



*engineering  
proceedings*

Proceedings Reprint

---

# The 10th International Electronic Conference on Sensors and Applications

Volume II

---

Edited by  
Stefano Mariani, Francisco Falcone, Stefan Bosse and Jean-Marc Laheurte

[mdpi.com/journal/engproc](https://mdpi.com/journal/engproc)



**The 10th International Electronic  
Conference on Sensors and  
Applications—Volume II**



# The 10th International Electronic Conference on Sensors and Applications—Volume II

Editors

**Stefano Mariani**

**Francisco Falcone**

**Stefan Bosse**

**Jean-Marc Laheurte**



Basel • Beijing • Wuhan • Barcelona • Belgrade • Novi Sad • Cluj • Manchester

*Editors*

Stefano Mariani  
Politecnico di Milano  
Milan  
Italy

Francisco Falcone  
Public University of Navarre  
Pamplona  
Spain

Stefan Bosse  
University of Bremen  
Bremen  
Germany

Jean-Marc Laheurte  
Université Gustave Eiffel  
Champs-sur-Marne  
France

*Editorial Office*

MDPI AG  
Grosspeteranlage 5  
4052 Basel, Switzerland

This is a reprint of articles from the Proceedings published online in the open access journal *Engineering Proceedings* (ISSN 2673-4591) (available at: <https://www.mdpi.com/2673-4591/58/1>).

For citation purposes, cite each article independently as indicated on the article page online and as indicated below:

Lastname, A.A.; Lastname, B.B. Article Title. <i>Journal Name</i> <b>Year</b> , <i>Volume Number</i> , Page Range.
--

**Volume II**

ISBN 978-3-7258-1287-5 (Hbk)

ISBN 978-3-7258-1288-2 (PDF)

[doi.org/10.3390/books978-3-7258-1288-2](https://doi.org/10.3390/books978-3-7258-1288-2)

**Set**

ISBN 978-3-7258-1283-7 (Hbk)

ISBN 978-3-7258-1284-4 (PDF)

© 2024 by the authors. Articles in this book are Open Access and distributed under the Creative Commons Attribution (CC BY) license. The book as a whole is distributed by MDPI under the terms and conditions of the Creative Commons Attribution-NonCommercial-NoDerivs (CC BY-NC-ND) license.

# Contents

About the Editors . . . . .	xi
Preface . . . . .	xiii
<b>Parsa Hooshyar, Atieh Zamani, Deniz Rezapour Kiani, Shayan Fakhraeelotfabadi and Mehdi Fardmanesh</b> Electrical and Optical Properties of Controlled Reduced Graphene Oxide Prepared by a Green and Facile Route † Reprinted from: <i>Eng. Proc.</i> <b>2023</b> , 58, 68, doi:10.3390/ecs-a-10-16175 . . . . .	1
<b>Miguel Ángel Remiro, Manuel Gil-Martín and Rubén San-Segundo</b> Improving Hand Pose Recognition Using Localization and Zoom Normalizations over MediaPipe Landmarks † Reprinted from: <i>Eng. Proc.</i> <b>2023</b> , 58, 69, doi:10.3390/ecs-a-10-16215 . . . . .	8
<b>Tarek Berghout and Mohamed Benbouzid</b> Getting a Better Sense of Data Drift in Dynamic Systems: Sequence-Based Deep Learning for Monitoring Slowly Evolving Degradation Processes † Reprinted from: <i>Eng. Proc.</i> <b>2023</b> , 58, 70, doi:10.3390/ecs-a-10-16229 . . . . .	15
<b>Alagumariappan Paramasivam, Jaya Prakash Abimanyu, Pavan Sai Kiran Reddy Pittu, Sankaran Vijayalakshmi and Mohana Krishnan Kaushal Mayur</b> The Design and Development of an Internet of Things-Based Condition Monitoring System for Industrial Rotating Machines † Reprinted from: <i>Eng. Proc.</i> <b>2023</b> , 58, 71, doi:10.3390/ecs-a-10-16240 . . . . .	21
<b>Onur Toker</b> A High-Level Synthesis Approach for a RISC-V RV32I-Based System on Chip and Its FPGA Implementation † Reprinted from: <i>Eng. Proc.</i> <b>2023</b> , 58, 72, doi:10.3390/ecs-a-10-16212 . . . . .	27
<b>Neelamadhab Padhy</b> Predicting Heart Disease Using Sensor Networks, the Internet of Things, and Machine Learning: A Study of Physiological Sensor Data and Predictive Models † Reprinted from: <i>Eng. Proc.</i> <b>2023</b> , 58, 73, doi:10.3390/ecs-a-10-16239 . . . . .	39
<b>Marut Deo Sharma and Juwesh Binong</b> Performance Evaluation of a Specialized Pressure Sensor for Pick and Place Operations † Reprinted from: <i>Eng. Proc.</i> <b>2023</b> , 58, 74, doi:10.3390/ecs-a-10-16586 . . . . .	46
<b>Rubén Nicolás Ibáñez, Antonio Guerrero González and Juan Carlos Molina Molina</b> Indirect Assessment of Implementation of Industry 4.0 Technologies in Regional Companies † Reprinted from: <i>Eng. Proc.</i> <b>2023</b> , 58, 75, doi:10.3390/ecs-a-10-16225 . . . . .	56
<b>Tobias Sukianto, Matthias Wagner, Sarah Seifi, Maximilian Strobel and Cecilia Carbonelli</b> Federated Learning for Frequency-Modulated Continuous Wave Radar Gesture Recognition for Heterogeneous Clients † Reprinted from: <i>Eng. Proc.</i> <b>2023</b> , 58, 76, doi:10.3390/ecs-a-10-16194 . . . . .	62
<b>Pavan Sai Kiran Reddy Pittu, Vijayalakshmi Sankaran, Paramasivam Alagu Mariappan, Gauri Pramod, Nikita and Yash Sharma</b> Design of Artificial Intelligence-Based Novel Device for Fault Diagnosis of Integrated Circuits † Reprinted from: <i>Eng. Proc.</i> <b>2023</b> , 58, 77, doi:10.3390/ecs-a-10-16242 . . . . .	69

<b>Sibo Prasad Patro and Neelamadhab Padhy</b> A Secure Remote Health Monitoring for Heart Disease Prediction Using Machine Learning and Deep Learning Techniques in Explainable Artificial Intelligence Framework <sup>†</sup> Reprinted from: <i>Eng. Proc.</i> <b>2023</b> , 58, 78, doi:10.3390/ecsa-10-16237 . . . . .	77
<b>Oksana Gutsul, David Rutherford, Marketa Barinkova, Vsevolod Slobodyan and Bohuslav Rezek</b> The Detection of <i>E. coli</i> and <i>S. aureus</i> on Sensors without Immobilization by Using Impedance Spectroscopy <sup>†</sup> Reprinted from: <i>Eng. Proc.</i> <b>2023</b> , 58, 79, doi:10.3390/ecsa-10-16073 . . . . .	85
<b>Jumar Cadondon, James Roy Lesidan, Jejomar Bulan, Edgar Vallar, Tatsuo Shiina and Maria Cecilia Galvez</b> Algal Organic Matter Fluorescence Analysis of <i>Chlorella</i> sp. for Biomass Estimation <sup>†</sup> Reprinted from: <i>Eng. Proc.</i> <b>2023</b> , 58, 80, doi:10.3390/ecsa-10-16220 . . . . .	92
<b>Nivine Guler and Ali Gunes</b> Optimal Resource Allocation Scheme Based on Time Slot Switching for Point-to-Point SISO SWIPT Systems <sup>†</sup> Reprinted from: <i>Eng. Proc.</i> <b>2023</b> , 58, 81, doi:10.3390/ecsa-10-16247 . . . . .	97
<b>Daniel Calegaro, Stefano Mariani, Massimiliano Merli and Giacomo Ferrari</b> Optimization of the Geometry of a Microelectromechanical System Testing Device for SiO <sub>2</sub> —Polysilicon Interface Characterization <sup>†</sup> Reprinted from: <i>Eng. Proc.</i> <b>2023</b> , 58, 82, doi:10.3390/ecsa-10-16033 . . . . .	104
<b>Tarek Berghout, Mohamed Benbouzid and Jaouher Ben Ali</b> ProgMachina: Feature Extraction and Processing Package for Prognostic Studies <sup>†</sup> Reprinted from: <i>Eng. Proc.</i> <b>2023</b> , 58, 83, doi:10.3390/ecsa-10-16222 . . . . .	110
<b>Songhua Huang, Maocheng Hong, Ge Lin, Bo Tang and Shaobin Shen</b> The Implementation and Advantages of a Discrete Fourier Transform-Based Digital Eddy Current Testing Instrument <sup>†</sup> Reprinted from: <i>Eng. Proc.</i> <b>2023</b> , 58, 84, doi:10.3390/ecsa-10-16214 . . . . .	115
<b>Rajan Prasad, Rajinder Tiwari and Adesh Kumar Srivastava</b> Internet of Things-Based Fuzzy Logic Controller for Smart Soil Health Monitoring: A Case Study of Semi-Arid Regions of India <sup>†</sup> Reprinted from: <i>Eng. Proc.</i> <b>2023</b> , 58, 85, doi:10.3390/ecsa-10-16208 . . . . .	123
<b>Judith Falkhofen, Bernd Baumann and Marcus Wolff</b> New Photoacoustic Cell Design for Solid Samples <sup>†</sup> Reprinted from: <i>Eng. Proc.</i> <b>2023</b> , 58, 86, doi:10.3390/ecsa-10-16198 . . . . .	129
<b>Rabai Boudershem</b> Privacy and Regulatory Issues in Wearable Health Technology <sup>†</sup> Reprinted from: <i>Eng. Proc.</i> <b>2023</b> , 58, 87, doi:10.3390/ecsa-10-16206 . . . . .	135
<b>Radu Tamaian</b> Aptamer-Based Biosensor Design for Simultaneous Detection of Cervical Cancer-Related MicroRNAs <sup>†</sup> Reprinted from: <i>Eng. Proc.</i> <b>2023</b> , 58, 88, doi:10.3390/ecsa-10-16203 . . . . .	141

<b>Maria Cecilia Galvez, Jumar Cadondon, Paulito Mandia, Ernest Macalalad, Edgar Vallar and Tatsuo Shiina</b> Characterization of Porcine Skin Using a Portable Time-Domain Optical Coherence Tomography System † Reprinted from: <i>Eng. Proc.</i> <b>2023</b> , 58, 89, doi:10.3390/ecsa-10-16213 . . . . .	150
<b>Md. Humayun Kabir, Mohammad Nadib Hasan, Ahmad and Hassan Jaki</b> Transfer Learning-Based Anomaly Detection System for Autonomous Vehicle † Reprinted from: <i>Eng. Proc.</i> <b>2023</b> , 58, 90, doi:10.3390/ecsa-10-16248 . . . . .	155
<b>Kim-Ming Tsoi, King-Pong Yu, Chu-Kei Ng, Suk-Mun Wong, Riggs Ng, Tsz-Yan Yeung, et al.</b> Development of an Embedded Device for Quantifying and Recording Daily Standing Profiles in Individuals with Lower Limb Motor Impairment Using an Assistive Standing Mobile Device † Reprinted from: <i>Eng. Proc.</i> <b>2023</b> , 58, 91, doi:10.3390/ecsa-10-16011 . . . . .	162
<b>Zeynab Alipour, Seyed Iman Mirzaei and Mehdi Fardmanesh</b> Design, Fabrication and Characterization of a Wideband Metamaterial Absorber for THz Imaging † Reprinted from: <i>Eng. Proc.</i> <b>2023</b> , 58, 92, doi:10.3390/ecsa-10-16210 . . . . .	169
<b>MD Jiabul Hoque, Md. Saiful Islam and Md. Khaliluzzaman</b> A Fuzzy Logic- and Internet of Things-Based Smart Irrigation System † Reprinted from: <i>Eng. Proc.</i> <b>2023</b> , 58, 93, doi:10.3390/ecsa-10-16243 . . . . .	176
<b>Sergey Goncharov and Andrey Nechesov</b> AI-Driven Digital Twins for Smart Cities † Reprinted from: <i>Eng. Proc.</i> <b>2023</b> , 58, 94, doi:10.3390/ecsa-10-16223 . . . . .	187
<b>Egor Mikharev, Andrey Lunev, Alexander Sidorov and Dmitry Redka</b> Modeling and Characterization of Microspheres with Silver Molecular Clusters for Sensor Applications † Reprinted from: <i>Eng. Proc.</i> <b>2023</b> , 58, 95, doi:10.3390/ecsa-10-16196 . . . . .	194
<b>Marianna Portaccio, Carlo Camerlingo, Fabrizia d’Apuzzo, Ludovica Nucci and Maria Lepore</b> Validation of the Use of ATR Mode in FT-IR Spectroscopy on Gingival Crevicular Fluid Samples in Orthodontics † Reprinted from: <i>Eng. Proc.</i> <b>2023</b> , 58, 96, doi:10.3390/ecsa-10-16232 . . . . .	200
<b>P. Ayesha Barvin and T. Sampradeepraj</b> Crop Recommendation Systems Based on Soil and Environmental Factors Using Graph Convolution Neural Network: A Systematic Literature Review † Reprinted from: <i>Eng. Proc.</i> <b>2023</b> , 58, 97, doi:10.3390/ecsa-10-16010 . . . . .	206
<b>Antonio Tupek, Mladen Zrinjski, Marko Švaco and Đuro Barković</b> Early Results on GNSS Receiver Antenna Calibration System Development † Reprinted from: <i>Eng. Proc.</i> <b>2023</b> , 58, 98, doi:10.3390/ecsa-10-16227 . . . . .	217
<b>Hee Yun Suh, Helena Hahn and James West</b> Wearable Impedance-Matched Noise Canceling Sensor for Voice Pickup † Reprinted from: <i>Eng. Proc.</i> <b>2023</b> , 58, 99, doi:10.3390/ecsa-10-16153 . . . . .	224
<b>Alexander M. Lloyd, Willem J. Perold and Pieter R. Fourie</b> Electrospun Nano- and Microfiber Mesh-Based Transducer for Electrochemical Biosensing Applications † Reprinted from: <i>Eng. Proc.</i> <b>2023</b> , 58, 100, doi:10.3390/ecsa-10-16217 . . . . .	230



<b>Ojodomo J. Achadu, Gideon L. Elizur and Owolabi M. Bankole</b> The Synthesis of Anisotropic 3D Nanomagnets for Magnetic Actuation and Sensing in Piezoelectric Polyvinylidene Fluoride towards Magnetic Nanogenerator Device Fabrication † Reprinted from: <i>Eng. Proc.</i> <b>2023</b> , <i>58</i> , 101, doi:10.3390/ecsa-10-16228 . . . . .	236
<b>Hamid Errachdi, Ivan Felis, Eduardo Madrid and Rosa Martínez</b> Bridging the Gap: Challenges and Opportunities of IoT and Wireless Sensor Networks in Marine Environmental Monitoring † Reprinted from: <i>Eng. Proc.</i> <b>2023</b> , <i>58</i> , 102, doi:10.3390/ecsa-10-16158 . . . . .	244
<b>Oliver Chojnowski, Dario Luipers, Caterina Neef and Anja Richert</b> Forecasting Vital Signs in Human–Robot Collaboration Using Sequence-to-Sequence Models with Bidirectional LSTM: A Comparative Analysis of Uni- and Multi-Variate Approaches † Reprinted from: <i>Eng. Proc.</i> <b>2023</b> , <i>58</i> , 103, doi:10.3390/ecsa-10-16190 . . . . .	258
<b>Md. Humayun Kabir, Arif Hasnat, Ahmed Jaser Mahdi, Mohammad Nadib Hasan, Jaber Ahmed Chowdhury and Istiak Mohammad Fahim</b> Enhancing Insider Malware Detection Accuracy with Machine Learning Algorithms † Reprinted from: <i>Eng. Proc.</i> <b>2023</b> , <i>58</i> , 104, doi:10.3390/ecsa-10-16234 . . . . .	264
<b>Samira Azizi, Kaveh Karami and Stefano Mariani</b> Full-Field Modal Analysis Using Video Measurements and a Blind Source Separation Methodology † Reprinted from: <i>Eng. Proc.</i> <b>2023</b> , <i>58</i> , 105, doi:10.3390/ecsa-10-16199 . . . . .	272
<b>Muhammad Bilal, Muhammad Tayyab, Ali Hamza, Kiran Shahzadi and Farva Rubab</b> The Internet of Things for Smart Farming: Measuring Productivity and Effectiveness † Reprinted from: <i>Eng. Proc.</i> <b>2023</b> , <i>58</i> , 106, doi:10.3390/ecsa-10-16012 . . . . .	278
<b>Massimo Barbieri and Giuseppe Andreoni</b> Carbon Allotrope-Based Textile Biosensors: A Patent Landscape Analysis † Reprinted from: <i>Eng. Proc.</i> <b>2023</b> , <i>58</i> , 107, doi:10.3390/ecsa-10-16216 . . . . .	285
<b>Jiří Přibíl, Anna Přibilová and Ivan Frollo</b> Wearable Two-Channel PPG Optical Sensor with Integrated Thermometers for Contact Measurement of Skin Temperature † Reprinted from: <i>Eng. Proc.</i> <b>2023</b> , <i>58</i> , 108, doi:10.3390/ecsa-10-16249 . . . . .	296
<b>Lucas Pires Bernardes, Pedro Oliveira Conceição Júnior, Fabio Romano Lofrano Dotto, Alessandro Roger Rodrigues and Marcio Marques Silva</b> Damage Detection in Machining Tools Using Acoustic Emission, Signal Processing, and Feature Extraction † Reprinted from: <i>Eng. Proc.</i> <b>2023</b> , <i>58</i> , 109, doi:10.3390/ecsa-10-16258 . . . . .	303
<b>Warakorn Karasaeng, Jitjark Nualkham, Chuthong Summatta and Somchat Sonasang</b> Measurement of Soil Moisture Using Microwave Sensors Based on BSF Coupled Lines † Reprinted from: <i>Eng. Proc.</i> <b>2023</b> , <i>58</i> , 110, doi:10.3390/ecsa-10-16029 . . . . .	309
<b>Nikolay G. Petrov, Tim J. Mulroy and Alexander N. Kalashnikov</b> Prototyping Bespoke Sensor Industrial Internet-of-Things (IIoT) Systems for Small and Medium Enterprises (SMEs) † Reprinted from: <i>Eng. Proc.</i> <b>2023</b> , <i>58</i> , 111, doi:10.3390/ecsa-10-16000 . . . . .	316
<b>Vijayaraja Loganathan, Dhanasekar Ravikumar, Gokul Raj Kusala Kumar, Sarath Sasikumar, Theerthavasan Maruthappan and Rupa Kesavan</b> Multipurpose Smart Shoe for Various Communities † Reprinted from: <i>Eng. Proc.</i> <b>2023</b> , <i>58</i> , 112, doi:10.3390/ecsa-10-16284 . . . . .	324

<b>Sofia Batsi and Stefano Tennina</b> QoS Performance Evaluation for Wireless Sensor Networks: The AQUASENSE Approach † Reprinted from: <i>Eng. Proc.</i> <b>2023</b> , 58, 113, doi:10.3390/ecsa-10-16181 . . . . .	332
<b>Ali Elyounsi, Tim J. Mulroy and Alexander N. Kalashnikov</b> Experimental Measurement of Air Temperature in an Enclosure Using Ultrasonic Oscillating Temperature Sensors (Uotses) † Reprinted from: <i>Eng. Proc.</i> <b>2023</b> , 58, 114, doi:10.3390/ecsa-10-16001 . . . . .	339
<b>Ivanna Kruglenko, Julia Burlachenko and Borys Snopok</b> Interaction of the Fluorescent Cell-Labeling Dye Rhodamine 6G with Low-Molecular-Weight Compounds: A Comparative QCM Study of Adsorption Capacity of Rh6G for Gaseous Analytes † Reprinted from: <i>Eng. Proc.</i> <b>2023</b> , 58, 115, doi:10.3390/ecsa-10-16200 . . . . .	345
<b>Ejay Nsugbe, Halin Buruno, Stephanie Connelly, Oluwarotimi Williams Samuel and Olusayo Obajemu</b> On the Use of Muscle Activation Patterns and Artificial Intelligence Methods for the Assessment of the Surgical Skills of Clinicians † Reprinted from: <i>Eng. Proc.</i> <b>2023</b> , 58, 116, doi:10.3390/ecsa-10-16231 . . . . .	353
<b>Alexander Isiani, Leland Weiss and Kelly Crittenden</b> Statistical Analysis of Gyroscopic Data to Determine Machine Health in Additive Manufacturing † Reprinted from: <i>Eng. Proc.</i> <b>2023</b> , 58, 117, doi:10.3390/ecsa-10-16218 . . . . .	358
<b>Patricia Iweka, Shuso Kawamura, Tomohiro Mitani and Takashi Kawaguchi</b> Cow Milk Quality Determination Using a Near-Infrared Spectroscopic Sensing System for Smart Dairy Farming † Reprinted from: <i>Eng. Proc.</i> <b>2023</b> , 58, 118, doi:10.3390/ecsa-10-16020 . . . . .	370
<b>Md. Humayun Kabir, Jaber Ahmed Chowdhury, Istiak Mohammad Fahim, Mohammad Nadib Hasan, Arif Hasnat and Ahmed Jaser Mahdi</b> Design and Simulation of AI-Enabled Digital Twin Model for Smart Industry 4.0 † Reprinted from: <i>Eng. Proc.</i> <b>2023</b> , 58, 119, doi:10.3390/ecsa-10-16235 . . . . .	377
<b>Ángel Niebla-Montero, Iván Froiz-Míguez, José Varela-Barbeito, Paula Fraga-Lamas and Tiago M. Fernández-Caramés</b> IOTA and Smart Contract Based IoT Oxygen Monitoring System for the Traceability and Audit of Confined Spaces in the Shipbuilding Industry † Reprinted from: <i>Eng. Proc.</i> <b>2023</b> , 58, 120, doi:10.3390/ecsa-10-16226 . . . . .	384
<b>Stefan Bosse</b> Automated Damage and Defect Detection with Low-Cost X-ray Radiography Using Data-Driven Predictor Models and Data Augmentation by X-ray Simulation † Reprinted from: <i>Eng. Proc.</i> <b>2023</b> , 58, 121, doi:10.3390/ecsa-10-16126 . . . . .	390
<b>Sahar Mahdie Klim Al-Zaidawi and Stefan Bosse</b> A Pore Classification System for the Detection of Additive Manufacturing Defects Combining Machine Learning and Numerical Image Analysis † Reprinted from: <i>Eng. Proc.</i> <b>2023</b> , 58, 122, doi:10.3390/ecsa-10-16024 . . . . .	402
<b>Rajesh Kumar Dhanaraj and Md. Akkas Ali</b> Deep Learning-Enabled Pest Detection System Using Sound Analytics in the Internet of Agricultural Things † Reprinted from: <i>Eng. Proc.</i> <b>2023</b> , 58, 123, doi:10.3390/ecsa-10-16205 . . . . .	415

<b>Enric Dorca, Daniel Bonet-Solà, Pau Bergadà, Carme Martínez-Suquía and Rosa Ma Alsina-Pagès</b> Sons al Balcó: A Subjective Approach to the WASN-Based $L_{Aeq}$ Measured Values during the COVID-19 Lockdown † Reprinted from: <i>Eng. Proc.</i> <b>2023</b> , 58, 124, doi:10.3390/ecsa-10-16241 . . . . .	422
<b>Ejay Nsugbe, Oluwarotimi Williams Samuel, Jose Javier Reyes-Lagos, Dawn Adams and Olusayo Obajemu</b> Bio-Magneto Sensing and Unsupervised Deep Multiresolution Analysis for Labor Predictions in Term and Preterm Pregnancies † Reprinted from: <i>Eng. Proc.</i> <b>2023</b> , 58, 125, doi:10.3390/ecsa-10-16245 . . . . .	429
<b>Luis Otávio de Angeles Dias, Pedro Oliveira Conceição Junior and Paulo Monteiro de Carvalho Monson</b> Computational Feasibility Study for Time-Frequency Analysis of Non-Stationary Vibration Signals Based on Wigner-Ville Distribution † Reprinted from: <i>Eng. Proc.</i> <b>2023</b> , 58, 126, doi:10.3390/ecsa-10-16193 . . . . .	434
<b>Hichem Ferhati, Tarek Berghout, Abderraouf Benyahia and Faycal Djeflal</b> Machine Learning DFT-Based Approach to Predict the Electrical Properties of Tin Oxide Materials † Reprinted from: <i>Eng. Proc.</i> <b>2023</b> , 58, 127, doi:10.3390/ecsa-10-16017 . . . . .	440
<b>Abdelhak Maoucha, Faycal Djeflal, Tarek Berghout and Hichem Ferhati</b> Photoresponsivity Enhancement of SnS-Based Devices Using Machine Learning and SCAPS Simulations † Reprinted from: <i>Eng. Proc.</i> <b>2023</b> , 58, 128, doi:10.3390/ecsa-10-16014 . . . . .	446
<b>Alyssa Dainelle T. Alcantara, Ramon Balancer H. Balbuena III, Venlester B. Catapang, John Patrick M. Catchillar, Rick Edmond P. De Leon, Steven Niño A. Sanone, et al.</b> Internet of Things-Based Smart Helmet with Accident Identification and Logistics Monitoring for Delivery Riders † Reprinted from: <i>Eng. Proc.</i> <b>2023</b> , 58, 129, doi:10.3390/ecsa-10-16238 . . . . .	452
<b>Ejay Nsugbe, Dephney Mathebula and Dawn Adams</b> A Novel Ensemble of Fourier Transform Infrared Spectroscopic Biosensing and Deep Learning Postprocessing for Diagnosis of Endometrial Cancer † Reprinted from: <i>Eng. Proc.</i> <b>2023</b> , 58, 130, doi:10.3390/ecsa-10-16244 . . . . .	460
<b>Ejay Nsugbe, Dephney Mathebula, Evi Viza, Oluwarotimi W. Samuel, Stephanie Connelly and Ian Mutanga</b> On the Clinical Use of Artificial Intelligence and Haematological Measurements for a Rapid Diagnosis and Care of Paediatric Malaria Patients in West Africa † Reprinted from: <i>Eng. Proc.</i> <b>2023</b> , 58, 131, doi:10.3390/ecsa-10-16246 . . . . .	465
<b>Khalida Mimoune, Mohamed Yacine Hammoudi and Wail Hamdi</b> Designing Unknown Input Observers for Fault Reconstruction in Disturbed Takagi-Sugeno Fuzzy Systems † Reprinted from: <i>Eng. Proc.</i> <b>2023</b> , 58, 132, doi:10.3390/ecsa-10-16283 . . . . .	472

# About the Editors

## **Stefano Mariani**

Dr. Stefano Mariani received an M.S. degree (cum laude) in civil engineering in 1995 and a Ph.D. degree in structural engineering in 1999; both of his degrees were awarded by the Polytechnic University of Milan. He is currently a Full Professor in the Department of Civil and Environmental Engineering at the Polytechnic University of Milan. He was a research scholar at the Danish Technical University in 1997, an adjunct professor at Penn State University in 2007, and a visiting professor at the Polytechnic Institute of New York University in 2009. He is a member of the Editorial Boards of several journals, including *Algorithms*, the *International Journal on Advances in Systems and Measurements*, *Inventions*, *Machines*, *Micro and Nanosystems*, *Micromachines*, and *Sensors*. He was a recipient of the Associazione Carlo Maddalena Prize for graduate students (1996), and of the Fondazione Confalonieri Prize for PhD students (2000). His main research interests are the reliability of MEMS that are subject to shocks and drops; the structural health monitoring of composite structures through MEMS sensors; numerical simulations of ductile fracture in metals and of quasi-brittle fracture in heterogeneous and functionally graded materials; extended finite element methods; the calibration of constitutive models via extended and sigma-point Kalman filters; and multi-scale solution methods for dynamic delamination in layered composites.

## **Francisco Falcone**

Dr. Francisco Falcone received both his Telecommunication Engineering Degree (1999) and his PhD in Communication Engineering (2005) from the Public University of Navarre in Spain. From 1999 to 2000, he was Microwave Network Engineer, Siemens-Italtel, Málaga. From 2000 to 2008, he was Mobile Access Network Engineer, Telefónica Móviles, in Pamplona. In 2009 he co-founded Tafco Metawireless, spin-off of the UPNA, of which he was the first manager. In parallel, from 2003 to 2009 he was Assistant Lecturer, EEC Dept., UPNA. In June 2009 he became Associate Professor at UPNA and since September 2022, Full Professor. From January 2012 to July 2018 and from July 2019 to November 2021 he was Head of the EEC Dept., UPNA. In 2018 he was Visiting Professor at Kuwait College of Science and Technology, Kuwait, for three months. He is also affiliated with the Smart Cities Institute-UPNA, a multidisciplinary research institute with over 100 researchers, being Head of the Institute since May 2021, working on contextual and interactive environments solutions, through the integration of heterogeneous wireless communications networks. Since June 2022, he is Distinguished Visiting Professor in Telecommunications, School of Engineering and Science, Tecnológico de Monterrey, Mexico. His research area is artificial EM media, complex electromagnetic scenarios and wireless system analysis, with applications to context aware environments, Smart Cities and Smart Regions. He has over 500 contributions to journal and conference publications. He has been awarded several research awards: CST Best Paper Award 2003/2005, COIT 2005 Best Doctoral Thesis, UPNA PhD Award 2004-2006, 1st Prize Juan López de Peñalver 2010, Real Academia de Ingeniería de España, XII Talgo Foundation Award for Technological Innovation, ECSA-2 Best Paper Award (2015), Best Paper Award IISA (2015), ECSA Award -3 Best Paper Award (2016), ECSA-4 Best Paper Award (2018), Best Paper Award ISSI (2019) and IIoT 2020 Best Paper Award.

## **Stefan Bosse**

Dr. Stefan Bosse studied physics at the University of Bremen. He received a PhD/doctoral degree in physics in the year 2002 from the University of Bremen, and a post-doctoral degree (Habilitation) and the Venia Legendi in Computer Science in the year 2016 from the University of

Bremen. Since 2016 he is teaching and researching as a Privatdozent (assoc. prof.) at the University of Bremen, Department of Computer Science. From 2018 to 2019 he was an interim professor at the University of Koblenz-Landau, Faculty Computer Science, Institute of Software Technologies. Since 2022 he is also a lecturer at the University of Siegen, Department of Mechanical Engineering. His research is dedicated to distributed artificial intelligence in general and sensor-driven data processing and sensor networks in special. This covers the design of embedded systems, virtualization, distributed and massive parallel system design, distributed and tiny machine learning, agent-based methods including simulation and material-integrated sensing systems with a high interdisciplinary and technological background. Typical applications are Structural Health Monitoring (SHM) and Mobile Crowd Sensing (MCS) at the boundaries of technical systems, humans and society.

He published more than 100 journal and conference papers and four books, and he acts as a reviewer and a Guest Editor for several international journals and is a member of a broad range of international conference program and organizing committees. He is member of several scientific committees and chairs the International Electronic Conference on Sensors and Applications since 2019. Since 2019 he is also a principal investigator of the transregional and interdisciplinary DFG founded research unit 3022 and conducts the subproject "Data-driven Damage Diagnostics", with its origin in the scientific center "Integrated Solutions in Sensorial Structure Engineering" (ISIS) as well as membership in the MAPEX Center for Materials and Processes.

### **Jean-Marc Laheurte**

Dr. Jean-Marc Laheurte received M.Sc. and Ph.D. degrees in electrical engineering and a Habilitation to Supervise Research from the University of Nice, France, in 1989, 1992 and 1997, respectively. From 1989 to 1990, he was a research assistant at the École Polytechnique Fédérale de Lausanne, Switzerland. In 1992, he served as a postdoctoral researcher at the University of Michigan, Ann Arbor, MI, USA. From 1993 to 2002 he was an Associate Professor at the University of Nice Sophia Antipolis, France. Since 2002, he has been a Professor at the University Gustave Eiffel, France. In 2012, he spent a year as a senior RF engineer at Tagsys, La Ciotat, France. For the past eight years he has been the director of the 75-member Electronics, SYstèmes de COmmunications and Microsystems Laboratory (ESYCOM Laboratory). He is the author or co-author of two books, two book chapters, ninety technical papers in international journals and more than a hundred conference papers. He holds two patents on RFID technologies. His current research interests include the design of antennas in matter, RFID technologies, RFID localization, body array antennas (BANs).

# Preface

This Issue of *Engineering Proceedings* assembles the papers presented at the 10th International Electronic Conference on Sensors and Applications (ECSA-10), held online on 15–30 November 2023, through the sciforum.net platform developed by MDPI. The annual ECSA conference was initiated in 2014 on an online basis to allow for global participation without concerns for travel and related expenditures. This year's edition saw significantly increased collaboration among the authors and the audience through live session presentations of a limited number of contributions that were selected among the over 200 submissions, which were all reviewed and accepted by the chairs and/or by the conference committee members.

After the success of the nine editions of the conference that were held from 2014 to 2022, this year's edition, ECSA-10, collected contributions concerning five thematic areas which are deeply affected by the rapid development of sensors and data processing: Chemo- and Biosensors; Physical Sensors; Sensor Networks, IoT and Structural Health Monitoring; Sensor Data Analytics; and Sensors and Artificial Intelligence. Five specific sessions were also included: Smart Agriculture Sensors; Materials for Sensing Applications; Electronic Sensors, Devices and Systems; Wearable Sensors and Healthcare Applications; and Robotics, Sensors and Industry 4.0. Three keynote presentations were delivered by Sabina Merlo, a Full Professor of Electrical and electronic measurements at the Department of Electrical, Computer and Biomedical Engineering, University of Pavia, Pavia (Italy), by Leyre Azpilicueta, from the Department of Electrical, Electronic and Communication Engineering, Institute of Smart Cities, Public University of Navarre (UPNA), and by Dirk Lehmus, from the Department of Casting Technology and Lightweight Construction, Fraunhofer IFAM.

**Stefano Mariani, Francisco Falcone, Stefan Bosse, and Jean-Marc Laheurte**

*Editors*



# Electrical and Optical Properties of Controlled Reduced Graphene Oxide Prepared by a Green and Facile Route <sup>†</sup>

Parsa Hooshyar <sup>1</sup>, Atieh Zamani <sup>1,2,\*</sup>, Deniz Rezapour Kiani <sup>1</sup>, Shayan Fakhraeilotfabadi <sup>1</sup>  
and Mehdi Fardmanesh <sup>1,\*</sup>

<sup>1</sup> Superconductive Electronics Research Laboratory (SERL), Electrical Engineering Department, Sharif University of Technology, Tehran 14588-89694, Iran; parsahooshyar77@yahoo.com (P.H.); denizrezapur@gmail.com (D.R.K.); shayan.fakhraee@gmail.com (S.F.)

<sup>2</sup> Department of Converging Technologies, Khatam University, Tehran 19916-33357, Iran

\* Correspondence: atieh.zamani.mail@gmail.com (A.Z.); fardmanesh@sharif.edu (M.F.)

<sup>†</sup> Presented at the 10th International Electronic Conference on Sensors and Applications (ECSA-10), 15–30 November 2023; Available online: <https://ecsa-10.sciforum.net/>.

**Abstract:** Three distinct homogeneous multilayer self-standing thin films, composed of stacked reduced graphene oxide (rGO) planes, were produced by the improved Hummer's method. In order to investigate their structural, electrical, and optical properties, the samples were characterized by Raman spectroscopy, field emission scanning electron microscopy (FESEM), four-point probe measurements, and Fourier-transform infrared spectroscopy (FTIR). The Raman spectra of the samples indicate the presence of minor surface defects and a relatively low oxygen content of rGOs. The FESEM images obtained from the samples reveal a smooth sheet-like surface with few wrinkles. Additionally, the cross-sectional images provide confirmation of the presence of multi-stacked layer structures. Based on the resistance decreasing by about 0.35 to 0.65 percent per kelvin within the region of ambient temperature, the electrical resistance vs. temperature curves imply semiconducting behavior in the rGOs. The FTIR analysis of the samples conducted within the wavelength range of 2.5 to 25  $\mu\text{m}$  demonstrates a significant absorption value exceeding 90%. This observation shows that the developed materials possess favorable characteristics, making them an excellent absorber candidate for sensing detectors in the infrared range. We systematically analyzed and confirmed that the structural as well as optical and electrical properties of our obtained rGOs may be fine-tuned by adjusting the initial reactants concentration and annealing temperature.

**Keywords:** graphene; spectrally wide absorber; free-standing films; thermal stability; electrical conductivity

**Citation:** Hooshyar, P.; Zamani, A.; Rezapour Kiani, D.; Fakhraeilotfabadi, S.; Fardmanesh, M. Electrical and Optical Properties of Controlled Reduced Graphene Oxide Prepared by a Green and Facile Route. *Eng. Proc.* **2023**, *58*, 68. <https://doi.org/10.3390/ecsa-10-16175>

Academic Editor: Stefano Mariani

Published: 15 November 2023



**Copyright:** © 2023 by the authors. Licensee MDPI, Basel, Switzerland. This article is an open access article distributed under the terms and conditions of the Creative Commons Attribution (CC BY) license (<https://creativecommons.org/licenses/by/4.0/>).

## 1. Introduction

Since the emergence of graphene in 2004, numerous studies have been conducted on graphene and its derivatives due to their remarkable properties. As a monolayer of carbon atoms held together by  $\text{sp}^2$  covalent bonds in a honeycomb-resembling lattice, graphene was first extracted from graphite by Geim and Novoselov [1,2]. Graphene oxide (GO) and reduced graphene oxide (rGO) are considered the two main derivatives of graphene. GO, the oxidized form of graphene, comprises a variety of oxygen-containing functional groups, including hydroxyl and carboxyl moieties. Meanwhile, rGO is produced through the reduction process of GO, resulting in fewer oxygen-containing groups [3]. Additionally, when arranged in a stacked configuration, they form many other derivatives, including monolayer, few-layer, and multilayer graphene-based materials, each exhibiting distinct characteristics and properties [4].

Graphene and its derivatives possess distinctive characteristics that render them promising subjects for research across different applications. For instance, graphene has high electron mobility, high electrical conductivity, high thermal conductivity, and high



optical transparency [2,5–7]. These distinct characteristics make graphene-based materials appropriate for an extensive range of applications. For instance, graphene is utilized in a variety of thermal, optical, and electrical systems, such as temperature sensors [8,9], transparent electrodes [10], conductive composites (electrically, thermally, or both) [11–13], solar cells [14], and thermal imaging [15].

Most graphene synthesis methods involve the utilization of complex and costly techniques, as well as the need for three-dimensional crystal, posing difficulties for its operation and investigation [16]. On the other hand, free-standing samples offer more flexibility and versatility. In this regard, we have developed a green and facile route towards the synthesis of free-standing rGO samples. This eco-friendly route is based on the modified Hummer's method, which uses the least possible chemicals. In addition to structural analyses, the obtained samples were subjected to electrical and optical examinations to ascertain their distinct features. The interesting properties of these samples, along with their low chemical content, make them a great candidate for many applications, including medical uses such as biomedical imaging, contrast agents, and monitoring electrodes [17,18].

## 2. Materials and Methods

### 2.1. Materials

Aqueous GO solution has been initially prepared by a modified Hummers method. The pre-treatment of graphite powder favored a lower amount of reactants during synthesis. Also, the reaction time was prolonged to 34 h, which provides good GO exfoliation without compromising the quality of the dispersion [19–22]. The concentration of the solution was 12 mg/mL, which was then air-dried overnight. This was followed by thermal reduction processes to obtain rGO free-standing layers [23]. This provides an eco-friendly and safer yet facile rGO synthesis and oxygen reduction route, which also enables mass production.

We produced three distinct rGO samples, designated *rGO1*, *rGO2*, and *rGO3*, using the described method. Notably, this approach makes no use of any mechanical or shear force. Finally, it should be mentioned that these three rGO samples were fine-tuned by adjusting the initial reactant concentration and annealing temperature. In this work, the following chemical species were used: graphite flakes (99.0%, Acros Organics, Geel, Belgium), sodium nitrate (84.99, R&M Chemicals, Chandigarh, India), sulfuric acid (98.0%, Sigma-Aldrich, Sofia, Bulgaria), potassium permanganate (99.0%, Sigma Aldrich, Sofia, Bulgaria), and hydrogen peroxide (27% *w/w*, Alfa Aesar graded, provided by a local company).

### 2.2. Methods

The experimental approaches used in this work necessitated the use of specialized instruments to perform the relevant measurements. The Field-Emission Scanning Electron Microscope (FESEM) images of the samples were taken using a TESCAN MIRA 3 LMU (TESCAN, Brno, Czech Republic). A four-point probe technique was used to conduct electrical measurements. The four-point probe measurement was performed utilizing a KEITHLEY 6221 (Keithley Instruments, Solon, OH, USA) current source (with sub pico ampere resolution) and a KEITHLEY 2182A NANOVOLTMETER (Keithley Instruments, Solon, OH, USA). Finally, The Fourier-Transform Infrared (FTIR) spectra of the samples were obtained using Bruker's VERTEX 70 FT-IR Spectrometer (Bruker, Billerica, MA, USA) for the purpose of analyzing their optical absorption values.

## 3. Results and Discussion

### 3.1. Structural Properties

Finding a sample's structural properties is always the initial step in learning about its properties. In order to accomplish this, our samples were initially analyzed by FESEM and Raman spectroscopy, two powerful techniques in the field of material characterization. FESEM facilitates the acquisition of high-resolution images, allowing for the detailed examination of the morphology and structural characteristics of diverse materials at the nanoscale level [24]. The images of the rGO samples obtained through FESEM are presented

in Figure 1. The multi-stacked layer architectures of these free-standing thin films are immediately apparent from these cross-sectional views. Each stacked layer is approximately between 2  $\mu\text{m}$  and 3  $\mu\text{m}$  thick and is made up of multiple rGO planes. Moreover, while looking at the surface morphology of the samples, it can be seen that they have a relatively smooth sheet-like surface with few wrinkles.

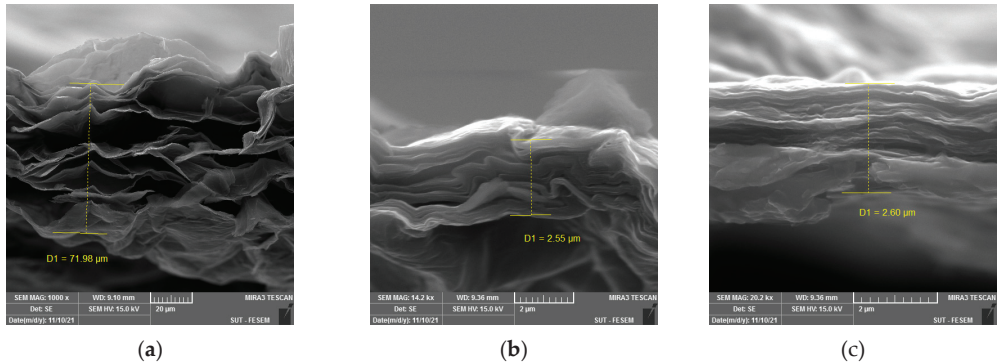


**Figure 1.** FESEM images of (a) *rGO1*, (b) *rGO2*, and (c) *rGO3*.

Raman spectroscopy complements the capabilities of FESEM by providing information on chemical structures and physical forms. Based on the Raman effect, irradiating a sample with monochromatic light and measuring the scattered light has revealed that all the materials derived from graphene exhibit a G peak in their Raman spectra, which corresponds to the first-order scattering of the E<sub>2g</sub> mode. Additionally, when examining the oxidized derivatives of graphene, such as GO and rGO, a D band is also detected. The presence of this D band signifies a decrease in the size of the in-plane sp<sup>2</sup> domains due to the process of oxidation [25,26]. The Raman spectra obtained from our rGO samples confirm these findings and also disclose a shift of the G bands towards lower wavenumbers when compared to the G bands of the GO, which is indicative of a lower oxygen content in the rGOs. In addition, the intensity ratio between the D band and the G band (I<sub>D</sub>/I<sub>G</sub>) shows that the number of surface defects is small [27].

### 3.2. Electrical Properties

To evaluate the electrical properties of the rGO samples, we first conducted resistance measurements using the four-point probe technique at room temperature. The samples were tested in various directions to ensure comprehensive analysis. Additionally, the measurements were performed on different days to assess the stability of the samples under varying conditions. The recorded measurements demonstrate a remarkable homogeneity as the resistance values for each sample differ only slightly across different directions.

Upon analyzing the data, we found that *rGO1* exhibited an average resistance of approximately 19.38  $\Omega$ , with a deviation of  $\pm 1.6 \Omega$ , representing a variation of about  $\pm 8.2\%$  from the average. For *rGO2*, the average resistance was approximately 294.25  $\Omega$ , with a deviation of  $\pm 12 \Omega$ , corresponding to a variation of around  $\pm 4.1\%$  from the average. Finally, *rGO3* displayed an average resistance of 5849.7  $\Omega$ , with a deviation of  $\pm 9.5 \Omega$ , indicating a variation of less than  $\pm 0.2\%$  from the average. These minimal variations in resistance values, ranging from 0.2% to 8.2%, across different directions and measurements conducted on various days are indicative of the low degree of uncertainty associated with our measurements. The consistent and stable resistance values obtained underscore the environmental and thermal stability of the samples.

According to this result, *rGO1* has the highest conductivity and is interpreted to be the most oxygen-reduced sample, while *rGO3* has high resistivity and behaves the least like conductors. These results indicate that rGO samples can be produced with any desired

conductivity. This brings us the versatility and tunability needed to synthesize rGO samples that have distinct resistances over a broad spectrum of electrical conductivity by modifying the fabrication steps. These samples were also analyzed by AC measurements, and no phase change was observed between the voltage and current passing through them. As a result, these free-standing homogeneous thin films are laterally pure-resistive.

Given the potential applications of graphene-based materials as electrothermal devices, it becomes imperative to exert precise control over the impact of temperature on electrical parameters, specifically their resistivity [28]. To acquire the electrical resistance versus temperature (RT) curves for the samples at temperatures exceeding room temperature, we progressively increased their temperature with a heater while simultaneously monitoring their resistance. These curves are presented in Figure 2, where all the resistance values have been normalized to each sample resistance value at 300 K. With an increase in temperature, the resistance of *rGO1*, *rGO2*, and *rGO3* decreases at a rate of 0.35, 0.55, and 0.65 percent per Kelvin, in turn implying semiconducting behavior in the rGOs. It is worth noting that the sample with higher conductivity and therefore a higher reduction degree, suggesting a higher carbon to oxygen ratio, has a lower temperature coefficient of resistance (TCR), implying a decrease in its semiconducting energy gap [29].

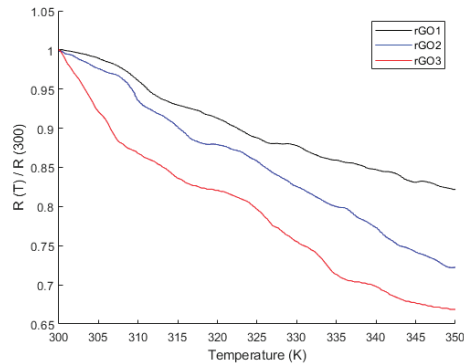


**Figure 2.** Resistance versus temperature curves of *rGO1*, *rGO2*, and *rGO3*.

### 3.3. Optical Properties

*rGO1* and *rGO2* were measured and analyzed by FTIR spectroscopy in order to investigate their optical properties. The analysis was conducted within the wavelength range of 2.5 to 25  $\mu\text{m}$ . The resulting absorbance spectra of *rGO1* and *rGO2* are shown in Figure 3, indicating that both *rGO1* and *rGO2* exhibit exceptional performance across the whole spectrum. To be more specific, for *rGO1*, the absorption value exceeds 93% at wavelengths shorter than 4  $\mu\text{m}$ , and its minimum absorption, observed around 12.5  $\mu\text{m}$ , remains at a remarkable value of 91%. Similarly, *rGO2* demonstrates excellent absorption, with values surpassing 91.5% before 4  $\mu\text{m}$  and maintaining a minimum absorption of approximately 90% at wavelengths around 12  $\mu\text{m}$  and above. These results highlight the significant absorption values of the samples exceeding 90% across the entire spectrum, indicating their potential use as spectrally wide absorbers.

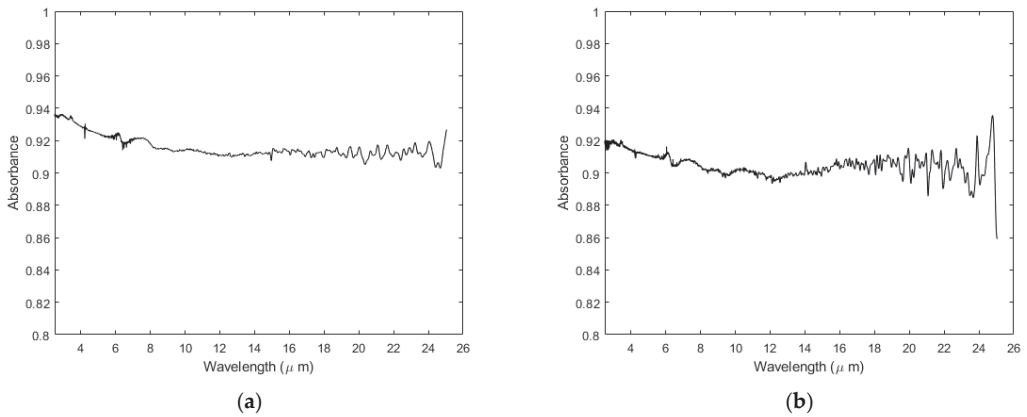


**Figure 3.** FTIR spectra of (a) *rGO1* and (b) *rGO2*.

#### 4. Conclusions

The findings presented in this study provide a valuable understanding of the electrical and optical properties of three multilayer rGO thin films. By using a modified version of Hummer's method, which is a facile, versatile, and environmentally friendly approach, these self-standing samples were successfully synthesized. Despite the absence of shear stress in the production process of these samples, their cross-sectional FESEM images validate the commendable attainment of a well-organized stacking arrangement. Although all samples displayed minor surface defects and a smooth sheet-like structure with few wrinkles, suggesting their high quality and uniformity, additional morphological analyses, such as Grazing-Incidence Small-Angle X-ray Scattering (GISAXS), are required to investigate the structures of the samples in more detail.

According to our electrical investigations, the semiconducting behavior of the samples was evidenced by a temperature-dependent decrease in their electrical resistance, and according to the optical investigations, they showcased substantial absorption values exceeding 90% in a wide infrared range. Different electrical and optical characteristics exhibited by each sample indicate that it is possible to fine-tune the properties of rGO samples by adjusting the reactants' concentration and annealing temperature, thereby enhancing their potential for a variety of applications, including electronics, thermoelectric, and optoelectronics devices. For instance, the fact that as few chemicals as possible were used to produce the samples, coupled with their high optical absorption even in electrically conductive ranges, makes them a clean and favorable option for many biomedical applications.

**Author Contributions:** P.H. and A.Z. have shared the first authorship, and all the authors have contributed to writing and preparing the manuscript; the samples were synthesized by A.Z., and the sample preparation and measurements were conducted by P.H., S.F., and D.R.K. under the supervision of M.F. All authors have read and agreed to the published version of the manuscript.

**Funding:** This research received no external funding.

**Institutional Review Board Statement:** Not applicable.

**Informed Consent Statement:** Not applicable.

**Data Availability Statement:** Data sharing not applicable.

**Conflicts of Interest:** The authors declare no conflicts of interest.

## References

- Novoselov, K.S.; Geim, A.K.; Morozov, S.V.; Jiang, D.-E.; Zhang, Y.; Dubonos, S.V.; Grigorieva, I.V.; Firsov, A.A. Electric field effect in atomically thin carbon films. *Science* **2004**, *306*, 666–669. [CrossRef] [PubMed]
- Geim, A.K.; Novoselov, K.S. The rise of graphene. *Nat. Mater.* **2007**, *6*, 183–191. [CrossRef]
- Tahriri, M.; Del Monico, M.; Moghanian, A.; Yarak, M.T.; Torres, R.; Yadegari, A.; Tayebi, L. Graphene and its derivatives: Opportunities and challenges in dentistry. *Mater. Sci. Eng. C* **2019**, *102*, 171–185. [CrossRef]
- Parvin, N.; Kumar, V.; Joo, S.W.; Park, S.-S.; Mandal, T.K. Recent Advances in the Characterized Identification of Mono-to-Multi-Layer Graphene and Its Biomedical Applications: A Review. *Electronics* **2022**, *11*, 3345. [CrossRef]
- Balandin, A.A.; Ghosh, S.; Bao, W.; Calizo, I.; Teweldebrhan, D.; Miao, F.; Lau, C.N. Superior thermal conductivity of single-layer graphene. *Nano Lett.* **2008**, *8*, 902–907. [CrossRef]
- Ghosh, S.; Calizo, I.; Teweldebrhan, D.; Pokatilov, E.P.; Nika, D.L.; Balandin, A.A.; Bao, W.; Miao, F.; Lau, C.N. Extremely high thermal conductivity of graphene: Prospects for thermal management applications in nanoelectronic circuits. *Appl. Phys. Lett.* **2008**, *92*, 151911. [CrossRef]
- Rokmana, A.W.; Asriani, A.; Suhendar, H.; Triyana, K.; Kusumaatmaja, A.; Santoso, I. The optical properties of thin film reduced graphene oxide/poly (3, 4 ethylenedioxythiophene): Poly (styrene sulfonate)(pedot: Pss) fabricated by spin coating. *Proc. J. Phys. Conf. Ser.* **2018**, *1011*, 012007. [CrossRef]
- Zeng, Y.; Li, T.; Yao, Y.; Li, T.; Hu, L.; Marconnet, A. Thermally conductive reduced graphene oxide thin films for extreme temperature sensors. *Adv. Funct. Mater.* **2019**, *29*, 1901388. [CrossRef]
- Liu, G.; Tan, Q.; Kou, H.; Zhang, L.; Wang, J.; Lv, W.; Dong, H.; Xiong, J. A flexible temperature sensor based on reduced graphene oxide for robot skin used in internet of things. *Sensors* **2018**, *18*, 1400. [CrossRef]
- Rana, K.; Singh, J.; Ahn, J.-H. A graphene-based transparent electrode for use in flexible optoelectronic devices. *J. Mater. Chem. C* **2014**, *2*, 2646–2656. [CrossRef]
- Kumar, P.; Yu, S.; Shahzad, F.; Hong, S.M.; Kim, Y.-H.; Koo, C.M. Ultrahigh electrically and thermally conductive self-aligned graphene/polymer composites using large-area reduced graphene oxides. *Carbon* **2016**, *101*, 120–128. [CrossRef]
- Yu, H.; Chen, C.; Sun, J.; Zhang, H.; Feng, Y.; Qin, M.; Feng, W. Highly thermally conductive polymer/graphene composites with rapid room-temperature self-healing capacity. *Nano-Micro Lett.* **2022**, *14*, 135. [CrossRef] [PubMed]
- Yu, S.; Li, N.; Higgins, D.; Li, D.; Li, Q.; Xu, H.; Spindel, J.S.; Wu, G. Self-assembled reduced graphene oxide/polyacrylamide conductive composite films. *ACS Appl. Mater. Interfaces* **2014**, *6*, 19783–19790. [CrossRef] [PubMed]
- Das, S.; Sudhagar, P.; Kang, Y.S.; Choi, W. Graphene synthesis and application for solar cells. *J. Mater. Res.* **2014**, *29*, 299–319. [CrossRef]
- Hsu, A.L.; Herring, P.K.; Gabor, N.M.; Ha, S.; Shin, Y.C.; Song, Y.; Chin, M.; Dubey, M.; Chandrakasan, A.P.; Kong, J. Graphene-based thermopile for thermal imaging applications. *Nano Lett.* **2015**, *15*, 7211–7216. [CrossRef] [PubMed]
- Dato, A.; Radmilovic, V.; Lee, Z.; Phillips, J.; Frenklach, M. Substrate-free gas-phase synthesis of graphene sheets. *Nano Lett.* **2008**, *8*, 2012–2016. [CrossRef] [PubMed]
- Nurunnabi, M.; Parvez, K.; Nafuijman, M.; Revuri, V.; Khan, H.A.; Feng, X.; Lee, Y.-k. Bioapplication of graphene oxide derivatives: Drug/gene delivery, imaging, polymeric modification, toxicology, therapeutics and challenges. *RSC Adv.* **2015**, *5*, 42141–42161. [CrossRef]
- Cui, T.-R.; Li, D.; Huang, X.-R.; Yan, A.-Z.; Dong, Y.; Xu, J.-D.; Guo, Y.-Z.; Wang, Y.; Chen, Z.-K.; Shao, W.-C. Graphene-based flexible electrode for electrocardiogram signal monitoring. *Appl. Sci.* **2022**, *12*, 4526. [CrossRef]
- Paulchamy, B.; Arthi, G.; Lignesh, B. A simple approach to stepwise synthesis of graphene oxide nanomaterial. *J. Nanomed. Nanotechnol.* **2015**, *6*, 1.
- Segal, M. Selling graphene by the ton. *Nat. Nanotechnol.* **2009**, *4*, 612–614. [CrossRef]
- Sharma, N.; Sharma, V.; Jain, Y.; Kumari, M.; Gupta, R.; Sharma, S.; Sachdev, K. Synthesis and characterization of graphene oxide (GO) and reduced graphene oxide (rGO) for gas sensing application. *Macromol. Symp.* **2017**, *376*, 1700006. [CrossRef]
- Chen, X.; Qu, Z.; Liu, Z.; Ren, G. Mechanism of oxidation of graphite to graphene oxide by the hummers method. *ACS Omega* **2022**, *7*, 23503–23510. [CrossRef] [PubMed]
- Roy Chowdhury, S.; Maiyalagan, T. CuCo<sub>2</sub>S<sub>4</sub>@B, N-doped reduced graphene oxide hybrid as a bifunctional electrocatalyst for oxygen reduction and evolution reactions. *ACS Omega* **2022**, *7*, 19183–19192. [CrossRef] [PubMed]
- Akhtar, K.; Khan, S.A.; Khan, S.B.; Asiri, A.M. Scanning electron microscopy: Principle and applications in nanomaterials characterization. In *Handbook of Materials Characterization*; Springer: Cham, Switzerland, 2018; pp. 113–145.
- Smith, E.; Dent, G. Introduction, Basic Theory and Principles. In *Modern Raman Spectroscopy—A Practical Approach*; John Wiley & Sons, Ltd.: Hoboken, NJ, USA, 2004; pp. 1–21. [CrossRef]
- Stankovich, S.; Dikin, D.A.; Piner, R.D.; Kohlhaas, K.A.; Kleinhammes, A.; Jia, Y.; Wu, Y.; Nguyen, S.T.; Ruoff, R.S. Synthesis of graphene-based nanosheets via chemical reduction of exfoliated graphite oxide. *Carbon* **2007**, *45*, 1558–1565. [CrossRef]
- Palaniselvam, T.; Aiyappa, H.B.; Kurungot, S. An efficient oxygen reduction electrocatalyst from graphene by simultaneously generating pores and nitrogen doped active sites. *J. Mater. Chem.* **2012**, *22*, 23799–23805. [CrossRef]

28. Sibia, S.; Bertocchi, F.; Chiodini, S.; Cristiano, F.; Ferrigno, L.; Giovinco, G.; Maffucci, A. Temperature-dependent electrical resistivity of macroscopic graphene nanoplatelet strips. *Nanotechnology* **2021**, *32*, 275701. [CrossRef]
29. Jung, I.; Dikin, D.A.; Piner, R.D.; Ruoff, R.S. Tunable electrical conductivity of individual graphene oxide sheets reduced at “low” temperatures. *Nano Lett.* **2008**, *8*, 4283–4287. [CrossRef]

**Disclaimer/Publisher’s Note:** The statements, opinions and data contained in all publications are solely those of the individual author(s) and contributor(s) and not of MDPI and/or the editor(s). MDPI and/or the editor(s) disclaim responsibility for any injury to people or property resulting from any ideas, methods, instructions or products referred to in the content.

Proceeding Paper

# Improving Hand Pose Recognition Using Localization and Zoom Normalizations over MediaPipe Landmarks <sup>†</sup>

Miguel Ángel Remiro, Manuel Gil-Martín \* and Rubén San-Segundo

Speech Technology and Machine Learning Group (T.H.A.U. Group), Information Processing and Telecommunications Center, E.T.S.I. de Telecomunicación, Universidad Politécnica de Madrid, 28040 Madrid, Spain; ma.remiro@alumnos.upm.es (M.Á.R.); ruben.sansegundo@upm.es (R.S.-S.)

\* Correspondence: manuel.gilmartin@upm.es; Tel.: +34-91-067-2500

<sup>†</sup> Presented at the 10th International Electronic Conference on Sensors and Applications (ECSA-10), 15–30 November 2023; Available online: <https://ecsa-10.sciforum.net/>.

**Abstract:** Hand pose recognition presents significant challenges that need to be addressed, such as varying lighting conditions or complex backgrounds, which can hinder accurate and robust hand pose estimation. This can be mitigated by employing MediaPipe to facilitate the efficient extraction of representative landmarks from static images combined with the use of Convolutional Neural Networks. Extracting these landmarks from the hands mitigates the impact of lighting variability or the presence of complex backgrounds. However, the variability of the location and size of the hand is still not addressed by this process. Therefore, the use of processing modules to normalize these points regarding the location of the wrist and the zoom of the hands can significantly mitigate the effects of these variabilities. In all the experiments performed in this work based on American Sign Language alphabet datasets of 870, 27,000, and 87,000 images, the application of the proposed normalizations has resulted in significant improvements in the model performance in a resource-limited scenario. Particularly, under conditions of high variability, applying both normalizations resulted in a performance increment of 45.08%, increasing the accuracy from  $43.94 \pm 0.64\%$  to  $89.02 \pm 0.40\%$ .

**Keywords:** deep learning; computer vision; human activity recognition; hand pose recognition; landmarks; location normalization; zoom normalization

**Citation:** Remiro, M.Á.; Gil-Martín, M.; San-Segundo, R. Improving Hand Pose Recognition Using Localization and Zoom Normalizations over MediaPipe Landmarks. *Eng. Proc.* **2023**, *58*, 69. <https://doi.org/10.3390/ecsa-10-16215>

Academic Editor: Stefano Mariani

Published: 15 November 2023



**Copyright:** © 2023 by the authors. Licensee MDPI, Basel, Switzerland. This article is an open access article distributed under the terms and conditions of the Creative Commons Attribution (CC BY) license (<https://creativecommons.org/licenses/by/4.0/>).

## 1. Introduction

Recent advances in deep learning and computer vision have been driving the development of Human Activity Recognition (HAR) [1,2], which consists of classifying the physical activities that people perform. One of the HAR research fields is Hand Pose Recognition, which has numerous applications and a great impact on individuals who are deaf or have limited speech and communicate using Sign Language.

In this context, many of the latest works focused on the use of MediaPipe to extract representative landmarks from hands combined with the use of neural networks. Using this approach, a previous work [3] obtained an accuracy of nearly 88% for the recognition of signs of the American Sign Language (ASL) alphabet, using 87,000 images.

Even using MediaPipe, there are still aspects such as the variability of the location of the hand or its size that can negatively impact the performance of the model that previous works have not been focused on. This variability can significantly hinder the accurate recognition of hand poses, particularly when employing deep-learning algorithms, because they heavily rely on data for training. Most datasets contain standardized hand positions and sizes images, so the ones with diverse locations and sizes could be misclassified and may hinder the models to generalize.

This paper aims to study the impact of hand location and zoom variability to propose efficient normalization techniques to mitigate these effects.

## 2. Materials and Methods

This section describes the datasets used in the experiments, the signal processing, the deep-learning approach, and the evaluation methodology to assess the performance of the model.

### 2.1. Datasets

In this work, we used three ASL Alphabet datasets. The ASL Alphabet Test dataset, [4] or so-called Dataset 1, has 870 images, 29 classes, 30 images per class, and is variable in terms of hand location and zoom. The synthetic ASL Alphabet [5], or so-called Dataset 2, has 27,000 images, 27 classes, 1000 images per class, and is static in terms of hand location and zoom. The ASL Alphabet [6], or so-called Dataset 3, has 87,000 images, 29 classes, 3000 images per class, and is variable in terms of hand location and zoom.

### 2.2. Signal Processing

#### 2.2.1. MediaPipe Hands

In this work, we used MediaPipe Hands [7,8], a specific module within the MediaPipe open source project capable of empowering real-time hand detection and tracking in images and videos, providing essential information regarding the precise position of 21 landmarks and key points on each hand. Each landmark is composed of the x and y coordinates and is related to a specific point in the hands, as shown in Figure 1.

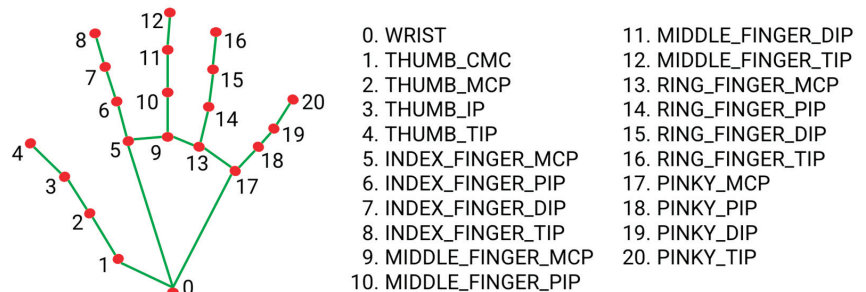


**Figure 1.** The specific location of the hand landmarks extracted by MediaPipe Hands [8].

Once these points are extracted, they serve as inputs to a neural network, enabling the model to discern patterns and effectively differentiate between various signs.

#### 2.2.2. Modules to Include Location and Zoom Variability

To analyze the effect of normalizations under more extreme conditions of variability, two modules have been designed to include location and zoom variability. Their application to a dataset will generate another artificial dataset with the same number of images with a wider heterogeneity in terms of location or zoom.

To include location variability, the first module adds or subtracts equiprobably the same random value to the coordinates of the landmarks of each image. In this way, a new dataset is generated with the landmarks relocated at new random locations.

Similarly, the second module generates an artificial dataset by multiplying or dividing by the same coefficient all the coordinates of the landmarks. Thus, the size of the hands is randomly modified and the variability of the zoom is substantially increased.

Under these conditions of higher variability, the performance of the system may decrease but the potential of normalization algorithms can be tested.

#### 2.2.3. Normalization Algorithms

To mitigate the location and zoom variability of the dataset, several algorithms have been developed. The Norm\_Loc algorithm used the landmark of the wrist (landmark 0) as the origin of coordinates and normalized all other points concerning it. In the



Norm\_Zoom algorithm, the maximum coordinate value is moved to the edge of the square of vertices (0,0), (0,1), (1,0), and (1,1), transforming the rest of the points proportionally so as not to lose the aspect ratio of the hand. The correct functioning of this normalization makes either the largest X-axis coordinate or the largest Y-axis coordinate become worth 1, while the rest of the points are multiplied by the same coefficient. The last algorithm is called Norm\_Loc\_Zoom and applies the two previous modules sequentially. These algorithms mitigate the location and zoom variability because they standardize these image characteristics considering the wrist location and the hand size. As these algorithms consist on simple mathematical operations, there is no increase in the overall computational cost.

### 2.3. Deep Learning

A deep-learning structure with a feature-learning subnet composed of a convolutional layer and a classification subnet composed of fully connected layers is used to recognize the different hand poses. This architecture is represented in Figure 2.

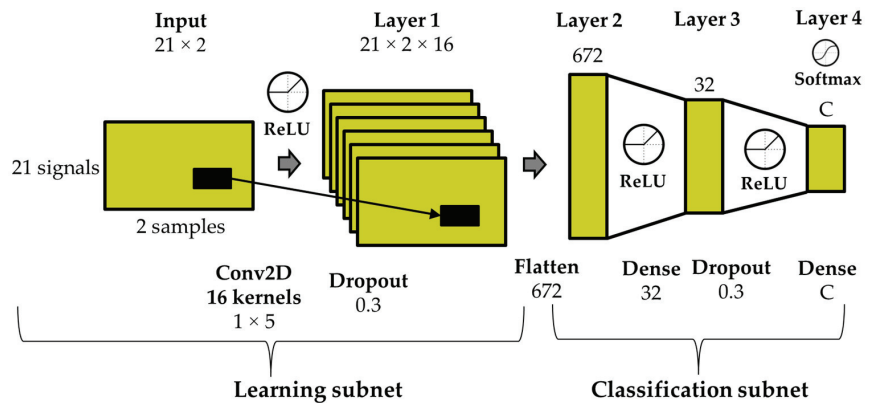


**Figure 2.** Deep-learning architecture used in this work to classify the hand poses.

First, a two-dimensional convolutional layer is added following the input layer. This layer uses the Conv2D function to apply 16 filters to the input of the network, performing convolution operations to facilitate feature extraction. This layer learns feature engineering by itself via filter optimization. The ReLU activation function is applied to the output of this layer to introduce non-linearity and enable the neural network to learn more complex representations of the data. Next, the Dropout layer is added to regularize the network and prevent overfitting. Specifically, a Dropout rate of 0.3 is applied, meaning that 30% of the outputs from the previous layer are randomly deactivated during training. This helps to prevent the network from becoming too dependent on specific neurons and thus avoids overfitting. The Flatten layer converts the output of the previous layer into a one-dimensional vector. The data is then processed by a Dense layer. In this case, this layer consists of 32 neurons directly connected to all neurons from the previous layer. Thus, the neural network performs a linear and non-linear transformation of the input data, allowing the network to learn more complex relationships between the features extracted by the previous layers. Another Dropout layer with the same rate of 0.3 is applied afterward. The ReLU activation function is also employed.

Finally, the output layer consists of a dense layer with a number of neurons corresponding to the number of classes. The softmax activation function is used to calculate the probability of belonging to each of the possible classes. The output layer produces the final outputs of the model, representing the probability distribution over the different classes.

### 2.4. Evaluation Methodology

In this work, k-fold cross-validation is used to assess model performance more accurately and robustly. The data set is divided into k subsets (or folds), and the system is trained on k−1 sets while the remaining set is tested. This process is repeated as many times as there are folds, obtaining a result for each one. In this way, a weighted average of the test results achieved can be calculated, obtaining a much more accurate and robust evaluation of the system, reaching to test all the available data.

Regarding the evaluation metrics, the model performance is measured with accuracy, which is the most common metric in classification problems. It calculates the proportion of correctly classified examples out of the total number of examples. As seen in Equation (1), it is obtained by dividing the sum of true positives and true negatives by the total number of instances. This way, an increment of accuracy implies that the overall system better recognizes the classes. In this work, we used a confidence interval with a 95% significance level attached to the accuracy values.

$$\text{Accuracy}(\%) = \frac{\text{True Positives} + \text{True Negatives}}{\text{True Positives} + \text{True Negatives} + \text{False Positives} + \text{False Negatives}} \quad (1)$$

## 3. Results

This section provides the results for the different datasets, using the original ones and the ones obtained after including the artificial hand and zoom variability. This way, the system was tested with four variants for each dataset: the original dataset (when no normalization algorithm was applied to the data) and the three versions with artificial variability in location, zoom, or both.

In this work, we have been focused on improving the performance in a resource-limited scenario, so we used 10 epochs and batch size values for each dataset according to this aspect and the number of frames in each dataset.

### 3.1. Results for Dataset 1

Table 1 below shows the accuracy rates obtained with Dataset 1 using a batch size of 15. Under these conditions, the system is not able to learn enough from the data in the given number of epochs, giving very low accuracy rates when no normalization is applied. When applied, significant improvements in rates are observed, raising the accuracy from  $46.18 \pm 3.49$  to  $88.17 \pm 2.26$  in conditions of high localization and zoom variability when applying the Norm\_Zoom normalization, which offers better results than the application of both normalizations (Norm\_Loc\_Zoom).

**Table 1.** Results for Dataset 1.

Dataset 1	Normalization Used	Accuracy (%)	Upgrade (%)
Original *	None	$43.77 \pm 3.47$	
	Norm_Loc	$67.94 \pm 3.26$	24.17
	Norm_Zoom	<b><math>78.63 \pm 2.87</math></b>	34.86
	Norm_Loc_Zoom	<b><math>79.64 \pm 2.81</math></b>	35.87
Artificial location	None	$34.22 \pm 3.32$	
	Norm_Loc	<b><math>61.45 \pm 3.40</math></b>	27.23
Artificial zoom	None	$33.84 \pm 3.31$	
	Norm_Zoom	<b><math>76.84 \pm 2.95</math></b>	43
Artificial location and zoom	None	$46.18 \pm 3.49$	
	Norm_Loc	$55.09 \pm 3.48$	8.91
	Norm_Zoom	<b><math>88.17 \pm 2.26</math></b>	41.99
	Norm_Loc_Zoom	$77.35 \pm 2.93$	31.17

\* The modules that include artificial hand location and zoom variability have been not applied.

### 3.2. Results for Dataset 2

For this dataset, we used a batch size of 1000. As can be seen in Table 2, the application of the different proposed normalizations supposes significant improvements in the different variability conditions.

**Table 2.** Results for Dataset 2.

Dataset 2	Normalization Used	Accuracy (%)	Upgrade (%)
Original *	None	79.95 ± 0.51	
	Norm_Loc	83.61 ± 0.48	3.66
	Norm_Zoom	87.61 ± 0.42	7.66
	Norm_Loc_Zoom	<b>94.64 ± 0.29</b>	14.69
Artificial location	None	48.15 ± 0.64	
	Norm_Loc	<b>87.22 ± 0.43</b>	39.07
Artificial zoom	None	67.53 ± 0.60	
	Norm_Zoom	<b>91.91 ± 0.35</b>	24.38
Artificial location and zoom	None	43.94 ± 0.64	
	Norm_Loc	74.42 ± 0.56	30.48
	Norm_Zoom	87.96 ± 0.42	44.02
	Norm_Loc_Zoom	<b>89.02 ± 0.40</b>	45.08

\* The modules that include artificial hand location and zoom variability have been not applied.

The improvement of the accuracy was 45.08% in conditions of high variability in location and zoom when both normalizations are applied. Moreover, the model achieves higher accuracy rates with zoom normalization than with location normalization.

With the original dataset, the model achieves an accuracy of  $87.61 \pm 0.42$  with Norm\_Zoom against  $83.61 \pm 0.48$  achieved with Norm\_Loc. This difference becomes even wider under conditions of high variability of location and zoom:  $87.96 \pm 0.42$  in contrast to  $74.42 \pm 0.56$ .

### 3.3. Results for Dataset 3

With this dataset, we used a batch size of 5000. The proposed normalizations continue to result in significant improvements in scenarios specified in Table 3.

**Table 3.** Results for Dataset 3.

Dataset 3	Normalization Used	Accuracy (%)	Upgrade (%)
Original *	None	44.99 ± 0.39	
	Norm_Loc	67.97 ± 0.36	22.98
	Norm_Zoom	<b>85.03 ± 0.28</b>	40.04
	Norm_Loc_Zoom	82.13 ± 0.30	37.14
Artificial location	None	58.68 ± 0.38	
	Norm_Loc	<b>61.18 ± 0.38</b>	2.50
Artificial zoom	None	57.90 ± 0.38	
	Norm_Zoom	<b>88.56 ± 0.25</b>	30.66
Artificial location and zoom	None	47.09 ± 0.39	
	Norm_Loc	69.86 ± 0.36	22.77
	Norm_Zoom	<b>86.43 ± 0.27</b>	39.34
	Norm_Loc_Zoom	82.85 ± 0.29	35.76

\* The modules that include artificial hand location and zoom variability have been not applied.

By applying zoom normalization, not only much higher accuracy rates are obtained than when applying localization normalization, but superior results are obtained than those obtained by applying both normalizations.

#### 4. Discussion and Conclusions

When a limited time of training is used, the performance of a hand pose recognizer model can decrease due to the variability of location and zoom in the instances used to train the neural network. The application of location and zoom normalizations results in significant accuracy improvements in this situation. These techniques are more impactful when the variability is higher. For example, the performance of the system was raised from  $43.94 \pm 0.64\%$  to  $89.02 \pm 0.40\%$  (45.08%), applying both normalizations.

Comparing both normalizations, the zoom normalization results in a better performance of the model compared to the location normalization, reaching higher rates in all the studied scenarios. In addition, the application of zoom normalization resulted in better results compared to applying both normalizations sequentially in some situations. From this, it can be deduced that this algorithm not only mitigates the effects of size variability, but it also mitigates those of location variability.

For future work, it could be interesting to apply the proposed techniques in other datasets related to hand pose recognition with a wide variety of classes, such as thumb up, thumb down, open hand, or okay.

**Author Contributions:** Conceptualization, M.Á.R., M.G.-M. and R.S.-S.; Methodology, M.Á.R., M.G.-M. and R.S.-S.; Software, M.Á.R. and M.G.-M.; Validation, M.G.-M. and R.S.-S.; Formal analysis, M.G.-M.; Investigation, M.Á.R. and M.G.-M.; Resources, R.S.-S.; Data curation, M.Á.R. and M.G.-M.; Writing—original draft preparation, M.Á.R. and M.G.-M.; Writing—review and editing, R.S.-S.; Visualization, M.G.-M.; Supervision, R.S.-S.; Project administration, R.S.-S.; Funding acquisition, R.S.-S. All authors have read and agreed to the published version of the manuscript.

**Funding:** This research received no external funding.

**Institutional Review Board Statement:** Not applicable.

**Informed Consent Statement:** Not applicable.

**Data Availability Statement:** The data presented in this study are openly available in Kaggle repository: ASL alphabet test: <https://www.kaggle.com/danrasband/asl-alphabet-test> (accessed on 1 June 2023); Synthetic ASL alphabet: <https://www.kaggle.com/datasets/lexset/synthetic-asl-alphabet> (accessed on 1 June 2023) and Asl alphabet: <https://www.kaggle.com/datasets/grassknotted/asl-alphabet> (accessed on 1 June 2023).

**Acknowledgments:** The work leading to these results was supported by the Spanish Ministry of Science and Innovation through the projects AMIC-PoC, BeWord, GOMINOLA, and TremorDetect: Detección de la enfermedad de Parkinson a través de señales inerciales (PDC2021-120846-C42, PID2021-126061OB-C43, PID2020-118112RB-C21, and PID2020-118112RB-C22 funded by MCIN/AEI/10.13039/501100011033, by E.T.S.I. de Telecomunicación, and by the European Union “NextGenerationEU/PRTR”), and ASTOUND (101071191 HORIZON-EIC-2021-PATHFINDERCHALLENGES-01) funded by the European Commission. We gratefully acknowledge the support of the NVIDIA Corporation with the donation of the Titan X Pascal GPU used for this research.

**Conflicts of Interest:** The authors declare no conflicts of interest.

#### References

1. Gil-Martín, M.; San-Segundo, R.; de Córdoba, R.; Pardo, J.M. Robust Biometrics from Motion Wearable Sensors Using a D-vector Approach. *Neural Process. Lett.* **2020**, *52*, 2109–2125. [CrossRef]
2. Gil-Martín, M.; López-Iniesta, J.; Fernández-Martínez, F.; San-Segundo, R. Reducing the Impact of Sensor Orientation Variability in Human Activity Recognition Using a Consistent Reference System. *Sensors* **2023**, *23*, 5845. [CrossRef] [PubMed]
3. Shin, J.; Matsuoka, A.; Hasan, M.A.; Srizon, A.Y. American Sign Language Alphabet Recognition by Extracting Feature from Hand Pose Estimation. *Sensors* **2021**, *21*, 5856. [CrossRef] [PubMed]
4. Rasband, D. ASL Alphabet Test. Available online: <https://www.kaggle.com/danrasband/asl-alphabet-test> (accessed on 1 June 2023).
5. Lexset. Synthetic ASL Alphabet. Available online: <https://www.kaggle.com/datasets/lexset/synthetic-asl-alphabet> (accessed on 1 June 2023).
6. Akash. Asl Alphabet. Available online: <https://www.kaggle.com/datasets/grassknotted/asl-alphabet> (accessed on 1 June 2023).

7. Lugesesi, C.; Tang, J.; Nash, H.; McClanahan, C.; Uboweja, E.; Hays, M.; Zhang, F.; Chang, C.L.; Yong, M.G.; Lee, J.; et al. MediaPipe: A Framework for Building Perception Pipelines. *arXiv* **2019**, arXiv:1906.08172.
8. Google. Hand Landmarks Detection Guide. Available online: [https://developers.google.com/mediapipe/solutions/vision/hand\\_landmarker](https://developers.google.com/mediapipe/solutions/vision/hand_landmarker) (accessed on 1 June 2023).

**Disclaimer/Publisher's Note:** The statements, opinions and data contained in all publications are solely those of the individual author(s) and contributor(s) and not of MDPI and/or the editor(s). MDPI and/or the editor(s) disclaim responsibility for any injury to people or property resulting from any ideas, methods, instructions or products referred to in the content.



# Getting a Better Sense of Data Drift in Dynamic Systems: Sequence-Based Deep Learning for Monitoring Slowly Evolving Degradation Processes <sup>†</sup>

Tarek Berghout <sup>1,\*</sup> and Mohamed Benbouzid <sup>2,3</sup>

<sup>1</sup> Laboratory of Automation and Manufacturing Engineering, University of Batna 2, Batna 05000, Algeria

<sup>2</sup> UMR CNRS 6027 IRDL, University of Brest, 29238 Brest, France; mohamed.benbouzid@univ-brest.fr

<sup>3</sup> Logistics Engineering College, Shanghai Maritime University, Shanghai 201306, China

\* Correspondence: t.berghout@univ-batna2.dz

<sup>†</sup> Presented at the 10th International Electronic Conference on Sensors and Applications (ECSA-10), 15–30 November 2023; Available online: <https://ecsa-10.sciforum.net/>.

**Abstract:** Deep Learning (DL) for monitoring slowly evolving degradation processes typically involves overcoming data drift, complexity, and unavailability issues resulting from dynamic and harsh conditions and the rarity of labeled failure patterns, respectively. While degradation patterns are mostly hidden in such complex data, observation-based DL is prone to producing uncertain predictions and/or overfit models during the training process. This problem is usually caused by the insignificance of certain data representations. Therefore, and particularly due to the sequential nature of data in such a degradation process, it is necessary to consider neighboring observations to judge the accuracy of a representation or improve it. In this context, instead of providing traditional observation-based learning philosophy, this paper presents data-driven sequential mapping while additionally showing that health indices can also be represented as a vector of sequential data and not as a single regressor output changing a model's architecture. Using a dataset generated from a mathematical model mimicking bearing degradation life cycles and responding to the aforementioned three main challenges, a comparative study built on investigating observation-based and sequence-based learning paths was conducted. According to a well-defined visual and numerical evaluation criterion, a sequence-based methodology reflects a better understanding of data representations through parameter tuning, achieving better approximation and generalization. Such results support the necessity of such a learning mechanism, especially for sequential data, dealing with some sort of correlation and degrading controversy. The files required to reproduce the findings of this work have been made publicly available.

**Keywords:** bearing; deep learning; degradation; prognostics and health management; remaining useful life; sequential data; vibration

**Citation:** Berghout, T.; Benbouzid, M. Getting a Better Sense of Data Drift in Dynamic Systems: Sequence-Based Deep Learning for Monitoring Slowly Evolving Degradation Processes. *Eng. Proc.* **2023**, *58*, 70. <https://doi.org/10.3390/ecsa-10-16229>

Academic Editor: Stefano Mariani

Published: 15 November 2023



**Copyright:** © 2023 by the authors. Licensee MDPI, Basel, Switzerland. This article is an open access article distributed under the terms and conditions of the Creative Commons Attribution (CC BY) license (<https://creativecommons.org/licenses/by/4.0/>).

## 1. Introduction

The monitoring of the slow degradation processes of dynamic systems under real conditions based on DL is generally a problem pertaining to the construction of a regression model where a specifically reconstructed health index needs to be predicted accurately for unseen health indicators [1]. This usually poses problem such as data drift, complexity, and unavailability [1]. The concept of drift refers to massive changes in the historical data features of a specific system lifecycle (i.e., run-to-failure data) [2]. Similarly, data complexity and unavailability refer to different kinds of distortions and the rarity of failure patterns [1]. Such distortions can be the result of the presence of noise and different outliers/anomalies in data affected by environmental conditions or physical damage propagation of the system itself. A high level of rarity of failure patterns is generally due to the fact that data are usually generated from physics-based models or accelerated aging experiments and not true

degradation phenomena for many reasons, including financial and critical safety-related issues, reducing emulation quality with respect to reality [3].

It should be mentioned that this paper focuses on the data drift problem, while a DL model must be continuously updated to account for new changes in data and be able to generalize better for unseen samples. As a result, research gaps in this paper will be revealed based upon analysis from this perspective. Basically, DL models for health monitoring are generally constructed based on an ordinary training process consisting of mapping each observation feature separately to outputs produced at each time instant. This means that when, for instance, an observation is misrepresented due to any possible data distortion, sensor malfunction, or other disturbances, the model will automatically be affected, potentially leading to bias, misprediction, overfitting, etc. [2]. In this case, it is necessary to mitigate the negative effects of such misleading information to maintain both approximation and the generalization process of a DL model.

### 1.1. Research Gaps

According to the brief previous analysis, gaps in research on this topic can consequently be highlighted as follows:

1. Observation-based learning does not consider correlations between time series data, which could cause a model to produce biased results if the samples are misrepresented due to the many aforementioned reasons;
2. Observation-based learning does not reflect the actual monitoring of concept drift and its detection at some point while data are subject to continuous change.

Overall, a single observation, even if driven in chunk-by-chunk form, is not expected to carry information about neighboring samples to the learning model itself. This is a significant learning problem, especially when slowly evolving degradation process monitoring is a time series analysis problem and this fact must be considered [4].

### 1.2. Contributions

Based on the highlighted analysis criteria of concept drift in dynamic systems for monitoring slowly evolving degradation processes, the following contributions are made in this paper:

1. **The consideration of a sequence-based learning methodology:** One of the main solutions that this paper proposes is to follow a sequence-based learning methodology for a task such as that outlined herein. In this case, a sequence of observations of a specific length will be flattened and used as an input to the DL network. It should be mentioned that this is different from sequence-to-sequence learning presenting a series of encoding–decoding patterns and processes, as proposed in [5]. Therefore, the output of the DL regressor will be a vector instead of a single health index during sequential mapping. The tuning mechanism of the DL model will make it possible to attain a sense of the data changes and to improve their representations, taking into account the loss result.
2. **The consideration of adaptive deep learning:** An additional step of adaptive deep learning is taken into account in this case by introducing a long short-term memory (LSTM) neural network. An LSTM has a strong advantage as it allows for the consideration of correlations between driven sequences of time series data. In another way, data drift, in this case, will be addressed in two main steps: (i) a preprocessing step, where data are organized in sequences instead of as observations, and (ii) a main step, where the learning algorithm itself considers adaptive learning. This will further strengthen the learning processes and allow for more-accurate adaptive learning.
3. **Using data generated from a mathematical model:** An experiment was conducted on data generated from a mathematical model mimicking the health degradation trajectories of bearings responding to the three aforementioned health-monitoring issues of slowly evolving degradation processes. Compared to traditional observation-based DL, the experiments encourage such data mapping, especially for sequential

data with similar degradation behavior. The necessary files for reproducing the findings of this work have been made online available at [6].

### 1.3. Outlines

In attempt to ensure that the contributions of this paper are clear and well-illustrated, making this study reproducible, this paper is organized as follows: Section 1 is dedicated to data description. Section 2 is devoted to the proposed methodology. Section 3 is dedicated to the results and discussion. Finally, Section 4 concludes this work.

## 2. Materials

In this work, we used a bearing degradation dataset extracted from a mathematical model describing an exponentially growing sinusoidal wave with additive noise and distortions in an attempt to mimic real-world conditions [7]. The dataset contains two subsets dedicated to outer-race and inner-race faults, where each subset contains 20 sequences with different degradation rates. The degradation rate is defined using a different number of vibration window sizes with 30, 50, 65, 80, and 100 time cycles. For each speed profile, 4 life cycles are generated, modifying the parameters influencing the fault signatures randomly by  $\pm 5\%$ . Each window has 16,348 samples, with a sampling frequency of 51.2 kHz, meaning that there are 40 life cycles in total. Row data from a single life cycle from the dataset are presented in Figure 1a, clearly showing an exponential shift in the data towards failure mode.

In this work, data were subjected to preprocessing, making it easier to extract any possible degradation signs at first glance. In this context, 11 time domain features that were the same as those used in previous work [8] (see [8], Section 2.3) were extracted. Similarly, the same denoising, outlier removing, and scaling steps applied in [8] were followed to make sure the data were ready for DL model training. Accordingly, Figure 1b is an example of extracted features from the life cycle in Figure 1a, as some degradation patterns clearly can be seen in this situation. Based on data visualization in Figure 1a,b, the health index function was defined as an exponential degradation function, better reflecting degradation mechanisms than linear trends, which also can be seen in Figure 1c.

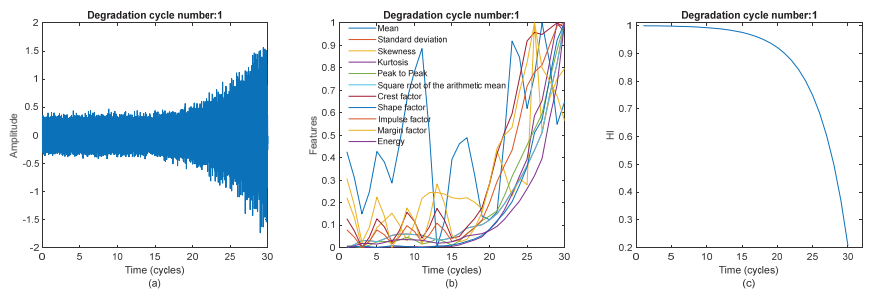


**Figure 1.** Dataset and preprocessing: (a) raw data of a single degradation life cycle; (b) prepared data for a single degradation life cycle; (c) health index of an entire life cycle.

## 3. Methods

In this work, a long-short term memory (LSTM) network was involved in the training process, as it is recommended for data drift and complexity problems (see Section 6.2 from [1]). In this context, for observation-based learning, a single-layer LSTM with trial-error-tuned parameters of 10 neurons, an  $l_2$  regularization parameter equal to 0.01, and a learning rate of 0.01 was used. The same parameters were retained for sequence-based training, while a sequence length was fixed to six observations. The only aspect that changes in this case is the input and output layers sizes, which are altered to fit changes in data mapping and sequence length. Figure 2a is an example of an ordinary deep network



commonly used in degradation process monitoring, while Figure 2b is the new network architecture reflecting sequence-based learning.

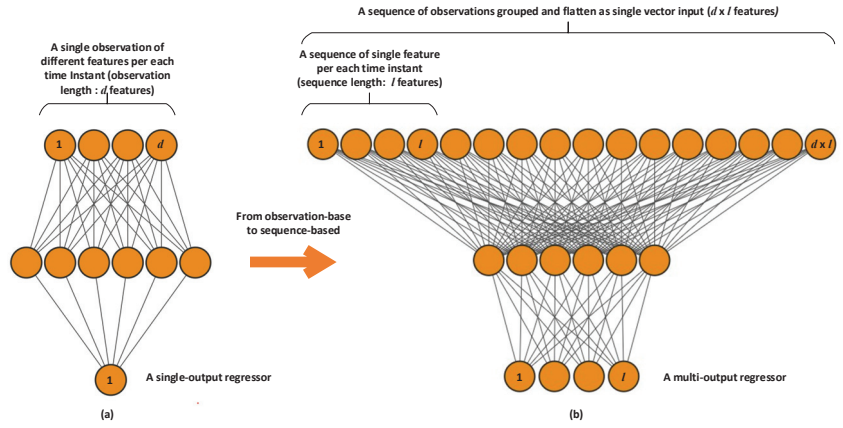


**Figure 2.** DL model architecture: (a) observation-based DL model; (b) sequence-based DL model.

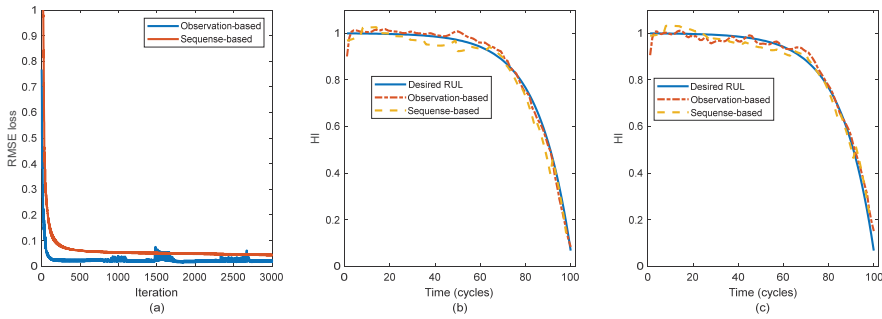
#### 4. Results and Discussion

In this work, from each previously mentioned speed profile, we selected three life cycles for training and one file for testing. Thus, 30 degradation profiles were used for training, and 10 degradation profiles were used for testing. This includes files of both subsets for both inner- and outer-race fault scenarios. Mini-batch size, maximum number of epochs, and iterations were fixed to 10, 1000, and 3000, respectively, for both DL networks under the same tuning mechanism with an error-trial basis. Two types of metrics were used in this case to judge the accuracy of the training process: visual and numeric. Visual metrics including curve-fitting examples, loss function behavior, and some scoring function behavior, as will be illustrated by the following numerical metrics. The numerical metrics include the root mean squared error (RMSE) in Equation (1) and the score function in Equation (2), the latter of which is usually used to evaluate data-driven models for bearing degradation analysis [9].  $n$ ,  $y$ , and  $\tilde{y}$  are the number of samples, the desired health index, and the predicted health index, respectively. The score function penalizes early and late predictions differently to satisfy certain decision-making constraints related to maintenance planning [9]. Meanwhile, the RMSE designed to study the actual distance between a prediction reflecting a real significant measurement.

$$RMSE = \frac{1}{n} \sum_{i=1}^n y_i - \tilde{y}_i \quad (1)$$

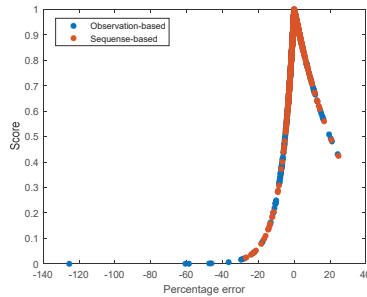
$$Score = \begin{cases} e^{-\ln(0.5)\left(\frac{100(y-\tilde{y})}{5}\right)}, & \frac{100(y-\tilde{y})}{5} < 0 \\ e^{+\ln(0.5)\left(\frac{100(y-\tilde{y})}{5}\right)}, & \frac{100(y-\tilde{y})}{5} \geq 0 \end{cases} \quad (2)$$

Figure 3a shows the loss function behavior. For observation-based learning, we can observe faster convergence and reduced loss values. However, the model soon encounters an overfitting problem showing fluctuations in loss values (e.g., iterations 1000, 1500, and 2500). Meanwhile, despite the late convergence and slightly larger values of the loss function for sequence-based learning, the DL model shows better stability, with no signs of overfitting. The curve-fitting examples of the test set for both inner-race and outer-race profiles for a speed profile of 100 time cycles in Figure 3b,c show that the sequence-based results are closer and smoother, leading to better predictions.



**Figure 3.** Obtained results: (a) loss function behavior; (b) curve fit result example for inner-race fault degradation cycles; (c) curve fit result example for outer-race fault degradation cycles.

Figure 4 is dedicated to addressing the behavior of the suggested scoring function. The score function was designed to explain both early prediction scores (where the percentage error is > 0) and late prediction scores (with a percentage error < 0). These predictions are related to maintenance decisions. What we see in Figure 4 are observation-based prediction scores that are further dispersed compared to the sequence-based ones when approaching a value of 1. This means that the DL model with respect to the latter has a better generalization ability (prediction using the test set). This proves the necessity of sequential learning in improving data presentation, consequently improving approximation and generalization through accurate tuning.



**Figure 4.** Score function behavior.

For numerical evaluation, the RMSE and score results are shown in Table 1. The results encourage using sequence-based mapping when dealing with such slowly evolving degradation process rather than observation-based mapping due to the clear gap between them in term of performance. Also, the sequence-based methodology seems less computationally expensive than the observation-based one, especially when considering the computation time results in Table 1, which confirm this information.

**Table 1.** Final numerical evaluation results.

Method	RMSE	Score	Training Time (s)
Sequence-based LSTM	0.0243	0.8401	16.4235
Observation-based LSTM	0.0246	0.7989	30.9235

**5. Conclusions**

In this work, we introduced a health index assessment experiment using deep learning under slowly evolving degradation processes. We discussed the use of a sequential learning philosophy versus the traditional observation philosophy when training a DL model for

approximating a degraded function. A bearing degradation dataset of multiple fault scenarios was used in these cases while adopting LSTM learning rules for DL model reconstruction. Many visual and numerical assessment metrics were used to evaluate the performance of the investigated approaches. The results encourage adopting the sequence-based methodology as it allows for the mitigation of misrepresented observations occurring as a result of harsh operating conditions. As a future perspective, further highly dynamic systems need to be studied to solve this problem, including those with deeper architectures and targeting other problems regarding data complexity and availability, not only data drift problems. In doing so, further performance details about this methodology will be revealed.

**Author Contributions:** Conceptualization, T.B.; methodology, T.B. and M.B.; T.B. and M.B.; validation, T.B. and M.B.; formal analysis, T.B. and M.B.; investigation, T.B.; resources, T.B.; data curation, T.B. and M.B.; writing—original draft preparation, T.B.; writing—review and editing, T.B. and M.B.; All authors have read and agreed to the published version of the manuscript.

**Funding:** This research received no external funding.

**Institutional Review Board Statement:** Not applicable.

**Informed Consent Statement:** Not applicable.

**Data Availability Statement:** Data used in this work can be downloaded at [https://figshare.com/articles/dataset/Simulated\\_Bearing\\_Degradation\\_Data\\_mat/12554690](https://figshare.com/articles/dataset/Simulated_Bearing_Degradation_Data_mat/12554690) (accessed on 14 November 2023). The necessary files for reproducing the findings of this work can be downloaded at <https://doi.org/10.5281/zenodo.8142676> (accessed on 14 November 2023).

**Acknowledgments:** The authors thank Koceila, A.; Mouchaweh, M.S.; Cornez, L.; and Chimentin, X for making their simulated bearing degradation dataset public and easily accessible, enabling the results presented in this work to be produced.

**Conflicts of Interest:** The authors declare no conflict of interest.

## References

1. Berghout, T.; Benbouzid, M. A Systematic Guide for Predicting Remaining Useful Life with Machine Learning. *Electronics* **2022**, *11*, 1125. [CrossRef]
2. Khamassi, I.; Sayed-Mouchaweh, M.; Hammami, M.; Ghédira, K. Discussion and Review on Evolving Data Streams and Concept Drift Adapting. *Evol. Syst.* **2018**, *9*, 1–23. [CrossRef]
3. Lei, Y.; Li, N.; Guo, L.; Li, N.; Yan, T.; Lin, J. Machinery Health Prognostics: A Systematic Review from Data Acquisition to RUL Prediction. *Mech. Syst. Signal Process.* **2018**, *104*, 799–834. [CrossRef]
4. Ding, C.; Zhao, J.; Sun, S. Concept Drift Adaptation for Time Series Anomaly Detection via Transformer. *Neural Process. Lett.* **2023**, *55*, 2081–2101. [CrossRef]
5. Sutskever, I.; Vinyals, O.; Le, Q.V. Sequence to Sequence Learning with Neural Networks. *Adv. Neural Inf. Process. Syst.* **2014**, *4*, 3104–3112.
6. Berghout, T. *Sequence-Based Instead of Observation-Based Deep Learning: Monitoring Slowly Evolving Degradation Processes*, Version 1.0.0; Zenodo: Geneva, Switzerland, 2023. [CrossRef]
7. Koceila, A.; Mouchaweh, M.S.; Cornez, L.; Chimentin, X. *Simulated Bearing Degradation Data*, 2020. [CrossRef]
8. Berghout, T.; Benbouzid, M.; Amirat, Y. Towards Resilient and Secure Smart Grids against PMU Adversarial Attacks: A Deep Learning-Based Robust Data Engineering Approach. *Electronics* **2023**, *12*, 2554. [CrossRef]
9. Gouriveau, R.; Medjaher, K.; Ramasso, E.; Zerhouni, N. PHM-Prognostics and Health Management De La Surveillance Au Pronostic de Défaillances de Systèmes Complexes. *Tech. l'ingénieur Fonct. Strat. la Maint.* **2013**, *9*, MT 9570 2–MT 9570 16. [CrossRef]

**Disclaimer/Publisher's Note:** The statements, opinions and data contained in all publications are solely those of the individual author(s) and contributor(s) and not of MDPI and/or the editor(s). MDPI and/or the editor(s) disclaim responsibility for any injury to people or property resulting from any ideas, methods, instructions or products referred to in the content.



Proceeding Paper

# The Design and Development of an Internet of Things-Based Condition Monitoring System for Industrial Rotating Machines <sup>†</sup>

Alagumariappan Paramasivam <sup>1,\*</sup>, Jaya Prakash Abimanyu <sup>1</sup>, Pavan Sai Kiran Reddy Pittu <sup>1</sup>, Sankaran Vijayalakshmi <sup>2</sup> and Mohana Krishnan Kaushal Mayur <sup>1</sup>

<sup>1</sup> Department of Biomedical Engineering, Vel Tech Rangarajan Dr. Sagunthala R&D Institute of Science and Technology, Chennai 600062, India; vtu12390@veltech.edu.in (J.P.A.); vtu18106@veltech.edu.in (P.S.K.R.P.); vtu12076@veltech.edu.in (M.K.K.M.)

<sup>2</sup> Department of Electronics and Communication Engineering, Vel Tech Rangarajan Dr. Sagunthala R&D Institute of Science and Technology, Chennai 600062, India; drvijayalakshmis@veltech.edu.in

\* Correspondence: drparamasivam@veltech.edu.in or parama.ice@gmail.com; Tel.: +91-984-378-0801

<sup>†</sup> Presented at the 10th International Electronic Conference on Sensors and Applications (ECSA-10), 15–30 November 2023; Available online: <https://ecsa-10.sciforum.net/>.

**Abstract:** In general, the industries utilize more rotating machines and the efficient functioning of these machines is vital for the smooth operation of industrial processes. Further, the detection and identification of motor issues in a timely manner is crucial to prevent unexpected downtime and expensive repairs. In this work, a novel approach is proposed to monitor and assess the condition of motors in real-time by analyzing the environmental parameters using sensors which are capable of measuring temperature and humidity, to gather data about the operating environment of motors in industrial settings. Also, by continuously monitoring these environmental factors, deviations from optimal conditions can be detected, allowing for proactive maintenance actions to be taken. The proposed system consists of a network of temperature and humidity sensors strategically placed in proximity to the motors being monitored. Further, these sensors collect temperature and humidity data at regular intervals and transmit them to an Internet of Things (IoT) cloud platform. Finally, the data are analyzed using a fuzzy logic decision-making algorithm and are compared against predefined threshold values to determine if the motor is operating within acceptable conditions. This work appears to be of high industry relevance since automated notifications or alerts are to be sent to maintenance personnel when abnormal conditions are detected.

**Keywords:** fuzzy logic control; internet of things (IoT); motor condition assessment; proactive maintenance; real-time monitoring

**Citation:** Paramasivam, A.; Abimanyu, J.P.; Pittu, P.S.K.R.; Vijayalakshmi, S.; Kaushal Mayur, M.K. The Design and Development of an Internet of Things-Based Condition Monitoring System for Industrial Rotating Machines. *Eng. Proc.* **2023**, *58*, 71. <https://doi.org/>

Academic Editor: Francisco Falcone

Published: 15 November 2023



**Copyright:** © 2023 by the authors. Licensee MDPI, Basel, Switzerland. This article is an open access article distributed under the terms and conditions of the Creative Commons Attribution (CC BY) license (<https://creativecommons.org/licenses/by/4.0/>).

## 1. Introduction

In this modern era, industries are mainly concerned with the quality and quantity of production over a period of time. The deployment of motors to complete operational requirements is a practice that has been embraced by all sectors [1]. Induction motors are the most common among AC motors used in industries nowadays. The motors are subjected to several electrical and mechanical stresses during prolonged operation. An initial fault results in motor disfunction, which leads to downtime and loss and if it is not diagnosed it will lead to decreased safety, dependability, and motor overheating problems [2,3]. The main problems in the induction motors are single phase failures and overheating. So, the insulation fails and produces high heat for the motor windings to handle. In overheating, the supply mechanism drawing more current than necessary leads to the motor overheating. At the time of overloading, the motor draws an excessive amount of current from the power source, which increases the heat [4]. To avoid such failures, a method of condition-based monitoring techniques for the prediction and prevention of motors bearing health conditions on a timely basis is used. A fair number of those industries

have progressed towards the decreasing activity of human reliability and proceeded further over the area of automation; this in turn has led to a new domain called the fourth industrial revolution, or industry 4.0. The mentioned industry 4.0 depends highly on Wireless Sensor Networks (WSNs) and the Internet of Things (IoT). IoT devices work by contributing to the main application of processing acquired data from WSN devices and transmitting them to various remote locations [5].

The Industrial Internet of Things (IIoT) is relatively a new approach for existing and fairly new industries; it is opening horizons to a wide range of opportunities in aiding industries to operate more effectively and ensure safety while fairly increasing the efficiency percentage and cutting an ample amount of cost. Businesses are expected to pay out around 80 percent of their initial investment in technology and it is predicted that this would grow to a value close to USD 4 trillion in the specific market of technology by the year 2025 (Nasscom, 2018). Thus, the help of the connectivity of all devices into one network gives the ability for a human being to access technology in a very effective and efficient way; hence, the IIoT will revolutionize the ways of production and distribution in industries in a very productive way, while offering safety at the same time [6,7].

The IIoT is one of the most dependable ways of connecting sensors and industrial machinery with one another, providing the user with the ability and accessibility to connect these devices and process the acquired data in a very efficient manner. IoT technology architectures include the technology of cloud computing. Before the IoT, Bluetooth and Radio Frequency (RF) methods were employed in industrial applications, which enabled the user to control the device remotely but was limited only to a short distance. The operator or the user had to be in the range of the Bluetooth or RF in order to operate; with the help of the IIoT, this tedious process is replaced, as they can be connected via the internet and the range can extend as much as the user requires [8].

Humidity and temperature are condemning ecological factors that can remarkably affect the performance and life span of industrial motors. Fairly high humid levels can lead to the reduction of resistance of insulation in the motor windings. This could gradually lead to electrical leakage and failures. Also, temperature changes can lead to condensation inside the motor; this could result in electrical shorts [9]. The overall efficiency of industrial motors can be lowered by both high temperatures and humidity. This might result in drastic changes such as a greater loss in energy efficiency and an increase in running expenses [10]. Sudden temperature changes might result in the failure of cooling systems, which may lead to the overheating and gradual failure of the motor. Cooling systems such as fans and heat exchangers work less comparatively to normal temperatures. Temperature fluctuations can result in thermal expansion; that is, the motor components may become contracted and they may lead to excessive stress and misalignment [11].

The objective of this work is to propose a novel approach to monitor and assess the condition of motors in real-time by analyzing the environmental parameters using sensors which are capable of measuring temperature and humidity.

## 2. Literature Survey

Recently, several researchers have proposed the IoT-based condition monitoring of induction machines [12–20]. Jeyalakshmi et al. [13] (2020) have developed a smart motor condition monitoring system to monitor the vibration and temperature of the motor using MyRio software platform. Agyare et al. [14] (2019) have developed a three-phase induction motor model in MATLAB/Simulink software with a FL controller. Furthermore, the authors have showed the results by monitoring the health condition of motors using a fuzzy logic controller.

Lilo et al. [15] (2020) have proposed a wireless system for detecting and monitoring the faults of induction motors. Further, the authors have used a FL controller and showed the results that the proposed system detects at a faster rate and reduced the maintenance costs. Purwanto et al. [16] (2018) have proposed a fuzzy logic-based microcontroller to monitor the temperature and humidity controller of the server room. Further, the authors

have stored and monitored the data in an IoT-based system, also accessed using remote control. Caicedo [17] (2020) has developed a monitoring system to detect and collect the thermal and magnetic parameters of coil winding during short circuits. Further, the author has proposed a cloud-based storage system to store the monitored data.

Kang et al. [18] (2020) have proposed the detection method of high voltage motors during end-to-end winding faults. Further, the authors have proposed an online monitoring partial discharge identification method to detect and identify the pattern of faults under different temperature conditions. Li et al. [20] (2020) have proposed a machine-learning-based IoT technique to collect data during the condition monitoring of machineries. Mykoniatas [21] (2020) has developed an IoT-based real-time condition monitoring system which detects and monitors the temperature and vibration data of industrial motors.

### 3. Materials and Methods

In general, rotating machines are the most commonly used device in industries such as manufacturing, power systems, textiles, etc. To overcome the heating issues of the rotating machines due to its continuous operation, cooling systems are provided. Further, the cooling shall be given through natural and artificial methods. The natural cooling occurs due to the presence of air around the environment. This air is otherwise known as coolant air, which sucks in the heat produced the rotating machines and is delivered to the outside environment. Also, the coolant air can be purposely provided to any rotating machine to remove heat by artificial methods. However, the coolant air with high humidity degrades the insulation quality of windings and in turn reduces the life of the machine.

Figure 1 shows the overall block diagram for the proposed work. Further, the temperature and humidity of the coolant air for the rotating machine is monitored and stored. Also, the temperature of the rotating machine is monitored and stored. The proposed system consists of device components such as sensors, a microcontroller unit and an IoT cloud platform with Graphical User Interface.

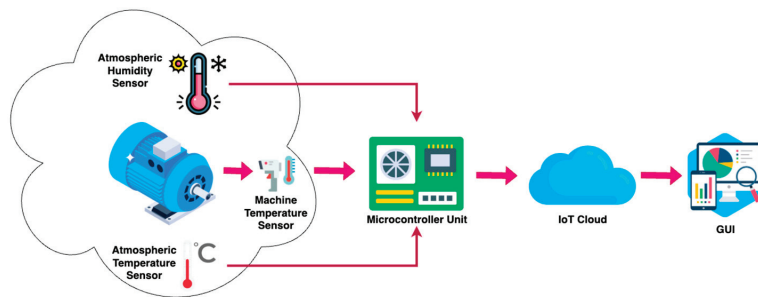


**Figure 1.** Overall block diagram for the proposed work.

#### 3.1. Sensors

In this work, three different sensors such as ambient temperature sensors, humidity sensors (DHT11) and machine temperature sensors (MLX90614) are explored. The DHT11 measures both temperature and humidity, which are easy to interface with a microcontroller unit. Furthermore, the DHT11 measures temperature ranges from 0 to 50 degrees Celsius and measures humidity ranges from 20 to 90% (relative humidity). Also, the MLX90614 is a non-contact temperature sensor module which can be used to measure object temperature ranges from  $-70$  to 380 degree Celsius. The output of the non-contact-type machine temperature sensor module is transferred to the microcontroller unit through inter-integrated circuit (I2C) protocol.

### 3.2. The Microcontroller Unit

An ESP8266 microcontroller unit is utilized in this work to read the temperature and humidity from the appropriate sensors. Further, the ESP8266 or Node MCU has an in-built Wi-Fi module, which helps to feed sensor data to IoT cloud platform. Also, the DHT11-based temperature and humidity sensor module is connected to the analog pin of ESP8266. The MLX90614-based object temperature measurement sensor is connected to the serial clock (SCL) and serial data (SDA) pins of the node MCU controller. The sensor values such as machine temperature, ambient temperature and ambient humidity are measured and the data is fed to the microcontroller unit.

### 3.3. IoT Cloud Platform

The sensor data are stored to the user account of the ThingSpeak platform, and these data are accessed by MATLAB R2023a software. For every user account, the unique read and write Application Programming Interface (API) key is created. Further, any data sent to the user's account is be stored or accessed with the help of read and write API key, respectively. Fuzzy logic control algorithm is coded In the MATLAB software and the sensor data stored in the ThingSpeak are accessed by the MATLAB software using write API key. Fuzzy Logic Controller (FLC) is most popular nowadays in automatic process control and it has four main steps, namely, fuzzification, fuzzy inference, fuzzy rule base and de-fuzzification [22]. Further, FLC uses a fuzzifier for the fuzzification process and the most commonly used type of fuzzifier is the Mamdani fuzzifier. In this work, the same Mamdani fuzzifier is utilized as a fuzzifier. The input values given to fuzzifier are machine temperature, ambient temperature and ambient humidity, which derives the condition of the machine. The error ( $E$ ) and the change in error ( $\Delta E$ ) from the fuzzifier is provided as an input to the fuzzy inference system. Also, the fuzzy inference is performed by a decision-making algorithm named fuzzy rule base. Finally, the output of the fuzzy inference system is provided to de-fuzzifier and these outputs are the conditions of the machine.

## 4. Results and Discussion

Figure 2a shows the ThingSpeak IoT cloud platform, which was used to log three different sensor values. Further, it is observed that there are three different field charts which were used to store and monitor three different sensor values. Also, the pseudo-code for the proposed work is shown in Figure 2b. At first, the three different sensors' data were logged in the ThingSpeak IoT cloud platform. In the user account of the ThingSpeak IoT platform, the four different field charts were created to log three different sensors' data, namely ambient temperature, ambient humidity and machine temperature, and to log the decision output of the FLC algorithm. All these sensors' data and fuzzy outputs were logged with respect to time and date, which helps the user to have a clear picture about whether the machine is operating at acceptable conditions. Once the sensor data was logged, these data were utilized by the FLC algorithm, which was coded using MATLAB software with the help of the read API key. The output of the FLC algorithm were the conditions of the motor, which were further stored in the Field 4 chart.

The log of the ambient/atmospheric temperature acquired by the DHT11-based temperature is shown in Figure 2a. It is clearly seen that the values of ambient humidity are logged at the Field 1 chart. Also, it is shown that the values of ambient temperature are logged at Field 2 chart. Figure 2a shows the log for the machine temperature acquired using the MLX90614-based temperature sensor. Further, the decision output of the FLC was logged relating to environmental conditions, which is shown in the Field 4 chart. Also, from the figures, it is seen that the increase in ambient temperature increases the temperature of the rotating machine during its continuous operation. In the Field 4 chart, the y-axis of the graph shows the acceptable conditions for the operations of rotating machines. Further, the 0, 1 and 2 scale are worse, poor and good or acceptable conditions, respectively. According to the three different inputs, namely ambient temperature, ambient humidity and machine temperature, the FLC generates the decision of whether the machine is operating within

acceptable conditions. Also, if the machine is operated at the permissible conditions, this increases its lifetime.

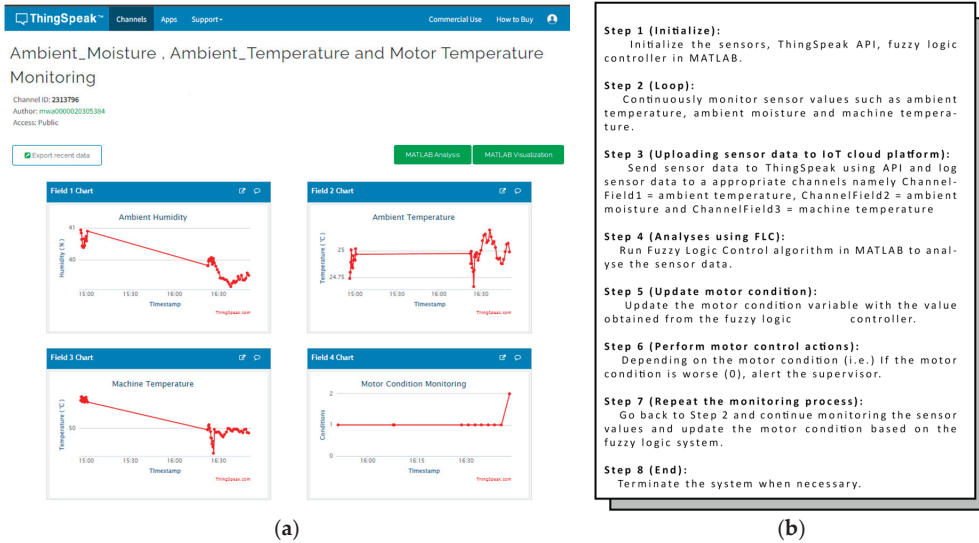


Figure 2. (a) ThingSpeak IoT cloud Platform. (b) Pseudo-code for the proposed work.

### 5. Conclusions

The main aim of this work is to continuously monitor the air coolant’s moisture and temperature provided to the rotatory machine. Due to the increased moisture and temperature content, the degradation of the winding insulation is caused. And this, in turn, reduces the lifetime of the machine when it is operated for a prolonged period of time. Furthermore, an internet of things (IoT)-based condition monitoring technique is utilized to monitor the moisture and temperature of the air coolant continuously. Also, this is performed by placing sensors near to the winding insulation surface. These sensors are connected to the controllers, which receive sensor parameters as input data. A Fuzzy Logic Control algorithm (FLC) is used to alert the user if a high moisture content of the air is sensed. So, the FL-based controller continuously monitors and allows the user to control ambient temperature. The advantage of using IoT-based condition monitoring is that the measured parametric data can be stored in cloud storage and it can be monitored or accessed from any remote place, as it is a web- or Internet-based application. Also, the instant alerts can be received regarding the health condition, which improves the lifetime of rotating machines.

**Author Contributions:** M.K.K.M., J.P.A. and A.P. conceptualized this work. S.V. provided the required resources. P.S.K.R.P. designed and developed the hardware. P.S.K.R.P. and J.P.A. carried out the investigation and data curation. S.V. designed the visualization. A.P. validated the acquired results and prepared the original draft. M.K.K.M. and J.P.A. reviewed and edited the original draft. S.V. supervised, and A.P. administered the work. All authors have read and agreed to the published version of the manuscript.

**Funding:** This research received no external funding.

**Institutional Review Board Statement:** Not applicable.

**Informed Consent Statement:** Not applicable.

**Data Availability Statement:** Data are contained within the article.

**Conflicts of Interest:** The authors declare no conflicts of interest.



## References

1. Goundar, S.S.; Pillai, M.R.; Mamun, K.A.; Islam, F.R.; Deo, R. Real time condition monitoring system for industrial motors. In Proceedings of the 2015 IEEE 2nd Asia-Pacific World Congress on Computer Science and Engineering (APWC on CSE), Nadi, Fiji, 2–4 December 2015; pp. 1–9.
2. Tong, W. *Mechanical Design of Electric Motors*; CRC Press: Boca Raton, FL, USA, 2014.
3. Crowder, R. *Electric Drives and Electromechanical Systems: Applications and Control*; Butterworth-Heinemann: Cambridge, MA, USA, 2019.
4. Shaikh, S.; Kumar, D.; Hakeem, A.; Soomar, A.M. Protection System Design of Induction Motor for Industries. *Model. Simul. Eng.* **2022**, *2022*, 7423018. [CrossRef]
5. Majid, M.; Habib, S.; Javed, A.R.; Rizwan, M.; Srivastava, G.; Gadekallu, T.R.; Lin, J.C.W. Applications of wireless sensor networks and internet of things frameworks in the industry revolution 4.0: A systematic literature review. *Sensors* **2022**, *22*, 2087. [CrossRef] [PubMed]
6. Kumar, A.S.; Iyer, E. An industrial iot in engineering and manufacturing industries—Benefits and challenges. *Int. J. Mech. Prod. Eng. Res. Dev. (IJMPERD)* **2019**, *9*, 151–160.
7. Sorooshian, S.; Panigrahi, S. Impacts of the 4th Industrial Revolution on Industries. *Walailak J. Sci. Technol. (WJST)* **2020**, *17*, 903–915. [CrossRef]
8. Niranjani, M.; Madhukar, N.; Ashwini, A.; Muddasar, J.; Saish, M. IoT based industrial automation. *IOSR J. Comput. Eng. (IOSR-JCE)* **2017**, *2*, 36–40.
9. Fenger, M.; Stone, G.C.; Lloyd, B.A. The impact of humidity on PD inception voltage as a function of rise-time in random wound motors of different designs. In Proceedings of the IEEE Annual Report Conference on Electrical Insulation and Dielectric Phenomena, Cancun, Mexico, 20–24 October 2002; pp. 501–505.
10. Fenger, M.; Stone, G.C. Investigations into the effect of humidity on stator winding partial discharges. *IEEE Trans. Dielectr. Electr. Insul.* **2005**, *12*, 341–346. [CrossRef]
11. Stone, G.C.; Warren, V.; Fenger, M. Case studies on the effect of humidity on stator winding partial discharge activity. In Proceedings of the Conference Record of the 2002 IEEE International Symposium on Electrical Insulation (Cat. No. 02CH37316), Boston, MA, USA, 7–10 April 2002; pp. 579–581.
12. Vijayalakshmi, S.; Karthikha, R.; Paramasivam, A.; Bhaskar, K.B. Condition Monitoring of Industrial Motors using Machine Learning Classifiers. In Proceedings of the ICICNIS 2020, Kottayam, India, 10–11 December 2020; pp. 1–7.
13. Jeyalakshmi, C.; Subhasri, G.; Muruganantham, T. Smart Industrial Motor Monitoring and Control using myRIO. In Proceedings of the 2020 IEEE Fourth International Conference on Inventive Systems and Control (ICISC), Coimbatore, India, 8–10 January 2020; pp. 1–5.
14. Agyare, O.R.; Asiedu-Asante, A.B.; Biney, A.R. Fuzzy Logic Based Condition Monitoring of a 3-Phase Induction Motor. In Proceedings of the 2019 IEEE AFRICON, Accra, Ghana, 25–27 September 2019; pp. 1–8.
15. Lilo, M.A.; Mohammad, M.J. Design and implementation of wireless system for vibration fault detection using fuzzy logic. *IAES Int. J. Artif. Intell.* **2020**, *9*, 545.
16. Purwanto, F.H.; Utami, E.; Pramono, E. Design of server room temperature and humidity control system using fuzzy logic based on microcontroller. In Proceedings of the 2018 IEEE International Conference on Information and Communications Technology (ICOIACT), Yogyakarta, Indonesia, 6–7 March 2018; pp. 390–395.
17. Caicedo-Narvaez, C. Just-in-time Detection of Stator Short Circuit Faults in Electric Machines. Doctoral Dissertation, University of Texas at Dallas, Ann Arbor, MI, USA, 2020.
18. Kang, A.; Tian, M.; Li, C.; Song, J.; Suraci, S.V.; Li, W.; Lin, L.; Lei, Z.; Fabiani, D. Development and pattern identification of end-winding discharge under effect of relative humidity and temperature for HV motors. *High Voltage* **2020**, *5*, 434–443. [CrossRef]
19. Zuraidah, T.; Hamdani, Melly, A.; Solly, A.; Siti, A. Enhance Method Power Point Tracking Wear Method DC-DC Converter based on Fuzzy Logic of Bayu Power Plant. *Int. J. Phys. Appl. Sci.* **2020**, *7*, 1–6.
20. Li, C.; Mo, L.; Tang, H.; Yan, R. Lifelong Condition Monitoring Based on NB-IoT for Anomaly Detection of Machinery Equipment. *Procedia Manuf.* **2020**, *49*, 144–149.
21. Mykoniatis, K. A Real-Time Condition Monitoring and Maintenance Management System for Low Voltage Industrial Motors Using Internet-of-Things. *Procedia Manuf.* **2020**, *42*, 450–456. [CrossRef]
22. Kececiloglu, O.F.; Gani, A.; Sekkeli, M. Design and Hardware Implementation Based on Hybrid Structure for MPPT of PV System Using an Interval Type-2 TSK Fuzzy Logic Controller. *Energies* **2020**, *13*, 1842. [CrossRef]

**Disclaimer/Publisher’s Note:** The statements, opinions and data contained in all publications are solely those of the individual author(s) and contributor(s) and not of MDPI and/or the editor(s). MDPI and/or the editor(s) disclaim responsibility for any injury to people or property resulting from any ideas, methods, instructions or products referred to in the content.

# A High-Level Synthesis Approach for a RISC-V RV32I-Based System on Chip and Its FPGA Implementation <sup>†</sup>

Onur Toker

Electrical and Computer Engineering, Florida Polytechnic University, Lakeland, FL 33805, USA; otoker@floridapoly.edu

<sup>†</sup> Presented at the 10th International Electronic Conference on Sensors and Applications (ECSA-10), 15–30 November 2023; Available online: <https://ecsa-10.sciforum.net/>.

**Abstract:** In this paper, we present a RISC-V RV32I-based system-on-chip (SoC) design approach using the Vivado high-level synthesis (HLS) tool. The proposed approach consists of three separate levels: The first one is an HLS design and simulation purely in C++. The second one is a Verilog simulation of the HLS-generated Verilog implementation of the CPU core, a RAM unit initialized with a short assembly code, and a simple output port which simply forwards the output data to the simulation console. Finally, the third level is the implementation and testing of this SoC on a low-cost FPGA board (Basys3) running at a clock speed of 100 MHz. A sample C code was compiled using the GNU RISC-V compiler tool chain and tested on the HLS-generated RISC-V RV32I core as well. The HLS design consists of a single C++ file with fewer than 300 lines, a single header file, and a testbench in C++. Our design objectives are that (1) the C++ code should be easy to read for an average engineer, and (2) the coding style should dictate minimal area, i.e., minimal resource utilization, without significantly degrading the code readability. The proposed system was implemented for two different I/O bus alternatives: (1) a traditional single clock cycle delay memory interface and (2) the industry-standard AXI bus. We present timing closure, resource utilization, and power consumption estimates. Furthermore, by using the open-source synthesis tool *yosys*, we generated a CMOS gate-level design and provide gate count details. All design, simulation, and constraint files are publicly available in a GitHub repo. We also present a simple dual-core SoC design, but detailed multi-core designs and other advanced futures are planned for future research.

**Keywords:** high-level synthesis; RISC-V; system on chip; FPGA; multi-core architectures

**Citation:** Toker, O. A High-Level Synthesis Approach for a RISC-V RV32I-Based System on Chip and Its FPGA Implementation. *Eng. Proc.* **2023**, *58*, 72. <https://doi.org/10.3390/ecsa-10-16212>

Academic Editor: Jean-marc Laheurte

Published: 15 November 2023



**Copyright:** © 2023 by the authors. Licensee MDPI, Basel, Switzerland. This article is an open access article distributed under the terms and conditions of the Creative Commons Attribution (CC BY) license (<https://creativecommons.org/licenses/by/4.0/>).

## 1. Introduction

In this paper, we present a RISC-V RV32I-based system-on-chip (SoC) design and implementation using a high-level synthesis (HLS) approach. The complete core design was carried out with HLS and then simulated at the C level, then at the Verilog level, and finally tested on a low-cost FPGA board at 100 MHz clock speed. Both assembly programs and C programs compiled with the GNU RISC-V toolchain were used as RAM images for testing the HLS-generated core. The proposed HLS core design has a single C++ file with fewer than 300 lines and is designed to be both highly-readable and use minimal hardware resources.

There are several published papers for CPU design in different hardware description languages (HDLs). In [1], a very simple reduced instruction set (RISC) processor design is presented with about 120 lines of Verilog code. See [2–4] and references therein for related work. RISC-V is a free and open source instruction set architecture [5,6]. The standard defines various ISAs starting with the base architecture RV32I. There are numerous Verilog implementations of RISC-V architectures, with varying degrees of performance and resource utilization. The paper [7] presents a review of some of the well-known open source designs and links to relevant GitHub repos for source codes. One disadvantage of these

Verilog implementations is the length of the source codes, which is the main motivation for the HLS-based approach adapted in this work. The HLS-based approach can be quite useful for rapid prototyping of complex ideas, especially for systems with complex state machines. To the best of author's knowledge, there is limited published work where an HLS-based approach is used for a RISC-V core design. In [8], an HLS design is presented, but the source code is split into multiple files, making it difficult to read. This work presents a single file design which is relatively short, easily readable, and yet suitable for an FPGA implementation with clock speeds of 100 MHz. Open source RISC-V cores can be quite useful for computer architecture education too; see [9]. The proposed HLS RISC-V RV32I core source codes are available in the public GitHub repo [10]. Finally, the author would like to cite [11] as a source of inspiration for this work.

This paper is organized as follows: In Section 2, we summarize the RISC-V RV32I instruction set architecture. In Section 3, a high-level synthesis approach for design and simulation is presented. Verilog simulations of our RISC-V SoC are presented in Section 4, CMOS gate-level design using the open-source synthesis tool yosys and gate count details are given in Section 5, and the FPGA implementation and testing are presented in Section 6. A sample C program was used for testing the HLS-generated core, as outlined in Section 7. A multi-core RISC-V SoC approach is outlined in Section 8, and finally some concluding remarks are given in Section 9.

## 2. RISC-V RV32I Architecture

In this section, we summarize the RISC-V RV32I instruction set architecture (ISA) [5,6] in Table 1. From a programming perspective, there are 32 registers  $x0 \dots x31$  and a program counter PC, all having 32-bit size. The register  $x0$  is hardwired to 0, and the instructions are divided into six different groups R (Register), I (Immediate), S (Store), B (Branch), J (Jump), and U (Upper) [5,6]. Full details of the instruction encoding and instruction fields are given in [5,6]. For the HLS implementation of the instruction decoder stage, we divide I type instructions into IA (Immediate arithmetic), IM (Immediate memory), IJ (Immediate jump), and IE (Immediate exception) groups. Furthermore, U type instructions are divided into U1 (Upper1) and U2 (Upper2). All of the instructions are 32 bits in size and have a 7-bit opcode field located between bits 6 down to 0. Furthermore, there are 3-bit `func3`, 7-bit `func7`, and `imm` fields, but not all instructions have all of these three additional fields [5,6].

The `sra` and `srai` instructions use the most significant bit (MSB) extension rule, whereas the instructions `sltu`, `sltiu`, `lbu`, `lhu`, `bltu`, and `bgeu` use the zero extension rule. The instructions `ecall` and `ebreak` are implemented as trap/halt. All unaligned memory accesses are also implemented as trap/halt.

**Table 1.** RV32I instructions [5,6].

Inst	Type	Description
<code>add</code>	R	$rd = rs1 + rs2$
<code>sub</code>	R	$rd = rs1 - rs2$
<code>xor</code>	R	$rd = rs1 \wedge rs2$
<code>or</code>	R	$rd = rs1 \vee rs2$
<code>and</code>	R	$rd = rs1 \& rs2$
<code>sll</code>	R	$rd = rs1 \ll rs2$
<code>srl</code>	R	$rd = rs1 \gg rs2$
<code>sra</code>	R	$rd = rs1 \ggg rs2$
<code>slt</code>	R	$rd = (rs1 < rs2)?1:0$
<code>sltu</code>	R	$rd = (rs1 < rs2)?1:0$

Table 1. Cont.

Inst	Type	Description
addi	IA	$rd = rs1 + imm$
xori	IA	$rd = rs1 \wedge imm$
ori	IA	$rd = rs1   imm$
andi	IA	$rd = rs1 \& imm$
slli	IA	$rd = rs1 \ll imm[0:4]$
srlr	IA	$rd = rs1 \gg imm[0:4]$
srai	IA	$rd = rs1 \gg imm[0:4]$
slti	IA	$rd = (rs1 < imm)?1:0$
sltiu	IA	$rd = (rs1 < imm)?1:0$
lb	IM	$rd = M[rs1+imm][0:7]$
lh	IM	$rd = M[rs1+imm][0:15]$
lw	IM	$rd = M[rs1+imm][0:31]$
lbu	IM	$rd = M[rs1+imm][0:7]$
lhu	IM	$rd = M[rs1+imm][0:15]$
sb	S	$M[rs1+imm][0:7] = rs2[0:7]$
sh	S	$M[rs1+imm][0:15] = rs2[0:15]$
sw	S	$M[rs1+imm][0:31] = rs2[0:31]$
beq	B	$if(rs1 == rs2) PC += imm$
bne	B	$if(rs1 != rs2) PC += imm$
blt	B	$if(rs1 < rs2) PC += imm$
bge	B	$if(rs1 \geq rs2) PC += imm$
bltu	B	$if(rs1 < rs2) PC += imm$
bgeu	B	$if(rs1 \geq rs2) PC += imm$
jal	J	$rd = PC+4; PC += imm$
jalr	IJ	$rd = PC+4; PC = rs1 + imm$
lui	U1	$rd = imm \ll 12$
auipc	U2	$rd = PC + (imm \ll 12)$
ecall	IE	Trap/Halt
ebreak	IE	Trap/Halt

### 3. HLS Approach for Design and Simulation

The HLS design consists of the C++ file `riscv32i.cc` and the header file `riscv32i.h`. There is also a C simulation testbench file `riscv32i_tb.cc`. In this section, we simply summarize the main design ideas. The full source code is available in our GitHub repo [10].

We start with the outline of the design file `riscv32i.cc`; see Outline I. This file has only the `cpu()` function, which has two pointer arguments. For C simulation, they have the usual semantics, but for hardware synthesis, the first one is interpreted as a single-port RAM, and the other is implemented as a 4-bit write-strobe signal. The local array `reg_file[]` is interpreted as a multi-port RAM for hardware synthesis, which will correspond to the internal register file. The HLS tool has a standard C compiler which works according to standard semantic rules for simulations, but for hardware synthesis semantic details are different and can be controlled by using the `#pragma HLS` directives. Full details are available in the Vivado HLS User Guide [12].

Outline I: Outline of the design file `riscv32i.cc`

```

#include "riscv32i.h"
#include <stdio.h>
#include <stdint.h>

// Write strobe
#define wstrb (*ptrb)

void cpu(arch_t mem[MEM_SIZE], volatile strb_t* ptrb) {
#pragma HLS RESOURCE variable=mem core=RAM_1P_BRAM
#pragma HLS INTERFACE ap_none port=ptrb

    // Register file
    arch_t reg_file[REGFILE_SIZE];

    for (int i = 0; i < REGFILE_SIZE; i++)
        reg_file[i] = 0;

    arch_t pc = 0;

    PROGRAM_LOOP: while (true) {
        // Fetch
        arch_t insn = mem[pc >> 2];

        // Decode
        opcode_t opcode = insn(6,0);
        ...

        // Execute
        switch (opcode) {
            case OPCODE_R:
                case OPCODE_IA:
                    switch(...) {
                        ...
                    }
                    break;
            ...
        }

        // Write back to reg_file or memory or PC

        // Branch handling
    }
}

```

As seen in Outline I, immediately after resetting the program counter and all of the registers are initialized to zero, there is an infinite while loop which will be exited if an ECALL or EBREAK instruction is executed or an unaligned memory access is requested, basically causing the CPU core to halt.

The HLS tool converts this while loop to a state machine with 11 states using the one-hot encoding. Inside the loop, we have the usual instructions fetch, decode, execute, write-back, and branch handling. For example, `insn = mem[pc >> 2]` will be synthesized as a memory read operation, and `opcode = insn(6,0)` will be synthesized as selecting the least significant 7 bits of the 32-bit value read from the memory. Note that, by using the operator overloading features of C++, we are able to express slicing and concatenation in C++; see [10,12] for full details. For example, in the instruction decode stage, we have the lines

```

immI = ( ((ap_int<ARCH>) insn) >> 20 );
immS = ( immI(31,5), insn(11,8), insn(7,7) );
immB = ...
immJ = ...
immU = ( insn(31,12), ((ap_uint<12>) 0) );

```

which correspond to generating the 32-bit immediate value for various types of instructions. Note that `ap_uint<p>` is used for p-bit unsigned integers, `insn(p,q)` corresponds to slicing, and `( ... , ... , ... )` corresponds to concatenation. These are possible because of the standard operator loading features of C++. Note that the C simulation semantics and the hardware synthesis semantics are different.

There are various switch statements, which are synthesized as wide-multiplexers. Nested switch statements correspond to cascaded multiplexers. To make sure that minimal number of adders, comparators, barrel-shifters, etc., are synthesized, and no hardware resources are wasted or underutilized, we defined first program variables `src1`, `src2`, `res` and then wrote several switch statements. This coding style may appear slightly unusual but is still highly readable and is adapted purely for optimal hardware synthesis. In other words, the C++ coding style used in HLS greatly affects the final generated

hardware, and we tried to keep a reasonable balance between C++ code readability and hardware optimality.

The HLS tool automatically generates Verilog files in a human-readable format but also allows C-simulation-based testing using the file `riscv32i_tb.cc`. This C-simulation testbench reads a text file of hexadecimal values in a human-readable format, initializes the memory by using these values, and passes the control to the `cpu()` function. Immediately after return, all register values and the memory are dumped to separate text files. In Figure 1, Vivado HLS C simulation for the following short assembly program is given:

```

li      x1, 1020
sw      x0, 0(x1)
loop: lw  x2, 0(x1)
      addi x2, x2, 1
      sw   x2, 0(x1)
      j    loop

```

Values stored in registers and memory as well as internal signals are displayed in the debug window. Hexadecimal values for each instruction are written to the file `mem.txt`, and conversion is carried out by using an online assembler tool. See [10] for full details.

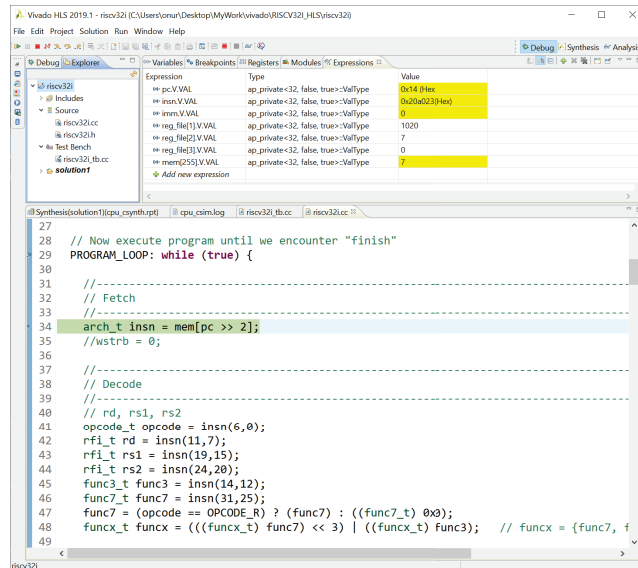


Figure 1. Vivado HLS C simulation.

#### 4. RISC-V SoC Simulation in Verilog

In this section, we present Verilog simulation of the HLS-generated RISC-V core. Either one can copy the HLS-generated Verilog files to the Vivado project folder or create an IP object for a block-diagram-based design. We simply copy and paste the generated Verilog files from one folder to the other, but in the next FPGA-based design we will use the block-diagram-based design approach for better visualization of the overall system.

## Outline II: Outline of the System Verilog testbench

```

module sys_tb();

localparam T=10;

logic clk, reset, start, done, idle, ready, we, ce, vld;
logic [3:0] wstrb;
logic [9:0] addr;
logic [31:0] val_i, val_o;

cpu U1(
    .ap_clk(clk),
    .ap_rst(reset),
    .ap_start(start),
    .ap_idle(idle),
    .ap_ready(ready),
    .mem_V_address0(addr),
    .mem_V_ce0(ce),
    .mem_V_we0(we),
    .mem_V_d0(val_i),
    .mem_V_q0(val_o),
    .pstrb_V(wstrb)
);

mem U3(.clk(clk), .we(we), .addr(addr),
    .din(val_i), .dout(val_o), .wstrb(wstrb) );

//SRAM U4 (.clka(clk), .wea({4{we}} & wstrb), .addr(addr),
//    .dina(val_i), .douta(val_o) );

initial clk = 0;
always #(T/2) clk = ~clk;

initial
begin
    ...
    wait(idle==1);
    $stop;
end
endmodule

```

The simulation testbench outline is given in Outline II, and the RAM with the I/O devices is presented in Outline III. Basically, we have a simple system on chip consisting of a single RISC-V RV32I core, a 4 KB RAM with single clock cycle read/write delay, and a 32-bit output port at memory address 0x0ff.

## Outline III: Outline of the RAM and I/O devices

```

module mem(clk, we, addr, din, dout, wstrb);

input clk, we;
input [3:0] wstrb;
input [9:0] addr, read_addr;
input [31:0] din, dout;
logic [31:0] ram [0:1023];

always @(posedge clk)
begin
    if (we) begin
        if (wstrb[0]) ram[addr][ 7: 0] <= din[ 7: 0];
        if (wstrb[1]) ram[addr][15: 8] <= din[15: 8];
        if (wstrb[2]) ram[addr][23:16] <= din[23:16];
        if (wstrb[3]) ram[addr][31:24] <= din[31:24];
        /* add memory-mapped IO here */
        if (addr == 255)
            $write("%c", din[7:0]); // Change %c to %x
    end
    read_addr <= addr;
end
assign dout = ram[read_addr];

initial
    $readmemh("C:/Users/onur/Desktop/MyWork/vivado/RISCv32I_HLS/mem.txt", ram);

//initial begin
//    ram[0] = 32'h 3fc00093; //    l1    x1,1020
//    ram[1] = ...
//end
endmodule

```

In Figure 2, Verilog simulation results are shown. We are using the assembly program given in the previous section, which basically writes the values 0, 1, 2, ... to the address 0x0ff. The program counter PC is shown in the timing diagram, and the values written to the output port at address 0x0ff are shown both in the simulation console and the timing diagram. There is a specific reason why `$write("%c", din[7:0])` is used for the memory mapped I/O at address 0x0ff. If we use a C-compiler and implement `putc()` as a write to the I/O address 0x0ff, then all `printf(...)` and `cout << ...` will write to

the Verilog simulation console. This allows more complex C/C++ programs to be tested with the HLS-generated RISC-V core.

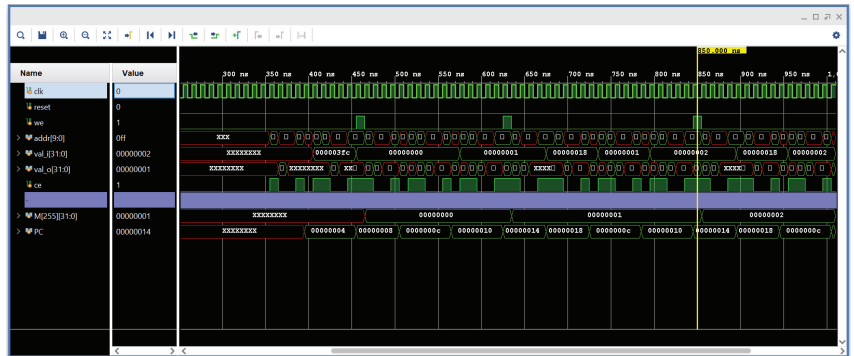


Figure 2. Verilog simulation.

In our simulation testbench, we also have a block RAM option, shown as SRAM. This allows the HLS-generated RISC-V core to be tested using block RAMs available on most Xilinx FPGAs; see Figure 3.

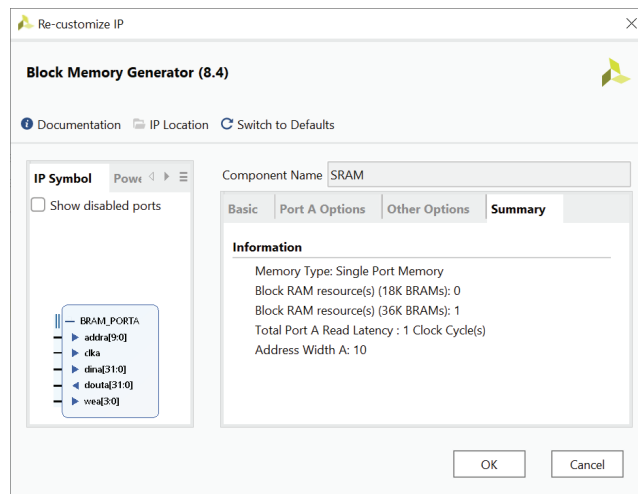


Figure 3. Block RAM should have single clock cycle read/write delay.

### 5. RISC-V RV32I Core Synthesis Gate Counts

In this short section, we present gate count results for the CMOS gate-level design generated by the open-source synthesis tool yosys. The following script is for the synthesis tool

```
read_verilog cpu.v cpu_reg_file.V.v
hierarchy -check
proc; opt; fsm; opt; memory; opt
techmap; opt
read_liberty -lib cmos_cells.lib
abc -liberty cmos_cells.lib
splitnets -ports; opt
stat
```

and the following gate-count results are reported by the synthesis tool:



```

=== cpu ===

Number of wires:          8282
Number of cells:
  $_DFF_P_                321
  NAND                   2689
  NOR                     3714
  NOT                     924

=== cpu_reg_file_V ===

Number of wires:          7714
Number of cells:
  $_DFF_P_                1056
  NAND                   4726
  NOR                     1505
  NOT                     387
    
```

In summary, a total of 1377 D-type flip-flops are used, including the register file of depth 32 and width 32. We have forced the synthesis tool to design using only two input NAND and NOR gates, and with that constraint the total number of two-input NAND gates is 7415, two-input NOR gates is 5219, and NOT gates is 1311.

### 6. RISC-V SoC Implementation on an FPGA

In this section, we will present a simple RISC-V SoC implemented on an FPGA. High-level details are presented in Figure 4, and the elaborated design is shown in Figure 5.

The elaborated design has 1296 cells and 1968 nets.

The resource utilization of the implemented design is 1078 LUT (5.18%), 326 FF (0.78%), and 3% of the BRAM. The final system has 1.41 ns worst-case negative slack for the setup time for 100 MHz clock. The power consumption is estimated as 81 mW at 100 MHz clock. Figure 6 shows the FPGA implementation of the SoC for the Basys3 board. Note that the whole SoC design fits into a portion of the clock region X0Y0. The large rectangular block at the center of Figure 6 is the 4 KB RAM used for the system on chip.

We use the same assembly program given in Section 3 and make sure that the hex values corresponding to assembly instructions are loaded to the SoC RAM. After the system is reset using the button btnC, the CPU core can be started using the button btnU. Figure 7 shows a Basys3 board implementation of our RISC-V SoC with the output port connected to the on-board LEDs. Note that bits 20 down-to 13 of the 32-bit value written to memory are routed to the I/O port using the slice block shown in Figure 4. The assembly program given in Section 3 has a loop execution time of 170 ns, i.e., 17 clock cycles loop execution time. The slicing block effectively slows down the counting speed so that counting can be observed by the naked eye.

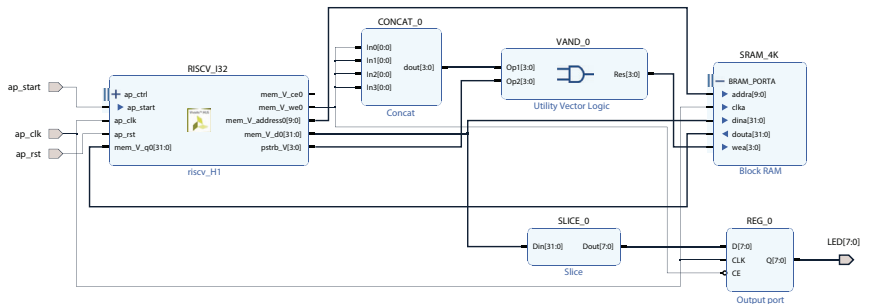
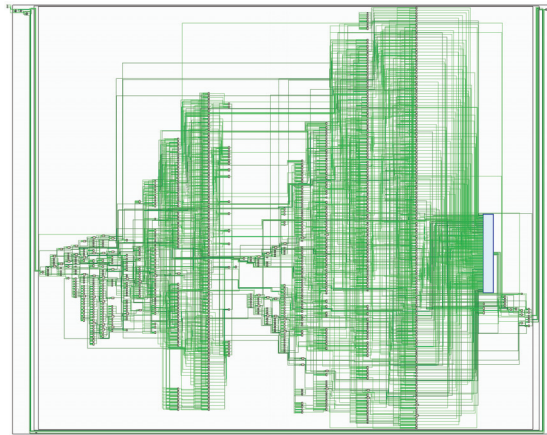
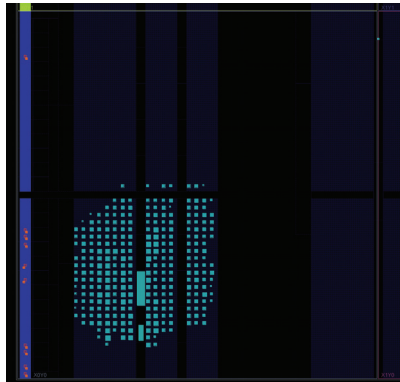


Figure 4. A RISC-V SoC block diagram for FPGA implementation.



**Figure 5.** Elaborated design of the RISC-V SoC. The blue box on the right corresponds to the register file.



**Figure 6.** RISC-V SoC FPGA implementation for the Basys3 board fits into a portion of the clock region X0Y0.



**Figure 7.** RISC-V SoC implemented on a Basys3 board.

### 7. Testing with a Sample C Program

We used a short C program for simulating the RISC-V H1 core designed earlier. Our testcode is given below

```
#define OUTPUTPORT (0x0ff)
#include <stdint.h>

void main(void);
```

```

void main(void) {
*((volatile uint32_t*)OUTPORT) = 'R';
*((volatile uint32_t*)OUTPORT) = 'I';
*((volatile uint32_t*)OUTPORT) = 'S';
*((volatile uint32_t*)OUTPORT) = 'C';
*((volatile uint32_t*)OUTPORT) = '\n';
}

```

It is compiled with the GNU RISC-V compiler to generate the RAM image. As shown in Outline III, we have a \$readmemh to initialize the RAM for the Verilog simulation. Again as shown in the Outline III, all writes to address 0x0ff are forwarded to the simulation console using the \$write command. In summary, when the SoC is simulated with the GNU RISC-V compiler to generate the RAM image, we see the string 'RISC' written to the console followed by a newline, which serves as another verification of the H1 core. In a future version of the paper, we will use longer C programs for more comprehensive testing.

### 8. A Multi-Core RISC-V SoC

In this section, we briefly summarize our multi-core RISC-V SoC implementation. We started by changing the memory interface from block RAM to a AXI master, i.e., changing the HLS directive to #pragma HLS INTERFACE m\_axi depth=1024 port=mem. This resulted in a different RISC-V RV32I core equipped with the AXI master interface. The Vivado HLS generates a Verilog implementation with 42 states, which we call the H2 core. For this AXI-equipped H2 core, we need to delete the write-strobe port, wstrb, and use

```

(mem[addr >> 2])( 7,0) = res;
(mem[addr >> 2])(16,0) = res;
(mem[addr >> 2])(32,0) = res;

```

to implement byte, word, and double-word sized memory write operations, respectively. Note that the bit-slicing operator (. . .) can be used both on the left- and right-hand side of expressions.

In Figure 8, we have a dual-core RISC-V RV32I system with 8K on-chip RAM, two 8-bit output ports, a 16-bit input port, and a single UART port. The H2 core does not have a tightly coupled memory (TCM) inside the unit, but this will be addressed in a future version of the paper. Basically, in the current implementation, both cores are using the on-chip static RAM over the AXI bus. All GPIOs and the UART unit are also on the AXI-bus. We have added a JTAG to AXI unit which can be used for debugging and initialization of the on-chip static RAM. For this dual-core SoC to function properly, both cores should have different reset vectors so that they can execute different programs independently.

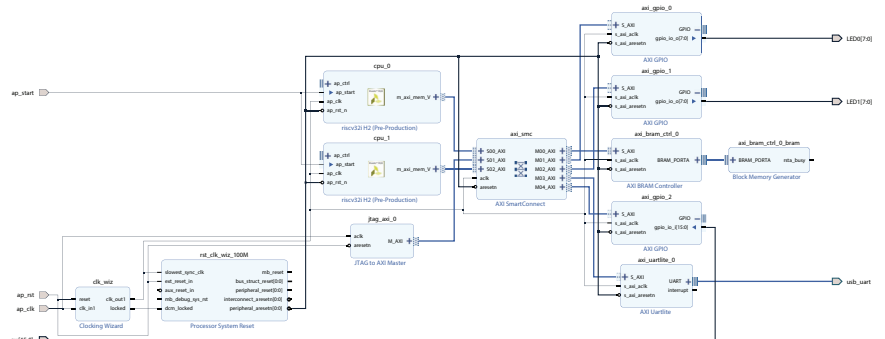


**Figure 8.** A dual-core RISC-V SoC for FPGA implementation.

Based on our preliminary results, we see that the dual-core RISC-V system shown in Figure 8 does fit into a Basys3 board.

## 9. Conclusions

In this paper, we have presented a high-level synthesis approach for RISC-V RV32I system design. The CPU core was designed and simulated at the C level, then the HLS-generated Verilog code was tested with RAM and I/O devices at the Verilog simulation level. Finally, the complete system-on-chip design with memory and I/O devices was implemented and tested on a low-cost FPGA board. Timing closure, resource utilization, and power consumption estimates are presented. The CMOS gate-level design and gate counts were generated by using an open-source synthesis tool. We have also outlined a dual-core system design. The HLS-generated CPU core has 14 states for a traditional single clock cycle delay memory interface and 42 states if the AXI bus support is needed. For such more complex systems, design in Verilog will be more demanding and error-prone compared to an HLS-based approach. Detailed analysis of multi-core designs are planned for future research.

**Funding:** Funding is provided by NSF-1919855, Advanced Mobility Institute grants GR-2000028, GR-2000029, and Florida Polytechnic University startup grant GR-1900022.

**Institutional Review Board Statement:** Not applicable.

**Informed Consent Statement:** Not applicable.

**Data Availability Statement:** Not applicable.

**Acknowledgments:** The author would like to acknowledge the support from NSF-1919855, Florida Polytechnic University, and AMI.

**Conflicts of Interest:** The author declares no conflicts of interest.

## References

- Depablo, S.; Cebrián, J.A.; Herrero-de Lucas, L.C.; Rey-Boué, A.B. A very simple 8-bit RISC processor for FPGA. In Proceedings of the FPGAWorld Conference 2006, Stockholm, Sweden, November 2006; pp. 9–15.
- Archana, H.R.; Sanjana, T.; Bhavana, H.T.; Sunil, S.V. System Verification and Analysis of ALU for RISC Processor. In Proceedings of the 2021 7th International Conference on Advanced Computing and Communication Systems (ICACCS), Coimbatore, India, 19–20 March 2021; Volume 1, pp. 1785–1789. [CrossRef]
- Wang, L.; Yu, Z.; Zhang, D.; Qin, G. Research on Multi-Cycle CPU Design Method of Computer Organization Principle Experiment. In Proceedings of the 2018 13th International Conference on Computer Science Education (ICCSE), Colombo, Sri Lanka, 8–11 August 2018; pp. 1–6. [CrossRef]
- Eljhani, M.M.; Kepuska, V.Z. Reduced Instruction Set Computer Design on FPGA. In Proceedings of the 2021 IEEE 1st International Maghreb Meeting of the Conference on Sciences and Techniques of Automatic Control and Computer Engineering MI-STA, Tripoli, Libya, 25–27 May 2021; pp. 316–321. [CrossRef]
- Waterman, A.; Asanović, K. *The RISC-V Instruction Set Manual, Volume I: Unprivileged ISA Version 20191213*; RISC-V International: San Francisco, CA, USA, 2021.
- RV32I Base Integer Instruction Set, Version 2.1. Available online: <https://five-embeddev.com/riscv-isa-manual/latest/rv32.html> (accessed on 14 November 2023).
- Höller, R.; Haselberger, D.; Ballek, D.; Rössler, P.; Krapfenbauer, M.; Linauer, M. Open-Source RISC-V Processor IP Cores for FPGAs — Overview and Evaluation. In Proceedings of the 2019 8th Mediterranean Conference on Embedded Computing (MECO), Budva, Montenegro, 10–14 June 2019; pp. 1–6. [CrossRef]
- Rokicki, S.; Pala, D.; Paturel, J.; Sentiéys, O. What You Simulate Is What You Synthesize: Design of a RISC-V Core from C++ Specifications. In Proceedings of the RISC-V Workshop 2019, Zurich, Switzerland, June 2019; pp. 1–2.
- Harris, S.L.; Chaver, D.; Piñuel, L.; Gomez-Perez, J.; Liaqat, M.H.; Kakakhel, Z.L.; Kindgren, O.; Owen, R. RVfpga: Using a RISC-V Core Targeted to an FPGA in Computer Architecture Education. In Proceedings of the 2021 31st International Conference on Field-Programmable Logic and Applications (FPL), Dresden, Germany, 30 August–3 September 2021; pp. 145–150. [CrossRef]
- Toker, O. GitHub Repo for RISC-V RV32I HLS CPU Core H1. 2021. Available online: [https://github.com/onurtoker/hls\\_riscv](https://github.com/onurtoker/hls_riscv) (accessed on 14 November 2023).

11. Moreau, T. CPU Design in HLS. 2018. Available online: <https://gitlab.cs.washington.edu/cse599s/hls-tutorials/-/tree/master/part3> (accessed on 14 November 2023).
12. Vivado Design Suite User Guide, High-Level Synthesis. 2019. Available online: [https://www.xilinx.com/support/documentation/sw\\_manuals/xilinx2019\\_1/ug902-vivado-high-level-synthesis.pdf](https://www.xilinx.com/support/documentation/sw_manuals/xilinx2019_1/ug902-vivado-high-level-synthesis.pdf) (accessed on 14 November 2023).

**Disclaimer/Publisher's Note:** The statements, opinions and data contained in all publications are solely those of the individual author(s) and contributor(s) and not of MDPI and/or the editor(s). MDPI and/or the editor(s) disclaim responsibility for any injury to people or property resulting from any ideas, methods, instructions or products referred to in the content.

Proceeding Paper

# Predicting Heart Disease Using Sensor Networks, the Internet of Things, and Machine Learning: A Study of Physiological Sensor Data and Predictive Models <sup>†</sup>

Neelamadhab Padhy

School of Engineering and Technology, Department of Computer Science and Engineering, GIET University, Gunupur 765022, Odisha, India; dr.neelamadhab@giet.edu or dr.neelamadhab@gmail.com

<sup>†</sup> Presented at the 10th International Electronic Conference on Sensors and Applications (ECSA-10), 15–30 November 2023; Available online: <https://ecsa-10.sciforum.net/>.

**Abstract:** The Internet of Things (IoT) and sensor networks are used for structural health monitoring (SHM). This study aimed to create a model for predicting cardiac disease using sensor networks, the IoT, and machine learning. Through wearable sensors, physiological data, such as heart rate, blood pressure, and oxygen saturation levels, were collected from patients. Data were subsequently processed and translated into an analysis-ready format. The most important predictors of heart disease were identified using feature selection techniques. Accuracy, precision, recall, F1-score, etc., were used to evaluate the performance of the proposed model. An SVM obtained the highest accuracy 93.87%.

**Keywords:** sensory data; CVD; machine learning; performance analysis

## 1. Introduction

In the 21st century, heart disease is one of the important causes of death in the world. Several researchers have discussed HDP using machine learning. However, early prediction and detection are important components in the healthcare sector. Wearable sensors play a crucial role in tracking physiological variables like heart rate, blood pressure, pulse oximeters, activity sensors, temperature sensors, respiration sensors, and electrocardiogram (ECG) signals. With the help of these sensors, a heart disease system can be properly monitored, and any irregularities can be easily identified. Machine learning algorithms can be suitable in this situation to create predictive models that can identify those who have a high risk of acquiring heart disease and allow for early therapies. Structural health monitoring is one of the leading technologies in the health industry, and focuses on the sensors that monitor health issues. SHM allows monitoring of the health of the cardiovascular system and detects any structural abnormalities or defects. A ML algorithm effectively finds unseen data in the database and provides an early warning signal to patients and healthcare providers. This can enable timely interventions, such as lifestyle changes, medication, or surgery, and improve patient outcomes. The objective of this project was to develop a predictive model for heart disease using sensor-based monitoring and machine learning algorithms. The model was trained using a dataset of physiological parameters collected from patients using wearable sensors. The model's effectiveness was assessed using established benchmarks like accuracy, precision, recall, F1-score, and the area under the receiver operating characteristic (ROC) curve. The ultimate objective is to create a sturdy and dependable model that can anticipate the probability of heart disease in patients, allowing for timely interventions that can enhance patient results and decrease healthcare expenses. The main motivation of this article is to enhance HDP models' accuracy using sensory data. Sensory data are electrocardiography (ECG) and blood tests, which are often limited by their reliance on intermittent measurements and

**Citation:** Padhy, N. Predicting Heart Disease Using Sensor Networks, the Internet of Things, and Machine Learning: A Study of Physiological Sensor Data and Predictive Models. *Eng. Proc.* **2023**, *58*, 73. <https://doi.org/10.3390/ecsa-10-16239>

Academic Editor: Francisco Falcone

Published: 15 November 2023



**Copyright:** © 2023 by the author. Licensee MDPI, Basel, Switzerland. This article is an open access article distributed under the terms and conditions of the Creative Commons Attribution (CC BY) license (<https://creativecommons.org/licenses/by/4.0/>).

subjective interpretation. These data are provided continuously and analyzed using novel classification approaches. These algorithms provide patterns and predict outcomes. The goal is to establish a heart disease prediction model employing sensor-based monitoring of the model's accuracy.

This paper includes four sections. Section 1 introduces structural health monitoring systems along with sensory devices. Section 2 provides insight into heart disease prediction through machine learning classifiers. Section 3 describes the proposed model and is followed by Section 4, results and discussion.

## 2. Literature Review

Many wearable sensor-based systems have been recently proposed to enhance the process of predicting heart disease. Tang, C. et al. [1] used mechanical sensors that allowed the monitoring of heart diseases. Their objective was to check pulse waves, heart rhythms, and BP. They also focused real-time sensory data for CVD prediction. Lin, J. et al. [2] conducted a systematic literature review (SLR) about various physiological signals for cardio problems. They also provided future direction. The authors Esther, G. M. et al. [3] developed one android App that monitors a patient's record and provides information to the patient's doctors. Finally, they integrated into the cloud, where machine learning predictions occurred. Salvi, S. et al.'s [4] research used machine learning to present a combined hybrid feature selection and classification strategy for heart disease prediction in a cloud-based IoT healthcare system. Kumar, R. et al.'s [5] study examined the application of linear regression as a machine learning approach for air quality time-series predictions. This study employed sensor data from three separate locations in Delhi and the National Capital Region to estimate air quality for the following day using linear regression as a machine learning approach, and the findings were significant. Kumar, P. M. et al. [6] applied various machine learning methods to predict heart disease, and logistic regression with majority voting achieved 88.59% accuracy, which is superior to that of previous techniques. A framework for dependable at-home assistance in healthcare was proposed by Hongxu and Niraj [7]. The primary focus of this architecture was data transmission between installed servers located in patient homes and distant hospitals. Daniele et al.'s [8] Their main finding was to increase the accuracy of the classifiers using deep learning techniques. They have proposed deep learning algorithms for enhancing accuracy and demonstrated their method that performs well in real-time on-node processing on smartphones and a wearable sensor platform. In their line of work, these gadgets serve as data collection points.

## 3. Proposed Model

The model consists into 4 different phases.

- **Phase 1:** We developed the proposed model for heart disease prediction using machine-learning classification algorithms. These are some of the steps followed: Data was collected from different sources through sensors. We deployed sensors (heart rate and blood pressure sensors, pulse oximeters, activity sensors, temperature sensors, respiration sensors, and electrocardiogram (ECG) signals) into the patient's body for testing.
- **Phase 2:** The major steps were data cleansing, normalization, and feature engineering (data preparation and analysis (DPA)). The objective of this step was to train the model. During DPA, we also identified relevant features in the dataset and then performed standard statistical tests and correlation analysis. When feature engineering was completed, we used novel machine learning classification algorithms (RF, DTC, K-NN, SVM, GNB, AdaBoost, Bagging, KNN, and LR) for CVD prediction. Figure 1 presents the structural healthcare monitoring model for cardiovascular prediction. In our proposed model we used machine learning classification algorithms like random forest, decision tree, K-NN, Gussian Naive Bayes, AdaBoost, bagging, and logistic regression are examples of ensemble learning algorithm that generates multiple numbers of decision trees during training and produces output of the predicted classes of the

individual trees. Normally, this classifier is satisfactory when we are dealing with high-dimensional data, as well as when found missing values in the dataset. A decision tree (DT) is one of the classifiers that allow splitting data into different homogeneous sets based on good features. It is simple because this classifier can handle both numerical and categorical data. K-NN is used for the same purpose, and classifies the unseen heart disease instances of a patient. A support vector machine is one of the powerful classifiers that finds the best hyperplane and separates data into different classes. It performs well using high-dimensional data and is capable of handling both linear and non-linear data. Gaussian Naive Bayes (GNB) is a probabilistic method that computes the likelihood of each class given the input data and chooses the class with the highest likelihood. It is simple and quick, and can handle data with multiple dimensions. AdaBoost is another type of ensemble learning technique which combines different weak classifiers to create another strong classifier. As our dataset was large, we used this algorithm to handle the imbalance issue, which can enhance the performance of weak classifiers. Bagging is also an ensemble learning technique that generates different subsets of training data and trains a classifier using each subset. We used bagging classifiers to address overfitting and enhance the overall performance of our model. This technique involves training multiple models on different subsets of the data and combining their predictions to achieve better generalization to new, unseen data. Logistic regression was also used for classification purposes to estimate the probability of a binary outcome. Mutual information feature selection (MIFS) is a technique that chooses relevant features by evaluating their mutual information using the target variable. MIFS can be particularly beneficial when working with sensor data because it can identify features that have a strong correlation with the target variable. This method evaluates how much information a feature provides about the target variable and selects those that have a high degree of mutual information. Using MIFS, it is possible to select the most relevant features and reduce the dimensionality of a dataset. This can improve the accuracy and efficiency of heart disease prediction models that use sensor data. Figure 1 shows the proposed structural healthcare monitoring model for cardiovascular prediction.

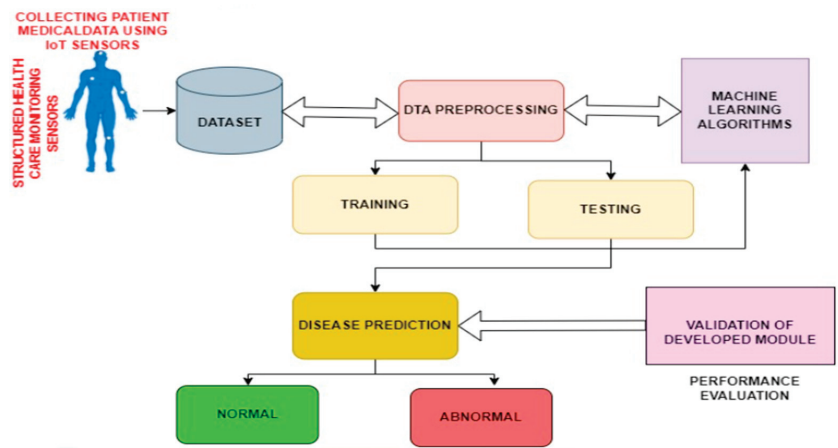


**Figure 1.** Structural healthcare monitoring model for cardiovascular prediction.

- Phase 3:** In this phase, we mainly trained the model and tested its effectiveness. The best model was identified during the training phase, and the model, after being trained, faced a challenging task of being tested on unfamiliar data. Performance metrics such as accuracy, precision, recall, F1-score, and area under the receiver operating characteristic (ROC) curve were evaluated. The required hyper parameters were used to enhance CVD prediction accuracy.



- Phase 4:** The model was validated using performance evaluation parameters on the test dataset, which we originally collected from patients through sensory data to ensure that it was not over fitting to the training data validation required.

#### 4. Results and Discussion

Table 1 presents analyses of classification models. Here, we compare the performance metrics of the ensemble classification models, including accuracy, precision, recall, F1-score, true-negative rate (TNR), and true-positive rate (TPR). Nine classification models were created to implement the proposed model: random forest (RF), decision tree classifier (DTC), K-nearest neighbour (K-NN), support vector machine (SVM), Gaussian Naive Bayes (GNB), AdaBoost, bagging, KNN, and logistic regression (LR) models. Our observations were that the SVM achieved the best accuracy (93.87%). Similarly, when, considering the TPR, LR achieved an accuracy of 90.20%. Table 2 shows the confusion matrices for the various classifiers.

**Table 1.** Comparative analyses of the ensemble classification models.

Algorithms	Accuracy	Precision	Recall	F1-Score	TNR	TPR
RF	89.90	88.47	87.07	85.11	78.4%	84%
DTC	88.87	85.62	86.82	82.30	82.5%	54%
K-NN	87.16	86.34	85.99	88.40	89.2%	82%
SVM	93.87	93.33	93.67	93.35	77.6%	82%
GNB	87.25	89.20	87.54	91.20	89.2%	86%
AdaBoost	85.20	88.45	85.56	87.20	78.6%	84%
Bagging	89.54	89.99	90.20	81.25	87.7%	86%
KNN	87.55	89.25	88.89	90.20	89.7%	87%
LR	92.25	90.20	89.99	90.09	90.4%	88%

**Table 2.** Confusion matrices and ROC curve values for the various classifiers.

Name of the Model	Accuracy	AUC	TNR	TPR	F-Score
RF	89.90	0.88	78.4%	84%	85.11
DTC	88.87	0.87	82.5%	54%	82.30
K-NN	87.16	0.86	89.2%	82%	88.40
SVM	93.87	0.91	77.6%	82%	93.35
GNB	87.25	0.88	89.2%	86%	91.20
AdaBoost	85.20	0.85	78.6%	84%	87.20
Bagging	89.54	0.90	87.7%	86%	81.25
KNN	87.55	0.87	89.7%	87%	90.20
LR	92.25	0.93	90.4%	88%	90.09

#### The Critical Observation

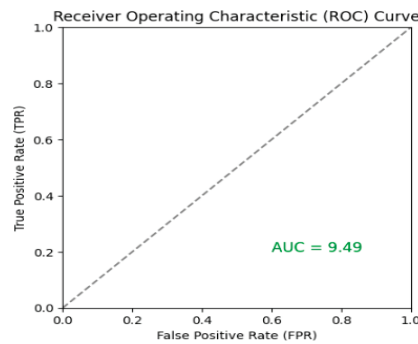
In the results mentioned above, the highest accuracy obtained is SVM, while AdaBoost had the lowest accuracy; accuracies ranged from 85.20% to 93.87%. Similarly, when we considered the AUC (area under the curve), it ranged from 0.85 to 0.93. The TPR and TNR are important components of any type of classifier. The highest TPR and TNR were found using the SVM and LR methods, whereas the lowest TPR was found using the DTC. Similarly, when we considered the F1-score as well as precision, the SVM obtained the highest classifier that could find positive cases.

Table 3 presents error analyses for several machine learning algorithms. We used nine models to indicate performance in Tables 1 and 2, as well for errors in Table 3. MSE and RMSE are considered the best error measurements for the classification model. Based on results presented in Table 3, it was concluded that the SVM had the lowest MSE and RMSE, which indicates that the SVM was the most accurate model for heart disease prediction. The model with the greatest MSE and the second-highest RMSE was LR, indicating that LR was the least accurate model.

**Table 3.** Details of the implementation environment used in the current study.

Model	MSE	RMSE
RF	0.37322	0.47185
DTC	0.33547	0.57805
K-NN	0.45281	0.59233
SVM	0.18752	0.32589
GNB	0.32558	0.50785
AdaBoost	0.45287	0.60890
Bagging	0.32897	0.54780

The dataset is one type of binary class classification nature and performed AUC = 0.94, which perfectly classified the positive and negative classifications. The ranges of AUC value start from zero to one. Here, zero indicates the random classifier and one indicates the perfect classifier. Figure 2 shows an AUC value of 0.94, and the model suggested a good level of discrimination between positive and negative classes. This graph is meant to illustrate the performance of the binary classifier. The below mentioned-Figure 2 represents the true positive vs true negative values and it is represented in the form of ROC curve. Similarly Figure 3 CVD prediction through boxplot representation.



**Figure 2.** True-positive rate vs. false-positive rate.

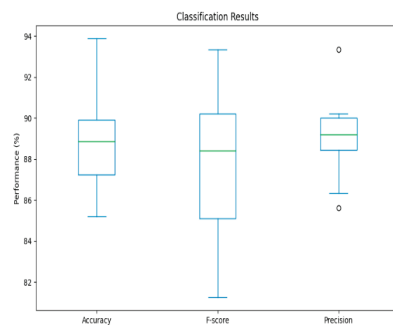


**Figure 3.** Boxplot representation of CVD prediction.

The above Figure 4 demonstrates the classification results for heart disease prediction. Regarding precision metrics, our results demonstrated that the highest result, i.e., 93.33%, indicated a low false-positive rate. The above figure represents the normalized confusion matrix for the heart disease classification task. This graph has a square matrix in which columns represent predicted classes and rows represent actual classes. These classes were divided into the total number of samples in each true class, which is why this graph is called a normalized matrix. The reason for doing this was to compare the performance of

different classes even though they each contain a number of independent samples. In the above figure, the diagonal matrix of each graph indicates the correctly identified classes and the off-diagonal value indicates misclassified observations. A classifier is said to be good when the diagonal matrix value represents one, which means all collected observations correctly classified the heart disease. The below-mentioned Figure 5 is the normalized confusion matrices.

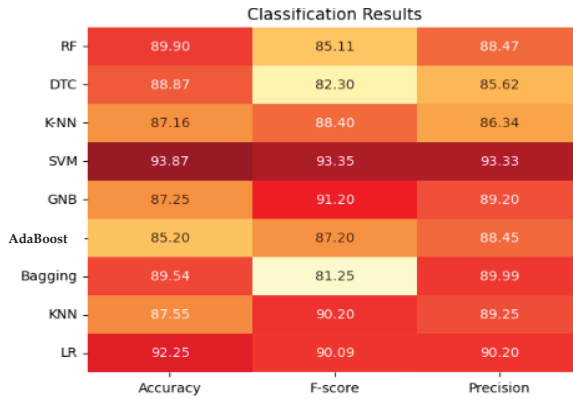


Figure 4. Classification results for heart disease data.

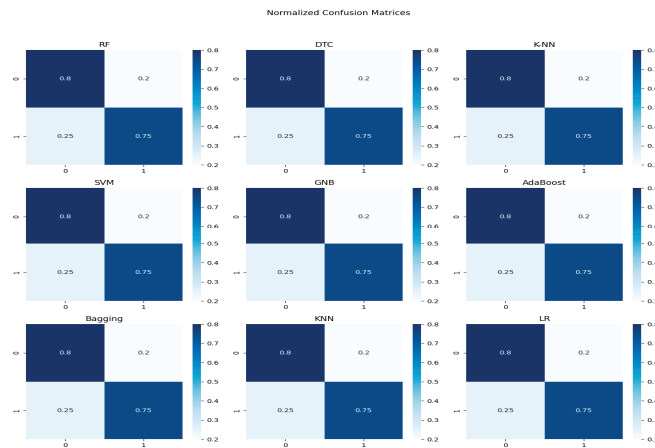


Figure 5. Normalized confusion matrices.

### 5. Conclusions

The heart disease prediction model developed in this study has the potential to improve patient outcomes while also lowering healthcare costs by identifying patients at risk of developing heart disease and offering appropriate interventions and treatments. Future research can expand on the possibilities of sensor networks, the IoT, and machine learning approaches in healthcare, allowing the development of more accurate and effective predictive models for heart disease and other medical diseases. The SVM had the highest accuracy (93.87%), followed by LR (92.25%). Overall, the SVM and LR seem to be the most effective models for this dataset, while AdaBoost may need further optimization. The SVM had the best overall performance, with the lowest mean-squared error (MSE) and root-mean-squared error (RMSE) of 0.18752 and 0.32589, respectively.

**Funding:** This research received no external funding.

**Institutional Review Board Statement:** Not applicable.

**Informed Consent Statement:** Not applicable.

**Data Availability Statement:** The data that support the findings of this study are openly available in "UCI" at <https://www.kaggle.com/datasets/aasheesh200/framingham-heart-study-dataset> (accessed on 5 February 2023).

**Conflicts of Interest:** The authors declare no conflicts of interest.

## References

1. Tang, C.; Liu, Z.; Li, L. Mechanical sensors for cardiovascular monitoring: From battery-powered to self-powered. *Biosensors* **2022**, *12*, 651.
2. Lin, J.; Fu, R.; Zhong, X.; Yu, P.; Tan, G.; Li, W.; Zhang, H.; Li, Y.; Zhou, L.; Ning, C. Wearable sensors and devices for real-time cardiovascular disease monitoring. *Cell Rep. Phys. Sci.* **2021**, *2*, 100541.
3. Esther, G.M.; Ahila, S.S.; Kumar, P.H. Coronary Heart Disease (Cad) Monitoring System Based On Wireless Sensors. *J. Physics Conf. Series* **2019**, *1362*, 012045.
4. Salvi, S.; Dhar, R.; Karamchandani, S. IoT-Based Framework for Real-Time Heart Disease Prediction Using Machine Learning Techniques. In *Innovations in Cyber Physical Systems: Select Proceedings of ICICPS 2020*; Springer: Singapore, 2021; pp. 485–496.
5. Kumar, R.; Kumar, P.; Kumar, Y. Time series data prediction using IoT and machine learning technique. *Procedia Comput. Sci.* **2020**, *167*, 373–381. [CrossRef]
6. Kumar, P.M.; Gandhi, U.D. A novel three-tier Internet of Things architecture with machine learning algorithm for early detection of heart diseases. *Comput. Electr. Eng.* **2018**, *65*, 222–235. [CrossRef]
7. Yin, H.; Jha, N.K. A health decision support system for disease diagnosis based on wearable medical sensors and machine learning ensembles. *IEEE Trans. Multi-Scale Comput. Syst.* **2017**, *3*, 228–241. [CrossRef]
8. Ravi, D.; Wong, C.; Lo, B.; Yang, G.Z. A deep learning approach to on-node sensor data analytics for mobile or wearable devices. *IEEE J. Biomed. Health Inform.* **2016**, *21*, 56–64. [CrossRef] [PubMed]

**Disclaimer/Publisher's Note:** The statements, opinions and data contained in all publications are solely those of the individual author(s) and contributor(s) and not of MDPI and/or the editor(s). MDPI and/or the editor(s) disclaim responsibility for any injury to people or property resulting from any ideas, methods, instructions or products referred to in the content.

# Performance Evaluation of a Specialized Pressure Sensor for Pick and Place Operations <sup>†</sup>

Marut Deo Sharma \* and Juwesh Binong

Department of Electronics and Communication Engineering, North Eastern Hill University, Shillong 793022, India; jbinong@nehu.ac.in

\* Correspondence: marut.devsharma@mwu.edu.et; Tel.: +91-9411491786

<sup>†</sup> Presented at the 10th International Electronic Conference on Sensors and Applications (ECSA-10), 15–30 November 2023; Available online: <https://ecsa-10.sciforum.net/>.

**Abstract:** A piezoresistive electrical bagging material with minimal cost and profile, such as linqstat or velostat, is a good choice for pressure-sensing systems in robotic arm grippers. This paper's main objective is to examine the performance of a unique velostat-based pressure sensor system for supplying real-time grasping pressure profiles during the lifting of calibrated weights. Copper conductive tape was used to build the sensor, and it was positioned on top of and beneath a velostat sheet to serve as an electrode. The accuracy, repeatability, and hysteresis responses of the pressure sensor system were examined through a variety of experiments, as well as through testing with calibrated weights ranging from 100 gm to 2000 gm in steps. The sensor's hysteresis and nonlinear characteristics were discovered through the experimental results of loading cycle measurements. Velostat proved to be a realistic option as a sensitive material for sensors with a single electrode pair, depending on the sensor's sensitivity, hysteresis, reaction time, loading conditions, and deformation. The area where the velostat sensor might be implemented was verified by experimental results.

**Keywords:** pressure sensor; Arduino board; velostat; calibrated weights; hysteresis; grippers; wearable sensors

## 1. Introduction

In research using the haptic approach and robotics applications utilizing wearable technology, force distribution sensors and contact pressure sensors are frequently used. As a result, it is crucial to thoroughly research the design and characterization of these sensors in order to produce accurate results. Three distinct physical phenomena occurring in various materials—the piezoresistive effect, the piezoelectric effect, and variable capacitance—provide the three most popular approaches to designing electronic sensors for measuring force and pressure [1–3]. In numerous sorts of sensing applications, the three phenomena have been thoroughly researched. However, among these three categories of physical phenomenon, piezoresistive materials enable better metrical pressure distribution monitoring in biomedical applications given their affordability and deterministic behavior [4].

The electrical resistance of piezoresistive materials varies in response to deformation caused by an applied force [5,6] and has an inversely proportional relationship [7]. When no force is applied, the material's electrical resistance is somewhere between megaohms and kiloohms or less [8]. In this, a paper piezoresistive sensor was tested in response to load, hysteresis, and temporal drift tests.

## 2. Materials and Methods

### 2.1. Sensor Fabrication

The materials needed for sensor fabrication are a velostat sheet, adhesive copper tape, silver conductive fabric, a silicone foam layer, etc. The velostat sheet is sandwiched in

**Citation:** Sharma, M.D.; Binong, J. Performance Evaluation of a Specialized Pressure Sensor for Pick and Place Operations. *Eng. Proc.* **2023**, *58*, 74. <https://doi.org/10.3390/ecsa-10-16586>

Academic Editor: Francisco Falcone

Published: 5 December 2023



**Copyright:** © 2023 by the authors. Licensee MDPI, Basel, Switzerland. This article is an open access article distributed under the terms and conditions of the Creative Commons Attribution (CC BY) license (<https://creativecommons.org/licenses/by/4.0/>).

between two pieces of copper conductive tape, and then, silver conductive fabric is also placed, covering the copper conductive tape as shown in Figures 1 and 2. Experimental setup for the entire system is shown in Figure 3. Over the conductive tape, a layer of silicone foam is placed so that applied pressure or force is uniformly distributed over the entire surface area of the sensor strip [9,10] The piezoresistive velostat core of the sensor has a length of 5 mm, and a thickness of 0.06 mm. The main goal of the sensor design is to reduce the size and cost of this customized sensor. Velostat is the core material of the sensor; it has a length of 105 mm, a breadth of 65 mm, and a thickness of 0.06 mm. Given the micro-Brownian motion of the carbon filler particles in the polymer, the material's resistance decreases as force is applied to it [11,12]. Electron microscopy diagram of velostat paper is shown in Figure 4 showing the molecular structure of carbon material used.

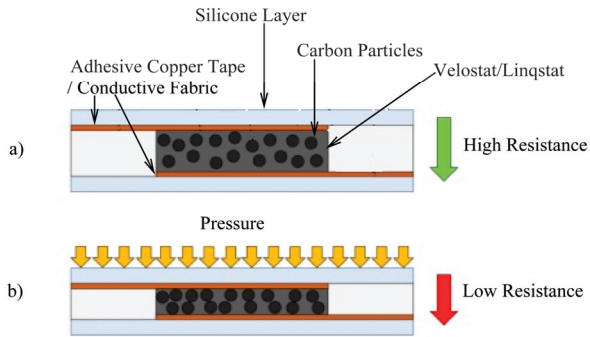


Figure 1. Sensor construction, (a) unloaded, (b) loaded [13].

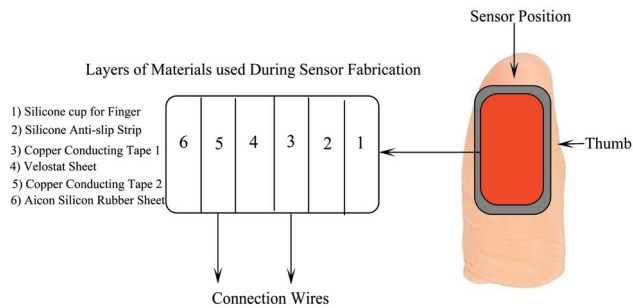


Figure 2. Layers of materials used in sensor fabrication [13].

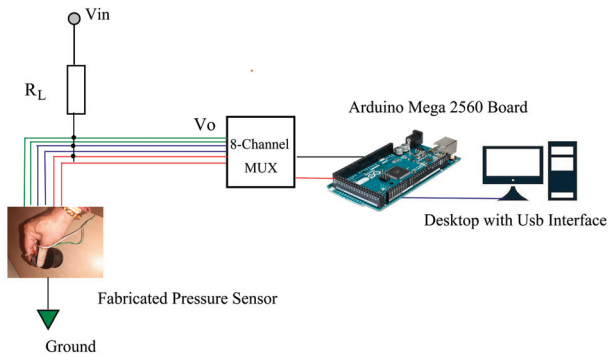
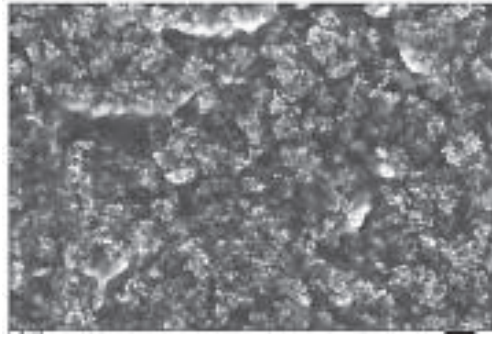


Figure 3. Experimental setup [13].



**Figure 4.** Electron microscopic image of velostat [14].

## 2.2. Design Parameters of Conditioning Circuit

Equation (1) accurately shows the resistance–force relation for velostat [15].

$$R = \frac{\rho' \times k}{F} \quad (1)$$

$R$ : resistance of piezoresistive material;  
 $K$ : surface roughness factor/coefficient;  
 $\rho'$ : resistivity of the contacting surfaces;  
 $F$ : force applied normal to the contact surfaces.

The effect of the change in force is inversely proportional to the resistance of the sensor; moreover,  $k$  has a direct impact on the force applied while holding an object. If the value of the surface is rougher, the resistance will be greater, and the force required to lift an object will be lesser. As shown in Figure 3, a voltage divider circuit was used to transform the resistance of the sensors into a voltage signal by connecting them in series with a fixed resistor,  $R$  (10 K $\Omega$ ). Applying Ohm's law, as illustrated in Equation (2), yields the voltage read at the sensor–resistor junction.

$$V_O = V_{in} \left[ \frac{\rho' \times k}{F \times R_L + \rho' \times k} \right] \quad (2)$$

$R_L$ : voltage divider circuit's resistance;  
 $V_{in}$ : sensor's input voltage;  
 $V_O$ : voltage divider's output voltage.

By taking into account Equations (1) and (2), the voltage force relationship is established. A linear response might be obtained by connecting the sensor resistor between a voltage source and the current input of a voltage converter (a virtual ground), obtaining a voltage output proportional to the piezoresistive sensor's resistance [15].

## 2.3. Experimental Design Parameters [8–10]

The experiments focused on sensor response characteristics for distinct load levels, continuous cyclical loads, drift characteristics, and variation due to loading rate changes.

### 2.3.1. Hysteresis

The greatest output variation between loading and unloading a single load was referred to as hysteresis.

$$\text{Hysteresis} = \frac{|V_{Load} - V_{Unload}|}{|V_{Max} - V_{Min}|} \times 100\% \quad (3)$$

where  $V_{Load}$  and  $V_{Unload}$  are the sensor voltages corresponding to the greatest difference between the loading and unloading responses, and  $V_{Max}$  and  $V_{Min}$  are the sensor voltages at maximum and minimum loads, respectively [16]. Loading test with calibrated weights is shown in Figure 5.

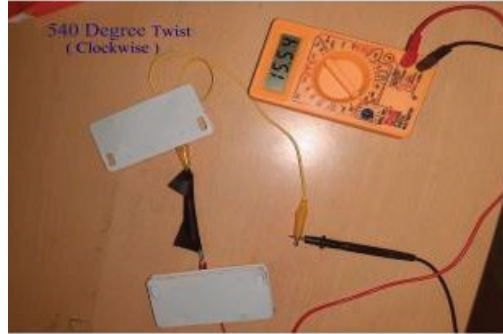


**Figure 5.** Loading test with calibrated weights [17].

### 2.3.2. Drift

Drift is described as a shift in sensor output over time for a specific load, typically an increase in value. With weights kept for five minutes, the sensor was loaded from 200 gm to 2000 gm in steps, and the variations in resistance and pressure values were noted.

### 2.3.3. Repeatability

The variation in output produced when a sensor is loaded to the same pressure is known as repeatability. Each sensor was loaded with a calibrated weight ranging from 100 gm to 2000 gm.

### 2.3.4. Effect of Temperature

The sensors were heated using a hot plate or hair dryer from room temperature up to 60 °C in steps of 5 degrees. At these temperatures, the sensor response was recorded for roughly 30 min with no loads and loads ranging from 200 gm to 2000 gm [11,12]. The temperature test is shown in Figure 6.

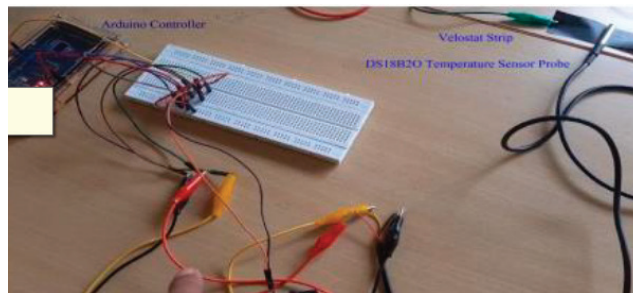


**Figure 6.** Temperature test [17].

## 2.4. Experimental Methods

### 2.4.1. Pre-Commissioning Test

The fabricated sensor has to undergo various pre-commissioning tests, which include the twisting effect, bending effect, and stretching effect as in Figure 7.



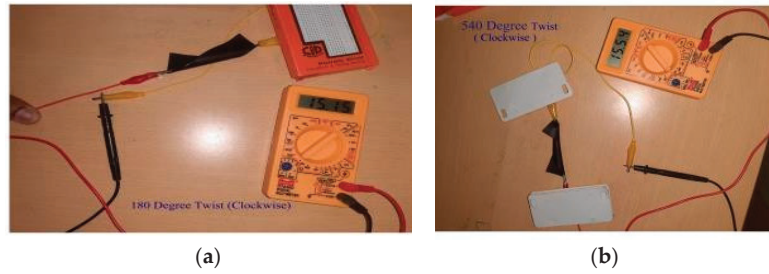


**Figure 7.** (a) The 180° twisting of a velostat strip (Clockwise); (b) 540° twisting of a velostat strip (clockwise) [17].

2.4.2. Pre- and Post-Commissioning Tests

The results are shown in Tables 1–8 and their related curves are shown in Figures 8–12.

**Table 1.** Variation in velostat resistance (clockwise).

S. No	Twisting Angle in Degree(Clockwise)	Rvelostat (KΩ)	% Change in Resistance ( $\Delta R_{velostat}/R_{velostat} \times 100\%$ )
1	0° Twist (Flat Surface)	14.70–14.81	0.673%
2	180° Twist	15.15	2.292%
3	360° Twist	15.40	1.655%
4	540° Twist	15.56	1.039%

**Table 2.** Variation in velostat resistance (anti-clockwise).

S. No	Twisting Angle in Degree (Anti-Clockwise)	Rvelostat (KΩ)	% Change in Resistance ( $\Delta R_{velostat}/R_{velostat} \times 100\%$ )
1	0° Twist (Flat Surface)	14.77–14.80	0.673%
2	180° Twist	15.13	2.292%
3	360° Twist	15.32	1.655%
4	540° Twist	15.50	1.039%

**Table 3.** Bending test on velostat strip.

S. No	Bend Angle (Degree)	Rvelostat (KΩ)	% Change in Velostat Resistance ( $\Delta R_{velostat}/R_{velostat} \times 100\%$ )
1	0° (Flat Surface)	14.70	0.673%
2	30° (Light Bend)	14.82	2.297%
3	45° (Moderate bend)	14.90	1.256%
4	90° (Omega Bend)	15.56	1.173%
5	Pinch Bend	13.05	−16.124%

**Table 4.** Stretching test on velostat strip.

S. No	Velostat Strip Length (L + $\delta L$ ) cm	Rvelostat (KΩ)	% Change in Velostat Resistance ( $\Delta R_{velostat}/R_{velostat} \times 100$ )
1	No Stretch (10.5)	14.55–14.68	0.855%
2	Light Stretch (10.55)	15.60	6.768%
3	Med. Stretch (10.6)	15.90	1.923%
4	High Stretch (10.7)	15.73	1.173%
5	Pinch Bend	13.05	−16.124%

**Table 5.** Loading test on the sensor (ascending weights) [18].

S. No	Calibrated Weights (Grams)	Resistance Range R <sub>velostat</sub> (K $\Omega$ )	% Change in Resistance ( $\Delta R_{\text{velostat}}/R_{\text{velostat}} \times 100$ )
1	0	17.1–18.2	–30%
2	250	12.23–12.60	–11.90%
3	500	10.99–11.10	–0.09%
4	750	10.85–10.93	–4.55%
5	1000	10.15–10.50	–12.38%
6	1250	9.11–9.20	–2.17%
7	1500	8.94–9.00	–0.89%
8	1750	8.67–8.92	–4.71%
9	2000	8.45–8.50	0%

**Table 6.** Loading test on the sensor (descending weights).

S. No	Calibrated Weights (Grams)	Resistance Range R <sub>velostat</sub> (K $\Omega$ )	% Change in Resistance ( $\Delta R_{\text{velostat}}/R_{\text{velostat}} \times 100$ )
1	2000	8.63–8.69	0%
2	1750	8.85–8.92	2.55%
3	1500	9.10–9.17	2.83%
4	1250	9.23–9.57	1.43%
5	1000	10.60–10.85	14.84%
6	750	11.03–11.86	4.06%
7	500	13.50–13.84	22.40%
8	250	14.00–15.56	3.70%
9	0	16.44–17.54	25.29%

**Table 7.** Effect of temperature on velostat material.

S. No	Ambience Temperature in Degree Celsius	R <sub>velostat</sub> (K $\Omega$ )	% Change in Resistance ( $\Delta R_{\text{velostat}}/R_{\text{velostat}} \times 100$ )
1	24.44 (Room Temp.)	13.1	0%
2	27	14.2	8.40%
3	32	14.7	3.52%
4	37	15.3	3.92%
5	42	18.7	22.22%
6	47	21.9	17.10%
7	52	26.1	19.18%
8	57	20.4	–21.83%
9	62	18.5	–9.31%

**Table 8.** Hysteresis and drift tests on the sensor with calibrated weights.

S. No	Calibrated Weights (Grams)	Hysteresis	Voltage Drift	
			$\Delta V_0$	$\Delta R_{\text{velostat}} (\Omega)$
1	0	0%	0	0
2	250	–1.408451%	0.47	58002.11
3	500	12.67606%	0.09	4705.14
4	750	1.408451%	0.12	5565.36
5	1000	21.121761%	0.08	4154.8
6	1250	–14.08451%	0.14	5512.6
7	1500	–42.25352%	0.06	2733.62

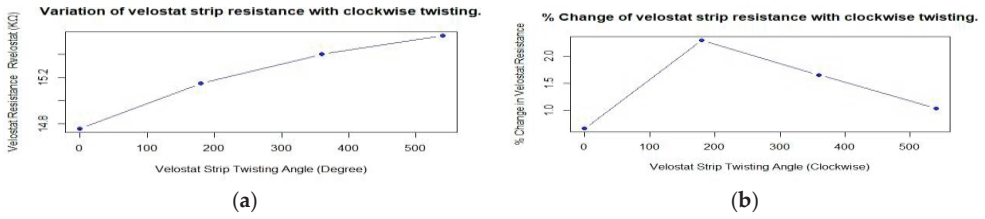


Figure 8. (a) Variation in velostat resistance with clockwise twisting; (b) % change in velostat resistance with clockwise twisting.

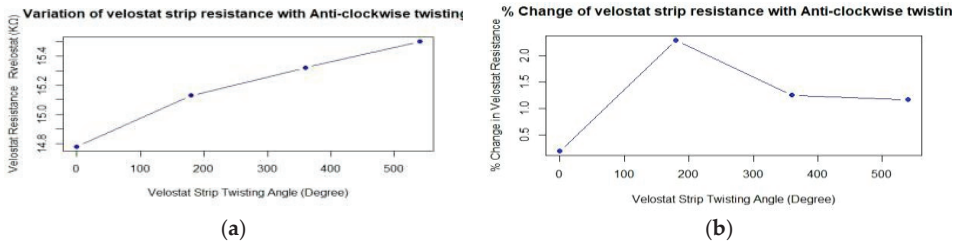


Figure 9. (a) Variation in velostat resistance; (b) % change in resistance with anti-clockwise twisting.

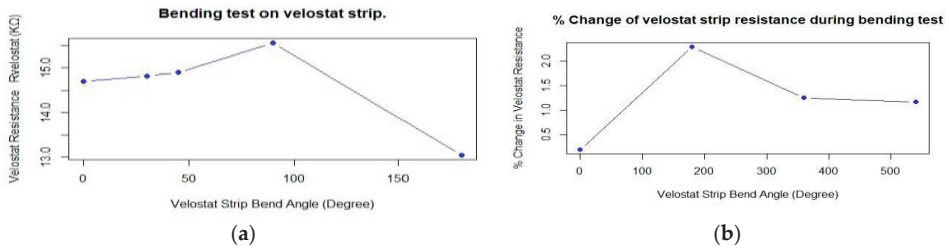


Figure 10. (a) Resistance variation in bending test; (b) % change in resistance in bending test.

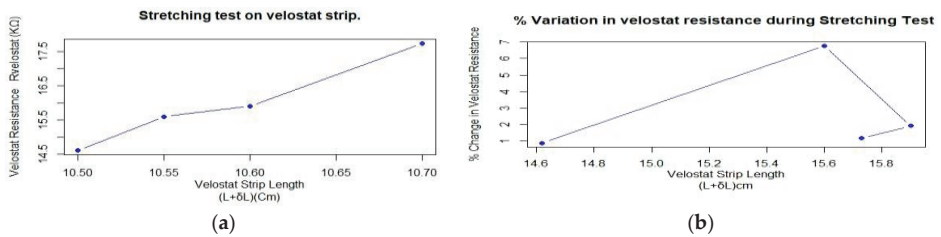


Figure 11. (a) Variation in velostat resistance with stretching test; (b) % change in velostat resistance during stretching test.

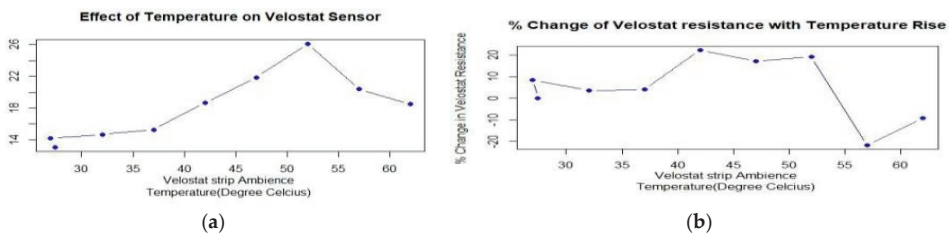


Figure 12. (a) Effect of temperature on velostat sensor; (b)%change in resistance with temperature.

Calculations

For a calibrated weight of 1000 grams:

$$\text{Drift in voltage} = 1.10 - 1.02 = 0.08 \text{ V}$$

$$\text{Drift in fabricated sensor resistance} = 39420.29 - 35245.29 = 4175.00 \Omega$$

$$\text{Hysteresis} = \frac{|1.10 - 0.95|}{|1.50 - 0.79|} \times 100 \% = 21.121761\%$$

For calibrated weight of 250 grams, drift in voltage = 0.91 – 0.44 = 0.47 V

$$\text{Drift in fabricated sensor resistance} = 102417 - 44414.89 = 58002.11 \Omega$$

$$\text{Hysteresis} = \frac{|0.42 - 0.79|}{|1.50 - 0.79|} \times 100 \% = -1.408451\%$$

3. Results and Discussion

In the fabricated sensor, hysteresis errors were observed in a range of 21.121% to -42.253% for ascending and descending weights, as shown in Figure 13a,b, Figure 14a,b and Figure 15 and observations shown in Table 8.

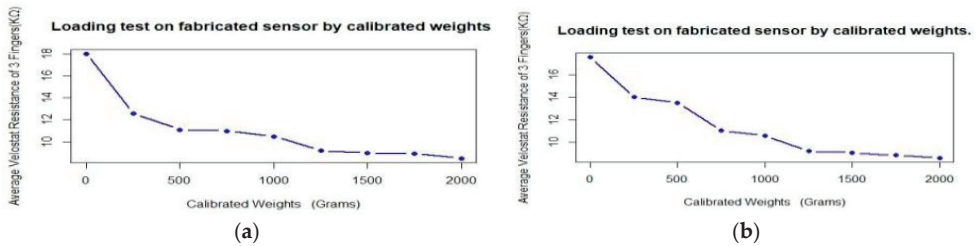


Figure 13. (a) Effect of descending weight on Sensor Resistance (b) effect of ascending weight on sensor Resistance.

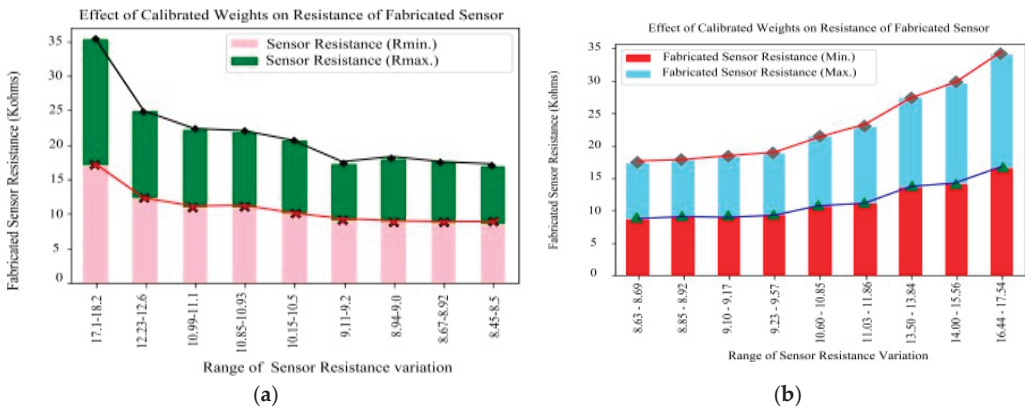


Figure 14. (a) Sensor resistance range (descending weights); (b) Sensor resistance range (ascending weights).

The sensor sensitivity changes swiftly when exceeding a load of 1000 gm, as variations in resistance are significant; therefore, a range of readings are taken and then found optimal values shown in Figure 15a,b.

The voltage drift is also quantized in the sensor, ranging from 0.06 V to 0.47 V, as shown in Table 8. The effectiveness of the sensor is greatly affected when temperature increases above 60 °C, as shown in Table 7. After 55 °C, the resistance of the sensor drops significantly, as shown in Figure 12a The significance of this sensor fabrication is that it provides sensing solutions spanning consumer, industrial, and biomedical applications, as many different engineering principles and physics phenomena are employed to sense pressure.

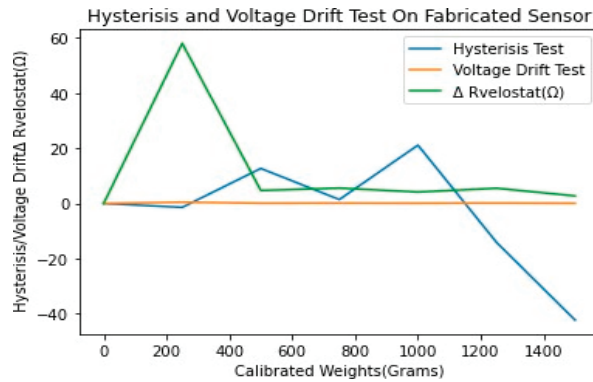


Figure 15. Performance curve of the sensor [19,20].

The advantage of using velostat as a pressure-sensing element is that it is low cost, low power consumption, and has simple electronic circuitry. The limitations include its high sensitivity to pressure variations since output from the sensor is temperature-dependent, and problems with coating material and adhesives at temperatures beyond the sensor's permissible values. Hysteresis can also affect performance matrices like accuracy, stability, precision, etc.

#### 4. Conclusions

It is evident from the above observations and performance curves that the proposed specialized pressure sensor works satisfactorily during pick-and-place operation with calibrated weights and can safely be deployed with robotic arm grippers to grasp objects.

**Author Contributions:** The following are the contributions of the main author and coauthor of this manuscript. Conceptualization, M.D.S.; methodology, M.D.S.; software, M.D.S.; validation, J.B.; formal analysis, M.D.S.; investigation, M.D.S.; resources, M.D.S.; data curation, M.D.S.; writing—original draft preparation, M.D.S.; writing—review end editing, M.D.S. All authors have read and agreed to the published version of the manuscript.

**Funding:** This research received no external funding.

**Institutional Review Board Statement:** Not applicable.

**Informed Consent Statement:** Not applicable.

**Data Availability Statement:** The data that support the findings of this research are available at <https://github.com/marutdevsharma/performance-evaluation-of-especialized-Pressure-Sensor> (accessed on 14 June 2023) or at DOI.

**Acknowledgments:** This research would not have been possible without the exceptional support of Juwesh Binong. He also looked over my transcriptions and numerous questions about the sensor system design and its implementations.

**Conflicts of Interest:** The authors declare no conflicts of interest.

## References

1. Tao, L.Q.; Zhang, K.N.; Tian, H.; Liu, Y.; Wang, D.Y.; Chen, Y.Q.; Yang, Y.; Ren, T.L. Graphene-paper pressure sensor for detecting human motions. *ACS Nano* **2017**, *11*, 8790–8795. [CrossRef] [PubMed]
2. Ruth SR, A.; Feig, V.R.; Tran, H.; Bao, Z. Micro engineering pressure sensor active layers for improved performance. *Adv. Funct. Mater.* **2020**, *30*, 2003491. [CrossRef]
3. Li, J.; Bao, R.; Tao, J.; Peng, Y.; Pan, C. Recent progress in flexible pressure sensor arrays: From design to applications. *J. Mater. Chem. C* **2018**, *6*, 11878–11892. [CrossRef]
4. Li, R.; Zhou, Q.; Bi, Y.; Cao, S.; Xia, X.; Yang, A.; Xiao, X. Research progress of flexible capacitive pressure sensor for sensitivity enhancement approaches. *Sens. Actuators A Phys.* **2021**, *321*, 112425. [CrossRef]
5. Luo, Z.P.; Berglund, L.J.; An, K.N. Validation of F-Scan pressure sensor system: A technical note. *J. Rehabil. Res. Dev.* **1998**, *35*, 186–191. [PubMed]
6. Patra, J.C.; Kot, A.C.; Panda, G. An intelligent pressure sensor using neural networks. *IEEE Trans. Instrum. Meas.* **2000**, *49*, 829–834. [CrossRef]
7. Shirinov, A.V.; Schomburg, W.K. Pressure sensor from a PVDF film. *Sens. Actuators A Phys.* **2008**, *142*, 48–55. [CrossRef]
8. Hopkins, M.; Vaidyanathan, R.; Mcgregor, A.H. Examination of the performance characteristics of velostat as an in-socket pressure sensor. *IEEE Sensors J.* **2020**, *20*, 6992–7000. [CrossRef]
9. Zang, Y.; Zhang, F.; Di, C.A.; Zhu, D. Advances of flexible pressure sensors toward artificial intelligence and health care applications. *Mater. Horiz.* **2015**, *2*, 140–156. [CrossRef]
10. Ashruf, C.M.A. Thin flexible pressure sensors. *Sensor Rev.* **2002**, *22*, 322–327. [CrossRef]
11. Vehec, I.; Livovsky, L. Flexible resistive sensor based on velostat. In Proceedings of the 2020 43rd International Spring Seminar on Electronics Technology (ISSE), Demanovska Valley, Slovakia, 14–15 May 2020; pp. 1–6.
12. Giovanelli, D.; Farella, E. Force sensing resistor and evaluation of technology for wearable body pressure sensing. *J. Sens.* **2016**, *2016*, 9391850. [CrossRef]
13. Fatema, A.; Poondla, S.; Mishra, R.B.; Hussain, A.M. A low-cost pressure sensor matrix for activity monitoring in stroke patients using artificial intelligence. *IEEE Sensors J.* **2021**, *21*, 9546–9552. [CrossRef]
14. Yuan, L.; Qu, H.; Li, J. Velostat Sensor Array for Object Recognition. *IEEE Sens. J.* **2022**, *22*, 1692–1704. [CrossRef]
15. Sergio, M.; Manaresi, N.; Tartagni, M.; Guerrieri, R.; Canegallo, R. A textile based capacitive pressure sensor. *Sensors* **2002**, *2*, 1625–1630.
16. Gála, M.; Barabáš, J.; Kopásková, M. User presence monitoring based on Velostat pressure sensors and Arduino platform. In Proceedings of the 2020 IEEE 21st International Conference on Computational Problems of Electrical Engineering (CPEE), Online Conference, Poland, 16–19 September 2020; pp. 1–3.
17. Salibindla, S.; Ripoche, B.; Lai, D.T.; Maas, S. Characterization of a new flexible pressure sensor for body sensor networks. In Proceedings of the 2013 IEEE Eighth International Conference on Intelligent Sensors, Sensor Networks and Information Processing, Melbourne, VIC, Australia, 2–5 April 2013; pp. 27–31.
18. Chen, D.; Cai, Y.; Huang, M.C. Customizable pressure sensor array: Design and evaluation. *IEEE Sensors J.* **2018**, *18*, 6337–6344. [CrossRef]
19. Li, Y.; Samad, Y.A.; Liao, K. From cotton to wearable pressure sensor. *J. Mater. Chem. A* **2015**, *3*, 2181–2187. [CrossRef]
20. Meyer, J.; Lukowicz, P.; Troster, G. Textile pressure sensor for muscle activity and motion detection. In Proceedings of the 2006 10th IEEE International Symposium on Wearable Computers, Montreux, Switzerland, 11–14 October 2006; pp. 69–72.

**Disclaimer/Publisher’s Note:** The statements, opinions and data contained in all publications are solely those of the individual author(s) and contributor(s) and not of MDPI and/or the editor(s). MDPI and/or the editor(s) disclaim responsibility for any injury to people or property resulting from any ideas, methods, instructions or products referred to in the content.

Proceeding Paper

# Indirect Assessment of Implementation of Industry 4.0 Technologies in Regional Companies <sup>†</sup>

Rubén Nicolás Ibáñez \*, Antonio Guerrero González and Juan Carlos Molina Molina

Escuela de Ingeniería Industrial, Universidad Politécnica de Cartagena, 30203 Cartagena, Spain; antonio.guerrero@upct.es (A.G.G.); jcarlos.molina@upct.es (J.C.M.M.)

\* Correspondence: ruben.nicolas@edu.upct.es

<sup>†</sup> Presented at the 10th International Electronic Conference on Sensors and Applications (ECSA-10), 15–30 November 2023; Available online: <https://ecsa-10.sciforum.net/>.

**Abstract:** This article evaluates the implementation of Industry 4.0 technology in companies in a region using indirect methods such as web scrapping and the examination of publicly available information. By analyzing online data and reports, the level of adoption and integration of 4.0 technology is determined. This provides valuable information on the technological progress of companies to help policymakers promote widespread adoption, businesses benchmark and make informed technology investments and researchers analyze the impact on regional economies. The use of online data sources to assess Industry 4.0 implementation is essential to understanding the technological progress and growth potential of these technologies in various industries, contributing to the formulation of policies that encourage innovation.

**Keywords:** Industry 4.0; web scrapping; implementation of Industry 4.0; digital transformation; business competitiveness

## 1. Introduction

In a world in constant evolution, driven by the digital revolution, Industry 4.0 stands as a beacon guiding entrepreneurs and companies through uncharted waters towards an increasingly digitized and automated future. The work by Michela Piccarozzi, Barbara Aquilani and Corrado Gatti [1] seeks to shed light on this concept, offering a precise definition and pointing out gaps in existing research.

Industry 4.0, more than a simple evolution of manufacturing, represents a revolution that connects all aspects of the production chain, infusing intelligence into every phase. V. Alcácer and V. Cruz-Machado [2] explore how enabling technologies are transforming management and decision making in industry, moving away from traditional centralized applications to a more distributed and agile approach.

Roland Ortt, Stolwijk and Matthijs Punter [3] embark on a mission to summarize and combine numerous articles to address this crucial question. Their work provides a comprehensive overview of the implementation, evaluation methods and current status of Industry 4.0.

However, its implementation is not uniform everywhere. In developing countries, competitive pressure and government support are key drivers of technology adoption, as a study of manufacturing companies in developing economies reveals.

Industry 4.0 not only transforms manufacturing but also has a significant impact on business sustainability, as the study by Julian Marius Müller, Daniel Kiel and Kai-Ingo Voigt [4] shows. Opportunities drive adoption, but challenges vary by company size and sector.

However, a persistent issue in this field is the lack of a clear definition of Industry 4.0. Mario Hermann, Tobias Pentek and Boris Otto [5] set out to solve this problem by establishing a precise definition and presenting key implementation principles.

**Citation:** Ibáñez, R.N.; González, A.G.; Molina, J.C.M. Indirect Assessment of Implementation of Industry 4.0 Technologies in Regional Companies. *Eng. Proc.* **2023**, *58*, 75. <https://doi.org/10.3390/ecsa-10-16225>

Academic Editor: Stefano Mariani

Published: 15 November 2023



**Copyright:** © 2023 by the authors. Licensee MDPI, Basel, Switzerland. This article is an open access article distributed under the terms and conditions of the Creative Commons Attribution (CC BY) license (<https://creativecommons.org/licenses/by/4.0/>).

As countries and companies struggle to adapt to Industry 4.0, the adoption of national strategies becomes essential. The article by Batchkova I.A, Popov G.T, Ivanova Ts. A. and Belev Y.A. [6] discusses how different approaches assess countries' readiness for this industrial revolution.

In the European Union, the adoption of digital technologies has become a key competence in the single market. Isabel Castelo-Branco, Frederico Cruz-Jesus and Tiago Oliveira [7] explore key indicators of readiness and the importance of detailed data.

Meanwhile, in Turkey [8], the specific opportunities and challenges facing the country in adopting Industry 4.0 are assessed through the perceptions of managers in the home appliance industry.

But not all regions of the world are advancing at the same pace. In Kathmandu, Nepal [9], the limited availability of highly skilled labor poses significant barriers to Industry 4.0 adoption, while in Ethiopia [10], information technology implementation is a critical challenge.

The transformation of manufacturing through cyber-physical systems, as highlighted by the work of Joseph Flynn, Steven Dance and Dirk Schaefer [11], underscores the importance of preparing the workforce to deal with the changes that this new industrial era will bring.

To access the valuable information that fuels this revolution, we turn to web scraping, a crucial technique for extracting data from online sources. Chaimaa Lotfi, Swetha Srinivasan, Myriam Ertz and Imen Latrous [12] delve into this essential technique, covering its design and the tools and technologies involved.

For those immersed in academic research, the CRISP-DM framework, proposed by Hossam El-Din Hassanien [13], offers a valuable solution for analyzing the literature in scientific web repositories, addressing challenges related to unstructured data.

Ultimately, web scraping proves to be a vital bridge between the vast ocean of online information and its application in various fields, facilitating informed decision making in an increasingly digital world. Industry 4.0 continues to advance, and those who understand its concepts and challenges are better prepared to navigate this Fourth Industrial Revolution.

## 2. Materials and Methods

Within the framework of our project, we used the SABI (Sistema de Análisis de Balances Ibéricos) database. SABI, provided by the Spanish firm Informa D&B, represents a fundamental tool used predominantly in Spain and Portugal to carry out financial analyses of companies. It stands out as one of the most prominent sources of business information on the Iberian Peninsula, as it compiles and stores detailed financial and commercial data on both Spanish and Portuguese companies. This information covers aspects such as balance sheets, income statements, shareholders, managers, economic activity and other key indicators.

The percentage of companies with websites has been determined using the SABI database through an exhaustive analysis of the information collected in the database. The process involved the identification of companies with website records in their profiles, followed by a calculation that related the number of companies with websites to the total number of companies included in the SABI database. This assessment provided an accurate picture of the extent of the online presence of the companies in the dataset and allowed us to obtain a percentage that reflects the level of adoption of web presence in the business context analyzed.

The process of determining the level of Industry 4.0 implementation in a company through a visit and survey was carried out as follows: First, a thorough preparation was carried out, and clear objectives were defined. During the visit, an interview was conducted with management, a tour of the facility was conducted, employees were spoken to and systems and data were evaluated. A targeted survey was then used to gather additional information. The data collected were then analyzed to rank the level of implementation in



key areas. Finally, recommendations for improving Industry 4.0 adoption were provided and tailored to the specific needs of the assessed company.

In our research process to assess the level of Industry 4.0 implementation in companies, we carefully identified and defined a number of key terms related to this emerging industry. These key terms were used as a basis for formulating questions and conducting targeted searches in the analyzed companies. By focusing on essential concepts such as "Internet of Things (IoT)", "Artificial Intelligence (AI)", "Automation", "Big Data" and "Cybersecurity", we were able to address key aspects of Industry 4.0 and more accurately assess the degree of technological adoption and sophistication in the organizations studied.

Web scraping is used in a variety of applications, such as data collection for market research, online price monitoring, news aggregation, information extraction for data analysis and many other areas. However, it is important to note that web scraping must be carried out in an ethical manner and in compliance with the websites' terms of service, as unauthorized access or excessive requests can have legal and ethical implications.

Web scraping is a technique that automates the extraction of data from websites in order to collect information efficiently and use it in various applications.

In the project we developed, we applied a number of fundamental Python techniques and libraries to carry out web scraping effectively. To extract data from web pages, we employed HTML Document Object Model (DOM) navigation techniques using BeautifulSoup and Scrapy. These tools were essential for analyzing the structure of the web pages and extracting relevant information in a systematic way. In addition, we made use of other key libraries such as Requests to handle HTTP requests, Selenium to automate interaction with web browsers, PyQuery to perform jQuery-like parsing of HTML documents and Lxml for efficient processing of XML and HTML data. Thanks to these techniques and libraries, we were able to perform accurate and efficient data extraction for our project successfully.

### *Methodology*

In the development of our project, we followed a specific methodology to analyze the level of implementation of 4.0 technologies in companies. The general steps we have applied are as follows:

- Identification of information sources: we started the process by identifying relevant online information sources that host data on the adoption of 4.0 technologies in companies. This includes news websites, research reports, specialized blogs and social media platforms where companies share their technological advances.
- Selection of target pages: We identified specific web pages or sections of websites that contained relevant information on the implementation of 4.0 technologies in companies. This included press releases, annual reports, case studies, company blogs and other resources that provided meaningful data.
- Use of web scraping libraries: To automate data extraction from the selected web pages, we opted for Python web scraping libraries, such as BeautifulSoup and Scrapy. These tools facilitated the navigation through the HTML code of the pages and the extraction of relevant data.
- Development of a web scraping script: We created a Python script that used the selected library to collect information from the target web pages. This involved sending HTTP requests to download the content of the pages, parsing the HTML to extract relevant data and then storing it in a data structure, such as a CSV file or a database.
- Definition of analysis criteria: We established clear criteria to assess the level of implementation of 4.0 technologies in companies. This included identifying keywords and phrases related to Industry 4.0, such as "Internet of Things (IoT)", "Artificial Intelligence (AI)", "Automation" and more.
- Data processing and analysis: Once we collected data from various sources, we proceeded to process and analyze the information collected to assess the level of

- adoption of 4.0 technologies in companies. We employed word processing, text mining and data analysis techniques to quantify and classify relevant information.
- Data visualization: In order to effectively present our findings, we created graphs and visualizations that showed the level of implementation of 4.0 technologies in companies in a clear and concise manner. For this, we used tools such as Matplotlib, Seaborn and D3.js.
  - Data validation: To ensure the accuracy and consistency of the data collected, we validated and verified the information. This involved a manual review of some results and a comparison of data from multiple sources.
  - Results report: We documented our findings in a report detailing the level of implementation of 4.0 technologies in the companies analyzed. The report included information on the methodology used, the analysis criteria and any significant observations or trends identified.
  - Continuous update: Given the constantly evolving nature of 4.0 technology implementation, we considered automating the web scraping and analysis process to continuously track trends and changes in the level of technology adoption by companies.

### 3. Results

Prior to applying the web scraping techniques, the number of Murcian companies with a website was analyzed from the SABI database. A total of 5913 Murcian companies were counted out of the 19,921 companies with a website in 2021. This corresponds to 29.68% of the companies. In this study, the level of implementation was analyzed by economic activities, locations, income, age, employees and export level.

Thirteen essential KETs have been identified and evaluated, including the Internet of Things (IoT), Cloud/Edge Computing, Artificial Intelligence (AI), Systems Integration, Visualization and Data Management Systems, Augmented, Virtual and Mixed Reality (AR/VR/MR), Drones, Cybersecurity, Additive Manufacturing, Collaborative Robotics, Smart Factory, Building Information Modeling (BIM), Big Data and Digital Twin. These KETs have been used for web scraping searches on their websites.

This paper shows the results obtained for a sample consisting of two 4.0 enabler companies as it is shown in Table 1, one in the drone sector and another in the collaborative robotics sector. In the first company, 254 websites were analyzed. From the second company, 178 websites were analyzed using the web scraping technique.

**Table 1.** Web scraping results versus interviews and company visits.

KETs	Enabler 1	Enabler 2
IoT	0 (0%) [0]	48 (11.40%) [2]
Cloud/Edge Computing	380 (23.7%) [1]	52 (12.3%) [2]
IA	237 (14.7%) [1]	36 (8.5%) [1]
Vertical and horizontal integration	14 (8.7%) [1]	159 (37.7%) [3]
Data Visualization	465 (29.8%) [3]	206 (48.9%) [4]
RA, RV, RM	45 (2.8%) [1]	14 (3.3%) [1]
Drones	1606 (100%) [5]	35 (8.31%) [1]
Cybersecurity	54 (3.36%) [1]	43 (10.1%) [1]
Additive Fabrication	23 (1.4%) [1]	13 (3.01%) [1]
Collaborative Robotics	0 [0]	421 (100%) [5]
Smart Factory	0 [0]	68 (16.15%) [1]
BIM	154 (9.5%) [2]	0
Big Data	[0]	15 (3.5%) [1]
Digital Twin	[0]	12 (2.8%) [1]

The tables show the number of times the keyword or terms related to KETs were found on their website, and in parentheses, the percentage measured with respect to the number of times the main topic was found. Personal interviews were conducted as indicated in the methodology. The interview findings are presented within parentheses on a scale from one

to five (with zero denoting no implementation and five representing high implementation). The percentages of keyword encounters on the web are related to the encounters on the company's main topic. A correlation is found between the results obtained from the interviews and those obtained from the web scraping techniques.

#### 4. Discussion

This study demonstrates the usefulness of using indirect methods, such as web scraping and public information analysis, to assess the adoption of Industry 4.0 technologies in companies in a region.

The results obtained through web scraping correlate well with the direct assessments made through company visits, interviews and surveys. This validates the use of web mining techniques to extract relevant data from corporate websites and other online sources.

The analysis of the SABI database was also very useful to obtain an overview of the level of online presence of companies in the region. This information allows us to focus our web scraping efforts on the companies most likely to disclose data on their digital transformation.

An important finding is the considerable variability in the adoption of 4.0 technologies depending on the economic activity, location, revenue and other factors of the companies. This underscores the need for customized digital transformation strategies according to the characteristics of each organization.

Among the limitations of the study is the impossibility of covering all the companies in the region through manual web scraping. However, the automation of this process using scripts would make it possible to significantly expand the sample analyzed.

Another limitation is the reliance on the information that companies publish on their websites and other online media. Not all companies disclose their technological advances, which may underestimate their level of Industry 4.0 adoption.

In conclusion, this work lays the groundwork for continuous monitoring of the progress of digital transformation in the business fabric using web mining techniques. This information is essential for the formulation of policies that encourage innovation and for companies to assess their capabilities in relation to those of their competitors.

**Author Contributions:** Conceptualization, R.N.I.; methodology, A.G.G. and J.C.M.M.; software, R.N.I., A.G.G. and J.C.M.M.; validation, A.G.G. and R.N.I.; formal analysis, R.N.I. investigation, R.N.I., A.G.G. and J.C.M.M.; resources, R.N.I.; data curation, J.C.M.M.; writing—original draft preparation, R.N.I.; writing—review and editing, A.G.G.; visualization, R.N.I. and A.G.G.; supervision, R.N.I. and A.G.G.; project administration, A.G.G.; funding acquisition, A.G.G. All authors have read and agreed to the published version of the manuscript.

**Funding:** This research was funded by Comunidad Autónoma de la Región de Murcia, Project: Cátedra Industria 4.0.

**Institutional Review Board Statement:** Not applicable.

**Informed Consent Statement:** Not applicable.

**Data Availability Statement:** Data are contained within the article.

**Acknowledgments:** The authors would like to thank the Instituto de fomento de la Región de Murcia for the support for this work.

**Conflicts of Interest:** The authors declare no conflicts of interest.

#### References

1. Piccarozzi, M.; Aquilani, B.; Gatti, C. Industry 4.0 in management studies: A systematic literature review. *Sustainability* **2018**, *10*, 3821. [CrossRef]
2. Alcácer, V.; Cruz-Machado, V. Scanning the industry 4.0: A literature review on technologies for manufacturing systems. *Eng. Sci. Technol. Int. J.* **2019**, *22*, 899–919. [CrossRef]
3. Ortt, R.; Stolwijk, C.; Punter, M. Implementing industry 4.0: Assessing the current state. *J. Manuf. Technol. Manag.* **2020**, *31*, 825–836. [CrossRef]

4. Müller, J.M.; Kiel, D.; Voigt, K.I. What Drives the Implementation of Industry 4.0? The Role of Opportunities and Challenges in the Context of Sustainability. *Sustainability* **2018**, *10*, 247. [CrossRef]
5. Herman, M.; Pentek, T.; Otto, B. *Design Principles for Industry 4.0 Scenarios: A Literature Review*; Business Engineering Institute St. Gallen: St. Gallen, Switzerland, 2015; Volume 10, p. 16.
6. Batchkova, I.A.; Popov, G.T.; Ivanova, T.A.; Belev, Y.A. Assessment of readiness for “Industry 4.0”. *Int. Sci. J.* **2021**, *6*, 288–291.
7. Castelo-Branco, I.; Cruz-Jesus, F.; Oliveira, T. Assessing Industry 4.0 readiness in manufacturing: Evidence for the European Union. *Comput. Ind.* **2019**, *107*, 22–32. [CrossRef]
8. Demirbağ, K.Ş.; Yıldırım, N. Getting the measure of the fourth industrial revolution: Advantages and challenges of Industry 4.0 in the Turkish white goods industry. *Cent. Eur. Manag. J.* **2022**, *31*, 82–101. [CrossRef]
9. Rajbhandari, S.; Devkota, N.; Khanal, G.; Mahato, S.; Paudel, U.R. Assessing the industrial readiness for adoption of industry 4.0 in Nepal: A structural equation model analysis. *Heliyon J.* **2022**, *10*, 1–11. [CrossRef] [PubMed]
10. Beza, M. Readiness Assessment of Ethiopian Industrial Park for Industry 4.0. Master Thesis, College of Social Science Addis Ababa Science and Technology University, Addis Ababa, Ethiopia, 2020.
11. Flynn, J.; Dance, S.; Schaefer, D. Industry 4.0 and its potential impact on employment demographics in the UK. *Adv. Transdiscipl. Eng.* **2017**, *6*, 239–244.
12. Lotfi, C.; Srinivasan, S.; Ertz, M.; Latrous, I. Web Scraping Techniques and Applications: A Literature Review. In *SCRS Conference Proceedings on Intelligent Systems*; SCRS Publications: Delhi, India, 2022; pp. 381–394. [CrossRef]
13. Hassanien, H.E.D. Web Scraping Scientific Repositories for Augmented Relevant Literature Search Using CRISP-DM. *Appl. Syst. Innov.* **2019**, *2*, 37. [CrossRef]

**Disclaimer/Publisher’s Note:** The statements, opinions and data contained in all publications are solely those of the individual author(s) and contributor(s) and not of MDPI and/or the editor(s). MDPI and/or the editor(s) disclaim responsibility for any injury to people or property resulting from any ideas, methods, instructions or products referred to in the content.



# Federated Learning for Frequency-Modulated Continuous Wave Radar Gesture Recognition for Heterogeneous Clients <sup>†</sup>

Tobias Sukianto <sup>1,2,\*</sup>, Matthias Wagner <sup>2</sup>, Sarah Seifi <sup>1,3</sup>, Maximilian Strobel <sup>1</sup> and Cecilia Carbonelli <sup>1</sup>

<sup>1</sup> Infineon Technologies AG, 81726 Munich, Germany; Sarah.Seifi@infineon.com (S.S.); Maximilian.Strobel@infineon.com (M.S.); Cecilia.Carbonelli@infineon.com (C.C.)

<sup>2</sup> Institute for Signal Processing, Johannes Kepler University Linz, 4040 Linz, Austria; matthias.wagner@jku.at

<sup>3</sup> Chair for Design Automation, Technical University of Munich, 80333 Munich, Germany

\* Correspondence: tobias.sukianto@infineon.com

<sup>†</sup> Presented at the 10th International Electronic Conference on Sensors and Applications (ECSA-10), 15–30 November 2023; Available online: <https://ecsa-10.sciforum.net/>.

**Abstract:** Federated learning (FL) is a field in distributed optimization. Therein, the collection of data and training of neural networks (NN) are decentralized, meaning that these tasks are carried out across multiple clients with limited communication and computation capabilities. In FL, the client NNs are first trained with locally available data. Next, they are aggregated to update a global NN. FL suffers from non-independent and identically distributed (iid) data and asynchronous communication between the server and the clients, which degrades the NN's overall performance. In this work, we investigate FL for a small-live-gesture-sensing NN, using a low-power 60 GHz frequency modulated continuous wave radar from Infineon Technologies. The challenges of data sparsity, i.e., only a fraction of a gesture recording corresponds to an executed gesture combined with non-iid data, pose issues during neural network training. It is shown that FL reaches an accuracy higher than 96.2% for an iid setting. However, an increasing level of non-iid data degrades the accuracy to 64.8%. To tackle the accuracy degradation, we propose to dynamically adapt the class weights during the training procedure based on each client's varying ratio of data sparsity. Moreover, regularization terms are included in the loss function to prevent client drift and overconfidence in the client's NN prediction. Finally, it is shown that the proposed modifications increase the NN's performance, such that an accuracy of 97% is obtained despite a high degree of non-iid data.

**Keywords:** radar sensors; gesture recognition; machine learning; federated learning; IoT

**Citation:** Sukianto, T.; Wagner, M.; Seifi, S.; Strobel, M.; Carbonelli, C. Federated Learning for Frequency-Modulated Continuous Wave Radar Gesture Recognition for Heterogeneous Clients. *Eng. Proc.* **2023**, *58*, 76. <https://doi.org/10.3390/ecsa-10-16194>

Academic Editor: Francisco Falcone

Published: 15 November 2023



**Copyright:** © 2023 by the authors. Licensee MDPI, Basel, Switzerland. This article is an open access article distributed under the terms and conditions of the Creative Commons Attribution (CC BY) license (<https://creativecommons.org/licenses/by/4.0/>).

## 1. Introduction

Gesture recognition revolutionizes human-machine interfaces by providing a contact-free and intuitive method of interaction. Unlike touch-based systems, gesture-controlled systems introduce a touchless approach that enhances hygiene and enables interaction without direct hand exposure. Consequently, gesture sensing is one of the leading solutions for effortlessly managing a wide range of consumer and IoT devices [1]. Gesture recognition using radar sensing is a prominent application, merging signal processing-based feature extraction with the classification capabilities of neural networks (NNs). Radar sensors are advantageous to vision-based sensors in terms of privacy preservation, monetary cost, and memory efficiency. Early studies by Lien et al. in 2016 on gesture recognition with radar sensors propose a feature extraction based on range-Doppler images [2], which relies on intricate two-dimensional (2D) data processing. Furthermore, the training of NNs requires a rich database with broad distributional coverage that is then transmitted to a central server. While radar gesture sensing protects user privacy, data collection often involves sensitive user data, mainly because the radar sensor is paired with cameras to obtain accurate ground truth labels.

Federated learning (FL) offers a solution by shifting the training of a global NN to different clients, where all clients train a client NN with local data. These client NNs are then aggregated to learn a global NN, ensuring that the data remain local and are not transmitted to a central server. Although FL has gained significant traction over the past years, the used NN architectures are primarily large and require substantial computational power for training and inference. This poses a challenge in situations where the NNs should be implemented in computational and memory-efficient devices. In 2017, McMahan et al. [3] introduced the idea of FL and suggested an efficient way to train deep networks collaboratively. The challenge of heterogeneous FL, introduced by Zhao et al. [4], involves the training of NNs across different devices or servers with varying characteristics, such as data distributions and features. Challenges in FL when dealing with data heterogeneity, also known as non-independent and identically distributed (iid) data, were also addressed in [5–8]. They investigated how fluctuating data distributions in the clients affect the NN's convergence and proposed strategies to mitigate the impact of non-iid data. Communication efficiency is also a crucial research domain in FL, where the objective is to reach a high accuracy while minimizing the data exchange or the required communication rounds between the clients and the server. In [9,10], communication efficiency is enhanced by introducing various optimization techniques, and reducing the communication overhead while maintaining the NN's performance. Within the relatively unexplored domain of using FL for radar sensors, Savazzi et al. [11] investigated in 2021 a serverless FL approach, which addresses the task of tracking the position of individuals. In 2022, Yang et al. proposed an autoencoder-based technique to encode local gradients from client NNs into a lower-dimensional latent representation to decrease the transmission error within a three-class classification task across three clients [12]. However, these current state-of-the-art methods of FL in the context of radar do not account for the effects of data sparsity, imbalanced data distributions, or varying levels of non-iid data. Furthermore, they require significant changes in the NN architecture while utilizing computationally intensive 2D processing and large network architectures.

In this work, we apply FL on a small real-time gesture sensing NN designed for a low-power 60 GHz frequency modulated continuous wave (FMCW) radar sensor developed by Infineon Technologies and Google [1]. The NNs are designed to be efficient in terms of computational power and memory usage, aiming for minimal hardware requirements. The presented FL algorithms are evaluated on a diverse dataset, including approximately 26,000 gesture recordings. Our approach adopts the lightweight 1-dimensional (1D) radar processing algorithm from Strobel et al. [13], which requires fewer computational operations and smaller NNs than the 2D radar processing in [2]. Besides computationally efficient architectures, we address client heterogeneity and asynchronous client communication. To effectively overcome these training challenges, our main contribution involves dynamically adjusting the training process by assigning weights to the gesture recordings. These weights are based on the ratio of distinct gesture recordings and background within client's data, where all non-gesture recordings are considered as background. This strategy aims to counteract the accuracy degradation due to increasing levels of non-iid data and to decrease the number of communication rounds. An overview of our novel radar-based FL approach compared to prior work is highlighted in Table 1. The remainder of this paper is organized as follows. Section 2 discusses the radar processing setup and the neural network architectures and outlines the proposed contributions. The results are presented and discussed in Section 3. Section 4 concludes this paper.

**Table 1.** Comparison of radar-based FL approaches.

	Radar Processing	Parameters	Mitigates Non-lid Data	Task
This work	1D	1.000	Yes	6-class classification
Savazzi et al. [11]	2D	3.000.000	No	Regression
Yang et al. [12]	2D	30.400	No	3-class Classification

## 2. Methods

In this section, the necessary radar processing steps, the sensor setup, and the utilized NN architectures are briefly discussed. Furthermore, the proposed modifications in the NN's learning method are introduced.

### 2.1. Radar Setup and Processing

The radar sensor emits a chirp signal, which ranges from 58.5 GHz to 62.5 GHz. This chirp signal is reflected by all objects in front of the sensor such that the reflected signal is received by the receive antenna. The received signal is downconverted with the transmit signal, yielding the intermediate frequency (IF) signal which is digitized with a sampling rate of 2 MHz into 64 so-called fast time samples which translates to a range resolution of 0.0375 m and a maximum detectable range of 1.2 m. Transmitting multiple (32) chirps allows to store the corresponding IF signals in a  $32 \times 64$  matrix as illustrated in Figure 1, left. Note that the row index along the chirps is referred to as slow time. Computing a discrete Fourier transform (DFT) along fast time yields the range profile, wherein each peak at a range bin corresponds to an object at a certain radial distance. This is illustrated by Figure 1, center, where the range bins related to the hand and the body are highlighted in black. Finally, computing the so-called Doppler DFT along slow time at the hand's range bin yields another peak (Figure 1, right). The position of this peak relates to the radial velocity of the hand and the magnitude will be referred to as amplitude. As suggested by [13] only the hand's range bin is used for further processing. Hence, this is referred to as 1D radar processing. In addition to radial distance and radial velocity, the angle in azimuth and elevation of an object may be estimated by using three receive antennas arranged in an L-shape [14]. Consequently, five input features, i.e., radial distance, radial velocity, azimuth angle, elevation angle and the amplitude averaged over all receive antennas, are extracted from the radar data. Note that the radar data required to compute all five features will be referred to as a radar frame throughout this work. Within the classification task, we consider six gestures, i.e., swipe left, swipe right, swipe up, swipe down and push, and no gesture which is referred to as background.

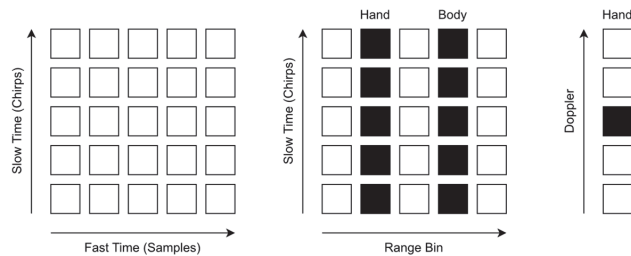


**Figure 1.** Illustration of the reduced 1D radar processing algorithm. Raw radar involves illustrated data for one antenna (**left**). The hand and the body are resolved with a discrete Fourier transform along the fast time samples (**center**). The discrete Fourier transform is applied to the detected hand range bin to resolve its velocity (**right**).

The network consists of a long short-term memory (LSTM)-based architecture to capture the time dependencies for the gesture recordings that are each comprised of a sequence of radar frames. In our model, the inputs are sequences of the five extracted features, while the output consists of gesture predictions. The start until the end of each gesture is labeled as the executed gesture to allow a real-time recognition of the gestures, while the remainder of the gesture recording is labeled as background. The LSTM layer is initialized with 16 hidden units, followed by a dense layer with six output neurons and a softmax activation representing the five gestures and the background.

### 2.2. Learning Methods

In each communication round  $t$  of the FL method,  $d$  NN weights  $\mathbf{w}_t \in \mathbb{R}^d$  are transmitted from the server to a selected group of  $K \in \mathbb{N}$  clients with  $n_i \in \mathbb{N}$  data samples. These clients collectively possess  $n = \sum_{i=1}^K n_i$  data samples, allowing them to engage in localized learning using their local data samples while referencing the server's weights for their individual NNs. The resulting client weights  $\mathbf{w}_{t+1}^i$  are then sent to the server after local training, which aggregates them into an updated set of global weights,

$$\mathbf{w}_{t+1} = \sum_{i=1}^K \frac{n_i}{n} \mathbf{w}_{t+1}^i. \tag{1}$$

The server and clients repeat this procedure through multiple communication rounds to fit the global NN to the client data without exchanging training data between clients and server. Given that the gesture execution constitutes only a fraction of each recording, we are confronted with an imbalanced dataset, wherein the majority of ground truth labels correspond to background. Hence, we propose to adapt the loss function with respect to the ratio of background and gesture samples for each recording with length  $F \in \mathbb{N}$ , and for all  $C \in \mathbb{N}$  classes during the training procedure. Specifically, the loss function may be written as

$$L_S = -\frac{1}{F} \sum_{i=1}^F \sum_{c=1}^C \left( \frac{F}{\sum_{j=1}^F y_{j,0}} y_{i,c} \log(\hat{y}_{i,c}) + y_{i,0} \log(\hat{y}_{i,0}) \right), \tag{2}$$

where  $y_{i,c}$  and  $\hat{y}_{i,c}$  is the actual and predicted probability of the  $i$ -th frame to be the gesture  $c$ , where the index 0 corresponds to the background class. Furthermore, a constraint proposed in [9] prevents non-iid and asynchronous clients' weights from drifting too strongly compared to the server's weights  $\mathbf{w}_t$  and serves as the regularization term

$$L_{\text{cons}} = \|\mathbf{w}_t - \mathbf{w}_{t+1}^i\|^2. \tag{3}$$

A different loss function, known as the confidence constraint, is utilized when multiple client NNs encounter varying label distributions and undergo different numbers of local training epochs. In such scenarios, these client NNs are sensitive to overfitting to their respective heterogeneous distributions, resulting in overly confident predictions on their individual local datasets. To address this issue, we utilize the constraint from [15],

$$L_C = \sum_{c=0}^C \log(\hat{y}_{i,c}), \tag{4}$$

enhancing the generalization capabilities. The final loss function is defined as

$$L = L_S + \lambda L_C + \mu L_{\text{cons}}, \tag{5}$$

with  $\lambda \in [0, 1]$  and  $\mu \in [0, 1]$  as weighting coefficients. For the baseline approach, (2) is replaced in (5) with the cross-entropy loss.



### 3. Results and Discussion

The first study includes varying degrees of non-iid data in each client. The data are split in an iid partition, where the data are shuffled, and an equal number of gesture recordings is assigned to each client. In the non-iid configuration, each client is assigned an equal number of gesture recordings. However, the client’s dataset only contains a subset of classes ranging from 1 to 4. The batch size, referring to the number of gesture recordings utilized in one iteration of the training, is fixed at 32. The stochastic gradient descent optimizer is used with a learning rate of 0.0001, and the algorithms are evaluated in 800 communication rounds. The total number of clients is 100, and the number of selected clients in each communication round is 10. Furthermore, a model is trained where all the data are centralized based on Strobel et al. [13] to compare FL with classical ML. Table 2 illustrates the test accuracy. In the synchronous client setting, all clients complete the same number of local epochs (Table 2, columns 2–3), whereas in the asynchronous client setting, the number of local epochs can vary across clients (Table 2, columns 4–5). A fixed number of five local epochs is used for all clients in the synchronous client scenario, while in the asynchronous client scenario, the number of local epochs is randomized for each client within the range of 1 to 20 epochs. The results in Table 2 reveal that, as the degree of non-iid data increases, there is a noticeable drop in accuracy for the baseline approaches. The proposed approaches prevent the effects of non-iid-related accuracy degradation for synchronous and asynchronous clients. For instance, higher than 97% accuracy is achieved in the one label per client setting, which is comparable to the iid case with an accuracy higher than 98%. One should note, also for the baseline approaches, that randomizing local epochs within the clients does not affect the accuracy drastically. The underlying reason could be ascribed to the regularization terms in (3) and (4), which might effectively mitigate the effects of asynchronous clients or that the randomization of the local epochs effectively yields more training iterations. As can be seen in Figure 2, by integrating the proposed approach, not only the necessary communication rounds are reduced, but also superior performance is achieved even in scenarios with increased levels of non-iid data. Furthermore, classical ML outperforms FL scenarios by a small margin. Nevertheless, FL has the advantage of not requiring to aggregate the client data in a centralized fashion.

**Table 2.** Gesture accuracy for varying levels of non-iid data and asynchronous clients.

Labels Per Client	This Work: 5 Local Epochs (Synchronous)	Baseline: 5 Local Epochs (Synchronous)	This Work: 1 to 20 Local Epochs (Asynchronous)	Baseline: 1 to 20 Local Epochs (Asynchronous)	Baseline: Traditional Learning
5 (iid)	98.2%	96.2%	98.4%	96.0%	98.8%
4	98.0%	86.2%	98.4%	91.9%	-
3	97.7%	83.2%	97.8%	90.0%	-
2	97.4%	79.0%	97.4%	88.1%	-
1	97.0%	64.8%	96.1%	78.5%	-

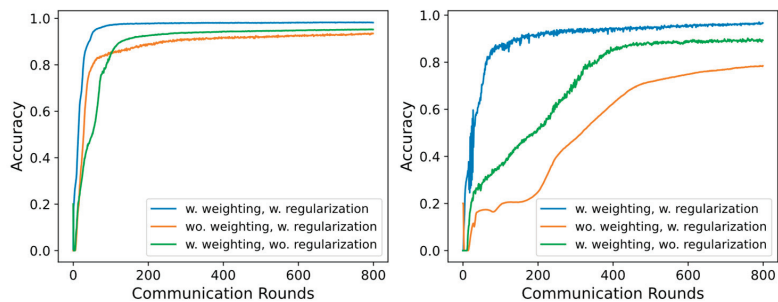


**Figure 2.** FL accuracy for five labels for each client (iid, left) and one label for each client (non-iid, right). The number of local epochs is randomized in each client between 1 and 20.

The second study illustrates the effects of the regularization terms denoted in (3) and (4). As may be seen in Figure 2, it is evident that the inclusion of those regularization terms in the loss function enhances the training of the NN, considering an increasing level of non-iid data. This results in a substantial reduction of required communication rounds. Asynchronously aggregating the clients' NNs into the global NN negatively impacts the accuracy of both the iid and the non-iid data partition. It should further be noted that combining the proposed loss function (2) and the regularization terms (3) and (4) is beneficial to achieve high accuracy and reduce the communication rounds. When only applying the weighted loss, significantly more communication rounds are needed to achieve comparable accuracy. Moreover, the negative impact of asynchronous clients increases with rising degrees of non-iid data, while synchronous clients achieve high performance without requiring the regularization term. This approach might be limited by the data quality available to the clients. In this work, it is assumed that the gestures are executed correctly. Falsely executed gestures could, therefore, degrade the performance of this approach. Therefore, future research should also address the open topic of varying data quality in the clients and could weight each client based on this.

#### 4. Conclusions

In this work, we utilized FL in the scope of varying levels of non-iid data and client asynchronicity for low-power and small NN architectures within FMCW radar gesture sensing. We introduce a modified loss function to mitigate accuracy degradation caused by varying levels of non-iid data and client asynchronicity. We showed how an increasing degree of non-iid data decreases the NN's accuracy. By introducing a new loss function that incorporates the varying degrees of label sparsity in the training procedure, the gesture accuracy is increased by up to 33%. Furthermore, we identified adapting the class weights as a crucial component in the training procedure to maintain high accuracy and low communication overhead.

**Author Contributions:** Conceptualization, methodology and software, T.S.; validation and formal analysis, T.S., M.W., S.S., M.S. and C.C.; writing, T.S., M.W., S.S., M.S. and C.C.; supervision, C.C. All authors have read and agreed to the published version of the manuscript.

**Funding:** This work received no external funding.

**Institutional Review Board Statement:** Not applicable.

**Informed Consent Statement:** Not applicable.

**Data Availability Statement:** The data presented in this study are available on request from the corresponding author.

**Conflicts of Interest:** The authors declare no conflicts of interest.

#### References

1. Trotta, S.; Weber, D.; Jungmaier, R.W.; Baheti, A.; Lien, J.; Noppeney, D.; Tabesh, M.; Rumpler, C.; Aichner, M.; Albel, S.; et al. 2.3 SOLI: A tiny device for a new human machine interface. In Proceedings of the 2021 IEEE International Solid-State Circuits Conference (ISSCC), San Francisco, CA, USA, 13–22 February 2021.
2. Lien, J.; Gillian, N.; Karagozler, M.E.; Amihhood, P.; Schwesig, C.; Olson, E.; Raja, H.; Poupyrev, I. Soli: Ubiquitous gesture sensing with millimeter wave radar. *ACM Trans. Graph. (TOG)* **2016**, *35*, 1–19. [CrossRef]
3. McMahan, B.; Moore, E.; Ramage, D.; Hampson, S.; Arcas, B.A. Communication-efficient learning of deep networks from decentralized data. In Proceedings of the Artificial Intelligence and Statistics, Ft. Lauderdale, FL, USA, 20–22 April 2017.
4. Zhao, Y.; Li, M.; Lai, L.; Suda, N.; Civin, D.; Chandra, V. Federated learning with non-iid data. *arXiv* **2018**, arXiv:1806.00582. [CrossRef]
5. Diao, E.; Ding, J.; Tarokh, V. Heterofl: Computation and communication efficient federated learning for heterogeneous clients. *arXiv* **2020**, arXiv:2010.01264.
6. Li, X.; Huang, K.; Yang, W.; Wang, S.; Zhang, Z. On the convergence of fedavg on non-iid data. *arXiv* **2019**, arXiv:1907.02189.
7. Rodio, A.; Faticanti, F.; Marfoq, O.; Neglia, G.; Leonardi, E. Federated Learning under Heterogeneous and Correlated Client Availability. *arXiv* **2023**, arXiv:2301.04632.

8. Li, T.; Sahu, A.K.; Zaheer, M.; Sanjabi, M.; Talwalkar, A.; Smith, V. Federated optimization in heterogeneous networks. *Proc. Mach. Learn. Syst.* **2020**, *2*, 429–450.
9. Sattler, F.; Wiedemann, S.; Müller, K.R.; Samek, W. Robust and communication-efficient federated learning from non-iid data. *IEEE Trans. Neural Netw. Learn. Syst.* **2019**, *31*, 3400–3413. [CrossRef] [PubMed]
10. Lohana, A.; Rupani, A.; Rai, S.; Kumar, A. Efficient privacy-aware federated learning by elimination of downstream redundancy. *IEEE Des. Test* **2021**, *3*, 73–81. [CrossRef]
11. Savazzi, S.; Kianoush, S.; Rampa, V.; Bennis, M. A framework for energy and carbon footprint analysis of distributed and federated edge learning. In Proceedings of the 2021 IEEE 32nd Annual International Symposium on Personal, Indoor and Mobile Radio Communications (PIMRC), Helsinki, Finland, 13–16 September 2021.
12. Yang, Y.; Hong, Y.G.; Park, J. Federated learning over wireless backhaul for distributed micro-Doppler radars: Deep learning aided gradient estimation. *IET Radar Sonar Navig.* **2022**, *16*, 885–895. [CrossRef]
13. Strobel, M.; Schoenefeld, S.; Daugalas, J. Gesture recognition for fmcw radar on the edge. *arXiv* **2023**, arXiv:2310.08876.
14. Gerstmair, M.; Melzer, A.; Onic, A.; Huemer, M. On the safe road toward autonomous driving: Phase noise monitoring in radar sensors for functional safety compliance. *IEEE Signal Process. Mag.* **2019**, *36*, 60–70. [CrossRef]
15. Zhang, B.B.; Zhang, D.; Li, Y.; Hu, Y.; Chen, Y. Unsupervised domain adaptation for device-free gesture recognition. *arXiv* **2021**, arXiv:2111.10602.

**Disclaimer/Publisher’s Note:** The statements, opinions and data contained in all publications are solely those of the individual author(s) and contributor(s) and not of MDPI and/or the editor(s). MDPI and/or the editor(s) disclaim responsibility for any injury to people or property resulting from any ideas, methods, instructions or products referred to in the content.



# Design of Artificial Intelligence-Based Novel Device for Fault Diagnosis of Integrated Circuits <sup>†</sup>

Pavan Sai Kiran Reddy Pittu <sup>1</sup>, Vijayalakshmi Sankaran <sup>2</sup>, Paramasivam Alagu Mariappan <sup>1,\*</sup>, Gauri Pramod <sup>1</sup>, Nikita <sup>1</sup> and Yash Sharma <sup>1</sup>

<sup>1</sup> Department of Biomedical Engineering, Vel Tech Rangarajan Dr. Sagunthala R&D Institute of Science and Technology, Chennai 600062, India; vtu18106@veltech.edu.in (P.S.K.R.P.); vtu21593@veltech.edu.in (G.P.); vtu22402@veltech.edu.in (N.); vtu23335@veltech.edu.in (Y.S.)

<sup>2</sup> Department of Electronics and Communication Engineering, Vel Tech Rangarajan Dr. Sagunthala R&D Institute of Science and Technology, Chennai 600062, India; drvijayalakshmis@veltech.edu.in

\* Correspondence: drparamasivam@veltech.edu.in or parama.ice@gmail.com; Tel.: +91-984-378-0801

<sup>†</sup> Presented at the 10th International Electronic Conference on Sensors and Applications (ECSA-10), 15–30 November 2023; Available online: <https://ecsa-10.sciforum.net/>.

**Abstract:** The rapid advancement of integrated circuit (IC) technology has revolutionized various industries, but it has also introduced challenges in detecting faulty ICs. Traditional testing methods often rely on manual inspection or complex equipment, resulting in time-consuming and costly processes. In this work, a novel approach is proposed which uses a thermal camera and an Internet of Things (IoT) physical device, namely a Raspberry PI microcontroller, for the detection of faulty and non-faulty ICs. Further, a deep learning algorithm, namely You Only Look Once (YOLO), is coded inside the Raspberry PI controller using Python programming software to detect faulty ICs efficiently and accurately. Also, the various images of faulty and non-faulty ICs are used to train the algorithm and once the algorithm is trained, the thermal camera along with the Raspberry PI microcontroller is used for the real-time detection of faulty ICs and the YOLO algorithm analyzes the thermal images to identify regions with abnormal temperature patterns, indicating potential faults. The proposed approach offers several advantages over traditional methods, including increased efficiency and improved accuracy.

**Keywords:** deep learning; fault diagnosis; object detection; temperature variation; thermal camera; YOLO algorithm

**Citation:** Pittu, P.S.K.R.; Sankaran, V.; Alagu Mariappan, P.; Pramod, G.; Nikita; Sharma, Y. Design of Artificial Intelligence-Based Novel Device for Fault Diagnosis of Integrated Circuits. *Eng. Proc.* **2023**, *58*, 77. <https://doi.org/10.3390/ecsa-10-16242>

Academic Editor: Stefano Mariani

Published: 15 November 2023



**Copyright:** © 2023 by the authors. Licensee MDPI, Basel, Switzerland. This article is an open access article distributed under the terms and conditions of the Creative Commons Attribution (CC BY) license (<https://creativecommons.org/licenses/by/4.0/>).

## 1. Introduction

Recent advancements in integrated circuits (ICs) and system on chip (soc) technology have significantly transformed numerous industries, including electronics, telecommunications, and automotive sectors. However, this progress has also presented significant challenges in detecting and ensuring the reliability of integrated circuits (ICs). The system faults can lead to critical system failures, reduced performance, the loss of production, and substantial financial losses. However, it is essential to locate/identify the fault and to isolate it in order to ensure recovery and safe mode operation [1].

Due to design or manufacturing defects and normal wear and tear, faults are developed [2]. The traditional methods of detecting faulty ICs often rely on manual visual inspection or complex and expensive testing equipment. Contact methods are used to identify the discontinuity in connections to ICs. Furthermore, non-contact methods such as X-ray, ultrasound, optical comparators, vision systems, computerized tomography (CT) scanning, long range, laser radar, thermal imaging, etc., are used for fault detection [3]. These approaches are not only time-consuming but also prone to human error and subjective interpretations. Also, it is essential to develop a module to diagnose a fault (fault detection) that may affect these system operations and to locate their root causes (fault

isolation) [4]. As a result, there is a growing need for automated techniques that can streamline the detection process, improve efficiency, and enhance accuracy.

Thermal imaging has been gaining focus for its efficiency and reliability [3,5–9]. All objects in nature, as long as their temperature is not higher than the absolute temperature ( $-273\text{ }^{\circ}\text{C}$ ), display the irregular movement of molecules and atoms, which causes their surface to continuously radiate infrared light. In general, thermal imaging collects infrared light in the thermal infrared band between  $8\text{ }\mu\text{m}$  and  $14\text{ }\mu\text{m}$ , which lies in the electromagnetic spectrum between visible and microwave regions [9]. However, humans are not capable of visualizing these thermal radiations, the thermal cameras are utilized to visualize the thermal radiation emitted by the object. Once the thermal radiation emitted by the object is detected, the data are converted into gray value and the differences in gray value of each object are used for imaging. Furthermore, the thermal profiles of each object can be assessed in order to detect various parameters such as hotspots and the extent of heat spread and its location [3,9–11]. Thermal infrared imaging has proven its significance across various industries, including the medical, building and construction, agriculture, automotive, etc., industries. Furthermore, these industries showed improved efficiency, safety, and decision-making by making use of thermal imaging [12].

Non-contact thermal imaging combined with computer vision and machine learning are accurate, fast, and non-destructive to detect faults as in recent years, computer vision and machine learning algorithms have emerged as powerful tools for automated defect detection in various domains, and the fault diagnosis for integrated circuits with the help of automated defect detection can be generally classified into two stages, namely data acquisition and image classification [3,5–9,12].

Data acquisition is the process of collecting data, while image classification involves categorizing images based on their content. Further, the data acquisition process includes data acquisition, data pre-processing, the extraction of features, the training of learning models, and inference output. Common approaches for model training in image classification are support vector machines (SVMs), random forests, and deep learning, namely convolutional neural networks (CNNs), which can be time-consuming and resource-intensive [13,14]. These methods often require powerful hardware, such as graphical processing units (GPUs) or tensor processing units (TPUs), to train models effectively [14]. Also, real-time monitoring with these approaches can be challenging due to the computational demands involved in processing images in real-time. So, there is an increasing demand for a real-time approach that does not rely on high computational power, aiming to simplify the detection process.

## 2. Literature Survey

Over the last few years, many contact and non-contact methods have been used for the detection of fault diagnosis of ICs. Nowadays, non-contact methods are widely used for better performance and the detection of faults and are faster than contact methods. Further, non-contact methods are mainly carried out using X-ray, ultrasound, vision systems, computerized tomography (CT) scanning, long range lasers, laser-based radar, structured light, thermal imaging, etc. Of these mentioned techniques, thermal imaging is considered the best for the process.

Silva et al. (2013) proposed a technique using machine learning methods. The proposed method comprised three common steps, namely the extraction of features using principal component analysis (PCA), classification using the nearest neighbor (k-NN) and other methods, and the evaluation of the classifier's performance using cross-validation (CV) technique [1]. Lo et al. (2019) presented a review on the diagnosis of systems using artificial intelligence (AI) approaches. Further, the authors discussed its applications, especially in the field of the diagnosis of complex systems [5]. Al-Obaidy et al. (2017) compared various soft computing methods, which were utilized for the fault detection of ICs. Also, the histogram thresholding is used to extract features that can be further reduced through principal component analysis. Furthermore, these minimized features can be given as input to the classifier which enables the classification of defects in PCB at IC level [3].

Redon et al. (2020) proposed a condition monitoring system via thermal image using a denoising technique for reducing noise. Denoising methods comprise two types, namely continuous wavelet transform and stationary wavelet transform [15]. Huo et al. (2017) proposed a self-adaptive fault diagnosis of roller bearings using infrared thermal images. In stage one, the authors decomposed the images using two-dimensional discrete wavelet transform (2D-DWT) and Shannon entropy. Furthermore, the authors utilized the histograms of selected coefficients as the input of the feature space selection method by using the genetic algorithm (GA) and nearest neighbor (NN) for the purpose of selecting two salient features that exhibit the highest classification accuracy [16].

The objective of this work is to combine thermal imaging with the YOLO algorithm and to develop an efficient and accurate system for the real-time monitoring and detection of faulty ICs based on their thermal characteristics and to overcome the limitations of existing methods.

### 3. Materials and Methods

The proposed device comprises components such as a thermal sensor, a Raspberry PI 4 Model B controller, and a battery. Figure 1 shows the overall block diagram of a proposed device. Further, the AMG8833-based thermal sensor is an  $8 \times 8$  (64 pixels) two-dimensional non-contact type temperature detection module. Also, the thermal sensor is capable of transmitting infrared temperature readings through the inter-integrated circuits (I2C) protocol to the utilized Raspberry PI microcontroller.

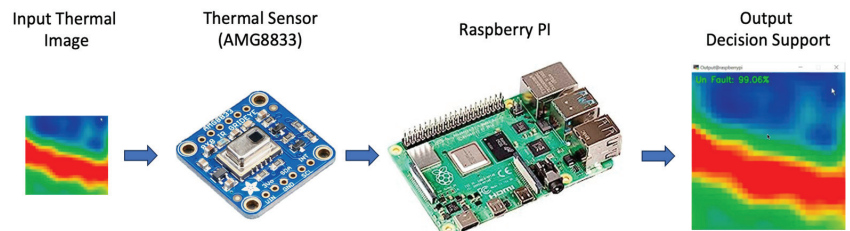


**Figure 1.** Overall diagram of a proposed device.

Figure 2 shows the connection diagram of AMG8833 thermal sensor module with Raspberry PI microcontroller. The I2C utilizes two different pins, namely serial data (SDA) and serial clock (SCL). Further, the SDA and SCL of AMG8833 are connected to the SDA and SCL pins of the PI controller, respectively, which is shown in Figure 2. Also, the AMG8833 thermal sensor requires 3.3 volts for its operation, and it is fed using the Raspberry PI controller. In this work, a fast and compact module is proposed, which can be used to identify the IC fault conditions based on thermal profiles. Further, the short circuit faults based on electrical over stress are detected. Also, electrical overstress can be caused because of high voltage.

The proposed device is a simple handy device shown in Figure 2 and can be moved over any integrated circuits through non-contact types.

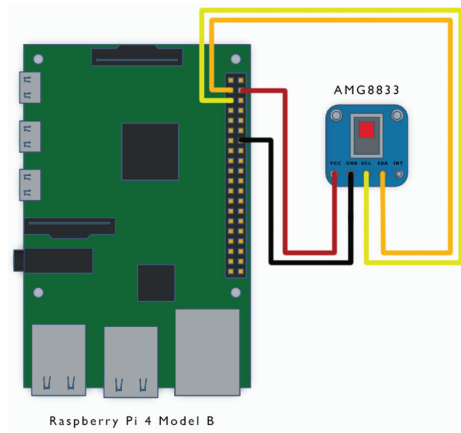


**Figure 2.** Connection diagram of thermal camera (AMG8833) with Raspberry Pi microcontroller.

### 3.1. Proposed Approach for Fault Diagnosis

Figure 3 shows the proposed approach for fault diagnosis, which is composed of various stages, such as the preprocessing of input images and the training and testing phases of the YOLOV7 model.

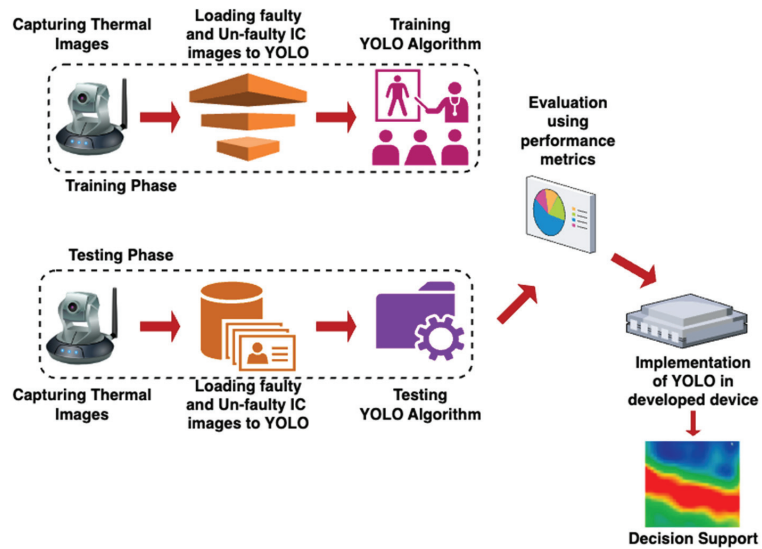


**Figure 3.** Procedure for fault diagnosis using proposed approach.

#### 3.1.1. Preprocessing of Images

Data preprocessing is a crucial step before feeding data to a model. Labeling is used to annotate faulty and un-faulty IC in images by drawing bounding boxes around them. These bounding boxes help the YOLO model to look for objects during training and testing. After labeling images, these data are converted into the .txt file format, which YOLO understands. This format includes details like the positions of the objects and their class labels.

#### 3.1.2. YOLOV7 Algorithm

YOLO stands for “You Only Look Once”, and it is one of the most effective object identification methods for partitioning images into a grid system. Each divided cell within

the grid is in charge of detecting objects on its own. Because of its precision and quickness, YOLO (you only look once) is one of the most well-known object identification techniques. When comparing YOLOV5 and YOLOV6 in terms of accuracy, YOLOV7 has a 100% accuracy rate. As a result, the algorithm used in this proposed work is YOLOV7. The design and development of YOLOV7 involves two stages, namely the training phase and testing phase.

In the training phase, 80% of the total input preprocessed faulty and unfaulty thermal images are given to the proposed YOLOV7 algorithm for training purposes. Once the YOLOV7 model is trained, the testing process is carried out. In the testing phase, 20% of the total input preprocessed faulty and unfaulty thermal images are given to the proposed YOLOV7 algorithm for testing purposes. Further, the performance metrics are evaluated to determine the efficacy of the proposed YOLOV7 model. The entire algorithm is coded using Python programming software and is executed using the Raspberry PI controller. Furthermore, the Raspberry PI, along with the thermal sensor module, acts as a handy device integrated with YOLOV7 and provides decision support regardless of whether the IC is faulty or unfaulty.

#### 4. Results and Discussion

The normal circuit boards, especially ICs and the boards with faulty ICs, were considered for this study. For both faulty and unfaulty ICs, the required power supply was applied and the thermal images were obtained using AMG8833 thermal sensor module. Also, a total of 720 images, encompassing 360 faulty and 360 unfaulty thermal images, were acquired and stored. Further, these 720 faulty and unfaulty thermal images were utilized in this work to train and test the proposed YOLOV7 model. Out of 720 images, 576 images were used for training phase and the remaining 144 images were used for the testing phase of the YOLOV7 model. Further, the 576 faulty and unfaulty images were annotated using labeling software. Figure 4 shows the faulty and unfaulty image preprocessing using labeling software. Further, the faulty and unfaulty IC images were annotated by drawing bounding boxes around them and was given to the YOLOV7 model for training images.

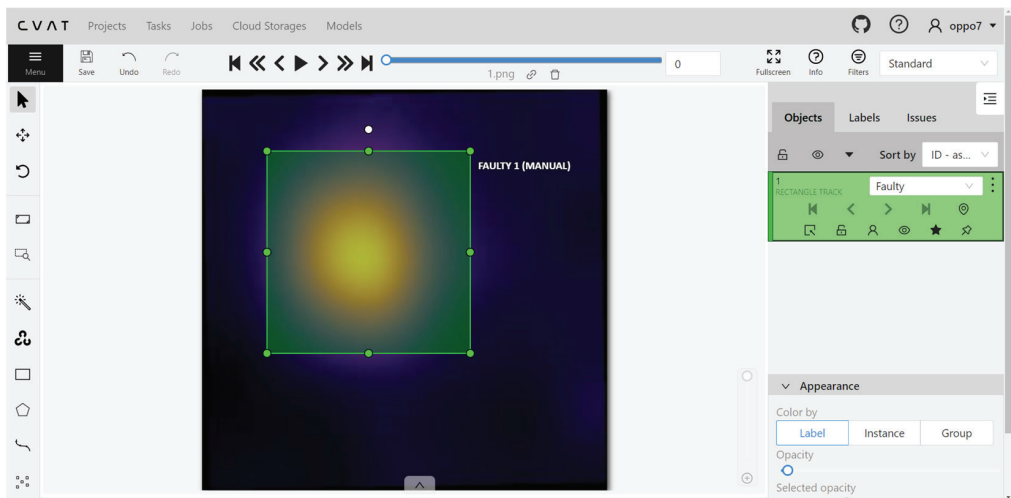


**Figure 4.** Data preprocessing using labeling software.

Once the faulty and unfaulty thermal images were acquired and processed, the fault diagnosis was carried out. Further, 144 preprocessed faulty and unfaulty thermal images were utilized to carry out the performance of the proposed YOLOV7 model. Also, these 144 preprocessed faulty and unfaulty thermal images were fed to the proposed YOLOV7 model as the test images and the output prediction was obtained.



Figure 5 shows the fault diagnosis of ICs using YOLOV7 model. Further, it is seen that the prediction output of the YOLOV7 is given in terms of a bounding box. Also, the faulty and unfaulty ICs are predicted, and the prediction output is given as a caption at the top of the bounding box. Figure 6 shows the confusion matrix for faulty and unfaulty prediction using the YOLOV7 model. Further, the confusion matrix given in Figure 6 was generated after the testing process.

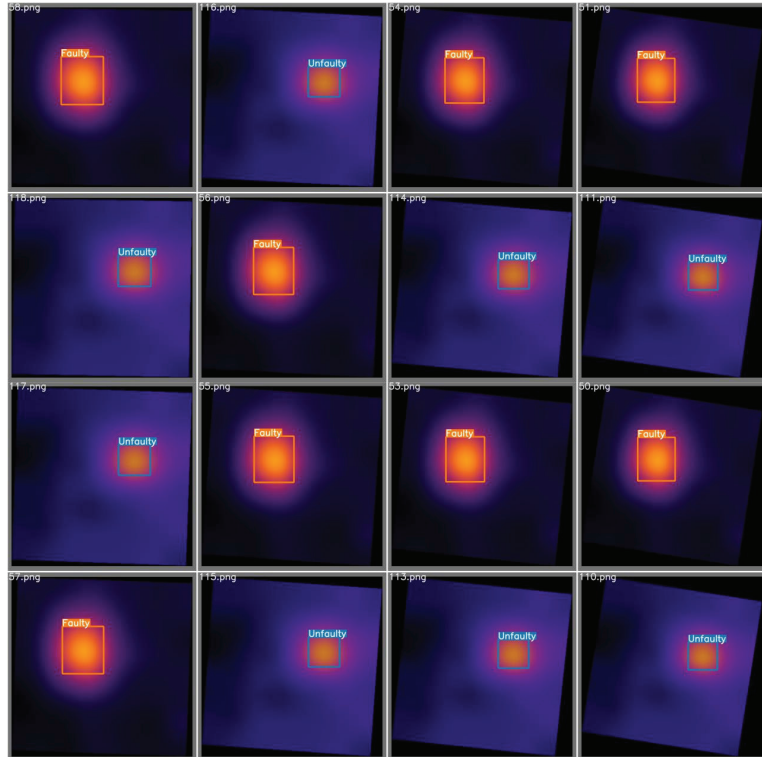


Figure 5. Fault diagnosis of integrated circuits using YOLOV7 model.

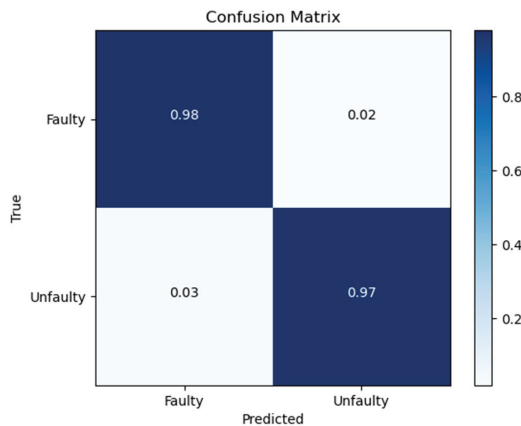


Figure 6. Confusion matrix for faulty and unfaulty prediction using YOLOV7 model.

The four different performance metrics of the YOLOV7 model are evaluated and presented in Table 1. Also, the performance metrics are expressed in terms of %. Further, it can be observed that the proposed YOLOV7 model has an accuracy of 97%. Also, the precision and recall of the proposed YOLOV7 model on faulty and unfaulty IC images are 97% and 98%, respectively. Also, the F1\_Score of the proposed YOLOV7 model is around 98%. From the performance measures, it is evident that the proposed device integrated with the YOLOV7 model is highly efficient for classifying faulty and unfaulty ICs, which gains more prominence in IC fault diagnosis applications.

**Table 1.** Performance metrics of YOLOV7 model.

Performance Metrics	Percentage (%)
Accuracy	97
Precision	97
Recall	98
F1_Score	98

## 5. Conclusions

In this study, an efficient technique using thermal image processing was proposed to inspect faulty ICs located on PCB. Further, the thermal images were collected from AMG8833 thermal sensor module and the acquired images were preprocessed. These preprocessed images were given to the YOLOV7 algorithm for image classification. Results demonstrate that the proposed method provides 97 percent accuracy in detecting faulty and unfaulty images with less computational time. Further, by integrating the capabilities of thermal camera and the YOLOV7 algorithm, the user can be alerted regarding the fault conditions of the circuit. In the near future, the proposed method could be automatized and the faults could be identified and monitored remotely using the Internet of Things (IoT).

**Author Contributions:** P.S.K.R.P., V.S. and P.A.M. conceptualized this work. P.A.M. provided the required resources. P.S.K.R.P. designed and developed the hardware. N. and Y.S. carried out the investigation. P.S.K.R.P., N. and Y.S. acquired data and managed data curation. G.P. implemented the YOLO algorithm. N. designed visualization. P.A.M. validated the acquired results. V.S. prepared the original draft. N. and Y.S. reviewed and edited the original draft. V.S. supervised and P.A.M. administered the work. All authors have read and agreed to the published version of the manuscript.

**Funding:** This research received no external funding.

**Institutional Review Board Statement:** Not applicable.

**Informed Consent Statement:** Not applicable.

**Data Availability Statement:** The raw data supporting the conclusions of this article will be made available by the authors on request.

**Conflicts of Interest:** The authors declare no conflicts of interest.

## References

1. Silva, A.A.; Bazzi, A.M.; Gupta, S. Fault diagnosis in electric drives using machine learning approaches. In Proceedings of the 2013 IEEE International Electric Machines & Drives Conference, Chicago, IL, USA, 12–15 May 2013; pp. 722–726.
2. Kabisatpathy, P.; Barua, A.; Sinha, S. *Fault Diagnosis of Analog Integrated Circuits*; Springer Science & Business Media: Dordrecht, The Netherlands, 2005; Volume 30.
3. Al-Obaidy, F.; Yazdani, F.; Mohammadi, F. Fault detection using thermal image based on soft computing methods: Comparative study. *Microelectron. Reliab.* **2017**, *14*, 56–64. [CrossRef]
4. Lo, N.G.; Flaus, J.M.; Adrot, O. Review of machine learning approaches in fault diagnosis applied to IoT systems. In Proceedings of the 2019 IEEE International Conference on Control, Automation and Diagnosis (ICCAD), Grenoble, France, 2–4 July 2019; pp. 1–6.
5. Sarawade, A.A.; Charniya, N.N. Detection of faulty integrated circuits in PCB with thermal image processing. In Proceedings of the 2019 IEEE International Conference on Nascent Technologies in Engineering (ICNTE), Navi Mumbai, India, 4–5 January 2019; pp. 1–6.

6. Haque, A.; Bharath, K.V.S.; Khan, M.A.; Khan, I.; Jaffery, Z.A. Fault diagnosis of photovoltaic modules. *Energy Sci. Eng.* **2019**, *7*, 622–644. [CrossRef]
7. Alagu Mariappan, P.; Krishnamurthy, K. A Thermal Sensor-Based Decision Support System for the Identification of Roof Leaks and Cracks. *Proceedings* **2019**, *42*, 7.
8. Laxmi; Mehra, R. Thermal imaging-based fault diagnosis of electronics circuit boards. In *Advances in Energy Technology: Select Proceedings of EMSME 2020*; Springer: Singapore, 2022; pp. 111–121.
9. Alagu Mariappan, P.; Fathima, I. Identification of Electrical Faults in Underground Cables Using Machine Learning Algorithms. *Proceedings* **2019**, *42*, 20.
10. Morain, S.A.; Budge, A.M. Fundamentals of Electromagnetic Radiation. In *Manual of Remote Sensing*, 4th ed.; American Society for Photogrammetry and Remote Sensing: Baton Rouge, LA, USA, 2019; Volume 1, pp. 1–120.
11. Coudrain, P.; Souare, P.; Colonna, J.P.; Vivet, P.; Prieto, R.; Ben-Jamaa, H.; Fiori, V.; Dutoit, D.; de Crecy, F.; Dumas, S.; et al. Experimental insights into thermal dissipation in TSV-based 3D integrated circuits. *IEEE Des. Test Comput.* **2016**, *33*, 21–36. [CrossRef]
12. Wilson, A.N.; Gupta, K.; Koduru, B.H.; Kumar, A.; Jha, A.; Cenkeramaddi, L.R. Recent advances in thermal imaging and its applications using machine learning: A review. *IEEE Sens. J.* **2023**, *23*, 3395–3407. [CrossRef]
13. Ozcanli, A.K.; Yaprakdal, F.; Baysal, M. Deep learning methods and applications for electrical power systems: A comprehensive review. *Int. J. Energy Res.* **2020**, *44*, 7136–7157. [CrossRef]
14. Wei, Y.; Zhou, J.; Wang, Y.; Liu, Y.; Liu, Q.; Luo, J.; Huang, L. A review of algorithm & hardware design for AI-based biomedical applications. *IEEE Trans. Biomed. Circuits Syst.* **2020**, *14*, 145–163. [PubMed]
15. Redon, P.; Rodenas, M.P.; Antonino-Daviu, J. Development of a diagnosis tool, based on deep learning algorithms and infrared images, applicable to condition monitoring of induction motors under transient regime. In Proceedings of the IECON 2020 The 46th Annual Conference of the IEEE Industrial Electronics Society, Singapore, 18–21 October 2020; pp. 2505–2510.
16. Huo, Z.; Zhang, Y.; Sath, R.; Shu, L. Self-adaptive fault diagnosis of roller bearings using infrared thermal images. In Proceedings of the IECON 2017-43rd Annual Conference of the IEEE Industrial Electronics Society, Beijing, China, 29 October–1 November 2017; pp. 6113–6118.

**Disclaimer/Publisher’s Note:** The statements, opinions and data contained in all publications are solely those of the individual author(s) and contributor(s) and not of MDPI and/or the editor(s). MDPI and/or the editor(s) disclaim responsibility for any injury to people or property resulting from any ideas, methods, instructions or products referred to in the content.

# A Secure Remote Health Monitoring for Heart Disease Prediction Using Machine Learning and Deep Learning Techniques in Explainable Artificial Intelligence Framework<sup>†</sup>

Sibo Prasad Patro \* and Neelamadhab Padhy

Department of Computer Science and Engineering, GIET University, Gunupur 765022, India; dr.neelamadhab@giet.edu

\* Correspondence: sibofromgiyet@giyet.edu; Tel.: +91-94372-34031

<sup>†</sup> Presented at the 10th International Electronic Conference on Sensors and Applications (ECSA-10), 15–30 November 2023; Available online: <https://ecsa-10.sciforum.net/>.

**Abstract:** Cardiovascular diseases (CVD) are the most prevalent cause of death worldwide and have become an important concern for the physicians. Clinical practices have often failed to achieve high accuracy in CVD prediction. Machine learning provides benefits not only for clinical prediction but also for feature ranking, which improves clinical professionals' interpretation of outputs. The explainable artificial intelligence (XAI) concept seeks to address the lack of explainability in machine learning and deep learning models and provides healthcare professionals with patient-tailored decision-making tools for improving treatments and diagnostics. This paper aims to predict heart disease using a RHMIoT model in the XAI framework.

**Keywords:** machine learning; deep learning; artificial intelligence; IoT; XAI

## 1. Introduction

CVDs are the most prevalent cause of morbidity and mortality throughout the world. CVDs enforce significant social and financial costs, including direct costs for diagnostic equipment and treatment by the specialists, as well as indirect costs resulting from decreased quality of life, morbidity, and loss of productivity. Furthermore, diagnostic equipment is primarily available in specialized hospitals in large cities. Patients that live in small towns receive a lack of such services. Computational methods can assist in identifying high-risk individuals and motivating them to change their behaviors for the purposes of preventive medicine. Based on their risk score outputs, these CVD models are divided into four groups: 1. If-then models, 2. Formula-based models, 3. Machine learning models, and 4. Chart-based models. These models either have accuracy or interoperability limitations [1]. Machine learning (ML) and deep learning (DL) are the subfields of artificial intelligence (AI). ML and AI are emerging technologies that play significant roles in healthcare and personalized clinical support. Clinical data in healthcare consist of electronic health data and sensor data from Internet of Things (IoT) devices. The data are available in both unstructured and structured forms. Deriving meaningful and decision-making information from these data by a human effort is difficult. The IoT and cloud-enabled technologies work together closely to provide medical assistance and maintain the electronic health records of patients. With the help of knowledge-based systems and digital medical devices, AI expert systems can be designed to provide an expert opinion. AI algorithms examine IoT data from smart watches, medicines, wearable monitoring devices, and other sources. The data assist patients, doctors, and pharmaceutical companies in evaluating medical conditions and providing feedback on treatments, medication therapy, patient outcomes, and so on.

In recent years, an additional concept known as explainability has emerged, called XAI in some contexts [2]. XAI is a type of AI in which the outcome can be understood by humans.

**Citation:** Patro, S.P.; Padhy, N. A Secure Remote Health Monitoring for Heart Disease Prediction Using Machine Learning and Deep Learning Techniques in Explainable Artificial Intelligence Framework. *Eng. Proc.* **2023**, *58*, 78. <https://doi.org/10.3390/ecsa-10-16237>

Academic Editor: Francisco Falcone

Published: 15 November 2023



**Copyright:** © 2023 by the authors. Licensee MDPI, Basel, Switzerland. This article is an open access article distributed under the terms and conditions of the Creative Commons Attribution (CC BY) license (<https://creativecommons.org/licenses/by/4.0/>).

Explainable ML models or interpretable ML models enable medical professionals to make reasonable and data-driven decisions to provide individualized care that may ultimately result in high-quality healthcare services. These models are part of the XAI field that defines a set of ML techniques to produce more explainable models while maintaining a high level of learning performance and enabling humans to understand, appropriately trust, and effectively manage the emerging generation of artificially intelligent partners [3]. The major challenges in healthcare are model interoperability and data interpretation. Another challenge is the distribution of heterogeneous data storage. Medical aid can easily reach people in remote locations and those who only need preliminary medical assistance with the aid of IoT and ML techniques. The aim of this study is to identify cardiac diseases using machine learning and deep learning algorithms using a secured remote health care application.

The aims of the study are listed below.

- A RHMIoT system is proposed using medical sensors to perform automated analysis, clustering, processing and, finally, visualize the predicted results.
- The data are transferred to cloud storage using encryption and decryption techniques to prevent unauthorized users access.
- The XAI-based SHAP and PCA feature selection techniques are applied on the dataset to select the best features, and the accuracy of the XAI-based method's performance is evaluated using a variety of evaluation metrics, including accuracy, recall, and precision.

## 2. Literature Review

Moreno-Sanchez, P. A. et al. [4] discussed the development of a heart failure-survival prediction model using ensemble trees and ML techniques. XGBoost outperformed with 83% accuracy in unseen data compared to the other ensemble tree options. The feature selection technique is performed to identify the relevant features and produce the model's results. The model's interpretability and fidelity are then quantitatively assessed, resulting in a balanced ratio between these two variables. Yang, G. et al. [5] conducted a survey on XAI progress and its efficacy in the field of the healthcare sector. The authors proposed a XAI solution for multi-center and multi-model data fusion. Compared to the current model, the previously proposed models are incapable of explaining the decision-making strategy used in categorizing results. Hence, a model was proposed to classify data and can explain the outcome of the decision. Das, S. et al. [6] focused on dimensionality reduction, using XAI to increase the accuracy of heart disease classification. Four SHAP-based explainable ML models were developed for classification, reflecting the feature contributions and calculating each feature's weight to generate the final findings. With the help of dimensional reduction, the feature subset was created through FC and FW. Finally, the XGBoost classifier outperformed as the best explanation for heart diseases with a 2% increase in model accuracy. Dave, D. et al. [7] proposed an interpretability technique to investigate a heart disease dataset using XAI techniques for deep learning systems. The SHAP technique was applied to explain the prediction of heart failure on a coronary heart disease dataset, which contained 1562 data items over three years. After screening six machine learning methods, the SHAP technique was applied to explain the XGBoost model. The performance of the model proved that the mortality rate had dropped over a three-year period. Chen, T. et al. [8] used the LightGBM (light gradient boosting machine) to predict the failure of extubation using the MIMIC-III clinical database. By using the SHAP method, they carried out an analysis of feature importance and visualized the key features. All of the models discussed above are insufficient to explain the decision-making method used in categorizing these cases. The development of a model that can classify data while explaining the outcome of the decision made is this desired.

## 3. Proposed Methodology

The approaches in this paper are discussed step by step in this section. To improve the capacity of the model, XAI was introduced to increase the effectiveness of AI. Figure 1

depicts the model for predicting cardiovascular disease using the XAI system integrated with the ML and DL model in a secured RHMIoT.

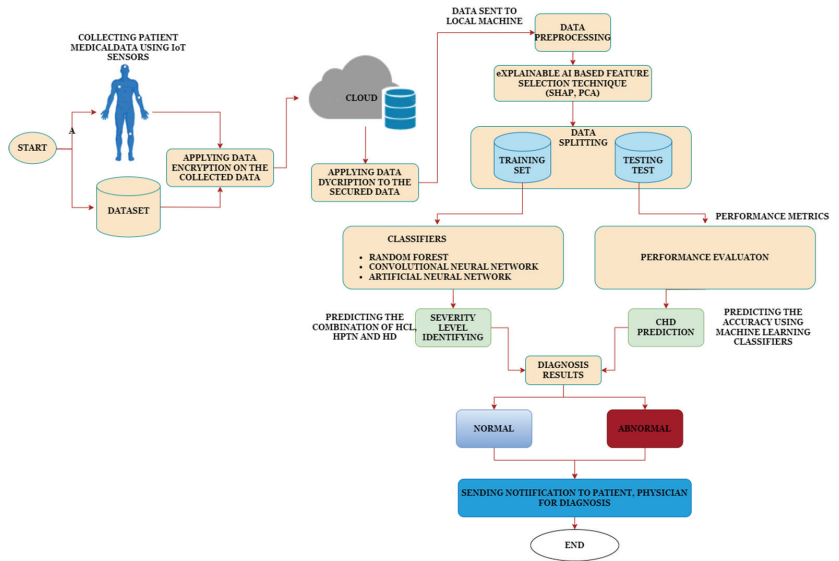


**Figure 1.** Proposed RHMIoT framework.

The model comprises a sensor layer, transport layer, and an application layer. The sensor layer is used to collect the data using various medical IoT sensors. Using ML-based applications, physicians can continuously analyze their patients’ diseases and health status using IoT-medical sensors [9]. After the patient data are collected through the sensors, the data are transferred to cloud storage using encryption and decryption techniques to prevent unauthorized users from accessing it. A performance algorithm is used to encrypt sensitive patient data. An algorithm was designed for enhancing security with a key-dependent dynamic S-Box and a hyper elliptic curve. In the application layer, heart disease was predicted using ML and deep learning algorithms. The RHMIoT framework is divided into two phases. In phase-1, the patient’s risk of HPTN and its severity level is calculated. The DM algorithm is applied to the patient’s medical data to calculate HPTN and its severity levels [10]. In phase-2 heart, disease accuracy is calculated using machine learning and deep learning classifiers. The Framingham dataset was used to train our model, and was retrieved from Kaggle. The heart disease dataset contained 4238 records with 16 attributes. The data pre-processing was carried out using feature selection and classification techniques. After the training process, the IoT medical device sensor data are tested by classifying and contrasting the results. To accurately predict the presence of heart disease, the proposed RHMIoT framework used Artificial Neural Network (ANN), Convolutional Neural Network(CNN) and Random Forest (RF). The following section provides a detailed explanation of the training procedure.

### 3.1. Data Preprocessing

A data preprocessing method was used to replace missing data or remove noise. The missing values in the dataset were identified and updated by a median value of the attribute. A studentized residual technique was used to lower the residuals. It finds the correlation among the features and helps to find the outliers in a given dataset. The preprocessing of data aids in improving heart disease detection. After data pre-processing, the dataset is normalized using a min–max normalization technique.

$$\hat{V}_I = \frac{V_I - \text{MIN}_A}{\text{MAX}_A - \text{MIN}_A} (\text{NEW\_MAX}_A - \text{NEW\_MIN}_A) + \text{NEW\_MIN}_A \quad (1)$$

### 3.2. Feature Selection

Explainable AI (XAI)-based feature selection techniques are used to identify and select the most relevant features from a dataset while maintaining interpretability and transparency in the feature selection process. These techniques are particularly useful when you need to understand why certain features were chosen or excluded from a predictive model. SHAP (SHapley Additive exPlanations) and PCA (Principal Component Analysis) used for feature selection.

#### 3.2.1. SHAP (Shapley Additive Explanations)

SHAP is an extremely effective XAI approach. It assigns values to prediction characteristics, showing their contributions to the model's output. SHAP allows for us to discover the factors that influence AI decisions, making them more interpretable and trustworthy. The following dependence plot in Figure 2 shows how a particular characteristic (in this case, 'age') effects the model's output (in this case, the chance of belonging to class 1, which might signify a favorable conclusion in your binary classification problem). The y-axis (SHAP Value) displays the SHAP values for the 'age' characteristic. The SHAP values represent the feature's influence on the model's prediction for each data point. Positive SHAP values increase the model's output, whereas negative values decrease it. The X-axis represents the values of a test data's 'age' feature. Each point on the diagram represents one of the test data's points. The point's vertical location corresponds to the SHAP value for 'age' for that individual data point. If the trend line is generally flat, it suggests that the 'age' attribute has little to no link with the model's output. In other words, changes in 'age' have no discernible effect on the model's forecast. If the trend line is favorably sloping, it indicates that as 'age' increases, so does the model's prediction (probability of belonging to class 1). According to this concept, it was suggested that older people are more likely to belong to class 1. The results ranged between  $-2.0$  to  $-1.0$ . The dependence plot's main function is to show how changes in the feature of interest ('age') affect the model's output. The data and SHAP values for a specific dataset and model determine the specific axis values and ranges.

#### 3.2.2. PCA (Principal Component Analysis)

PCA is a technique for reducing dimensionality in data analysis and visualization. Reducing SHAP values can be high-dimensional, especially when features are greater in a dataset. It can be difficult to visualize high-dimensional data in a single graph. PCA aids in dimensionality reduction while maintaining as much information as feasible. PCA finds linear combinations of features that capture the most significant variances in the data. These primary components can aid in the discovery of underlying patterns and correlations between features. Figure 3 shows the PCA visualization of SHAP values. SHAP and PCA can identify the features that are most relevant for heart disease prediction in sensor data. Patients' heart conditions were determined using training and testing dataset with an 80:20% ratio. The following research questions address how the XAI environment aids in heart disease prediction.

RQ1: How can a machine learning model make predictions for a specific data point in an Explainable AI environment, in this case, "patient 0"?

Solution: The decision plot in Figure 4 shows the most critical features that influence the model's prediction for "patient 0". The absolute SHAP values of these attributes are ranked from top to bottom. SHAP factors: Each feature's SHAP values are represented by horizontal bars. Positive SHAP values (on the right) indicate that the feature raises the model's prediction (towards a positive class), whereas negative SHAP values (on the left) reduce the prediction (towards a negative class). In binary classification, the probability threshold (generally 0.5) is what distinguishes the two classes. If the projected value line is to the right of the vertical centerline, the class is predicted to be positive.

RQ2: How effectively does a Random Forest classifier perform in distinguishing between individuals with heart disease and those without, as demonstrated by the confusion

matrix heatmap, and what insights can be gained from the distribution of TP, TN, FP, and FN predictions in the context of heart disease classification?

Solution: The confusion matrix heatmap generated using a Random Forest classifier on the heart disease dataset provides valuable insights into the model's performance, which is shown in Figure 5. It reveals the distribution of TP, TN, FP, and FN predictions. These metrics are crucial for understanding the classifier's ability to correctly identify individuals with heart disease TP, correctly identify those without heart disease TN, misclassify healthy individuals as having heart disease FP, and misclassify individuals with heart disease as healthy FN.

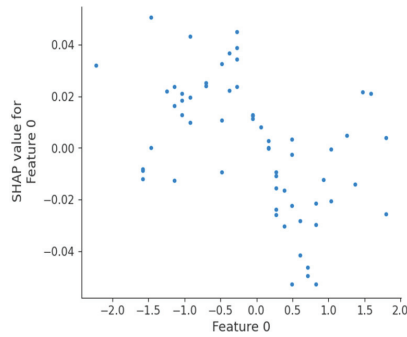


Figure 2. Dependence plot.

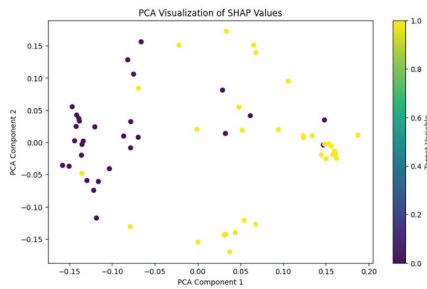


Figure 3. Decision plot for PCA visualization.

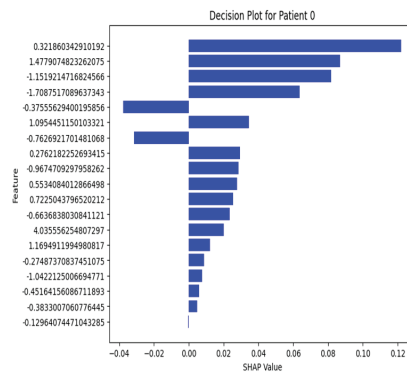
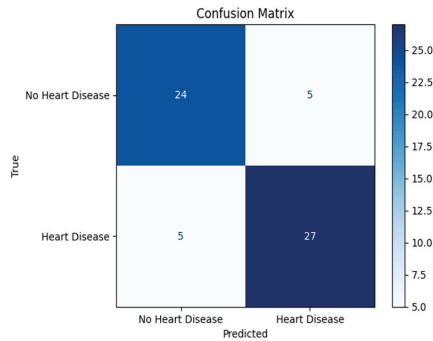


Figure 4. Decision plot.





**Figure 5.** Confusion matrix.

### 3.3. Machine Learning Algorithms

The flow of the RHMIoT model begins with the dataset's input parameters. After data preprocessing and feature selection, the dataset is passed on to the proposed framework. For comparative analysis, RF, ANN, and CNN algorithms were used in study.

**Random Forest (RF):** An AI ensemble method combining several learning algorithms to produce accurate prediction. Compared to a statistical ensemble, a machine learning ensemble is typically much more flexible in its structure. During the training phase, the RF algorithm constructs multiple decision trees. The RF selects the majority decision of the trees as the final decision. The "forest" is an ensemble of decision trees, which are typically trained through the "bagging" method. Bagging is used to combine several learning models to improve the overall result.

#### 3.3.1. Convolutional Neural Network (CNN)

CNN has the ability of feature learning. Hence, CNN is a suitable algorithm for heart disease prediction at an earlier stage. We can use CNN for binary classification. In heart disease prediction, a patient suffering from CHD is classified as "1" and not-suffering is classified as "0", which is called a binary classification. CNN architecture operates in a single-input and single-output sequential mode. CNN architecture relies heavily on the convolution layer for feature extraction.

#### 3.3.2. Artificial Neural Network (ANN)

ANN is interrelated with input, hidden, and output units. The patient's risk factors are accepted as the input unit for medical diagnosis. ANN has proven to be more effective in the field of healthcare and medicine. In the proposed model, eight neurons were constructed for the input layer to correlate with eight important characteristics. The output class variable generates either 0 or 1, where 0 indicates that the person does not have heart disease and 1 indicates the person suffers with heart disease.

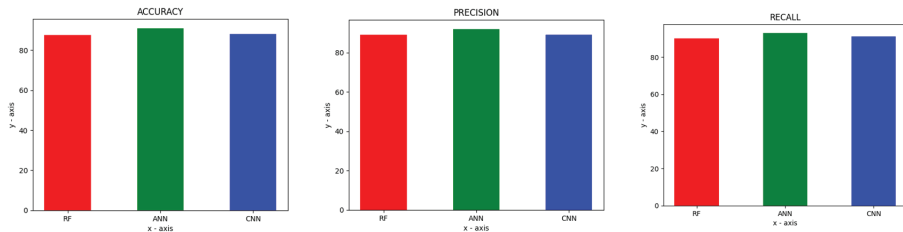
## 4. Results and Discussion

The aim of this study was to calculate the severity level of heart disease and prediction accuracy. In the proposed RHMIoT model, three different classification algorithms, RF, ANN, and CNN, were applied to a heart disease test dataset.

Table 1 shows the performance metrics of the proposed classifiers. The performance of each experiment was compared through performance metrics and statistical results. For the early diagnosis of heart disease, more attention was given to achieving maximum true positives. The deep learning algorithms performed well compared to the machine learning classifiers in terms of testing accuracy, precision, and recall. RF is recognized as a weak classifier for the proposed work because it demonstrated low accuracy. Figure 6 shows a plot graph representation of the proposed classifiers.

**Table 1.** Experimental results.

Classifier	Accuracy	Precision	Recall
RF	87.69%	89.00%	90.00%
ANN	91.00%	92.00%	93.00%
CNN	88.10%	89.10%	91.00%

**Figure 6.** Box plot bar graph for accuracy, precision, and recall.

## 5. Conclusions

Due to the rapid increase in CVDs, remote health monitoring has become more popular over the globe. This technique helps patients receive diagnoses at home or in a remote area. A lightweight block encryption and decryption technique is provided to secure the RHMloT. A variety of IoT medical sensors are used to gather data to test the suggested model. XAI-based SHAP and PCA techniques were used for feature selection. Heart disease accuracy was calculated using various deep learning and machine learning algorithms. The outcomes were determined using several performance matrices. In comparison to other machine learning and deep Learning techniques, ANN provided the greatest accuracy of 91.00%. In the future, we will try to improve the speed and precision of our model by making a few dynamic adjustments in accordance with the requirements of the user.

**Author Contributions:** N.P., designed, directed and coordinated the study, verified the analytical methods, conceived the original idea and supervised the findings of this work; S.P.P., developed the model, preparation of images, developed the theoretical formalism, data collection, performed the analytic calculations, computational framework, analyzed the data, carried out the experiment, interpretation of the results, analysis of the results, visualization, implementation of the research and took the lead in writing-review and editing the manuscript. All authors have read and agreed to the published version of the manuscript.

**Funding:** The research received no external funding.

**Institutional Review Board Statement:** Not applicable.

**Informed Consent Statement:** Not applicable.

**Data Availability Statement:** The data support the findings of this study are openly available in “Kaggle” at <https://www.kaggle.com/datasets/aasheesh200/framingham-heart-study-dataset> (accessed on 15 March 2023).

**Conflicts of Interest:** The authors declare no conflicts of interest.

## References

- Ordikhani, M.; Saniee Abadeh, M.; Prugger, C.; Hossain, R.; Mohammadifard, N.; Sarrafzadegan, N. An evolutionary machine learning algorithm for cardiovascular disease risk prediction. *PLoS ONE* **2022**, *17*, e0271723. [CrossRef] [PubMed]
- Guleria, P.; Naga Srinivasu, P.; Ahmed, S.; Almusallam, N.; Alarfaj, F.K. XAI framework for cardiovascular disease prediction using classification techniques. *Electronics* **2022**, *11*, 4086. [CrossRef]
- Ahsan, M. Heart Attack Prediction Using Machine Learning and XAI. Ph.D. Thesis, Brac University, Dhaka, Bangladesh, 2022.
- Moreno-Sanchez, P.A. Development of an explainable prediction model of heart failure survival by using ensemble trees. In Proceedings of the 2020 IEEE International Conference on Big Data (Big Data), Atlanta, GA, USA, 10–13 December 2020; pp. 4902–4910.

5. Yang, G.; Ye, Q.; Xia, J. Unbox the black-box for the medical explainable AI via multi-modal and multi-centre data fusion: A mini-review, two showcases and beyond. *Inf. Fusion* **2022**, *77*, 29–52. [CrossRef] [PubMed]
6. Das, S.; Sultana, M.; Bhattacharya, S.; Sengupta, D.; De, D. XAI-reduct: Accuracy preservation despite dimensionality reduction for heart disease classification using explainable AI. *J. Supercomput.* **2023**, *79*, 18167–18197. [CrossRef] [PubMed]
7. Dave, D.; Naik, H.; Singhal, S.; Patel, P. Explainable ai meets healthcare: A study on heart disease dataset. *arXiv* **2020**, arXiv:2011.03195.
8. Chen, T.; Xu, J.; Ying, H.; Chen, X.; Feng, R.; Fang, X.; Gao, H.; Wu, J. Prediction of extubation failure for intensive care unit patients using light gradient boosting machine. *IEEE Access* **2019**, *7*, 150960–150968. [CrossRef]
9. Patro, S.P.; Padhy, N.; Sah, R.D. An improved ensemble learning approach for the prediction of cardiovascular disease using majority voting prediction. *Int. J. Model. Identif. Control* **2022**, *41*, 68–86. [CrossRef]
10. Patro, S.P.; Padhy, N. An RHMIoT Framework for Cardiovascular Disease Prediction and Severity Level Using Machine Learning and Deep Learning Algorithms. *Int. J. Ambient. Comput. Intell.* **2022**, *13*, 1–37. [CrossRef]

**Disclaimer/Publisher’s Note:** The statements, opinions and data contained in all publications are solely those of the individual author(s) and contributor(s) and not of MDPI and/or the editor(s). MDPI and/or the editor(s) disclaim responsibility for any injury to people or property resulting from any ideas, methods, instructions or products referred to in the content.

# The Detection of *E. coli* and *S. aureus* on Sensors without Immobilization by Using Impedance Spectroscopy<sup>†</sup>

Oksana Gutsul<sup>1,2,\*</sup>, David Rutherford<sup>1</sup>, Marketa Barinkova<sup>1</sup>, Vsevolod Slobodyan<sup>3</sup> and Bohuslav Rezek<sup>1</sup>

<sup>1</sup> Physics Department, Faculty of Electrical Engineering, Czech Technical University in Prague, 16227 Prague, Czech Republic

<sup>2</sup> Biological Physics and Medical Informatics Department, Bukovinian State Medical University, 58000 Chernivtsi, Ukraine

<sup>3</sup> Electronics and Energy Department, Applied-Physics and Computer Sciences Institute, Yuriy Fedkovich Chernivtsi National University, 58012 Chernivtsi, Ukraine

\* Correspondence: gutsul@bsmu.edu.ua

<sup>†</sup> Presented at the 10th International Electronic Conference on Sensors and Applications (ECSA-10), 15–30 November 2023; Available online: <https://ecsa-10.sciforum.net/>.

**Abstract:** The impedance spectroscopy method (AC  $f = 4\text{--}8$  MHz at a constant amplitude of 1 V) and Pt-IDE sensors were used to detect and monitor different concentrations ( $10^3$ ,  $10^6$ , and  $10^9$  CFU/mL) of both live and dead bacteria cells (*Escherichia coli* and *Staphylococcus aureus*). The analysis of the impedance spectra shows the differences in resistance with increasing concentrations for both types of bacteria and the presence of characteristic changes in the frequency range 10–100 kHz. The presence of live bacteria led to a decrease in the impedance value compared to dead cells, and the value of  $R_s + R_{ct}$  decreased about two times.

**Keywords:** impedance spectroscopy; IDE sensors; bacteria detection; *Escherichia coli*; *Staphylococcus aureus*

## 1. Introduction

The detection of bacteria is important in various fields, including healthcare, food safety, and environmental monitoring. The rapid and accurate identification of bacterial pathogens such as *Escherichia coli* (*E. coli*) and *Staphylococcus aureus* (*S. aureus*) is essential for public health and safety. Traditional methods of bacterial detection often involve time-consuming sample preparation steps, specialist personnel, and equipment that involves complex analyses. In the last decade, more innovative methods have been developed that greatly simplify the approach to the real-time detection of bacteria [1–4], such as electrical impedance spectroscopy (EIS).

Electrical impedance spectroscopy (EIS) is used to study various biological samples in suspension and is capable of characterizing their properties [5–8]. The native negative surface charge on live bacterial cells enables their detection and characterization using electrical impedance measurements. The impedance  $Z$  is the ratio of the applied voltage to the measured current and is a function of resistance ( $R$ ), capacitance ( $C$ ), and the applied frequency:  $Z = V/I = R + 1/j \omega C$  [7,9].

The metabolic activity of bacteria can be controlled by changes in the conductivity of the nutrient medium [10–12]. EIS has successfully been used to monitor changes related to adhesion, the growth of bacteria, and their behavior in real time [1–3]. The impedance-based detection of bacteria has several advantages over more traditional detection methods, such as low cost, versatility, and ease of implementation [5,6]. However, very few works have been devoted to the direct detection of bacteria by impedance spectroscopy on interdigitated electrode (IDE) sensors without bacterial immobilization [1,6,13]. Modern biosensors typically require the immobilization of specific antibodies onto the surface of the sensor to offer high specificity but have a low sensitivity mainly due to low capture efficiency

**Citation:** Gutsul, O.; Rutherford, D.; Barinkova, M.; Slobodyan, V.; Rezek, B. The Detection of *E. coli* and *S. aureus* on Sensors without Immobilization by Using Impedance Spectroscopy. *Eng. Proc.* **2023**, *58*, 79. <https://doi.org/10.3390/ecsa-10-16073>

Academic Editor: Stefano Mariani

Published: 15 November 2023



**Copyright:** © 2023 by the authors. Licensee MDPI, Basel, Switzerland. This article is an open access article distributed under the terms and conditions of the Creative Commons Attribution (CC BY) license (<https://creativecommons.org/licenses/by/4.0/>).

(<35%), even after careful optimization [2,14]. Therefore, the search for alternative methods of bacteria detection that do not depend on the immobilization of the electrode surface is still relevant.

In this paper, we introduce the principle, methodology, and application of direct detection of *E. coli* and *S. aureus* on IDE sensors using immobilization-free impedance spectroscopy. We propose an approach for the direct detection of bacteria on IDE sensors by measuring the change in impedance. This method avoids complex surface modification and immobilization stages, simplifying the detection process while maintaining high measurement sensitivity [6,9,11,13,15]. The presented method is capable of detecting bacterial concentration ( $10^3$ – $10^9$  CFU/mL) in a short time (30 s) across a wide frequency range (4–8 MHz) and demonstrates selectivity for two different types of bacterial cells (*E. coli* and *S. aureus*). We also demonstrate the ability to distinguish between live and dead cells. At the same time, the processes for preparing the sensor surface are simplified, thereby increasing the economic efficiency of this method and reducing the need for specialized personnel. There is an obvious prospect of practical application of this method for selective detection of various types of bacteria.

## 2. Materials and Methods

### 2.1. Preparation of the Biological Samples (Gram-Positive *S. aureus* and Gram-Negative *E. coli*)

Gram-negative *E. coli* (CCM3954) and Gram-positive *S. aureus* (CCM 3953) were stored at  $-20\text{ }^\circ\text{C}$  in single-use vials and thawed at room temperature before use. A 1-in-10 dilution series was performed from the stock vial using sterile 0.9% NaCl (Penta), and 500  $\mu\text{L}$  of each dilution was added to Petri dishes containing Mueller Hinton (MH) agar that were placed overnight in an incubator ( $37\text{ }^\circ\text{C}$ ). The following day, a single colony was removed from the MH agar plate and reconstituted in 5 mL MH broth and grown overnight at  $37\text{ }^\circ\text{C}$  in an orbital shaker (150 rpm). After culturing, the bacteria were centrifuged (13,000 rpm at 10 min) to separate bacterial cells from MH broth and resuspended in sterile deionized water ( $\text{DH}_2\text{O}$ ,  $\sigma = 0.1\text{ }\mu\text{S/cm}$ ). This process was repeated additionally two times to remove any residual MH broth. To obtain dead bacteria, the first wash step was preceded by an additional wash using 99.9% ethanol and the absence of live bacteria was confirmed by the absence of growth on MH agar. The bacteria were then adjusted to McFarland's density 6.0, which is equivalent to  $1.8 \times 10^9$  colony forming units per milliliter (CFU/mL) before sequential dilution using  $\text{DH}_2\text{O}$  to the desired concentrations ( $10^3$ ,  $10^6$ , and  $10^9$  CFU/mL).

### 2.2. Preparation of the IDE Sensor Surface

Prior to use, the surface of the IDE sensor platform was cleaned with isopropanol then rinsed with deionized water and dried under a stream of nitrogen.

### 2.3. Electrical Impedance Measurements

The electrical impedance spectroscopy (EIS) measurements with IDE sensors type CC1.Au and CC1.Pt (BVT Technologies, Czech Republic) were made by using an IM 3536 LCR meter and application software (V1.40 Hioki, Nagano, Japan) in the frequency range from 4 Hz up to 8 MHz. The sample was placed in a Faraday cage. The electrodes were fixed using a clamp and connected to the LCR meter. Experimental Nyquist plots of the impedance  $-Z_{\text{im}} = f(Z_{\text{rel}})$  were constructed to analyze the electron transport processes occurring at the interface of the Pt-IDE sensor and two types of bacteria cells (*E. coli* and *S. aureus*). All measurements were conducted at a temperature of  $24 \pm 1\text{ }^\circ\text{C}$ , the immersion sample volume was 1 mL. The general scheme of the proposed method for the detection of bacteria using impedance spectroscopy on IDE sensors is shown in Figure 1.

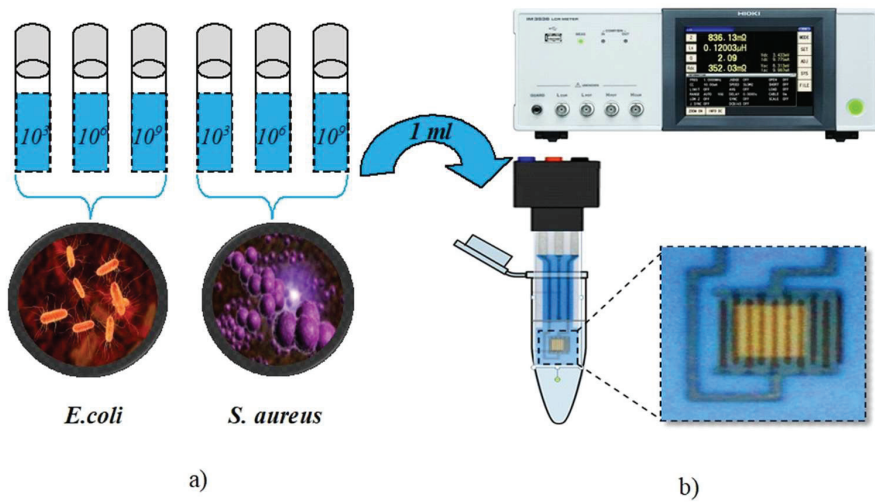


**Figure 1.** Schematic image of bacteria detection by EIS on IDE sensor: (a) preparation of different concentrations of bacteria; (b) IM 3536 LCR and IDE sensor (overall view and zoomed image of the IDE measurement part).

### 3. Results and Discussion

#### Detection of Bacteria Cells—Characterization of Impedance Spectrum Data

Impedance spectroscopy was performed in deionized water (DH<sub>2</sub>O) (non-Faraday EIS) with increasing *E. coli* concentrations ( $10^3$ ,  $10^6$ , and  $10^9$  CFU/mL) in a frequency range between 4 Hz and 8 MHz at a formal voltage of 1 V. The effect of different concentrations of *E. coli* bacteria cells on DH<sub>2</sub>O pH was previously measured (Figure 2a). The growth of live and dead cells was monitored using agar plates for 24 h at 37 °C (Figure 2b).

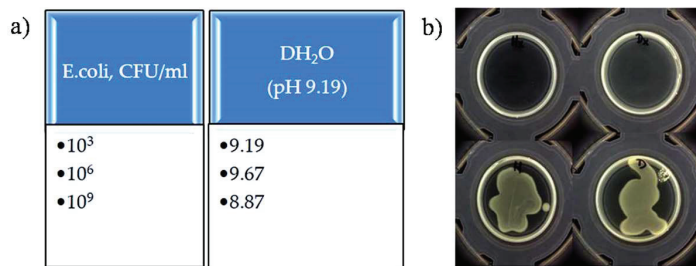


**Figure 2.** *E. coli* in DH<sub>2</sub>O: (a) pH of *E. coli* for different CFU/mL; (b) recultivated *E. coli* colonies ( $10^8$  CFU/mL) (live (H/D) and dead (H<sub>x</sub>/D<sub>x</sub>) with HPLC (H) and DH<sub>2</sub>O (D) on LB agar plate after incubation).

The Nyquist plots (Figure 3) were fitted with an equivalent circuit (the inset of Figure 3), showing that the  $R_{ct}$  is a relevant parameter that depends on the bacterial cell concentration. The Nyquist curves were fitted using the EIS analyzer software, and the best results were obtained with the equivalent circuit (inset of Figure 3), where CPE is a constant phase element included in the circuit in parallel and in series with the charge transfer resistance  $R_{ct}$ .  $R_s$  is the solution resistance. A decrease in the charge transfer resistance  $R_{ct}$  was observed with an increase in the concentration of bacterial cells, both live (Figure 3a) and dead (Figure 3b), in deionized water.

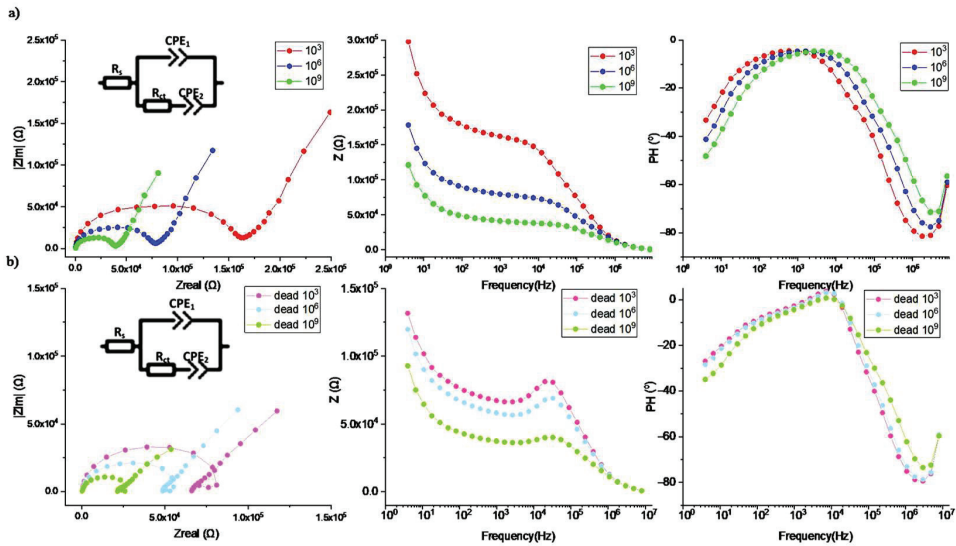


**Figure 3.** Impedance spectra (Nyquist and Bode plots) of *E. coli* ( $10^3$ ,  $10^6$ , and  $10^9$  CFU/mL): (a) live and (b) dead bacteria.

The semicircle-shaped portion of the Nyquist plots obtained at high frequencies corresponds to the faradic transfer of electrons on the electrodes, while the spectrum obtained at low frequencies provides information on the diffusion process of transferring bacterial waste products in solution to the electrode surface. For dead *E. coli* bacteria, characteristic changes were observed at frequencies of 10–100 kHz, which were absent in the impedance spectra for live cells, which can serve as an identifier for distinguishing live cells from dead ones.

The obtained estimated parameters of charge transfer resistance, series resistance, and for series and parallel CPE are shown in Table 1.

**Table 1.** Evaluated parameters for *E. coli* EIS (live and dead cells).

CFU/mL	Live					
	$R_s, \Omega$ ( $\times 10^{-14}$ )	$R_{ct}, k\Omega$	$CPE1$ ( $\times 10^{-10}$ )	n1	$CPE2$ ( $\times 10^{-7}$ )	n2
$10^3$	9.31	166	5.55	0.74	5.86	0.69
$10^6$	9.01	80.53	7.04	0.74	7.59	0.71
$10^9$	8.79	41.08	8.86	0.73	9.56	0.72
CFU/mL	Dead					
	$R_s, \Omega$ ( $\times 10^{-14}$ )	$R_{ct}, k\Omega$	$CPE1$ ( $\times 10^{-11}$ )	n1	$CPE2$ ( $\times 10^{-6}$ )	n2
$10^3$	8.69	70.24	1.37	0.99	1.88	0.60
$10^6$	8.64	50.52	4.05	0.93	1.85	0.61
$10^9$	7.26	22.67	1.33	1.00	4.08	0.50

For dead cells, a decrease in the CPE values by an order of magnitude is observed (Table 1). Moreover, the value of CPE1 decreases by an order of magnitude, which is associated with a change in the capacitive properties of the membranes of dead cells. CPE2, responsible for the change in mass transfer in solution, increases by an order of magnitude,

indicating an increase in ion diffusion in solution due to changes in osmotic pressure inside and outside the dead cells. There is a significant decrease in resistance for suspensions with dead *E. coli* cells. For comparison, the impedance spectra for live and dead cells with a concentration of  $10^3$  and  $10^6$  CFU/mL are shown below in one plot (Figure 4a).

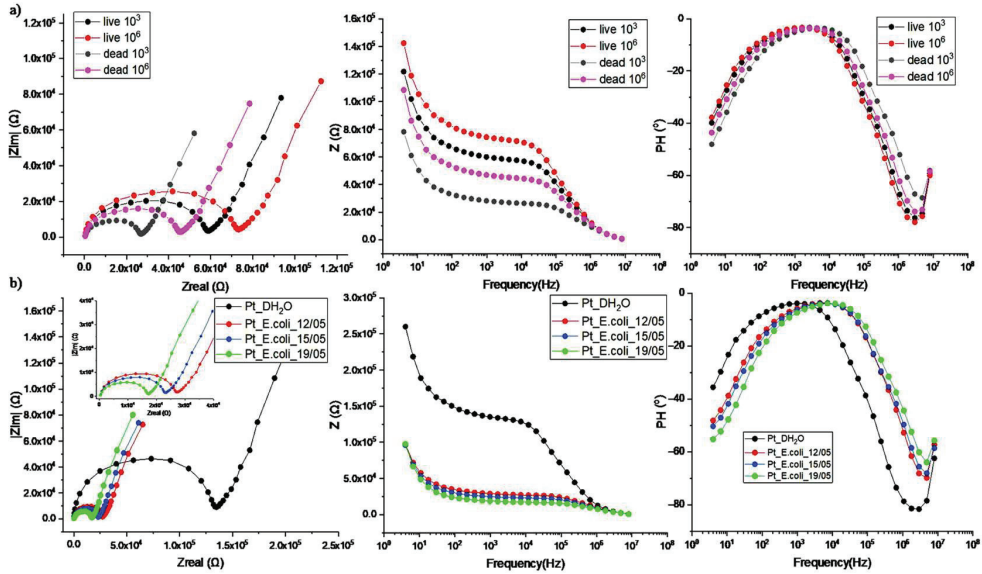


**Figure 4.** Comparison of impedance spectra of *E. coli* (Nyquist and Bode plots): (a) *E. coli* live and dead; (b) *E. coli*  $10^8$  CFU/mL (during 1st, 4th, and 8th day) and  $\text{DH}_2\text{O}$ .

Impedance measurements were also performed for live *E. coli*  $10^8$  CFU/mL cells in  $\text{DH}_2\text{O}$  on the 1st, 4th, and 8th day after suspension preparation. There was a tendency to decrease the charge transfer resistance with increasing storage time of the suspension, which is associated with an increase in bacteria waste products. For comparison, the impedance spectrum for pure  $\text{DH}_2\text{O}$  is shown (Figure 4b–black curve). It is obvious that the increase in the electrical conductivity of the suspension is due to the presence of bacterial cells.

To compare the impedance spectra of *E. coli* and *S. aureus* in  $\text{DH}_2\text{O}$ , suspensions with a concentration of  $10^9$  CFU/mL were chosen. The Nyquist and Bode curves are shown in Figure 5a,b.

The obtained estimated parameters of the charge transfer resistance  $R_{ct}$  and series resistance  $R_s$ , as well as the values of the CPEs included in parallel and in series with the charge transfer resistance  $R_{ct}$ , are given below in Table 2.

**Table 2.** Evaluated parameters for live and dead bacterial cells.

$10^9$ CFU/mL	$R_s, \Omega$ ( $\times 10^{-14}$ )	$R_{ct}, \text{k}\Omega$	CPE1	n1	CPE2 ( $\times 10^{-6}$ )	n2
<i>E. coli</i>						
Live	1.60	9.21	$8.86 \times 10^{-09}$	0.70	2.26	0.70
Dead	1.62	32.70	$5.39 \times 10^{-10}$	0.77	1.35	0.72
<i>S. aureus</i>						
Live	9.59	73.46	$1.36 \times 10^{-10}$	0.85	1.23	0.70
Dead	9.58	58.37	$1.73 \times 10^{-10}$	0.83	1.40	0.67



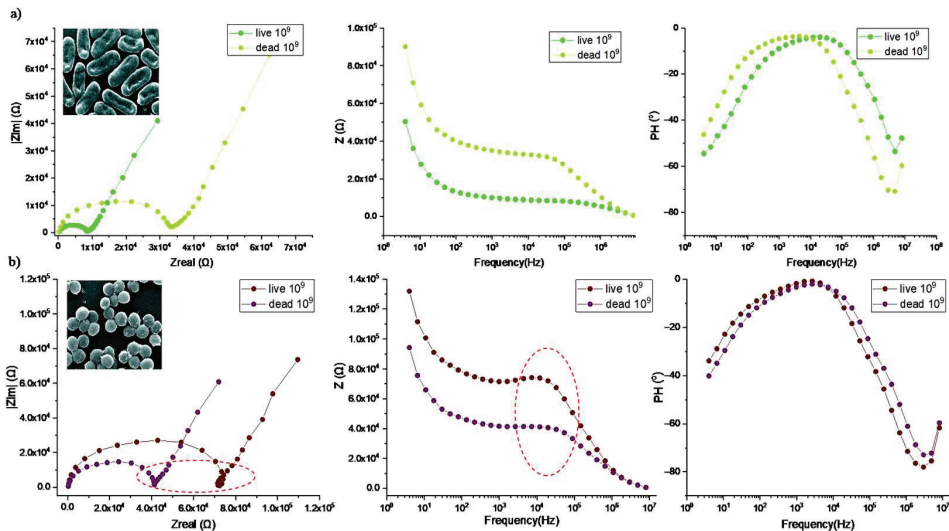


**Figure 5.** Nyquist and Bode plots of impedance spectra live/dead: (a) *E. coli*; (b) *S. aureus*.

Opposite dependencies of the change in charge transfer resistance and the obtained values of the total impedance for live and dead cells for the two types of bacteria are observed. This difference can be related to the structural features of these types of bacteria and their size. *S. aureus* are spherical cells that tend to form larger agglomerates, whereas *E. coli* are rod-shaped cells and preferentially exist as individual cells. For *S. aureus*, increased CPE1 (the capacity of the double layer  $C_{dl}$ ) is due to the difference in bacterial membrane structure.

#### 4. Conclusions

The proposed method of selective detection of bacterial cells can be used to differentiate between two types of bacteria, specifically *E. coli* and *S. aureus*, as well as qualitatively characterize their physiological state, i.e., dead or alive, and to estimate their concentration in samples with an unknown number of bacteria per unit volume.

**Author Contributions:** Conceptualization, O.G. and V.S.; methodology, O.G. and V.S.; software, O.G.; validation, B.R., V.S. and D.R.; formal analysis, O.G., V.S., D.R. and M.B.; investigation, O.G., D.R. and M.B.; writing—original draft preparation, O.G.; writing—review and editing, B.R.; visualization, O.G. and V.S.; supervision, B.R.; project administration, B.R.; funding acquisition, B.R. All authors have read and agreed to the published version of the manuscript.

**Funding:** This research was financially supported by the TACR project TM0300033 (TACOM) and by the MEYS project CZ.02.1.01/0.0/0.0/16\_019/0000778 (CAAS).

**Institutional Review Board Statement:** Not applicable.

**Informed Consent Statement:** Not applicable.

**Data Availability Statement:** All data is available upon request to the corresponding author.

**Conflicts of Interest:** The authors have no financial/commercial conflicts of interest.

#### References

- Mallén-Alberdi, M.; Mas, J.; Fernández-Sánchez, C.; Baldi, A. Impedance spectral fingerprint of *E. coli* cells on interdigitated electrodes: A new approach for label free and selective detection. *Sens. Bio-Sens. Res.* **2016**, *7*, 100–106. [CrossRef]
- Wang, R.; Lum, J.; Callaway, Z.; Lin, J.; Bottje, W.; Li, Y. A Label-Free Impedance Immunosensor Using Screen-Printed Interdigitated Electrodes and Magnetic Nanobeads for the Detection of *E. coli* O157:H7. *Biosensors* **2015**, *5*, 791–803. [CrossRef] [PubMed]

3. Yang, H.; Zhou, H.; Hao, H.; Gong, Q.; Nie, K. Detection of *Escherichia coli* with a label-free impedimetric biosensor based on lectin functionalized mixed self-assembled monolayer. *Sens. Actuators B Chem.* **2016**, *229*, 297–304. [CrossRef]
4. Ahmed, A.; Rushworth, J.V.; Hirst, N.A.; Millner, P.A. Biosensors for Whole-Cell Bacterial Detection. *Clin. Microbiol. Rev.* **2014**, *27*, 631–646. [CrossRef] [PubMed]
5. Santos, M.B.D.; Sporer, C.; Sanvicens, N.; Pascual, N.; Errachid, A.; Martinez, E.; Marco, M.-P.; Teixeira, V.; Samiter, J. Detection of pathogenic Bacteria by Electrochemical Impedance Spectroscopy: Influence of the immobilization strategies on the sensor performance. *Procedia Chem.* **2009**, *1*, 1291–1294. [CrossRef]
6. Brosel-Oliu, S.; Abramova, N.; Uria, N.; Bratov, A. Impedimetric transducers based on interdigitated electrode arrays for bacterial detection—A review. *Anal. Chim. Acta* **2019**, *1088*, 1–19. [CrossRef] [PubMed]
7. Swami, P.; Sharma, A.; Anand, S.; Gupta, S. DEPIs: A combined dielectrophoresis and impedance spectroscopy platform for rapid cell viability and antimicrobial susceptibility analysis. *Biosens. Bioelectron.* **2021**, *182*, 113190. [CrossRef] [PubMed]
8. Jira, J.; Rezek, B.; Kriha, V.; Artemenko, A.; Matolínová, I.; Skakalova, V.; Stenclova, P.; Kromka, A. Inhibition of *E. coli* Growth by Nanodiamond and Graphene Oxide Enhanced by Luria-Bertani Medium. *Nanomaterials* **2018**, *8*, 140. [CrossRef] [PubMed]
9. Kivirand, K.; Min, M.; Rinken, T. Challenges and Applications of Impedance-Based Biosensors in Water Analysis. In *Biosensors for Environmental Monitoring*; Rinken, T., Kivirand, K., Eds.; IntechOpen: London, UK, 2019. [CrossRef]
10. Lanzoni, M.G.M. Data Transformation Algorithm for Reliable Bacterial Concentration Detection Using the Impedance Method. *J. Electr. Eng. Electron. Technol.* **2014**, *3*, 1–5. [CrossRef]
11. Cimafronte, M.; Fulgione, A.; Gaglione, R.; Pappaianni, M.; Capparelli, R.; Arciello, A.; Censi, S.B.; Borriello, G.; Velotta, R.; Della Ventura, B. Screen Printed Based Impedimetric Immunosensor for Rapid Detection of *Escherichia coli* in Drinking Water. *Sensors* **2020**, *20*, 274. [CrossRef] [PubMed]
12. Kundu, A.; Ausaf, T.; Rajasekaran, P.; Rajaraman, S. Multimodal Microfluidic Biosensor with Interdigitated Electrodes (IDE) and Microelectrode Array (MEA) for Bacterial Detection and Identification. In Proceedings of the 2019 20th International Conference on Solid-State Sensors, Actuators and Microsystems & Eurosensors XXXIII (TRANSDUCERS & EUROSENSORS XXXIII), Berlin, Germany, 23–27 June 2019; pp. 1199–1202. [CrossRef]
13. Singh, V.; Rawal, V.; Lakhanpal, S.; Jain, P.; Dahiya, S.; Tripathi, C.C. Immobilized bacteriophage used for specific detection of *E. coli* using electrochemical impedance sensing. *Int. J. Pharm. Sci. Res.* **2015**, *6*, 3913–3919.
14. Gehring, A.G.; Albin, D.M.; Bhunia, A.K.; Reed, S.A.; Tu, S.-I.; Uknalis, J. Antibody Microarray Detection of *Escherichiacoli* O157:H7: Quantification, Assay Limitations, and Capture Efficiency. *Anal. Chem.* **2006**, *78*, 6601–6607. [CrossRef] [PubMed]
15. Al-Jumaili, A.; Zafar, M.A.; Bazaka, K.; Weerasinghe, J.; Jacob, M.V. Bactericidal vertically aligned graphene networks derived from renewable precursor. *Carbon Trends* **2022**, *7*, 100157. [CrossRef]

**Disclaimer/Publisher's Note:** The statements, opinions and data contained in all publications are solely those of the individual author(s) and contributor(s) and not of MDPI and/or the editor(s). MDPI and/or the editor(s) disclaim responsibility for any injury to people or property resulting from any ideas, methods, instructions or products referred to in the content.



Proceeding Paper

# Algal Organic Matter Fluorescence Analysis of *Chlorella* sp. for Biomass Estimation <sup>†</sup>

Jumar Cadondon <sup>1,2,\*</sup>, James Roy Lesidan <sup>1,3</sup>, Jejomar Bulan <sup>1</sup>, Edgar Vallar <sup>1</sup>, Tatsuo Shiina <sup>4</sup>  
and Maria Cecilia Galvez <sup>1</sup>

<sup>1</sup> Environment and Remote Sensing Research (EARTH) Laboratory, Department of Physics, College of Science, De La Salle University, 1004 Taft Avenue, Manila 0922, Philippines; jejomar\_bulan@dlsu.edu.ph (J.B.); edgar.vallar@dlsu.edu.ph (E.V.)

<sup>2</sup> Division of Physical Sciences and Mathematics, College of Arts and Sciences, University of the Philippines Visayas, Miagao 5023, Philippines

<sup>3</sup> Department of Physics, College of Arts and Sciences, Visayas State University, Visca, Baybay City 6521, Philippines

<sup>4</sup> Graduate School of Engineering, Chiba University, 1-33 Yayoi-cho, Inage-ku, Chiba 263-8522, Japan

\* Correspondence: jgcadondon@up.edu.ph

<sup>†</sup> Presented at the 10th International Electronic Conference on Sensors and Applications (ECSA-10), 15–30 November 2023; Available online: <https://ecsa-10.sciforum.net/>.

**Abstract:** Algal Organic Matter (AOM) is derived from the dissolved organic matter composition of the algal species being observed. In this study, excitation–emission fluorescence spectroscopy was used to determine *Chlorella* sp.’s AOM and pigment characteristics in varying algal biomass concentrations. The AOM and pigment characteristics were observed at 400–600 nm and 600–800 nm fluorescence emission, respectively, with an excitation spectrum of 300–450 nm. F450/680 was computed based on the ratio between the dissolved organic matter contribution at 450 nm and chlorophyll-a at 680 nm. F450/680 positively correlated with algal biomass ( $r = 0.96$ ) at an excitation wavelength of 405 nm. This study is a good reference for those interested in algal biomass estimation and production in natural waters.

**Keywords:** algal organic matter; *Chlorella* sp.; biomass estimation; fluorescence

**Citation:** Cadondon, J.; Lesidan, J.R.; Bulan, J.; Vallar, E.; Shiina, T.; Galvez, M.C. Algal Organic Matter Fluorescence Analysis of *Chlorella* sp. for Biomass Estimation. *Eng. Proc.* **2023**, *58*, 80. <https://doi.org/10.3390/ecsa-10-16220>

Academic Editor: Stefano Mariani

Published: 15 November 2023



**Copyright:** © 2023 by the authors. Licensee MDPI, Basel, Switzerland. This article is an open access article distributed under the terms and conditions of the Creative Commons Attribution (CC BY) license (<https://creativecommons.org/licenses/by/4.0/>).

## 1. Introduction

Algae are mostly abundant in rivers and reservoirs connected to drinking water facilities and factories [1,2]. With rapid urbanization and industrialization, effluents can severely affect the environment. This may result in an increase in algal organic matter (AOM) in surface waters. Organic substances produced by algae lead to water discoloration, odor and toxicity problems, and algal blooms [3–5].

Different techniques have been used to characterize organic matter in aquatic systems, which can be used to understand the composition of AOM in natural waters. These include specific ultraviolet absorption (SUVA), excitation–emission matrix (EEM) fluorescence spectroscopy, and lidar systems [6–9]. These techniques are promising tools for understanding the behaviors and composition of AOM and the pigment chlorophyll-a in natural waters.

The behavior and composition of *Chlorella* sp. has been studied using spectroscopic techniques. We aimed to study excitation–emission (Ex/Em) pairs for algal organic matter and pigment measurement in natural waters. This EEM fluorescence analysis may improve the existing portable fluorescence lidar systems used in algal biomass estimation. A specific fluorescence ratio was used to understand the contributions of chlorophyll-a and AOM in the different growth phases of microalgae. The in situ and real-time monitoring technique was the focus of this study, as it provides new information with faster interpretation.

## 2. Materials and Methods

### 2.1. Algal Preparation

*Chlorella* sp. inoculum was provided by the Microalgae Systematics and Applied Phycology Research Unit of De La Salle University using a BG-11 culture medium. The initial optical density was 0.6, with a pH between 8 and 9. The light/dark cycle was controlled at 12 h/12 h, with a light intensity of 75  $\mu\text{mol}/\text{m}^2/\text{s}$ .

The extracted AOM was obtained via the following processes. The algal supernatant was processed through centrifugation at 8000  $\text{r}\cdot\text{min}^{-1}$  for 5 min. It was then filtered with deionized water using 0.47  $\mu\text{m}$  glass filter fiber (Whatman, Marlborough, MA, USA).

### 2.2. Spectral Characterization

#### 2.2.1. Measuring UV-Vis Using Absorbance Spectroscopy

The aromaticity, size, and aromatic substances of algae can be interpreted by measuring SUVA<sub>254</sub>. The protein-like structures of algae can also be characterized by measuring SUVA<sub>280</sub>. The method performed was based on the characterization of water quality in rivers and estuaries [10,11].

#### 2.2.2. Measuring Fluorescence Using Excitation–Emission Spectroscopy

The fluorescence measurements, expressed in normalized units, described in this paper are the EEM of AOM and their pigments at varying biomass concentrations. Excitation–emission pairs were obtained by changing the excitation wavelength at 5 nm intervals. A 3D EEM of varying algal biomass and pigments of *Chlorella* sp. was analyzed. A detailed discussion on the fluorescence set-up and data analysis is provided in our previous paper on algal growth and real-time monitoring in natural waters [12–14].

### 2.3. The Application of the EEM to Fluorescence Lidar Measurements

The fluorescence EEM provides preliminary guidelines for constructing a fluorescence lidar by identifying excitation–emission combinations. This study explores the possibility of using fluorescence intensity profiles with 380 nm and 405 nm excitation wavelengths. The region of interest for AOM is 400–600 nm, and the region of interest for pigment measurements is 600–800 nm. Developing a fluorescence lidar system for biomass estimation is recommended since it is an in situ and non-invasive technique.

### 2.4. Comparisons of the Fluorescence EEM

In recent studies, biomass measurements have been taken using indirect or direct techniques. The results from the introduced fluorescence ratio are correlated (Pearson's  $r$ ) with optical density measurements, biomass estimation, and estimated chlorophyll-*a* concentrations.

## 3. Results and Discussion

The growth of *Chlorella* sp. in controlled culture media was analyzed for its AOM, and its pigments were analyzed for biomass estimation. The fluorescence EEM is crucial in developing a new fluorescence lidar system for biomass estimation.

### 3.1. The Spectral Characterization of *Chlorella* sp.

The variance in the SUVA<sub>254</sub> and SUVA<sub>280</sub> in varying biomass are shown in Figure 1a. The SUVA<sub>254</sub> measured in the AOM ranges from 0.3 to 1.4  $\text{L}\cdot\text{mg}^{-1}\cdot\text{m}^{-1}$ . This means that the aromaticity of AOM is low, indicating a smaller number of protein-like substances [15]. The same trend was observed between SUVA<sub>254</sub> and SUVA<sub>280</sub>, which shows a positive correlation between aromaticity and protein-like structures ( $r = 0.89$ ,  $p < 0.05$ ). These changes in organic matter from the logarithmic phase to the decline phase are helpful in algal growth monitoring.

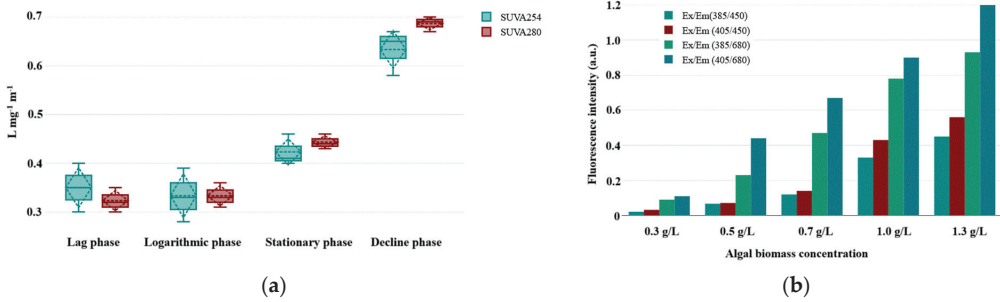


**Figure 1.** (a) Whisker and box plot of AOM in different growth phases. This figure represents the absorbance at SUVA<sub>254</sub> and SUVA<sub>280</sub> (n = 6). (b) Fluorescence intensity from the 3D EEMs at varying algal biomass concentrations.

The fluorescence intensity results from the 3D EEMs at varying algal biomass are presented in Figure 1b. The fluorescence EEMs, based on Ex/Em peaks, are valuable for distinguishing different types of organic matter components and types of natural waters. All algal biomass showed similar fluorescence EEM trends for the AOM and pigments. The total organic matter contribution was measured at a fluorescence emission wavelength of 450 nm [16]. Fluorescence emission spectroscopy is commonly used for surface water and terrestrial systems [17]. The observed excitation/emission pairs for algal organic matter are 385 nm/405 nm and 405 nm/450 nm. Higher fluorescence intensity profiles were measured using 405 nm/450 nm, but no significant differences were shown at 385 nm/450 nm ( $p < 0.05$ ).

The same trend was reflected in the 405 nm/680 nm and 385 nm/680 nm pairs for our measurement of chlorophyll-a ( $p < 0.05$ ). The mean values were compared using Pearson's r correlation ( $p < 0.05$ ), as shown in Figure 2. The Ex/Em 385 nm/450 nm pair showed a higher correlation compared to the Ex/Em 405 nm/450 nm with the algal biomass concentration. This was also the case when using a fluorescence emission wavelength of 680 nm. On the other hand, the fluorescence ratio showed opposite results. F<sub>450/680</sub> at an excitation wavelength of 405 nm ( $r = 0.96$ ) positively correlates with F<sub>450/680</sub> at an excitation wavelength of 385 nm ( $r = 0.94$ ) with algal biomass. This F-ratio is recommended to understand the dry-weight algal biomass in natural waters.

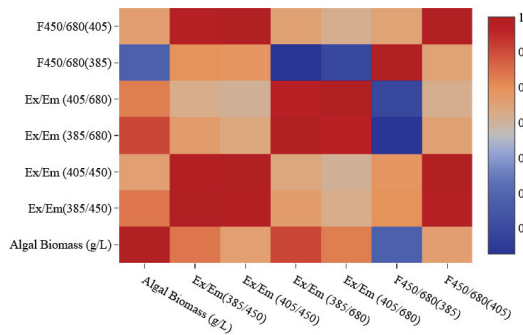


**Figure 2.** Heat map depicting the correlations between the Ex/Em pairs, F ratio, and algal biomass of *Chlorella* sp.

### 3.2. The Analysis of the Fluorescence EEM regarding the Development of the Lidar System

Developing a portable fluorescence lidar system is vital for the real-time monitoring and estimation of algal biomass in natural waters. With the guidance of the excitation-emission pairs used in this study, improving the existing fluorescence lidar system with a

new excitation wavelength at 405 nm is recommended. Simultaneous measurements at 450 and 680 nm are also suggested to understand the behavior of AOM and the chlorophyll concentrations of microalgae, respectively (Figure 3). F450/680 was used to calculate dry-weight measurements of algal biomass of *Chlorella* sp. for excitation wavelengths of 385 nm and 405 nm. Similar trends were observed, but a higher positive correlation was computed at an excitation wavelength of 405 nm.

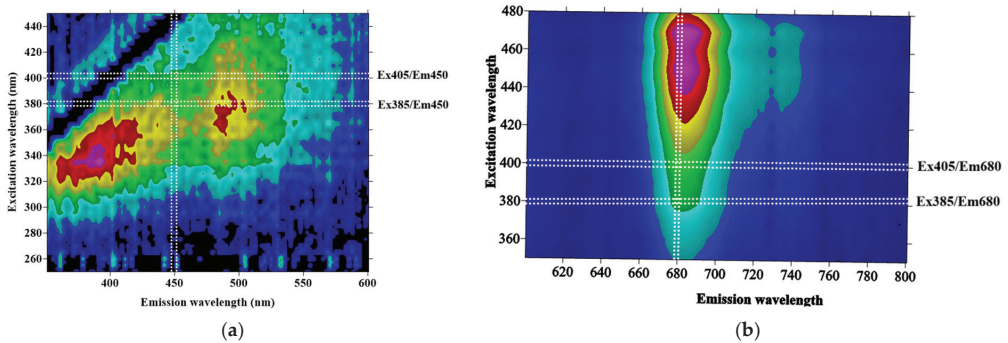


**Figure 3.** Fluorescence EEMs of *Chlorella* sp. at 0.3 g/L. (a) Algal organic matter EEM showing Ex/Em 405 nm/450 nm and Ex/Em 385 nm/450 nm. (b) Chlorophyll-a pigment EEM showing Ex/Em 405 nm/680 nm and Ex/Em 385 nm/680 nm.

The developed fluorescence lidar system discussed in our previous study showed its unique features and robustness [13,14]. It uses a pulsed LED circuit at an excitation wavelength of 385 nm, which serves as a transmitting system. With our new understanding of Ex/Em pairs, we suggest the development of a portable pulsed laser diode (LD) at an excitation wavelength of 405 nm. This study paves the way for the discovery of a new technique for developing a fluorescence lidar system using excitation–emission pairs [8].

**Author Contributions:** Conceptualization, J.C., J.R.L. and J.B.; methodology, J.C.; validation, formal analysis, J.C., J.R.L., J.B. and T.S.; investigation, J.C.; writing—original draft preparation, J.C., J.R.L. and J.B.; writing—review and editing, J.C., M.C.G., E.V. and T.S.; supervision, M.C.G., E.V. and T.S.; funding acquisition, M.C.G. and T.S. All authors have read and agreed to the published version of the manuscript.

**Funding:** This study received no external funding.

**Institutional Review Board Statement:** Not Applicable.

**Informed Consent Statement:** Not Applicable.

**Data Availability Statement:** Data are contained within the article, further inquiries can be directed to the corresponding author.

**Acknowledgments:** The authors would like to acknowledge the support they received from the University of the Philippines Visayas, De La Salle University, Chiba University, Department of Science and Technology-Accelerated Science and Technology Human Resource Development Program, and Visayas State University. We also thank DLSU-URCO project No. 16 IR2TAY19-2TAY21 for supporting this project.

**Conflicts of Interest:** The authors declare no conflicts of interest.

## References

1. Ebrahimzadeh, G.; Alimohammadi, M.; Kahkah, M.; Mahvi, A.H. Relationship between algae diversity and water quality—a case study: Chah Niemeh reservoir Southeast of Iran. *J. Environ. Health Sci. Eng.* **2021**, *19*, 437–443. [CrossRef] [PubMed]
2. Feng, J.; Zhou, L.; Zhao, X.; Chen, J.; Li, Z.; Liu, Y.; Ou, L.; Xie, Z.; Wang, M.; Yin, X.; et al. Evaluation of environmental factors and microbial community structure in an important drinking-water reservoir across seasons. *Front. Microbiol.* **2023**, *14*, 1091818. [CrossRef] [PubMed]
3. Caron, D.A.; Garneau, M.E.; Seubert, E.; Howard, M.D.A.; Darjany, L.; Schnetzer, A.; Cetinic, I.; Filteau, G.; Lauri, P.; Jones, B.; et al. Harmful algae and their potential impacts on desalination operations off southern California. *Water Res.* **2010**, *44*, 385–416. [CrossRef] [PubMed]
4. Villacorte, L.O.; Ekowati, Y.; Neu, T.R.; Kleijn, J.M.; Winters, H.; Amy, G.; Schippers, J.C.; Kennedy, M.D. Characterisation of algal organic matter by bloom-forming marine and freshwater algae. *Water Res.* **2015**, *73*, 216–230. [CrossRef] [PubMed]
5. Du, Y.; An, S.; He, H.; Wen, S.; Xing, P.; Duan, H. Production and transformation of organic matter driven by algal blooms in a shallow lake: Role of sediments. *Water Res.* **2022**, *219*, 118560. [CrossRef] [PubMed]
6. Chu, H.; Yu, H.; Tan, X.; Zhang, Y.; Zhou, X.; Yang, L.; Li, D. Extraction procedure optimization and the characteristics of dissolved extracellular organic matter (bEOM) from *Chlorella pyrenoidosa*. *Coll. Surf. B Biointerfaces* **2015**, *125*, 238–246. [CrossRef] [PubMed]
7. Tan, L.; Zhang, Z.; Wang, Z.; Zhang, P.; Xiong, C.; Kuang, Y.; Peng, X.; Yu, M.; Qian, Y. Compositional variations in algal organic matter during distinct growth phases in karst water. *Front. Environ. Sci.* **2023**, *11*, 1112522.
8. Saito, Y.; Hosokawa, T.; Shiraishi, K. Collection of excitation-emission-matrix fluorescence of aerosol-candidate-substances and its application to fluorescence lidar monitoring. *Appl. Opt.* **2022**, *61*, 653–660. [CrossRef] [PubMed]
9. Cadondon, J.G.; Vallar, E.A.; Beltran, A.B.; Orbecido, A.H.; Galvez, M.C.D. Variation in Dissolved Organic Matter Using Absorbance and Fluorescence Measurements during Dry Season in St. Rosa and Cabuyao Rivers, Philippines. *Water* **2022**, *14*, 1444. [CrossRef]
10. Lal, P.P.; Juste-Poinapen, M.S.N.; Poinapen, J. Assessing the water quality of Suva foreshore for the establishment of estuary and marine recreational water guidelines in the Fiji Islands. *Water Sci. Technol.* **2021**, *84*, 3040–3054. [CrossRef] [PubMed]
11. Sanyal, P.; Ray, R.; Paul, M.; Gupta, V.K.; Acharya, A.; Bakshi, S.; Jana, T.K.; Mukhopadhyay, S.K. Assessing the Dynamics of Dissolved Organic Matter (DOM) in the Coastal Environments Dominated by Mangroves, Indian Sundarbans. *Front. Earth Sci.* **2020**, *8*, 218. [CrossRef]
12. Cadondon, J.; Vallar, E.; Belo, L.; Orbecido, A.; Galvez, M.C. UV-Vis Absorbance and Fluorescence Characterization of Pasig River Surface Water Samples Towards the Development of an LED Fluorescence Lidar System. *Int. J. Adv. Sci. Eng. Inf. Technol.* **2021**, *11*, 968–980. [CrossRef]
13. Cadondon, J.G.; Ong, P.M.B.; Vallar, E.A.; Shiina, T.; Galvez, M.C.D. Chlorophyll-a pigment measurement of spirulina in algal growth monitoring using portable pulsed LED fluorescence lidar system. *Sensors* **2022**, *22*, 2940. [CrossRef]
14. Cadondon, J.G.; Vallar, E.A.; Shiina, T.; Galvez, M.C.D. Real-time Chlorophyll-a Pigment Monitoring of *Chlamydomonas reinhardtii* in a Controlled Environment Using Pulsed LED Fluorescence LiDAR System. *Photonics* **2023**, *10*, 144. [CrossRef]
15. Li, L.; Gao, N.; Deng, Y.; Yao, J.; Zhang, K. Characterization of intracellular & extracellular algae organic matters (AOM) of Microcystic aeruginosa and formation of AOM-associated disinfection byproducts and odor & taste compounds. *Water Res.* **2012**, *46*, 1233–1240. [PubMed]
16. Lee, S.; Park, J. Identification of Dissolved Organic Matter Origin Using Molecular Level Analysis Methods. *Water* **2022**, *14*, 1317. [CrossRef]
17. Harjung, A.; Schweichhart, J.; Rash, G.; Griebler, C. Large-scale study on groundwater dissolved organic matter reveals a strong heterogeneity and a complex microbial footprint. *Sci. Total Environ.* **2023**, *854*, 158542. [CrossRef] [PubMed]

**Disclaimer/Publisher’s Note:** The statements, opinions and data contained in all publications are solely those of the individual author(s) and contributor(s) and not of MDPI and/or the editor(s). MDPI and/or the editor(s) disclaim responsibility for any injury to people or property resulting from any ideas, methods, instructions or products referred to in the content.

# Optimal Resource Allocation Scheme Based on Time Slot Switching for Point-to-Point SISO SWIPT Systems <sup>†</sup>

Nivine Guler <sup>1,\*</sup> and Ali Gunes <sup>2</sup><sup>1</sup> Department of Informatics Engineering, University of Technology Bahrain, Salmabad 18041, Bahrain<sup>2</sup> Department of Computer Engineering, Istanbul Aydin University, Istanbul 34295, Turkey; [aligunes@aydin.edu.tr](mailto:aligunes@aydin.edu.tr)\* Correspondence: [n.guler@utb.edu.bh](mailto:n.guler@utb.edu.bh); Tel.: +973-33361859<sup>†</sup> Presented at the 10th International Electronic Conference on Sensors and Applications (ECSA-10), 15–30 November 2023; Available online: <https://ecsa-10.sciforum.net/>.

**Abstract:** This paper presents an optimal resource allocation scheme based on time slot switching (TS) for point-to-point single-input single-output (SISO) simultaneous wireless information and power transfer (SWIPT) systems, aiming to maximize the average achievable rate. The proposed scheme considers the nonlinear energy harvesting (EH) characteristic, and thus, the problem is formulated as a nonconvex optimization problem in the presence of a binary TS ratio. Hence, solving the problem is performed using the time-sharing strong duality theorem and Lagrange dual method. Simulations showed that the proposed scheme improves energy efficiency with respect to different transmission powers by 20%, 10%, and 3% for high-SNR, medium-SNR, and low-SNR regions, respectively. Improvement with respect to average energy efficiency versus other system performance metrics has also been noted for the proposed scheme.

**Keywords:** energy harvesting; information decoding; SWIPT; time slot switching; SNR

## 1. Introduction

Energy shortage is considered as one of the main issues faced by energy-constrained wireless networks [1]; hence, energy shortage directly affects the network lifetime and performance. Energy harvesting (EH) becomes a promising solution for reducing energy consumption and extending the lifetime of energy-constrained wireless networks where nodes harvest energy from the surrounding environment. The simultaneous wireless information and power transfer (SWIPT) is one of the EH technologies, where energy harvesting is performed through the radio frequency (RF) signals since RF signals are able to carry both information and electromagnetic energy simultaneously. Thus, SWIPT is currently an area of high research interests due to its higher efficiency compared to that of information and power transmission with orthogonal resources, i.e., time or frequency channels [2]. Authors of [3,4] present a trade-off between the amount of harvested energy and the achievable rate for the SWIPT systems in the frequency selection channel with additive white Gaussian noise (AWGN). TS and power splitting (PS) SWIPT receivers were first proposed in [5], and since then, the idea of using TS and PS SWIPT receivers has been adopted in the literature. Authors of [6] present multiuser single-input single-output (SISO) orthogonal frequency-division multiplexing (OFDM) system where the TS and PS ratios are optimized to maximize the weighted sum rate of all receivers. Authors of [7] propose an energy efficiency maximization optimization scheme for the multiuser multicarrier energy-constrained amplify-and-forward (AF) multi-relay network. Aiming at minimizing the transmission power, the power allocation problem for the multiuser system is studied, and the optimal PS ratio is obtained in [8]. Power allocation and subcarrier allocation schemes are presented in [9,10] for energy-efficient, large-scale, multiple-antenna SWIPT systems. Most of the proposed SWIPT systems in the literature consider the linear EH

**Citation:** Guler, N.; Gunes, A. Optimal Resource Allocation Scheme Based on Time Slot Switching for Point-to-Point SISO SWIPT Systems. *Eng. Proc.* **2023**, *58*, 81. <https://doi.org/10.3390/ecsa-10-16247>

Academic Editor: Stefano Mariani

Published: 15 November 2023



**Copyright:** © 2023 by the authors. Licensee MDPI, Basel, Switzerland. This article is an open access article distributed under the terms and conditions of the Creative Commons Attribution (CC BY) license (<https://creativecommons.org/licenses/by/4.0/>).



model, where the power conversion efficiency factor of the EH receiver is assumed to be constant. However, this assumption was rejected by [11], after showing the saturation behavior of the output power of the RF to direct current converter as the input power exceeds a certain threshold. In [12–14], a nonlinear EH model is presented to optimize the power split factor to minimize the outage probability for the AF relay system with the PS receiver. In this paper, an SISO point-to-point SWIPT communication system with TS receiver is considered where the nonlinear saturation input–output characteristic of EH circuit is modeled, and a simple optimal resource allocation scheme based on the time slot-switching strategy to maximize the average achievable rate for the system is proposed. The main contribution of this paper is the consideration of the effect of the saturation characteristic of the nonlinear EH model, and the achievable rate in the TS SWIPT system is mathematically formulated where the scheme shows the regions that the receiver can use to harvest energy or decode information based on the value of SNR. Another contribution is that the proposed resource allocation scheme maximizes the network energy efficiency.

The rest of this paper is organized as follows. Section 2 presents the system model. Section 3 presents the proposed model. Simulation results are discussed in Section 4. Section 5 concludes the paper.

### 2. System Model

We consider an SISO point-to-point SWIPT communication system as shown in Figure 1, where both the receiver and the transmitter have single antenna and Rx is assumed to be energy limited and can harvest energy from the received signals with a TS scheme. The channel between the transmitter and the receiver is subjected to frequency flat and the block Rayleigh fading. The channel coefficient is denoted as  $h$ , which is a random variable following the complex Gaussian distribution with zero mean and variance  $\sigma^2$ . The optimal problem is formulated as a nonconvex optimization, which we have proved meets the time-sharing condition, and then, the problem is solved by using the time-sharing strong duality theorem and Lagrange dual method. Without the loss of generality, we assume that each time slot is normalized transmission time. In each time slot, the TS ratio  $\mathcal{T}$  is equal to 0 or 1, indicating that the receiver implements EH or ID operations, respectively. The received signal  $S_R$  is provided in Equation (1) and is as follows:

$$S_R = \sqrt{\theta P_t}hx + n_i \tag{1}$$

where  $P_t$  is the transmit power,  $x$  is the data symbol with unity power, i.e.,  $E[|x|^2] = 1$ , where  $E[\cdot]$  is the mathematical expectation,  $n_i \sim \text{CN}(0, \sigma^2)$  is the channel noise,  $\theta = d^{-m}$  represents the path loss,  $d$  is the distance between the source and the destination nodes, and  $m$  represents the pathloss exponent. The achievable rate  $\mathfrak{R}$  of the system based on the TS scheme is provided in Equation (2) and is as follows:

$$\mathfrak{R}(\mathcal{T}) = \mathcal{T} \log_2 \left( 1 + \frac{\theta P_t H}{\sigma^2} \right), \tag{2}$$

where  $H = h^2$  is the channel power gain.

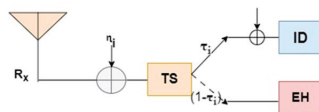


Figure 1. The SISO point-to-point SWIPT system.

We use the piece-wise linear function to model the nonlinear saturation input–output characteristic of the EH receiver. The harvested power at the EH receiver is provided by Equation (3) and is as follows:

$$P_h = \begin{cases} \varepsilon\theta HP_t, & \varepsilon\theta HP_t < P_m \\ P_m, & \varepsilon\theta HP_t \geq P_m \end{cases} \quad (3)$$

where  $\varepsilon(0 < \varepsilon < 1)$  is the energy conversion efficiency of the energy harvester in the linear region, and  $P_m$  is the maximum saturation harvested power of the EH receiver. When the conversion power of the energy receiver,  $\varepsilon\theta HP_t$ , exceeds the saturation output power,  $P_m$ , the output power of the energy receiver remains unchanged and some of the power is wasted, which means that in such a case, the receiver should perform ID instead of EH to avoid the wastage of this power.

### 3. An Optimal Resource Allocation Scheme

In this section, we propose an optimal resource allocation scheme based on a simple time slot-switching strategy to achieve the balance between the maximum average achievable rate and the maximum average harvested energy. The harvested energy can be expressed as mentioned in Equation (4). The proposed optimal resource allocation scheme maximizes the average achievable rate and is provided by Equation (5).

$$\mathcal{E}(\mathbb{T}) = (1 - \mathbb{T})P_h \quad (4)$$

$$\max_{\mathbb{T}} E[\mathfrak{R}(\mathbb{T})] \quad (5)$$

$$\text{s.t. } E[\mathcal{E}(\mathbb{T})] \geq \mathcal{E}_m, \mathbb{T} \in \{0,1\},$$

where  $\mathcal{E}_m$  is the minimum value of the EH required to maintain the normal operation of the EH receiver. As shown in Equation (5), it is a combination of series of nonconvex problems due to the binary aspect of  $\mathbb{T}$ , making it difficult to solve. In addition, the complexity of solving the optimization problem increases with the number of time slots. Hence, we use the time-sharing strong duality theorem [15]. According to the time-sharing strong duality theorem, the primal problem of Equation (5) has the same optimal solution as its dual problem and can be solved with the Lagrange dual method. The Lagrange function of Equation (5) is expressed in Equation (6):

$$L(\mathbb{T}, \lambda) = E[\mathfrak{R}(\mathbb{T})] + \lambda(E[\mathcal{E}(\mathbb{T})] - \mathcal{E}), \quad (6)$$

where  $\lambda \geq 0$  is the Lagrange multiplier associated with  $E[\mathcal{E}(\mathbb{T})] \geq \mathcal{E}$ . Accordingly, the Lagrange dual function is described by Equation (7), and the dual problem is then described by Equation (8):

$$g(\lambda) = \max_{\mathbb{T} \in \{0,1\}} L(\mathbb{T}, \lambda), \quad (7)$$

$$\min g(\lambda), \quad (8)$$

$$\text{s.t. } \lambda \geq 0.$$

In order to effectively solve Equation (8), first, we decouple the optimization problem in Equation (7) into  $N$  parallel subproblems that have the same structure as Equation (7). The  $k$ th ( $k = 1, 2, \dots, N$ ) subproblem is expressed in Equation (9):

$$\max_{\mathbb{T} \in \{0,1\}} L_k(\mathbb{T}), \quad (9)$$

where  $L_k(\mathcal{T}) = \Re(\mathcal{T}) + \lambda \mathcal{E}(\mathcal{T})$ . First, we consider the values of  $\mathcal{T} = 0,1$ , and we substitute  $\mathcal{T}$  in Equations (4) and (6). Then, Equations (10) and (11) express the Lagrange functions, respectively:

$$L_k(\mathcal{T} = 0) = \lambda P_h \tag{10}$$

$$L_k(\mathcal{T} = 1) = \log_2 \left( 1 + \frac{\theta P_t H}{\sigma^2} \right) \tag{11}$$

Therefore, the optimal solution,  $\mathcal{T}^*$ , of Equation (7) is provided in Equation (12) and is as follows:

$$\mathcal{T}^* = \begin{cases} 1, & \log_2 \left( 1 + \frac{\theta P_t H}{\sigma^2} \right) > \lambda P_h \\ 0, & \text{else} \end{cases} \tag{12}$$

Hence, for a given value of  $\lambda$ ,  $\mathcal{T}^*$  can be obtained from (12) according to the channel state in each time slot. Let  $\lambda^*$  be the optimal dual variable, which is associated with the required minimum harvested energy value  $\mathcal{E}_m$  in Equation (5). The optimal dual variable  $\lambda^*$  is found using iterative search until the average energy meets the minimum energy constraint, i.e.,  $|E[\mathcal{E}(\mathcal{T})] - \mathcal{E}_m| \leq \delta$ . The proposed optimal resource allocation scheme is based on the optimal TS strategy according to the channel state in each time slot in Equation (12). Based on the value of  $P_h$  in Equation (3) and  $\mathcal{T}^*$  in Equation (12), we define two channel gain functions CG1 and CG2 with respect to the channel power gain in Equations (13) and (14), respectively:

$$CG1(H) = \log_2 \left( 1 + \frac{\theta P_t H}{\sigma^2} \right) - \lambda^* \epsilon \theta H P_t \tag{13}$$

$$CG2(H) = \log_2 \left( 1 + \frac{\theta P_t H}{\sigma^2} \right) - \lambda^* P_m \tag{14}$$

Evidently, Equation (13) is a combination of logarithmic and linear functions, hence, solving it is performed by traversing the value of  $H$  from 0 until the difference is approximately  $10^{-6}$ , and thus,  $CG1(H) = 0$ . Then, we can determine an approximate nonzero  $H_1$ . Also,  $\lambda$  is found when  $G1(H)$  increases in range  $(0, H_1)$ . As  $CG1(0) = 0$  and  $CG1(H_1) = 0$ , when  $H \in (0, H_1)$ ,  $CG1(H) > 0$ . From Equations (3) and (12),  $\log_2 \left( 1 + \frac{\theta P_t H}{\sigma^2} \right) > \lambda^* P_h$ ;  $\log_2 \left( 1 + \frac{\theta P_t H}{\sigma^2} \right) > \lambda^* \epsilon \theta H P_t$ ; hence,  $\mathcal{T}^* = 1$ . Similarly,  $CG2(H)$  is an increasing function, when  $H \in (H_2, \infty)$ , where  $H_2$  is a nonzero real root of  $CG2(H) = 0$ . Then, when  $H \in [H_1, H_2]$ ,  $\mathcal{T}^* = 0$ . The optimal TS strategy is provided in Equation (15):

$$\mathcal{T}^* = \begin{cases} 1, & H < H_1 \text{ or } H > H_2 \\ 0, & H_1 \leq H \leq H_2 \end{cases} \tag{15}$$

The optimal TS thresholds  $H^*1$  and  $H^*2$  depend on the optimal dual variable  $\lambda^*$  determined from Equation (5) where  $E[\mathcal{E}(\mathcal{T}(H))] = \mathcal{E}_m$ . The average energy collection depends on the probability density function of  $H$ ,  $f_H(x)$ , and is provided in Equation (16) and is as follows:

$$E[\mathcal{E}(\mathcal{T}(H))] = \int_{H_1}^{H_{th}} \epsilon \theta x P_t f_H(x) dx + \int_{H_{th}}^{H_2} P_m * f_H(x) dx \tag{16}$$

The optimal resource allocation scheme first divides the information block  $K$  into  $k$  time slots. For each time slot,  $k$  ( $1 \leq k \leq K$ ), the optimal TS thresholds  $H^*1$  and  $H^*2$  are found by applying algorithm, and the channel gain  $H_k$  is compared to  $H^*1$  and  $H^*2$ . The receiver will switch to ID if  $H_k < H^*1$  or  $H_k > H^*2$ ; otherwise, the receiver will perform EH.

### 4. Simulation Results

In this section, simulation results for the proposed optimal resource allocation scheme are presented. In each time slot  $k$ , the channel obeys the Rayleigh distribution. The distance between the source node and the destination node is  $d = 5$  m, and the pathloss exponent  $m = 2.0$ , and. The power transmitted,  $P_t = 1$  W,  $\mathcal{E}_m = 5$  mW,  $P_m = 24$  mW,  $H_{th} = P_m/\epsilon\theta P_t$ . The energy efficiency with various SNR [5,15] is analyzed for different values of transmission power  $P_t$ . For verification purposes, the proposed resource allocation scheme is compared with [16] in terms of the energy efficiency ( $\epsilon_f$ ) of a system that is defined as the ratio of the total achievable rate to the total power consumption as described in Equation (17). Hence, the average energy efficiency  $\hat{\epsilon}_f$  is provided by Equation (18).

$$\epsilon_f = \mathfrak{R}(\mathcal{U}) / (P_t - E[\mathcal{E}(\mathcal{U})]) \tag{17}$$

$$\hat{\epsilon}_f = \frac{1}{K} \sum_{ts=1}^K \epsilon_f(ts) \tag{18}$$

In Figure 2, as the transmit power increases, the average energy efficiency,  $\hat{\epsilon}_f$ , decreases in the region where SNR is 15 dB or 25 dB, whereas it stays unchanged when SNR is 5 dB. This is because the receiver of the traditional scheme will waste the power in the nonlinear regions, thus resulting in a bigger gap. The proposed scheme improves the average energy efficiency by 20%, 10%, and 5% when SNR = 25 dB, 15 dB, and 5 dB, respectively.

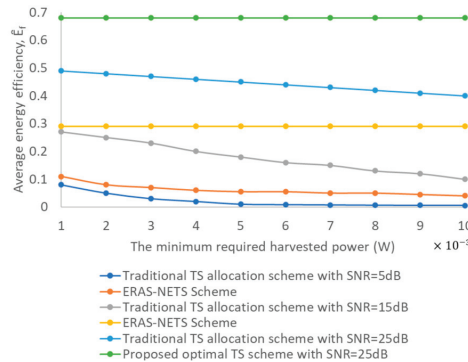


Figure 2. Average energy efficiency versus power.

In Figure 3, as the distance increases, the average energy efficiency decreases. In the intermediate regions where SNR = 15 dB and 25 dB, the gap between the traditional scheme and the proposed scheme becomes obvious due to the saturation characteristic of the EH model. In Figure 4, as the minimum required harvested power increases, the average energy efficiency of the traditional scheme decreases, whereas it remains unchanged with the proposed scheme.

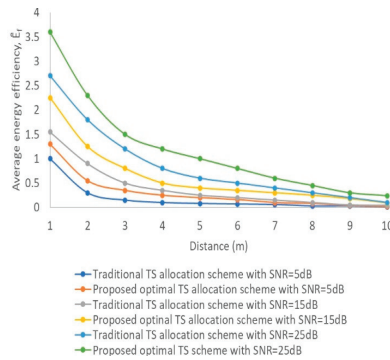


Figure 3. Average energy efficiency versus distance.

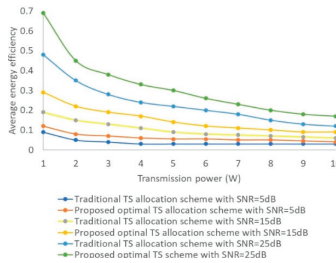


Figure 4. Average energy efficiency versus minimum required harvested energy.

### 5. Conclusions

In this paper, an optimal resource allocation scheme for point-to-point SISO SWIPT systems with a nonlinear EH model is presented. The proposed scheme is based on TS to maximize the average information rate by which the receiver performs information decoding in the regions of either low or high SNR, whereas switching to energy harvesting is performed in the intermediate region. In comparison with the traditional TS resource allocation scheme, the proposed scheme improves energy efficiency with different transmission powers by 20%, 10%, and 3% for high-SNR, medium-SNR, and low-SNR regions, respectively. We have also investigated the impact of the minimum required harvested energy on the average energy efficiency performance. It has been demonstrated that the average energy efficiency decreases with the increase in the minimum required harvested energy for the traditional TS allocation scheme, whereas it is hardly affected for the proposed scheme.

**Author Contributions:** Conceptualization, N.G. and A.G.; methodology, N.G.; software, N.G.; validation, N.G. and A.G.; formal analysis, N.G.; investigation, N.G.; resources, N.G.; data curation, N.G.; writing—original draft preparation, N.G. and A.G.; writing—review and editing. All authors have read and agreed to the published version of the manuscript.

**Funding:** This research received no external funding.

**Institutional Review Board Statement:** Not applicable.

**Informed Consent Statement:** Not applicable.

**Data Availability Statement:** The data presented in this study are available on request from the corresponding author.

**Conflicts of Interest:** The authors declare no conflicts of interest regarding the publication of this paper.

## References

1. Varshney, L. Transporting information and energy simultaneously. In Proceedings of the IEEE International Symposium on Information Theory, Toronto, ON, Canada, 6–11 July 2008.
2. Krikidis, I.; Timotheou, S.; Nikolaou, S.; Zeng, G.; Ng, D.; Schober, R. Simultaneous wireless information and power transfer in modern communication systems. *IEEE Commun. Mag.* **2014**, *52*, 104–110. [CrossRef]
3. Grover, P.; Sahai, A. Shannon meets Tesla: Wireless information and power transfer. In Proceedings of the IEEE International Symposium on Information Theory, Austin, TX, USA, 13–18 June 2010. [CrossRef]
4. Liu, L.; Zhang, R.; Chua, K. Wireless information and power transfer: A dynamic power splitting approach. *IEEE Trans. Wirel. Commun.* **2014**, *61*, 3990–4001. [CrossRef]
5. Zhang, R.; Ho, C. MIMO broadcasting for simultaneous wireless information and power transfer. *IEEE Trans. Wirel. Commun.* **2013**, *61*, 1989–2001. [CrossRef]
6. Zhou, X.; Zhang, R.; Ho, C. Wireless information and power transfer in multiuser OFDM systems. *IEEE Trans. Wirel. Commun.* **2014**, *13*, 2282–2294. [CrossRef]
7. Gupta, A.; Singh, K.; Sellathurai, M. Time-switching EH-based joint relay selection and resource allocation algorithms for multi-user multi-carrier AF relay networks with SWIPT. *IEEE Syst. J.* **2020**, *14*, 196–207. [CrossRef]
8. Shi, Q.; Liu, L.; Xu, W.; Zhang, R. Joint transmit beamforming and receive power splitting for MISO SWIPT Systems. *IEEE Trans. Wirel. Commun.* **2014**, *13*, 3269–3280. [CrossRef]
9. Ng, D.; Lo, E.; Schober, R. Wireless information and power transfer: Energy efficiency optimization in OFDMA systems. *IEEE Trans. Wirel. Commun.* **2013**, *12*, 6352–6370. [CrossRef]
10. Chen, X.; Wang, X. Energy-efficient optimization for wireless information and power transfer in large-scale MIMO systems employing energy beamforming. *IEEE Wirel. Commun. Lett.* **2013**, *2*, 667–670. [CrossRef]
11. Boshkoovska, E.; Ng, D.; Zlatanov, N.; Schober, R. Practical non-linear energy harvesting model and resource allocation for SWIPT systems. *IEEE Commun. Lett.* **2015**, *19*, 2082–2085. [CrossRef]
12. Kang, M.; Kim, I.; Kim, D. Joint Tx power allocation and Rx power splitting for SWIPT system with multiple nonlinear energy harvesting circuits. *IEEE Wirel. Commun. Lett.* **2019**, *8*, 53–56. [CrossRef]
13. Dong, Y.; Hossain, M.; Cheng, J. Performance of wireless powered amplify and forward relaying over Nakami-m fading channels with nonlinear energy harvester. *IEEE Commun. Lett.* **2016**, *20*, 672–675. [CrossRef]
14. Wang, K.; Li, Y.; Ye, Y.; Zhang, H. Dynamic power splitting schemes for nonlinear EH relaying networks: Perfect and imperfect CSI. In Proceedings of the IEEE 86th Vehicular Technology Conference(VTC.Fall), Toronto, ON, Canada, 24–27 September 2017. [CrossRef]
15. Yu, W.; Lui, R. Dual methods for nonconvex spectrum optimization of multicarrier systems. *IEEE Trans. Commun.* **2006**, *54*, 1310–1322. [CrossRef]
16. Zhou, X.; Zhang, R.; Ho, C. Wireless information and power transfer: Architecture design and rate-energy tradeoff. *IEEE Trans. Commun.* **2013**, *61*, 4754–4767. [CrossRef]

**Disclaimer/Publisher’s Note:** The statements, opinions and data contained in all publications are solely those of the individual author(s) and contributor(s) and not of MDPI and/or the editor(s). MDPI and/or the editor(s) disclaim responsibility for any injury to people or property resulting from any ideas, methods, instructions or products referred to in the content.

# Optimization of the Geometry of a Microelectromechanical System Testing Device for SiO<sub>2</sub>—Polysilicon Interface Characterization <sup>†</sup>

Daniel Calegario <sup>1,\*</sup>, Stefano Mariani <sup>1</sup>, Massimiliano Merli <sup>2</sup> and Giacomo Ferrari <sup>2</sup>

<sup>1</sup> Dipartimento di Ingegneria Civile e Ambientale, Politecnico di Milano, Piazza Leonardo da Vinci, 32, 20133 Milano, Italy; stefano.mariani@polimi.it

<sup>2</sup> STMicroelectronics, 20007 Cornaredo, Italy; massimiliano.merli@st.com (M.M.); giacomo.ferrari@st.com (G.F.)

\* Correspondence: daniel.calegario@polimi.it

<sup>†</sup> Presented at the 10th International Electronic Conference on Sensors and Applications (ECSA-10), 15–30 November 2023; Available online: <https://ecsa-10.sciforum.net/>.

**Abstract:** Microelectromechanical systems (MEMSs) are small-scale devices that combine mechanical and electrical components made through microfabrication techniques. These devices have revolutionized numerous technological applications, owing to their miniaturization and versatile functionalities. However, the reliability of MEMS devices remains a critical concern, especially when operating in harsh conditions like high temperatures and humidities. The unknown behavior of their structural parts under cyclic loading conditions, possibly affected by microfabrication defects, poses challenges to ensuring their long-term performance. This research focuses on addressing the reliability problem by investigating fatigue-induced delamination in polysilicon-based MEMS structures, specifically at the interface between SiO<sub>2</sub> and polysilicon. Dedicated test structures with piezoelectric actuation and sensing for closed-loop operation were designed, aiming to maximize stress in regions susceptible to delamination. By carefully designing these structures, a localized stress concentration is induced to facilitate the said delamination and help understand the underlying failure mechanism. The optimization was performed by taking advantage of finite element analyses, allowing a comprehensive analysis of the mechanical responses of the movable parts of the polysilicon MEMS under cyclic loading.

**Keywords:** MEMS; reliability; fatigue and fracture; geometry optimization

**Citation:** Calegario, D.; Mariani, S.; Merli, M.; Ferrari, G. Optimization of the Geometry of a

Microelectromechanical System Testing Device for SiO<sub>2</sub>—Polysilicon Interface Characterization. *Eng. Proc.* **2023**, *58*, 82. <https://doi.org/10.3390/ecsa-10-16033>

Academic Editor: Francisco Falcone

Published: 15 November 2023



**Copyright:** © 2023 by the authors. Licensee MDPI, Basel, Switzerland. This article is an open access article distributed under the terms and conditions of the Creative Commons Attribution (CC BY) license (<https://creativecommons.org/licenses/by/4.0/>).

## 1. Introduction

In the realm of microelectromechanical systems (MEMSs), the fusion of miniaturized mechanical and electrical components through microfabrication techniques has spearheaded a technological revolution. These devices have demonstrated immense potential for multiple applications, driven by their compact form and multifaceted functionalities [1–4]. However, amid the proliferation of their application, the crucial concern of reliability looms large [2,5–7], particularly when they are exposed to challenging operational conditions such as high load cycles, elevated temperatures, and high humidities [8]. A thorough assessment of their mechanical reliability stands as a crucial requirement to propel the ongoing development of MEMSs.

The dominance of polycrystalline silicon in crafting MEMSs designed to sustain high-frequency oscillations is driven by its exceptional mechanical properties, outperforming many alternative materials. Despite its inherent brittleness and the absence of dislocation motion at temperatures below 900 °C, its operating conditions do not typically induce fatigue mechanisms [5,8]. Nevertheless, in some cases, MEMS devices exhibit heightened susceptibility to environmental factors that impact both the mechanical and electrical characteristics of the device. Paradoxically, fatigue stands as one of the critical failure

mechanisms in such systems, highlighting the importance of thorough consideration and analysis of the mechanical properties of polysilicon [9–15]; see also [16,17].

An additional failure mode, likely to manifest under cyclic loading due to elevated interfacial stress levels and often in conjunction with fatigue, is delamination. This localized cracking-like failure mode typically occurs at the interface between silicon dioxide and polycrystalline silicon. The fatigue and delamination phenomena both lead to a progressive shift in resonance frequency, structural stiffness (also affected by uncertainties at the microscale; see [18–22]), and electrical resistance, thereby affecting the long-term reliability of these devices [9,23–25].

Effectively replicating fatigue failures through experimental tests requires the utilization of setups enabling relatively high-frequency testing, ideally in the range of kHz. Such high-frequency driving enables a significant number of cycles to be achieved within a reasonable timeframe, which is critical for an accurate fatigue analysis. In this context, on-chip tests emerge as the optimal choice, given their capability to operate over large frequency ranges [26].

By employing purpose-built test structures leveraging piezoelectric actuation and sensing for closed-loop operation, this research seeks to optimize the stress field within the movable structure of ad hoc-designed MEMS test structures. We take advantage of finite element analyses to enhance the stress concentrations at the interface between SiO<sub>2</sub> and polysilicon in order to possibly induce fatigue-driven delamination. The optimization procedure is based on static analyses to obtain an idea of the best shape of the mechanical parts to induce a large stress concentration at the said interface, thus leading to the failure analysis in the experimental section to follow.

## 2. Materials and Methods

As anticipated, a polysilicon-based MEMS test structure was ad hoc designed to maximize the stress concentration, possibly leading to delamination-driven failure modes. The optimization of the geometry of the structure was made possible by the finite element software COMSOL Multiphysics®, through its MEMS module [27].

Figure 1 displays the initial geometry used for the optimization process, which is a bridge-like test structure actuated in bending mode. The main material layers are single-crystal silicon and silicon dioxide, on top of which the polycrystalline silicon movable structure is laid. In addition, four PZT-based patches are used for actuation and sensing, as highlighted in red in the figure. The shape optimization procedure was carried out by varying the length of the beam connecting the plate and the SiO<sub>2</sub>–polycrystalline silicon interface and also by allowing for the following constraints:

- The failure-governing principal stress component at the interface should be as high as possible, ideally close to 1 GPa, in order to speed up the fatigue tests.
- The stress field in the polysilicon layer should not exceed the one at the interface to avoid inducing brittle cracking in the latter region [28–39].

The numerical investigation includes two types of analysis (see Figure 2): (i) a stationary analysis performed on the entire structure and characterized by a coarse mesh optimized to achieve a trade-off between accuracy and computational cost requirements; (ii) a stationary analysis performed only on the region under study, namely on the central portion of the device, characterized by a finer mesh optimized to achieve accuracy in terms of the stress field. To take into account the non-linear geometric effects linked to the deformed configuration of the structure, a sufficiently high driving voltage is adopted in the first stationary analysis. Afterward, this solution is used as the starting configuration for the evaluation of the stress field using the finer mesh of the second analysis.



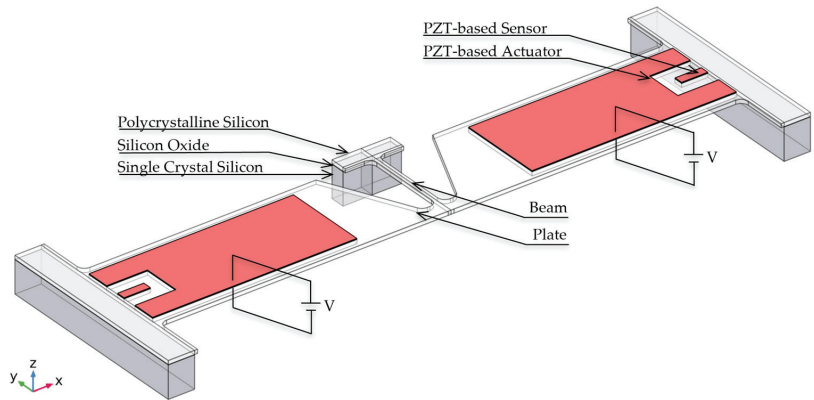


Figure 1. Sketch of the polysilicon-based MEMS test structure.

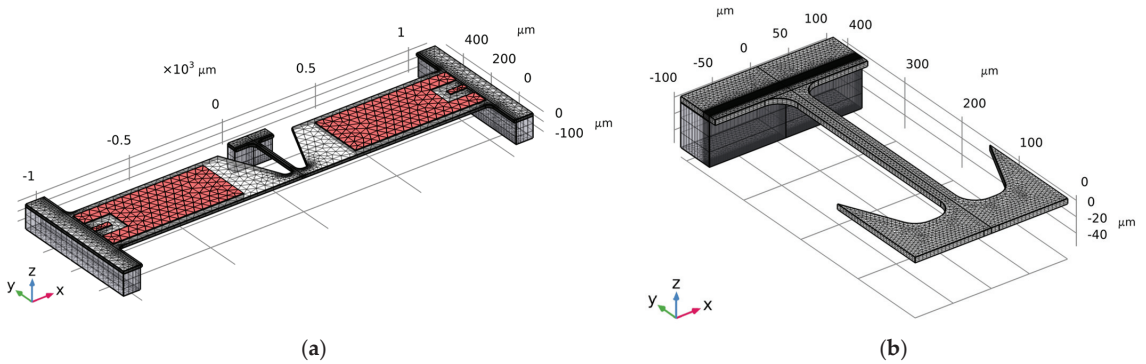


Figure 2. (a) Coarse mesh of the entire structure; (b) refined mesh on a smaller part of the structure.

The mechanical properties of the main materials that make up the test structure are gathered in Table 1. The properties of single-crystal silicon in the  $\langle 100 \rangle$  crystallographic direction are shown [40].

Table 1. Electromechanical properties of the main materials of the test structure.

Material	Thickness ( $\mu\text{m}$ )	Mass Density ( $\text{kg}/\text{m}^3$ )	Young's Modulus (GPa)	Poisson's Ratio	Shear Modulus (GPa)
Single-Crystal Silicon	110	2330	130	0.278	79.6
Silicon Oxide	1	2200	70	0.17	29.9
Polycrystalline Silicon	13	2320	160	0.22	65.6
PZT	2	7600	70	0.33	26.3

### 3. Results and Discussion

A series of stationary analyses were conducted for a beam length,  $L$ , ranging between  $60 \mu\text{m}$  and  $300 \mu\text{m}$  at a given applied driving voltage. Taking advantage of the 3-1 piezoelectric coupling mechanism of the PZT, an axial deformation of the beam is induced, leading to a bending-dominated structural deformation mode and, therefore, to displacements in the out-of-plane  $z$ -direction. With the structure being fully constrained at its two side ends, the load is transmitted through the beam and measured through the deflection at the center to also quantify the induced solution at the interface where the stress must be intensified.

The results of the local analyses featuring the finest mesh are depicted in Figure 3. It is shown that, as expected, for very high values of  $L$ , the structure becomes very compliant, as highlighted by the large deflection values attained, and the stress transmitted to the

SiO<sub>2</sub>–polysilicon interface becomes very small if compared to the stress exhibited in the polysilicon layer, specifically along the rounded corners highlighted in red in the figure. As the beam length,  $L$ , decreases, the vertical displacement at the middle point decreases as well due to a stiffening of the structure, along with the principal stress in the rounded region. On the contrary, the stress at the SiO<sub>2</sub>–polysilicon interface keeps increasing until it reaches a maximum value of about 800 MPa, notably higher than the stress in the polysilicon, amounting to about 700 MPa. Afterward, the stress at the interface starts to drop due to the constrain joint at the center of the movable plate, which induces a stress redistribution throughout the entire structure.

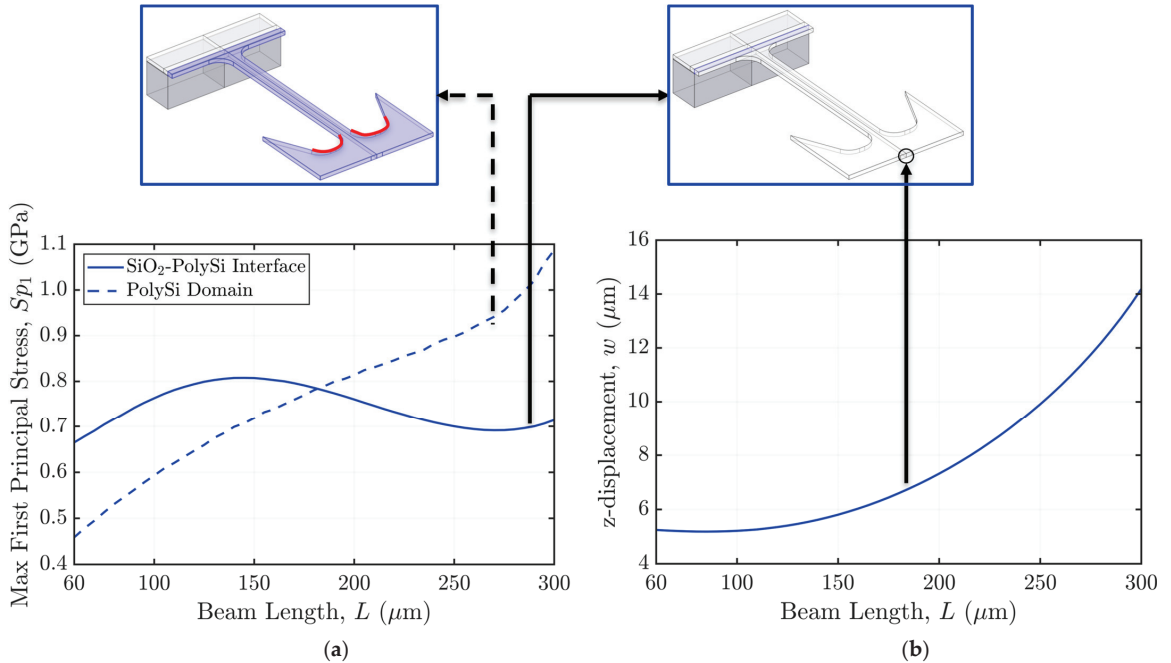


**Figure 3.** Effects of the beam length ( $L$ ): (a) on the maximum stress in the polycrystalline silicon domain (dashed line) and on the SiO<sub>2</sub>–polycrystalline silicon interface (continuous line); (b) on the out-of-plane displacement or deflection at the central point, highlighted by the black circle.

#### 4. Conclusions

In this study, a new design for a MEMS test structure based on piezoelectric actuation and sensing for closed-loop operation was reported. By means of finite element analyses, its geometry was optimized in order to maximize the stress at the SiO<sub>2</sub>–polysilicon interface, as a concentration can lead, in real-life situations, to delamination events. A maximum stress equivalent to about 800 MPa was attained, which resulted in being higher than the stress in the polysilicon to increase the probability of a localized crack-driven failure at such an interface and close to the target value of 1 GPa needed to speed up the fatigue tests.

These findings will be further developed by taking into consideration other geometric parameters in the optimization process that may lead to a higher stress intensification at the interface. The actual dynamic response of the structures to a sinusoidal, time-varying electric potential will also be assessed and compared to the outcome of an experimental study.

**Author Contributions:** Conceptualization, D.C., S.M., M.M. and G.F.; methodology, D.C.; software, D.C.; formal analysis, D.C., S.M., M.M. and G.F.; investigation, D.C., S.M., M.M. and G.F.; resources, D.C. and S.M.; data curation, D.C.; writing—original draft preparation, D.C.; writing—review and editing, S.M.; visualization, S.M.; supervision, S.M.; project administration, S.M.; funding acquisition, S.M. All authors have read and agreed to the published version of the manuscript.

**Funding:** The project was funded by STMicroelectronics under the Joint Research Platform STEAM, project Steam-P5 “Reliability of MEMS”.

**Institutional Review Board Statement:** Not applicable.

**Informed Consent Statement:** Not applicable.

**Data Availability Statement:** The data presented in this study are available on request from the corresponding author. The data are not publicly available due to some confidentiality issues.

**Acknowledgments:** The authors are indebted to Roberto Carminati, Carlo Valzasina, and Aldo Ghisi for a number of fruitful discussions in the early stages of the present study.

**Conflicts of Interest:** The authors declare no conflicts of interest.

## References

- Frangi, A.; Cercignani, C.; Mukherjee, S.; Aluru, N. *Advances in Multiphysics Simulation and Experimental Testing of Mems*, 1st ed.; Imperial College Press: London, UK, 2008.
- Tsuchiya, T. Mechanical reliability of silicon microstructures. *J. Micromech. Microeng.* **2021**, *32*, 013003. [CrossRef]
- Younis, M.I. *MEMS Linear and Nonlinear Statics and Dynamics*, 1st ed.; Springer: New York, NY, USA, 2011.
- Gad-el-Hak, M.; Seemann, W. *MEMS Handbook*, 1st ed.; CRC Press: Boca Raton, FL, USA, 2002.
- Corigliano, A.; Ardito, R.; Comi, C.; Frangi, A.; Ghisi, A.; Mariani, S. *Mechanics of Microsystems*, 1st ed.; Wiley: Chichester, UK, 2018.
- Saleem, M.; Nawaz, H. A Systematic Review of Reliability Issues in RF-MEMS Switches. *Micro Nanosyst.* **2019**, *11*, 11–33. [CrossRef]
- Rajagopalan, J. Microelectromechanical Systems (MEMS)-Based Testing of Materials. In *Handbook of Mechanics of Materials*, 2nd ed.; Schmauder, S., Chen, C.S., Chawla, K., Chawla, N., Chen, W., Kagawa, Y., Eds.; Springer: Singapore, 2019; pp. 1955–1979.
- Bhalerao, K.; Soboyejo, A.B.O.; Soboyejo, W.O. Modeling of fatigue in polysilicon MEMS structures. *J. Mater. Sci.* **2003**, *38*, 4157–4161. [CrossRef]
- Muhlstein, C.L.; Ritchie, R.O. High-cycle fatigue of micron-scale polycrystalline silicon films: Fracture mechanics analyses of the role of the silica/silicon interface. *Int. J. Fract.* **2003**, *120*, 449–474. [CrossRef]
- Ritchie, R.O.; Kruzic, J.J.; Muhlstein, C.L.; Nalla, R.K.; Stach, E.A. Characteristic dimensions and the micro-mechanisms of fracture and fatigue in “nano” and “bio” materials. *Int. J. Fract.* **2004**, *128*, 1–15. [CrossRef]
- Osterberg, P.M.; Senturia, S.D. M-TEST: A test chip for MEMS material property measurement using electrostatically actuated test structures. *J. Microelectromech. Syst.* **1997**, *6*, 107–118. [CrossRef]
- Mitul, B.M.; Suresh, K.S. Interfacial fracture toughness measurement for thin film interfaces. *Eng. Fract. Mech.* **2004**, *71*, 1219–1234.
- Tuck, K.; Jungen, A.; Geisberger, A.; Ellis, M.; Skidmore, G. A Study of Creep in Polysilicon MEMS Devices. *J. Eng. Mater. Technol.* **2005**, *127*, 90–96. [CrossRef]
- Chen, K.-S.; Ayon, A.A.; Zhang, X.; Spearing, S.M. Effect of process parameters on the surface morphology and mechanical performance of silicon structures after deep reactive ion etching (DRIE). *J. Microelectromech. Syst.* **2002**, *11*, 264–275. [CrossRef]
- Gao, X.; Joyce, J.A.; Roe, C. An investigation of the loading rate dependence of the Weibull stress parameters. *Eng. Fract. Mech.* **2008**, *75*, 1451–1467. [CrossRef]
- Mariani, S.; Martini, R.; Corigliano, A.; Beghi, M. Overall elastic domain of thin polysilicon films. *Comput. Mater. Sci.* **2011**, *50*, 2993–3004. [CrossRef]
- Mariani, S.; Martini Ghisi, A.R.; Corigliano, A.; Beghi, M. Overall elastic properties of polysilicon films: A statistical investigation of the effects of polycrystal morphology. *Int. J. Multiscale Comput. Eng.* **2011**, *9*, 327–346. [CrossRef]
- Mirzazadeh, R.; Eftekhar Azam, S.; Mariani, S. Micromechanical characterization of polysilicon films through on-chip tests. *Sensors* **2016**, *16*, 1191. [CrossRef] [PubMed]
- Mirzazadeh, R.; Mariani, S. Uncertainty quantification of microstructure-governed properties of polysilicon MEMS. *Micromachines* **2017**, *8*, 248. [CrossRef] [PubMed]
- Mirzazadeh, R.; Eftekhar Azam, S.; Mariani, S. Mechanical characterization of polysilicon MEMS: A hybrid TCMC/POD-kriging approach. *Sensors* **2018**, *18*, 1243. [CrossRef]
- Mariani, S.; Ghisi, A.; Mirzazadeh, R.; Eftekhar Azam, S. On-Chip testing: A miniaturized lab to assess sub-micron uncertainties in polysilicon MEMS. *Micro Nanosyst.* **2018**, *10*, 84–93. [CrossRef]
- Quesada Molina, J.P.; Mariani, S. Hybrid model-based and data-driven solution for uncertainty quantification at the microscale. *Micro Nanosyst.* **2022**, *14*, 281–286. [CrossRef]
- Zhang, M.; Lu, F.; Shao, J. Research on MEMS failure modes and failure mechanisms. In Proceedings of the 2017 Second International Conference on Reliability Systems Engineering (ICRSE), Beijing, China, 10–12 July 2017.

24. Muhlstein, C.L.; Brown, S.B.; Ritchie, R.O. High-cycle fatigue and durability of polycrystalline silicon thin films in ambient air. *Sens. Actuator A Phys.* **2001**, *94*, 177–188. [CrossRef]
25. Muhlstein, C.L.; Howe, R.T.; Ritchie, R.O. Fatigue of polycrystalline silicon for microelectromechanical system applications: Crack growth and stability under resonant loading conditions. *Mech. Mater.* **2004**, *36*, 13–33. [CrossRef]
26. Ballarini, R.; Kahn, H.; Boer, M.P.; Dugger, M. MEMS Structures for On-chip Testing of Mechanical and Surface Properties of Thin Films. *Compr. Struct. Integr.* **2007**, *8*, 325–356.
27. COMSOL Multiphysics®, v.6.0; COMSOL AB: Stockholm, Sweden. Available online: www.comsol.com (accessed on 30 September 2023).
28. Mariani, S.; Ghisi, A.; Corigliano, A.; Martini, R.; Simoni, B. Two-scale simulation of drop-induced failure of polysilicon MEMS sensors. *Sensors* **2011**, *11*, 4972–4989. [CrossRef] [PubMed]
29. Mariani, S.; Martini, R.; Ghisi, A.; Corigliano, A.; Simoni, B. Monte Carlo simulation of micro-cracking in polysilicon MEMS exposed to shocks. *Int. J. Fract.* **2011**, *167*, 83–101. [CrossRef]
30. Mulay, S.; Becker, G.; Vayrette, R.; Raskin, J.-P.; Pardoën, T.; Galceran, M.; Godet, S.; Noels, L. Multiscale modelling framework for the fracture of thin brittle polycrystalline films: Application to polysilicon. *Comput. Mech.* **2015**, *55*, 73–91. [CrossRef]
31. Hintsala, E.D.; Bhowmick, S.; Yueyue, X.; Ballarini, R.; Asif, S.A.S.; Gerberich, W.W. Temperature dependent fracture initiation in microscale silicon. *Ser. Mater.* **2017**, *130*, 78–82. [CrossRef]
32. Geraci, G.; Aliabadi, M.H. Micromechanical boundary element modelling of transgranular and intergranular cohesive cracking in polycrystalline materials. *Eng. Fract. Mech.* **2017**, *176*, 351–374. [CrossRef]
33. Bernal, R.A. On the application of Weibull statistics for describing strength of micro and nanostructures. *Mech. Mater.* **2021**, *162*, 104057. [CrossRef]
34. Brezmes, A.O.; Reuther, G.; Gneupel, A.; Breitkopf, C. Characterization of critical conditions for fracture during wafer testing by FEM and experiments. *Mater. Sci. Semicond. Process.* **2017**, *67*, 124–140. [CrossRef]
35. Buchheit, T.E.; Phinney, L.M. Fracture strength characterization for 25 micron and 125 micron thick SOI-MEMS structures. *J. Micromech. Microeng.* **2015**, *25*, 075018. [CrossRef]
36. Chen, M.; Pethö, L.; Sologubenko, A.; Ma, H.; Michler, J.; Spolenak, R.; Wheeler, J. Achieving micron-scale plasticity and theoretical strength in Silicon. *Nat. Commun.* **2020**, *11*, 2681. [CrossRef]
37. Somà, A.; Pistorio, F.; Saleem, M.M. Study of notched MEMS specimen: Elasto-plastic modeling and experimental testing. *J. Micromech. Microeng.* **2022**, *32*, 025006. [CrossRef]
38. Kozhushko, V.V.; Hess, P. Comparison of mode-resolved fracture strength of silicon with mixed-mode failure of diamond crystals. *Eng. Fract. Mech.* **2010**, *77*, 193–200. [CrossRef]
39. DelRio, F.W.; Cook, R.F.; Boyce, B.L. Fracture strength of micro- and nano-scale silicon components. *Appl. Phys. Rev.* **2015**, *2*, 021303. [CrossRef]
40. Masolin, A.; Bouchard, P.-O.; Martini, R.; Bernacki, M. Thermo-mechanical and fracture properties in single-crystal silicon. *J. Mater. Sci.* **2013**, *48*, 979–988. [CrossRef]

**Disclaimer/Publisher’s Note:** The statements, opinions and data contained in all publications are solely those of the individual author(s) and contributor(s) and not of MDPI and/or the editor(s). MDPI and/or the editor(s) disclaim responsibility for any injury to people or property resulting from any ideas, methods, instructions or products referred to in the content.

Proceeding Paper

# ProgMachina: Feature Extraction and Processing Package for Prognostic Studies <sup>†</sup>

Tarek Berghout <sup>1,\*</sup>, Mohamed Benbouzid <sup>2,3</sup> and Jaouher Ben Ali <sup>4</sup>

<sup>1</sup> Laboratory of Automation and Manufacturing Engineering, University of Batna 2, Batna 05000, Algeria

<sup>2</sup> UMR CNRS 6027 IRDL, University of Brest, 29238 Brest, France; mohamed.benbouzid@univ-brest.fr

<sup>3</sup> Logistics Engineering College, Shanghai Maritime University, Shanghai 201306, China

<sup>4</sup> Laboratory of Signal Image and Energy Mastery (SIME), National Higher School of Engineers of Tunis, University of Tunis, 5 Av. Taha Hussein, Tunis 1008, Tunisia; benali.jaouher@essths.u-sousse.tn

\* Correspondence: t.berghout@univ-batna2.dz

<sup>†</sup> Presented at the 10th International Electronic Conference on Sensors and Applications (ECSA-10), 15–30 November 2023; Available online: <https://ecsa-10.sciforum.net/>.

**Abstract:** Prognostic studies of industrial systems essentially focus on health deterioration analysis that has recently been oriented toward data analytics and learning systems. In general, real degradation phenomena suffer from complex drifted data in which degradation patterns are hidden and change over time. Accordingly, such a process requires a well-structured processing and extraction mechanism to reveal such patterns, which facilitates the transition to other model reconstruction and investigation tasks. In this context, to provide additional simplicity of data processing in the field, a complete software package is designed and grouped into a single function that is fully automated and does not require human intervention. The package named ProgMachina (i.e., prognostic machine) provides a featured list of processed features from a life cycle that passed through denoising, filtering, outlier removal, and scaling process to ensure data significance in terms of degradation. The package allows for the use of a time window with a specific overlap to ensure that the scanning process of all possible degradation patterns is properly done. Additionally, an exponential function is used to identify a corresponding health index of degraded signals. In addition, a set of well-known metrics is used to assess the degradation of extracted features. Data visualization and many previous experiments on machines show the effectiveness of such a methodology in terms of obtained prediction accuracy and degradation assessment. The package is designed with Matlab software and made available online to be exploited in similar fields.

**Keywords:** degradation; feature extraction; health index; machine learning; prognostics and health management; remaining useful life

**Citation:** Berghout, T.; Benbouzid, M.; Ali, J.B. ProgMachina: Feature Extraction and Processing Package for Prognostic Studies. *Eng. Proc.* **2023**, *58*, 83.

<https://doi.org/10.3390/ecsa-10-16222>

Academic Editor: Stefano Mariani

Published: 15 November 2023



**Copyright:** © 2023 by the authors. Licensee MDPI, Basel, Switzerland. This article is an open access article distributed under the terms and conditions of the Creative Commons Attribution (CC BY) license (<https://creativecommons.org/licenses/by/4.0/>).

## 1. Introduction

Nowadays, prognostic studies rely heavily on data analysis and learning systems for condition monitoring rather than highly complex traditional physics-based modeling. Physics-based modeling is primarily needed when the systems under study are both safety-critical and financially expensive, rarely fail under working conditions, and cannot be subjected to real deterioration or accelerated aging laboratory experiments. However, physics-based modeling is used for generative modeling and is also hybridized with learning systems to ensure efficient predictions. In this case, the acquisition, extraction, and processing of run-to-failure data are crucial steps for data analysis and reconstruction of the learning model [1]. When it comes to building a learning model for system prognostics, run-to-failure is usually a challenge of complexity and data drift, while degradation patterns are hidden and buried with ever-changing noise and different distortion patterns, respectively, resulting from harsh system operating conditions. In this case, training a learning model with such data will certainly mislead the predictions and over-fit the model. In this context,

the need for a well-structured feature extraction and processing methodology is urgent to ensure that data are well presented in terms of providing a reliable source of information to improve the performance of the learning model.


In the literature, many paths have been proposed, including most importantly, denoising, extraction, and outlier removal. Accordingly, since these methodologies are proven to be necessary for progressive degradation analysis in terms of prognostics studies, the main goal of this paper is to combine them as a single and full package as an important contribution to facilitating such a complex process. In this case, this paper introduces ProgMachina, a full package designed specifically to deal with such run-to-failure data features passing via different important steps. Each of these steps is used to uncover and extract degradation patterns from row data of entire life cycles. The package also allows for the release of an exponentially deteriorating health index for the intended life cycle.

This paper is organized as follows: Section 2 represents the package descriptions, its main features, and its relationship with run-to-failure data besides some illustrative examples. Section 3 is specifically dedicated to introducing the impact of this package on prognostics studies, while the conclusion is dedicated to limitations and future improvements of the package.

## 2. ProgMachina Package Description

ProgMachina is a function designed in Matlab software (<https://www.mathworks.com/products/matlab.html>, accessed on 14 November 2023) to deliver well-processed run-to-failure data with a corresponding health index (HI) ready to feed a learning system for training and evaluation. Table 1 gives further details about the metadata of the package. ProgMachina allows the acquisition of a run-to-failure dataset per life cycle (i.e., a single degradation unit from normal operating conditions to a complete failure of the system), which is organized vertically as observations and channels (i.e., different sensor measurements) only and uses them to generate an extracted and well-prepared list of features and corresponding HI. According to previous literature [2], ProgMachina follows specific steps of extraction, denoising, and outlier removal as the main steps of uncovering hidden degradation patterns in provided life cycles, while smoothening, filtering, and scaling brings further enhanced representations and builds strange connections and correlations between data samples. Accordingly, this section is dedicated to exploring such steps in detail.

**Table 1.** Important metadata of ProgMachina.

Package Name	ProgMachina
Current code version	v1.0.0
Permanent link to the software	<a href="https://doi.org/10.5281/zenodo.8174085">https://doi.org/10.5281/zenodo.8174085</a>
Software code languages, tools, and services used	Matlab
Compilation requirements	Matlab $\geq$ r2023a
Logo	

### 2.1. Features Extraction

A set of well-used features in the literature is included in ProgMachina. These features include mean, standard deviation (Std), skewness, kurtosis, peak to peak, square root of the arithmetic mean (RMS), crest factor, shape factor, impulse factor, margin factor, energy, mean value spectral kurtosis (SKMean), standard deviation of spectral kurtosis (SKStd), spectral kurtosis of skewness (SKSkewness), and spectral kurtosis of kurtosis (SK kurtosis). More details of these features background and their mathematical background can be found in the following references [3]. These features are extracted for each time window that overlaps all over the signal and have been selected as they are well-known signal descriptors and used for such slowly evolving degradation process analysis while reducing

problem complexity and prevent information loss [4]. It should be mentioned that these features need further analysis of whether they describe a degradation mechanism or not. In this case, metrics like Monotonicity, Tenability, Prognosability, and Robustness (MTPR) are well investigated for such purposes [4]. Accordingly, ProgMachina also includes such metrics to further provide insights about the degradation ability of extracted features and also to provide further information about feature selections. The goal of measuring MTPR is to guarantee that the signal is monotonic to specific degradation trends and given in a meaningful way through the degradation path reflecting actual system health, while prognosability mainly indicates the possibility of separating faulty and healthy degradation patterns.

## 2.2. Denoising

Slowly evolving degradation processes are well known with the complex dynamics resulting in a very complex feature space with higher levels of noise with unknown sources [5]. In this context, the collected features unquestionably need to be subject to a noise reduction procedure. ProgMachina offers an empirical Bayesian wavelet transformation to create more reliable representations by reducing the amount of noise of such features. This method successfully minimizes the effect of noise in the feature space by combining a Cauchy prior with a posterior median threshold rule [6,7]. This process is accomplished by including the default “`wdenoise(---)`” Matlab function.

## 2.3. Outlier Removal

Besides the existence of noise in recorded signals as well as per extracted features, different random pulses of higher magnitude disturbances can be found in such a degradation process. Therefore, an outlier remover is necessary to eliminate/reduce their effects on the recorded data. Subsequently, the denoised characteristics of the entire tire life cycle will be further processed using an outlier removal tool. This distinct outlier removal approach was implemented to distinguish differences in data characteristics. The removal of outliers was carried out by default, using a moving median function “`rmoutliers(---)`” [8].

## 2.4. Smoothing and Filtering

Additional filtering and smoothing processes are required to further enhance signal quality and provide further appearance to degradation patterns. While the Markov-switching dynamic regression model models data, we employed the state probabilities of the active latent states in the regime transition for smoothing “`smooth(---)`”. It conducts reverse recursion after performing forward recursion [9]. For the filtering process, an additional step of median filtering is involved to further enhance signal quality “`medfilt1(---)`”.

## 2.5. Scaling and Health Index Identification

A min-max normalization in the range  $[0, 1]$  is used as normal to unify feature measurement scales after each process of denoising and smoothing and outlier removal. From such data, ProgMachina defines a deteriorating HI according to an exponential function (see Equation (2) from [10]).

## 2.6. Illustrative Example

As an illustrative example, a life cycle of bearing dataset generated from a mathematical model is used in this case [11]. The dataset represents a vibration run-to-failure measurement. Figure 1a is an example of vibration measurement while degradation grows exponentially. ProgMachina is used to find out both features in Figure 1b and HI in Figure 1c. The extracted features are smoother, cleaner, and even more representative of degradation than the original raw signal and the HI signal. This is demonstrated by the fact that Figure 1d,e,g show values closer to 1 for all features. This means that the features reflect the degradation mechanism. Meanwhile, Figure 1f provides further instructions for feature selection if dimensionality reduction is required.

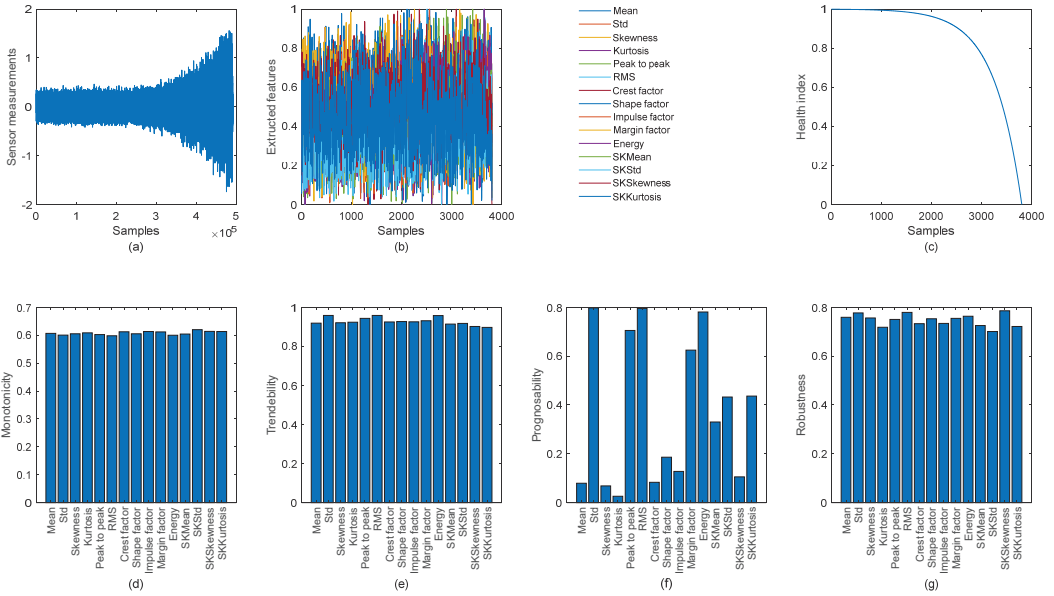


**Figure 1.** ProgMachina package inputs and outputs: (a) raw vibration data; (b) extracted and processed features; (c) identified health index; (d–g) Monotonicity, trendability, prognosability, robustness.

### 3. ProgMachina Impact

ProgMachina as an easy-to-use single package is expected to draw several advantages for prognostics studies including the most important ones listed as follows:

- Bringing more simplicity in learning model reconstruction;
- Needing less human intervention as everything is done automatically;
- Easily investigating the variability of new features by simply adding them to the open source code;
- Providing a reliable source of information, especially by involving outlier removal and denoising;
- Making the feature selection process further simplified by studying signal degradations metrics;
- Spending more time on developing learning systems rather than processing.

### 4. Conclusions

This paper has introduced ProgMachina, a full package for feature extraction and processing degradation signals recorded from slowly evolving degradation processes. It follows different important steps of extraction, denoising, outlier removal, smoothing, filtering, and scaling to reach quality signals that can be used to feed learning systems and prepare for investigations. We should mention that ProgMachina is built based on a limited set of both time domain and frequency domain feature extraction and processing. Therefore, future opportunities in improving such a package are to consider other features and further signal processing tools to produce better quality and clean data with better illustration of degradation. It is also important to consider the tempo-frequency domain. Additionally, we can use methods of attribute reduction to define health indicators in a new space whose evolution will surely be more linear.



**Author Contributions:** Conceptualization, T.B.; methodology, T.B. and M.B.; validation, T.B., M.B. and J.B.A.; formal analysis, T.B., M.B. and J.B.A.; investigation, T.B.; resources, T.B.; data curation, T.B., M.B. and J.B.A.; writing—original draft preparation, T.B.; writing—review and editing, T.B., M.B. and J.B.A. All authors have read and agreed to the published version of the manuscript.

**Funding:** This research received no external funding.

**Institutional Review Board Statement:** Not applicable.

**Informed Consent Statement:** Not applicable.

**Data Availability Statement:** This work used data from [https://figshare.com/articles/dataset/Simulated\\_Bearing\\_Degradation\\_Data\\_mat/12554690](https://figshare.com/articles/dataset/Simulated_Bearing_Degradation_Data_mat/12554690) (accessed 14 November 2023). Necessary files to reproduce the findings of this work can be downloaded at: <https://doi.org/10.5281/zenodo.8174085>.

**Conflicts of Interest:** The authors declare no conflicts of interest.

## References

1. Berghout, T.; Benbouzid, M. A Systematic Guide for Predicting Remaining Useful Life with Machine Learning. *Electronics* **2022**, *11*, 1125. [CrossRef]
2. Ali, J.B.; Saidi, L. A New Suitable Feature Selection and Regression Procedure for Lithium-Ion Battery Prognostics. *Int. J. Comput. Appl. Technol.* **2018**, *58*, 102. [CrossRef]
3. Qiu, W.; Zhu, K.; Teng, Z.; Tang, Q.; Yao, W.; Dong, Y.; Liu, Y. Cyber-Attack Identification of Synchronphasor Data Via VMD and Multi-Fusion SVM. In Proceedings of the 2020 IEEE Industry Applications Society Annual Meeting, IEEE, Detroit, MI, USA, 10–16 October 2020; pp. 1–6.
4. Qiu, G.; Gu, Y.; Chen, J. Selective Health Indicator for Bearings Ensemble Remaining Useful Life Prediction with Genetic Algorithm and Weibull Proportional Hazards Model. *Meas. J. Int. Meas. Confed.* **2020**, *150*, 107097. [CrossRef]
5. Saxena, A.; Goebel, K.; Simon, D.; Eklund, N. Damage Propagation Modeling for Aircraft Engine Run-to-Failure Simulation. In Proceedings of the 2008 International Conference on Prognostics and Health Management, IEEE, Denver, CO, USA, 6–9 October 2008; pp. 1–9.
6. Donoho, D.L. De-Noising by Soft-Thresholding. *IEEE Trans. Inf. Theory* **1995**, *41*, 613–627. [CrossRef]
7. Johnstone, I.M.; Silverman, B.W. Needles and Straw in Haystacks: Empirical Bayes Estimates of Possibly Sparse Sequences. *Ann. Stat.* **2004**, *32*, 1594–1649. [CrossRef]
8. Blázquez-García, A.; Conde, A.; Mori, U.; Lozano, J.A. A Review on Outlier/Anomaly Detection in Time Series Data. *arXiv* **2020**, arXiv:2002.04236v1. [CrossRef]
9. Kim, C.-J. Dynamic Linear Models with Markov-Switching. *J. Econom.* **1994**, *60*, 1–22. [CrossRef]
10. Berghout, T.; Mouss, L.-H.; Bentrícia, T.; Benbouzid, M. A Semi-Supervised Deep Transfer Learning Approach for Rolling-Element Bearing Remaining Useful Life Prediction. *IEEE Trans. Energy Convers.* **2022**, *37*, 1200–1210. [CrossRef]
11. Koceila, A.; Mouchaweh, M.S.; Cornez, L.; Chiementin, X. Simulated Bearing Degradation Data. 2020. Available online: [https://figshare.com/articles/dataset/Simulated\\_Bearing\\_Degradation\\_Data\\_mat/12554690](https://figshare.com/articles/dataset/Simulated_Bearing_Degradation_Data_mat/12554690) (accessed on 14 November 2023).

**Disclaimer/Publisher’s Note:** The statements, opinions and data contained in all publications are solely those of the individual author(s) and contributor(s) and not of MDPI and/or the editor(s). MDPI and/or the editor(s) disclaim responsibility for any injury to people or property resulting from any ideas, methods, instructions or products referred to in the content.

# The Implementation and Advantages of a Discrete Fourier Transform-Based Digital Eddy Current Testing Instrument <sup>†</sup>

Songhua Huang <sup>1,2,\*</sup>, Maocheng Hong <sup>3</sup>, Ge Lin <sup>1,2</sup>, Bo Tang <sup>1</sup> and Shaobin Shen <sup>1</sup>

<sup>1</sup> CGN Inspection Technology Co., Ltd., 191 Yangpu Road, Suzhou 215012, China; mr.linge@163.com (G.L.); qtfytb@163.com (B.T.); simensshen@hotmail.com (S.S.)

<sup>2</sup> National Engineering Research Center for Nuclear Power Plant Safety & Reliability, Suzhou 215012, China

<sup>3</sup> School of Electronic Science & Engineering, Southeast University, No.2 Sipailou, Nanjing 211189, China; hmc\_2019@163.com

\* Correspondence: huangsonghua\_2008@126.com

<sup>†</sup> Presented at the 10th International Electronic Conference on Sensors and Applications (ECSA-10), 15–30 November 2023; Available online: <https://ecsa-10.sciforum.net/>.

**Abstract:** An eddy current testing instrument is the core equipment for non-destructive testing (NDT) in nuclear power plants, and its performance is of great significance to ensure the safety of nuclear power units throughout their life cycle. At present, mainstream eddy current instruments use analog circuits for signal processing, whose structure is complex, and there are shortcomings such as large noise and weak anti-interference ability. To improve the performance of eddy current instruments, this paper creatively proposes a digital signal processing method. In this method, ARM+FPGA is used as the core of signal processing, and a DFT digital signal processing algorithm is used instead of traditional hardware detection circuits to complete the processing of eddy current signals. The parallel DFT operation is realized in the algorithm, and up to 10 superimposed signals of different frequencies can be operated simultaneously, which further improves the detection efficiency of the instrument. The measured results show that the digital instrument designed in this paper greatly simplifies the hardware circuit, reduces the overall electronic noise level, and improves the signal-to-noise ratio and detection efficiency. The instrument supports BOBBIN, MRPC and ARRAY detection technologies, which fully meets the application needs of NDT in nuclear power plants.

**Keywords:** eddy current instrument; Discrete Fourier transform (DFT); nuclear power plants; signal processing

**Citation:** Huang, S.; Hong, M.; Lin, G.; Tang, B.; Shen, S. The Implementation and Advantages of a Discrete Fourier Transform-Based Digital Eddy Current Testing Instrument. *Eng. Proc.* **2023**, *58*, 84. <https://doi.org/10.3390/ecsa-10-16214>

Academic Editor: Stefano Mariani

Published: 15 November 2023



**Copyright:** © 2023 by the authors. Licensee MDPI, Basel, Switzerland. This article is an open access article distributed under the terms and conditions of the Creative Commons Attribution (CC BY) license (<https://creativecommons.org/licenses/by/4.0/>).

## 1. Introduction

Eddy current testing technology is a non-destructive testing (NDT) method based on the principle of electromagnetic induction [1]. If the defect in a conductor interferes with the trajectory of the eddy currents, the equilibrium state will be changed, and the defect information can be obtained by detecting the change of the eddy current magnetic field [2]. Figure 1a shows the trajectory of eddy currents in a defect-free conductor when the excitation coil is applied. Figure 1b depicts the changes when there is a crack in the conductor.

Eddy current testing is essentially a magnetic field disturbance problem that can be calculated using the Maxwell equation. When the excitation signal changes in time harmonics, its mathematical model can be regarded as a derivation issue from the beginning of the time-harmonic electromagnetic field to the disturbance electromagnetic field generated

by the defect. Taking the harmonic factor  $e^{j\omega t}$ ,  $\omega > 0$ , the Maxwell equation can be written as Equation (1) [3].

$$\begin{cases} \nabla * H = J_s + (\sigma + j\omega\epsilon)E \\ \nabla * E = -j\omega B \\ \nabla * B = 0 \\ \nabla * D = \rho \end{cases} \quad (1)$$

where H is the magnetic field strength,  $J_s$  is the current density of the conductor surface, D is the electric displacement, B is the magnetic induction, E is the electric field intensity, and  $\rho$  is the bulk density of free charge. The solution of this equation is complex, and not suitable for engineering applications.

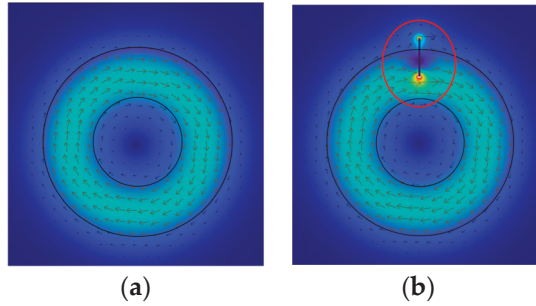


**Figure 1.** (a) Distribution of eddy currents when there are no defects in the conductor, (b) distribution of eddy currents when there is a crack in the conductor.

Further research shows that changes in various factors of conductors will cause changes in impedance of the detection coil [1]. Eddy current detection can be abstracted into monitoring impedance value of the sensing coil with the following functional formula:

$$Z = F(\rho, \mu, x, f, r, h) \quad (2)$$

where Z represents the detection coil impedance,  $\rho$  represents the conductivity,  $\mu$  represents the magnetic permeability, x represents the material defect, f represents the excitation coil frequency, r represents the probe radius, and h represents the distance between the test piece and the probe. In engineering applications,  $\rho$ ,  $\mu$ , f, r, and h are kept unchanged, so that the correspondence between the sensor coil impedance Z and the material defect x can be established. This makes eddy current testing easier to implement.

To facilitate defect analysis, changes in coil impedance are usually converted into changes in the real and imaginary parts of the signal [1]. Figure 2b is an impedance plane plot showing the trajectory of the impedance change of the test coil. Strip charts are formed on the basis of impedance plane diagram. Figure 2a shows the strip chart in the horizontal direction, representing the real part signal of the test coil; Figure 2c shows in vertical direction, representing the imaginary part signal of the coil.

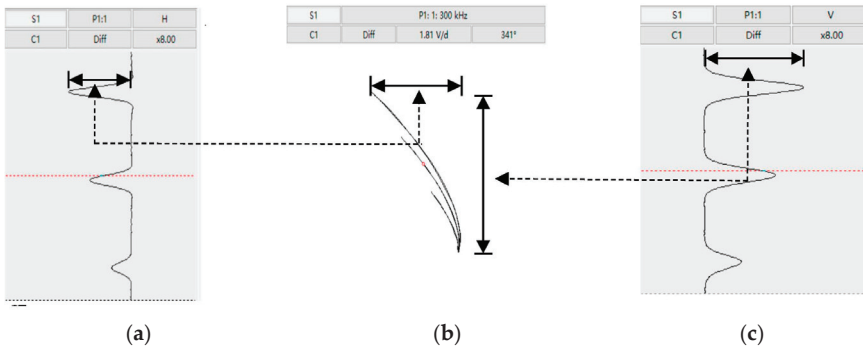


**Figure 2.** (a) Strip chart in horizontal direction, showing changes in real part of coil impedance; (b) impedance plan, characterizing the trajectory of coil impedance changes; (c) strip chart in vertical direction, showing changes in the imaginary part of coil impedance.

**2. Implementation of Digital Eddy Current Testing Instrument**

The eddy current instrument designed in this paper is mainly used for the NDT of core components in nuclear power plants. To eliminate the influence of strong interference signals generated by adjacent support plates, multi-frequency eddy current inspection technology is required [4]. Multi-frequency eddy current testing refers to technology that can be inspected at two or more operating frequencies simultaneously. The mixing channel superimposes the response signals of different frequencies to eliminate the response signal of the support plate and extract the defect signal. In the eddy current test of the heat transfer tube of the steam generator, five frequencies are generally used at the same time [4]. This section focuses on how to implement a digital multi-frequency eddy current instrument.

Figure 3 is the schematic diagram of the digital eddy current signal processing method, the main functions of which are implemented by ARM+FPGA. ARM is used for interaction with the host computer, receiving configuration information, and uploading detection data. FPGA is mainly used to control the generation of excitation signals and the extraction of detection signals.

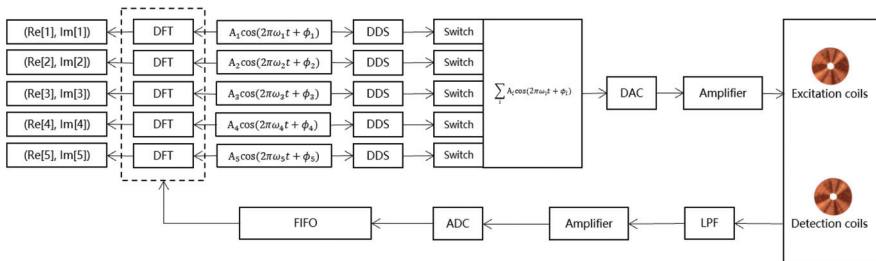


**Figure 3.** Digital eddy current signal processing.

The specific implementation process is described as follows:

1. Digitization of excitation signals.

Depending on the characteristics of the object to be inspected, different combinations of frequencies are set. Figure 3 shows the flow when configuring five different frequencies.

Each frequency can be individually configured for its frequency, phase, and amplitude. The sinusoidal signals of different frequencies are converted into digital sine waves through Direct Digital Frequency Synthesis (DDS) technology. DDS is based on sampling theory, sampling the signal waveform at very small phase intervals, and calculating the amplitude corresponding to the phase to form a phase-amplitude table for generating the desired

waveform [5]. The resulting excitation signal has the advantages of high resolution and fast conversion speed, and its stability and accuracy are improved to the same level as the reference frequency, and fine frequency adjustment can be performed over a wide range.

As shown in Figure 4a, the excitation signal of an eddy current instrument usually uses continuous sine waves, which is easy to implement. In the application, a continuous signal of a specific length is intercepted according to the set eddy current signal sampling rate ( $f_s$ ) and, for subsequent calculations, the specific length is called timeslot (T). It is easy to obtain  $T = 1/f_s$ . It is difficult for T to be exactly an integer multiple of the excitation signal period, resulting in inconsistency in each intercepted signal, affecting the detection results.

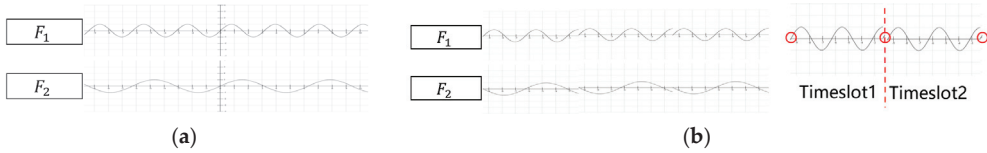


**Figure 4.** (a) Continuous sinusoidal signals, (b) repeated sinusoidal excitation signals.

As shown in Figure 4b, in this article, DDS is used to generate stable repetitive signals to ensure that the excitation signal is the same in each timeslot, so that the ADC sampling values are identical under the same defects. Enhance the repeatability of the instrument’s response to the same defect.

2. Excitation signal and detection signal processing.

The digitized sinusoidal signals are superimposed by calculation  $\sum_i A_i \cos(2\pi\omega_i t + \phi_i)$ , and it should be noted that when superimposing, the phase of different frequencies needs to be adjusted to avoid signal peaks superimposed together and cause amplitude overrange.

Then, the digital signal is converted to analog by DAC, where the signal has no drive capability and needs to be amplified by a power amplifier to drive the excitation probe.

The induced signal generated on the detection coil contains a lot of high-frequency noise that needs to be filtered out by a low-pass filter. The amplitude of the detection signal is generally only a few millivolts, which is prone to attenuation, and when attenuated to a certain extent, it will become an invalid signal. Therefore, this method adds an amplifier to the detection circuit to further improve the signal quality and anti-interference ability.

3. Discrete Fourier Transform (DFT).

Using DFT to complete signal parsing is core of this method, which is detailed below.

The amplified detection signal is converted into digital signal after AD conversion. The digital signal is a multi-frequency superimposed signal, which contains the defect information of the inspected object, and the real and imaginary parts corresponding to each frequency signal need to be calculated to complete the signal analysis. The analytical method adopted in this paper is to make DFT of the multi-frequency detection digital signal at the set frequency point, through which the signal is transformed from time domain to frequency domain, the spectral structure of each different frequency signal is separated, and the real and imaginary parts of each frequency signal are calculated at the same time.

The detection signal obtained by the ADC conversion is a discrete time-domain signal, based on the principle of signal processing, and it can be expressed in form of Equation (3).

$$x[i] = \sum_{k=0}^{N/2} ReX[k] \cos(2\pi ki/N) + \sum_{k=0}^{N/2} ImX[k] \sin(2\pi ki/N) \tag{3}$$

The DFT is calculated using the correlation-based method, and formulas are as follows [6]:

$$ReX[k] = \sum_{i=0}^{N-1} x[i] \cos(2\pi ki/N) \tag{4}$$

$$ImX[k] = -\sum_{i=0}^{N-1} x[i] \sin(2\pi ki/N) \tag{5}$$

From Equations (4) and (5), it can be seen that the DFT transformation can extract the real and imaginary parts corresponding to different frequency signals in the detection signal, and  $(ReX[k], ImX[k])$  can be obtained, so as to complete the analysis of the detection signal.

Improper use of the DFT method will lead to spectrum leakage; that is, the spectral lines in the signal spectrum affect each other, so that the measurement results deviate from the actual value, and some false spectra with smaller amplitudes will appear at other frequency points on both sides of the spectral line [7]. From the perspective of the time domain, DFT treats signals as infinitely long periodic signals when processing them; therefore, the signal needs to be extended processing, and the non-periodic signal should also be extended into a periodic signal. During splicing, if the repeated fragments can be spliced exactly to be consistent with the original signal, it is called perfect stitching. If not, there will be sudden changes at the splicing point, resulting in the generation of other frequency components, and the surrounding frequencies will bisect the frequencies in the original signal, resulting in inaccurate frequency amplitude and spectral leakage [8,9].

In order to avoid spectrum leakage, this method conducted in-depth research on DFT algorithm, and found that when the relationship of Equation (6) is strictly satisfied, there will be no spectrum leakage at all, where  $M$  is the number of periods in time domain,  $N$  is the number of sampling points, and  $F_s$  is the sampling frequency,  $F_{in}$  is the signal frequency.

$$M/N = F_{in}/F_s \quad (6)$$

Because when the above relationship is satisfied, the repeated periodic signal can be spliced exactly to coincide with the original signal, thus avoiding spectral leakage. Figure 5a is the impedance plane when spectral leakage occurs, and Figure 5b is the impedance plane when the relationship (6) is satisfied.

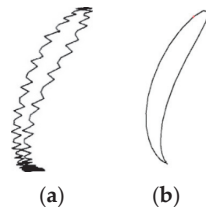


**Figure 5.** (a) Impedance plane plot when spectral leakage occurs, (b) normal impedance plane.

Then, the parsed  $(ReX[k], ImX[k])$  values are transmitted to the host computer for professional analysts to complete the analysis and evaluation of eddy current detection results.

### 3. Advantages of Digital Eddy Current Instrument

Compared with the eddy current instrument using analog circuits for signal processing, the digital instrument designed in this paper mainly has the following advantages:

1. Higher detection efficiency.

Due to the limitations of the implementation mechanism, the analog eddy current instrument uses hardware multiplier to extract the detection signals. The hardware detection circuit needs to complete the extraction of different frequency signals in order, which is inefficient and can only set up to five different detection frequencies simultaneously.

The digital eddy current meter can use the computing power of the FPGA to extract the real and imaginary parts of different frequency signals in parallel, which greatly improves the detection efficiency, and this method can support up to 10 signals of different frequencies at the same time, expanding the application scenarios of the instrument [10].

2. Higher signal-to-noise ratio.

It can be seen from the principle of DFT that when doing N-point DFT operation on the signal of a certain frequency, because the signal is superimposed in phase, sampling

N times will increase the amplitude in the frequency domain by N times, and the signal power will increase by  $N^2$  times. There is white noise in the detection signal, the DFT operation of noise is non-in-phase superposition, the amplitude of the noise signal increases by  $\sqrt{N}$  times in the frequency domain, and the noise power increases N times. Therefore, the signal-to-noise ratio (signal power divided by noise power) of the digital instrument increases N times.

Analog instruments, on the other hand, extract effective signals through hardware circuits without improving the signal-to-noise ratio. When the noise floor is large, there is a risk that the measured signal will be drowned out by strong noise in engineering applications.

Therefore, the digital instrument designed in this paper has a higher signal-to-noise ratio.

### 3. Greater dynamic range.

Figure 6a shows the circuit block diagram of an analog eddy current instrument, which has a complex circuit structure. The digital instrument, on the other hand, uses high-performance 24-bit ADC with a signal-to-noise ratio of up to 100 dB, enabling a large dynamic range in the digital domain and greatly improving the ability to acquire tiny induced signals. In addition, the multi-stage amplification circuit and program-controlled circuit at the front end of the analog circuit are simplified, the influence of the analog circuit on the induced signal is reduced, and the performance of the eddy current meter is improved.

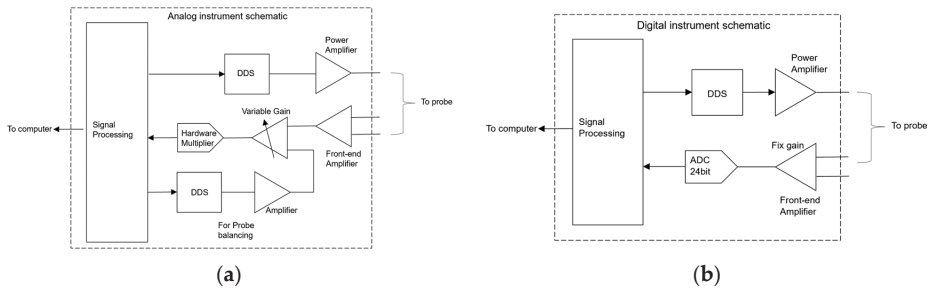


Figure 6. (a) Circuit diagram of analog instrument, (b) circuit diagram of digital instrument.

## 4. Application Testing and Conclusions

### 4.1. Application Testing

The eddy current instruments designed in this paper have been successfully applied to non-destructive testing of nuclear power plants with excellent test results. Wear damage in heat transfer tubes in nuclear power plants is often difficult to measure; Figure 7 shows the results obtained by testing the wear damage of the same heat transfer tube separately using the digital eddy current instrument designed in this article and the traditional analog instrument. It can be seen that the digital instrument has a higher signal-to-noise ratio, and the result is much clearer, which is conducive to analysis.

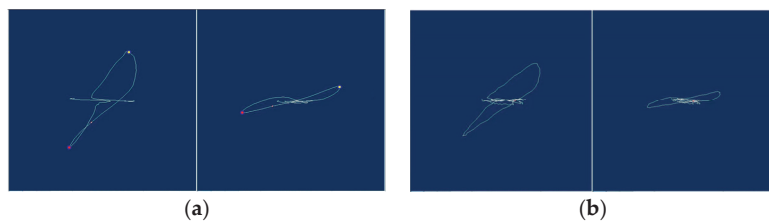
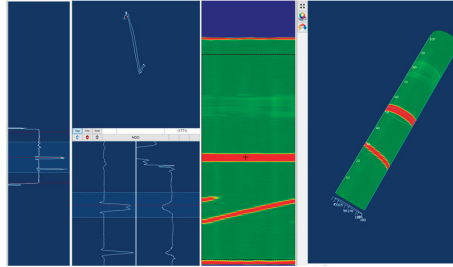


Figure 7. (a) Test result of digital instrument, (b) test result of analog instrument.

To better present the results, 3D imaging techniques were used in this design. Figure 8 shows the 3D imaging obtained when performing a heat transfer tube eddy current inspection using an array probe. The “+” sign in the figure is the position of the cursor, and the signal of the coil indicated by this cursor is shown on the left side of the figure. This allows the location and size of the various injuries in the tube to be clearly seen, so that the analysis can be completed more accurately.



**Figure 8.** Array probe 3D test results.

#### 4.2. Conclusions

Through scientific research on eddy current detection, this paper creatively puts forward the design scheme for a digital eddy current instrument, solves a series of problems such as architecture design, signal-to-noise ratio improvement, anti-electromagnetic interference, high-speed data processing, and three-dimensional data imaging of the digital eddy current instrument, and finally realizes the successful research and development of a high-end eddy current instrument. The research and development results mentioned in this paper have been successfully applied to eddy current testing in many nuclear power plants, providing a guarantee for the safe and stable operation of nuclear power plants.

**Author Contributions:** Conceptualization, S.H. and G.L.; methodology, S.H. and M.H.; software, B.T. and S.H.; validation, S.S., M.H. and G.L.; formal analysis, M.H. and B.T.; investigation, S.H. and G.L.; data curation, B.T.; writing—original draft preparation, S.H.; writing—review and editing, M.H.; visualization, B.T.; supervision, G.L.; project administration, S.H.; funding acquisition, G.L. All authors have read and agreed to the published version of the manuscript.

**Funding:** This research received no external funding.

**Institutional Review Board Statement:** Not applicable.

**Informed Consent Statement:** Not applicable.

**Data Availability Statement:** The data and intellectual property rights belong to CGN Inspection Technology Co., Ltd.; Any sharing needs to be evaluated and approved by the company.

**Conflicts of Interest:** The authors declare no conflicts of interest.

#### References

1. Kebei, X.; Junhua, Z. *Eddy Current Testing*, 1st ed.; China Machine Press: Beijing, China, 2004; pp. 21–44.
2. Xie, S.; Yamamoto, T. Pulsed ECT method for evaluation of pipe wall-thinning of nuclear power plants using magnetic sensor. *Stud. Appl. Electromagn. Mech.* **2011**, *35*, 203–210.
3. Li, X.; Yinzhao, L. Uniqueness and stability of solution to the linear transient eddy current electromagnetic field problem for determining solution. *Acta Phys. Sin.* **2006**, *55*, 4397–4406.
4. MIL-STD-2023(SH) *Eddy Current Inspection of Heat Exchanger Tubing on Ships of the United States Navy*; Department of Defense, United States of America: Arlington, VA, USA, 1990.
5. Junzhe, G.; Feilu, L. Modular Multi-Frequency Eddy Current Test System Design Based on DDS Technology. *Instrum. Tech. Sens.* **2009**, *10*, 104–107.
6. Junzhe, G.; Mengchun, P. Research on signal processing method of multi-frequency eddy current testing based on spectrum analysis. *J. Electron. Meas. Instrum.* **2011**, *25*, 16–22.



7. Lei, C.; Qingsheng, Z. Real-time Frequency and Amplitude Measurement Algorithm Based on Improved Discrete Fourier Transformation. *Sci. Technol. Eng.* **2018**, *18*, 240–245.
8. Tao, J.; Yiyang, C. Research on Synchronous Phasor Measurement Algorithm of Power System Based on Improved DFT. *Trans. China Electrotech. Soc.* **2017**, *32*, 1–10.
9. Tanaka, M.; Tsuboi, H. Transient eddy current analysis by the boundary element method using fourier transforms. *IEEE Trans. Magn.* **1993**, *29*, 1722–1725. [CrossRef]
10. Tong, H.; Xing, C. High-precision frequency detection with APFFT based on FPGA. *Electron. Meas. Technol.* **2013**, *36*, 80–88.

**Disclaimer/Publisher’s Note:** The statements, opinions and data contained in all publications are solely those of the individual author(s) and contributor(s) and not of MDPI and/or the editor(s). MDPI and/or the editor(s) disclaim responsibility for any injury to people or property resulting from any ideas, methods, instructions or products referred to in the content.



Proceeding Paper

# Internet of Things-Based Fuzzy Logic Controller for Smart Soil Health Monitoring: A Case Study of Semi-Arid Regions of India <sup>†</sup>

Rajan Prasad <sup>1,\*</sup>, Rajinder Tiwari <sup>2</sup> and Adesh Kumar Srivastava <sup>3</sup>

<sup>1</sup> Department of Computer Science and Engineering, Babu Banarasi Das University, Lucknow 226028, Uttar Pradesh, India

<sup>2</sup> Department of Electronics and Communication Engineering, Babu Banarasi Das University, Lucknow 226028, Uttar Pradesh, India; trajan@rediffmail.com

<sup>3</sup> School of Management, Babu Banarasi Das University, Lucknow 226028, Uttar Pradesh, India; adsri6@bbdu.ac.in

\* Correspondence: rajan18781@gmail.com

<sup>†</sup> Presented at the 10th International Electronic Conference on Sensors and Applications (ECSA-10), 15–30 November 2023; Available online: <https://ecsa-10.sciforum.net/>.

**Abstract:** The human population continues to grow, and specific efforts must be made in order to meet foreseeable food demands. In this paper, it is suggested that an IoT-based fuzzy control system be used for smart soil monitoring systems. This study is based on the semi-arid regions of India. A fuzzy classifier is used to categorize the real-time data into three parameters, such as sodium, potassium, and calcium, based on the proposed model, which gets trained from a dataset and then chooses the optimal solution. The real-time data are collected from NPK sensors, which are suitable for sensing the content of nitrogen, phosphorus, and potassium in the territory, which helps in determining the fertility of the soil by facilitating the systematic assessment of the soil condition. With the aid of this system, a farmer would be able to monitor soil health in a real-time environment and also track the growth of their plants. Farmers will be able to enhance productivity while decreasing resource waste with the aid of an IoT-enabled fuzzy system. Experimental data have been collected from Mahoba district, Uttar Pradesh provinces in India, and the results show that the suggested system is a more reliable and precise concept used for precision farming that will certainly enhance the overall production of crops with better quality. These results obtained with the help of the proposed model system have been compared with the existing one with data accuracy that has been improved and well accepted.

**Keywords:** soil health; fuzzy logic controller; internet of things

**Citation:** Prasad, R.; Tiwari, R.; Srivastava, A.K. Internet of Things-Based Fuzzy Logic Controller for Smart Soil Health Monitoring: A Case Study of Semi-Arid Regions of India. *Eng. Proc.* **2023**, *58*, 85. <https://doi.org/10.3390/ecsa-10-16208>

Academic Editor: Francisco Falcone

Published: 15 November 2023



**Copyright:** © 2023 by the authors. Licensee MDPI, Basel, Switzerland. This article is an open access article distributed under the terms and conditions of the Creative Commons Attribution (CC BY) license (<https://creativecommons.org/licenses/by/4.0/>).

## 1. Introduction

A networked machine ecosystem is a fitting way to define the Internet of Things [1]. This technology has the potential to be widely used in agriculture for crop production improvement and soil health detection. Sensors are frequently employed to monitor soil parameters important for crop development [2]. Farmers receive several forms of data from the sensors, which are processed to improve agricultural productivity [3]. These sensors are managed by software applications designed expressly for this purpose. Sensors are used primarily for monitoring and control, security and warning, and diagnostics and analysis. It moves farming one step closer to self-sufficiency and independence from human involvement [4]. This study covers the IoT technology based on fuzzy logic that is used to monitor soil health in semi-arid locations. To make optimal judgments for precision agricultural activities, the research focuses on sensor technologies for real-time data collection and fuzzy logic controllers (FLCs) [5] for approximate decision-making. This

research looks at the uses of various sensors in the agricultural process. These products are for sale in the marketplace. How these sensors are employed in different types of farms and how they benefit farmers, consumers, and the economy [6,7], the materials and procedures used for the testing, the study area, a brief overview of the NPK sensor, fuzzy logic controller, and suggested technique for alert generation system are all included in Section 2 of the paper. Section 3 describes the modeling of various sensor parameters and fuzzy variables. Section 4 details the system’s performance study and comparison with existing systems. Section 5 discusses the conclusion and improvement plan.

## 2. Materials and Methods

Dry areas with an aridity index of 0.20 to 0.50 are referred to as semi-arid zones [8]. Due to historical land use, semi-arid soils commonly experience degradation, which leads to low levels of soil organic carbon (SOC) and poor structure. Human-caused erosion, salinity, and deterioration pose significant difficulties to semi-arid soils. Our research is centered on the Mahoba district of Uttar Pradesh, India, which is classified as semi-arid. We put up numerous sensors in one area to collect datasets for the construction of fuzzy rules based on the proposed model. We use real-world inputs from a few selected sensors for testing. Figure 1 displays the recommended model’s block diagram, which is made up of five parts. The first section is concerned with the design of NPK sensors, while the second part is concerned with converting the analog signal to a digital signal (obtained from the NPK sensors). The third step is to create the fuzzy logic controller and inference rules based on the acquired dataset. The fourth step is to install the model in a cloud database, and the fifth step is to generate alarm messages.

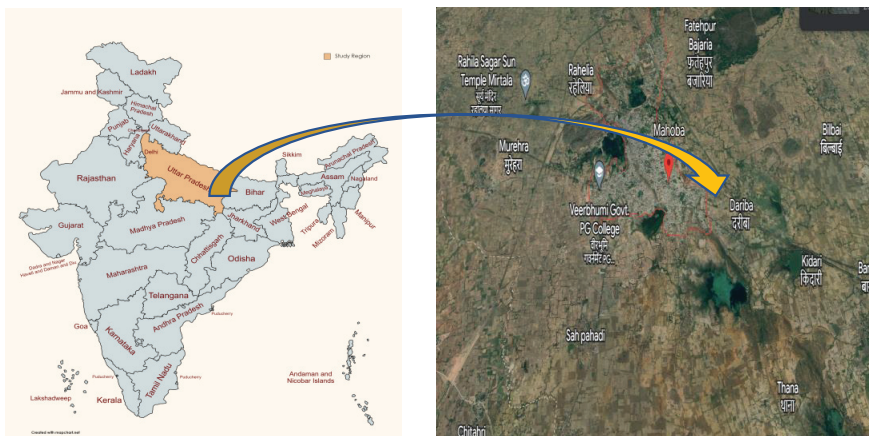


**Figure 1.** Study location of Mahoba district, Uttar Pradesh provinces in India (credit to Google map of geo-tagged image).

### 2.1. NPK Sensor

The NPK sensor [9] setup includes four 10K resistors to detect the nutrients present in the soil while guarding against LED current overload. To determine the nutritional level of the soil solution, LEDs first transmit light into it. The colorimetric principle states that the chemical composition of the soil affects how much light will be reflected from the solution. An LDR absorbs this light (using the concept of photoconductivity), and the amount of light absorbed will be recorded. The quantity of light absorption (A) in the LDR will be calculated using the Beer–Lambert equation, in Equation (1).

$$A = K \times l \times c \tag{1}$$

where 'l' stands for the length of the light path, 'c' is the solution concentration, and 'K' stands for the molar absorptivity. Equation (2) states that the resistance level ( $R_L$ ) in a light-diffusing device (LDR) impacts how much light will reflect per unit of area (Lux), and Equation (3) uses this information to compute the output voltage across an LDR.

$$R_L = \frac{500}{Lux} \tag{2}$$

$$V_o = I \times R_L \tag{3}$$

The voltage that results shows the nitrogen, phosphorus, and potassium concentrations in the test soil along with the data gathered by the sensor.

### 2.2. Fuzzy Logic Controller (FLC) for Soil Analysis

A mathematical concept called fuzzy logic deals with information that is imprecise. Fuzzy logic, as opposed to conventional binary logic, allows the representation of degrees of truth. A FLC is a decision-making system that interprets and reacts to input data using fuzzy logic concepts. The inference engine infers the correspondence fuzzy value with the aid of pre-defined fuzzy rules available in the knowledge base, and finally, the defuzzification block converts the fuzzy output value to the corresponding crisp value [10]. The fuzzy logic controller's block design is in Figure 2. It receives input data from an NPK sensor and fuzzify it to translate it into desired language phrases (in Figure 3). The inference engine determines the correspondence fuzzy value using pre-defined fuzzy rules from the knowledge base, which is subsequently translated into a corresponding crisp value by the defuzzification block [10].

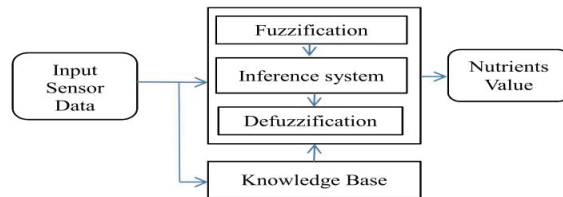


Figure 2. Proposed structure of FLC.

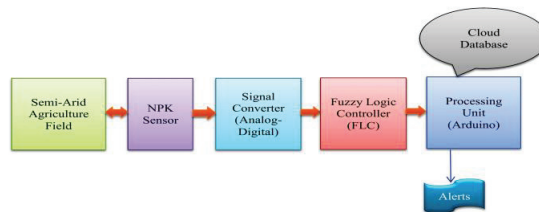


Figure 3. Schematic flow of IoT-based soil health-monitoring module.

### 2.3. Alert Generation System Using IoT

Analog signals are sensed by an NPK sensor connected to an A-to-D converter [11]. This produces a digital output linked to an Arduino device equipped with a WI-FI networking module to carry out more investigation into the soil's nutritional insufficiency. After receiving the LDR output voltage, the first step is to run a Python program that employs a fuzzy inference technique to diagnose soil nutrients.

A system with software is uploaded in accordance with the detected value, and it also alerts the field owners about required fertilizer on a regular basis. The best fertilizer for the soil is selected in the second stage using the results of the fuzzy rule system. This process generates fertilizer in text form. The third stage of the program flow links the message

agent and transmits the message about fertilizer over the internet. The sensor value and fuzzy logic system response are saved in the embedded program’s link to the Google Cloud database for later use. The modeling of fuzzy input parameters and their correspondence with fuzzy outputs is shown in Figure 4.

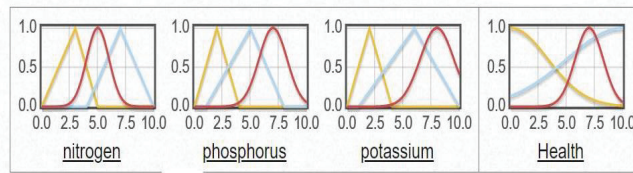


Figure 4. Modeling of the input and output linguistic parameters.

### 3. Modeling of Sensor and Fuzzy Parameters

The simulation program is used to transport data from the NPK sensor kit to the cloud server and assess performance factors such as throughput, end-to-end latency, and average jitter. It is accomplished by adjusting the network density. Table 1 shows the fuzzy rules created by the fuzzy inference module and the associated output.

Table 1. Fuzzy inference rules generated by the system.

If N is Low and P is Low and K is Low	then Health is Low
If N is High and P is Low and K is Low	then Health is Medium
If N is Low and P is High and K is High	then Health is High

The network protocols were implemented in Python3.8, and to assess network performance, several simulated scenarios were developed. For testing the model, we chose ten nodes. Similar setups, including internet servers with 6, 7, 14, 19, 23, and 35 nodes, were used to analyze end-to-end throughput, latency, and jitter [12]. The implemented network performance was tested in terms of scalability. The proposed system can deploy in real time to examine any type of soil in semi-arid lands. The hardware settings for the sensor nodes are shown in Table 2.

Table 2. Simulation parameters.

Sl. No.	Parameters	Values
1	Time of Simulation	300 s
2	Area Covered	1500 m × 1500 m
3	Frequency of Channel	2.4 GHz
4	Path Loss	Free space
5	Propagation Limit	−111 dBm
6	Transmission power	15 dBm

### 4. Results and Performance Analysis

The sensor’s active mode determines how much energy it uses. The proposed system’s sensor has not been used for more than 24 h. Regular soil nutrient monitoring takes two to three days, or roughly 36 h, during the crop’s growth. The crops grown in each agricultural area determine the relatively low sensing frequency and data transfer to the cloud. The proposed system outperformed the mentioned algorithms in the experiment using various machine learning algorithms, as shown in Figure 5 [13–20]. We adjusted the frequency of data transmission of numerous sensors to estimate energy conservation. Each sensor takes less than 0.14 mJ of energy to detect, analyze, and transmit data.

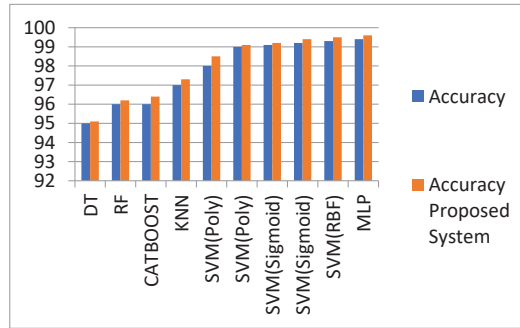


Figure 5. Comparative performance analysis of proposed system.

Throughput, or data transport rate through a network, is changed with network density. When analyzing throughput changes, the data transfer frequency is kept constant. Over a node density of 20, the throughput reaches saturation. The average end-to-end latency for every network density is calculated from the latency of the circuit (from the sensor to the server). The average latency increases as node density climbs; as a result, the shared network becomes increasingly congested during data transmission. The average jitter, which varies with node density, is 4 ms. The experimental results show that the suggested system can be deployed in semi-arid agricultural areas to improve soil health and yields. The performance appears to be scalable, viable, and employable. Internet agents (as depicted in Figure 6) send out SMSs about the appropriate fertilizer application depending on the present soil nutrient level in accordance with the system’s output.

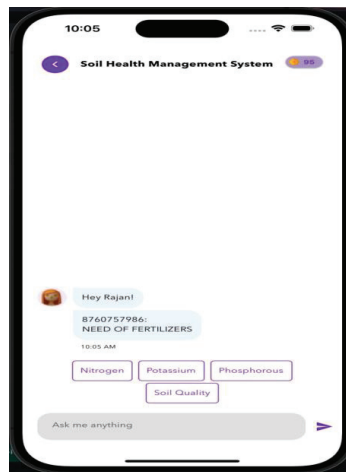


Figure 6. Alert message received by the land owner.

### 5. Conclusions

It is challenging to routinely evaluate soil nutrients in agricultural fields by conventional testing methods. The suggested system notifies the farmer by SMS of the absence of critical soil nutrients, specifically nitrogen, phosphorus, and potassium. It does this through the system’s integrated NPK sensor and fuzzy system. The outcomes of the proposed model performed are to better understand how the built IoT system works and to describe its intended purpose. The experiment shows that the suggested system is an accurate, low-cost, and intelligent Internet of Things (IoT) system that instantly alerts the farmer by SMS about the fertilizer that needs to be applied at the right moment. This system might be a helpful tool for farmers in the agricultural industry.

**Author Contributions:** Conceptualization, R.P. and A.K.S.; Methodology, R.T. and A.K.S.; Software, R.P.; Validation, R.P. and R.T.; Formal Analysis, A.K.S.; Investigation, R.T.; Resources, R.P.; Data Curation, R.P. and R.T.; Writing Original Draft Preparation, R.P. and R.T.; Writing Review & Editing; R.T.; Visualization, A.K.S.; Supervision, R.P. and R.T.; Project Administration, R.P., R.T. and A.K.S. All authors have read and agreed to the published version of the manuscript.

**Funding:** This research received no external funding.

**Institutional Review Board Statement:** Not applicable.

**Informed Consent Statement:** Not applicable.

**Data Availability Statement:** Data are contained within the article.

**Conflicts of Interest:** The authors declare no conflict of interest.

## References

1. Sankarasubramanian, P.; Ganesh, E.N. IoT Based Prediction for Industrial Ecosystem. *Int. J. Eng. Adv. Technol. (IJEAT)* **2019**, *8*, 1544–1548.
2. Young, R. *Soil Properties and Behaviour*; Elsevier: Amsterdam, The Netherlands, 2012; Volume 5.
3. Kim, H.-J.; Sudduth, K.A.; Hummel, J.W. Soil macronutrient sensing for precision agriculture. *J. Environ. Monit.* **2009**, *11*, 1810–1824. [CrossRef] [PubMed]
4. Zhang, Q.; Wu, C.-H.; Tilt, K. Application of fuzzy logic in an irrigation control system. In Proceedings of the IEEE International Conference on Industrial Technology (ICIT'96), Shanghai, China, 2–6 December 1996.
5. Lee, C.-C. Fuzzy logic in control systems: Fuzzy logic controller. I. *IEEE Trans. Syst. Man Cybern.* **1990**, *20*, 404–418. [CrossRef]
6. McCulley, R.L.; Jobbágy, E.G.; Pockman, W.T.; Jackson, R.B. Nutrient uptake as a contributing explanation for deep rooting in arid and semi-arid ecosystems. *Oecologia* **2004**, *141*, 620–628. [CrossRef] [PubMed]
7. Adham, A.; Riksen, M.; Ouessar, M.; Ritsema, C. Identification of suitable sites for rainwater harvesting structures in arid and semi-arid regions: A review. *Int. Soil Water Conserv. Res.* **2016**, *4*, 108–120.
8. Arora, V.K. The use of the aridity index to assess climate change effect on annual runoff. *J. Hydrol.* **2002**, *265*, 164–177. [CrossRef]
9. Misbah, K.; Laamrani, A.; Khechba, K.; Dhiba, D.; Chehbouni, A. Multi-sensors remote sensing applications for assessing, monitoring, and mapping NPK content in soil and crops in African agricultural land. *Remote Sens.* **2021**, *14*, 81. [CrossRef]
10. Haban, J.J.I.; Puno, J.C.V.; Bandala, A.A.; Billones, R.K.; Dadios, E.P.; Sybingco, E. Soil Fertilizer Recommendation System using Fuzzy Logic. In Proceedings of the 2020 IEEE REGION 10 CONFERENCE (TENCON), Osaka, Japan, 16–19 November 2020.
11. Walden, R.H. Analog-to-digital converter survey and analysis. *IEEE J. Sel. Areas Commun.* **1999**, *17*, 539–550. [CrossRef]
12. Iwasaki, A. Detection and estimation satellite attitude jitter using remote sensing imagery. *Adv. Spacecr. Technol.* **2011**, *13*, 257–272.
13. Rajeswari, S.; Suthendran, K. C5. 0: Advanced Decision Tree (ADT) classification model for agricultural data analysis on cloud. *Comput. Electron. Agric.* **2019**, *156*, 530–539. [CrossRef]
14. Hengl, T.; Heuvelink, G.B.M.; Kempen, B.; Leenaars, J.G.B.; Walsh, M.G.; Shepherd, K.D.; Sila, A.; MacMillan, R.A.; de Jesus, J.M.; Tamene, L.; et al. Mapping soil properties of Africa at 250 m resolution: Random forests significantly improve current predictions. *PLoS ONE* **2015**, *10*, e0125814. [CrossRef] [PubMed]
15. Zhang, C.; Chen, X.; Wang, S.; Hu, J.; Wang, C.; Liu, X. Using CatBoost algorithm to identify middle-aged and elderly depression, national health and nutrition examination survey 2011–2018. *Psychiatry Res.* **2021**, *306*, 114261. [PubMed]
16. Li, H.; Leng, W.; Zhou, Y.; Chen, F.; Xiu, Z.; Yang, D. Evaluation models for soil nutrient based on support vector machine and artificial neural networks. *Sci. World J.* **2014**, *2014*, 478569.
17. Prasad, R.; Shukla, P.K. A Review on the Hybridization of Fuzzy Systems and Machine Learning Techniques. In *Computer Vision and Robotics. Algorithms for Intelligent Systems*; Bansal, J.C., Engelbrecht, A., Shukla, P.K., Eds.; Springer: Singapore, 2022. [CrossRef]
18. Prasad, R.; Shukla, P.K. Identification of Ischemic Stroke Origin Using Machine Learning Techniques. In *Advances in Data-driven Computing and Intelligent Systems. Lecture Notes in Networks and Systems*; Das, S., Saha, S., CoelloCoello, C.A., Bansal, J.C., Eds.; Springer: Singapore, 2023; Volume 653. [CrossRef]
19. Prasad, R.; Shukla, P.K. Indeterminacy Handling of Adaptive Neuro-fuzzy Inference System Using Neutrosophic Set Theory: A Case Study for the Classification of Diabetes Mellitus. *Int. J. Intell. Syst. Appl. (IJISA)* **2023**, *15*, 1–15. [CrossRef]
20. Prasad, R.; Shukla, P.K. Interpretable Fuzzy System for Early Detection Autism Spectrum Disorder. *Int. J. Intell. Syst. Appl. (IJISA)* **2023**, *15*, 26–36. [CrossRef]

**Disclaimer/Publisher's Note:** The statements, opinions and data contained in all publications are solely those of the individual author(s) and contributor(s) and not of MDPI and/or the editor(s). MDPI and/or the editor(s) disclaim responsibility for any injury to people or property resulting from any ideas, methods, instructions or products referred to in the content.



# New Photoacoustic Cell Design for Solid Samples <sup>†</sup>

Judith Falkhofen <sup>1,2,\*</sup>, Bernd Baumann <sup>1</sup> and Marcus Wolff <sup>1</sup>

<sup>1</sup> Heinrich Blasius Institute of Physical Technologies, Hamburg University of Applied Sciences, 20099 Hamburg, Germany; bernd.baumann@haw-hamburg.de (B.B.); marcus.wolff@haw-hamburg.de (M.W.)

<sup>2</sup> School of Computing, Engineering and Physical Sciences, University of the West of Scotland, Paisley PA1 2BE, UK

\* Correspondence: judith.falkhofen@haw-hamburg.de

<sup>†</sup> Presented at the 10th International Electronic Conference on Sensors and Applications (ECSA-10), 15–30 November 2023; Available online: <https://ecsa-10.sciforum.net/>.

**Abstract:** We have developed a new design for a photoacoustic (PA) cell particularly suited for quartz-enhanced photoacoustic spectroscopy (QEPAS), where a quartz tuning fork (QTF) is used as a sound detector for the PA signal. The cell is designed for the investigation of solid and semi-solid samples and represents a unilateral open cylinder. The antinode of the sound pressure of the fundamental longitudinal mode of the half-open cylinder occurs directly at the sample, where a measurement is difficult. Therefore, the first harmonic is used. A small hole in the resonator wall at the location of the pressure antinode allows signal detection outside the cylinder without (or only minimally) changing the resonance conditions. This design is particularly simple and easy to manufacture. A finite element (FE) simulation is applied to determine the optimal cell length for the given frequency and the location of the pressure maximum. One difficulty is that the open end dramatically changes the acoustic sound field. We answer the following research questions: where is the sound pressure maximum located and do simple analytical equations agree with the results of the FE simulation?

**Keywords:** photoacoustic spectroscopy; QEPAS; solid samples; higher harmonics; resonator design; FE simulation

## 1. Introduction

In photoacoustic spectroscopy, a sound pressure wave is generated by modulated laser radiation. The molecules absorb the light energy by converting it into bending and stretching oscillations and rotations or electronic transitions. The associated temperature variation pulsates due to the modulated excitation, which leads to the development of sound waves. Over a wide range, the sound pressure amplitude is proportional to the concentration of the molecules under investigation. In contrast to gaseous samples, where the photoacoustic signal is often generated over the length of the laser beam within the cell, the signal of solid samples is generated directly at the surface of the sample or even slightly below it [1,2].

Often, acoustic resonances of the sample cell are exploited to improve the signal-to-noise ratio (SNR) of the PAS measurement. Special cells have been developed for the photoacoustic investigation of solid samples, e.g., in a cuboid [3,4] or a T shape [5,6]. The latter was also modelled using Finite Element Methods (FEM) and optimised concerning the signal amplitude [7].

Recently, quartz tuning forks (QTF) with resonance frequencies beginning in the kHz region are used to detect the acoustic signal. QTFs possess a high specificity for separating noise in other frequency ranges from the signal. Further advantages are a high frequency stability over a wide temperature range, insensitivity to magnetic fields and a high resonance quality factor. Their low costs and small size make them suitable for small sensors in mass production [8–10].

**Citation:** Falkhofen, J.; Baumann, B.; Wolff, M. New Photoacoustic Cell Design for Solid Samples. *Eng. Proc.* **2023**, *58*, 86. <https://doi.org/10.3390/ecsa-10-16198>

Academic Editor: Stefano Mariani

Published: 15 November 2023



**Copyright:** © 2023 by the authors. Licensee MDPI, Basel, Switzerland. This article is an open access article distributed under the terms and conditions of the Creative Commons Attribution (CC BY) license (<https://creativecommons.org/licenses/by/4.0/>).



In this article, we present the design of a half-open cylindrical resonator for the photoacoustic investigation of solid samples particularly suited for QEPAS. One end of the tube is tightly sealed by the sample. The laser beam enters at the opening on the other side. The cell is considerably simpler to manufacture than a cuboid or T-shaped cell. The T cell consists of two different cylinders coupled together. Often, the larger one is referred to as the cavity cylinder and the one leading to the acoustic sensor as the resonance cylinder. The sample is attached to the cavity cylinder and the sound generated there has to couple into the second, geometrically much narrower resonance cylinder, which is accompanied by an additional damping because impedance discontinuities between large and small pipes usually lead to considerable energy losses [11]. It is expected that the signal of the new cell will be significantly higher compared to the T cell.

The following section briefly comprises the theoretical background of sound propagation in a resonant cell in the case of the PA signal of a solid sample. Chapter 3 describes the finite element (FE) model and the results of the simulation. Chapter 4 contains a discussion and the study's outlook.

## 2. Acoustically Resonant PA Cell

PAS experiments with solid samples have already been carried out by Alexander Bell [12]. The absorption spectrum of solid samples can be observed more easily with PAS than with conventional spectroscopy techniques since scattered light does not play an important role in the PA signal. The primary source of the PA signal is the result of periodic heat flow from the solid to the surrounding gas [13].

The SNR of the PA signal is intended to be enlarged by the resonator described here. In the cylinder, a standing wave is developing due to reflections at the tube's ends and the superposition of the waves. If the radius  $a$  of the tube is much smaller than the wavelength, the acoustic wave is basically longitudinal. At open ends, the sound wave does not undergo a phase shift, whereas closed ends lead to a phase shift of 180 degrees. In this application of a half-open cylinder, the tube will be in resonance if its length  $l'$  and the frequency  $f_m$  are connected by the following equation [14]

$$f_m = \frac{(2m-1)c}{4l'}, \quad m = 1, 2, 3 \dots \quad (1)$$

Here,  $l' = l + \Delta l$ , where  $l$  is the geometric length of the cylinder and  $\Delta l$  is called the end correction. At the open end, it can be assumed that the reflection takes place at an imaginary point  $\Delta l$  away from the plane defined by the open end of the cylinder. The end correction is an effect resulting from a mismatch between the essentially one-dimensional acoustic field inside the pipe and the three-dimensional field radiated by its open end [14]. The corrected overall length  $l'$  is also called the effective length of the cylinder. The end correction can be calculated from [15]

$$\Delta l = 0.6133 \cdot a. \quad (2)$$

Due to loss effects, the true resonance frequencies are slightly lower than the eigenfrequencies. Therefore, the real end correction is slightly larger than the calculated value according to Equation (2). In order to obtain the highest possible photoacoustic signal, the radiation should be modulated with a frequency corresponding to the most intense acoustic resonance. Since the intensity decreases with increasing mode order [16] and the fundamental longitudinal resonance leads to a sound pressure maximum directly at the sample, the first harmonic of the longitudinal resonance is used. The according sound pressure distribution is schematically shown in Figure 1.

In upcoming experiments, a commercial quartz tuning fork will serve as a sound detector for the photoacoustic signal [17]. Its resonance frequency is  $f_R = 32.768$  kHz. The placement of the tuning fork in the so-called off-beam configuration is shown in Figure 2.

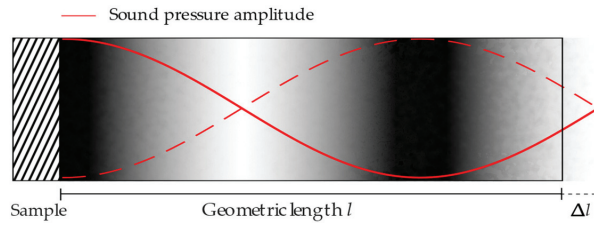


**Figure 1.** Sound pressure distribution of the first harmonic longitudinal resonance of a half-open cylinder.

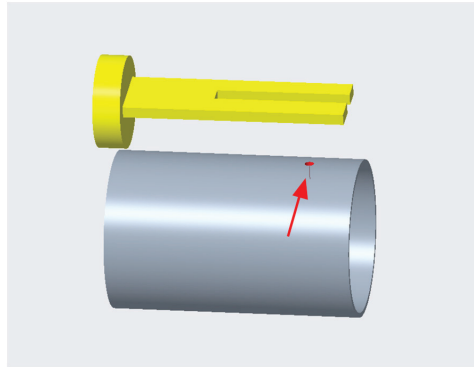


**Figure 2.** Cell with hole (marked with arrow) in a QEPAS off-beam configuration.

Since the sample is stimulated by a laser beam, the diameter of the cylinder has to be larger than the beam width. The laser beam must not hit the wall of the tube. Otherwise, this results in a wall signal that interferes with the wanted PA signal of the sample. In this investigation, the radius of the tube is

$$a = 2 \text{ mm.} \quad (3)$$

Combining the end correction formula Equation (2) with the resonance frequency of the first harmonic  $f_2$  matching the QTF resonance frequency,  $f_R$ , leads to a geometric length of the pipe

$$l = 6.6240 \text{ mm.} \quad (4)$$

where, for the speed of sound, the value  $343\text{m/s}$  has been used.

### 3. Finite Element Simulation

To obtain an independent and presumably more accurate result for  $l$ , we performed a simulation using the FE tool COMSOL Multiphysics®. Also, we aimed to obtain information on the location of the maximum sound pressure.

The simulation numerically solves the homogenous Helmholtz equation

$$\nabla^2 p(\vec{r}) + k^2 p(\vec{r}) = 0. \quad (5)$$

For the acoustic pressure field  $p(\vec{r})$  with the wave number  $k$ . At the sound hard walls (the cylinder walls, the closed end and a plane surface defined by the flange at the resonator's open end), the boundary condition applies. The normal derivative of the pressure is zero at the boundary

$$\frac{\partial p}{\partial n} = 0. \quad (6)$$

For the Helmholtz Equation, the truncation of a simulation domain for the open cylinder end is non-trivial. Conventional or periodic boundary conditions generate artifacts. A well-established method to deal with this problem is to define a perfectly matched layer (PML). PMLs can be imagined as non-reflecting wave absorbers [18].

The solutions of the differential Equation (5) subject to the described boundary conditions comprise the modes  $p_m(\vec{r})$  and the corresponding value  $k_m$ . The eigenfrequencies are given by

$$\omega_m = ck_m, \quad (7)$$

where  $c$  is the velocity of sound [19]. It is assumed that the sample is sound-hard, closes the tube soundproof and that vibrations of the resonator walls are negligible.

To determine the geometric length of the tube and the location of the antinode of the sound pressure near the open end of the cylinder, a 2D axially symmetric FE model is used. Initially,  $l$  is set to the estimate of Equation 4. Then, the cylinder length is gradually varied until the eigenfrequency matches with the resonance frequency of the QTF (trial and error). The result of this procedure is

$$l_{FE} = 6.6605 \text{ mm}. \quad (8)$$

In comparison to the analytical result (Equation (4)), the result of the FE simulation is 0.55% (0.037 mm) higher. The difference between the two methods is remarkably small. The FEM is supposed to rely on fewer approximations and is therefore considered to be more accurate.

Figure 3a shows the resulting sound pressure distribution of the first harmonic longitudinal mode in the centre plane of the cylinder closed by the sound-hard sample at the lower end. The semi-circle-shaped domain attached to the upper end of the resonator represents the outer space. The PML is implemented in the semi annulus. In Figure 3b, the FE mesh used for the simulations is depicted. The mesh is the result of a convergence study. The number of degrees of freedom is approximately 4500.

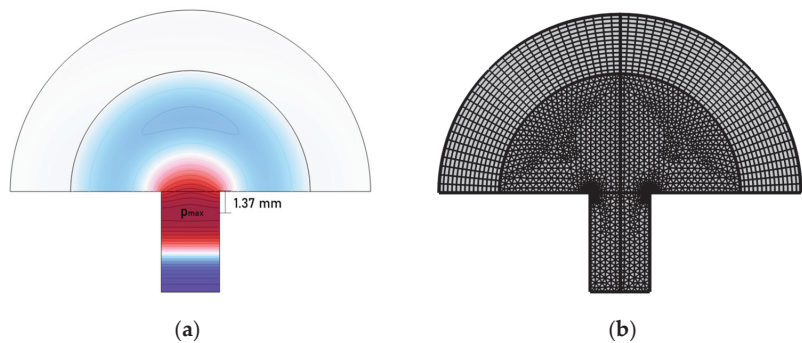


**Figure 3.** (a) Sound pressure distribution at the central plane of the new cell at  $f_1 = 32.768$  kHz. Dark blue and dark red correspond to the highest pressure values, which are 180 degrees out of phase. The distance of the maximum sound pressure to the open end is marked. (b) FE mesh. The PML is defined on the outer semi annulus.

As expected, the sound pressure of the mode spreads into the exterior space. The sound pressure maximum is located 1.37 mm from the open end. This is supposed to be the optimal location for the sound detector. In order to avoid a substantial distortion of the sound field, a small hole could be drilled and the QTF placed in front of it (see Figure 2).

#### 4. Discussion and Outlook

A simple cylindrical cell design of a PAS cell for measurements with QEPAS and solid samples has been developed. For the first harmonic longitudinal resonance, the results for the end correction of an analytical estimate and a numerical calculation are similar.

It is expected that the properties of the QTF can optimally complement the resonance behaviour of the small cylinder. The simple and inexpensive sensor design is also suitable for a miniaturised mass product. Since the expectation for the signal is that the SNR is larger than that of a T-shaped cell, these will be compared in the following experimental test series.

The next step will be to consider the effect of the hole in the cylinder wall on the sound pressure field. In the experimental testing of the sensor, we plan to investigate the dependency of the PA signal on the distance between the sound detector and the outer tube wall. Furthermore, the sample attachment can be examined more closely. Since the signal is generated at the surface of the sample, it is essential that it has a flat and smooth surface and is aligned perpendicular and acoustically sealed to the cylinder end.

**Author Contributions:** Conceptualization, M.W.; methodology, B.B. and J.F.; software, B.B.; writing—original draft preparation, J.F. and B.B.; writing—review and editing, J.F., B.B. and M.W.; visualization, J.F.; supervision, M.W. All authors have read and agreed to the published version of the manuscript.

**Funding:** This research received no external funding.

**Institutional Review Board Statement:** Not applicable.

**Informed Consent Statement:** Not applicable.

**Data Availability Statement:** Besides those shown, no further data were created or analysed in this study. Data sharing is not applicable to this article.

**Acknowledgments:** We would like to thank the 3D printing teams of the Hamburg University of Applied Sciences for their friendly support, and the company MeKo for their cooperation in creating the small cylinders.

**Conflicts of Interest:** The authors declare no conflicts of interest.

## References

- Friedrich, C.S. *Photoakustik Mit Halbleiterlasern*; Cuvillier Verlag: Lower Saxony, Germany, 2012.
- Sarode, A.; Mahajan, O. Theoretical aspects of Photoacoustic Signal Generation with Solid Crystals. *Bull. Karaganda Univ. Phys. Ser.* **2021**, *104*, 61–67. [CrossRef]
- Raghu, O.; Philip, J. A dual channel photoacoustic cell for imaging experiments on solid samples. *J. Instrum. Soc. India* **2003**, *33*, 155–158.
- Rabasović, M.D.; Nikolić, M.G.; Dramićanin, M.D.; Franko, M.; Markushev, D.D. Low-cost, portable photoacoustic setup for solid samples. *Meas. Sci. Technol.* **2009**, *20*, 095902. [CrossRef]
- El-Busaidy, S.; Baumann, B.; Wolff, M.; Duggen, L.; Bruhns, H. Experimental and Numerical Investigation of a Photoacoustic Resonator for Solid Samples: Towards a Non-Invasive Glucose Sensor. *Sensors* **2019**, *19*, 2889. [CrossRef] [PubMed]
- El-Busaidy, S.A.S.; Baumann, B.; Wolff, M.; Duggen, L. Modelling of open photoacoustic resonators. *Photoacoustics* **2020**, *18*, 100161. [CrossRef] [PubMed]
- El-Busaidy, S.; Baumann, B.; Wolff, M.; Duggen, L. Shape Optimization of an Open Photoacoustic Resonator. *Appl. Sci.* **2021**, *11*, 2571. [CrossRef]
- Patimisco, P.; Sampaolo, A.; Zheng, H.; Dong, L.; Tittel, F.K.; Spagnolo, V. Quartz-enhanced photoacoustic spectrophones exploiting custom tuning forks: A review. *Adv. Physics X* **2017**, *2*, 169–187. [CrossRef]
- Zifarelli, A.; Menduni, G.; Giglio, M.; Sampaolo, A.; Patimisco, P.; Wu, H.; Dong, L.; Spagnolo, V. Latest Advances in Quartz Enhanced Photoacoustics Spectroscopy for Environmental and Industrial Applications. In Proceedings of the 23rd International Conference on Transparent Optical Networks (ICTON), Bucharest, Romania, 2–6 July 2023; pp. 1–3.
- Ayache, D.; Rousseau, R.; Kniazeva, E.; Charenso, J.; Seoudi, T.; Bahriz, M.; Gouzi, F.; Spagnolo, V.; Vicet, A. Commercial and Custom Quartz Tuning Forks for Quartz Enhanced Photoacoustic Spectroscopy: Stability under Humidity Variation. *Sensors* **2023**, *23*, 3135. [CrossRef]
- Peat, K. The acoustical impedance at discontinuities of ducts in the presence of a mean flow. *J. Sound Vib.* **1988**, *127*, 123–132. [CrossRef]
- Manohar, S.; Razansky, D. Photoacoustics: A historical review. *Adv. Opt. Photon* **2016**, *8*, 586–617. [CrossRef]
- Rosencwaig, A.; Gersho, A. Theory of the photoacoustic effect with solids. *J. Appl. Phys.* **1976**, *47*, 64–69. [CrossRef]
- Miklós, A.; Hess, P.; Bozóki, Z. Application of acoustic resonators in photoacoustic trace gas analysis and metrology. *Rev. Sci. Instrum.* **2001**, *72*, 1937–1955. [CrossRef]
- Levine, H.; Schwinger, J. On the Radiation of Sound from an Unflanged Circular Pipe. *Phys. Rev. B* **1948**, *73*, 383–406. [CrossRef]

16. Wu, D.; Gao, S.; Li, J.; Yao, L.; Yu, X.; Zhang, Z.; Zhang, H.; Wang, X. Amplitude and phase relation of harmonics in nonlinear focused ultrasound. *AIP Adv.* **2022**, *12*, 065317. [CrossRef]
17. Ma, Y. Review of Recent Advances in QEPAS-Based Trace Gas Sensing. *Appl. Sci.* **2018**, *8*, 1822. [CrossRef]
18. Johnson, S.G. Notes on perfectly matched layers (PMLs). *arXiv* **2021**, arXiv:2108.05348.
19. Baumann, B.; Wolff, M.; Kost, B.; Groninga, H. Finite element calculation of photoacoustic signals. *Appl. Opt.* **2007**, *46*, 1120–1125. [CrossRef] [PubMed]

**Disclaimer/Publisher’s Note:** The statements, opinions and data contained in all publications are solely those of the individual author(s) and contributor(s) and not of MDPI and/or the editor(s). MDPI and/or the editor(s) disclaim responsibility for any injury to people or property resulting from any ideas, methods, instructions or products referred to in the content.

# Privacy and Regulatory Issues in Wearable Health Technology <sup>†</sup>

Rabai Boudherhem <sup>1,2</sup>

<sup>1</sup> College of Law, Prince Mohammad Bin Fahd University, P.O. Box 1664, Al Khobar 31952, Saudi Arabia; rboudherhem@pmu.edu.sa

<sup>2</sup> CREDIMI FRE 2003 CNRS, University of Burgundy, 21000 Dijon, France

<sup>†</sup> Presented at the 10th International Electronic Conference on Sensors and Applications (ECSA-10), 15–30 November 2023; Available online: <https://ecsa-10.sciforum.net/>.

**Abstract:** This paper is based on a research literature review for identifying and evaluating the technical, ethical and regulatory challenges to adequately regulate the use of wearable health technology. The objective is to analyze how researchers address the use of smart wearables in healthcare under the scope of data privacy. The main challenges faced by states in regulating e-health wearables were identified, especially the different methods to ensure the privacy of personal health information (PHI) and the legal voids and complexities of regulating wearable health technology at both national and international levels. Finally, a few recommendations were made to more efficiently regulate wearable health technology at both national and international levels. AI could be used as a regulatory tool to monitor the use of e-wearables in healthcare. Also, European Union (EU) law—the upcoming EU Data Act and AI Act—can serve as models and guidance for the World Health Organization (WHO), which has a constitutional mandate to regulate the use of wearable health technology.

**Keywords:** data collection; health monitoring; privacy; regulations; smart wearables

## 1. Introduction

Wearable [1] health technology is a global new trend that could disrupt healthcare by tracking health information in real time. However, real-time health monitoring systems such as e-wearables also raise ethical and regulatory challenges regarding health data privacy. E-wearables collect, process, store and share a considerable amount of data, including in the cloud from where third parties may be granted access to it [2]. The biggest challenge is data privacy [3] as health data is sensitive and confidential by nature [4]. It is important for all stakeholders—public and private actors—to find a consensus and an acceptable balance between regulation and innovation [5]. Technical, ethical and regulatory challenges such as data collection [6], data quality, security [7], interoperability between different operating systems (OS), health equity and fairness [8] need to be addressed by states at both national and international levels. Concrete national and international regulations should be developed such as the implementation of quality standards, conditions to access health data, interoperability and representativity. Most importantly, compliance with key regulations such as the EU General Data Protection Regulation (GDPR) or the upcoming EU Data Act is a requirement. Self-regulation should also be encouraged as it will help to build public confidence in health wearable technology as important volumes of personal data are processed. Companies operating in this field are making efforts [9] and want to be seen as actors caring about personal health data and its processing, storing and sharing. Guidelines and voluntary codes of conduct developed by the private sector are concrete illustrations [10]. Despite the existence of such challenges, health wearables are an opportunity to improve healthcare systems, as these devices could become a substantial addition to everyday healthcare practice [11]. Indeed, health wearables could save lives as they act as computational systems allowing healthcare providers to adjust to patients' needs and situations; they can also be an important tool for people living in remote areas

**Citation:** Boudherhem, R. Privacy and Regulatory Issues in Wearable Health Technology. *Eng. Proc.* **2023**, *58*, 87. <https://doi.org/10.3390/ecsa-10-16206>

Academic Editor: Stefano Mariani

Published: 15 November 2023



**Copyright:** © 2023 by the author. Licensee MDPI, Basel, Switzerland. This article is an open access article distributed under the terms and conditions of the Creative Commons Attribution (CC BY) license (<https://creativecommons.org/licenses/by/4.0/>).

or far from hospitals or physicians. As observed, there is today a global adoption of health wearables such as smartwatches or fitness trackers; this trend demonstrates that individuals have already embraced health wearable technology which could help monitor people's health condition [12]. A balance between the use of health wearable technology and data privacy is a necessity from a regulatory and ethical perspective [13], as several challenges need to be solved. Different measures can be adopted to ensure privacy and security of health data; AI can also be used as a regulatory tool for audits and inspections in wearable health technology.

## 2. Challenges Posed by Wearable Health Technology

There are several challenges posed by wearable health technology ranging from technical [14] issues such as the development of powerful batteries to ethical and regulatory gaps at both national and international levels. Data [15] accuracy is also a concern acknowledged by companies as physicians or lay people need precise data to be able to rely on it and monitor their health [16]. Data security [17] and privacy [18] are other crucial challenges to be addressed. Improper device wearing [19] could be another obstacle to health monitoring. From a scientific perspective, the use of consumer wearables [20] in health research could be a limitation as data may not be accurate (see Table 1 below).

**Table 1.** Challenges posed by wearable health technology.

Main Challenges Posed by Wearable Health Technology
1. Data privacy
2. Data collection and storage
3. Data quality and accuracy
4. Interoperability between different OS (Apple, Android, etc.)
5. Bias
6. Health equity
7. Access to technology in developing countries
8. Lack of regulations at both national and international level
9. Ability to control third-party access to personal health data
10. Security

## 3. How Can We Ensure the Privacy and Security of Personal Health Data?

Different measures can be taken to ensure the privacy and security of personal health data [21]. Companies and health professionals can help to secure patient privacy and data confidentiality (see Table 2 below).

**Table 2.** Measures to ensure privacy and security of personal health data.

Potential Measures and Safeguards for Effective Data Protection
1. Educate healthcare personnel
2. Conduct routine risk assessment
3. Secure data with a VPN
4. Restrict access to data
5. Implement role-based access
6. Two-factor authentication
7. Encryption
8. Security awareness training
9. AI to conduct regular inspections and audits to ensure compliance with regulations

It has been demonstrated [22] that most data breaches are attributable to human errors. Adequate training and education should be provided by healthcare institutions to their personnel. Employees have to be well aware of all risks associated with personal health data and security issues. Risk assessments on a regular basis are a requirement [23] as they could help to identify intrinsic limitations—such as data security breaches—of any healthcare institution and help with their resolution. Health personal data can also be protected and secured with a virtual private network (VPN) [24]. A VPN allows users to encrypt and mask their digital footprint. Healthcare institutions could protect themselves from data breaches and cyber attacks such as ransomware. Access to patients' health records has to be limited to certified personnel and restricted [25] for better data security and confidentiality. Healthcare institutions could implement improved authentication processes such as two-factor authentication. Based on the confidential and sensitive nature of health data, healthcare providers should implement role-based access control systems [26]; employees should only have access to a specific assigned system level.

In the US, the Health Insurance Portability and Accountability Act (HIPAA) 1996 [27] regulates health data and ensures its security and confidentiality. As such, when physicians assign health wearables to their patients, all data collected are considered protected health information (PHI). According to US federal regulations, all data collected, processed and shared must be protected and secured at all times [28]. Companies commercializing health wearables should first consider data privacy and security issues to be reliable alternatives to healthcare providers. This could be achieved through the adoption of international standards for e-wearables in sport for instance [29]. Health data privacy requires not only built-on security features, but also guarantees that the network is safe, as well as third-party applications available on the App Store or Google Store. Transparency is a key aspect of data privacy as users should know who can access their data, whether it is a third party or the healthcare provider itself. Here, some gaps exist in the US legal framework applicable to health data and its handling. Indeed, HIPAA only targets specifically health data and not all wearables such as smartwatches which also collect health data. However, US authorities could provide a regulatory answer if such companies start dealing with health data and promote their products as health devices.

EU law offers today detailed rules and guidelines relating to privacy and the handling of personal data. The GDPR [30] is indeed a key regulation and a law model that offers a comprehensive legal framework with stringent obligations and duties for service providers and manufacturers [31]. Recently, the European Union Commission made a proposal [32] for an EU Data Act for adequate regulation of data specifically processed, stored or shared by electronic devices, including health wearables. In June 2023, the Council Presidency and the European Parliament came to a consensus and adopted the EU Data Act as a provisional agreement [33]. The objective of the EU Data Act is to harmonize rules relating to fair access to data and its use by public and private actors. As its predecessor the GDPR, the EU Data Act will help wearable users to keep control over their health data more efficiently. It could also serve as a guideline or law model for the rest of the world and enshrine key international standards relating to health data privacy and security.

#### **4. The Complexity to Regulate Wearable Health Technology at Both National and International Levels**

The regulation [34] of wearable health technology at both national and international levels is a complex issue but potential solutions exist (see Table 3 below).

As stated, ethical and regulatory challenges need to be addressed by both states and international organizations such as the World Health Organization (WHO). There is a need for clear guidelines and standards [35] and how wearable health technology can help to promote healthcare systems worldwide. International guidelines and recommendations should be detailed as much as possible considering especially some important challenges such as accuracy, security, data privacy as well as ethics in the use of health wearables and data collected [36]. Ethical issues [37] with health wearable technology include users' data



privacy, transparency and the necessity to ensure that users have given informed consent to the processing of their personal data. Indeed, health wearables are small computers able to collect, process and store a considerable volume of personal data. Unauthorized access by third parties is an ethical issue and a violation of data privacy and informed consent [38]. Potential threats such as cybersecurity need to be tackled as well. Wearable health technology will play an important role in the near future as it facilitates health monitoring and can save lives. However, public authorities will need to create new regulatory bodies or give new powers and attribution to existing watchdogs [39]. Throughout audits and inspections, regulatory bodies such as the FDA in the US and the Medicines and Healthcare products Regulatory Agency (MHRA) in the UK play a crucial role by monitoring all stakeholders and ensuring that they comply with their obligations in terms of privacy, efficiency, safety and quality. The promotion of transparency and accountability [40] is fundamental as companies know that they might face severe consequences such as financial sanctions, especially regarding their sharing practices. They should also be held accountable for any breaches of data privacy or security. Self-regulation should be encouraged as codes of conduct can help to promote international standards such as data protection [41]. As mentioned, states and international organizations need to cooperate, harmonize their national regulations and promote the safe and ethical use of wearable health technology [42].

**Table 3.** Solutions to adequately regulate wearable health technology at both national and international levels.

Potential Solutions to Adequately Regulate Wearable Health Technology
1. Establishing clear guidelines and standards under WHO
2. Strengthening regulatory oversight
3. Promoting transparency and accountability
4. Encouraging industry self-regulation
5. Fostering international cooperation
6. Ethics in using personal health data

## 5. AI as a Regulatory Tool

Artificial Intelligence (AI) can play a key role in the regulation of wearable health technology [43]. AI tools already exist for fast and reliable analysis of data [44] generated by wearables. AI can also identify deviations or anomalies in health measurements. This can help healthcare providers save lives but also allow them to make more accurate diagnoses or provide better treatment. Regulatory authorities such as the FDA in the US and the MHRA in the UK can use AI to conduct regular inspections and audits to ensure compliance with established standards and regulations. At the international level, key players such as the European Union [45], the United Nations [46] (UN) and the WHO have also published proposals and guidance [47] on the ethical use of AI in healthcare. The objective of these regulations is to tackle the risks associated with the use of AI in healthcare. AI tools can help implement and regulate wearable health technology through data analysis, and facilitate compliance with established standards and regulations.

## 6. Conclusions

Wearable health technology can help build better healthcare systems. However, the novelty of this technology is the source of ethical and regulatory challenges, especially the necessity to comply with the right to privacy by protecting personal health data. Existing regulations such as the GDPR or upcoming ones such as the EU Data Act can provide reliable legal frameworks and established standards to be implemented by healthcare providers. States and international organizations such as the WHO need to cooperate and elaborate new guidelines and legally binding rules in this field. Also, AI promises to be a powerful tool with its ability to conduct automated audits and investigations.

**Funding:** This research received no external funding.

**Institutional Review Board Statement:** Not applicable.

**Informed Consent Statement:** Not applicable.

**Data Availability Statement:** Publicly available data.

**Conflicts of Interest:** The author declares no conflicts of interest.

## References

- Godfrey, A.; Hetherington, V.; Shum, H.; Bonato, P.; Lovell, N.H.; Stuart, S. From A to Z: Wearable technology explained. *Maturitas* **2018**, *113*, 40–47. [CrossRef] [PubMed]
- Escobar-Linero, E.; Muñoz-Saavedra, L.; Luna-Perejón, F.; Sevillano, J.L.; Domínguez-Morales, M. Wearable Health Devices for Diagnosis Support: Evolution and Future Tendencies. *Sensors* **2023**, *23*, 1678. [CrossRef] [PubMed]
- Vidhi, K.; Singh, R.; Reddy, R.; Churi, P. Privacy issues in wearable technology: An intrinsic review. In Proceedings of the International Conference on Innovative Computing & Communications (ICICC), Delhi, India, 20–22 February 2020.
- da Silva, J.P. *Privacy Data Ethics of Wearable Digital Health Technology*; Center for Digital Health: Providence, RI, USA, 2023. Available online: <https://digitalhealth.med.brown.edu/news/2023-05-04/ethics-wearables> (accessed on 1 November 2023).
- Thierer, A.D. The internet of things and wearable technology: Addressing privacy and security concerns without derailing innovation. *Richmond J. Law Technol.* **2015**, *21*. Available online: <https://jolt.richmond.edu/jolt-archive/v21i2/article6.pdf> (accessed on 1 November 2023). [CrossRef]
- Huang, K.-H.; Yu, T.H.-K.; Lee, C.F. Adoption model of healthcare wearable devices. *Technol. Forecast. Soc. Chang.* **2022**, *174*, 121286. [CrossRef]
- Barua, A.; Al Alamin, M.A.; Hossain, M.S.; Hossain, E. Security and privacy threats for Bluetooth low energy in IoT and wearable devices: A comprehensive survey. *IEEE Open J. Commun. Soc.* **2022**, *3*, 251–281. [CrossRef]
- Canali, S.; Schiaffonati, V.; Aliverti, A. Challenges and recommendations for wearable devices in digital health: Data quality, interoperability, health equity, fairness. *PLoS Digit. Health* **2022**, *1*, e0000104. [CrossRef] [PubMed]
- Chikwetu, L.; Miao, Y.; Woldetensae, M.K.; Bell, D.; Goldenholz, D.M.; Dunn, J. Does deidentification of data from wearable devices give us a false sense of security? A systematic review. *Lancet Digit. Health* **2023**, *5*, E239–E247. [CrossRef]
- Paul, M.; Maglaras, L.; Ferrag, M.A.; AlMomani, I. Digitization of healthcare sector: A study on privacy and security concerns. *ICT Express* **2023**, *9*, 571–588. [CrossRef]
- Powell, D.; Godfrey, A. Considerations for integrating wearables into the everyday healthcare practice. *NPJ Digit. Med.* **2023**, *6*, 70. [CrossRef]
- Loucks, J.; Stewart, D.; Bucaille, A.; Crossan, G. Deloitte Insights, Wearable Technology in Health Care: Getting Better All the Time, 1 December 2021. Available online: [https://www2.deloitte.com/content/dam/insights/articles/GLOB164601\\_Wearable-healthcare/DI\\_Wearable-healthcare.pdf](https://www2.deloitte.com/content/dam/insights/articles/GLOB164601_Wearable-healthcare/DI_Wearable-healthcare.pdf) (accessed on 1 November 2023).
- Boumpa, E.; Tsoukas, V.; Gkogkidis, A.; Spathoulas, G.; Kakarountas, A. Security and Privacy Concerns for Healthcare Wearable Devices and Emerging Alternative Approaches. In *Wireless Mobile Communication and Healthcare. MobiHealth 2021*; Gao, X., Jamalipour, A., Guo, L., Eds.; Lecture Notes of the Institute for Computer Sciences, Social Informatics and Telecommunications Engineering; Springer: Cham, Switzerland, 2022; Volume 440. [CrossRef]
- Devine, J.K.; Schwartz, L.P.; Hursh, S.R. Technical, regulatory, economic, and trust issues preventing successful integration of sensors into the mainstream consumer wearables market. *Sensors* **2022**, *22*, 2731. [CrossRef]
- Azodo, I.; Williams, R.; Sheikh, A.; Cresswell, K. Opportunities and challenges surrounding the use of data from wearable sensor devices in health care: Qualitative interview study. *J. Med. Internet Res.* **2020**, *22*, e19542. [CrossRef] [PubMed]
- Smith, A.A.; Li, R.; Tse, Z.T.H. Reshaping healthcare with wearable biosensors. *Sci. Rep.* **2023**, *13*, 4998. [CrossRef] [PubMed]
- Dinh-Le, C.; Chuang, R.; Chokshi, S.; Mann, D. Wearable health technology and electronic health record integration: Scoping review and future directions. *JMIR Mhealth Uhealth* **2019**, *7*, e12861. [CrossRef] [PubMed]
- Banerjee, S.; Hemphill, T.; Longstreet, P. Wearable devices and healthcare: Data sharing and privacy. *Inf. Soc.* **2018**, *34*, 49–57. [CrossRef]
- Xue, Y. A review on intelligent wearables: Uses and risks. *Hum. Behav. Emerg. Technol.* **2019**, *1*, 287–294. [CrossRef]
- Sui, A.; Sui, W.; Liu, S.; Rhodes, R. Ethical considerations for the use of consumer wearables in health research. *Digit. Health* **2023**, *9*, 20552076231153740. [CrossRef] [PubMed]
- Pirbhulal, S.; Samuel, O.W.; Wu, W.; Sangaiah, A.K.; Li, G. A joint resource-aware and medical data security framework for wearable healthcare systems. *Future Gener. Comput. Syst.* **2019**, *95*, 382–391. [CrossRef]
- Hughes-Lartey, K.; Li, M.; Botchey, F.E.; Qin, Z. Human factor, a critical weak point in the information security of an organization's Internet of things. *Heliyon* **2021**, *7*, e06522. [CrossRef]
- Khan, F.; Kim, J.H.; Mathiassen, L.; Moore, R. Data breach management: An integrated risk model. *Inf. Manag.* **2021**, *58*, 103392. [CrossRef]
- Prabakaran, D.; Ramachandran, S. Multi-factor authentication for secured financial transactions in cloud environment. *CMC-Comput. Mater. Contin.* **2022**, *70*, 1781–1798. [CrossRef]

25. Javaid, M.; Haleem, A.; Singh, R.P.; Suman, R. Towards insighting cybersecurity for healthcare domains: A comprehensive review of recent practices and trends. *Cyber Secur. Appl.* **2023**, *1*, 100016. [CrossRef]
26. Saha, S.; Chowdhury, C.; Neogy, S. A novel two phase data sensitivity based access control framework for healthcare data. *Multimed. Tools Appl.* **2023**, 1–26. [CrossRef]
27. Edemekong, P.F.; Annamaraju, P.; Haydel, M.J. Health Insurance Portability and Accountability Act. [Updated 2022 Feb 3]. In *StatPearls*; StatPearls Publishing: Treasure Island, FL, USA, 2023. Available online: <https://www.ncbi.nlm.nih.gov/books/NBK500019/> (accessed on 1 November 2023).
28. Jayanthilladevi, A.; Sangeetha, K.; Balamurugan, E. Healthcare biometrics security and regulations: Biometrics data security and regulations governing phi and hipaa act for patient privacy. In Proceedings of the 2020 International Conference on Emerging Smart Computing and Informatics (ESCI), Pune, India, 12–14 March 2020; pp. 244–247.
29. Ash, G.I.; Stults-Kolehmainen, M.; Busa, M.A.; Gaffey, A.E.; Angeloudis, K.; Muniz-Pardos, B.; Gregory, R.; Huggins, R.A.; Redeker, N.S.; Weinzimer, S.A.; et al. Establishing a global standard for wearable devices in sport and exercise medicine: Perspectives from academic and industry stakeholders. *Sports Med.* **2021**, *51*, 2237–2250. [CrossRef] [PubMed]
30. EU General Data Protection Regulation (GDPR). Regulation (EU) 2016/679 of the European Parliament and of the Council of 27 April 2016 on the Protection of Natural Persons with Regard to the Processing of Personal Data and on the Free Movement of Such Data, and Repealing Directive 95/46/EC (General Data Protection Regulation), OJ 2016 L 119/1. Available online: <https://eur-lex.europa.eu/eli/reg/2016/679/oj> (accessed on 1 November 2023).
31. Mulder, T.; Tudorica, M. Privacy policies, cross-border health data and the GDPR. *Inf. Commun. Technol. Law* **2019**, *28*, 261–274. [CrossRef]
32. EU Commission, Press Release, 23 Feb. 2022, Brussels, Data Act: Commission Proposes Measures for a Fair and Innovative Data Economy. Available online: [https://ec.europa.eu/commission/presscorner/detail/en/ip\\_22\\_1113](https://ec.europa.eu/commission/presscorner/detail/en/ip_22_1113) (accessed on 1 November 2023).
33. Council of the EU, Press Release, 27 June 2023, Data Act: Council and Parliament Strike a Deal on Fair Access to and Use of Data. Available online: <https://www.consilium.europa.eu/en/press/press-releases/2023/06/27/data-act-council-and-parliament-strike-a-deal-on-fair-access-to-and-use-of-data/#:~:text=The%20data%20act%20will%20give,objects,%20machines,%20and%20devices> (accessed on 1 November 2023).
34. Iqbal, J.D.; Biller-Andorno, N. The regulatory gap in digital health and alternative pathways to bridge it. *Health Policy Technol.* **2022**, *11*, 100663. [CrossRef]
35. Espinoza, J.; Xu, N.Y.; Nguyen, K.T.; Klonoff, D.C. The need for data standards and implementation policies to integrate CGM data into the electronic health record. *J. Diabetes Sci. Technol.* **2023**, *17*, 495–502. [CrossRef]
36. Taka, A.M. A deep dive into dynamic data flows, wearable devices, and the concept of health data. *Int. Data Priv. Law* **2023**, *13*, 124–140. [CrossRef]
37. Leese, J.; Zhu, S.; Townsend, A.F.; Backman, C.L.; Nimmon, L.; Li, L.C. Ethical issues experienced by persons with rheumatoid arthritis in a wearable-enabled physical activity intervention study. *Health Expect.* **2022**, *25*, 1418–1431. [CrossRef]
38. Segura Anaya, L.H.; Alsadoon, A.; Costadopoulos, N.; Prasad, P.W.C. Ethical Implications of User Perceptions of Wearable Devices. *Sci. Eng. Ethics* **2018**, *24*, 1–28. [CrossRef]
39. Korjian, S.; Gibson, C.M. Digital technologies and the democratization of clinical research: Social media, wearables, and artificial intelligence. *Contemp. Clin. Trials* **2022**, *117*, 106767. [CrossRef]
40. Tahri Sqalli, M.; Aslonov, B.; Gafurov, M.; Nurmatov, S. Humanizing AI in medical training: Ethical framework for responsible design. *Front. Artif. Intell.* **2023**, *6*, 1189914. [CrossRef] [PubMed]
41. Winter, J.S.; Davidson, E. Harmonizing regulatory regimes for the governance of patient-generated health data. *Telecommun. Policy* **2022**, *46*, 102285. [CrossRef]
42. Colloud, S.; Metcalfe, T.; Askin, S.; Belachew, S.; Ammann, J.; Bos, E.; Kilchenmann, T.; Strijbos, P.; Eggenspieler, D.; Servais, L.; et al. Evolving regulatory perspectives on digital health technologies for medicinal product development. *NPJ Digit. Med.* **2023**, *6*, 56. [CrossRef] [PubMed]
43. Venkatesh, K.P.; Raza, M.M.; Kvedar, J.C. Health digital twins as tools for precision medicine: Considerations for computation, implementation, and regulation. *NPJ Digit. Med.* **2022**, *5*, 150. [CrossRef]
44. Padoan, A.; Plebani, M. Flowing through laboratory clinical data: The role of artificial intelligence and big data. *Clin. Chem. Lab. Med. (CCLM)* **2022**, *60*, 1875–1880. [CrossRef]
45. EU Commission. Brussels, 21.4.2021, COM(2021) 206 Final, 2021/0106(COD), Proposal for a Regulation of the European Parliament and of the Council Laying Down Harmonised Rules on Artificial Intelligence (Artificial Intelligence Act) and Amending Certain Union Legislative Acts. Available online: <https://eur-lex.europa.eu/legal-content/EN/TXT/?uri=celex:52021PC0206> (accessed on 1 November 2023).
46. United Nations. UN Decade of Healthy Ageing. United Nations. Available online: <https://www.who.int/initiatives/decade-of-healthy-ageing> (accessed on 1 November 2023).
47. *Ethics and Governance of Artificial Intelligence for Health: WHO Guidance*; World Health Organization: Geneva, Switzerland, 2021. Available online: <https://www.who.int/publications/i/item/9789240029200> (accessed on 1 November 2023).

**Disclaimer/Publisher’s Note:** The statements, opinions and data contained in all publications are solely those of the individual author(s) and contributor(s) and not of MDPI and/or the editor(s). MDPI and/or the editor(s) disclaim responsibility for any injury to people or property resulting from any ideas, methods, instructions or products referred to in the content.

# Aptamer-Based Biosensor Design for Simultaneous Detection of Cervical Cancer-Related MicroRNAs<sup>†</sup>

Radu Tamaian

ICSI Analytics, National Institute for Research and Development for Cryogenic and Isotopic Technologies—ICSI Rm. Vâlcea, 4th Uzinei Street, 240050 Râmnicu Vâlcea, Romania; radu.tamaian@icsi.ro

<sup>†</sup> Presented at the 10th International Electronic Conference on Sensors and Applications (ECSA-10), 15–30 November 2023; Available online: <https://ecsa-10.sciforum.net/>.

**Abstract:** This study presents the design of an innovative aptamer-based biosensor for the detection of circulating microRNAs (miRNAs) associated with cervical cancer development. The selected panel includes circulating miRNAs known to play vital roles in cervical cancer pathogenesis, regulating processes such as cellular proliferation, migration, invasion, angiogenesis, apoptosis, inflammatory responses, and metastasis. The biosensor's design can be optimized to ensure high sensitivity, low limits of detection, and robust performance in clinical settings. This novel biosensor design holds great promise for facilitating non-invasive detection and personalized therapeutic approaches for cervical cancer patients.

**Keywords:** aptamer; biosensor; cervical cancer; circulating microRNAs

## 1. Introduction

Cervical cancer is a significant global health burden with a high prevalence in many regions [1], being the fourth most common cancer among women and accounting for 90% of new cases and fatalities in low- and middle-income countries [2]. To address this challenge, there is an urgent need for innovative diagnostic tools that can enable early detection and personalized therapeutic interventions. One such promising approach involves the design and development of aptamer-based biosensors (aptasensors) [3,4]. Aptamers are single-stranded DNA or RNA molecules that can bind specifically to target molecules with high affinity. They are often referred to as “chemical antibodies” due to their ability to recognize and bind to specific targets, including biomarkers associated with various diseases, such as cancer [5].

This paper refers to a design study for the further development of an aptasensor for the detection of circulating microRNAs (miRNAs) associated with cervical cancer development. In the context of cancer, including cervical cancer, altered expression levels of specific miRNAs have been identified in the bloodstream, known as circulating miRNAs. These circulating miRNAs can serve as potential biomarkers for early cancer detection and monitoring disease progression [6,7].

Aptasensors offer several advantages over traditional diagnostic methods. They are highly specific and sensitive, allowing for the detection of very small quantities of target molecules in complex biological samples. Aptasensors can be engineered to detect multiple miRNA targets simultaneously, providing a comprehensive profile of miRNA expression patterns associated with cervical cancer. Aptasensors offer a non-invasive and cost-effective diagnostic approach. Blood samples, which are easy to obtain, can be used for miRNA detection. Aptasensors, when used in place of more intrusive procedures such as biopsies, reduce patient discomfort and the risk of complications.

**Citation:** Tamaian, R. Aptamer-Based Biosensor Design for Simultaneous Detection of Cervical Cancer-Related MicroRNAs. *Eng. Proc.* **2023**, *58*, 88. <https://doi.org/10.3390/ecsa-10-16203>

Academic Editor: Stefano Mariani

Published: 15 November 2023



**Copyright:** © 2023 by the author. Licensee MDPI, Basel, Switzerland. This article is an open access article distributed under the terms and conditions of the Creative Commons Attribution (CC BY) license (<https://creativecommons.org/licenses/by/4.0/>).

## 2. Materials and Methods

An extended panel of circulating miRNAs known to play crucial roles in the pathogenesis of cervical cancer (regulating processes such as cellular proliferation, migration, invasion, angiogenesis, apoptosis, inflammatory responses, and metastasis) [8] was chosen for the design of the aptasensor.

The RNA sequences of the circulating miRNAs were extracted from the *RNAcentral database* (v22) [9].

All the aptamer sequences corresponding to the circulating miRNA panel were predicted with the help of the web-based software tool *NHLBI-AbDesigner* [10]. The best-ranked sequences were selected with the help of the Immunogenicity Score. Immunogenicity Score is calculated based on a hydrophathy scale (range:  $-4.5$  to  $4.5$ ), and helps assess the likelihood that the chosen peptide sequence will be specifically recognized.

The *RNA Folding Form* from the *mfold* web server [11] was used for modeling, displaying, and analyzing the secondary structure of designed aptamers. The preset folding temperature of software is fixed at  $37^{\circ}$ ; meanwhile, the ionic conditions were set to  $1.0$  M NaCl and no divalent ions. The Gibbs free energy ( $\Delta G$ ) was utilized to predict the stability of RNA aptamer secondary structures. In this context, a positive value for  $\Delta G$  means that the folding process is not spontaneous and requires an input of energy. This could be due to an unfavorable change in enthalpy ( $\Delta H$ ) or a decrease in entropy ( $\Delta S$ ) that is not compensated by a favorable change in enthalpy. In other words, the RNA molecule is more stable in its unfolded state than in its folded state under these conditions [12].

## 3. Results and Discussion

The Immunogenicity Score ranking of *NHLBI-AbDesigner* was used to select the most immunogenic aptamers (RNA sequence), while the *RNA Folding Form* was used to predict the most stable RNA aptamer secondary structures (Table 1).

**Table 1.** The best-ranked predicted aptamer sequences (Immunogenicity Score rank = 1) and the corresponding  $\Delta G$  of their secondary structures.

miRNA	Aptamer (Predicted) Sequence (N <sub>1</sub> –N <sub>n</sub> )	Aptamer Folding—Secondary Structure ( $\Delta G$ in kcal/mol)
miR-10b	CGAUUCUAGGGAAU (8–22) UCGAUUCUAGGGAA (7–21)	3xST: $-0.5/-0.2/0.4$ 3xST: $0.4/0.7/1.0$
miR-15b-3p	CAUUAUUUGCUGCUC (6–20)	2xST: $2.0/2.8$
miR-15b-5p	AGCAGCACAUCAUGG (2–16)	2xST: $0.9/1.9$
miR-17-3p <sup>PC</sup>	CUGCAGUGAAGGCAC (2–16)	2xST: $-1.1/-0.2$
miR-17-5p <sup>PC</sup>	GCUUACAGUGCAGGU (7–21)	$-1.2$
	UGCUUACAGUGCAGG (6–20)	$-1.9$
	GUGCUUACAGUGCAG (5–19)	4xST: $-2.7/-2.5/-2.5/-2.1$
miR-21 <sup>BC</sup>	CAGACUGAUGUUGAC (9–23)	$-0.4$
miR-27b-3p	GUGGCUAAGUUCUGC (7–21)	3xST: $0.2/1.0/1.1$
miR-27b-5p	AGCUGAUUGGUGAAC (8–22)	$-0.2$
miR-32-3p	AGUGUGUGUGAUUU (7–21)	$1.0$
	UAGUGUGUGUGAUUU (6–20)	$1.3$
	UUAGUGUGUGUGAUA (5–19)	3xST: $2.80/3.3/3.3$
	AUUUAGUGUGUGUGA (3–17)	6xST: $3.2/3.5/3.7/4.0/4.1/4.2$
	AAUUAGUGUGUGUG (2–16)	3xST: $2.9/3.2/3.7$
miR-32-5p	CAUUACUAAGUUGCA (8–22)	3xST: $2.8/3.2/3.7$
	ACAUUACUAAGUUGC (7–21)	3xST: $2.3/2.3/3.2$
	CACAUUACUAAGUUG (6–20)	2xST: $2.0/2.7$
	GCACAUUACUAAGUU (5–19)	2xST: $2.0/2.9$
	UGCACAUUACUAAGU (4–18)	2xST: $2.1/2.8$
	UUGCACAUUACUAAG (3–17)	2xST: $3.2/4.2$

Table 1. Cont.

miRNA	Aptamer (Predicted) Sequence (N <sub>1</sub> –N <sub>n</sub> )	Aptamer Folding—Secondary Structure (ΔG in kcal/mol)
miR-124-3p <sup>PC</sup>	GGCACGCGGUGAAUG (4–18)	2xST: 0.1/1.1
miR-124-5p <sup>PC</sup>	GUGUUCACACGCGGAC (2–16) CGUGUUCACACGCGGA (1–15)	–0.9 2xST: –1.1/–0.5
miR-130a-3p	GCAAUGUUAAAAGGG (5–19)	4xST: 3.6/4.1/4.5/4.5
miR-130a-5p	UCACAUUGUGCUACU (8–22) UUCACAUUGUGCUAC (7–21)	0.9 0.9
miR-138-1-3p	CACAACACCAGGGCC (8–22)	No folding is possible
miR-138-2-3p	CACGACACCAGGGUU (8–22) UCACGACACCAGGGU (7–21) UUCACGACACCAGGG (6–20)	2xST: 0.6/0.7 0.7 4xST: 2.9/3.4/3.7/3.9
miR-138-5p	GUGUUGUGAAUCAGG (6–20) GGUGUUGUGAAUCAG (5–19) AGCUGGUGUUGUGAA (1–15)	2xST: 0.9/1.5 –0.1 2xST: 0.3/0.9
miR-143-3p <sup>PC</sup>	GAUGAAGCACUGUAG (4–18) GAGAUGAAGCACUGU (2–16) UGAGAUGAAGCACUG (1–15)	5xST: 2.7/2.9/3.2/3.3/3.7 2xST: 1.8/2.5 3xST: 1.8/2.2/2.5
miR-143-5p <sup>PC</sup>	GGUGCAGUGCUGCAU (1–15)	–4.5
miR-146a	ACUGAAUCCAUGGG (7–21)	5xST: 1.3/1.5/1.8/1.8/2.5
miR-192-3p	UCCAUAAGGUCACAG (8–22) GCCAAUCCAUAAGGU (3–17) UGCCAAUCCAUAAGG (2–16)	1.7 –0.4 2xST: 1.4/2.3
miR-192-5p	UAUGAAUUGACAGCC (7–21) CUAUGAAUUGACAGC (6–20) CCUAUGAAUUGACAG (5–19) GACCUAUGAAUUGAC (3–17)	1.6 1.6 1.6 2xST: 3.1/4.0
miR-214	GGCACAGACAGGCAG (7–21) GCAGGCACAGACAGG (4–18)	–0.9 No folding is possible
miR-218-1-3p	CGUCAAGCACCAUUG (8–22)	7xST: 1.4/1.4/1.7/2.1/2.2/2.3/2.3
miR-218-2-3p	CUGUCAAGCACCGCG (8–22)	3xST: 0.4/1.2/1.3
miR-218-5p	GUGCUUGAUCUAACC (3–17)	2.1
miR-328-3p	GGCCUCUCUGCCCU (3–17) UGGCCUCUCUGCCC (2–16) CUGGCCUCUCUGCC (1–15)	–2.4 –2.4 –1.6
miR-328-5p	GGGGGGCAGGAGGGG (2–16) GGGGGGCAGGAGGG (1–15)	No folding is possible No folding is possible
miR-409-3p	GAAUGUUGCUCGGUG (1–15)	2xST: 1.3/2.1
miR-409-5p	GGUUAACCCGAGCAAC (2–16)	2xST: –0.40/0.2
miR-429	GUCUGGUAAAACCGU (8–22) UGUCUGGUAAAACCG (7–21)	3xST: –1.3/–1.2/–1.0 3xST: –1.3/–1.0/–0.6
miR-432-3p	CUGGAUGGCCUCCUCC (1–15)	–1.6
miR-432-5p	GAGUAGGUCAUUGGG (6–20) GGAGUAGGUCAUUGG (5–19)	1.3 2xST: 1.3/1.9
miR-454-3p	AUAUUGCUUAUAGGG (8–22)	4xST: 1.4/1.8/1.9/2.4
miR-454-5p	CAUAUUGUCUCUGC (8–22)	3xST: 2.6/3.1/3.5
miR-466	ACACGCAACACACAU (9–23) UACACGCAACACACA (8–22) AUACACGCAACACAC (7–21) CAUACACGCAACACACA (6–20) ACAUAACACGCAACAC (5–19) CACAUACACGCAACA (4–18) ACACAUACACGCAAC (3–17)	No folding is possible No folding is possible No folding is possible No folding is possible No folding is possible No folding is possible No folding is possible

(N<sub>1</sub>–N<sub>n</sub>): corresponding position of the nucleotides from the circulating miRNA sequence; xST = number of possible secondary structures (predicted folding variants); <sup>PC</sup>: circulating miRNA also expressed in breast cancer [8]; <sup>PC</sup>: circulating miRNA also expressed in prostate cancer [8].

From Table 1, it can be observed that for 19 of the selected circulating miRNAs, a single aptamer sequence was predicted, while for the rest of the 17 circulating miRNAs, up to seven possible variants of sequence were predicted, with all the presented sequences having an Immunogenicity Score rank equal to 1. This suggests that the 19 miRNAs may have relatively straightforward binding requirements, and a single aptamer sequence is sufficient for specific interaction. However, for the remaining 17 circulating miRNAs, the prediction process has led to the identification of multiple possible variants of aptamer sequences. This indicates that these particular miRNAs may have more complex structural features or binding requirements that necessitate multiple candidate aptamers to achieve the desired specificity. Regardless of whether a single sequence or multiple variants were predicted, all the presented aptamer sequences have an Immunogenicity Score rank equal to 1. This implies that these aptamers are unlikely to trigger an immune response when used in practical applications, which is a favorable characteristic for diagnostic or therapeutic purposes.

Additionally, from Table 1, it can be observed that for the 19 circulating miRNAs with only a single aptamer sequence predicted, there was also a single secondary structure variant predicted for five of them: miR-21 (negative  $\Delta G$ , also expressed in breast cancer), miR-27b-3p (negative  $\Delta G$ ), miR-143-5p (negative  $\Delta G$ , also expressed in prostate cancer), miR-218-5p (positive  $\Delta G$ ), and miR-432-3p (negative  $\Delta G$ ).

In terms of the Gibbs free energy ( $\Delta G$ ), utilized to predict the stability of aptamer secondary structures, the following outcome can be observed from Table 1:

- At least one valid secondary structure (folding variant) with negative  $\Delta G$  for aptamers corresponding to 14 circulating miRNAs. Negative  $\Delta G$  values suggest that these aptamers are likely to form stable secondary structures; the folding process of RNA aptamers is spontaneous and thermodynamically favored.
- At least one folding variant with positive  $\Delta G$  for 19 circulating miRNAs and no folding secondary structure variants with negative  $\Delta G$ . This indicates that for these miRNAs, the secondary structures of the aptamers might not be as thermodynamically stable, which could influence their binding kinetics and specificity.
- In the case of three aptamers, the folding process was not possible, and the prediction of the secondary structure failed, namely the corresponding aptamers for miR-138-1-3p (a single aptamer sequence predicted), miR-328-5p (two aptamer sequences predicted), and miR-466 (seven aptamer sequences predicted). This suggests that these particular miRNAs might pose challenges in terms of aptamer design due to their structural complexity or other factors.

Hereinafter are presented three different case studies for folding predicted aptamer structures: (1) aptamer for miR-21 (only one predicted aptamer sequence and a single secondary structure variant with negative  $\Delta G$ ; Table 2), aptamers for miR-124-5p (two predicted aptamer sequences and more than one secondary structure variant, all with negative  $\Delta G$ ; Table 3), and miR-146a (only one predicted aptamer sequence and multiple secondary structure variants, all with positive  $\Delta G$ —Table 4).

The miR-21 aptamer (Table 2) exhibits a single structure with a negative  $\Delta G$  ( $-0.4$  kcal/mol), indicating favorable stability and binding potential. Moreover, as a single structure was predicted for the miR-21 aptamer, the folding process is straightforward.

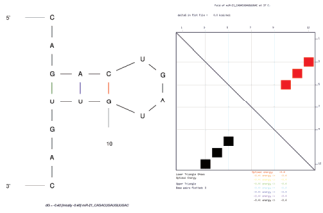
Two sequences were predicted for miR-124-5p (Table 3), each with a single structure variant, indicating some structural diversity but not as complex as in miR-146a (Table 4). Both miR-124-5p aptamers (Table 3) have negative  $\Delta G$  values ( $-0.9$  kcal/mol and  $-1.1$  kcal/mol, respectively), suggesting favorable folding and stability.

In contrast, all structures for the miR-146a aptamer (Table 4) have positive  $\Delta G$  values, ranging from 1.3 kcal/mol to 2.5 kcal/mol, indicating unfavorable folding and instability.

Hairpin loops are significant as they often form the functional binding sites of aptamers. In all case studies, hairpin loops are present, but their thermodynamic contributions vary. For instance, they contribute positively to the stability of the miR-21 aptamers (Table 2)

and miR-124-5p aptamers (Table 3) but not for the miR-146a aptamers, where positive  $\Delta G$  values dominate (Table 4).

**Table 2.** Case study: aptamer for miR-21, predicted sequence and folding of secondary structure.

Folding of Predicted Sequence		Thermodynamics of Folding	
<p><b>Sequence:</b> CAGACUGAUGUUGAC</p> 		<p><b>Structure</b> <math>\Delta G = -0.4</math> kcal/mol</p>	
Structural element	$\delta G$	Information	
External loop	-0.5	5 ss bases and 1 closing helix	
Stack	-1.3	External closing pair is G <sub>3</sub> -U <sup>12</sup>	
Stack	-2.2	External closing pair is A <sup>4</sup> -U <sup>11</sup>	
<b>Helix</b>	-3.5	3 base pairs	
Hairpin loop	3.6	Closing pair is C <sup>5</sup> -G <sup>10</sup>	

ss: single stranded;  $\delta G$  values are expressed in kcal/mol.

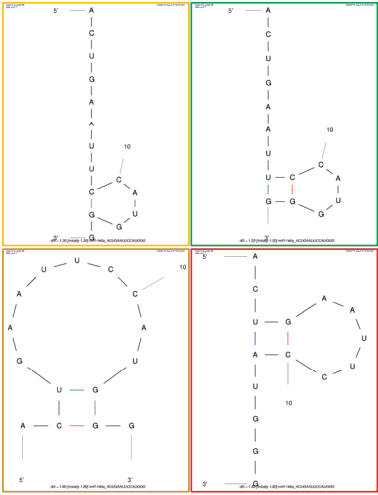


**Table 3.** Case study: aptamers for miR-124-5p, predicted sequences and folding variants.

Folding of Predicted Sequence		Thermodynamics of Folding																									
<p><b>Sequence 1: GUGUUCACAGCGGAC</b></p>		<p><b>Structure</b>  <math>\Delta G = -0.9</math> kcal/mol</p> <table border="1"> <thead> <tr> <th>Structural element</th> <th><math>\delta G</math></th> <th>Information</th> </tr> </thead> <tbody> <tr> <td>External loop</td> <td>0.0</td> <td>2 ss bases and 1 closing helix</td> </tr> <tr> <td>Stack</td> <td>-2.2</td> <td>External closing pair is G<sup>3</sup>-C<sup>15</sup></td> </tr> <tr> <td>Stack</td> <td>-1.3</td> <td>External closing pair is U<sup>4</sup>-A<sup>14</sup></td> </tr> <tr> <td>Stack</td> <td>-1.5</td> <td>External closing pair is U<sup>5</sup>-G<sup>13</sup></td> </tr> <tr> <td><b>Helix</b></td> <td>-5.0</td> <td>4 base pairs</td> </tr> <tr> <td>Hairpin loop</td> <td>4.1</td> <td>Closing pair is C<sup>6</sup>-G<sup>12</sup></td> </tr> </tbody> </table>		Structural element	$\delta G$	Information	External loop	0.0	2 ss bases and 1 closing helix	Stack	-2.2	External closing pair is G <sup>3</sup> -C <sup>15</sup>	Stack	-1.3	External closing pair is U <sup>4</sup> -A <sup>14</sup>	Stack	-1.5	External closing pair is U <sup>5</sup> -G <sup>13</sup>	<b>Helix</b>	-5.0	4 base pairs	Hairpin loop	4.1	Closing pair is C <sup>6</sup> -G <sup>12</sup>			
Structural element	$\delta G$	Information																									
External loop	0.0	2 ss bases and 1 closing helix																									
Stack	-2.2	External closing pair is G <sup>3</sup> -C <sup>15</sup>																									
Stack	-1.3	External closing pair is U <sup>4</sup> -A <sup>14</sup>																									
Stack	-1.5	External closing pair is U <sup>5</sup> -G <sup>13</sup>																									
<b>Helix</b>	-5.0	4 base pairs																									
Hairpin loop	4.1	Closing pair is C <sup>6</sup> -G <sup>12</sup>																									
<p><b>Sequence 2: CGUGUUCACAGCGGA</b></p>		<p><b>Structure 1 (red on dot plot folding comparison)</b>  <math>\Delta G = -1.1</math> kcal/mol</p> <table border="1"> <thead> <tr> <th>Structural element</th> <th><math>\delta G</math></th> <th>Information</th> </tr> </thead> <tbody> <tr> <td>External loop</td> <td>-1.3</td> <td>2 ss bases and 1 closing helix</td> </tr> <tr> <td>Stack</td> <td>-2.4</td> <td>External closing pair is C<sup>1</sup>-G<sup>13</sup></td> </tr> <tr> <td>Stack</td> <td>-2.5</td> <td>External closing pair is G<sup>2</sup>-C<sup>12</sup></td> </tr> <tr> <td><b>Helix</b></td> <td>-4.9</td> <td>3 base pairs</td> </tr> <tr> <td>Hairpin loop</td> <td>5.1</td> <td>Closing pair is U<sup>3</sup>-G<sup>11</sup></td> </tr> </tbody> </table>		Structural element	$\delta G$	Information	External loop	-1.3	2 ss bases and 1 closing helix	Stack	-2.4	External closing pair is C <sup>1</sup> -G <sup>13</sup>	Stack	-2.5	External closing pair is G <sup>2</sup> -C <sup>12</sup>	<b>Helix</b>	-4.9	3 base pairs	Hairpin loop	5.1	Closing pair is U <sup>3</sup> -G <sup>11</sup>						
Structural element	$\delta G$	Information																									
External loop	-1.3	2 ss bases and 1 closing helix																									
Stack	-2.4	External closing pair is C <sup>1</sup> -G <sup>13</sup>																									
Stack	-2.5	External closing pair is G <sup>2</sup> -C <sup>12</sup>																									
<b>Helix</b>	-4.9	3 base pairs																									
Hairpin loop	5.1	Closing pair is U <sup>3</sup> -G <sup>11</sup>																									
		<p><b>Structure 2 (green on dot plot folding comparison)</b>  <math>\Delta G = -0.5</math></p> <table border="1"> <thead> <tr> <th>Structural element</th> <th><math>\delta G</math></th> <th>Information</th> </tr> </thead> <tbody> <tr> <td>External loop</td> <td>-1.3</td> <td>2 ss bases and 1 closing helix</td> </tr> <tr> <td>Stack</td> <td>-2.4</td> <td>External closing pair is C<sup>1</sup>-G<sup>13</sup></td> </tr> <tr> <td><b>Helix</b></td> <td>-2.4</td> <td>2 base pairs</td> </tr> <tr> <td>Bulge loop</td> <td>1.6</td> <td>External closing pair is G<sup>2</sup>-C<sup>12</sup></td> </tr> <tr> <td>Stack</td> <td>-2.1</td> <td>External closing pair is U<sup>3</sup>-A<sup>10</sup></td> </tr> <tr> <td><b>Helix</b></td> <td>-2.1</td> <td>2 base pairs</td> </tr> <tr> <td>Hairpin loop</td> <td>3.7</td> <td>Closing pair is G<sup>4</sup>-C<sup>9</sup></td> </tr> </tbody> </table>		Structural element	$\delta G$	Information	External loop	-1.3	2 ss bases and 1 closing helix	Stack	-2.4	External closing pair is C <sup>1</sup> -G <sup>13</sup>	<b>Helix</b>	-2.4	2 base pairs	Bulge loop	1.6	External closing pair is G <sup>2</sup> -C <sup>12</sup>	Stack	-2.1	External closing pair is U <sup>3</sup> -A <sup>10</sup>	<b>Helix</b>	-2.1	2 base pairs	Hairpin loop	3.7	Closing pair is G <sup>4</sup> -C <sup>9</sup>
Structural element	$\delta G$	Information																									
External loop	-1.3	2 ss bases and 1 closing helix																									
Stack	-2.4	External closing pair is C <sup>1</sup> -G <sup>13</sup>																									
<b>Helix</b>	-2.4	2 base pairs																									
Bulge loop	1.6	External closing pair is G <sup>2</sup> -C <sup>12</sup>																									
Stack	-2.1	External closing pair is U <sup>3</sup> -A <sup>10</sup>																									
<b>Helix</b>	-2.1	2 base pairs																									
Hairpin loop	3.7	Closing pair is G <sup>4</sup> -C <sup>9</sup>																									

ss: single stranded;  $\delta G$  values are expressed in kcal/mol.

**Table 4.** Case study: aptamers for miR-146a, predicted sequences and folding variants.

Folding of Predicted Sequence	Thermodynamics of Folding	
<b>Sequence: ACUGAAUCCAUGGG</b> 	<b>Structure 1 (orange on dot plot folding comparison)</b> $\Delta G = 1.3$ kcal/mol	
	<b>Structural element</b>	<b>Information</b>
	External loop	9 ss bases and 1 closing helix
	Hairpin loop	Closing pair is C <sup>9</sup> -G <sup>14</sup>
	<b>Structure 2 (green on dot plot folding comparison)</b> $\Delta G = 1.5$ kcal/mol	
	<b>Structural element</b>	<b>Information</b>
	External loop	7 ss bases and 1 closing helix
	Stack	External closing pair is U <sup>8</sup> -G <sup>15</sup>
	<b>Helix</b>	2 base pairs
	Hairpin loop	Closing pair is C <sup>9</sup> -G <sup>14</sup>
	<b>Structure 3 (dark gold on dot plot folding comparison)</b> $\Delta G = 1.8$ kcal/mol	
	<b>Structural element</b>	<b>Information</b>
	External loop	2 ss bases and 1 closing helix
	Stack	External closing pair is C <sup>2</sup> -G <sup>14</sup>
	<b>Helix</b>	2 base pairs
	Hairpin loop	Closing pair is U <sup>3</sup> -G <sup>13</sup>
	<b>Structure 4 (red on dot plot folding comparison)</b> $\Delta G = 1.8$ kcal/mol	
	<b>Structural element</b>	<b>Information</b>
	External loop	6 ss bases and 1 closing helix
	Stack	External closing pair is U <sup>3</sup> -A <sup>11</sup>
	<b>Helix</b>	2 base pairs
	Hairpin loop	Closing pair is G <sup>4</sup> -C <sup>10</sup>
	<b>Structure 5 (blue on dot plot folding comparison)</b> $\Delta G = 2.5$ kcal/mol	
	<b>Structural element</b>	<b>Information</b>
	External loop	8 ss bases and 1 closing helix
	Stack	External closing pair is C <sup>9</sup> -G <sup>15</sup>
	<b>Helix</b>	2 base pairs
	Hairpin loop	Closing pair is C <sup>10</sup> -G <sup>14</sup>

ss: single stranded;  $\delta G$  values are expressed in kcal/mol.

The  $\Delta G$  values play a critical role in aptamer design because they reflect the stability of the interactions. Aptamers with negative  $\Delta G$  values are generally preferred as they are more likely to form stable complexes with their target molecules. A negative  $\Delta G$  value indicates that the aptamer-miRNA binding is thermodynamically driven and spontaneous, which is advantageous for applications such as biosensors, diagnostics, or targeted therapies. These

aptamers are more likely to function effectively. The positive  $\Delta G$  values indicate that these structures may struggle to form stable conformations, which could affect their binding affinity and specificity.

Accurate understanding and prediction of these values are crucial for the successful design and application of aptamers, especially in the context of cervical cancer-related miRNA detection. The structural complexity of miRNAs can pose serious challenges, and some miRNAs have intricately secondary and tertiary structures that may not be accurately captured in silico or even impossible to predict via certain computational tools in preset conditions (e.g., aptamers for miR-21, miR-124-5p, and miR-146a). This complexity can lead to difficulties in predicting  $\Delta G$  values, especially if multiple conformations are possible.

It is important to note that computational predictions of  $\Delta G$  values are an initial step. Experimental validation is essential to confirm the actual binding affinities and structural characteristics of these aptamers for their respective miRNA targets, especially in complex cases. Techniques such as isothermal titration calorimetry or surface plasmon resonance can provide precise  $\Delta G$  measurements and confirm the binding kinetics.

#### 4. Conclusions

In the context of cervical cancer research, these findings suggest that different circulating miRNAs may require different approaches when designing aptamers for their detection or targeting. The existence of multiple aptamer variants for some miRNAs indicates the need for careful selection and testing to determine which aptamers provide the best performance in terms of specificity and sensitivity for diagnostic or therapeutic applications related to cervical cancer.

In conclusion, the design of an innovative aptamer-based biosensor for the detection of circulating miRNAs associated with cervical cancer development holds great promise in the fight against this global health burden. By enabling early detection and personalized therapeutic interventions, this technology has the potential to improve patient outcomes and reduce the impact of cervical cancer on women's health worldwide. Continued research, validation, and collaboration are essential to realizing the full potential of this diagnostic tool and its translation into clinical practice.

**Funding:** This work has been financed by the Ministry of Research, Innovation and Digitization through Program 1—Development of the national research and development system; Subprogram 1.2—Institutional performance—Projects for financing excellence in R&D, contract no. 19PFE/2021.

**Institutional Review Board Statement:** Not applicable.

**Informed Consent Statement:** Not applicable.

**Data Availability Statement:** R.T is responsible for keeping and providing access to the data for the entire in silico work.

**Conflicts of Interest:** The author declares no conflicts of interest.

#### References

1. Zhao, M.; Wu, Q.; Hao, Y.; Hu, J.; Gao, Y.; Zhou, S.; Han, L. Global, Regional, and National Burden of Cervical Cancer for 195 Countries and Territories, 2007–2017: Findings from the Global Burden of Disease Study 2017. *BMC Women's Health* **2021**, *21*, 419. [CrossRef] [PubMed]
2. Sung, H.; Ferlay, J.; Siegel, R.L.; Laversanne, M.; Soerjomataram, I.; Jemal, A.; Bray, F. Global Cancer Statistics 2020: GLOBOCAN Estimates of Incidence and Mortality Worldwide for 36 Cancers in 185 Countries. *CA A Cancer J. Clin.* **2021**, *71*, 209–249. [CrossRef] [PubMed]
3. Zahra, Q.; Khan, Q.A.; Luo, Z. Advances in Optical Aptasensors for Early Detection and Diagnosis of Various Cancer Types. *Front. Oncol.* **2021**, *11*, 632165. [CrossRef] [PubMed]
4. Sharma, A.; Dulta, K.; Nagraik, R.; Dua, K.; Singh, S.K.; Chellappan, D.K.; Kumar, D.; Shin, D.-S. Potentialities of Aptasensors in Cancer Diagnosis. *Mater. Lett.* **2022**, *308*, 131240. [CrossRef]
5. Kher, G.; Trehan, S.; Misra, A. Antisense Oligonucleotides and RNA Interference. In *Challenges in Delivery of Therapeutic Genomics and Proteomics*; Misra, A., Ed.; Elsevier: London, UK, 2011; pp. 325–386. ISBN 978-0-12-384964-9.

6. Abbas, M.; Mehdi, A.; Khan, F.H.; Verma, S.; Ahmad, A.; Khatoon, F.; Raza, S.T.; Afreen, S.; Glynn, S.A.; Mahdi, F. Role of MiRNAs in Cervical Cancer: A Comprehensive Novel Approach from Pathogenesis to Therapy. *J. Gynecol. Obstet. Hum. Reprod.* **2021**, *50*, 102159. [CrossRef] [PubMed]
7. Doghish, A.S.; Ali, M.A.; Elyan, S.S.; Elrebehy, M.A.; Mohamed, H.H.; Mansour, R.M.; Elgohary, A.; Ghanem, A.; Faraag, A.H.I.; Abdelmaksoud, N.M.; et al. MiRNAs Role in Cervical Cancer Pathogenesis and Targeted Therapy: Signaling Pathways Interplay. *Pathol.—Res. Pract.* **2023**, *244*, 154386. [CrossRef] [PubMed]
8. Galvão-Lima, L.J.; Morais, A.H.F.; Valentim, R.A.M.; Barreto, E.J.S.S. MiRNAs as Biomarkers for Early Cancer Detection and Their Application in the Development of New Diagnostic Tools. *BioMedical Eng. OnLine* **2021**, *20*, 21. [CrossRef] [PubMed]
9. RNAcentral Consortium. RNAcentral 2021: Secondary Structure Integration, Improved Sequence Search and New Member Databases. *Nucleic Acids Res.* **2021**, *49*, D212–D220. [CrossRef] [PubMed]
10. Pisitkun, T.; Hoffert, J.D.; Saeed, F.; Knepper, M.A. NHLBI-AbDesigner: An Online Tool for Design of Peptide-Directed Antibodies. *Am. J. Physiol. Cell Physiol.* **2012**, *302*, C154–C164. [CrossRef] [PubMed]
11. Zuker, M. Mfold Web Server for Nucleic Acid Folding and Hybridization Prediction. *Nucleic Acids Res.* **2003**, *31*, 3406–3415. [CrossRef] [PubMed]
12. Zuber, J.; Schroeder, S.J.; Sun, H.; Turner, D.H.; Mathews, D.H. Nearest Neighbor Rules for RNA Helix Folding Thermodynamics: Improved End Effects. *Nucleic Acids Res.* **2022**, *50*, 5251–5262. [CrossRef] [PubMed]

**Disclaimer/Publisher’s Note:** The statements, opinions and data contained in all publications are solely those of the individual author(s) and contributor(s) and not of MDPI and/or the editor(s). MDPI and/or the editor(s) disclaim responsibility for any injury to people or property resulting from any ideas, methods, instructions or products referred to in the content.

Proceeding Paper

# Characterization of Porcine Skin Using a Portable Time-Domain Optical Coherence Tomography System <sup>†</sup>

Maria Cecilia Galvez <sup>1,2</sup>, Jumar Cadondon <sup>1,3,\*</sup>, Paulito Mandia <sup>1,4</sup>, Ernest Macalalad <sup>5</sup>, Edgar Vallar <sup>1,2</sup> and Tatsuo Shiina <sup>4</sup>

<sup>1</sup> Environment and Remote Sensing Research (EARTH) Laboratory, Department of Physics, De La Salle University, 2401 Taft Avenue, Manila 0922, Philippines

<sup>2</sup> Applied Research for Community, Health and Environment Resilience and Sustainability (ARCHERS), Center Natural Sciences and Environmental Research (CENSER), De La Salle University, 2401 Taft Avenue, Manila 0922, Philippines

<sup>3</sup> Division of Physical Sciences and Mathematics, College of Arts and Sciences, University of the Philippines Visayas, Miagao 5023, Philippines

<sup>4</sup> Graduate School of Engineering, Chiba University, 1-33 Yayoi-cho, Inage-ku, Chiba 2638522, Japan

<sup>5</sup> Department of Physics, Mapua University, 658 Muralla St., Intramuros, Manila 1002, Philippines

\* Correspondence: jgcadondon@up.edu.ph

<sup>†</sup> Presented at the 10th International Electronic Conference on Sensors and Applications (ECSA-10), 15–30 November 2023; Available online: <https://ecsa-10.sciforum.net/>.

**Abstract:** Optical coherence tomography (OCT) is an imaging tool used to visualize the cross-section of a sample. Additionally, this device can measure the sample's physical properties. This experiment used a portable version to measure the epidermal thickness and dermal extinction coefficient of porcine skin obtained from different anatomical sites. The thinnest epidermis was found to be from the ear region, while the thickest is from the leg. Meanwhile, the lowest dermal extinction coefficient was from the ear, while the highest was from the belly. These measured properties can be used as aids for diagnosing various skin conditions in humans and animals.

**Keywords:** time-domain optical coherence tomography; porcine skin; extinction coefficient; skin conditions

**Citation:** Galvez, M.C.; Cadondon, J.; Mandia, P.; Macalalad, E.; Vallar, E.; Shiina, T. Characterization of Porcine Skin Using a Portable Time-Domain Optical Coherence Tomography System. *Eng. Proc.* **2023**, *58*, 89. <https://doi.org/10.3390/ecsa-10-16213>

Academic Editor: Stefano Mariani

Published: 15 November 2023



**Copyright:** © 2023 by the authors. Licensee MDPI, Basel, Switzerland. This article is an open access article distributed under the terms and conditions of the Creative Commons Attribution (CC BY) license (<https://creativecommons.org/licenses/by/4.0/>).

## 1. Introduction

The skin is the outermost organ of the body. As such, it is the first line of defense of the organism from the environment and dehydration. Therefore, the skin needs to maintain its structural integrity to maintain homeostasis within the organism.

In an individual, skin properties can vary depending on anatomic location, age, sex, occupation, and many other factors [1,2]. The person's health condition may also alter the properties of the skin. Epidermal thickness has been used to study skin conditions. Increased epidermal thickness can be seen in patients with actinic keratosis, which is a condition that may lead to skin cancer [3]. On the other hand, decreased epidermal thickness can result from skin aging due to exposure to ultraviolet radiation [4]. Skin thickness can give a clue about the proliferation of epidermal cells; hence, it can be used to measure the degree of healing [5] and the effectiveness of drug delivery [6].

Traditionally, epidermal thickness was measured by excising a small skin region and viewing it under a light microscope [7]. While biopsy remains the gold standard in diagnostics, it is invasive and requires a significant amount of time for tissue processing. Newer methods of measuring epidermal thickness include high-resolution ultrasound [8] and optical coherence tomography (OCT) [9]. Both methods are non-invasive and can thus be used *in vivo*.

Studies have also shown that the extinction coefficient (EC) of tissue changes along with chemical and structural changes of the skin during disease states. Edematous areas are

caused by an increased water content, leading to reduced EC. Similarly, oral squamous cell carcinoma tissues showed lower extinction coefficient measurements than that of normal oral tissues [10], while pustular lesions have increased signal scattering, thus increasing the EC [11]. Due to ethical considerations and sample availability, animal tissue is the most suitable subject before testing on human volunteers, especially when using a diagnostic modality still under development.

The animal whose skin is found to have the closest resemblance to human skin regarding hair and lipid distribution, and immunogenicity is that of the pig [12,13]. Porcine skin is a possible model for studies on UV protection and epidermal morphology [14]. The wound-healing process and cell proliferation of human and porcine skin are similar [15]. It makes porcine skin the ideal candidate for our OCT study in human skin modeling. The first published OCT paper was in 1991, showing an image of the human retina [16]. OCT are vastly applied in dentistry [17], dermatology [18], and agriculture [19]. There are two types of OCT which are dependent on frequency and time. The absence of a movable reflector allows frequency domain (FD-OCT) to acquire signals faster than time domain (TD-OCT). FD-OCT is associated with a rapid scan speed and a higher resolution in contrast to TD-OCT. It also increases the signal-to-noise ratio [20,21]. However, the simple design and cheaper components make TD-OCT a viable type today [22]. It can also penetrate deeper when compared to FD-OCT. In this study, a time-domain OCT was developed.

This study aims to characterize porcine skin in terms of epidermal thickness and extinction coefficient of the dermis since these properties can easily be extracted from a single A-scan. Information derived from studies like these is useful in modeling human skin conditions, which can be later utilized for rapid, non-invasive screening and diagnosis of diseases. Furthermore, this study can also extend to veterinary medicine to benefit non-human species.

## 2. Materials and Methods

TD-OCT is based on the Michelson interferometer as shown in Figure 1a.

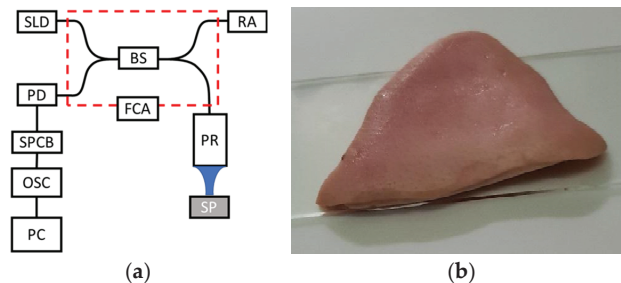


**Figure 1.** (a) The schematic diagram of the TD-OCT system. Superluminescent diode (SLD); Photodiode (PD); Signal processing circuit board (SPCB); Oscilloscope (Osc); Personal computer (PC); Beam splitter (BS); Reference arm (RA); Probe (PR); Sample (SP); Fiber coupler assembly (FCA) (enclosed in red box) [23]. (b) Porcine skin, ear part.

The reference mirror is designed as a rotating retroreflector instead of moving in translation motion [24]. The advantage of a rotating mechanism over a translational one is a more extended scanning range, which can be easily adjusted by changing the retroreflector's rotation radius. Using a rotating reflector, the repeatability has improved with an optical path difference at angles less than  $\pm 20$  degrees. A 1310 nm SLD (Anritsu Co. Ltd., Kanagawa, Japan) with a spectral width of 106 nm and an average axial resolution of 7  $\mu\text{m}$  in air. The detailed discussion on the mechanism was discussed by Shiina et al. [24]. This system has been used for gelatin-skin-based phantoms [23,25] and leaf structures [26]. The specifications of the TD-OCT system are summarized in Table 1.

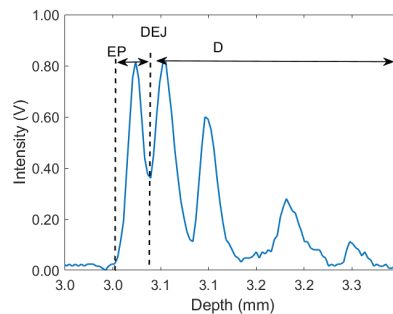
**Table 1.** Specifications of the TD-OCT system [22].

Specification	Value
Center wavelength	1310 nm
Spectral width	106 nm
Axial resolution	7 $\mu\text{m}$
Lateral resolution, spot size	6 $\mu\text{m}$
Numerical aperture	0.14
Scanning rate	25 scans/s
Scanning depth in air	12–14 mm

Porcine skin was bought from a local market. Skin samples were obtained from different parts, namely the belly, buttocks, leg, cheek, and ear. A piece of skin was mounted onto a glass slide, as shown in Figure 1b. The thickness can also be measured since the entire epidermal layer can be visualized from the A-scan. Light from the probe cannot penetrate the total thickness of the dermis; hence, dermal thickness cannot be assessed. On the other hand, the epidermal extinction coefficient cannot be obtained with the current specifications of the OCT system, so the dermal extinction coefficient was measured instead. A detailed discussion on the determination of extinction coefficients is previously published by Galvez et al. (2021) [23].

### 3. Results and Discussion

OCT attenuation has been increasingly used for tissue analysis and characterization. For heterogeneous samples like the skin, the A-scan may contain several prominent peaks representing boundaries of various surfaces [23,25]. Figure 2 is an A-scan of porcine skin at the belly. The use of multiple A-scans presents a possible use of OCT to characterize porcine skin at different sites [27].

**Figure 2.** A-scan of porcine skin: EP, epidermis; DEJ, dermo-epidermal junction; D, dermis.

Aside from the surface peak of the epidermis, another prominent peak is the dermis. Histologically, a very thin dermo-epidermal junction separates these two skin layers. Table 2 shows the epidermal thickness of porcine skin at various sites. It can be shown that the epidermal thickness in the belly produces higher standard deviations compared to other parts. Higher errors were also observed in the belly's extinction coefficient. Larger errors are partly due to having less particles at these regions which leads to low values and slow variation of backscatter intensity. It also causes significant scattering intensity fluctuations [28,29].

The ear epidermis was observed to be the thinnest, followed by the buttocks and cheek. These findings were consistent with other works [13,30], except for the belly, which in this research is one of the thickest compared to others. Since the epidermal layer is fragile, the data points were insufficient to compute the extinction coefficient. The high standard deviations of the values may be due to the heterogeneous nature of the skin. Another study limitation is that the skin samples were frozen for about a week before scanning.

**Table 2.** Epidermal thickness and extinction coefficient of porcine skin from various sites.

Epidermal Thickness (µm)	Belly	Leg	Buttocks	Cheek	Ear
Mean	92.38	95.22	64.64	77.72	60.13
Median	85.13	93.01	61.48	78.83	59.91
St Dev	27.30	16.64	13.18	12.03	4.70
Extinction Coefficient (1/mm)	Belly	Leg	Buttocks	Cheek	Ear
Mean	6.42	2.65	4.67	4.36	2.31
Median	6.33	2.45	3.80	3.82	2.48
St Dev	2.87	0.77	1.87	1.94	1.97

#### 4. Conclusions

Using OCT, epidermal thickness and dermal extinction coefficients were obtained at different pig body parts. The thinnest epidermis was found on the ear, consistent with the present literature. Even without using B-scans, which require more processing time than a single A-scan. This study showed preliminary measurements and the importance of an A-scan in epidermal thickness. Thus, we can use OCT as a rapid, non-invasive tool as an aid for the diagnosis of skin conditions, not just in humans but in other animals as well.

**Author Contributions:** Conceptualization, M.C.G.; methodology, T.S. and P.M.; software, E.M.; validation and formal analysis, M.C.G., J.C. and E.V.; investigation, P.M.; writing—original draft preparation, P.M. and J.C.; writing—review and editing, M.C.G., E.V., T.S. and J.C.; visualization, P.M. All authors have read and agreed to the published version of the manuscript.

**Funding:** This research was funded by the Commission on Higher Education (CHED) of the Philippine Government for the project entitled “Development of a Portable Optical Coherence Tomography System for the Evaluation of Human Skin Analogues”.

**Institutional Review Board Statement:** Not applicable.

**Informed Consent Statement:** Not applicable.

**Data Availability Statement:** The raw data supporting the conclusions of this article will be made available by the authors on request.

**Acknowledgments:** The authors are grateful for the support from the Commission on Higher Education, De La Salle University through the University Research Coordination Office (DLSU-URCO), Department of Science and Technology- ASTHRDP Program, University of the Philippines Visayas, Mapua University, and Chiba University.

**Conflicts of Interest:** The authors declare no conflicts of interest.

#### References

- Gambichler, T.; Matip, R.; Moussa, G.; Altmeyer, P.; Hoffmann, K. In Vivo Data of Epidermal Thickness Evaluated by Optical Coherence Tomography: Effects of Age, Gender, Skin Type, and Anatomic Site. *J. Dermatol. Sci.* **2006**, *44*, 145–152. [CrossRef]
- James, W.D.; Elston, D.K.; Treat, J.R.; Rosenbach, M.A.; Neuhaus, I.M. *Andrews’ Diseases of the Skin-Clinical Dermatology*, 13th ed.; Elsevier: Edinburgh, UK, 2020.
- Jerjes, W.; Hamdoon, Z.; Rashed, D.; Sattar, A.A.; Hopper, C. In Vivo Optical Coherence Tomography in Assessment of Suspicious Facial Lesions: A Prospective Study. *Photodiagn. Photodyn. Ther.* **2021**, *36*, 102493. [CrossRef] [PubMed]
- Olsen, J.; Gaetti, G.; Grandahl, K.; Jemec, G.B.E. Optical Coherence Tomography Quantifying Photo Aging: Skin Microvasculature Depth, Epidermal Thickness and UV Exposure. *Arch. Dermatol. Res.* **2022**, *314*, 469–476. [CrossRef]
- Mariia, K.; Arif, M.; Shi, J.; Song, F.; Chi, Z.; Liu, C. Novel Chitosan-Ulvan Hydrogel Reinforcement by Cellulose Nanocrystals with Epidermal Growth Factor for Enhanced Wound Healing: In Vitro and in Vivo Analysis. *Int. J. Biol. Macromol.* **2021**, *183*, 435–446. [CrossRef] [PubMed]
- Roberts, M.S.; Cheruvu, H.S.; Mangion, S.E.; Alinaghi, A.; Benson, H.A.E.; Mohammed, Y.; Holmes, A.; van der Hoek, J.; Pastore, M.; Grice, J.E. Topical Drug Delivery: History, Percutaneous Absorption, and Product Development. *Adv. Drug Deliv. Rev.* **2021**, *177*, 113929. [CrossRef]



7. Therkildsen, P.; Hædersdal, M.; Lock-Andersen, J.; Olivarius, F.D.F.; Poulsen, T.; Wulf, H.C. Epidermal Thickness Measured by Light Microscopy: A Methodological Study. *Ski. Res. Technol.* **1998**, *4*, 174–179. [CrossRef] [PubMed]
8. van Mulder, T.J.S.; de Koeijer, M.; Theeten, H.; Willems, D.; van Damme, P.; Demolder, M.; de Meyer, G.; Beyers, K.C.L.; Vankerckhoven, V. High Frequency Ultrasound to Assess Skin Thickness in Healthy Adults. *Vaccine* **2017**, *35*, 1810–1815. [CrossRef]
9. Czekalla, C.; Schönborn, K.H.; Lademann, J.; Meinke, M.C. Noninvasive Determination of Epidermal and Stratum Corneum Thickness in Vivo Using Two-Photon Microscopy and Optical Coherence Tomography: Impact of Body Area, Age, and Gender. *Skin Pharmacol. Physiol.* **2019**, *32*, 142–150. [CrossRef] [PubMed]
10. Yang, Z.; Shang, J.; Liu, C.; Zhang, J.; Liang, Y. Identification of Oral Cancer in OCT Images Based on an Optical Attenuation Model. *Lasers Med. Sci.* **2020**, *35*, 1999–2007. [CrossRef]
11. Welzel, J. Optical Coherence Tomography in Dermatology: A Review. *Ski. Res. Technol.* **2001**, *7*, 1–9. [CrossRef]
12. Summerfield, A.; Meurens, F.; Ricklin, M.E. The Immunology of the Porcine Skin and Its Value as a Model for Human Skin. *Mol. Immunol.* **2015**, *66*, 14–21. [CrossRef] [PubMed]
13. Khiao In, M.; Richardson, K.C.; Loewa, A.; Hedtrich, S.; Kaessmeyer, S.; Plendl, J. Histological and Functional Comparisons of Four Anatomical Regions of Porcine Skin with Human Abdominal Skin. *J. Vet. Med. Ser. C Anat. Histol. Embryol.* **2019**, *48*, 207–217. [CrossRef] [PubMed]
14. Brożyna, A.; Wasilewska, K.; Węsierska, K.; Barbara, W.; Chwirot, B.W. Porcine Skin as a Model System for Studies of Adverse Effects of Narrow-Band UVB Pulses on Human Skin Porcine Skin. *J. Toxicol. Environ. Health Part A* **2009**, *72*, 789–795. [CrossRef]
15. Vlig, M.; Boekema, B.K.H.L.; Ulrich, M.M.W. Porcine Models. In *Biomaterials for Skin Repair and Regeneration*; Garcia-Gareta, E., Ed.; Woodhead Publishing: Cambridge, UK, 2019; pp. 297–330. [CrossRef]
16. Huang, D.; Swanson, E.A.; Lin, C.P.; Schuman, J.S.; Stinson, W.G.; Chang, W.; Hee, M.R.; Flotte, T.; Gregory, K.; Puliafito, C.A.; et al. Optical Coherence Tomography. *Science* **1991**, *254*, 1178–1180. [CrossRef]
17. Schneider, H.; Park, K.-J.; Häfer, M.; Rüger, C.; Schmalz, G.; Krause, F.; Schmidt, J.; Ziebolz, D.; Haak, R. Dental Applications of Optical Coherence Tomography (OCT) in Cariology. *Appl. Sci.* **2017**, *7*, 472. [CrossRef]
18. Wan, B.; Ganier, C.; Du-Harpur, X.; Harun, N.; Watt, F.M.; Patalay, R.; Lynch, M.D. Applications and future directions for optical coherence tomography in dermatology. *Br. J. Dermatol.* **2020**, *184*, 1014–1022. [CrossRef] [PubMed]
19. Saleah, S.-A.; Lee, S.-Y.; Wijesinghe, R.E.; Lee, J.; Seong, D.; Ravichandran, N.K.; Jung, H.-Y.; Jeon, M.; Kim, J. Optical signal intensity incorporated rice seed cultivar classification using optical coherence tomography. *Comput. Electron. Agric.* **2022**, *198*, 107014. [CrossRef]
20. Gabriele, M.L.; Wollstein, G.; Ishikawa, H.; Kagemann, L.; Xu, J.; Folio, L.S.; Shuman, J.S. Optical Coherence Tomography: History, Current Status, and Laboratory Work. *Investig. Ophthalmol. Vis. Sci.* **2011**, *52*, 2425–2436. [CrossRef]
21. Wang, C.; Xia, X.; Tian, B.; Zhou, S. Comparison of Fourier-Domain and Time-Domain Optical Coherence Tomography in the Measurement of Thinnest Corneal Thickness in Keratoconus. *J. Ophthalmol.* **2015**, 402925. [CrossRef]
22. Liu, P. *Optical Coherence Tomography for Material Characterization*; Nanjing University of Aeronautics and Astronautics: Nanjing, China, 2014.
23. Galvez, M.C.; Vallar, E.; Shiina, T.; Macalalad, E.; Mandia, P. Time-Domain Optical Coherence Tomography System for Determining the Extinction Coefficient and Group Refractive Index of Gelatin-based Skin Phantoms. *Sci. Technol. Indones.* **2021**, *6*, 319–327. [CrossRef]
24. Shiina, T.; Moritani, Y.; Ito, M.; Okamura, Y. Long-Optical-Path Scanning Mechanism for Optical Coherence Tomography. *Appl. Opt.* **2003**, *42*, 3795–3799. [CrossRef] [PubMed]
25. Mandia, P.F.; Vallar, E.A.; Shiina, T.; Macalalad, E.P.; Galvez, M.C.D. Time-domain optical coherence tomography and gelatin-based skin phantom as training tools for venipuncture. *J. Phys. Conf. Ser.* **2020**, *1593*, 012032. [CrossRef]
26. Galvez, M.C.D.; de lara, R.; Mandia, P.; Vallar, E.; Macalalad, E.; Shiina, T. Leaf Structure and Attenuation Coefficients of Citrofornetella Microcarpa Leaves Using a Portbale TD-OCT System. *ECS Trans.* **2022**, *107*, 2243–2253. [CrossRef]
27. Gong, P.; Almasian, M.; Soest, G.; de Bruin, D.M.; van Leeuwen, T.G.; Sampson, D.D.; Faber, D.J. Parametric imaging of attenuation by optical coherence tomography: Review of models, methods, and clinical translation. *J. Biomed. Opt.* **2020**, *25*, 040901. [CrossRef] [PubMed]
28. Yang, H.; Zheng, G.; Li, M. A Discussion of Noise in Dynamic Light Scattering for Particle Sizing. *Part. Part. Syst. Charact.* **2008**, *25*, 406–413. [CrossRef]
29. Huang, R.; Zhang, Q.; Qi, P.; Liu, W. Concentration Measurement of Uniform Particles Based on Backscatter Sensing of Optical Fibers. *Water* **2019**, *11*, 1955. [CrossRef]
30. Faber, D.J.; van der Meer, F.J.; Aalders, M.C.G.; van Leeuwen, T.G. Quantitative Measurement of Attenuation Coefficients of Weakly Scattering Media Using Optical Coherence Tomography. *Opt. Express* **2004**, *12*, 4353. [CrossRef]

**Disclaimer/Publisher’s Note:** The statements, opinions and data contained in all publications are solely those of the individual author(s) and contributor(s) and not of MDPI and/or the editor(s). MDPI and/or the editor(s) disclaim responsibility for any injury to people or property resulting from any ideas, methods, instructions or products referred to in the content.



# Transfer Learning-Based Anomaly Detection System for Autonomous Vehicle <sup>†</sup>

Md. Humayun Kabir <sup>1,2,\*</sup>, Mohammad Nadib Hasan <sup>1</sup>, Ahmad <sup>3</sup> and Hassan Jaki <sup>1</sup>

<sup>1</sup> Department of Computer and Communication Engineering, International Islamic University Chittagong, Kumira Chattogram 4318, Bangladesh; nadibhasan@iiuc.ac.bd (M.N.H.); hassanjaki11@gmail.com (H.J.)

<sup>2</sup> Department of Electronics and Telecommunication Engineering, Chittagong University of Engineering and Technology (CUET), Chittagong 4349, Bangladesh

<sup>3</sup> Department of Electronics and Telecommunication Engineering, International Islamic University Chittagong, Kumira Chattogram 4318, Bangladesh; ahmadcse0@gmail.com

\* Correspondence: mdhkrabby@gmail.com; Tel.: +880-151-528-6984

<sup>†</sup> Presented at the 10th International Electronic Conference on Sensors and Applications (ECSA-10), 15–30 November 2023; Available online: <https://ecsa-10.sciforum.net/>.

**Abstract:** The advancements in technology have brought about significant changes in the automobile industry. A system that combines the control of a physical process with computing technology and communication networks is called a cyber–physical system (CPS). The enhancement of network communication has transitioned vehicles from purely mechanical to software-controlled technologies. The controller area network (CAN) bus protocol controls the communication network of autonomous vehicles. The convergence of technologies in autonomous vehicles (AVs) and connected vehicles (CVs) within Connected and Autonomous Vehicles (CAVs) leads to improved traffic flow, enhanced safety, and increased reliability. CAVs development and deployment have gained momentum, and many companies and research organizations have announced their initiatives and begun road trials. Governments worldwide have also implemented policies to facilitate and expedite the deployment of CAVs. Nevertheless, the issue of CAV cyber security has become a prevalent concern, representing a significant challenge in deploying CAVs. This study presents an intelligent cyber threat detection system (ICTDS) for CAV that utilizes transfer learning to detect cyberattacks on physical components of autonomous vehicles through their network infrastructure. The proposed security system was tested using an autonomous vehicle network dataset. The dataset was preprocessed and used to train and evaluate various pre-trained convolutional neural networks (CNNs), such as ResNet-50, MobileNetV2, AlexNet, GoogLeNet and YOLOV8. The proposed security system demonstrated exceptional performance, as demonstrated by its results in precision, recall, F1-score, and accuracy metrics. The system achieved an accuracy rate of 99.90%, indicating its high level of performance.

**Keywords:** autonomous vehicles; cyber–physical system; security; cyber-attacks; transfer learning

**Citation:** Kabir, M.H.; Hasan, M.N.; Ahmad; Jaki, H. Transfer Learning-Based Anomaly Detection System for Autonomous Vehicle. *Eng. Proc.* **2023**, *58*, 90. <https://doi.org/10.3390/ecsa-10-16248>

Academic Editor: Stefano Mariani

Published: 15 November 2023



**Copyright:** © 2023 by the authors. Licensee MDPI, Basel, Switzerland. This article is an open access article distributed under the terms and conditions of the Creative Commons Attribution (CC BY) license (<https://creativecommons.org/licenses/by/4.0/>).

## 1. Introduction

The emergence of connected and autonomous vehicles represents a shift towards a transportation system that utilizes intelligent automation and robust communication to replace traditional human-operated vehicles. These vehicles are designed to operate with the same level of intelligence, control, and agility as human drivers while minimizing the potential for errors in decision-making, making it the future of transportation [1]. AVs integrate advanced vehicle technologies to enable self-driving capabilities. AVs can perform complex functions, such as lane departure alerts, identification of traffic signs, and collision avoidance, which can decrease the burden on human drivers [2]. The increasing interest in autonomous vehicles has led to a proliferation of research and development efforts in the field, with various companies and organizations investing in developing autonomous vehicle technology. Furthermore, AVs can have a positive environmental

impact by decreasing energy consumption and air pollution. These vehicles are composed of intricate systems that necessitate advanced computing, sensing, actuation, networking, and communication technologies [3].

Initially, manual vehicles require additional connectivity to the exterior, making it challenging for hackers to attack, as they would need physical access to the vehicle. The researchers could control the vehicle through wired connections, such as altering the display dashboard, shutting down the engine, and interfering with steering. With the advancement of AV technology in recent years, vehicles are equipped with various sensors to aid human driving. Figure 1 shows the overview of CAV cyberattack AV systems [4].

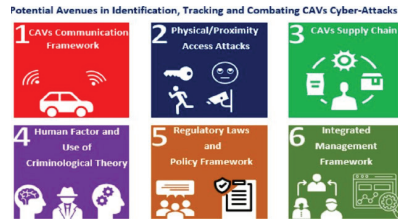


**Figure 1.** CAVs cyberattacks Holistic View.

The use of communication protocols is essential to guarantee the safety and stability of AVs. One commonly used protocol is CAN, which provides high-speed communication within the vehicle. Time-Triggered CAN (TTCAN) offers time-deterministic communication, an improvement from the basic CAN protocol. Local Interconnect Networks (LIN) connect low-cost sensors and actuators, providing a simple and economical communication solution [5]. FlexRay is a new protocol that offers high-speed and dependable communication for critical applications requiring real-time data transmission, like advanced driver assistance systems (ADASs). In autonomous vehicles, communication protocols such as CAN, TTCAN, LIN, and FlexRay are vital in addressing data transmission, real-time data analytics, bandwidth restrictions, privacy, and security [6]. The vulnerability of autonomous vehicles to security threats increases with their level of autonomy. The information from various control systems is transmitted to every node in the network through the Controller Area Network bus [7]. With data accessible to all nodes, it can expose the system to potential security risks from internal or external sources. Potential attack surfaces for AVs include the Airbag Electronic Control Unit (ECU), USB, Bluetooth, and the Vehicle Access System ECU. To ensure the safe and reliable operation of these vehicles, they must be equipped with advanced communication and sensing technology to counteract these potential threats [8].

Fully autonomous vehicles can carry out driving tasks and make instantaneous adjustments without requiring any input from the driver. The SAE has established a categorization of six levels to measure vehicle automation, taking into consideration factors such as the vehicle's ability to manage driving tasks and responses, detect objects and events, make corrections in case of system failures, and operate within specific domains. The responsibilities of the driver and the autonomous vehicle system vary with each level of automation, which can be seen in summary [9,10]:

**Level 0: Driver-Only Control:** At Level 0, the driver must handle all vehicle driving and control responsibilities. This includes being alert to their surroundings and responding to any events. If the system encounters any problems, it is up to the driver to fix the issue. This level does not specify any operational design domain.

**Level 1: Driver Assistance:** At Level 1 of automation, the vehicle is operated by collaborating with the driver and the system. The system can either control speed or direction, but not both. The driver is required to supervise the environment and respond to any situation. Additionally, if the system fails, the driver must control the vehicle. The operational design domain is also restricted to a small area at this level.

Level 2: Shared Control: At this level, the system is capable of controlling both the vertical and horizontal motions of the vehicle at the same time. However, the driver must still monitor the environment and take action if needed. In case of a system malfunction, the driver must regain vehicle control. The operational design domain is still limited at this level.

Level 3: Conditional Driving Automation: The system can control both longitudinal and lateral motion. It also monitors the environment and reacts to events and objects. If the system fails, the driver should be ready to respond to its request or take control of the vehicle. The operational design domain's extent is restricted at this level.

Level 4: Highly Automated Driving: The vehicle's system can manage both longitudinal and lateral driving tasks at the same time. The system is in charge of observing the surroundings and handling any events. If there is a system malfunction, the system must be able to recover without driver intervention. There are specific boundaries to the system's operating range at this level of automation.

Level 5: Complete Driving Automation: The vehicle can control both longitudinal and lateral driving tasks at the same time. The system is accountable for observing the environment and taking appropriate measures. In case of system failure, the vehicle's technology can recover without human intervention. This level of automation has no limitations in the operational design domain.

The vulnerability of CAVs to cyberattacks is amplified by their connectivity and autonomy capabilities when exchanging data with other vehicles and the environment. Autonomous vehicles face risks from cyberattacks such as cloning essential fobs, attacks on radars and telematics services, deception of sensors using ultrasonic or lidar technology, camera sensor attacks, and others. To counter these threats, a method has been proposed using a convolutional neural network (CNN) that has already been trained to detect cyberattacks on the connected physical parts of AVs through the CAN communication protocol. The technique employs transfer learning, a deep learning strategy that utilizes pre-trained models for various systems. This is important because it can be challenging and costly to gather enough data to train a model through traditional machine learning methods. The process of transfer learning involves adjusting a pre-trained model to a new and related model, enabling the model to learn from data from diverse domains [11,12].

This study proposes a solution for detecting cyberattacks on autonomous vehicles using a pre-trained CNN and the CAN communication protocol. The method consists of incorporating the CAN protocol into an AV simulation model that is built using Simulink from MathWorks. This model generates the dataset that is used to pre-train the CNN. The IIDS implemented uses four pre-trained networks and evaluates each network's performance. The results showed that the YOLOV8 network had the best performance, with an F1-score of 99.90%. The manuscript comprises four sections. The first part scrutinizes the latest studies on autonomous vehicle security. The second section delineates the research process, which includes integrating the AV-CPS. The third part presents the discoveries and debates, whereas the last segment concludes the paper.

## 2. Proposed Methodology

This study segment elaborates on the simulation methodology employed for analyzing autonomous vehicles. This section explains how the simulation of cyber-physical systems is incorporated to create the AV-CPS model shown in Figure 2. It also describes how data are collected from the AV-CPS simulation and discusses the application of this data in transfer learning.

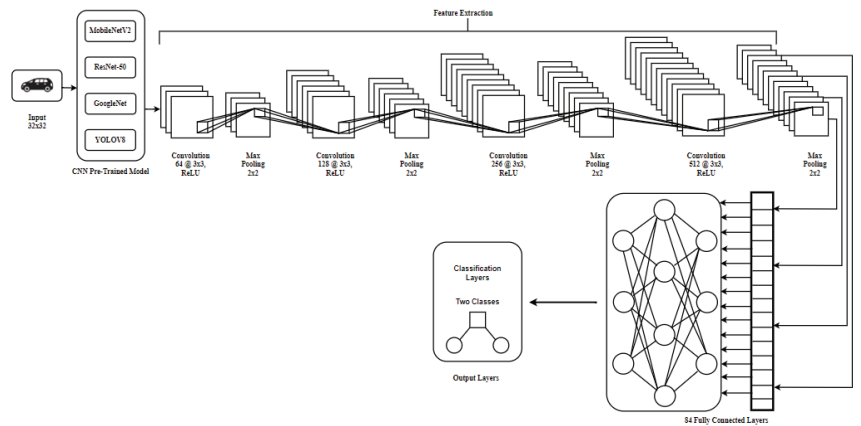


**Figure 2.** Architecture of the Proposed Pre-trained Models.

### 2.1. AV Simulation Scheme

The research employs a software-based simulation model to assess the performance of a self-driving car system before its deployment. The simulation model comprises an ego vehicle (i.e., the self-driving car) and a lead vehicle. The former utilizes an adaptive cruise controller (ACC) to maintain a safe distance from the latter while tracking its position and velocity. The simulation model integrates three crucial components: the ACC, a sensor to detect the position of both vehicles, and a sensor to record their velocity. The sensor measurements are relayed to the ACC, which subsequently regulates the speed of the vehicle in response to the movements of the lead vehicle.

### 2.2. CAN Communication Network

This study employed a simulation model of a self-driving car system to assess its performance before deployment. The simulation model for the AV-CPS was based on the ACC system, which consisted of an ACC, a position sensor, and a velocity sensor. However, there was no communication system component included in the model. To address this, the researchers used the Vehicle Network Toolbox on Simulink to implement a communication system based on the CAN protocol. The study focused on establishing the AV-CPS communication system using the CAN communication component to transmit and receive messages between the various elements. The signals were encapsulated and dispatched to the assigned CAN device, then received and decomposed into signals.

### 2.3. Autonomous Vehicle Cyber-Physical System

This study implemented an AV-CPS architecture to investigate the performance of the self-driving car system, which consisted of multiple components such as sensors, two CAN communication nodes, a controller, and actuators. The first communication node (Node A) receives and transmits signals such as the actual location, position, and speed of the ego and lead vehicles, as well as a constant time gap and desired speed. These signals are then used by the ACC to generate a control signal, which is sent to Node B. Node B then receives and transmits this control signal to the actuators, where it is converted into a mechanical movement that changes the speed of the vehicle. The entire process is repeated in a closed-loop simulation for a total of 81 s.

### 2.4. Generating Dataset

This research developed a cyber-physical system-based autonomous vehicle simulation, integrating a CAN communication system. The simulation model comprised a lead vehicle and a self-vehicle. The latter utilized sensors to monitor vehicles' position and velocity, maintaining a safe distance through the ACC. However, the researchers considered

a compromised communication node scenario where false data were inserted into the ego vehicle’s position sensor, causing the ACC to produce erroneous control signals. The data generated by the simulation was in a numerical format and consisted of five attributes, namely, the actual position and velocity of both vehicles and an anomaly detection label.

2.5. Transfer Learning

This section details the utilization of transfer learning in the research, which involves adapting pre-trained models to improve performance on a related task. This study utilized pre-trained models such as MobileNetV2, GoogLeNet, ResNet-18, and YOLOv8, all containing layers like Relu, Pooling, and Fully connected layers to ensure accurate image classification show in 3. These models have Relu, Pooling, and Fully connected layers to improve image classification. The final layer of each model has been modified to output only normal or anomaly categories. The dataset was preprocessed to be compatible with each CNN model. During AV-CPS simulation, feature responses were stored as numerical values in a matrix, which was reshaped from 1D to 2D. The resulting 2D matrix was saved as an image, and normal/anomaly images were stored separately for analysis.

3. Results and Discussion

This section covers the specifics of the experimentation, such as the tools and equipment employed to carry out the study. Additionally, the section will present and analyze the outcomes of the research. The study utilized Matlab and Simulink for experiments. Matlab is a programming language platform, whereas Simulink is a design platform based on Matlab. The AV simulation model was created using both Matlab and Simulink by MathWorks. The researchers used the Simulink network toolbox to integrate the CAN protocol component into the AV simulation. Matlab was used for implementing and evaluating pre-trained CNNs. A computer with a GPU was utilized for experiments to enhance performance and reduce computation time.

Figure 3 displays the overall steps taken in this research’s experiments. The initial stage involved importing a dataset into Matlab. The images were preprocessed by resizing them to comply with the input size requirements of pre-trained CNNs programmed to classify images as either normal or anomalous. The dataset contained two folders, one with normal images and the other with anomalous images. It was split into 70% for training and 30% for testing and validation. The dataset included 20,000 images, half normal and the other half anomalous. To ensure the training process’s accuracy, a 5-fold cross-validation technique was employed, and the expected output of each model was either normal, indicating no attack, or anomalous, indicating that an attack had occurred.

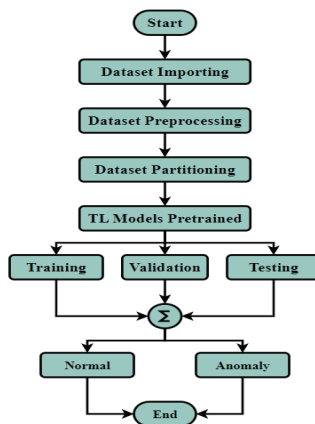


Figure 3. Research Experiment Steps.

The study evaluated pre-trained CNN model performance using several metrics, including precision, recall, F1-score, and accuracy classification. The accuracy of the models was determined by calculating true positive (TP), false positive (FP), false negative (FN), and true negative (TN). Table 1 displays the accuracy of the models, with YOLOV8 performing the best. Although all models had 100% precision, recall values ranged from 98.65% to 99.00%, indicating the misclassification of some anomalous images as normal.

**Table 1.** Performance Comparison of Pre-trained Model Accuracy.

Pre-Trained Model	Precision	Recall	F1 Score	Accuracy
ResNet-50	100%	98.86%	99.40%	99.40%
MobileNetV2	100%	98.65%	99.35%	99.35%
AlexNet	100%	98.90%	99.45%	99.45%
GoogLeNet	100%	98.96%	99.50%	99.50%
YOLOV8	100%	99.00%	99.90%	99.90%

To substantiate our findings, we conducted a comparative analysis of the performance outcomes of our research about existing intrusion detection system approaches employed in autonomous vehicle systems. In general, pre-trained convolutional neural networks, such as those discussed in research papers like ResNet-50, MobileNetV2, AlexNet, GoogLeNet, and YOLOV8, exhibited superior performance compared to alternative models, such as artificial neural networks (ANN) and Bayesian networks, as indicated in Table 1.

#### 4. Conclusions

The research proposed an IIDS that uses the CAN to identify cyberattacks on the physical components of AVs. The CAN was included in an AV simulation by MathWorks to illustrate the CPS concept, resulting in an AV-CPS. The AV-CPS created the dataset, which was transformed into images and inputted into pre-trained CNNs such as ResNet-50, MobileNetV2, AlexNet, GoogLeNet, and YOLOV8. The performance of each network was assessed and compared, and YOLOV8 had the best performance, with an F1 score of 99.90%. The proposed system's block architecture makes it adaptable and resilient to other CPS frameworks. The study suggested extending the AV-CPS system architecture to other CPS domains such as smart grids and drones.

**Author Contributions:** Conceptualization, M.H.K. and M.N.H.; methodology, M.H.K. and A.; software, M.N.H., H.J., A. and M.H.K.; formal analysis, M.H.K., M.N.H., A. and H.J.; writing—original draft preparation, M.H.K. and M.N.H.; writing—review and editing, M.H.K., A. and M.N.H.; supervision, M.H.K. All authors have read and agreed to the published version of the manuscript.

**Funding:** This research received no external funding.

**Institutional Review Board Statement:** Not applicable.

**Informed Consent Statement:** Not applicable.

**Data Availability Statement:** The raw data supporting the conclusions of this article will be made available by the authors on request.

**Conflicts of Interest:** The authors declare no conflicts of interest.

#### References

1. Park, K.J.; Zheng, R.; Liu, X. Cyber-physical systems: Milestones and research challenges. *Comput. Commun.* **2012**, *36*, 1–7. [CrossRef]
2. Rajkumar, R.; Lee, I.; Sha, L.; Stankovic, J. Cyber-physical systems: The next computing revolution. In Proceedings of the 47th Design Automation Conference, Anaheim, CA, USA, 13–18 June 2010.
3. Kim, S.; Park, K.-J. A Survey on Machine-Learning Based Security Design for Cyber-Physical Systems. *Appl. Sci.* **2021**, *11*, 5458. [CrossRef]

4. Aldhyani, T.H.H.; Alkahtani, H. Attacks to Automotous Vehicles: A Deep Learning Algorithm for Cybersecurity. *Sensors* **2022**, *22*, 360. [CrossRef] [PubMed]
5. Wang, Z.; Wei, H.; Wang, J.; Zeng, X.; Chang, Y. Security Issues and Solutions for Connected and Autonomous Vehicles in a Sustainable City: A Survey. *Sustainability* **2022**, *14*, 12409. [CrossRef]
6. NHTSA. SAE Define 5 Levels of Vehicle Automation. Available online: <https://www.sema.org/sema-enews/2017/11/ettn-tech-alert-nhtsa-sae-define-5-levels-of-vehicle-automation> (accessed on 19 October 2023).
7. Petit, J.; Shladover, S.E. Potential cyberattacks on automated vehicles. *IEEE Trans. Intell. Transp. Syst.* **2014**, *16*, 546–556. [CrossRef]
8. Parkinson, S.; Ward, P.; Wilson, K.; Miller, J. Cyber threats facing autonomous and connected vehicles: Future challenges. *IEEE Trans. Intell. Transp. Syst.* **2017**, *18*, 2898–2915. [CrossRef]
9. Lokman, S.F.; Othman, A.T.; Abu-Bakar, M.H. Intrusion detection system for automotive Controller Area Network (CAN) bus system: A review. *EURASIP J. Wirel. Commun. Netw.* **2019**, *2019*, 184. [CrossRef]
10. Young, C.; Zambreno, J.; Olufowobi, H.; Bloom, G. Survey of automotive controller area network intrusion detection systems. *IEEE Des. Test* **2019**, *36*, 48–55. [CrossRef]
11. Cao, Y.; Xiao, C.; Cyr, B.; Zhou, Y.; Park, W.; Rampazzi, S.; Chen, Q.A.; Fu, K.; Mao, Z.M. Adversarial Sensor Attack on LiDAR-based Perception in Autonomous Driving. In Proceedings of the 2019 ACM SIGSAC Conference on Computer and Communications Security (CCS '19), London, UK, 11–15 November 2019; Association for Computing Machinery: New York, NY, USA, 2019; pp. 2267–2281. [CrossRef]
12. Stottelaar, B.G. Practical Cyber-Attacks on Autonomous Vehicles. Master's Thesis, University of Twente, Enschede, The Netherlands, 2015.

**Disclaimer/Publisher's Note:** The statements, opinions and data contained in all publications are solely those of the individual author(s) and contributor(s) and not of MDPI and/or the editor(s). MDPI and/or the editor(s) disclaim responsibility for any injury to people or property resulting from any ideas, methods, instructions or products referred to in the content.





Proceeding Paper

# Development of an Embedded Device for Quantifying and Recording Daily Standing Profiles in Individuals with Lower Limb Motor Impairment Using an Assistive Standing Mobile Device<sup>†</sup>

Kim-Ming Tsoi, King-Pong Yu<sup>\*</sup>, Chu-Kei Ng, Suk-Mun Wong, Riggs Ng, Tsz-Yan Yeung, Ka-Leung Chan and Wai-Ling Ma

Community Rehabilitation Service Support Center, Hospital Authority, Hong Kong; tkm700@ha.org.hk (K.-M.T.); nck004@ha.org.hk (C.-K.N.); wsm712@ha.org.hk (S.-M.W.); riggs.ng@ha.org.hk (R.N.); ty.yeung1@ha.org.hk (T.-Y.Y.); ckl892@ha.org.hk (K.-L.C.); wlma@ha.org.hk (W.-L.M.)

<sup>\*</sup> Correspondence: ykp587@ha.org.hk

<sup>†</sup> Presented at the 10th International Electronic Conference on Sensors and Applications (ECSA-10), 15–30 November 2023; Available online: <https://ecsa-10.sciforum.net/>.

**Abstract:** The present study introduces an innovative device designed to objectively record and quantify the daily standing profiles of individuals with lower limb motor impairment. The device is specifically developed to be seamlessly embedded onto the standing platform of an assistive standing mobile device, without compromising its structural integrity or functional capabilities. The primary objective of this device is to provide objective evidence of patients' standing activities within their home environment, thus facilitating the assessment of patient performance and usage. The embedded device captures and stores comprehensive data regarding the duration, frequency, and interval of patients' standing sessions. Furthermore, the device integrates wireless connectivity to facilitate data transfer and analysis. The development process involved close collaboration between rehabilitation engineers and physiotherapists to ensure optimal functionality, user-friendliness, and unobtrusiveness. Extensive testing and validation procedures were conducted to assess the reliability, validity, and feasibility of the device. The results demonstrate its high accuracy and reliability in capturing and quantifying standing profiles. The proposed device addresses a critical need within the field of rehabilitation, providing clinicians, researchers, and funding organizations with objective evidence of patients' standing abilities and adherence to rehabilitation protocols. This evidence-based approach has the potential to enhance clinical decision making, improve treatment outcomes, and secure financial support for patients in need of assistive standing mobile devices. In conclusion, the embedded device presented in this study offers a novel and practical solution for quantifying and recording the daily standing profiles of individuals with lower limb motor impairment. By providing objective evidence of patients' standing activities, this device has the potential to advance the field of rehabilitation and facilitate improved access to assistive standing mobile devices for those in need.

**Keywords:** tele-monitoring; rehabilitation; standing training; patient compliance

**Citation:** Tsoi, K.-M.; Yu, K.-P.; Ng, C.-K.; Wong, S.-M.; Ng, R.; Yeung, T.-Y.; Chan, K.-L.; Ma, W.-L.

Development of an Embedded Device for Quantifying and Recording Daily Standing Profiles in Individuals with Lower Limb Motor Impairment Using an Assistive Standing Mobile Device. *Eng. Proc.* **2023**, *58*, 91. <https://doi.org/10.3390/ecsa-10-16011>

Academic Editor: Francisco Falcone

Published: 15 November 2023



**Copyright:** © 2023 by the authors. Licensee MDPI, Basel, Switzerland. This article is an open access article distributed under the terms and conditions of the Creative Commons Attribution (CC BY) license (<https://creativecommons.org/licenses/by/4.0/>).

## 1. Introduction

### 1.1. Background

Lower Limb Motor Impairment is one type of disability in which individuals lose part or whole coordination of lower limbs caused by stroke, spinal cord injuries, or cerebral palsy. Patients experiencing this medical condition have to deal with difficulty in standing and walking. In the scope of lower limb motor training, robotic lower limb exoskeletons are commonly adopted in rehabilitation clinics for user-driven or passive gait training to enhance proper gait patterns, especially in young patients [1]. For senior adults and

patients with upper body weakness, exoskeletons are not applicable due to their difficulties in maintaining body balance in upright posture. Although those patients are prohibited from walking due to restriction in operating lower limb exoskeletons, standing training is physiologically beneficial to reduce the risk of pressure sores, improve gastrointestinal function, strengthen bone density, etc. [2]. To help patients perform standing training, numerous standing training aids have been launched in the market such as standing frames and assistive standing mobile devices, robotic devices assisting patients in performing standing and sitting.

Traditional facility-based rehabilitation models provide important clinical supervision but can be resource intensive [3]. Accordingly, community-based rehabilitation has emerged as a cost-effective alternative to promote patient independence and functional recovery in real-world environments [4]. A recent study showed that home-based rehabilitation can effectively enhance functional and emotional recovery of various disabilities, including stroke and spinal cord injuries [5–7]. Well-planned remote rehabilitation programs have become acceptable by patients as they reduce their time in traffic and follow-up consultations, especially after the pandemic period. Therefore, home-based rehabilitation is not only beneficial to patients but is also treated as an alternative to traditional clinic-based therapies due to the reduced cost, time, manpower and capital.

However, home-based rehabilitation is not meant to be a let-go policy, and delivering rehabilitation programs remotely presents challenges in objectively monitoring patient compliance. According to the National Library of Medicine, about 40% of patients failed to follow the medical advice, including prescribed treatments [8]. To be a responsible healthcare service provider, the procedure and progress of rehabilitation programs are required to be monitored in order to understand the situation of patients. Phone interviews and home visits are currently the most common methods to monitor the progress of recovery. Patients may fail to accurately report participation in training by lying, false memory, or memory loss. The progress of the rehabilitation programs is hindered, which possibly causes deterioration of lower limb ability and development of physiological disorders such as osteoporosis or kidney malfunction in future.

Therefore, in this study, we propose the implementation of a Standing Tracking system to tele-monitor the rehabilitation progress of patients who are prescribed standing training programs with assistive standing mobile devices. An additional embedded device was developed to record the time spent in standing training and to then upload standing data to a cloud spreadsheet. To facilitate the upload process, a 4G mobile data communication module is integrated to the system, allowing data transfer in residential and community environments. When patients step on the platform of the assistive standing device, the Standing Tracking system is started.

### *1.2. Related Work*

There is a lack of specific research on the development of compliance monitoring about standing tasks with assistive standing devices. However, previous review studies have emphasized major considerations about the development and application of IoT services in rehabilitation [9]. Researchers have proposed that, in terms of system design, the ease of the system should be first considered since the tracking system is aims to provide timely feedback to patients [10]. Meanwhile, the system should be compatible with problems to be solved and patients with different proficiency in technology in order to avoid overuse of technology.

Devices and equipment were also recommended to be considered according to the system design, including the device for collecting, processing, and sharing data and information. Communication protocol was required to be considered according to the range of data transmission [11]. Additionally, understanding the methodology of the rehabilitation program was needed to develop an appropriate IoT system in order to promote significant system usability [12]. The studies also proposed that sensors should be included in IoT systems to capture the movement of patients. However, sensors should give minimum

influence on patients' actions. Sensors are expected to be ignored by patients even if sensors are detecting the activities of rehabilitation training [9].

## 2. Method and Material

The Standing Tracking system consists of 4 main components (Figure 1), including the microcontroller unit, 4G module, inertia measuring unit (IMU), and foot switch module. When the patient's weight is applied to the foot switch, the microcontroller would be powered up, as well as the 4G module and IMU. The 4G module starts initialization to connect to the 4G mobile data network. While the IMU is initialized to acquire the tilting angle. Then, the tilting angles data are uploaded to a cloud-based spreadsheet and are available to be reviewed by therapists.

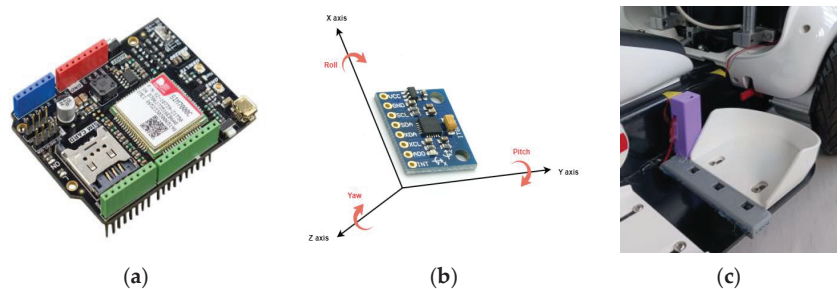


**Figure 1.** 4G module (a), inertia measuring unit (IMU) module used in the tracking device (b), and foot switch module (c) of the proposed Standing Tracking device.

### 2.1. Components

#### 2.1.1. Microcontroller Unit

In the tracking system, Arduino Mega 2560 (Arduino, Ivrea, Italy) is used as a microcontroller unit which distributes power to, initializes, and communicates with peripheral devices. The embedded microprocessor is ATmega2560 (Microchip Technology, Chandler, AZ, USA), which can operate with 16 MHz in maximum clock speed. The microprocessor also includes 8 KB of RAM, allowing processing of 2000 floating-point numbers per operation, which suits for acquiring 3-axis acceleration measurements from the IMU. A lithium rechargeable battery module is used as a power source for supplying the microcontroller unit. The program for data acquisition and transmission is flashed in the Microcontroller unit for operation.

#### 2.1.2. 4G Module

A 4G module is required to establish the connection between the cloud service and local data acquisition device. SIM7000C NB-IOT shield (DFROBOT) is used in the tracking system because it is compatible with the frequency band used for telecommunication in the Asia region and it is compatible with the microcontroller unit for data flow and operation. Hayes AT command set (AT command) is the major command language for operation, which can be sent by the microcontroller unit through Universal Asynchronous Receiver/Transmitter (UART) protocol. Meanwhile, a SIM Card with registered 4G mobile data service is required for activating the module.

#### 2.1.3. Inertia Measuring Unit (IMU)

Besides standing training, general assistive standing mobile devices offer sitting assistance to patients to avoid exhaustion. Therefore, the tilting angle of the upper body arm is a necessary indicator of standing. In the tracking system, a GY-521 6-axis IMU is included for tilting angle measurement (Figure 2). The tilting angle is derived from measuring 3 axes translational acceleration values. In terms of geometry, the tilting angle

is described by pitch angle, which is defined as the angle between the Z-axis and axis of gravity. The conversion of pitch angle and linear acceleration is

$$\text{Pitch angle} = \tan^{-1} \frac{\sqrt{A_x^2 + A_y^2}}{A_z} \quad (1)$$

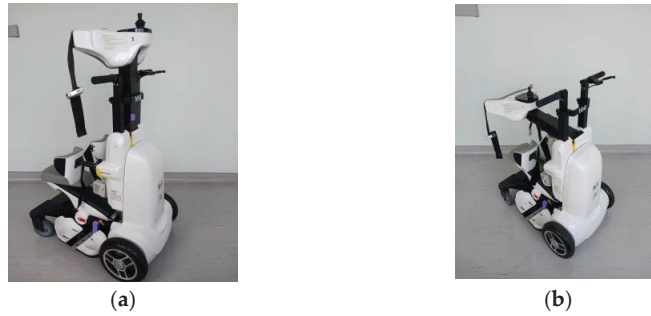


**Figure 2.** IMU integrated in assistive standing mobile device to measure the angle of the supporting arm. The device offers sitting mode (a) and standing mode (b).

The conversion is only valid if gravity is the only acceleration exerted on the IMU. Since standing mobile devices are prescribed for standing training only, angle calculation during driving, vibration, or collisions will be neglected.

#### 2.1.4. Foot Switch Module

The foot switch module, installed near the standing platform, is used to trigger the tracking device. The module consists of 2 ends, which are connected to the power source and power input pin of the Arduino Mega 2560, respectively. When patients are shifted to standing mobile devices, the patients' weight is applied on the foot switch module, and the Arduino Mega 2560 is powered on. For effectively capturing the applied weight, the foot switch module includes an array of mechanical switches which are connected in parallel. When either one or more switches are pressed, the tracking device will be powered on.

#### 2.1.5. Power Module

To power up the tracking device, 2 parallel connected 18,650 Lithium rechargeable batteries (2400 mAh at 3.7 V in total) are used as sources of power. A DC-DC transformer is installed to step up the supply voltage to 9 V for the input of the microcontroller unit and 4G module. The device consumes 9 V 100 mA in the data acquisition and processing period (80% time of cycle in average), while it consumes 9 V 140 mA while sending HTTP requests with the 4G module (20% time of cycle in average). Battery discharging tests have been conducted, and it is observed that 6 h of continuous usage is supported by the power module. For convenience of patients and caregivers, the battery module is charged by a 5 V DC power supply, which is common in domestic chargers for smartphones.

### 2.2. Mechanism

To start the standing training, the patient steps on the standing platform as well as the foot switch module. The battery module then powers on the microcontroller unit and 4G module. The Microcontroller unit sends AT commands to the 4G module to search for and register the mobile data station according to the mobile data service provider.

Meanwhile, the IMU is initiated to continuously acquire the 3 axes of acceleration data and computes the pitch angle according to Formula (1). The microcontroller unit then commands the 4G module to a HTTP POST request, which includes pitch angle data in the form of the JSON structure, and sends this to webhook. Once the request is received, webhook can automatically relay the data and additional timestamps to the

cloud spreadsheet. By using this network pathway, all data are directly streamed to a cloud spreadsheet and no local data storage is included in the system (Figure 3). Since all the configurations are performed before intervention, no extra settings are required after installation and distribution of the tracking device.



**Figure 3.** Mechanism of the proposed Standing Tracking device.

### 2.3. Data Validation

Data validation is crucial in tele-monitoring systems since it serves as an indicator of data corruption. It is expected that the value of IMU measurement is in the range of 0–90°, which is the range of movement of the upper body arm of the assistive standing mobile device. Therefore, any values out of this range or null values would be considered invalid data. As a result, corrective maintenance would be conducted once null values are received in order to reduce the disturbance of the rehabilitation program.

## 3. Conclusions and Discussion

The main contribution of this study is the development of a standing tracking system integrated with assistive standing mobile devices and the establishment of a connection between the system and cloud spreadsheet. The proposed system adopts the idea of the Internet-of-Things (IoT), providing a tele-monitoring function for device utilization and compliance of patients with prescribed home-based rehabilitation training. The system provides objective data for healthcare professionals to understand the progress of rehabilitation programs, and instant feedback can also be provided to patients as encouragement. Additionally, there are no extra operation requirements for the tracking device except recharging the battery module, which suits patients with different levels of proficiency in technology and reduces the risk of operation failure. The ultimate goal of this research is to enhance the connection among the assistive rehabilitation devices and the internet, adapting the IoT on medical devices to promote tele-healthcare and rehabilitation near residential communities.

### 3.1. Compliance of Prescribed Intervention

An effective rehabilitation program requires cooperation between patients and healthcare professionals. On the one hand, healthcare professionals have to provide adequate instruction and feedback to patients, while on the other hand, patients have to follow those instructions and perform the corresponding exercises. By installing the tracking device system, the usage will be comprehensively uploaded to the cloud spreadsheet, which can significantly improve the efficiency of data collection and eliminate human error during progress evaluation. With accurately collected data, more appropriate interventions can be provided to patients.

### 3.2. Privacy

Privacy is a major concern of patients or caregivers when adopting tele-monitoring systems. To solve this conflict, clinical professions should regularly share the standing records with patients and caregivers accordingly. Therapists can illustrate the progress and improvement using the acquired data to patients as positive feedback, which can pin a virtual target on patients psychologically. It is important to note that patient data will not be streamed to the cloud. Only standing profile information, such as duration and standing angle, will be accessible on the cloud. To maintain confidentiality, each patient

will be assigned a unique code, allowing us to match their demographic information at the backend.

### 3.3. Accessibility

The intended users of the device are individuals with lower limb motor impairment who are participating in rehabilitation training, particularly standing exercises prescribed by clinical professionals. This device serves as tele-rehabilitation equipment capable of monitoring patient compliance and capturing their standing profile over a specified period.

## 4. Limitation and Future Development

The foot switch module is a binary sensation module which considers only whether patients are performing standing training with assistive standing mobile devices. To obtain a comprehensive profile of the standing rehabilitation program, the distribution of weight bearing is also a key feature for indicating the quality of standing training. Uneven distribution of weight causes unequal force acting on tissues due to gravity, which causes extra pain, deformity, and contracture [4]. Therefore, a pressure sensor will be considered as an additional sensor in future improved versions, which could provide a description of the weight bearing symmetry. Feedback about symmetric standing posture would be available for patients in order to reduce the risk of injury and bone deformities.

Apart from additional pressure sensors, future work will also include recruiting patients with lower limb impairment to validate the standing tracker tele-monitoring system. Representing a major distribution of lower limb impairment, the stroke group will be the first stage of pilot study and it will then expand to other groups such as those with spinal cord injury. In preparation for the upcoming pilot trial involving patients, a formal research study will be conducted. Ethical approval will be sought from the hospital ethics committee to ensure compliance.

**Author Contributions:** Conceptualization, K.-M.T., K.-P.Y., C.-K.N. and S.-M.W.; methodology, K.-M.T. and K.-P.Y.; software, K.-M.T. and K.-P.Y.; resources, K.-P.Y. and K.-L.C.; data curation, K.-M.T. and K.-P.Y.; writing—original draft preparation, K.-M.T. and K.-P.Y.; writing—review and editing, K.-M.T.; visualization, K.-M.T.; supervision, K.-P.Y., K.-L.C. and W.-L.M.; project administration, K.-M.T., R.N. and T.-Y.Y. All authors have read and agreed to the published version of the manuscript.

**Funding:** This research received no external funding.

**Informed Consent Statement:** The authors affirm the work's originality and confirms that consent was obtained for the inclusion of the patient's photograph.

**Data Availability Statement:** The raw data supporting the conclusions of this article will be made available by the authors on request.

**Acknowledgments:** The study was supported by the Hospital Authority Community Rehabilitation Service Support Center (CRSSC).

**Conflicts of Interest:** The authors declare no conflict of interest.

## References

1. Sarajchi, M.; Sirlantzis, K. Design and Control of a Single-Leg Exoskeleton with Gravity Compensation for Children with Unilateral Cerebral Palsy. *Sensors* **2023**, *23*, 6103. [CrossRef] [PubMed]
2. Alekna, V.; Tamulaitiene, M.; Sinevicius, T.; Juocevicius, A. Effect of weight-bearing activities on bone mineral density in spinal cord injured patients during the period of the first two years. *Spinal Cord* **2008**, *46*, 727–732. [CrossRef] [PubMed]
3. Alfano, C.M.; Cheville, A.L.; Mustian, K. Developing high-quality cancer rehabilitation programs: A timely need. *Am. Soc. Clin. Oncol. Educ. Book* **2016**, *36*, 241–249.
4. Martelli, M.F.; Zasler, N.D.; Tiernan, P. Community based rehabilitation: Special issues. *Neuro Rehabil.* **2012**, *31*, 3–18. [CrossRef] [PubMed]
5. Rodby-Bousquet, E.; Agustsson, A. Postural Asymmetries and Assistive Devices Used by Adults with Cerebral Palsy in Lying, Sitting, and Standing. *Front. Neurol.* **2021**, *12*, 758706. [CrossRef] [PubMed]
6. Allen, L.; Richardson, M.; McIntyre, A.; Janzen, S.; Meyer, M.; Ure, D.; Willems, D.; Teasell, R. Community stroke rehabilitation teams: Providing home-based stroke rehabilitation in Ontario, Canada. *Can. J. Neurol. Sci.* **2014**, *41*, 697–703. [CrossRef] [PubMed]

7. Rezaei, M.; Sharifi, A.; Vaccaro, A.; Rahimi-Movaghar, V. Home-Based Rehabilitation Programs: Promising Field to Maximize Function of Patients with Traumatic Spinal Cord Injury. *Asian J. Neurosurg.* **2019**, *14*, 634–640. [CrossRef] [PubMed]
8. Martin, L.R.; Williams, S.L.; Haskard, K.B.; Dimatteo, M.R. The challenge of patient adherence. *Ther. Clin. Risk Manag.* **2005**, *1*, 189–199. [PubMed]
9. Camara Gradim, L.C.; Archanjo Jose, M.; Marinho Cezar da Cruz, D.; de Deus Lopes, R. IoT Services and Applications in Rehabilitation: An Interdisciplinary and Meta-Analysis Review. *IEEE Trans. Neural Syst. Rehabil. Eng. A Publ. IEEE Eng. Med. Biol. Soc.* **2020**, *28*, 2043–2052. [CrossRef] [PubMed]
10. Fan, Y.J.; Yin, Y.H.; Da Xu, L.; Zeng, Y.; Wu, F. IoT-based smart rehabilitation system. *IEEE Trans. Ind. Inform.* **2014**, *10*, 1568–1577.
11. Škraba, A.; Koložvari, A.; Kofjač, D.; Stojanović, R. Prototype of speech controlled cloud based wheelchair platform for disabled persons. In Proceedings of the 2014 3rd Mediterranean Conference on Embedded Computing (MECO), Budva, Montenegro, 15–19 June 2014; IEEE: Piscataville, NJ, USA, 2014; pp. 162–165.
12. Chiuchisan, I.U.L.I.A.N.A.; Geman, O.A.N.A. An approach of a decision support and home monitoring system for patients with neurological disorders using internet of things concepts. *WSEAS Trans. Syst.* **2014**, *13*, 460–469.

**Disclaimer/Publisher’s Note:** The statements, opinions and data contained in all publications are solely those of the individual author(s) and contributor(s) and not of MDPI and/or the editor(s). MDPI and/or the editor(s) disclaim responsibility for any injury to people or property resulting from any ideas, methods, instructions or products referred to in the content.

# Design, Fabrication and Characterization of a Wideband Metamaterial Absorber for THz Imaging <sup>†</sup>

Zeynab Alipour <sup>1,\*</sup>, Seyed Iman Mirzaei <sup>2</sup> and Mehdi Fardmanesh <sup>1</sup>

<sup>1</sup> Department of Electrical Engineering, Sharif University of Technology, Tehran 1458889694, Iran; fardmanesh@sharif.edu

<sup>2</sup> Department of Condensed Matter Physics, Faculty of Basic Sciences, Tarbiat Modares University, Tehran 1411944961, Iran; i.mirzaei@modares.ac.ir

\* Correspondence: alipour\_zeynab@ee.sharif.edu

<sup>†</sup> Presented at the 10th International Electronic Conference on Sensors and Applications (ECSA-10), 15–30 November 2023; Available online: <https://ecsa-10.sciforum.net/>.

**Abstract:** In this paper, the design and optimization of a wideband THz metamaterial absorber (MMA) are proposed. By simulation, we reached four structures with absorptions higher than 50%, 70%, 80%, and 90%, with relative absorption bandwidths (RABWs) of 1.43, 1.29, 0.93, and 0.72, respectively. Terahertz absorbers can be used in many potential applications, such as in imaging, energy harvesting, scattering reduction, and thermal sensing. Our intended application was to use the optimal absorber on a thermal detector for detectivity over a wide THz range. Since broadband absorption in the range of 0.3 to 2 terahertz is considered for use in medical imaging, the MMA with more than 50% absorption in the range of 0.35–2.1 THz was selected. The designs were also intended to have the capability of being implemented on different devices, such as bolometers. The cost of the fabrication of the proposed absorber was also low because of the implementation of a single-layer MMA design and the utilization of affordable and more accessible materials and techniques. Our proposed structure had a minimum feature size of 3  $\mu\text{m}$ , making the fabrication process convenient using the standard photolithography method as well. We used thin layers of nickel as the metal for both the single-layer pattern and ground layer, which were placed on the front and back sides of the structure, respectively. The nickel thin film layers were deposited using the sputtering technique and separated by a dielectric layer. The material chosen for the dielectric layer was SU8, which has proper electromagnetic properties and also good adhesion to nickel. Characterization of the fabricated absorber was performed using a terahertz spectroscopy system, and the experimental results verified the high absorption of the sample.

**Keywords:** terahertz; metamaterial absorber; THz imaging; detectivity; wideband absorption

**Citation:** Alipour, Z.; Mirzaei, S.I.; Fardmanesh, M. Design, Fabrication and Characterization of a Wideband Metamaterial Absorber for THz Imaging. *Eng. Proc.* **2023**, *58*, 92. <https://doi.org/10.3390/ecsa-10-16210>

Academic Editor: Jean-marc Laheurte

Published: 15 November 2023



**Copyright:** © 2023 by the authors. Licensee MDPI, Basel, Switzerland. This article is an open access article distributed under the terms and conditions of the Creative Commons Attribution (CC BY) license (<https://creativecommons.org/licenses/by/4.0/>).

## 1. Introduction

The extraordinary electromagnetic properties of materials, many of which are not found in nature, have been widely studied in recent years from the visible to the microwave [1,2]. They have received research attention for characteristics like negative refraction [3], invisible cloaking [4], energy harvesting [5], imaging lenses [6], and wave absorption [7,8]. The latter has been widely used in applications like THz radiation detection, imaging, filters, and spectroscopy.

To absorb the incident wave in a detector, we need an absorber of electromagnetic (EM) waves and we know that the detection rate is proportional to the amount of absorption [9]. Therefore, we need to design an absorber with significant absorption over a wide frequency range in the terahertz region, in other words, a broadband terahertz absorber. Most materials in nature absorb at separate frequencies, which results in small absorption bandwidths. This is where metamaterials come into play. Electromagnetic metamaterials are artificially



engineered materials arranged in sub-wavelength dimensions and can be modeled as materials with negative effective electrical permittivity ( $\epsilon(\omega)$ ) and magnetic permeability ( $\mu(\omega)$ ) values. Therefore, they have a refractive index of less than zero [10,11]. Veselago was the first person to publish a theoretical analysis of materials with negative electric permittivity and magnetic permeability [12]. Metamaterials are an excellent choice for use in electromagnetic wave absorbers in order to increase the absorption bandwidth [13]. Landy and Tao designed and fabricated the first metamaterial absorber [14].

Early-design metamaterial absorbers were not broadband, did not absorb (e.g., absorption above 50%) over a significant frequency range, and only had absorption peaks at some isolated frequencies. The need to increase the absorption bandwidth (in order to access a larger frequency range depending on their application) encouraged scientists to look at the design of broadband structures [15–22].

Here, we have designed four different THz broadband absorbers for different purposes. In these designs, we have used nickel as an absorbent layer material, which causes high losses and increased absorption due to its high permeability coefficient. Also, for the dielectric layer, we used a low-cost and available photoresist material so that the fabrication process can be achieved easily and at a low cost, and these absorbers can be implemented on different devices. In addition to the appropriate selection of materials, we have developed suitable designs for different structures. Thus, by using a combination of substructures with different dimensions and optimizing these dimensions, the absorption peaks caused by each substructure were brought closer to one another, and we finally achieved broadband structures. The proposed absorbers were designed and simulated using the numerical electromagnetic solver, Computer Simulation Technology (CST). The absorption results of these structures were compared with other similar works, and we realized excellent performance by the presented structures. The fabrication process was easily achieved using the standard processes of sputtering and photolithography. The structures and results are described in the following sections.

## 2. Materials and Methods

Generally, metamaterial absorbers are designed in three layers, with the metamaterial, being an array of periodic structures, separated from the ground plane (uniform metal plate) by a dielectric layer [23]. The existence of a metallic layer with high conductivity as the ground plane at the back of the structure is the reason that all of the incident wave that reaches the ground plane will be reflected, and all we have is absorption and reflection. In other words, because the transmission is zero ( $T = 0$ ), we have:

$$A = 1 - R, \tag{1}$$

where  $R$  and  $A$  are the reflectivity and absorptivity of the structure, respectively. For the reflectivity ( $R$ ) of TE and TM polarization of the incident wave with the angle of incidence ( $\theta$ ), by modeling the absorber by a material with  $\epsilon(\omega) = \epsilon_0 \epsilon_r(\omega)$  and  $\mu(\omega) = \mu_0 \mu_r(\omega)$ , where  $\epsilon_0 = \frac{1}{36\pi} \times 10^{-9} \text{Fm}^{-1}$  and  $\mu_0 = 4\pi \times 10^{-7} \text{Hm}^{-1}$ , and  $\epsilon_r(\omega)$  and  $\mu_r(\omega)$  are the relative permittivity and relative permeability, respectively, we have:

$$R_{TE} = |r_{TE}|^2 = \left| \frac{\cos \theta - \mu_r^{-1} \sqrt{n^2 - \sin^2 \theta}}{\cos \theta + \mu_r^{-1} \sqrt{n^2 - \sin^2 \theta}} \right|^2, R_{TM} = |r_{TM}|^2 = \left| \frac{\epsilon_r \cos \theta - \sqrt{n^2 - \sin^2 \theta}}{\epsilon_r \cos \theta + \sqrt{n^2 - \sin^2 \theta}} \right|^2 \tag{2}$$

where  $r$  is the reflection coefficient and  $n$  is the refractive index of the absorber ( $n = \sqrt{\epsilon_r(\omega)\mu_r(\omega)}$ ). So, the absorptivity ( $A$ ) of the absorber can be easily calculated from the reflectivity ( $R$ ) of the incident wave.

To design our structure and choose the feature sizes to achieve broadband absorption, we took advantage of the fact that each part of the pattern in the MMA induces resonance in the structure, and this resonance results in a peak in the absorption spectra,  $\frac{\lambda_0}{4} \propto L$ , where  $\lambda_0$  is the wavelength corresponding to the resonance frequency and  $L$  is the length of the

resonator in the structure. The absorption was maximized through independent engineering of the structural parameters. Due to the different effective permittivity and permeability of each material, optimizations were carried out for each material to enhance the overall absorption. The size of the metallic structure has the highest contribution to frequency tuning. The periodicity, fill factor, and dielectric thickness can modify the frequency as well, although they mainly affect the peak absorption and quality factor. The permeability coefficient of metallic components is also a key parameter to extend the bandwidth, since higher permeability shows a wider bandwidth. Therefore, we utilized nickel as the metallic layer as it is a ferromagnetic material and has a high permeability coefficient.

The designs reported in this paper combine different sizes of rings in a single layer to achieve broadband absorption behavior. Another phenomenon in these structures is that when the size values become a bit closer, coupling between neighbors of different sizes takes place as well. This adds an extra component in the frequency response of the absorber. We utilized this behavior to extend the absorption bandwidth.

We designed and simulated four different structures in the CST environment, as shown in Figure 1. Each structure's unit cell consisted of four rings that caused a high absorption bandwidth. Nickel was utilized as the ground and metamaterial metallic layer material, with a relative permeability of 600.

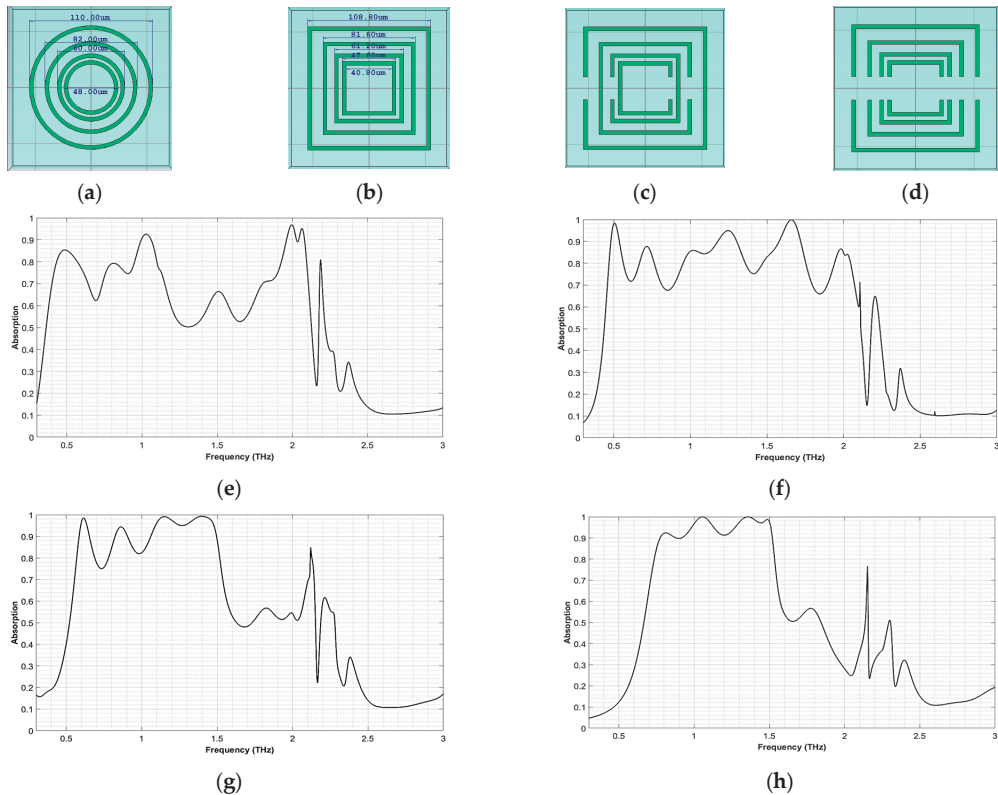


**Figure 1.** Unit cell structure and simulation results of the designed metamaterial absorbers. (a) Structure #1 with a unit cell size of  $142\ \mu\text{m}$  and dielectric thickness of  $37\ \mu\text{m}$ . (b) Structure #2 with a unit cell size of  $144\ \mu\text{m}$  and dielectric thickness of  $36\ \mu\text{m}$ . (c) Structure #3 with a unit cell size of  $143\ \mu\text{m}$  and dielectric thickness of  $34\ \mu\text{m}$ . (d) Structure #4 with a unit cell size of  $143\ \mu\text{m}$  and dielectric thickness of  $34\ \mu\text{m}$ . (e) Absorption spectra of structure #1. (f) Absorption spectra of structure #2. (g) Absorption spectra of structure #3. (h) Absorption spectra of structure #4.

In Table 1, we compare some basic properties of our MMAs with some other recent MMAs designed for THz frequencies, which indicates that the bandwidths of our proposed metamaterial absorbers were higher than those of similar works.

**Table 1.** Comparison of different structures based on number of layers, absorption BW, and absorption rate.

Ref.	MM Layer Material	Number of Layers	Absorption Frequency Range (THz)	Center Frequency (THz)	RABW	% Absorption
[24]	Gold	3	1.24–2.86	2.05	0.79	>50%
[25]	Gold and Graphene	4	22.02–36.61	29.3	0.50	>68%
[26]	Gold	19	5–7.75	6.37	0.43	>80%
[27]	Black phosphorus	10	4.77–6.49	5.63	0.30	>90%
This paper (#1)	Nickel	3	0.35–2.1	1.22	1.43	>50%
This paper (#2)	Nickel	3	0.45–2.07	1.25	1.29	>70%
This paper (#3)	Nickel	3	0.55–1.5	1.02	0.93	>80%
This paper (#4)	Nickel	3	0.7–1.5	1.1	0.72	>90%

Due to proper design and suitable selection of materials and parameters, fabrication of the absorber was easy, rapid, and low cost. We used standard photolithography for fabrication and the steps are given in Figure 2. Glass was chosen as the substrate, which can be replaced by any other device surface. After the RPA cleaning process, nickel was sputtered on the glass as the ground layer. Then, SU8 negative photoresist was spin-coated as the dielectric layer. For the metamaterial layer, nickel was sputtered again. For patterning, first S1813 positive photoresist was spin-coated. After chromium mask alignment and UV exposure, the excess photoresist was removed using NaOH as the developer. FeCl<sub>3</sub> was chosen as the Ni etchant. Finally, the photoresist was removed using acetone.

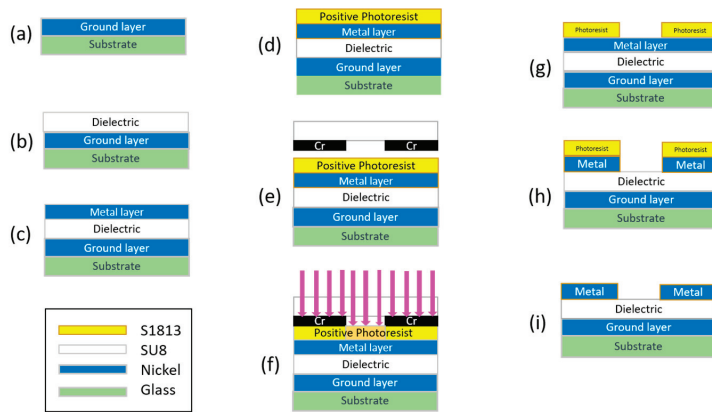


**Figure 2.** Fabrication process: (a) sputtering Ni as the ground layer, (b) spin-coating SU8 as the dielectric layer, (c) sputtering Ni as the top metal layer, (d) spin-coating positive photoresist (s1813), (e) aligning the chrome lithography mask, (f) exposure for 11 s, (g) removing the exposed photoresist using NaOH as the developer, (h) etching the top metal layer to achieve the pattern, and (i) removing excess photoresist utilizing acetone.

To evaluate the fabrication process and performance of the absorbers, we used structure #2, with the slight difference that instead of 37 μm, we coated a dielectric layer of 30 μm. This difference was implemented in order to investigate the effect of dielectric thickness on structure absorption. The final fabricated absorber is shown in Figure 3. The simulation and measurement results of this absorber are presented in the next section.

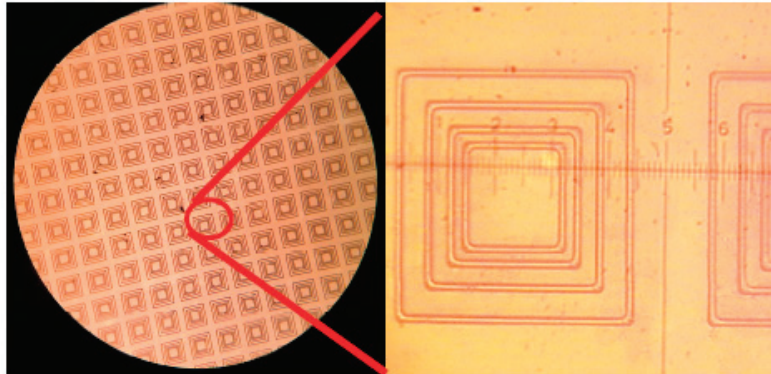


**Figure 3.** Fabricated MMA absorber.

### 3. Results and Discussion

We used a time-domain THz spectroscopy system to evaluate the absorption of our design in the fabricated structure. As shown in Figure 4, the simulation and measurement results were consistent. The slight difference was because we used a 100 nm thick gold layer to calibrate and normalize the graph. But, as we know, for this purpose we need a perfect reflective reference and gold material itself has a fingerprint in this frequency range. Also, due to its symmetrical design, this structure was polarization-independent, which is an advantage in many applications.

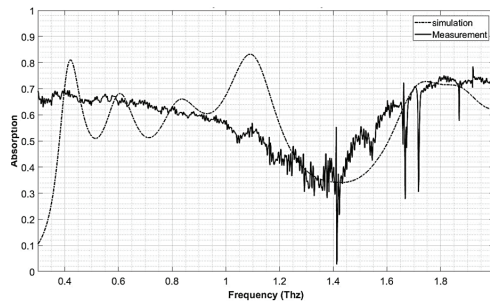


**Figure 4.** Measurement results of proposed MMA.

### 4. Conclusions

We introduced four ultra-wideband metamaterial THz absorbers that can be implemented on various devices, such as bolometer detectors, to increase detectivity. The absorptions of the structures were more than 50%, 70%, 80%, and 90%, with relative absorption bandwidths (RABWs) of 1.43, 1.29, 0.93, and 0.72, respectively. Simulations in the CST Studio Suite environment confirmed the correct operation of the designs. We used nickel as the ground and metamaterial layer material due to its ferromagnetic nature and high permeability coefficient, which caused more absorption by the structures. Also, we utilized SU8 negative photoresist as the dielectric material, which can be easily spin-coated on various surfaces. Also, the minimum feature size of the designs was 3  $\mu\text{m}$ . Using these available and low-cost materials and suitable designs, we successfully fabricated an absorber using a rapid, standard, and low-cost method. On the other hand, we designed the structures with only one patterned layer, which made our fabrication process more cost-effective, and this is one of the outstanding advantages of our MMAs over other broadband MMAs that employ more than one layer. Finally, we measured the absorption of the fabricated structure using a time-domain THz spectroscopy system. This special

design with broadband absorption will allow us to use the structure in various applications, such as bolometric imaging, scattering reduction, and thermal sensing.

**Author Contributions:** Conceptualization, Z.A. and M.F.; methodology, Z.A.; software, Z.A.; validation, Z.A.; investigation, Z.A.; resources, M.F.; data curation, Z.A. and S.I.M.; writing—original draft preparation, Z.A.; writing—review and editing, Z.A. and M.F.; visualization, Z.A.; supervision, M.F.; project administration, Z.A. and M.F.; All authors have read and agreed to the published version of the manuscript.

**Funding:** This research received no external funding.

**Institutional Review Board Statement:** Not applicable.

**Informed Consent Statement:** Not applicable.

**Data Availability Statement:** Data are available in this manuscript.

**Conflicts of Interest:** The authors declare no conflicts of interest.

## References

1. Cai, W.; Shalae, V.M. *Optical Metamaterials: Fundamentals and Applications*; Springer: New York, NY, USA, 2010; pp. 1–200. [CrossRef]
2. Smith, D.R.; Pendry, J.B.; Wiltshire, M.C.K. Metamaterials and Negative Refractive Index. *Science* **2004**, *305*, 788–792. [CrossRef] [PubMed]
3. Shelby, R.A.; Smith, D.R.; Schultz, S. Experimental Verification of a Negative Index of Refraction. *Science* **2001**, *292*, 77–79. [CrossRef] [PubMed]
4. Pendry, J.B.; Schurig, D.; Smith, D.R. Controlling Electromagnetic Fields. *Science* **2006**, *312*, 1780–1782. [CrossRef] [PubMed]
5. Alshareef, M.R.; Ramahi, O.M. Electrically Small Resonators for Energy Harvesting in the Infrared Regime. *J. Appl. Phys.* **2013**, *114*. [CrossRef]
6. Pendry, J.B. Negative Refraction Makes a Perfect Lens. *Phys. Rev. Lett.* **2000**, *85*, 3966–3969. [CrossRef]
7. Landy, N.I.; Sajuyigbe, S.; Mock, J.J.; Smith, D.R.; Padilla, W.J. Perfect Metamaterial Absorber. *Phys. Rev. Lett.* **2008**, *100*, 207402. [CrossRef] [PubMed]
8. Shen, X.; Yang, Y.; Zang, Y.; Gu, J.; Han, J.; Zhang, W.; Jun Cui, T. Triple-Band Terahertz Metamaterial Absorber: Design, Experiment, and Physical Interpretation. *Appl. Phys. Lett.* **2012**, *101*, 154102. [CrossRef]
9. Mofatkharzadeh, A.; Kokabi, A.; Bozbe, A.; Ghods-Elahi, T.; Vesaghi, M.; Khorasani, S.; Banzet, M.; Schubert, J.; Fardmanesh, M. Detectivity of YBCO Transition Edge Bolometer: Modulation Frequency, Bias Current and Absorber Effects. *J. Phys. Conf. Ser.* **2008**, *97*. [CrossRef]
10. Watts, C.M.; Liu, X.; Padilla, W.J. Metamaterial Electromagnetic Wave Absorbers. *Adv. Mater.* **2012**, *24*. [CrossRef]
11. Seetharamdoo, D. Resonant Negative Refractive Index Metamaterials. *Metamaterial* **2012**, 171–192. [CrossRef]
12. Veselago, V.G. The Electrodynamics of Substances with Simultaneously Negative Values of  $\epsilon$  and  $\mu$ . *Sov. Phys. Uspekhi* **1968**, *10*, 509–514. [CrossRef]
13. Zhu, W. Electromagnetic Metamaterial Absorbers: From Narrowband to Broadband. *Metamaterials Metasurfaces* **2018**. [CrossRef]
14. Tao, H.; Landy, N.I.; Bingham, C.M.; Zhang, X.; Averitt, R.D.; Padilla, W.J. A Metamaterial Absorber for the Terahertz Regime: Design, Fabrication and Characterization. *Opt. Express* **2008**, *16*, 7181. [CrossRef] [PubMed]
15. Luo, H.; Wang, T.; Gong, R.Z.; Nie, Y.; Wang, X. Extending the Bandwidth of Electric Ring Resonator Metamaterial Absorber. *Chinese Phys. Lett.* **2011**, *28*, 1–4. [CrossRef]
16. Lee, H.M.; Lee, H.S. A Method for Extending the Bandwidth of Metamaterial Absorber. *Int. J. Antennas Propag.* **2012**, *2012*, 859429. [CrossRef]
17. Yang, H.; Cao, X.Y.; Gao, J.; Li, W.; Yuan, Z.; Shang, K. Low RCS Metamaterial Absorber and Extending Bandwidth Based on Electromagnetic Resonances. *Prog. Electromagn. Res. M* **2013**, *33*, 31–44. [CrossRef]
18. He, X.J.; Yan, S.T.; Ma, Q.X.; Zhang, Q.F.; Jia, P.; Wu, F.M.; Jiang, J.X. Broadband and Polarization-Insensitive Terahertz Absorber Based on Multilayer Metamaterials. *Opt. Commun.* **2015**, *340*, 44–49. [CrossRef]
19. Ding, F.; Dai, J.; Chen, Y.; Zhu, J.; Jin, Y.; Bozhevolnyi, S.I. Broadband Near-Infrared Metamaterial Absorbers Utilizing Highly Lossy Metals. *Sci. Rep.* **2016**, *6*, 39445. [CrossRef]
20. Sood, D.; Tripathi, C.C. A Compact Ultrathin Ultra-Wideband Metamaterial Microwave Absorber. *J. Microwaves, Optoelectron. Electromagn. Appl.* **2017**, *16*, 514–528. [CrossRef]
21. Wu, L.; Shen, Q.; Yang, S.; Lei, L.; Xu, P. Plasmonic Metamaterial Ultra-Broadband Absorber from Visible to near-Infrared. *Int. Photonics Optoelectron. Meet.* **2018**, *26*, 5686–5693. [CrossRef]
22. Yu, P.; Besteiro, L.V.; Huang, Y.; Wu, J.; Fu, L.; Tan, H.H.; Jagadish, C.; Wiederrecht, G.P.; Govorov, A.O.; Wang, Z. Broadband Metamaterial Absorbers. *Adv. Opt. Mater.* **2019**, *7*, 1800995. [CrossRef]

23. Engheta, N. Thin Absorbing Screens Using Metamaterial Surfaces. In Proceedings of the IEEE Antennas and Propagation Society International Symposium (IEEE Cat. No.02CH37313), San Antonio, TX, USA, 16–21 June 2002; pp. 392–395.
24. Wang, B.X.; Tang, C.; Niu, Q.; He, Y.; Chen, R. A Broadband Terahertz Metamaterial Absorber Enabled by the Simple Design of a Rectangular-Shaped Resonator with an Elongated Slot. *Nanoscale Adv.* **2019**, *1*, 3621–3625. [CrossRef] [PubMed]
25. Xiong, H.; Wu, Y.-B.; Dong, J.; Tang, M.-C.; Jiang, Y.-N.; Zeng, X.-P. Ultra-Thin and Broadband Tunable Metamaterial Graphene Absorber. *Opt. Express* **2018**, *26*, 1681. [CrossRef] [PubMed]
26. Lu, X.; Xiao, Z.; Chen, M. A Broadband Metamaterial Absorber Based on Multilayer-Stacked Structure. *Mod. Phys. Lett. B* **2020**, *2050216*, 1–9. [CrossRef]
27. Wang, J.; Jiang, Y. Infrared Absorber Based on Sandwiched Two-Dimensional Black Phosphorus Metamaterials. *Opt. Express* **2017**, *25*, 5206. [CrossRef]

**Disclaimer/Publisher’s Note:** The statements, opinions and data contained in all publications are solely those of the individual author(s) and contributor(s) and not of MDPI and/or the editor(s). MDPI and/or the editor(s) disclaim responsibility for any injury to people or property resulting from any ideas, methods, instructions or products referred to in the content.

Proceeding Paper

# A Fuzzy Logic- and Internet of Things-Based Smart Irrigation System <sup>†</sup>

MD Jiabul Hoque <sup>1,2,\*</sup>, Md. Saiful Islam <sup>2</sup> and Md. Khaliluzzaman <sup>3</sup>

<sup>1</sup> Department of Computer and Communication Engineering, International Islamic University Chittagong (IIUC), Chattogram 4318, Bangladesh

<sup>2</sup> Department of Electronics and Telecommunication Engineering, Chittagong University of Engineering & Technology (CUET), Chattogram 4349, Bangladesh; saiful05eee@cuet.ac.bd

<sup>3</sup> Department of Computer Science and Engineering, International Islamic University Chittagong (IIUC), Chattogram 4318, Bangladesh; khalil@iiuc.ac.bd

\* Correspondence: jiabul.hoque@iiuc.ac.bd

<sup>†</sup> Presented at the 10th International Electronic Conference on Sensors and Applications (ECSA-10), 15–30 November 2023; Available online: <https://ecsa-10.sciforum.net/>.

**Abstract:** Conventional irrigation methods frequently generate excessive or inadequate watering, resulting in the wastage of water and energy and diminished agricultural yields. This study presents a novel intelligent irrigation system that incorporates fuzzy logic and the Internet of Things (IoT) to automate the control of water pumps, thereby eliminating the requirement for human intervention. This novel method enables users to effectively preserve water and electricity by mitigating the issues of excessive and insufficient irrigation of crops. The system utilizes climate sensors that are combined with electrical circuits and connected to an Arduino and a fuzzy inference system (FIS) model to consider climate conditions and soil moisture levels. The sensors are responsible for collecting data that are utilized by the FIS model to control the speed of the water pump effectively. The FIS model integrates fuzzy logic to analyse the data obtained by the Arduino. This analysis enables the Arduino to adjust the pump speed by considering a wide range of sensor inputs. The implementation of this autonomous system eliminates the requirement for human intervention and enhances agricultural productivity by accurately dispensing the optimal quantity of water at the proper intervals. The cessation of water supply occurs when the soil moisture levels reach a sufficient state and resumes when the moisture levels fall below predetermined limits, regulated by various environmental circumstances. A comparative analysis examines the suggested technology, drip irrigation, and manual flooding. The comparison results demonstrate that the intelligent irrigation system accomplishes water and energy conservation.

**Keywords:** fuzzy inference system; fuzzy logic; Internet of Things; sensors; smart irrigation

**Citation:** Hoque, M.J.; Islam, M.S.; Khaliluzzaman, M. A Fuzzy Logic- and Internet of Things-Based Smart Irrigation System. *Eng. Proc.* **2023**, *58*, 93. <https://doi.org/10.3390/ecsa-10-16243>

Academic Editor: Stefano Mariani

Published: 15 November 2023



**Copyright:** © 2023 by the authors. Licensee MDPI, Basel, Switzerland. This article is an open access article distributed under the terms and conditions of the Creative Commons Attribution (CC BY) license (<https://creativecommons.org/licenses/by/4.0/>).

## 1. Introduction

Agriculture plays a prominent role in the economy, and people recognize it as a vital cornerstone of the economic frameworks of developing nations. For several decades, there has been a close association between it and the growth of vital food crops [1]. The “Global Water Crisis” predicts that the increasing demand for clean water amid drought and hot weather conditions would seriously affect agriculture [2]. The presence of a water shortage in both agricultural and non-agricultural communities will significantly influence the quality of life for residents, particularly those who depend on these towns for food production on an intermittent basis [3]. When aiming to get a prosperous crop yield, it is vital to consider both the irrigation methodology that is employed and the volume of water that is consumed. It is imperative to ensure that the quantity of water provided aligns precisely with the specific requirements of the plants, thereby preventing any surplus [4].

Approximately 70% of the Earth's freshwater resources are allocated for agricultural and food production, making it the primary consumer of water globally [2,5]. Considering the substantial water consumption within the industrial sector, it is reasonable to expect a surplus allocation of water resources towards agricultural activities. Experts have identified low irrigation efficiency as a significant contributor to water wastage [6,7].

The United Nations Food and Agriculture Organization asserts that runoff and evapotranspiration cause the wastage of approximately 60% of the water that is used for irrigation. [8]. Digital advancements in agriculture are crucial, not just in less developed nations grappling with food and water scarcity but also in affluent nations due to climatic fluctuations, antiquated and ineffective irrigation systems, pandemics, and other unanticipated obstacles [4,9]. The implementation of automated agricultural irrigation systems provides farmers with the capacity to regulate water volumes accurately, regardless of the availability of labour for manual valve management and plant growth monitoring [10]. In the present era, automation has been widely implemented in various sectors, encompassing industries, household administration, and agriculture [11]. Using sensor-driven irrigation systems that are deployed throughout agricultural fields offers a promising option for managing irrigation and maximizing crop productivity while promoting water conservation. Intelligent agricultural systems provide a sophisticated technology that enables farmers to improve their crop output through cost-effective techniques [12].

The efficiency of intelligent irrigation systems utilizing IoT technology and a fuzzy logic controller (FLC) can be enhanced by evaluating data and implementing irrigation adjustments based on factors such as soil moisture and temperature [13]. Communication technologies such as Zigbee, LoRaWAN, and cloud computing facilitate monitoring and storing of data in real time [14]. The Internet of Things (IoT) employs diverse networks to gather data from the physical environment, employing optimization techniques to enhance operational efficiency. The abundance of applications provides evidence for the adaptability of fuzzy logic, a computational approach that effectively manages uncertainty and efficiently makes decisions in practical contexts [15].

Researchers have conducted a plethora of studies on utilizing fuzzy inference systems and Internet of Things (IoT) technologies in agriculture [16]. In their research, the authors in reference [17] provide a methodology for identifying meteorological condition variables and utilizing these data to quantify the frequency and quantity of water that is required for cultivation. The proposed system design [18] examines a fog wireless communication platform for monitoring and managing sensors and actuators, intending to determine the irrigation requirements for crops. Previous research [19] shows that implementing a decision support system can enhance regulated irrigation practices, ensuring consistent soil moisture levels. Additionally, such a system can prioritize areas with a low water content while minimizing the negative impacts of irrigation on regions with a high water content. In the study conducted by the authors of [20], novel irrigation techniques were devised to optimize agricultural water utilization through fuzzy logic. The researchers employed a Mamdani control system and utilized MATLAB and Simulink software to conduct simulations. The results exhibited accurate modelling and underscored the efficacy of the Mamdani fuzzy logic control system in optimizing the utilization of water resources in agriculture. In reference [21], fuzzy logic systems are employed to improve decision making assessments instead of standard acknowledgement control procedures. Fuzzy logic can enhance the adaptive capabilities of irrigation systems in response to the ever-changing dynamics of their surrounding environment. The manipulation of if-then rules in fuzzy inference systems can be efficiently achieved by applying fuzzy logic and set theory [22]. This article employs the widely adopted and accessible Mamdani methodology for irrigation control. This approach exhibits similarities to human cognition and linguistic processes.

This article explores implementing an intelligent irrigation system based on fuzzy logic. This technology calculates the optimal irrigation volume for crops by considering meteorological conditions. The attainment of an ideal crop yield is contingent upon



providing an appropriate quantity of water, avoiding excessive and inadequate amounts. The created fuzzy control system integrates four input parameters: soil moisture, solar radiation, air temperature, and air humidity. We have considered these specific components because they influence water evaporation from the soil. The management of the pump's speed influences the rate of water delivery, achieved through the regulation of the output parameter of the fuzzy logic control system. This invention differentiates itself from prior methodologies by using a more extensive set of input variables and formulating a direct fuzzy rule based on the interconnectedness between each input and output parameter. The system aims to enhance farmers' engagement and facilitate their transition to intelligent agriculture practices. The main contributions of this study can be summarized as follows:

- This study focuses on designing and implementing an intelligent irrigation system that utilizes fuzzy logic and leverages the Internet of Things (IoT) for real-time capture of meteorological and soil information. The system aims to enable informed irrigation decisions by applying a fuzzy inference system.
- The motor's activation or deactivation is automated based on the data obtained from the soil moisture sensor in order to mitigate excessive consumption of water and electricity.
- The engine is automatically deactivated in reaction to rain to conserve electricity resources.
- There is no need for human intervention.

The remaining sections are structured as follows: Section 2 explains the technique that was utilized in developing our work. Section 3 presents the outcomes that were achieved following the system's implementation, discussions, unresolved issues, and a comparison against other cited systems. Concluding the paper, Section 4 underscores the key takeaways of the research and outlines potential paths for future investigations.

## 2. Proposed System Model

By utilizing real-time data collected from sensors, an intelligent irrigation system enhances the efficacy of watering practices. The depicted system architecture, as illustrated in Figure 1, showcases the process flow.

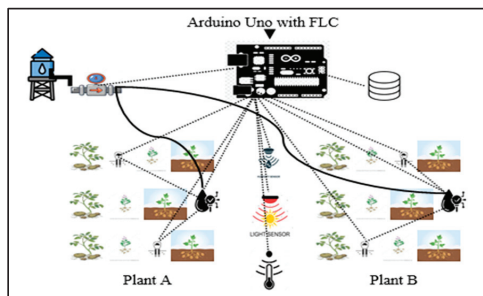


**Figure 1.** Proposed architecture of smart irrigation system.

In this arrangement, data are collected by sensors, afterwards interpreted by an Arduino, and ultimately utilized by the fuzzy controller to determine the optimal timing for grass irrigation. Integrating the Internet of Things (IoT) and Wireless Sensor Network (WSN) technology enables smooth communication between sensors and Arduino devices, facilitating efficient information exchange.

### 2.1. Sensors and Communication Media

The current study employed five sensors to monitor various environmental variables. We used the DHT11 sensor to measure humidity and temperature, the REES52 sensor to assess soil moisture, and the LM 393 sensor to analyse sun radiation. We employed a flow sensor to quantify the water flow rate to regulate irrigation. ZigBee technology facilitated

enhanced communication among system components, while the microcontroller effectively processed sensor data.

### 2.2. Fuzzy Inference System for Precision Agriculture

The fuzzy controllers utilized Mamdani’s fuzzy inference method in the present investigation. Figure 2 depicts the internal structure of the fuzzy inference system used for a water pump. The initial step of the fuzzy logic controller (FLC) involves acquiring data from sensors that are responsible for measuring a range of environmental characteristics, including temperature, humidity, sunshine intensity, and soil moisture.

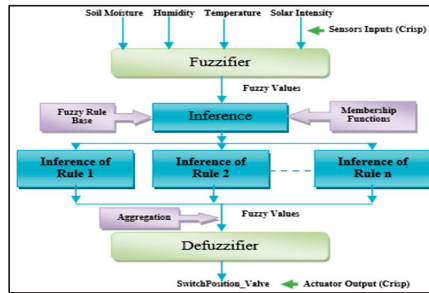


Figure 2. Internal structure of fuzzy logic controller.

We compute fuzzification rules by utilizing sensor data. The soil moisture sensor facilitates the determination of watering requirements. We initiate irrigation when the relative humidity drops below 17%. Fuzzy logic determines the length of irrigation in FLC. The rule-based approach determines the optimal frequency and duration of irrigation. The proposed fuzzy logic controller (FLC) utilized triangle and trapezoidal functions as piecewise linear membership functions to conduct the fuzzification process. The method for constructing a  $\mu_{\text{triangle}}$  is shown in (1) below:

$$\mu_{\text{triangle}}(x; a, b, c) = \begin{cases} 0, & x \leq a \\ \frac{x-a}{b-a}, & a \leq x \leq b \\ \frac{c-x}{c-b}, & b \leq x \leq c \\ 0, & c \leq x \end{cases} \quad (1)$$

$$\mu_{\text{trapezoidal}}(x; a, b, c) = \begin{cases} 0, & x \leq a \\ \frac{x-a}{b-a}, & a \leq x \leq b \\ 1, & b \leq x \leq c \\ \frac{d-x}{d-c}, & c \leq x \leq d \\ 0, & d \leq x \end{cases} \quad (2)$$

Tables 1–5 present the threshold values for the inputs and output. As mentioned earlier, the values play a critical role in the generation of rules through the utilization of membership functions in the fuzzification process. These reference points serve as a basis for identifying the appropriate linguistic phrases and fuzzy sets that are linked to each variable.

Table 1. Soil moisture threshold factor.

Soil Moisture Reading (%)	Category
0–17	Dry
18–50	Normal (Ideal)
51–100	Wet

**Table 2.** Solar radiation threshold factor.

Solar Radiation Reading (%)	Category
0–4	Dark
5–50	Medium
51–100	Light

**Table 3.** Humidity threshold factor.

Humidity Reading (%)	Category
0–49	Low
50–84	Medium (Ideal)
85–100	High

**Table 4.** Temperature threshold factor.

Temperature Reading (°C)	Category
0–16	Cold
17–22	Warm (Ideal)
23–45	Hot

**Table 5.** Irrigation duration threshold factor.

Irrigation Duration (Min)	Category
0–2	Very Short
3–5	Short
6–12	Medium
13–25	Long
26–45	Very Long

The system included fuzzy logic principles by formulating and exploiting the membership functions described in (1) and (2). The fuzzy logic controller (FLC) would require 81 rules to decide on the irrigation choice, considering four inputs with three membership functions each. However, employing careful examination, the established principles were refined to 49, resulting in optimization. Table 6 presents a compilation of exemplary firing rules.

**Table 6.** Fuzzy rules for proposed system.

1	If (Soil_Moisture is Normal) and (Humidity is Low) and (Air_Temperature is Cold) and (Solar_Radiation is Light), then (SwitchPosition_Valve is S) (1)
2	If (Soil_Moisture is Dry) and (Humidity is Low) and (Air_Temperature is Cold) and (Solar_Radiation is Light), then (SwitchPosition_Valve is M) (1)
·	· · · · ·
49	If (Soil_Moisture is Normal) and (Humidity is High) and (Air_Temperature is Hot) and (Solar_Radiation is Medium), then (SwitchPosition_Valve is S) (1)

Additionally, the MIN-MAX inference aggregation method and criteria were employed to ascertain the stress levels. We used the highest value to modify the output fuzzy region while employing the minimal value of the predicate truth to restrict the fuzzy union.

Employing the minor operator diminished the overall level of certainty of the stress state. Utilizing the MAX composition technique established the membership function for the irrigation time. The intelligent irrigation system uses four inputs, namely, moisture (M), temperature (T), humidity (H), and light (L). We use Equations (3) and (4) to compute the MIN-MAX aggregation inference.

$$M \cup T \cup H \cup L = \{x, \min(mM(x), mT(x), mH(x), mL(x)) | x \in X\} \tag{3}$$

$$M \cap T \cap H \cap L = \{x, \max(mM(x), mT(x), mH(x), mL(x)) | x \in X\} \tag{4}$$

The final stage in the intelligent irrigation system is the process of defuzzification, which entails converting the fuzzy output into a numerical value. The centroid defuzzification technique, as depicted in (5), is employed to ensure precise outcomes.

$$x^* = \frac{\int \mu_i(x).xdx}{\int \mu_i(x).dx} \tag{5}$$

$$Y_1 = \frac{(Y_{VS}C'_1 + Y_S C'_2 + Y_M C'_3 + Y_L C'_4 + Y_{VL} C'_5)}{(C'_1 + C'_2 + C'_3 + C'_4 + C'_5)} \tag{6}$$

Equation (5) illustrates the process of generating the de-fuzzified output, denoted as  $x^*$ , for the output variable  $x$  using the membership function  $\mu_i(x)$ . On the other hand, Equation (6) is employed to determine the Centroid of Area (CoA) for the proposed system. In this equation, (Y) represents the centroid of the output variable, while  $C'_1, C'_2, C'_3, C'_4,$  and  $C'_5$  correspond to the results of the membership functions. Additionally,  $Y_{VS} = \{VS_t = 2\}$ ,  $Y_S = \{S_t = 5\}$ ,  $Y_M = \{M_t = 12\}$ ,  $Y_L = \{L_t = 25\}$ , and  $Y_{VL} = \{VL_t = 45\}$  are the singleton functions associated with each output.

### 3. Results and Analysis

This work involved the development of a fuzzy inference system utilizing Mamdani-type fuzzy logic for the exact control of the irrigation switch position. The switch position, ranging from 1 to 5, was established based on four inputs: soil moisture, temperature, humidity, and light intensity. A numerical value of 1 signifies a reduced frequency and timing of water flow, whilst a value of 5 denotes the presence of a continuous and unrestricted water flow. We implemented the fuzzy inference system using the MATLAB software. Figures 3 and 4 exhibit the results obtained for water flow control, presenting the outcomes in diverse formats.

Upon examination of Figure 3, it becomes apparent that several environmental factors have a significant role in influencing the determination of the water valve's switch position and the irrigation duration. When we measure the soil moisture level at a low percentage of 9.69%, along with a relative humidity of 44.7%, an ambient temperature of 31.4 °C, and moderate sun radiation of 609 lux, we recommend adjusting the switch position to the extended position, which is the fourth position. The provided data suggest that the water flow will persist for an estimated duration of 14.4 min in order to facilitate the irrigation of the plants.

Likewise, Figure 4 illustrates an additional scenario whereby the soil moisture content is within a standard range of 43.5%, representing an optimal condition for the growth of potato plants. The relative humidity is at a moderate level, measuring 82.7%. The air temperature reads 13.7 °C, characterizing it as cold. Moreover, we observe negligible sun radiation. In this instance, the obtained output demonstrates a significantly diminished water flow value (4.91), implying that the switch position is close to the lower threshold. This adheres to the precise guidelines for this problem, as the predicted result in such situations will likely be extremely minor.

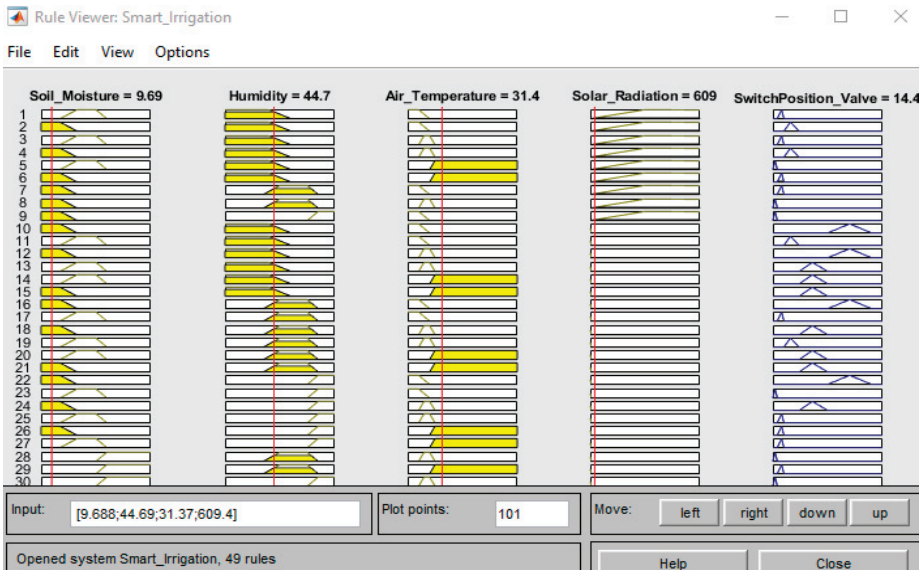


Figure 3. Switch position (long).

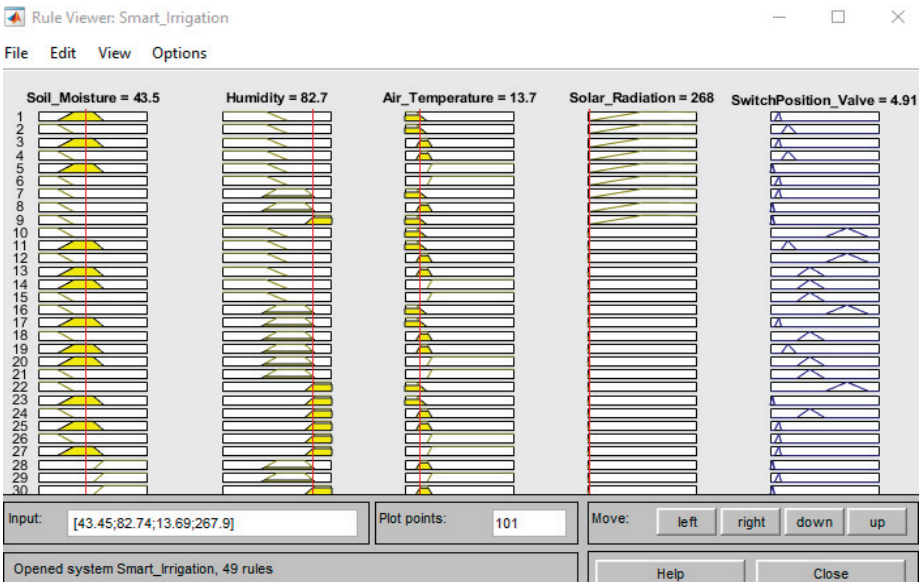
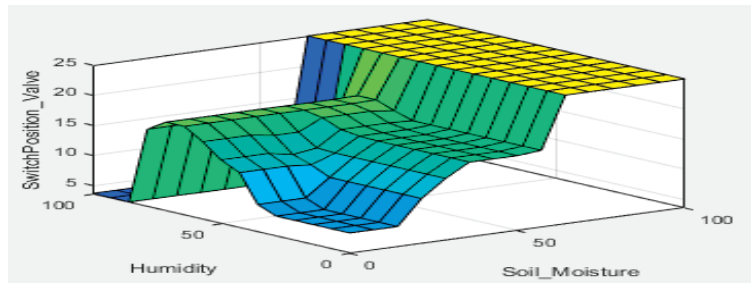


Figure 4. Switch position (short).

Moreover, Figure 5 illustrates the correlation between the two independent variables, namely, humidity and soil moisture, and the dependent variable, which is the switch position of the solenoid valve. The figure appears as a surface plot, generated using MATLAB. The figure demonstrates that in instances where moisture levels are low, resulting in a yellow colouration on the plot, there is a notable increase in the water flow through the system. In contrast, when moisture levels are elevated, as denoted by a blue hue on the graph, the magnitude of water flow is modest. The presented graphic illustrates the inverse correlation between moisture levels and water flow.



**Figure 5.** Relationship among humidity, soil moisture, and corresponding output for the FLC.

Similarly, Figure 6 illustrates the correlation between elevated temperatures and augmented evapotranspiration, hence requiring a larger quantity of water for irrigation.

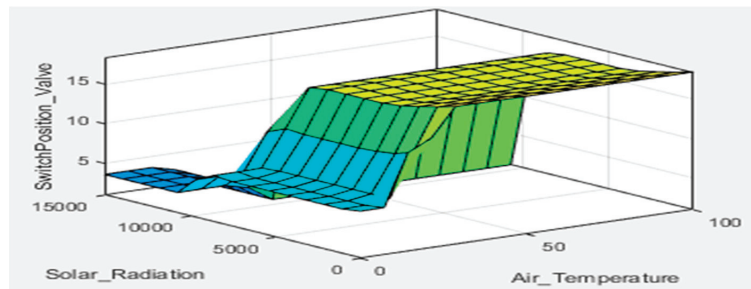


**Figure 6.** Relationship among temperature, solar radiation, and corresponding output for the FLC.

In order to provide empirical support for the conclusions drawn by the proposed system, a comparative evaluation is undertaken to compare its performance with that of the most recent systems [23,24]. These systems were selected as benchmarks based on their resemblance to the proposed irrigation approach. The evaluation process maintained consistency in the proposed system’s conditions, features, periods, and existing solutions to guarantee a comprehensive and unbiased assessment. This approach facilitated a realistic and meaningful comparison between the two.

Table 7 presents a comparative analysis of the proposed and existing models, focusing on three key parameters: weekly water volumes, actuator time, and energy consumption. The results indicate that the proposed model has a lower water use than alternative models, including those referenced in [23,24]. The reduced duration of pumping in the proposed system leads to decreased actuator operation time and diminished energy consumption. Significantly, the proposed model demonstrates an 11% reduction in energy use compared to the previous model. In Figure 7, a comparison is presented between the intelligent irrigation system that has been proposed and existing systems in terms of their water and energy consumption over four months. The chosen time frame has been determined based on its congruence with the ideal duration that is necessary for the growth and development of potato plants.

**Table 7.** Proposed system evaluation.

Irrigation Model	Water Consumption (L)	Operating Time of Actuators	Energy Consumption (Wh)
[23]	59	1 h 17 m 08 s	108
[24]	45	0 h 56 m 45 s	73

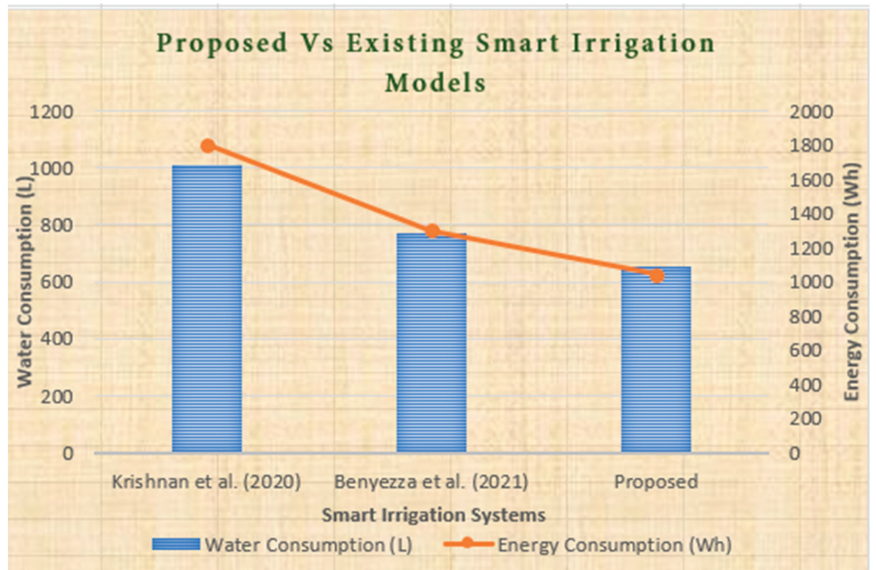


**Figure 7.** Comparison of proposed vs. existing smart irrigation systems [20,21].

The data presented in Figure 7 demonstrate the significant reduction in water consumption that is achieved by the suggested system. Specifically, it indicates a decrease of 360 litres (equivalent to 45%) compared to the approach described in reference [23] and a reduction of 121 litres (equivalent to 19%) compared to the method outlined in reference [24]. Additionally, it illustrates a decrease of 760 Wh and 260 Wh in energy consumption during the potato growth phase. This emphasizes the potential advantages of adopting the proposed methodology, which incorporates smart irrigation using a fuzzy inference system and the Internet of Things (IoT). That leads to significant cost reductions for farmers regarding water, energy, and labour expenditures.

#### 4. Conclusions

This article introduces a methodology for creating an intelligent irrigation system that tackles the difficulties posed by limited water resources in areas that are characterized by significant water limitations. The utilization of fuzzy inference systems and Internet of Things (IoT) technologies is employed by the system in order to facilitate the promotion of practical water usage and the enhancement of irrigation control. The fuzzy inference system, employing the Mamdani fuzzification method, effectively ascertains the ideal irrigation frequency and duration for potato cultivation. The system utilizes trapezoidal output membership functions and triangle input membership functions. The fuzzy control mechanism effectively preserves water and energy resources by regulating excessive runoff and ensuring that the soil moisture remains above a predetermined threshold through gradual adjustments. Additionally, the system compensates for the loss of water resulting from evapotranspiration throughout the winter season, a period characterized by frequent excessive irrigation. Significantly, the suggested methodology retains its user-friendly nature and economic viability, even when implemented across extensive agricultural landscapes. Potential areas for future research involve investigating the incorporation of intelligent farming technology based on artificial neural networks (ANNs). This integration can assist farmers and producers in reducing waste and improving productivity in multiple domains. For instance, it could optimize fertilizer use and enhance crop output.

**Author Contributions:** M.J.H.—Conceptualization, Methodology, Writing—original draft, Writing—review and editing, Software; M.S.I.—Writing—review and editing, Resources, Supervision, Validation; M.K.—Writing—review and editing, Resources, Validation. All authors have read and agreed to the published version of the manuscript.

**Funding:** This research received no external funding.

**Institutional Review Board Statement:** Not applicable.

**Informed Consent Statement:** Not applicable.

**Data Availability Statement:** The raw data supporting the conclusions of this article will be made available by the authors on request.

**Conflicts of Interest:** The authors declare no conflict of interest.

## References

1. FAO. The State of Food and Agriculture 2020. In *Overcoming Water Challenges in Agriculture*; FAO: Rome, Italy, 2020. [CrossRef]
2. World Resources Institute. Ranking the World's Most Water-Stressed Countries in 2040. 2018. Available online: <https://www.wri.org/insights/ranking-worlds-most-water-stressed-countries-2040> (accessed on 14 September 2022).
3. Veeramanikandasamy, T.; Sambath, K.; Rajendran, K.; Sangeetha, D. Remote Monitoring and Closed Loop Control System for Social Modernization in Agricultural System Using GSM and Zigbee Technology. In Proceedings of the 2019 International Conference on Advances in Electrical Engineering (ICAEE), Vellore, India, 7–9 March 2019; pp. 1–4. [CrossRef]
4. Abbasi, R.; Martinez, P.; Ahmad, R. The digitization of agricultural industry—A systematic literature review on agriculture 4.0. *Smart Agric. Technol.* **2022**, *2*, 100042. [CrossRef]
5. Hoque, M.J.; Ahmed, M.R.; Hannan, S. An Automated Greenhouse Monitoring and Controlling System using Sensors and Solar Power. *Eur. J. Eng. Res. Sci.* **2020**, *5*, 510–515. [CrossRef]
6. Veerachamy, R.; Ramalakshmi, R.; Kavin, B.P.; Hussain, I.; Almaliki, A.H.; Almaliki, A.A.; Elnaggar, A.Y.; Hussein, E.E. Exploiting IoT and its enabled technologies for irrigation needs in agriculture. *Water* **2022**, *14*, 719. [CrossRef]
7. Debo-Saiye, Y.; Okeke, H.S.; Mbamaluikem, P.O. Implementation of an Arduino-Based Smart Drip Irrigation System. *Int. J. Trend Sci. Res. Dev.* **2020**, *5*, 1130–1133.
8. Ullah, S.; Hafeez, G.; Rukh, G.; Albogamy, F.R.; Murawwat, S.; Ali, F.; Khan, F.A.; Khan, S.; Rehman, K. A Smart Sensors-Based Solar-Powered System to Monitor and Control Tube Well for Agriculture Applications. *Processes* **2022**, *10*, 1654. [CrossRef]
9. Vij, A.; Vijendra, S.; Jain, A.; Bajaj, S.; Bassi, A.; Sharma, A. IoT and machine learning approaches for automation of farm irrigation system. *Procedia Comput. Sci.* **2020**, *167*, 1250–1257. [CrossRef]
10. Muangprathub, J.; Boonnam, N.; Kajornkasirat, S.; Lekbangpong, N.; Wanichsombat, A.; Nillaor, P. IoT and agriculture data analysis for smart farm. *Comput. Electron. Agric.* **2019**, *156*, 467–474. [CrossRef]
11. Tsiropoulos, Z.; Skoubris, E.; Fountas, S.; Gravalos, L.; Gemtos, T. Development of an energy efficient and fully autonomous low-cost IoT system for irrigation scheduling in waterscarce areas using different water sources. *Agriculture* **2022**, *12*, 1044. [CrossRef]
12. Alomar, B.; Alazzam, A. A Smart Irrigation System Using IoT and Fuzzy Logic Controller. In Proceedings of the 2018 Fifth HCT Information Technology Trends (ITT), Dubai, United Arab Emirates, 11–13 March 2018; pp. 175–179. [CrossRef]
13. Veerachamy, R.; Ramar, R.; Balaji, S.; Sharmila, L. Autonomous Application Controls on Smart Irrigation. *Comput. Electr. Eng.* **2022**, *100*, 230–245. [CrossRef]
14. Zhang, H.; He, L.; Di Gioia, F.; Choi, D.; Elia, A.; Heinemann, P. LoRaWAN based Internet of Things (IoT) system for precision irrigation in plasticulture fresh-market tomato. *Smart Agric. Technol.* **2022**, *2*, 100053. [CrossRef]
15. Rao, R.N.; Sridhar, B. IoT Based Smart Crop-Field Monitoring and Automation Irrigation System. In Proceedings of the 2018 2nd International Conference on Inventive Systems and Control (ICISC), Coimbatore, India, 19–20 January 2018; pp. 478–483. [CrossRef]
16. Kurniawan, D.; Witanti, A. Prototype of Control and Monitor System with Fuzzy Logic Method for Smart Greenhouse. *Indones. J. Inf. Syst.* **2021**, *3*, 116–127. [CrossRef]
17. Soy, H.; Dilay, Y. Fuzzy Control of Agricultural Irrigation System through Wireless Sensor/Actuator Networks. *J. Multidiscip. Eng. Sci. Technol.* **2020**, *3*, 6093–6097.
18. Munir, M.S.; Bajwa, I.S.; Cheema, S.M. An Intelligent and Secure Smart Watering System Using Fuzzy Logic and Blockchain. *Comput. Electr. Eng.* **2019**, *77*, 109–119. [CrossRef]
19. Ibrahim, F.S. Smart Irrigation System Using a Fuzzy Logic Method. *Int. J. Eng. Res. Technol.* **2018**, *11*, 1417–1436.
20. Farkas, I.; Nagy, L. Improved Climate Control for Potato Stores by Fuzzy Controller. *Comput. Electron. Agric.* **2019**, *180*, 127–140.
21. Mamdani, E.H. Application of Fuzzy Logic to Approximate Reasoning Using Linguistic Synthesis. *IEEE Trans. Comput.* **1977**, *26*, 1182–1191. [CrossRef]



22. Izzuddin, T.A.; Johari, M.A.; Rashid, M.Z.A.; Jali, M.H. Smart Irrigation Using Fuzzy Logic Method. *ARPJ J. Eng. Appl. Sci.* **2018**, *13*, 2.
23. Krishnan, R.S.; Julie, E.G.; Robinson, Y.H.; Raja, S.; Kumar, R.; Son, L.H. Fuzzy Logic Based Smart Irrigation System Using Internet of Things. *J. Clean. Prod.* **2020**, *252*, 119902. [CrossRef]
24. Benyezza, H.; Bouhedda, M.; Rebouh, S. Zoning Irrigation Smart System Based on Fuzzy Control Technology and IoT for Water and Energy Saving. *J. Clean. Prod.* **2021**, *302*, 127001. [CrossRef]

**Disclaimer/Publisher's Note:** The statements, opinions and data contained in all publications are solely those of the individual author(s) and contributor(s) and not of MDPI and/or the editor(s). MDPI and/or the editor(s) disclaim responsibility for any injury to people or property resulting from any ideas, methods, instructions or products referred to in the content.

# AI-Driven Digital Twins for Smart Cities <sup>†</sup>

Sergey Goncharov \* and Andrey Nechesov

Sobolev Institute of Mathematics, Academician Koptyug's Avenue, 4, Novosibirsk 630090, Russia; nechesov@math.nsc.ru

\* Correspondence: s.s.goncharov@math.nsc.ru

<sup>†</sup> Presented at the 10th International Electronic Conference on Sensors and Applications (ECSA-10), 15–30 November 2023; Available online: <https://ecsa-10.sciforum.net/>.

**Abstract:** This paper explores the issues of building digital twins for smart cities, which can be controlled manually or with the assistance of intelligent systems. For these purposes, a specialized logic platform, Delta, is being built, which has such properties as transparency, reliability, and predictability. The Delta platform allows us to represent the digital twins of cities as a network of smart contracts that interact with each other within a unified multi-blockchain system. The inclusion of Delta-learning and Delta-connection modules facilitates knowledge acquisition and utilization for AI-driven process management and sensor integration within smart cities.

**Keywords:** smart cities; digital twins; Delta platform; artificial intelligence; multi-blockchain

## 1. Introduction

Smart cities [1] are the backbone of any digital economy [2]. This concept entails the end-to-end integration of IT technologies within a smart city, including tracking passenger traffic; monitoring transport and crime rates; managing household expenses, such as heating, water, and electricity; facilitating interaction between citizens and the government; providing automatic payroll and taxes; paying for health insurance; interacting with assistants and chatbots; and much more. All these achievements are aimed at improving reliability and the quality of life of ordinary citizens.

The successful implementation of these processes requires a robust IT infrastructure that includes computers, sensors, and controllers. This infrastructure generates huge amounts of data that require processing, storage, and analysis. Artificial intelligence algorithms play a pivotal role in addressing these challenges, encompassing pattern recognition, voice recognition, chatbots, and intelligent assistants. These sophisticated mechanisms enable the analysis and processing of the acquired information.

In this context, we are introducing a novel blockchain-based [3] platform, Delta. This platform enables the creation of digital twins of smart cities [4], accurately simulating all processes and relationships within them. The Delta platform implements a hierarchical approach to data storage and processing in which there are multi-blockchains using blockchains in combination with other big data stores as the underlying information stores. The work of intelligent systems in a smart city is described using smart contracts (SCs) that are executed within multi-blockchain structures, thereby ensuring efficient and secure functionality. To obtain new knowledge and predictions, we use a specially developed learning theory for intelligent systems based on the requirements of maximum specificity presented in the works of Carl Hempel [5].

## 2. Smart Cities

When we say smart city, what do we mean by it? This is not only the digitalization of all processes, but also the intellectual component. A smart city must independently solve some of the problems within the boundaries set by its developers. We cannot do

**Citation:** Goncharov, S.; Nechesov, A. AI-Driven Digital Twins for Smart Cities. *Eng. Proc.* **2023**, *58*, 94. <https://doi.org/10.3390/ecsa-10-16223>

Academic Editor: Stefano Mariani

Published: 15 November 2023



**Copyright:** © 2023 by the authors. Licensee MDPI, Basel, Switzerland. This article is an open access article distributed under the terms and conditions of the Creative Commons Attribution (CC BY) license (<https://creativecommons.org/licenses/by/4.0/>).

this without introducing artificial intelligence. IT solutions should make life as easy as possible for ordinary citizens in cities. Moreover, a compromise must be found between total surveillance and the personal lives of citizens. This compromise could be for each person to manually set the parameters they allow to be used to track their activities.

A living unsuccessful example of total digitalization is the South Korean city of Songdo [6], in which, according to the plans of the South Korean authorities and developer companies, several hundred thousand people were supposed to live, but in fact it is inhabited by only 10–20% of this. There can be many reasons for this, ranging from the lack of cultural and leisure facilities to tracking most of the actions of each person. And there are dozens and hundreds of such ghost towns all over the world.

Therefore, the creation and planning of smart cities must be approached with all care and seriousness. A very important criterion, in our opinion, is that an ordinary user can control the level of outside interference in their personal life. Moreover, it is necessary for the residents themselves to be able to influence what smart technologies are introduced in their city [7].

Many experts consider the following to be the main areas of development in smart cities: public and personal transport, smart homes, energy optimization, medicine, security, clean water, and waste recycling. In all these areas of development, we must not only create software, but we must teach these programs to think for themselves within their competences.

### 3. Digital Twins for Smart Cities

The first ideas of digital twins appeared in David Gelernter's book *Mirror Worlds* [8]. The concept of a digital twin was first described in 2002 by a professor at the University of Michigan, at a Society of Manufacturing Engineers conference in Troy, Michigan [9]. Over the past 20 years, the term has evolved significantly and today has several different definitions. Therefore, we understand the term digital twin as a digital copy of a physical object or process, and a change in the work of a digital copy entails a change in the work of the physical object or process itself and vice versa. A good example of a digital twin is ADNOC's technological solution to create a single control center for all processes for 20 oil refineries and oil production enterprises [10].

The digital twin of a smart city should not only be a decision-making system for the operator, but should also have AI solutions that would help manage all the city's processes, such as managing electricity, water resources, food delivery, waste recycling, automatic research on the health of citizens, the prevention of crimes in real time, traffic management of the city, and the control of unmanned vehicles, sensors, controllers, and other devices in the city.

#### 3.1. Delta Platform for Digital Twins

To build digital twins of large and complex systems such as smart cities, it is necessary to have stable and reliable software in which modular solutions based on neural networks [11] and other AI systems can be easily implemented. Such a solution is a combination of smart contracts and blockchains. Blockchains with a POW consensus algorithm [3] have already established themselves as one of the most reliable computer networks. Therefore, the technological platform must be implemented on the basis of blockchain technology, in which algorithms are implemented using smart contracts executed within these blockchains. This will ensure the security, decentralization, and transparency of all actions. But due to the well-known blockchain trilemma, high values of parameters of security, decentralization, and scalability cannot be achieved within a single blockchain. Therefore, multi-blockchains are entering the arena. Multi-blockchains gained great popularity after the release of the TON White Paper by the Durov brothers Nikolai and Pavel [12]. Their previous work made a splash in 2017 and forced us to turn our attention to this technology.

The Delta platform incorporates all of the above solutions that are necessary for the implementation of digital twins of smart cities. Due to multi-blockchains and other

data structures, we manage to achieve both high security and decentralization, as well as scalability. All processes occurring in a smart city are described by smart contracts using the p-complete language  $L^*$  [13]. The p-completeness of a high-level programming language provides a solution to the halting problem that occurs in Turing-complete languages. A program in a p-complete language is always executed in a time not exceeding a polynomial of the length of the input data. In this language, the program is some suitable term of the logical p-complete language  $L$  [13], in the construction of which both special termal constructions and  $\Delta_0$ -formulas can participate. The AI modules for learning and interaction between the platform and the smart city were also taken into account.

### 3.1.1. Multi-Blockchain Structures

As already shown in [3], the theory of blockchain structures can be axiomatized in first-order logic. This allows us to build computable models and simulate their work using special libraries.

Let us inductively define the class of multi-blockchains, MB:

- (1)  $MB_1 = \langle B_1 \rangle$  is a multi-blockchain if  $B_1$  is a blockchain.
- (2)  $MB_k = \langle MB_{k-1}, B_1, \dots, B_n \rangle$  is a multi-blockchain if  $MB_{k-1}$  is a multi-blockchain and all  $B_i$  are blockchains.

As shown in Figure 1, for each object (home, store, office, company), all data from sensors, controllers, and user requests are stored in local-level blockchains and, periodically, the hash of this blockchain is sent to higher-level blockchains. Moreover, any blockchain can store smart contracts that emulate the operation of certain internet devices in a smart city.

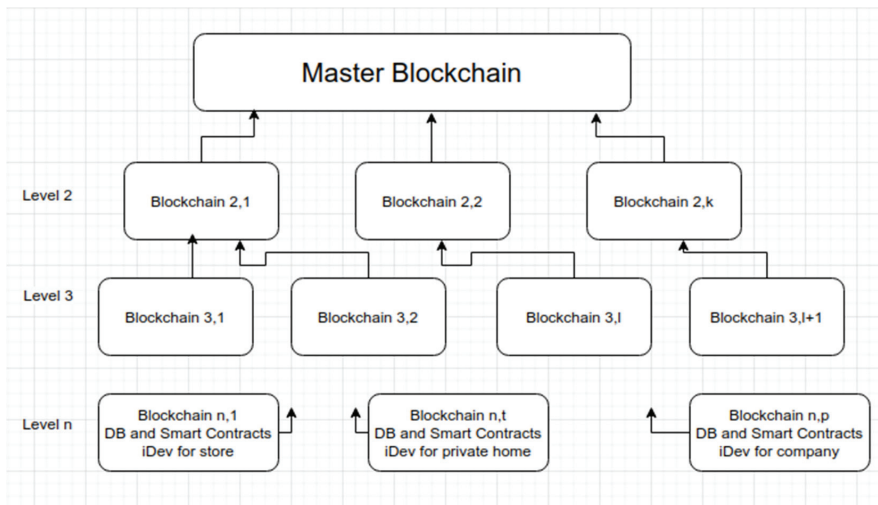


**Figure 1.** Multi-blockchain structure where iDev is an abbreviation for internet devices.

In a multi-blockchain structure, the most secure and decentralized blockchain is the Master Blockchain. Blockchains at the second level and beyond are less decentralized, but are cheaper for users or devices to interact with. The fastest and cheapest are the lowest-level blockchains. Information from internet devices, such as motion detectors, sensors, vehicles, houses, offices, companies, etc., is written to these blockchains.

Let some p-computable hereditarily finite list superstructure  $HW(m)$  of signature  $\sigma$  be fixed [14], in which some elements of the main set  $HW(M)$  are blockchains, and there is a one-place predicate blockchain that selects these elements. Using the polynomial analogue of Gandy’s fixed point theorem [14], as well as the process of constructing a monotone operator [14], one can easily obtain the following lemmas:

**Lemma 1.** *There is a generating family of L-formulas F which define a monotone operator  $\Gamma_F$  with the fixed point property. The smallest fixed point of this operator defines the class of multi-blockchains MB.*

**Lemma 2.** *The class MB is polynomially computable.*

3.1.2. Smart Contracts

Within the framework of the concept of semantic programming [13], we define the concept of L\* contract, which is an L\* program with the following syntactic constructions:

1. The special word Contract comes first, then the contract name.
2. After this comes the contract constructor, in which all variables are initialized when they are placed on the blockchain, including the public address of the contract owner.
3. After this comes a list of properties.
4. After this comes a list of functions with access modifiers.

Within one contract, you can call the properties and methods of another contract, but only if it has already been defined earlier and stored on the blockchain (recursive calls and looping are excluded). Due to the fact that the L\* contract is similar to an L\* program, the following lemma is true.

**Lemma 3.** *The computational complexity of any L\* contract is a polynomial.*

3.1.3. Delta-Connection Module (DCM)

In order for this platform to be flexible and smart, it is also necessary to introduce AI modules for managing the operation of all smart contracts within the multi-blockchain. For these purposes, we propose using a special Delta-connection module, which analyzes information inside the multi-blockchain and interacts with the necessary smart city systems. Delta-connection is a bridge between the multi-blockchain and smart city. Moreover, all information received from sensors can go either directly to the multi-blockchain or through the Delta-connection module, if this is allowed within the framework of security and access. It processes bidirectional interactions from the smart city to the multi-blockchain and from the multi-blockchain via the Delta-connection module to the smart city. Moreover, the Delta-connection module monitors the synchronization of the execution of smart contracts within the multi-blockchain with the processes, sensors, and states of a smart city (Figure 2).

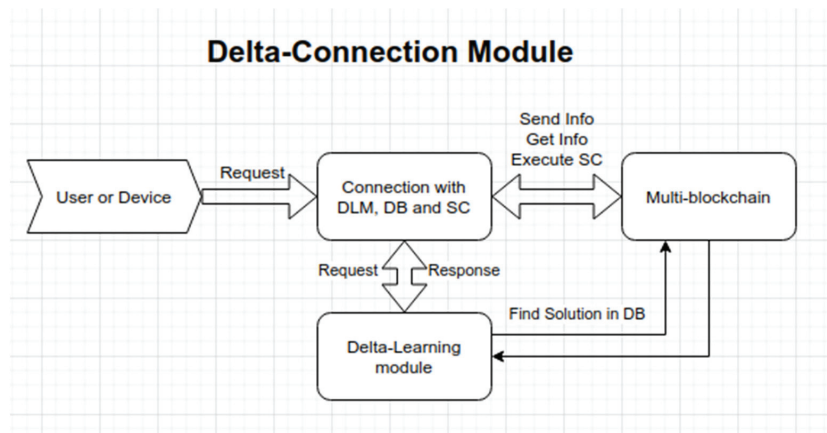


**Figure 2.** Delta-connection module.

### 3.1.4. Delta-Learning Module (DLM)

The Delta-learning module is a module that allows us to extract new knowledge and predict events based on the data contained in the multi-blockchain (Figure 3). For these purposes, both neural networks and logical-probabilistic inferences are used based on the theory of maximum specificity requirements announced by Carl Hempel in 1968 in [5]. This module can receive and store knowledge in special blockchains (databases).

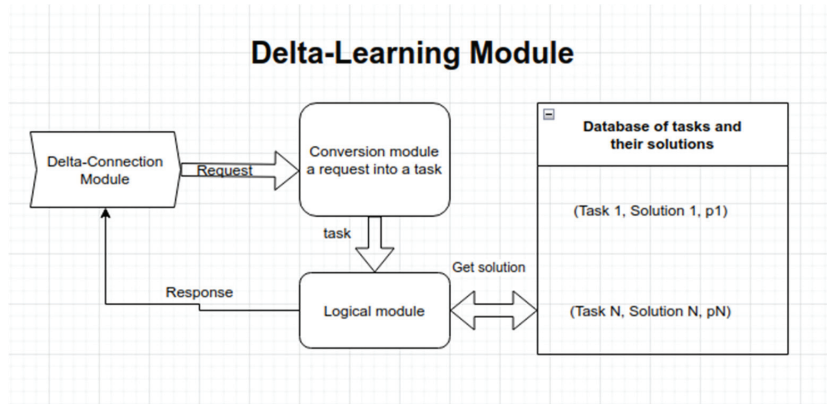


Figure 3. Delta-learning module.

The main idea of this module is to translate a natural request from a user or device via the Delta-Connection Module into a task (logical formula) and for this task to find the most effective solution, which is highly likely to be suitable (probability  $p_k$ ) for a given case. To perform this, all the facts and their generalizing problems with solutions are stored in the knowledge base.

All tasks are given by logical formulas of the following form:

$$\forall x \exists y \Phi(x,y) \rightarrow \Psi(x,y) \tag{1}$$

where the variable  $x$  can be considered a list of input parameters, and the variable  $y$  can be considered a list output parameters.

The conversion module can be either some neural network or some logical-probabilistic implementation. This module translates a user or device request from their language into the language of logical formulas. After that, a logical module is connected, whose task is to find the most effective solution to this logical formula (task) from the database.

Formulas of type (1) with the solution  $y = t(x)$  are generalizations with some probability  $p_k$  of facts from the database in the form

$$\Phi(c_i,t(c_i)) \rightarrow \Psi(c_i,t(c_i)), I \in I \tag{2}$$

From the database, we select the most effective solution  $y = t(x)$  for this task with the maximum probability  $p_k$ .

## 4. Results

This paper presented the blockchain-based Delta platform for building digital twins of smart cities. At the same time, the platform has a built-in Delta-learning module, which allows it to learn from multi-blockchain data as well as use the knowledge gained in managing smart cities. The Delta-connection module monitors the states of the multi-blockchain elements and issues commands and signals to the smart city elements. Through this module, it is also possible to transfer information to the multi-blockchain.

It was also shown that the computational complexity of smart contracts is also polynomial, and the smallest fixed point of the operator that inductively generates multi-blockchains is also polynomially computable.

## 5. Discussion

The development of smart cities has been actively happening for the last 10 years, but there is still a lot to be done. In this work, we have not touched on the financial issues that people face in their daily lives. It is also important to discuss the levels of citizens' access to various locations in the city, which is important for the safety of the city. We would also like to discuss issues related to a single control center for the digital twins of tens and hundreds of cities, and possibly for the management of entire countries.

## 6. Conclusions

This paper introduces the universal multi-blockchain-based Delta platform, which is designed for constructing digital twins of smart cities. This platform comprises multiple modules that enable the segregation of tasks such as data storage, interaction with smart city infrastructure, and real-time learning for extracting new insights. This instills optimism for its prompt deployment in practical scenarios. Furthermore, the platform facilitates the management of digital twins for multiple cities and the establishment of centralized and decentralized control hubs.

**Author Contributions:** Conceptualization, S.G. and A.N.; methodology, S.G. and A.N.; validation, S.G.; formal analysis, A.N.; investigation, S.G. and A.N.; writing—original draft preparation, A.N.; writing—review and editing, A.N.; visualization, A.N.; supervision, S.G.; project administration, S.G. All authors have read and agreed to the published version of the manuscript.

**Funding:** The work was performed within the state task of the Sobolev Institute of Mathematics, Novosibirsk, Russia. (project No. FWNF-2022-0011).

**Institutional Review Board Statement:** Not applicable.

**Informed Consent Statement:** Not applicable.

**Data Availability Statement:** The original contributions presented in the study are included in the article, further inquiries can be directed to the corresponding author.

**Acknowledgments:** We would like to thank all the staff in our department for the active discussion of our work. We also want to thank the Editors and Reviewers for your great work.

**Conflicts of Interest:** The authors declare no conflict of interest.

## References

1. Mohanty, S.; Choppali, U.; Kougiianos, E. Everything you wanted to know about smart cities: The Internet of things is the backbone. *IEEE Consum. Electron. Mag.* **2016**, *5*, 60–70. [CrossRef]
2. Popov, E.; Strielkowski, W.; Vlasov, M. Smart cities: Knowledge generation effectiveness in the digital economy. In *International Scientific and Practical Conference on Digital Economy (ISCDE 2019)*; Atlantis Press: Amsterdam, The Netherlands, 2019. [CrossRef]
3. Goncharov, S.; Nechesov, A. Axiomatization of Blockchain Theory. *Mathematics* **2023**, *11*, 2966. [CrossRef]
4. Deren, L.; Wenbo, Y.; Zhenfeng, S. Smart city based on digital twins. *Comput. Urban Sci.* **2021**, *1*, 4. [CrossRef]
5. Hempel, C. Maximal Specificity and Lawlikeness in Probabilistic Explanation. *Philos. Sci.* **1968**, *35*, 116–133. [CrossRef]
6. Shin, H.B. Envisioned by the state: Entrepreneurial urbanism and the making of Songdo City, South Korea. In *Book Mega-Urbanization in the Global South*, 1st ed.; Routledge: London, UK, 2016; ISBN 9781315797830. [CrossRef]
7. Lim, S.; Malek, J.A.; Hussain, M.Y.; Tahir, Z. Citizen participation in building citizen-centric smart cities. *Malays. J. Soc. Space* **2018**, *14*, 42–53. [CrossRef]
8. Gelernter, D. *Mirror Worlds*; Oxford University Press: Oxford, UK, 1993; p. 256.
9. Grieves, M. Virtually Intelligent Product Systems: Digital and Physical Twins. In *Complex Systems Engineering: Theory and Practice*; Flumerfelt, S., Shwartz, K., Mavris, D., Briceno, S., Eds.; American Institute of Aeronautics and Astronautics: Reston, VA, USA, 2019; pp. 175–200.
10. ADNOC at the Forefront of Digitization. Available online: <https://www.adnoc.ae/en/our-projects/hail-ghasha/at-the-forefront-of-digitization> (accessed on 1 July 2023).

11. Goncharov, S.; Nechesov, A. Polynomial-Computable Representation of Neural Networks in Semantic Programming. *J* **2023**, *6*, 48–57. [CrossRef]
12. Durov, N.; Durov, P. The Open Network. 2021. Available online: <https://docs.ton.org/ton.pdf> (accessed on 1 May 2023).
13. Goncharov, S.; Nechesov, A. Semantic programming for AI and Robotics. In Proceedings of the 2022 IEEE International Multi-Conference on Engineering, Computer and Information Sciences (SIBIRCON), Yekaterinburg, Russian, 11–13 November 2022; pp. 810–815. [CrossRef]
14. Goncharov, S.; Nechesov, A. Polynomial Analogue of Gandy’s Fixed Point Theorem. *Mathematics* **2021**, *9*, 2102. [CrossRef]

**Disclaimer/Publisher’s Note:** The statements, opinions and data contained in all publications are solely those of the individual author(s) and contributor(s) and not of MDPI and/or the editor(s). MDPI and/or the editor(s) disclaim responsibility for any injury to people or property resulting from any ideas, methods, instructions or products referred to in the content.



# Modeling and Characterization of Microspheres with Silver Molecular Clusters for Sensor Applications <sup>†</sup>

Egor Mikharev <sup>1,\*</sup>, Andrey Lunev <sup>1,\*</sup>, Alexander Sidorov <sup>2</sup> and Dmitry Redka <sup>1,3</sup>

<sup>1</sup> Department of Photonics, Faculty of Electronics, St. Petersburg Electrotechnical University “LETI”, St. Petersburg 197022, Russia; dnredka@etu.ru

<sup>2</sup> Research Center for Optical Material Engineering, ITMO University, St. Petersburg 197101, Russia; sidorov@oi.ifmo.ru

<sup>3</sup> Institute of Telecommunications, Riga Technical University, LV-1048 Riga, Latvia

\* Correspondence: eamikharev@stud.etu.ru (E.M.); ayulunyov@stud.etu.ru (A.L.)

<sup>†</sup> Presented at the 10th International Electronic Conference on Sensors and Applications (ECSA-10), 15–30 November 2023; Available online: <https://ecsa-10.sciforum.net/>.

**Abstract:** This study explores silver-molecular-cluster-containing microspheres for advanced sensors. These microspheres are synthesized through an ion exchange process with silver nitrate and sodium nitrate, creating unique optical properties. A simulation shows an enhanced radiation interaction due to extended fundamental mode propagation. This study investigates luminescence in the visible range (400–600 nm) when excited by long-wavelength UV light (360–410 nm), offering the potential for sensing applications. These microspheres find use in environmental sensing (pollutant detection), biomedicine (drug delivery, bioimaging), and industrial process monitoring.

**Keywords:** microspheres; silver molecular clusters; advanced sensor applications; ion exchange; glass matrix; refractive index gradient; optical characteristics; luminescence; UV light excitation; sensor technologies

## 1. Introduction

In recent years, Whispering Gallery Mode (WGM) microcavities have garnered significant attention as potential optical sensors for the label-free detection of various biological and chemical molecules and particles. These sensors can identify a range of molecules with refractive indices differing from that of the surrounding environment, eliminating the need for labeling. They rely on the observation of frequency shifts in WGM resonance due to minute perturbations in the mode volume. The efficacy of these sensors has been demonstrated in the detection of a variety of objects, including individual proteins, DNA molecules, and viruses [1,2].

In our current research, we explore a novel material for use in these WGM sensors. We focus on silicate glass microspheres containing ions and neutral molecular clusters (MC) of silver. These glasses are exceptional materials that exhibit intense luminescence in the visible spectrum [3]. They are characterized by high quantum yields and resistance to degradation, making them more appealing than organic dyes. The primary limitation of such sensors lies in the requirement for physical coupling between the WGM resonator and external optics, such as a tapered fiber or bus waveguide, to provide phase-matched evanescent coupling [4]. An alternative approach is the concept of WGM sensors with optically active resonators [5], which enables pumping in the UV region via LEDs and remote measurements through free space optics.

The ion exchange (IE) method is currently widely utilized for synthesizing multifunctional glasses. This method is straightforward to execute and enables the attainment of a high concentration of silver ions near the glass surface. Although studies on glasses with

**Citation:** Mikharev, E.; Lunev, A.; Sidorov, A.; Redka, D. Modeling and Characterization of Microspheres with Silver Molecular Clusters for Sensor Applications. *Eng. Proc.* **2023**, *58*, 95. <https://doi.org/10.3390/ecsa-10-16196>

Academic Editor: Stefano Mariani

Published: 15 November 2023



**Copyright:** © 2023 by the authors. Licensee MDPI, Basel, Switzerland. This article is an open access article distributed under the terms and conditions of the Creative Commons Attribution (CC BY) license (<https://creativecommons.org/licenses/by/4.0/>).

Ag<sup>+</sup> ions and silver ions obtained through the IO method have been conducted for more than half a century, their potential remains far from being fully explored.

In soda-silicate glass, silver initially exists in its ionic form as Ag<sup>+</sup>. Structural defects in the glass may contain uncompensated negative charges. These defects can arise from various factors, including defects in the crystal lattice of the glass or the presence of additional ions that can form negatively charged sites. In the presence of electronic defects near glass structural defects, silver ions Ag<sup>+</sup> can readily be reduced to neutral silver atoms Ag<sup>0</sup>. This reduction occurs when the glass is heated, and electrons are released from electronic defects. Neutral silver atoms Ag<sup>0</sup> can aggregate into molecular clusters, potentially comprising multiple silver atoms, each with unique optical and electronic properties. The formation of these molecular clusters can be induced by the characteristics of glass structure defects and heating conditions.

## 2. Materials and Methods

To create the silicate glass microspheres, we employed glass with the composition detailed in Table 1. The production process involved several steps. Initially, we crafted a thin fiber, and subsequently, we formed the microspheres by melting the fiber's end using a propane flame. The microspheres were then subjected to the Low-Temperature Ion Exchange (LTIE) process.

**Table 1.** Composition of glass used for making samples.

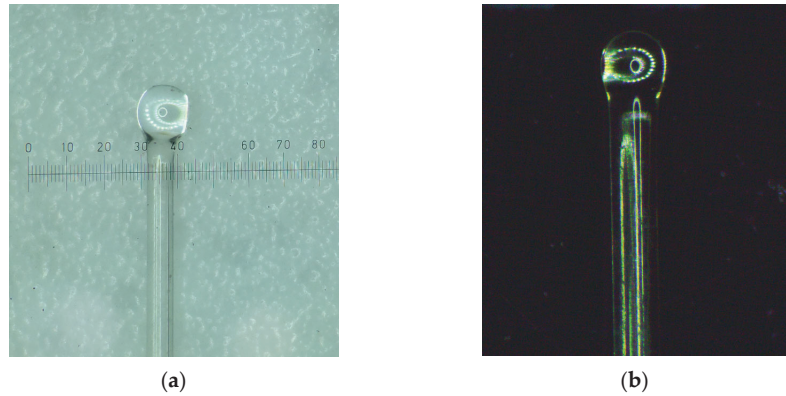
Chemical Constituents	Glass (% Mass)
SiO <sub>2</sub>	72.2%
Na <sub>2</sub> O	14.3%
K <sub>2</sub> O	1.2%
CaO	6.4%
MgO	4.3%
Al <sub>2</sub> O <sub>3</sub>	1.2%
Fe <sub>2</sub> O <sub>3</sub>	0.03%
SO <sub>3</sub>	0.3%

The ion exchange process occurred in a molten salt mixture of silver nitrate (AgNO<sub>3</sub>) and sodium nitrate (NaNO<sub>3</sub>) at a temperature of 330 °C for a duration of 15 min. To monitor the progress of the process, we also included witness glasses with the same composition. These glasses, with a thickness of 0.17 mm, underwent the ion exchange process alongside the microspheres in a common crucible.

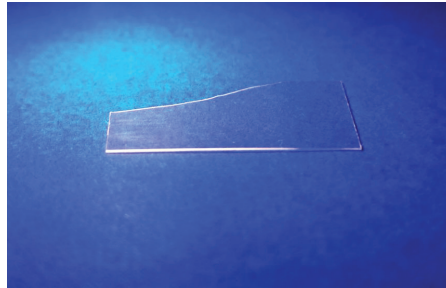
Following the LTIE process, we meticulously cleansed the samples. This cleansing process involved washing with distilled water and then with isopropyl alcohol to eliminate any residual salts remaining on the surface after the process.

Figure 1 display photographs of the samples we obtained. Notably, the smallest sample achievable through the described method had a diameter of 200 microns. Figure 2 shows one of the witness samples that was not completely immersed in the crucible; when the sample was illuminated with an LED with a wavelength of ≈390 nm, the luminescence of molecular clusters of silver was clearly visible, and the area where the glass passes was not immersed in the molten salts.

Comsol Multiphysics was employed to determine the resonant frequencies and fundamental modes of the resonator. For an effective modeling of the WGM resonator, a two-dimensional axisymmetric approach was adopted. The grid was manually adjusted to facilitate a two-dimensional axisymmetric natural frequency analysis.



**Figure 1.** The obtained microsphere samples: (a) microsphere with a diameter of 380  $\mu\text{m}$ ; (b) microsphere with a diameter of 200  $\mu\text{m}$ .



**Figure 2.** Witness sample visible luminescence.

The investigation of the properties of silicate glass containing silver molecular clusters, synthesized through the LTIE method, encompassed both absorption measurements and luminescence spectra measurements. Absorbance measurements were conducted on the witness samples using a UV-VIS spectrophotometer (PB 2201). Luminescence spectral acquisition measurements were performed using a Fluorolog<sup>®</sup>-3 instrument with FluorEssence<sup>™</sup> (HORIBA Jobin Yvon SAS, Palaiseau, France). For all luminescence measurements, the integration time was 0.1 s.

### 3. Results and Discussion

#### 3.1. Investigation of the Properties of Silicate Glass Containing Silver Molecular Clusters

An experiment was conducted to measure the absorption of glass samples that underwent Low-Temperature Ion Exchange (LTIE), as well as transparent glass samples that were not subjected to LTIE treatment. The resulting spectrum is depicted in Figure 3. Notably, the absorption spectrum of the samples after the LTIE process lacks characteristic absorption peaks. This absence is attributed to the fact that, under the same process parameters used in the treatment, predominantly silver molecular clusters, such as  $\text{Ag}_{2\dots5}$ , are formed [6].

Figure 4 presents the results of measuring the luminescence intensity. When excited at wavelengths of 370 nm and 390 nm, the luminescence spectra of all synthesized glasses exhibit a broad luminescence band within the visible spectrum. This broadband luminescence spanning from 500 to 900 nm corresponds to the emission emanating from a small quantity of silver microcrystals formed directly during the LTIE process [7]. To generate molecular clusters (MC), it is imperative to reduce silver ions to their atomic state. This transformation leads to the creation of a certain quantity of silver microcrystals during the LTIE process, consequently giving rise to weak luminescence across the entire visible range.

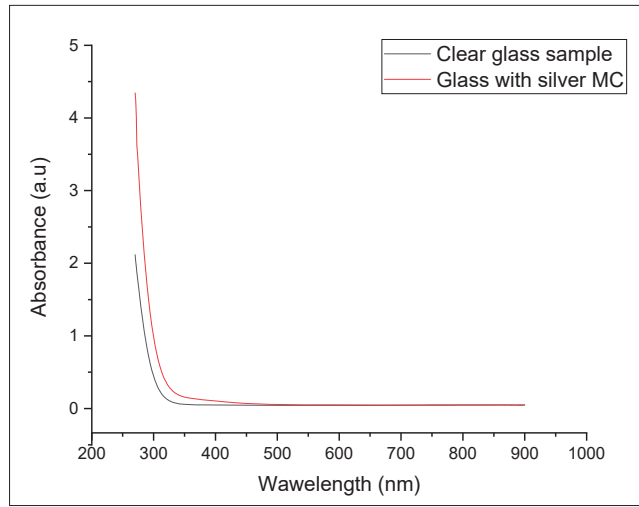


**Figure 3.** This is a figure. Schemes follow the same formatting.

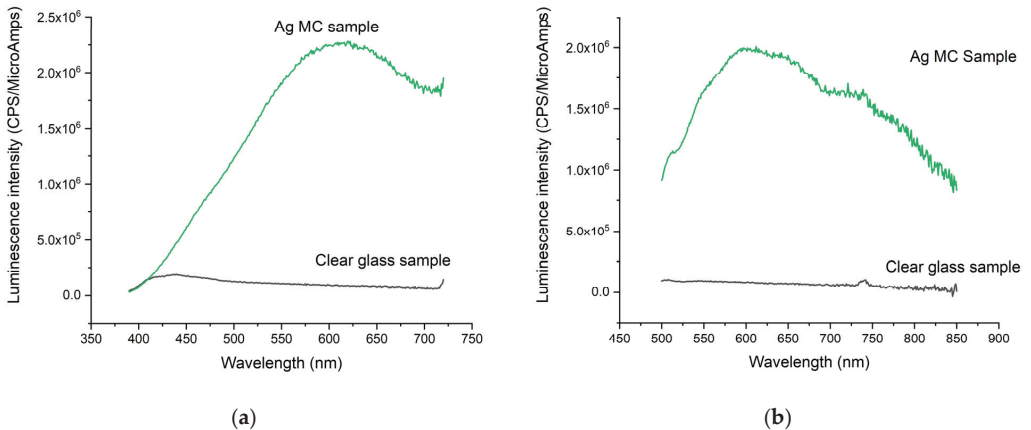


**Figure 4.** Luminescence intensity: (a) first sample,  $\lambda_{exc}$  370 nm; (b) second sample,  $\lambda_{exc}$  390 nm.

### 3.2. Modeling WGM Resonators

The simulated microspheres had a radius of 100  $\mu\text{m}$ . During the LTIE process with silver, glass changes its refractive index from 1.585 on the surface to 1.515. The simulated microsphere had a gradient refractive index from the edge of the microsphere to the center. To explore the potential of this material, simulations of microspheres in air and water were carried out. Figure 5 shows the distribution of the EM field in the cross-section of the microcavity in air (a) and water (b). The resonant wavelength for the fundamental mode of the microresonator near the luminescence peak was determined. For a microsphere in air, the resonant wavelength for the fundamental TE mode with azimuthal number 1608 was 600.988. For a microsphere in water, the resonant wavelength for the fundamental TE mode with azimuthal number 1608 was 601.294. The difference between the resonant wavelengths was 0.25 nm.

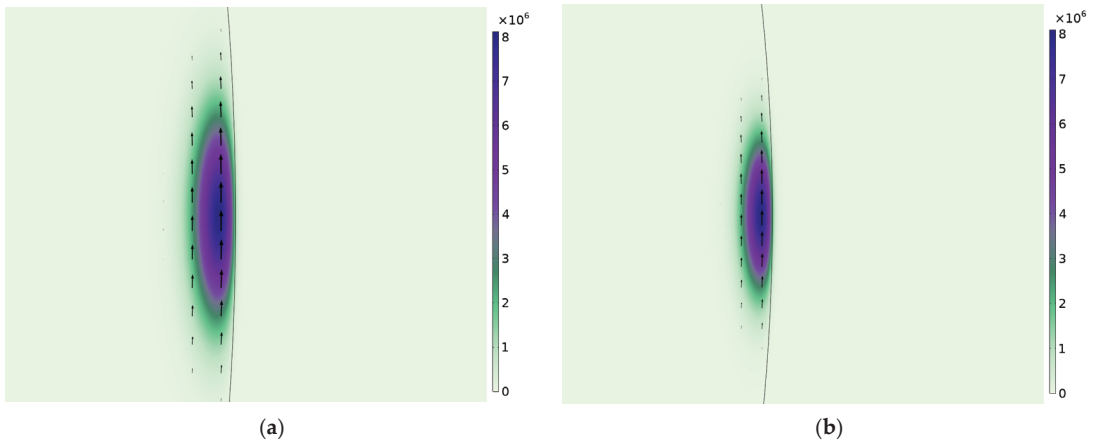


**Figure 5.** Fundamental mode localization: (a) microsphere in air; (b) microsphere in water.

#### 4. Conclusions

We have obtained a new material that is suitable for use in label-free sensors with active WGM resonators. This material is very simple to obtain and cost-effective. The experiment showed that glass samples subjected to Low-Temperature Ion Exchange (LTIE) showed distinct absorption characteristics, particularly the absence of characteristic absorption peaks, which was attributed to the formation of  $\text{Ag}_{2\dots5}$  molecular clusters of silver. Luminescence measurements demonstrated a broad emission band in the visible spectrum, especially in the 500–900 nm range, confirming the formation of silver microcrystals during the LTIE process.

According to the simulation results, the difference between the resonant wavelengths for media with different refractive indexes was 0.26 nm. This allows the material to be used for microsphere sensors without direct physical connection. The results obtained show the potential of soda silicate glass with molecular silver clusters as a material for WGM sensors.

**Author Contributions:** Conceptualization, E.M. and A.S.; methodology, A.S.; software, A.L.; validation, E.M. and A.L.; formal analysis, A.S.; investigation, A.L. and E.M.; resources, D.R.; data curation, A.S.; writing—original draft preparation, E.M.; writing—review and editing, E.M. and A.L.; visualization, A.L.; supervision, A.L.; project administration, D.R. All authors have read and agreed to the published version of the manuscript.

**Funding:** This research received no external funding.

**Institutional Review Board Statement:** Not applicable.

**Informed Consent Statement:** Not applicable.

**Data Availability Statement:** Data are contained within the article.

**Conflicts of Interest:** The authors declare no conflict of interest.

#### References

1. Foreman, M.R.; Swaim, J.D.; Vollmer, F. Whispering gallery mode sensors. *Adv. Opt. Photon.* **2015**, *7*, 168–240. [CrossRef] [PubMed]
2. Vollmer, F.; Arnold, S. Whispering-gallery-mode biosensing: Label-free detection down to single molecules. *Nat. Methods* **2008**, *5*, 591–596. [CrossRef] [PubMed]
3. Demichev, I.A.; Ignat'ev, A.I.; Nikonov, N.V.; Sgibnev, E.M.; Sidorov, A.I.; Khrushcheva, T.A.; Shakhverdov, T.A. Specific features of the luminescence of silicate glasses with silver introduced by ion exchange. *Opt. Spectrosc.* **2014**, *116*, 587–592. [CrossRef]

4. Wienhold, T.; Kraemmer, S.; Wondimu, S.F.; Siegle, T.; Bog, U.; Weinzierl, U.; Schmidt, S.; Becker, H.; Kalt, H.; Mappes, T.; et al. All-polymer photonic sensing platform based on whispering-gallery mode microgoblet lasers. *Lab Chip* **2015**, *15*, 3800–3806. [CrossRef] [PubMed]
5. Hanumegowda, N.M.; White, I.M.; Oveys, H.; Fan, X. Label-free protease sensors based on optical microsphere resonators. *Sens. Lett.* **2005**, *3*, 315–319. [CrossRef]
6. Sheng, J.; Li, J.; Yu, J. The development of silver nanoclusters in ion-exchanged soda-lime silicate glasses. *Int. J. Hydrog. Energy* **2007**, *32*, 2598–2601. [CrossRef]
7. Simo, A.; Polte, J.; Pfander, N.; Vainio, U.; Emmerling, F.; Rademann, K. Formation Mechanism of Silver Nanoparticles Stabilized in Glassy Matrices. *J. Am. Chem. Soc.* **2012**, *134*, 18824–18833. [CrossRef] [PubMed]

**Disclaimer/Publisher’s Note:** The statements, opinions and data contained in all publications are solely those of the individual author(s) and contributor(s) and not of MDPI and/or the editor(s). MDPI and/or the editor(s) disclaim responsibility for any injury to people or property resulting from any ideas, methods, instructions or products referred to in the content.

Proceeding Paper

# Validation of the Use of ATR Mode in FT-IR Spectroscopy on Gingival Crevicular Fluid Samples in Orthodontics <sup>†</sup>

Marianna Portaccio <sup>1</sup>, Carlo Camerlingo <sup>2</sup>, Fabrizia d'Apuzzo <sup>3</sup>, Ludovica Nucci <sup>3</sup> and Maria Lepore <sup>1,\*</sup>

<sup>1</sup> Dipartimento di Medicina Sperimentale, Università degli Studi della Campania Luigi Vanvitelli, 80138 Napoli, Italy; marianna.portaccio@unicampania.it

<sup>2</sup> CNR-SPIN, Istituto Superconduttori, Materiali Innovativi e Dispositivi, 80078 Pozzuoli, Italy; carlo.camerlingo@spin.cnr.it

<sup>3</sup> Dipartimento Multidisciplinare di Specialità Medico-Chirurgiche e Odontoiatriche, Università degli Studi, della Campania Luigi Vanvitelli, 80138 Napoli, Italy; fabrizia.dapuzzo@unicampania.it (F.d.); ludovica.nucci@unicampania.it (L.N.)

\* Correspondence: maria.lepore@unicampania.it

<sup>†</sup> Presented at the 10th International Electronic Conference on Sensors and Applications (ECSA-10), 15–30 November 2023; Available online: <https://ecsa-10.sciforum.net/>.

**Abstract:** Previous work has demonstrated the relevance of Fourier Tr and IR investigation on gingival crevicular fluid (GCF) for monitoring orthodontic treatments. Previously, FT-IR spectra of GCF samples have been acquired in reflectance mode by dropping a few microliters of GCF on a reflecting support. A faster procedure for collecting GCF spectra can be obtained by exploiting the Attenuated Total Reflection (ATR) contact sampling method, which allows the collection of good-quality infrared spectra with almost no sample preparation. The objective of the present investigation is to validate the ATR approach for GCF analysis by comparing the spectra acquired in reflectance using the GCF samples extracted via paper cones versus those directly collected from the blotter, employing the ATR approach.

**Keywords:** gingival crevicular fluid; orthodontic treatment; FT-IR spectroscopy; ATR collection geometry

**Citation:** Portaccio, M.; Camerlingo, C.; d'Apuzzo, F.; Nucci, L.; Lepore, M. Validation of the Use of ATR Mode in FT-IR Spectroscopy on Gingival Crevicular Fluid Samples in Orthodontics. *Eng. Proc.* **2023**, *58*, 96. <https://doi.org/10.3390/ecsa-10-16232>

Academic Editor: Stefano Mariani

Published: 15 November 2023



**Copyright:** © 2023 by the authors. Licensee MDPI, Basel, Switzerland. This article is an open access article distributed under the terms and conditions of the Creative Commons Attribution (CC BY) license (<https://creativecommons.org/licenses/by/4.0/>).

## 1. Introduction

Previous work has demonstrated the relevance of Fourier Transform Infrared (FT-IR) spectroscopic investigation on gingival crevicular fluid (GCF) for monitoring orthodontic tooth movement during treatment with fixed appliances in permanent dentition [1]. FT-IR spectra of GCF samples have been acquired in reflectance mode by dropping a few microliters of GCF on a reflecting support. A faster procedure for collecting GCF spectra can be obtained by exploiting a different acquisition geometry. The Attenuated Total Reflection (ATR) approach allows the collection of good-quality infrared spectra from any solid or liquid sample with almost no sample preparation and spectra are recorded in a few minutes [2].

It has been demonstrated that an unfolding process occurs during the initial stage of orthodontic treatments followed by some recovery during the following days. Modifications could also result from the formation of amyloid aggregates that can be induced by mechanical stress due to the application of orthodontic forces [3].

One of the advantages of using GCF is the fluid collection method, which is non-traumatic, minimally invasive, and relatively simple to perform. Several sampling and analyzing methods have been described to collect GSF samples, each with advantages and disadvantages.

The objective of this research is to validate the ATR approach for GCF investigation by comparing the spectra acquired from GCF samples extracted with paper cones, and examined using conventional reflecting supports, compared to those collected by employing

the ATR method. Using the ATR geometry, the measurement time is greatly shortened and there is no risk that the spectra can be affected by the extraction procedures. These findings can be pivotal for future research in order to make the GCF analysis fast and easy for the monitoring of orthodontic tooth movement in complex cases.

## 2. Materials and Methods

Patients aged between 13 and 21 years seeking an orthodontic treatment in full permanent dentition were recruited from the Orthodontic Program of the University of Campania Luigi Vanvitelli, Naples, Italy. GCF samples were collected before the beginning of the orthodontic treatment. Two different paper blotters were used: the standard sterile absorbent paper cones and PerioPaper strips, inserted 1 mm into the gingival crevice for about 30 s without any plaque or blood contamination of the fluid.

For FT-IR measurements in reflection geometry, GCF was extracted as reported in Ref. [4], whereas PerioPaper supports with GCF inside were directly used for the ATR acquisition mode. A Perkin Elmer Spectrum One FT-IR spectrometer was used for FT-IR in specular-reflection mode and a Universal ATR accessory was adopted for the other type of measurements.

Preliminary subtraction of the properly acquired background spectrum was performed for all spectra. Afterwards, the spectra were normalized using the Standard Normal Variate (SNV) method as described in Ref. [5]. The spectra were also analyzed using the convolution of Gaussian-shaped vibrational modes. The starting conditions of the procedure were manually selected and a best-fit routine from the GRAMS-AI software (2001, Thermo Fischer Scientific, Waltham, MA, USA) was used to estimate the optimized intensity, position, and width of the peaks. The  $\chi^2$  parameter was used to assess the convolution procedure performance.

For ATR spectra, it was also necessary to take into account the contribution of cellulose content of PerioPaper strips, since the measurements were performed on them after the GCF collection. In this case, both the cellulose component of PerioPaper and the GCF contribute to the spectroscopy signal; thus, a numerical data treatment needs to distinguish the two signal components. The measured ATR signals of GCF-embedded samples were compared with the signal obtained from bare PerioPaper.

The signal intensity was previously normalized with respect to the average value using the SNV method mentioned above. After that, the normalized signals were compared using linear regression, and the substrate signal, mainly assigned to cellulose, was subtracted from the whole signal, and thus obtained the spectral contributions due to GCF.

## 3. Results and Discussion

### 3.1. FT-IR Spectroscopy in Reflection Mode on Extracted Fluid

A typical FT-IR spectrum acquired in reflection mode is shown in Figure 1. Two regions of interest in the spectrum were identified: the 3020–2750  $\text{cm}^{-1}$  range (Figure 1a, high-wavenumber range) and the 1800–950  $\text{cm}^{-1}$  range (Figure 1b, fingerprint range).

The spectrum in Figure 1a is mainly related to the C-H vibrational modes of lipids [4]. Two prominent peaks occur at 2933  $\text{cm}^{-1}$  and 2884  $\text{cm}^{-1}$  that can be assigned to  $\text{CH}_2$  asymmetric and  $\text{CH}_3$  symmetric stretching, respectively. A smaller component at 2963  $\text{cm}^{-1}$  is attributed to the  $\text{CH}_3$  asymmetric stretching mode.

The spectrum in Figure 1b is mainly the result of protein vibrational modes. The spectrum is dominated by the Amide I band centered at about 1650  $\text{cm}^{-1}$ . The main component is assigned to  $\alpha$ -helix vibrational mode. This allows us to obtain essential information on the structural configuration of the proteins when the relative intensity of the  $\alpha$ -helix mode is compared with those of the other Amide I band components, namely the  $\beta$ -sheet modes, centered at 1588  $\text{cm}^{-1}$  and 1599  $\text{cm}^{-1}$  [5]. In addition to the Amide I band, two other major bands occur at about 1415  $\text{cm}^{-1}$  and 1075  $\text{cm}^{-1}$ . The former is attributed to  $\text{COO}^-$  stretching modes of amino acids. The band ranging into 1000–1100  $\text{cm}^{-1}$  is



related to C-O stretching mode. The prevalent component is centered at  $1075\text{ cm}^{-1}$  and it is assigned to the  $\text{PO}_2^-$  stretching mode of nucleic acid [4].

A list of the Gaussian components obtained using the deconvolution process of the spectrum of Figure 1a,b is reported in Table 1. As said before, the mode peaks have been modeled by Gaussian functions. For each component, the spectral position  $x_{ci}$ , the relative peak area (in percent)  $A_i$ , and the peak width at half signal  $\sigma_i$  are reported.

**Table 1.** Spectral features of GCF samples from FT-IR spectra acquired in reflection mode from the fluid extracted from the paper cones, and in ATR mode from GCF in PerioPapers. The analysis was performed using a deconvolution procedure using the overlap of Gaussian functions as model. The peak position, the normalized area, and the  $\sigma$  peak width are reported for each mode. The peak areas have been normalized to the whole area of  $3020\text{--}2750\text{ cm}^{-1}$  range and  $1800\text{--}950\text{ cm}^{-1}$  range, respectively.

Assignments	FT-IR in ATR Mode			FT-IR in Reflection Mode		
	$\sigma_i$ ( $\text{cm}^{-1}$ )	$A_i$ (%)	$x_{ci}$ ( $\text{cm}^{-1}$ )	$\sigma_i$ ( $\text{cm}^{-1}$ )	$A_i$ (%)	$x_{ci}$ ( $\text{cm}^{-1}$ )
C-O stretching of carbohydrates	13.5	$2 \pm 1$	$1050 \pm 4$	21	$10 \pm 4$	$1044 \pm 3$
Symm. $\text{PO}_2^-$ stretching of nucleic acids	15.1	$2 \pm 1$	$1077 \pm 17$	38	$18 \pm 9$	$1075 \pm 2$
asymmetric C-O stretching, COH bending of lipids	22	$6 \pm 3$	$1150 \pm 4$	35	$8 \pm 4$	$1152 \pm 3$
				38	$2 \pm 1$	$1211 \pm 1$
	38	$13 \pm 10$	$1234 \pm 7$			
				20	$2 \pm 2$	$1255 \pm 4$
	43	$8 \pm 4$	$1286 \pm 4$			
$\text{CH}_2$ twist of lipids and amino acids				30	$4 \pm 4$	$1307 \pm 26$
Stretching $\text{COO}^-$ of amino acids	43	$17 \pm 8$	$1417 \pm 8$	26	$12 \pm 7$	$1415 \pm 3$
	36	$10 \pm 4$	$1467 \pm 17$			
				22	$3 \pm 1$	$1500 \pm 3$
N-H bending of proteins (Amide II band)	25	$15 \pm 6$	$1542 \pm 4$			
$\beta$ -sheet ( $1612\text{--}1638\text{ cm}^{-1}$ )				31	$20 \pm 17$	$1580 \pm 27$
C=C stretching of amino acids						
$\beta$ -sheet ( $1612\text{--}1638\text{ cm}^{-1}$ ); C=C stretching of amino acids				33	$16 \pm 8$	$1599 \pm 1$
$\alpha$ -helix ( $1642\text{--}1661\text{ cm}^{-1}$ ); C=O stretching of proteins (Amide I band)	35	$27 \pm 5$	$1644 \pm 7$	12	$4 \pm 4$	$1650 \pm 8$
	8	$3 \pm 2$	$2798 \pm 3$			
	6	$20 \pm 6$	$2851 \pm 1$			
Symmetric $\text{CH}_3$ stretching of lipids	9	$13 \pm 5$	$2870 \pm 11$	16	$32 \pm 9$	$2884 \pm 3$
				10	$8 \pm 23$	$2903 \pm 9$
Asymmetric $\text{CH}_2$ stretching of lipids	9	$44 \pm 10$	$2919 \pm 2$	17	$17 \pm 1$	$2923 \pm 1$
				29	$29 \pm 11$	$2933 \pm 3$
Asymmetric $\text{CH}_3$ stretching of lipids	12	$21 \pm 13$	$2961 \pm 3$	14	$14 \pm 1$	$2963 \pm 5$

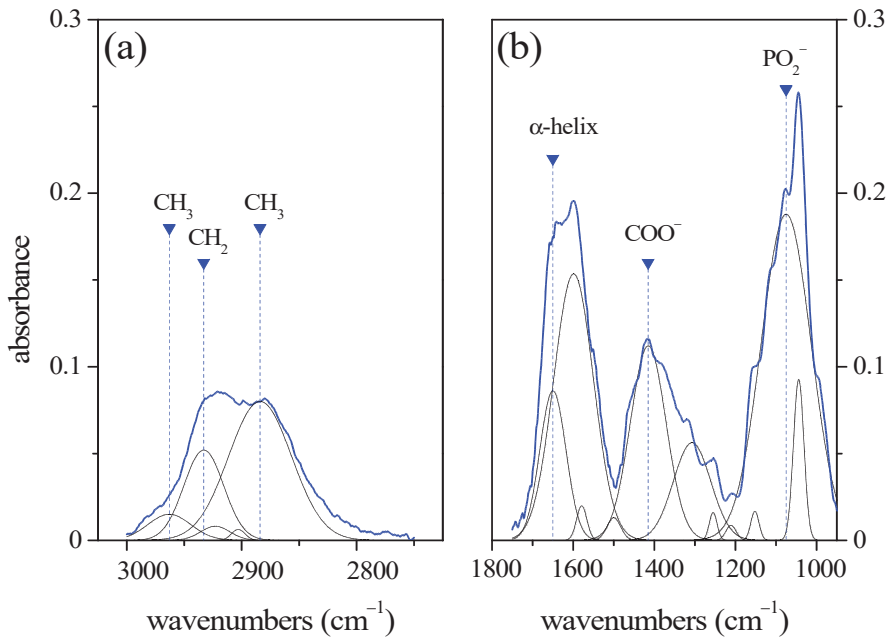


**Figure 1.** Typical FTIR spectrum of GCF acquired in reflectance mode. On the left, we see the 3020–2750  $\text{cm}^{-1}$  high-wavenumber range (a) and on the right, we see the 1800–950  $\text{cm}^{-1}$  fingerprint range (b). Blue curves refer to the experimental data. The positions, area, and width of the peaks are reported in Table 1.

### 3.2. ATR Spectroscopy on GCF in PerioPapers

The ATR configuration permitted the IR absorption spectrum of the GCF to appear directly on the PerioPapers supports, without any extraction process. The resulting IR spectrum of GCF in ATR configuration is reported in Figure 2. As in the case of conventional FT-IR, two regions of interest are shown in Figure 2a for wavenumbers ranging between 3020 and 2750  $\text{cm}^{-1}$ , and Figure 2b for the 1800–950  $\text{cm}^{-1}$  range. In the high-wavenumber region, (Figure 1a) the spectrum is similar to the one resulting from the FT-IR spectroscopy shown in Figure 1a, but the spectral features are better resolved, and four peaks are clearly evinced. They were assigned to symmetric and antisymmetric stretching modes of  $\text{CH}_2$  (2851  $\text{cm}^{-1}$  and 2919  $\text{cm}^{-1}$ ) and  $\text{CH}_3$  (2870  $\text{cm}^{-1}$  and 2961  $\text{cm}^{-1}$ ), respectively. The ATR spectrum of GCF in the 1800–950  $\text{cm}^{-1}$  wavenumber range is reported in Figure 2b. Also, in this region of the spectrum, it is possible to notice better-resolved spectral characteristics. The Amide I band located at 1644  $\text{cm}^{-1}$  and assigned to  $\alpha$ -helix mode and the peak at 1542  $\text{cm}^{-1}$  assigned to Amide II band are clearly evident. The  $\text{COO}^-$  stretching mode of amino acids occurs at 1150  $\text{cm}^{-1}$ , as in the case of spectra acquired in reflection mode. Instead, the intensity of the  $\text{PO}_2^-$  mode is drastically reduced due to the influence of the cellulose contained in the PerioPaper supports. In fact, in the FT-IR spectrum of cellulose, a large absorbance band occurs at 1083  $\text{cm}^{-1}$  due to the C-O stretching ring modes [6]. This dramatically increases the radiation attenuation of the excitation signal and affects the ATR signal of CGF in this wavenumber region.

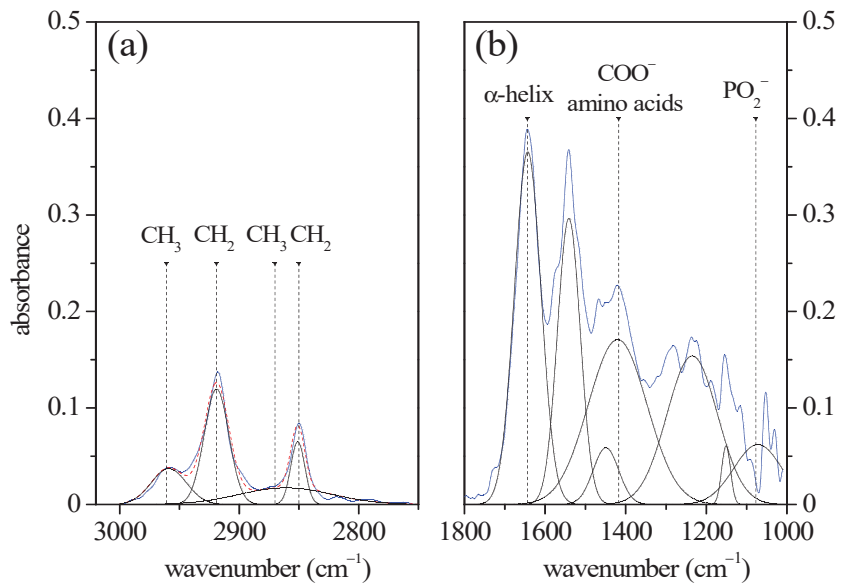


**Figure 2.** Typical FTIR spectrum of GCF acquired in ATR mode. On the left, we see the 3020–2750  $\text{cm}^{-1}$  high-wavenumber range (a) and on the right, we see the 1800–950  $\text{cm}^{-1}$  fingerprint range (b). Blue curves refer to the experimental data. The positions, area, and width of the peaks are reported in Table 1.

As in the case of FT-IR spectrum acquired in reflection mode, the deconvolution of the spectrum in Gaussian terms allowed us to determine the main vibrational modes. Their spectral positions, areas, and widths are reported in Table 1 and compared with FT-IR data. In general, a good agreement between the two acquisition geometries is found. In the high-wavenumber region, the broadening of the peak in the spectrum acquired in reflection mode determines some slight intensity differences, but the spectrum behavior is the same. In the fingerprint region, similarities occur between the spectra acquired in the two different geometries, even if the band intensity is drastically lowered in the 1000–1200  $\text{cm}^{-1}$  range.

#### 4. Conclusions

Analytical vibrational spectroscopies are widely recognized to have a relevant impact on new medical approaches and contribute to improving diagnosis and monitoring processes in terms of time, reliability, and sensitivity. The ATR approach for FT-IR investigation of CGF samples has been explored directly on the PerioPaper probe. This is an important aspect of clinical practice, since it facilitates the use of spectroscopy analysis.

A general agreement has been found between spectral data obtained via FT-IR in reflection mode and ATR spectroscopy of CGF. However, a reduced IR absorbance signal is measured in the 1000–1200  $\text{cm}^{-1}$  wavenumber range of the ATR spectrum, due to the influence of the cellulose contained in the PerioPaper. A more efficient procedure for subtracting cellulose contribution in this region that could offer better results is under investigation.

**Author Contributions:** Conceptualization, M.P., F.d. and M.L.; methodology, L.N. and C.C.; validation, M.P. and M.L.; investigation, F.d., M.P. and L.N.; data curation, C.C. and M.P.; writing—review and editing, C.C., F.d. and M.L. All authors have read and agreed to the published version of the manuscript.

**Funding:** This research received no external funding.

**Institutional Review Board Statement:** The study was conducted in accordance with the Declaration of Helsinki and approved by the Ethics Committee of University of Campania “L. Vanvitelli” (N. Prot. 207).

**Informed Consent Statement:** Informed consent was obtained from all subjects involved in the study.

**Data Availability Statement:** Data are available on request.

**Conflicts of Interest:** The authors declare no conflict of interest.

## References

1. d’Apuzzo, F.; Nucci, L.; Delfino, I.; Portaccio, M.; Minervini, G.; Isola, G.; Serino, I.; Camerlingo, C.; Lepore, M. Application of vibrational spectroscopies in the qualitative analysis of gingival crevicular fluid and periodontal ligament during orthodontic tooth movement. *J. Clin. Med.* **2021**, *10*, 1405. [CrossRef] [PubMed]
2. Vigano, C.; Manciu, L.; Buyse, F.; Goormaghtigh, E.; Ruysschaert, J.M. Attenuated total reflection IR spectroscopy as a tool to investigate the structure, orientation and tertiary structure changes in peptides and membrane proteins. *Biopolymers* **2000**, *55*, 373–380. [CrossRef] [PubMed]
3. Camerlingo, C.; Portaccio, M.; d’Apuzzo, F.; Nucci, L.; Perillo, L.; Delfino, I.; Lepore, M. An investigation on the Amide I band in vibrational spectra of gingival crevicular fluid during orthodontic treatments. In *SPIE 12627, Translational Biophotonics: Diagnostics and Therapeutics III*; SPIE: Munich, Germany, 2023; p. 1262732.
4. Portaccio, M.; d’Apuzzo, F.; Perillo, L.; Grassia, V.; Errico, S.; Lepore, M. Infrared spectroscopy characterization of gingival crevicular fluid during orthodontic treatment. *J. Mol. Struct.* **2019**, *1176*, 847–854. [CrossRef]
5. Camerlingo, C.; Portaccio, M.; d’Apuzzo, F.; Nucci, L.; Perillo, L.; Lepore, M.  $\mu$ -FTIR,  $\mu$ -Raman, and SERS analysis of Amide I spectral region in oral biofluid samples during orthodontic treatment. *Sensors* **2022**, *22*, 7874. [CrossRef] [PubMed]
6. Blackwell, J.; Vasko, P.D.; Koenig, J.L. Infrared and Raman Spectra of the Cellulose from the Cell Wall of *Valonia ventricosa*. *J. Appl. Phys.* **1970**, *41*, 4375–4379. [CrossRef]

**Disclaimer/Publisher’s Note:** The statements, opinions and data contained in all publications are solely those of the individual author(s) and contributor(s) and not of MDPI and/or the editor(s). MDPI and/or the editor(s) disclaim responsibility for any injury to people or property resulting from any ideas, methods, instructions or products referred to in the content.

Proceeding Paper

# Crop Recommendation Systems Based on Soil and Environmental Factors Using Graph Convolution Neural Network: A Systematic Literature Review <sup>†</sup>

P. Ayesha Barvin and T. Sampradeepraj \*

Department of Computer Science and Engineering, Kalasalingam Academy of Research and Education, Srivilliputhur 626138, Tamil Nadu, India; r9923104006@klu.ac.in

\* Correspondence: t.sampradeepraj@klu.ac.in

<sup>†</sup> Presented at the 10th International Electronic Conference on Sensors and Applications (ECSA-10), 15–30 November 2023; Available online: <https://ecsa-10.sciforum.net/>.

**Abstract:** Data-driven approaches and resource management to improve yield are becoming increasingly frequent in agriculture with the progress in technology. Based on a broad variety of environmental variables, this research compares two graph-based crop recommendation algorithms, GCN and GNN. Our methods select the optimal crop for a season based on nitrogen, potassium and phosphorus levels, as well as temperature, humidity, soil pH and rainfall. We assess the dataset's complexity using GCN and GNN, which can handle graph-based structured data well. We utilize supervised learning to structure input information as nodes in a graph with edges reflecting plausible feature relationships to predict the optimal crop based on environmental conditions. Our experiment creates a graph via data preprocessing. Crop recommendation effectiveness is assessed using F1-score, recall, accuracy and precision for both models. To prevent overfitting and ensure generalizability, we employ k-fold cross-validation. Our crop suggestion comparison of GCN vs. GNN shows their pros and cons. Due to its concentration on graph convolution and feature aggregation, GCN captures localized connections in the feature graph better than GNN, which competes in situations needing larger feature interactions. This research advances graph-based models in agriculture and highlights their potential to enhance precision agriculture. We prioritize choosing the optimum graph-based model based on the dataset's nature and inherent links to optimize crop management and resource allocation.

**Citation:** Ayesha Barvin, P.; Sampradeepraj, T. Crop Recommendation Systems Based on Soil and Environmental Factors Using Graph Convolution Neural Network: A Systematic Literature Review. *Eng. Proc.* **2023**, *58*, 97. <https://doi.org/10.3390/ecsa-10-16010>

Academic Editor: Stefano Mariani

Published: 15 November 2023



**Copyright:** © 2023 by the authors. Licensee MDPI, Basel, Switzerland. This article is an open access article distributed under the terms and conditions of the Creative Commons Attribution (CC BY) license (<https://creativecommons.org/licenses/by/4.0/>).

**Keywords:** crop recommendation; graph-based models; environmental factors; comparative analysis

## 1. Introduction

India is the leading producer of agricultural goods. The agriculture industry employs 58 percent of the total Indian population as well as contributes 17% to the country's GDP. Crops rely on a multitude of factors, including the type of soil, amount of rainfall and sunlight, irrigation, fertilizer use, insect presence, and land preparation [1,2]. One of the most frequent challenges that Indian farmers must overcome is choosing crops in accordance with the terrain and the climate [3]. Considering the fact that climatic conditions and characteristics of soil have a direct impact on crop yield, it is necessary to develop crop management practices that consider the appropriateness of the site and the soil [4]. Weather and agriculture are closely intertwined; therefore, it is essential to adapt to changing climatic trends in a productive way. Using climate-smart agricultural practices may help increase productivity and produce quality crops [5].

Precision agriculture has recently brought about significant advances in the world of agriculture, with an emphasis on irrigation systems, fertilization, crop monitoring and yield prediction [6]. Choosing the appropriate crop in relation to location-specific soil factors and climatic conditions is also vital for enhancing production [7]. Therefore, farmers must be

equipped with instruments that allow them to choose the best crop suited for the region’s unique meteorological and soil conditions [8]. The development of crop recommendation system using deep learning techniques are illustrated in Figure 1. In developing nations, using machine learning for agricultural planning objectives has resulted in the development of applications such as crop recommendation, crop disease diagnosis, fertilizer management and so on [9]. The farmers would profit from the development of crop recommendation systems that consider location-specific factors. The research described in this article tries to create a recommendation algorithm that offers highest produce based on terrain and climate factors unique to a particular region [10]. In this paper, the graph convolution neural networks model was utilized for developing a crop recommendation system that depends on terrain and environmental factors [11].

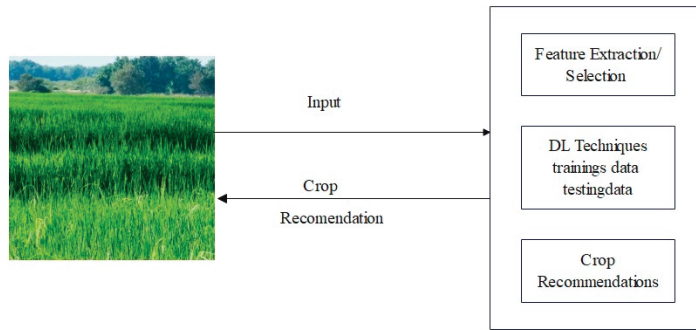


Figure 1. Crop recommendation system using deep learning.

## 2. Background

In this section, we discuss the proposed model graph convolution network (GCN) and the existing model graph neural network (GNN) along with their architectures.

### 2.1. Graph Convolution Network (GCN)

Graph-based neural networks, an extension of deep neural network models designed for data with inherent graph structures, have seen a surge in popularity in recent years. This trend is particularly notable in conjunction with the field of link prediction [12,13].

Consider a weighted undirected graph  $G$ , represented by its adjacency matrix  $A$ , where  $A(i, j)$  in the  $i$ th row and  $j$ th column signifies the weight of the edge  $(i, j)$ . The degree matrix,  $D$ , is defined as follows:

$$D(i, j) = \sum_{j=1}^n A(i, j) \tag{1}$$

The following normalized symmetric definition applies to the graph  $G$ 's Laplace matrix:

$$L = I - D^{-\frac{1}{2}} A D^{-\frac{1}{2}} \tag{2}$$

As a positive semidefinite real symmetry matrix,  $L$  may be divided into the following:

$$L = U \Lambda U^T \tag{3}$$

where  $U = (u_0, u_1, \dots, u_{n-1})$  is the matrix of eigenvectors and  $\Lambda = \begin{bmatrix} \lambda_1 & \dots & 0 \\ \dots & \dots & \dots \\ 0 & \dots & \lambda_n \end{bmatrix}$  is

the eigenvalues diagonal matrix. As shown by the Fourier transform ecosystem on the graph, the normalized Laplacian matrix,  $L$ , and its eigenvector,  $u$ , creates an orthogonal space [14,15]. The vector of features of each node in the graph represented by the graph

signal is  $x = (x_0, x_1, \dots, x_{n-1}) \in R^n$ . The Fourier transform of the graph signal,  $x$ , is shown below.

$$\hat{x} = U^T x \tag{4}$$

The convolution of the two signals is calculated as follows:

$$x * g = U((U^T x) (U^T g)) \tag{5}$$

If  $g_\theta = \text{diag}(U^T g)$  is used as a filter for a graph signal,  $x$ , the graph convolution may be defined as follows:

$$x * g_\theta = U g_\theta (\wedge) U^T x \tag{6}$$

However, because of matrix–vector multiplication, the model’s computational cost is  $O(n^2)$ , which is rather high. A  $K$ -degree polynomial filter is used in the convolutional layer of a model known as ChebNets to address this issue. The model’s  $k$ -th polynomial filter for the spectrum is written as follows.

$$g_\theta = \sum_{k=0}^K \theta_k \lambda_l^k \tag{7}$$

In order to ensure spatial locality, the  $K$ -order polynomial filter of the spectrum is represented in the node domain as an aggregate of  $K$ -order neighborhoods, and the number of filter parameters is also kept to  $O(K) = O(1)$  [16,17]. The model utilizes Chebyshev polynomial  $T_k(x) = 2T_{k-1}(x) - T_{k-2}(x)$  to further minimize computing complexity for recursive computation, where  $T_0(x) = 1$  and  $T_1(x) = x$ . As a result, the definition of the convolution of the filter and graph signal,  $x$ , is obtained as follows:

$$x * g_\theta = U \left( \sum_{k=0}^K \theta_k T_k(L) \right) U^T x \tag{8}$$

In order to achieve numerical stability, the matrix of adjacency,  $A$ , is modified to produce  $A$ , which yields a combined convolutional layer that is more straightforward.

$$H = X * g_\theta = f(D^{-\frac{1}{2}} A D^{-\frac{1}{2}} X \Theta) \tag{9}$$

where  $A = I + A$  and  $D_{ij} = \sum_j A_{ij}$ ,  $f(\cdot)$  is the activation function and  $\Theta$  is the matrix of the filter parameters. The GCN architecture and algorithm is followed.

### 2.2. Graph Neural Network

In 2005, a unique neural network model was created that demonstrated the capability to handle graph structure data. This model is known as the graph neural network. The objective of graph neural networks (GNNs) is to develop effective deep learning techniques for non-Euclidean spaces [18,19].

The following is an introduction to the relevant concepts. The input graph is  $G = (V, E, X_V, X_E)$ ,  $V = \{v_1, v_2, \dots, v_n\}$ , which depicts the collection of nodes, and  $E = \{(i, j) \mid \text{when } v_i \text{ is adjacent to } v_j\}$  is a collection of edges.  $x_i$  indicates the feature vector for node  $v_i$ , and  $X_V = \{x_1, x_2, \dots, x_n\}$  is the set of all nodes’ feature vectors.  $x(i, j)$  denotes the feature vector of edge  $(i, j)$ , and  $X_E = \{x(i, j) \mid (i, j) \in E\}$  is the collection of all edge feature vectors.

In a graph neural network model, the input graph  $G$  is turned into a dynamic graph  $G^t = (V, E, X_V, X_E, H^t)$ , where  $t = 1, 2, \dots, T$  denotes time and  $H^t = (h_1^{(t)}, h_2^{(t)}, \dots, h_n^{(t)})$ .

represents the state vectors of node  $v_i$  at time  $t$  that is dependent on the graph  $G^{t-1}$  at time  $t - 1$ . The  $h_i^{(t)}$  equation is as follows:

$$h_i^{(t)} = f_w(x_i, x_{co(i)}, h_{ne(i)}^{t-1}, x_{ne(i)}) \quad (10)$$

where  $f_w(\cdot)$  represents the local transformation function with parameters;  $w, x_{ne(i)}$  is the set of vectors of features of all nodes adjacent to node;  $v_i, x_{co(i)}$  is the set of feature vector of all edges linked to node  $v_i$ ;  $h_{ne(i)}^{(t)}$  is the collection of feature vectors of all edges linked to node  $v_i$ ; and the collection of state vector of all nodes that are adjacent to node  $v_i$  at time  $t$  [20].

### 3. Literature Review

This research unveils a straightforward yield forecast system crafted for the convenience of farmers. The proposed solution takes the form of a smartphone app, acting as a communicative tool to inform farmers about the myriad factors influencing crop yield. Various machine learning methods, including SVM, ANN, RF, MLR and KNN, are used to estimate agricultural production. The random forest method had the highest accuracy at 95% [21].

This study introduces Agro DSS, a unique system that connects agricultural systems with cutting-edge decision support. The tools include predictive modeling, accuracy assessment, time series grouping, decomposition and structural change detection. The users may use them to forecast simulated situations and comprehend domain relationships or interconnections [22].

This paper introduces Agro Consultant, a smart system that helps farmers in India choose crops based on the sowing season, farm geographical position, soil properties and environmental variables like climate and precipitation. The results of the Multi-Label Classification (MLC) model, in comparison with KNN and random forest, showed that it is better for prediction than the existing models [23].

This paper describes a system of recommendations using a majority voting ensemble model employing trees at random, CHAID, K-nearest neighbor and naive Bayes to suggest crops depending on site-specific parameters which are very effective and accurate. This system uses data on soil features, kinds of soil and crop yield to guide farmers in choosing the right crop [24].

The authors developed a crop recommendation system based on soil characteristics, employing a blend of ensemble models and majoritarian voting methods like K-nearest neighbor and naive Bayes. This approach aims to select crops with high efficiency and precision. These algorithms assess agricultural productivity under given weather circumstances utilizing statistical data like environmental factors, agricultural production and state/district crops to provide categorization pictures [25].

This article discusses AI-driven precision agriculture and an ML-powered cloud-based agricultural suggestion engine to help farmers grow crops based on data. Extreme gradient boosting, decision tree, random forest, KNN and support vector machine (SVM) methods are tested to find the best prediction machine learning (ML) method for a cloud-based recommendation platform. The advancement and widespread use of free and open-source precision agriculture solutions contribute to the cultivation and acceptance of high-quality crops [26].

Our study aims to solve the problem of choosing optimal crops by creating a machine learning-based recommendation system along with image manipulation. We compared KNN, XGBoost, random forest, as well as neural network-based picture augmentation methods in this article and discovered that XGBoost outperformed the other models. The developed model is accurate enough [27].

The goal of this review is to provide a thorough overview of the most recent research projects using deep convolutional neural networks (CNNs) for plant phenotyping applications. We particularly examine how different CNN architectures are used to evaluate



postharvest quality, monitor plant growth and measure plant stress. Finally, we provide a number of suggestions for further investigation into the use of CNN architecture for plant phenotyping [28].

This study demonstrated that, in addition to case-specific irrigation and drainage management optimization, combinations of soil amendments, conditioners and residue management may significantly increase crop yields while reducing soil salinity. These findings demonstrate that higher yields necessary for expanding and maintaining agricultural output may also be obtained via conservation agriculture [29].

In this article, we covered four topics: (1) the effect of conventional and unconventional cropping practices on soil health in agrosystems; (2) the evolution of plant–microbe soil complex and the biochemical mechanisms responsible for soil health under the pressure of agriculture; (3) changes in the notion of soil quality and health in recent decades in agrosystems and the key indicators currently used for evaluating soil health; and (4) the problems in agroecosystems that affect soil health [30].

## 4. Materials and Methods

### 4.1. Dataset

In this article, we used the following data set that can be found at <https://www.kaggle.com/datasets/siddharthss/crop-recommendation-dataset> (accessed on 21 August 2023). This dataset was built by augmenting datasets of rainfall, climate and fertilizer data available for India. The dataset which would allow the users to build a predictive model to recommend the most suitable crops to grow in a particular farm based on various parameters.

### 4.2. Data Preparation to Train GCN

Data preparation to train a graph convolutional network (GCN) entails many critical processes to guarantee that the model can successfully learn from the provided variables, which include edges, features and targets.

The creation of the graph structure is the initial stage of data preparation. This will include identification and organization of edges, which describe the connections among the nodes in the network. In order to do this, an adjacency matrix must be created to reflect the relationships between nodes. Additionally, node features need to be gathered. These features record data about each node and provide the GCN crucial input. In order to ensure proper information flow in the graph, it is essential to make sure that the node characteristics match with the associated nodes in an adjacency matrix.

Furthermore, for supervised learning tasks, target labels or values connected to certain nodes are crucial. These targets could represent actual data for regression tasks or categories for node classification. To set the baseline for the learning process, it is essential to match the goal values with their appropriate nodes.

After preparing the graph topology, node characteristics and goal values, data normalization should be considered. This stage improves training stability as well as convergence. Normalizing features and scaling target values eliminate problems caused by different magnitudes and distributions.

Finally, the data should be separated into three groups: training, validation and test. Care must be taken to make sure that the structure of graphs stays intact inside each set, maintaining the data's interconnectedness. Techniques such as stratified sampling are often used to maintain distribution of classes balance, especially for node tasks involving classification. Figure 2 depicts the flow chart for proposed methodology.

### 4.3. Model Training

After preprocessing the data, the graph convolutional network (GCN) requires many crucial training stages. The GCN model has graph convolutional units in each layer. These units transfer messages between neighboring nodes, allowing the model to reflect complex network interactions. This model minimizes a loss function that measures the difference among predicted and target values during training. The backpropagation procedure

computes loss gradients with respect to the model's parameters, permitting gradient descent or associated methods for optimization. Dropout or L2 regularization may avoid overfitting. Splitting the training dataset into batches improves memory efficiency and convergence. A validation set continually monitors the model's performance to avoid overfitting and picks the ideal model according to the validation criteria. After training converges, the example may be tested on a separate test set for generalization to new data. Hyper parameter tweaking, including learning rate, layers and hidden units per layer, significantly affects the GCN's predictive capability and convergence behavior, thereby making training successful.

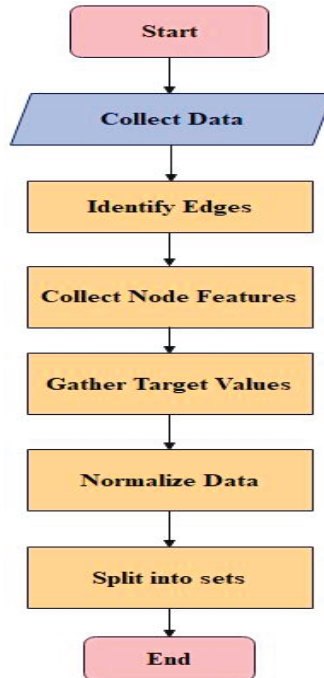


**Figure 2.** Flow chart of GCN data preparation.

#### 4.4. Model Evaluation

The capacity of a trained model to generalize to new data is assessed through model assessment. Metrics, such as the F1-score, precision, recall, accuracy, specificity and sensitivity reflect categorization task performance. Cross-validation guarantees that estimations are accurate. Confusion matrices, for example, provide extensive information. Evaluation guides deployment and improvement.

#### 4.5. Performance Metrics

**Accuracy:** A simple way to gauge accuracy is to look at how often the classifier predicts correctly. The ratio of the number of accurate forecasts to all of the model's predictions may be used to determine accuracy.

$$Accuracy = \frac{TP + TN}{S}$$

**Precision:** In terms of the total number of instances that have been categorized, precision is the proportion of cases that are accurately categorized.

$$Precision = \frac{TP}{TP + FP}$$

Recall: It is the ratio of the total number of true and false negatives to the correct positive numbers.

$$\text{Recall} = \frac{TP}{TP + FN}$$

F1-score: To compute the F1-score, the harmonic mean of the recall and accuracy scores is determined.

$$F1 = \frac{2 * \text{Precision} * \text{Recall}}{\text{Precision} + \text{Recall}}$$

Sensitivity: Memory, or sensitivity, is another name for recall, and it refers to the proportion of properly positive labels that our computer is able to identify as labels. This may also be expressed as a percentage.

$$\text{Sensitivity} = \frac{TP}{TP + FN}$$

Specificity: The algorithm identifies the negative labels as specificity, which is the proper classification.

$$\text{Specificity} = \frac{TN}{TN + FP}$$

## 5. Results

From Table 1 below, it can be seen that there are 22 classes, from 0 to 21. Class 0 is rice, Class 1 is wheat, and Class 2 is maize. The samples are as follows: 1—corn, 2—chickpeas, 3—kidney beans, 4—pigeon peas, 5—moth beans, 6—mung bean, 7—black gramme, 8—bean, 9—grape, 10—banana, 11—mango, 12—grapes, 13—watermelon, 14—muskmelon, 15—apple, 16—orange, 17—papaya, 18—coconut, 19—cotton, 20—jute and 21—coffee.

**Table 1.** Performance metrics.

Model	Accuracy	Precision	Recall	F1-Score	Specificity	Sensitivity
GCN	0.98	0.98	0.97	0.97	0.99	0.97
GNN	0.96	0.97	0.95	0.96	0.99	0.95
ANN	0.93	0.96	0.93	0.94	0.99	0.93
CNN	0.88	0.96	0.89	0.91	0.99	0.89

Figure 3 illustrates the confusion matrices for the proposed Graph Convolutional Network (GCN) and established methods like GNN, CNN), and ANN. Notably, the GCN exhibits the highest accuracy in correct predictions and a notably lower incidence of misclassifications compared to the other existing methods. Our analysis leads to the conclusion that the suggested model, the Graph Convolutional Network (GCN), demonstrates superior accuracy in classification tasks by minimizing misclassifications when compared to alternative models. Figure 4 depicts the comparison of performance metrics of proposed and existing methods.

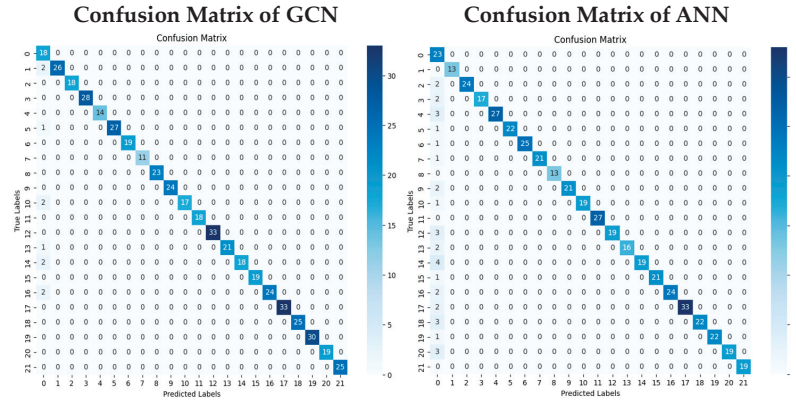


Figure 3. Cont.

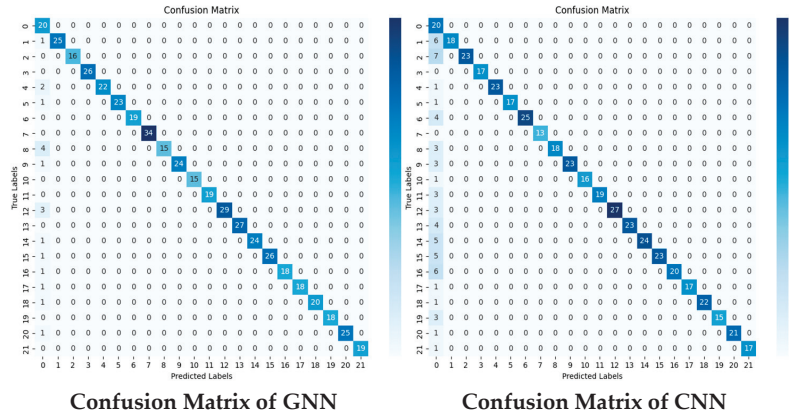


Figure 3. Comparison of proposed and existing methods.



Figure 4. Comparison of performance metrics.

## 6. Discussion

The GCN (graph convolutional network) model is clearly better than other crop recommendation models, as shown by the performance metrics in Table 1. The GCN model, which has a significantly higher accuracy rate of 0.98, not only performs well in this important measure but also routinely achieves excellent results in a number of other crucial assessment criteria, including accuracy, recall, F1-score, specificity and sensitivity. The unique ability of the GCN model to analyze the vast network of data related to agriculture through a lens of graphs topologies, thereby capturing intricate interconnections that are frequently elusive via conventional models, is what really sets it apart. Because of its amazing capacity for translating abstract knowledge into practical insights, the GCN model has the potential to revolutionize agricultural decision making. This model provides stakeholders with essential information to optimize plans and resource allocation by providing individualized and informed crop suggestions. In simple terms, the GCN model's strength goes beyond quantitative measurements. It has the potential to fundamentally alter the way we think about agriculture, ushering in a time where improving yields, long-term viability and overall production will be led by data-driven intelligence. The GCN model's superior ability to comprehend complex data structures sheds a positive light on the future of the agricultural sector, where innovation and pragmatism are combined for the benefit of the sector and the security of the world's food supply.

## 7. Conclusions

The extensive research reported in Table 1 supports the GCN (graph convolutional network) model as the indisputable leader in crop recommendation tasks. The GCN model, with an amazing 98% accuracy rate, establishes an incredibly high standard that is routinely matched by great performance across a range of essential measures such as recall, precision, F1-score, specificity and sensitivity. This comprehensive study not only confirms the GCN model's superiority but also highlights its potential to transform the landscape and agricultural decision making. The GCN model's unique capacity to untangle the complexities of agricultural data using graph topologies gives a multidimensional view unmatched by its competitors. This distinguishing feature enables it to provide personalized and contextually appropriate crop advice with remarkable granularity. The comparison analysis emphasizes the GCN model's clear advantage over competing models, establishing it as the only viable option for constructing an efficient crop recommendation system. The GCN model possesses the potential to optimize the use of resources, improve sustainability practices and significantly increase agricultural output by leveraging the power of modern data analytic tools. Its ability to achieve an accuracy rate of 98% attests to its resilience and highlights its potential for moving further improving precision agriculture. In a world of changing difficulties and agricultural needs, the GCN model's capacity to deliver insightful and exact suggestions is a spark of innovation. As technology continues to alter agriculture's future, the GCN model's efficacy demonstrates its critical contribution, highlighting its importance in driving transformative change in crop management and supporting a more environmentally friendly and productive agricultural industry.

**Author Contributions:** Conceptualization and methodology, and writing are done by P.A.B.; Resources, investigation, analysis part are done by T.S. All authors have read and agreed to the published version of the manuscript.

**Funding:** This research was conducted without external funding or financial support.

**Institutional Review Board Statement:** Not applicable.

**Informed Consent Statement:** Not applicable.

**Data Availability Statement:** In this research, we used kaggle website, where data supporting reported results can be found, including crop related images are used during the study. In this article, we used the following data set that can be found at <https://www.kaggle.com/datasets/siddharthss/crop-recommendation-dataset>.

**Conflicts of Interest:** The authors declare no conflict of interest.

## References

1. Tugrul, B.; Elfatimi, E.; Eryigit, R. Convolutional Neural Networks in Detection of Plant Leaf Diseases: A Review. *Agriculture* **2022**, *12*, 1192. [CrossRef]
2. Bandara, P.; Weerasooriya, T.; Ruchirawya, T.; Nanayakkara, W.; Dimantha, M.; Pabasara, M. Crop recommendation system. *Int. J. Comput. Appl.* **2020**, *975*, 8887. [CrossRef]
3. Sivanandhini, P.; Prakash, J. Crop Yield Prediction Analysis using Feed Forward and Recurrent Neural Network. *Int. J. Innov. Sci. Res. Technol.* **2020**, *5*, 1092–1096.
4. Pruthviraj; Akshatha, G.C.; Shastry, K.A.; Nagaraj; Nikhil. Crop and fertilizer recommendation system based on soil classification. In *Recent Advances in Artificial Intelligence and Data Engineering, Proceedings of AIDE 2020, Karkala, India, 22–23 December 2020*; Springer: Berlin/Heidelberg, Germany, 2022; pp. 29–40.
5. Motwani, A.; Patil, P.; Nagaria, V.; Verma, S.; Ghane, S. Soil Analysis and Crop Recommendation using Machine Learning. In *Proceedings of the 2022 International Conference for Advancement in Technology (ICONAT), IEEE, Goa, India, 21–22 January 2022*; pp. 1–7.
6. Sharma, A.; Bhargava, M.; Khanna, A.V. AI-Farm: A crop recommendation system. In *Proceedings of the 2021 International Conference on Advances in Computing and Communications (ICACC), IEEE, Kochi, Kakkannad, India, 21–23 October 2021*; pp. 1–7.
7. Bandi, R.; Likhit, M.S.S.; Reddy, S.R.; Bodla, S.R.; Venkat, V.S. Voting Classifier-Based Crop Recommendation. *SN Comput. Sci.* **2023**, *4*, 516. [CrossRef]
8. Fassa, V.; Pricca, N.; Cabassi, G.; Bechini, L.; Corti, M. Site-specific nitrogen recommendations' empirical algorithm for maize crop based on the fusion of soil and vegetation maps. *Comput. Electron. Agric.* **2022**, *203*, 107479. [CrossRef]
9. Sheddhi, S.; Shetty, A.; Shetty, R.R.; Alva, B.A.D.; Shetty, A.D. Machine Learning Techniques in Crop Recommendation based on Soil and Crop Yield Prediction System—Review. In *Proceedings of the 2022 International Conference on Artificial Intelligence and Data Engineering (AIDE), IEEE, Karkala, Karnataka, India, 22–23 December 2022*; pp. 230–235.
10. Hossain, D.; Kashem, M.A.; Mustary, S. IoT Based Smart Soil Fertilizer Monitoring and ML Based Crop Recommendation System. In *Proceedings of the 2023 International Conference on Electrical, Computer and Communication Engineering (ECCE), London, UK, 11–12 December 2023*; pp. 1–6.
11. Banerjee, S.; Mondal, A.C. A Region-Wise Weather Data-Based Crop Recommendation System Using Different Machine Learning Algorithms. *Int. J. Intell. Syst. Appl. Eng.* **2023**, *11*, 283–297.
12. Zhou, J.; Cui, G.; Hu, S.; Zhang, Z.; Yang, C.; Liu, Z.; Wang, L.; Li, C.; Sun, M. Graph neural networks: A review of methods and applications. *AI Open* **2020**, *1*, 57–81. [CrossRef]
13. Zhu, J.; Rossi, R.A.; Rao, A.; Mai, T.; Lipka, N.; Ahmed, N.K.; Koutra, D. Graph neural networks with heterophily. In *Proceedings of the AAAI Conference on Artificial Intelligence, Vancouver, BC, Canada, 2–9 February 2021*; pp. 11168–11176.
14. Zheng, X.; Liu, Y.; Pan, S.; Zhang, M.; Jin, D.; Yu, P.S. Graph neural networks for graphs with heterophily: A survey. *arXiv* **2022**, arXiv:2202.07082.
15. Wu, Z.; Pan, S.; Chen, F.; Long, G.; Zhang, C.; Yu, P.S. A comprehensive survey on graph neural networks. *arXiv* **2019**, arXiv:1901.00596. [CrossRef] [PubMed]
16. Scarselli, F.; Gori, M.; Tsoi, A.C.; Hagenbuchner, M.; Monfardini, G. The graph neural network model. *IEEE Trans. Neural Netw.* **2008**, *20*, 61–80. [CrossRef] [PubMed]
17. Zhang, X.-M.; Liang, L.; Liu, L.; Tang, M.-J. Graph Neural Networks and Their Current Applications in Bioinformatics. *Front. Genet.* **2021**, *12*, 690049. [CrossRef] [PubMed]
18. Chen, M.; Wei, Z.; Huang, Z.; Ding, B.; Li, Y. Simple and deep graph convolutional networks. In *Proceedings of the International Conference on Machine Learning, PMLR, Virtual, 13–18 July 2020*; pp. 1725–1735.
19. Tong, Z.; Liang, Y.; Sun, C.; Rosenblum, D.S.; Lim, A. Directed graph convolutional network. *arXiv* **2020**, arXiv:2004.13970.
20. Ma, Y.; Hao, J.; Yang, Y.; Li, H.; Jin, J.; Chen, G. Spectral-based graph convolutional network for directed graphs. *arXiv* **2019**, arXiv:1907.08990.
21. Pande, S.M.; Ramesh, P.K.; Anmol, A.; Aishwarya, B.R.; Rohilla, K.; Shaurya, K. Crop Recommender System Using Machine Learning Approach. In *Proceedings of the 2021 5th International Conference on Computing Methodologies and Communication (ICCMC), Erode, India, 8–10 April 2021*; pp. 1066–1071.
22. Rupnik, R.; Kukar, M.; Vračar, P.; Košir, D.; Pevec, D.; Bosnić, Z. AgroDSS: A decision support system for agriculture and farming. *Comput. Electron.* **2009**, *161*, 260–271. [CrossRef]
23. Doshi, Z.; Nadkarni, S.; Agrawal, R.; Shah, N. AgroConsultant: Intelligent Crop Recommendation System Using Machine Learning Algorithms. In *Proceedings of the 2018 Fourth International Conference on Computing Communication Control and Automation (ICCUBEA), Pune, India, 16–18 August 2018*; pp. 1–6.
24. Pudumalar, S.; Ramanujam, E.; Rajashree, R.H.; Kavya, C.; Kiruthika, T.; Nisha, J. Crop recommendation system for precision agriculture. In *Proceedings of the 2016 Eighth International Conference on Advanced Computing (ICoAC), Chennai, India, 19–21 January 2017*; pp. 32–36. [CrossRef]
25. Reddy, D.A.; Dadore, B.; Watekar, A. Crop Recommendation System to Maximize Crop Yield in Ramtek region using Machine Learning. *Int. J. Sci. Res. Sci. Technol.* **2019**, *6*, 485–489. [CrossRef]

26. Thilakarathne, N.N.; Abu Bakar, M.S.; Abas, P.E.; Yassin, H. A Cloud Enabled Crop Recommendation Platform for Machine Learning-Driven Precision Farming. *Sensors* **2022**, *22*, 6299. [CrossRef] [PubMed]
27. Chakraborty, S.; Mishra, S. A Smart Farming-Based Recommendation System Using Collaborative Machine Learning and Image Processing. In *Cognitive Informatics and Soft Computing, Proceedings of CISC 2021, Balasore, India, 21–22 August 2021*; Springer: Singapore, 2022; pp. 703–716.
28. Jiang, Y.; Li, C. Convolutional Neural Networks for Image-Based High-Throughput Plant Phenotyping: A Review. *Plant Phenomics* **2020**, *2020*, 4152816. [CrossRef] [PubMed]
29. Cuevas, J.; Daliakopoulos, I.N.; del Moral, F.; Hueso, J.J.; Tsanis, I.K. A Review of Soil-Improving Cropping Systems for Soil Salinization. *Agronomy* **2019**, *9*, 295. [CrossRef]
30. Yang, T.; Siddique, K.H.; Liu, K. Cropping systems in agriculture and their impact on soil health—A review. *Glob. Ecol. Conserv.* **2020**, *23*, e01118. [CrossRef]

**Disclaimer/Publisher’s Note:** The statements, opinions and data contained in all publications are solely those of the individual author(s) and contributor(s) and not of MDPI and/or the editor(s). MDPI and/or the editor(s) disclaim responsibility for any injury to people or property resulting from any ideas, methods, instructions or products referred to in the content.

Proceeding Paper

# Early Results on GNSS Receiver Antenna Calibration System Development <sup>†</sup>

Antonio Tupek <sup>1,\*</sup>, Mladen Zrinjski <sup>1</sup>, Marko Švaco <sup>2</sup> and Đuro Barković <sup>3</sup>

<sup>1</sup> Chair of Instrumental Technique, Faculty of Geodesy, University of Zagreb, Kačićeva 26, 10000 Zagreb, Croatia; mladen.zrinjski@geof.unizg.hr

<sup>2</sup> Department of Robotics and Production System Automation, Faculty of Mechanical Engineering and Naval Architecture, University of Zagreb, Ivana Lučića 5, 10000 Zagreb, Croatia; marko.svaco@fsb.hr

<sup>3</sup> Chair of Land Surveying, Faculty of Geodesy, University of Zagreb, Kačićeva 26, 10000 Zagreb, Croatia; djuro.barkovic@geof.unizg.hr

\* Correspondence: antonio.tupek@geof.unizg.hr

<sup>†</sup> Presented at the 10th International Electronic Conference on Sensors and Applications (ECSA-10), 15–30 November 2023; Available online: <https://ecsa-10.sciforum.net/>.

**Abstract:** Precise global navigation satellite system (GNSS) positioning is based on carrier phase observations, where the understanding of the receiver antenna's phase center corrections (PCCs) is critical. With the main goal of determining the PCC models of GNSS receiver antennas, only a few antenna calibration systems are in operation or under development worldwide. In this paper, a new automated GNSS receiver antenna calibration system, recently developed at the Laboratory for Measurements and Measuring Technique (LMMT) of the Faculty of Geodesy of the University of Zagreb in Croatia, is briefly presented. The developed system is an absolute field calibration system based on the utilization of a Mitsubishi MELFA RV-4FML-Q 6-axis industrial robot. The antenna's PCC modeling is based on triple-difference carrier phase observations and spherical harmonic (SH) expansion. Our early calibration results for the global positioning system (GPS) L1 frequency show sub-millimeter agreements with the IGS approved Geo++ GmbH values.

**Keywords:** GNSS; antenna calibration; industrial robot; phase center correction (PCC)

## 1. Introduction

For high-accuracy global positioning applications on the centimeter and millimeter level, global navigation satellite system (GNSS) receivers are essential sensors. To obtain the required accuracy level, all influential factors and error sources must be understood and, in an appropriate manner, accounted for. One such important influence is the phase center correction (PCC) of GNSS receiver antennas.

Because of the antenna's design characteristics and electromagnetic properties [1], the geometric location of the GNSS signal reception, i.e., the antenna phase center (PC), changes with respect to the incoming signal's direction and frequency [2–4]. Such variations cause advances and delays in carrier phase observations and corresponding range errors. Therefore, receiver antenna calibration is needed.

Today, *absolute filed calibration* is the state of the art when it comes to GNSS receiver antenna calibration. Only a few calibration systems utilizing a precise robot are operational or under development worldwide [5–12], and even fewer are accredited by the International GNSS Service (IGS) to provide antenna calibration results [13]. Since this topic is of high interest to the scientific antenna community, and a new calibration system is highly desirable, at the Laboratory for Measurements and Measuring Technique (LMMT) of the Faculty of Geodesy of the University of Zagreb in Croatia, a new antenna calibration system has been developed [14].

**Citation:** Tupek, A.; Zrinjski, M.; Švaco, M.; Barković, Đ. Early Results on GNSS Receiver Antenna Calibration System Development. *Eng. Proc.* **2023**, *58*, 98. <https://doi.org/10.3390/ecsa-10-16227>

Academic Editor: Francisco Falcone

Published: 15 November 2023



**Copyright:** © 2023 by the authors. Licensee MDPI, Basel, Switzerland. This article is an open access article distributed under the terms and conditions of the Creative Commons Attribution (CC BY) license (<https://creativecommons.org/licenses/by/4.0/>).



In this article, preliminary antenna calibration results for the Global Positioning System (GPS) L1 frequency (G01) are presented and elaborated. Furthermore, the results on LMMT calibration validation with Geo++ GmbH are presented and discussed.

## 2. Materials and Methods

### 2.1. The Receiver Antenna Phase Center Correction Model

To fulfill the requirements of high-accuracy positioning applications, the receiver antenna PCCs must be determined. In line with the IGS convention, and as depicted in Figure 1, PCC is divided into the phase center offset (PCO) vector and the azimuth- and elevation-dependent phase center variation (PCV) [4,6,10–12,14]:

$$PCC(\alpha^i, z^i) = -\mathbf{e}^T(\alpha^i, z^i) \cdot \mathbf{PCO} + PCV(\alpha^i, z^i) + r. \quad (1)$$

where  $\mathbf{e}(\alpha^i, z^i)$  is the line-of-sight unit vector from the receiver to the satellite  $i$ , and  $r$  is the constant part equal in all directions present due to the relative characteristics of GNSS measurements [4,6]. The PCO is a vector from the antenna reference point (ARP) to an arbitrarily defined mean phase center (MPC). The PCV is the direction-dependent range correction function, i.e., the difference between the real and ideal phase wavefront. The PCCs, and all corresponding antenna-related points, vectors, and scalars, are defined in a 3D antenna-fixed left-handed coordinate system (antenna frame–AF).

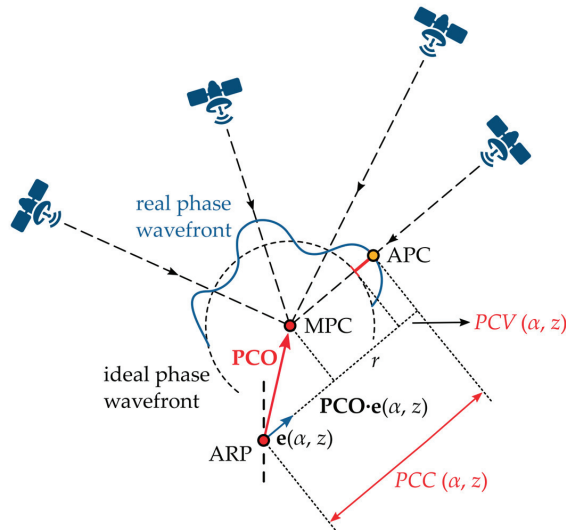


**Figure 1.** Definition and geometrical interpretation of the adopted GNSS receiver antenna phase center correction (PCC) model; ARP—antenna reference point; MPC—mean phase center; APC—actual phase center; PCO—phase center offset; PCV—phase center variation.

A set of PCCs of an antenna are transformed to PCO and PCVs using a least squares (LSQ) adjustment and by simultaneously fulfilling two conditions. Firstly, the PCV at the antenna zenith are constrained to zero, i.e., zero-zenith constraint, by  $PCV(\alpha^i, z^i = 0^\circ) = 0$ . Secondly, the PCO is determined such that the sum of the squared PCVs is minimal, i.e.,  $\Sigma [PCV(\alpha^i, z^i)^2] \rightarrow \min$ .

### 2.2. Antenna Calibration Method at LMMT

To efficiently sample the entire antenna-under-test (AUT) hemisphere during calibration, at LMMT, a 6-axis industrial robot Mitsubishi MELFA RV-4FLM-Q is utilized.

The robot turns the AUT in 2088 different antenna orientations, with stationary 2.5 s at every single orientation. Therefore, depending on the calibration timing parameters, a full calibration at LMMT lasts approx. 2 h. During calibration, a reference station (REF) on a 5 m short baseline is used. On both stations (REF and AUT), simultaneous 10 Hz raw carrier phase observations are registered with equal receiver settings. Afterwards, prior to PCC LSQ estimation, the carrier phase measurements are preprocessed to eliminate the majority of the GNSS error sources.

Generally, the calibration system at LMMT is based on the triple-difference (TD) approach, i.e., time-differenced double-difference carrier phase observations [15]. A generic GNSS observation equation from receiver A to satellite  $i$ , in units of length is expressed as follows [16]:

$$\Phi_A^i = \rho_A^i + c(\delta t_A - \delta t^i + dt^{\text{rel}}) + \zeta_A^i + c(dt_A - dt^i) + T_A^i - I_A^i + \lambda N_A^i + \lambda \omega_A^i + MP_A^i + \varepsilon_A^i, \quad (2)$$

where  $\rho_A^i$  is the geometric distance,  $c$  is the speed of light,  $\delta t_A$  and  $\delta t^i$  are the receiver and satellite clock errors,  $dt^{\text{rel}}$  is the relativistic effects term,  $\zeta_A^i$  is the combined satellite and receiver antennas' PCC value,  $dt_A$  and  $dt^i$  are the receiver and satellite hardware delays,  $T_A^i$  is the tropospheric delay,  $I_A^i$  is the ionospheric delay,  $\lambda$  is the signal wavelength,  $N_A^i$  is the integer phase ambiguity,  $\omega_A^i$  is the carrier phase wind-up (PWU) effect,  $MP_A^i$  is the multipath term, and  $\varepsilon_A^i$  is the phase observation noise term.

Forming the TD carrier phase observations needed for antenna calibration includes eight raw observations, from Equation (2), on the REF (R) and AUT (T) receivers for two satellites  $i$  and  $j$ , in two epochs  $t_k$  and  $t_{k+1}$ :

$$\begin{aligned} TD_{T,R}^{ij}(t_k, t_{k+1}) &= \Phi_R^j(t_{k+1}) - \Phi_T^j(t_{k+1}) - \Phi_R^i(t_{k+1}) + \Phi_T^i(t_{k+1}) - \Phi_R^j(t_k) + \Phi_T^j(t_k) + \Phi_R^i(t_k) - \Phi_T^i(t_k) \\ &= -PCC_T^j(t_{k+1}) + PCC_T^i(t_{k+1}) + PCC_T^j(t_k) - PCC_T^i(t_k) + \partial \varepsilon_{T,R}^{ij}. \end{aligned} \quad (3)$$

By exploiting the high spatial and temporal correlations of GNSS observations, and by forming TDs on a short baseline between two time-adjacent AUT orientations, the final TDs contain only the AUT PCCs and the differential phase noise  $\partial \varepsilon_{T,R}^{ij}$ . At LMMT, the PCCs are parametrized by spherical harmonic (SH) expansion with a degree and order resolution of  $m = n = 8$  as follows:

$$PCC(\alpha^i, z^i) = \sum_{m=0}^{m_{\max}} \sum_{n=0}^m \tilde{P}_{mn} [\cos(z^i)] \cdot [a_{mn} \cos(n\alpha^i) + b_{mn} \sin(n\alpha^i)]. \quad (4)$$

where  $\tilde{P}_{mn}$  is the fully normalized Legendre function,  $a_{mn}$  and  $b_{mn}$  are the SH coefficients, and  $\alpha^i$  and  $z^i$  are the azimuth and zenith angles in the AF.

The SH coefficients are determined by a constrained LSQ adjustment. Afterwards, the PCCs of the AUT are calculated for the entire antenna hemisphere according to Equation (4), transformed to PCO/PVC, and exported to the IGS ANTEX (ANTenna EXchange) format.

For an in-depth description of the antenna calibration methodology at LMMT, an interested reader is referred to Tupek et al. [14].

### 2.3. Antenna Calibration System at LMMT

The GNSS receiver antenna calibration system developed at LMMT consists of two major parts: hardware and software. Hardware-wise, the calibration system consists of a 6-axis industrial robot Mitsubishi MELFA RV-4FLM-Q with its corresponding controller Mitsubishi MELFA CR750, two GNSS receivers (Trimble NetR5) and antennas, and a personal computer. An on-site calibration set-up at LMMT is depicted in Figure 2. The in-house custom-made software components of the calibration system, all written in Python, are the antenna calibration module (ACM), time synchronization module (TISY), and the PCC estimation module. An in-depth description of the calibration system operation can be found in Tupek et al. [14].

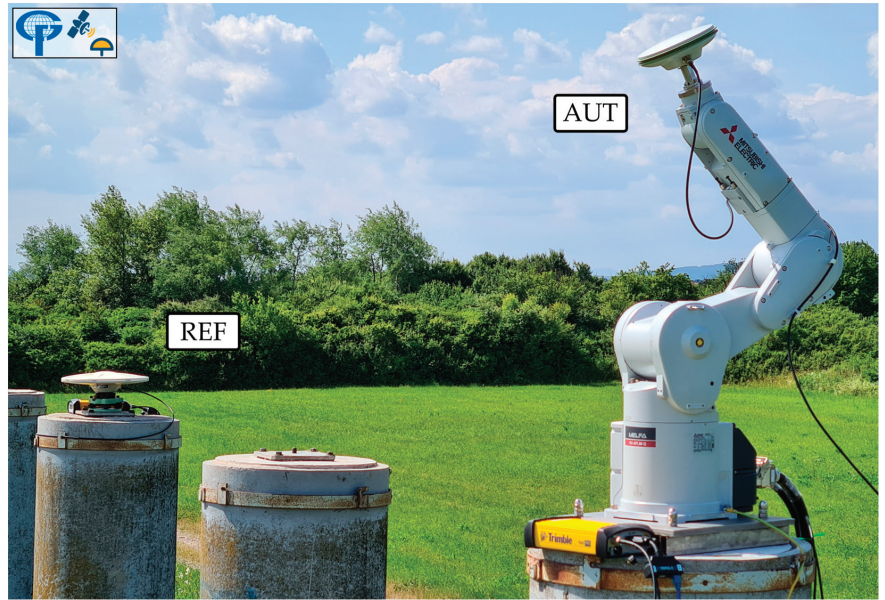


**Figure 2.** GNSS antenna calibration system at the Laboratory for Measurements and Measuring Technique (LMMT) of the Faculty of Geodesy of the University of Zagreb in Croatia; REF—reference antenna (TRM57971.00 NONE); AUT—antenna-under-test (LEIAX1202GG NONE). The calibration field consists of two 5-m-spaced pillars, which are part of the Calibration Baseline of the Faculty of Geodesy of the University of Zagreb [17].

### 3. Results and Discussion

To test the antenna calibration system at LMMT and to validate the calibration results with Geo++ GmbH, an IGS approved calibration institution, from April to June of 2023, four calibration campaigns of the same GNSS antenna Trimble Zephyr 2 Geodetic (TRM57971.00 NONE, S/N: 30739001) for the GPS L1 frequency were conducted. Figure 3 visualizes the main benefit of using a robot for antenna calibration, i.e., a full coverage of the entire antenna hemisphere, even after only approx. 2 h of calibration.

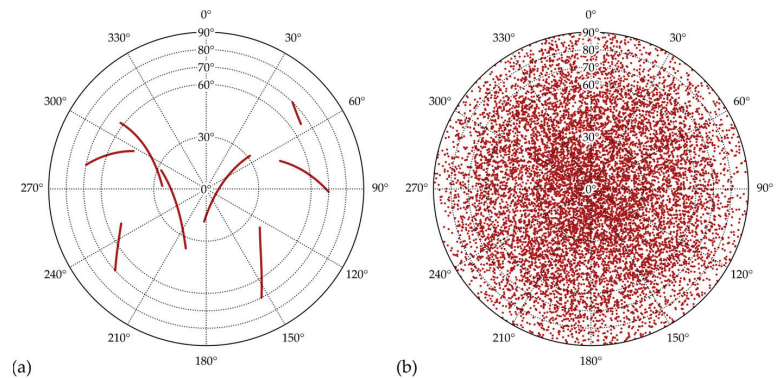


**Figure 3.** Satellite azimuth and zenith angle plot (sky-plot) during antenna calibration at LMMT: (a) topocentric frame (TF); (b) antenna frame (AF).

To validate the LMMT antenna calibration results, a comparison with an independent calibration was conducted. For that purpose, the investigated antenna was calibrated individually by Geo++ GmbH, an IGS approved institution, on 5 August 2022.

According to the new calibration method at LMMT, PCCs have been estimated for every conducted antenna calibration campaign. Lastly, to obtain a final solution, calibration results have been averaged, and the final PCO and PVC grids were exported to ANTEX. Table 1 summarizes the LMMT and Geo++ GmbH estimated PCOs. The PCO differences between the LMMT and Geo++ GmbH calibrations are on the sub-millimeter level. The PCVs of the investigated antenna for the GPS L1 frequency, per calibration institution, are depicted in Figure 4. Both individual calibration results show similar PCV behaviors over the entire antenna hemisphere, with noticeable larger values at the antenna horizon for the Geo++ calibrations. Also, for both calibration results (LMMT and Geo++ GmbH), small azimuthal variations are noticeable.

**Table 1.** PCO vector components of antenna TRM57971.00 NONE (S/N: 30739001) of GPS L1 (G01) frequency per calibration institution. All values are in millimeters (mm).

Calibration Institution	Phase Center Offset (PCO)		
	North	East	Up
Geo++ GmbH	0.79	0.32	66.96
LMMT	1.24	0.11	67.24

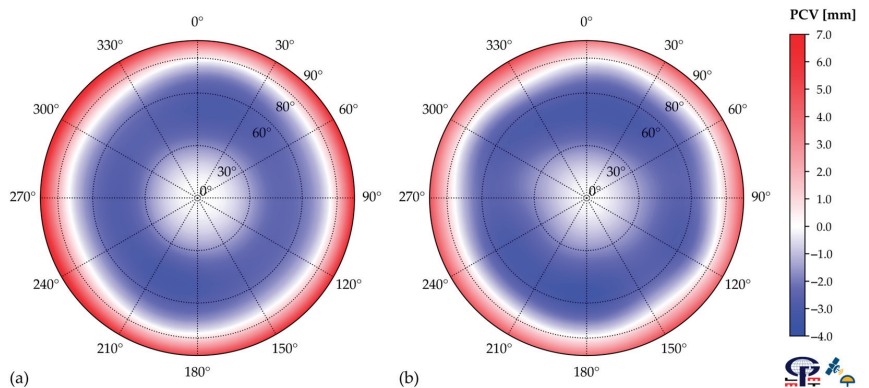


**Figure 4.** (a) Geo++ GmbH and (b) LMMT phase center variations (PCVs) of antenna TRM57971.00 NONE (S/N: 30739001) for GPS L1 (G01) frequency.

To estimate the accuracy of LMMT individual antenna calibration results, the Geo++ GmbH calibration results are taken as reference values. The PCC differences  $\Delta PCC$  of antenna TRM57971.00 NONE (S/N: 30739001) for GPS L1 (G01) frequency, over the entire antenna hemisphere, are calculated, and they are depicted in Figure 5. By a simple visualization of the gained difference pattern, it is evident that values around zero prevail with larger values mainly located at low antenna elevations, e.g., for an azimuth of approx. 300°.

To obtain a quantitative accuracy estimation of LMMT calibration results, the following scalar measures of the PCC difference pattern are calculated: minimum and maximum  $\Delta PCC$ , root-mean-square (RMS) deviation of  $\Delta PCC$ , range of the  $\Delta PCC$ , and the interquartile range (IQR) of the  $\Delta PCC$ . All calculated values are given in Table 2. Furthermore, because during the majority of GNSS applications, a standard elevation mask of a minimum of 10° is used, a 10° elevation-reduced antenna hemisphere analysis is justified. All accuracy measures were determined accordingly and are given in Table 2.

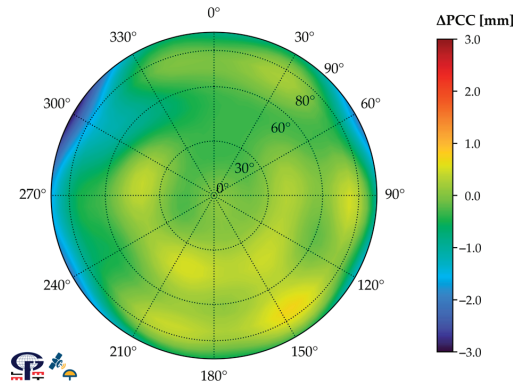


**Figure 5.** Geo++ GmbH and LMMT PCC differences ( $\Delta PCC$ ) of antenna TRM57971.00 NONE (S/N: 30739001) for GPS L1 (G01) frequency after transformation to common PCO and datum.

**Table 2.** Quantitative measures of the difference between Geo++ GmbH’s and LMMT’s individual absolute calibrations: minimum, maximum, root-mean-square (RMS) deviation, range, and interquartile range of  $\Delta PCC$ . All values are in millimeters (mm).

Full Antenna Hemisphere (0° Elevation Cut-Off)					Reduced Antenna Hemisphere (10° Elevation Cut-Off)				
Min.	Max.	RMS	Range	IQR	Min.	Max.	RMS	Range	IQR
-2.92	0.72	0.52	3.64	0.44	-1.64	0.72	0.34	2.36	0.41

Considering the full antenna hemisphere, the LMMT and Geo++ GmbH PCC differences are in the interval from  $-2.92$  to  $0.72$  mm, with the middle 50% of  $\Delta PCC$  being within  $0.44$  mm. The RMS of the differences is  $0.52$  mm. However, if only the elevation-reduced antenna hemisphere is considered, accuracy measures significantly improve. The range of all  $\Delta PCC$  is  $2.36$  mm with an RMS value of  $0.34$  mm whereby the middle 50% of the differences does not exceed  $0.41$  mm.

Therefore, to summarize, with the newly developed LMMT antenna calibration system, an estimated agreement with the accredited Geo++ GmbH calibrations, within  $0.52$  mm, was achieved.

#### 4. Conclusions

The new GNSS receiver antenna calibration system developed at the Laboratory for Measurements and Measuring Technique (LMMT) of the Faculty of Geodesy of the University of Zagreb in Croatia can provide meaningful antenna calibration results for the GPS L1 frequency. According to the obtained experimental research results regarding the Trimble Zephyr 2 Geodetic antenna, an estimated agreement within  $0.52$  mm, in terms of RMS, with the accredited Geo++ GmbH results, was achieved. Therefore, our calibration results also confirm the compatibility of LMMT GPS L1 calibrations with the IGS accredited Geo++ GmbH calibrations.

**Author Contributions:** Conceptualization, A.T., M.Z., M.Š. and Đ.B.; methodology, A.T., M.Z. and M.Š.; software, A.T.; validation, A.T. and M.Z.; formal analysis, A.T. and M.Z.; investigation, A.T.; resources, A.T. and M.Z.; data curation, A.T.; writing—original draft preparation, A.T.; writing—review and editing, M.Z., M.Š. and Đ.B.; visualization, A.T.; supervision, M.Z.; project administration, A.T.; funding acquisition, M.Z. All authors have read and agreed to the published version of the manuscript.

**Funding:** This research was funded by the University of Zagreb under the research project “Automatization of measurement procedure in the Laboratory for Measurements and Measuring Technique of the Faculty of Geodesy”.

**Institutional Review Board Statement:** Not applicable.

**Informed Consent Statement:** Not applicable.

**Data Availability Statement:** The data presented in this study are available on request from the corresponding author.

**Acknowledgments:** The authors would like to express their gratitude to the following: the Inea Group, the local Mitsubishi Electric authorized distributor, for great support regarding robotic automatization; the State Geodetic Administration of the Republic of Croatia for providing the GNSS equipment used for this research; Nenad Smolčak of Geomatika-Smolčak Ltd. for his many useful receiver-specific advices; Krunoslav Špoljar for his technical and logistical assistance during calibration field activities; and Sergej Baričević for his help during the production of antenna-robot mounting elements.

**Conflicts of Interest:** The authors declare no conflict of interest.

## References

1. Maqsood, M.; Gao, S.; Montenbruck, O. Antennas. In *Springer Handbook of Global Navigation Satellite Systems*; Teunissen, J.G.P., Montenbruck, O., Eds.; Springer International Publishing: Cham, Switzerland, 2017; pp. 505–534.
2. Wübbena, G.; Schmitz, M.; Menge, F.; Seeber, G.; Völksen, C. A New Approach for Field Calibration of Absolute GPS Antenna Phase Center Variations. *Navigation* **1997**, *44*, 247–255. [CrossRef]
3. Wübbena, G.; Schmitz, M.; Menge, F.; Böder, V.; Seeber, G. Automated Absolute Field Calibration of GPS Antennas in Real-Time. In Proceedings of the 13th International Technical Meeting of the Satellite Division of The Institute of Navigation (ION GPS 2000), Salt Lake City, UT, USA, 19–22 September 2000; The Institute of Navigation: Manassas, VA, USA, 2000; pp. 2512–2522.
4. Kröger, J.; Kersten, T.; Brevia, Y.; Schön, S. Multi-Frequency Multi-GNSS Receiver Antenna Calibration at IfE: Concept-Calibration Results-Validation. *Adv. Space Res.* **2021**, *68*, 4932–4947. [CrossRef]
5. Wübbena, G.; Schmitz, M.; Warneke, A. Geo++ Absolute Multi-Frequency GNSS Antenna Calibration. In Proceedings of the EUREF Analysis Centres Workshop, Warsaw, Poland, 16–17 October 2019.
6. Kröger, J.; Kersten, T.; Brevia, Y.; Schön, S. Multi-GNSS Receiver Antenna Calibration. In Proceedings of the FIG Working Week 2020, International Federation of Surveyors, Amsterdam, The Netherlands, 10–14 May 2020; pp. 1–13.
7. Riddell, A.; Moore, M.; Hu, G. Geoscience Australia’s GNSS Antenna Calibration Facility: Initial Results. In Proceedings of the International GNSS Society Symposium (IGNSS 2015), Gold Coast, QLD, Australia, 16–17 July 2015; pp. 1–12.
8. Bilich, A.; Erickson, B.; Geoghegan, C. 6-Axis Robot for Absolute Antenna Calibration at the US National Geodetic Survey. In Proceedings of the IGS Workshop 2018, International GNSS Service, Wuhan, China, 29 October–2 November 2018; International GNSS Service: Pasadena, CA, USA, 2018.
9. Hu, Z.; Cai, H.; Jiao, W.; Zhou, R.; Zhai, Q.; Liu, X.; Kan, H.; Zhao, Q. Preliminary Results of IGMAS BDS/GNSS Absolute Antenna Phase Center Field Calibration. In Proceedings of the China Satellite Navigation Conference (CSNC 2022), Beijing, China, 22–25 May 2022; Yang, C., Xie, J., Eds.; Springer: Singapore, 2022; pp. 147–160.
10. Willi, D.; Lutz, S.; Brockmann, E.; Rothacher, M. Absolute Field Calibration for Multi-GNSS Receiver Antennas at ETH Zurich. *GPS Solut.* **2020**, *24*, 28. [CrossRef]
11. Sutyagin, I.; Tatarnikov, D. Absolute Robotic GNSS Antenna Calibrations in Open Field Environment. *GPS Solut.* **2020**, *24*, 92. [CrossRef]
12. Dawidowicz, K.; Rapiński, J.; Śmieja, M.; Wielgosz, P.; Kwaśniak, D.; Jarmołowski, W.; Grzegory, T.; Tomaszewski, D.; Janicka, J.; Gołaszewski, P.; et al. Preliminary Results of an Astri/UWM EGNSS Receiver Antenna Calibration Facility. *Sensors* **2021**, *21*, 4639. [CrossRef] [PubMed]
13. IGS Antenna Working Group. Available online: <https://igs.org/wg/antenna/#files> (accessed on 1 August 2023).
14. Tupek, A.; Zrinjski, M.; Švaco, M.; Barković, Đ. GNSS Receiver Antenna Absolute Field Calibration System Development: Testing and Preliminary Results. *Remote Sens.* **2023**, *15*, 4622. [CrossRef]
15. Hauschild, A. Combinations of Observations. In *Springer Handbook of Global Navigation Satellite Systems*; Teunissen, J.G.P., Montenbruck, O., Eds.; Springer International Publishing: Cham, Switzerland, 2017; pp. 583–604.
16. Hauschild, A. Basic Observation Equations. In *Springer Handbook of Global Navigation Satellite Systems*; Teunissen, J.G.P., Montenbruck, O., Eds.; Springer International Publishing: Cham, Switzerland, 2017; pp. 561–582.
17. Zrinjski, M.; Barković, Đ.; Špoljar, K. Review of Precise Calibration Methods of Geodetic Calibration Baselines. *Geod. List.* **2022**, *76*, 25–52.

**Disclaimer/Publisher’s Note:** The statements, opinions and data contained in all publications are solely those of the individual author(s) and contributor(s) and not of MDPI and/or the editor(s). MDPI and/or the editor(s) disclaim responsibility for any injury to people or property resulting from any ideas, methods, instructions or products referred to in the content.

# Wearable Impedance-Matched Noise Canceling Sensor for Voice Pickup<sup>†</sup>

Hee Yun Suh, Helena Hahn and James West \*

Department of Electrical and Computer Engineering, Johns Hopkins University, Baltimore, MD 21218, USA; hshuh11@jhu.edu (H.Y.S.); helena@jhu.edu (H.H.)

\* Correspondence: jimwest@jhu.edu

<sup>†</sup> Presented at the 10th International Electronic Conference on Sensors and Applications (ECSA-10), 15–30

November 2023; Available online: <https://ecsa-10.sciforum.net/>.

**Abstract:** Communicating under extreme noise conditions remains challenging in spite of higher-order noise-canceling microphones, throat microphones, and signal processing. Both natural and human-made background ambient noise can disturb the conveyance of information because of high noise levels. Noise cancellation, which is used frequently in audio technology, has limits in noise reduction and does not guarantee clear vocal pickup in these severe situations. A contact microphone that is attached directly to the medium of interest has the potential to pick up vocal signals with reduced noise. In this study, an electrostatic transducer with an elastomer layer that is impedance-matched to the human body is used to pick up speech sounds through constant contact on the chin and cheek. By attaching the wearable device directly to the skin, the medium of air is bypassed, and airborne noise is passively canceled. Because of the acoustic impedance-matched layer, the sensor is more sensitive to low frequencies under 500 Hz, so frequency equalization was implemented to flatten the frequency response throughout the vocal range. The perceptual evaluation of speech quality (PESQ) scores of the wearable device with equalization averaged around 2.6 on a scale from −0.5 to 4.5. Speech recordings were also collected in a noise field of 85 dB, and the performance was compared to a cardioid lapel mic, a cardioid dynamic mic, and an omnidirectional condenser mic. The recordings revealed a significantly reduced presence of white noise in the contact sensor. This study provides preliminary results that show potential vocal applications for a wearable impedance-matched sensor.

**Keywords:** wearable device; acoustic noise; transducers; speech communication; microphones; noise cancellation

**Citation:** Suh, H.Y.; Hahn, H.; West, J.

Wearable Impedance-Matched Noise Canceling Sensor for Voice Pickup.

*Eng. Proc.* **2023**, *58*, 99. <https://doi.org/10.3390/ecsa-10-16153>

Academic Editor: Jean-marc Laheurte

Published: 15 November 2023



**Copyright:** © 2023 by the authors. Licensee MDPI, Basel, Switzerland. This article is an open access article distributed under the terms and conditions of the Creative Commons Attribution (CC BY) license (<https://creativecommons.org/licenses/by/4.0/>).

## 1. Introduction

Extreme noise conditions such as construction and heavy traffic can reduce the quality of communication. Active noise cancellation, piezoelectric throat microphones, and signal processing techniques are methods used to improve the conveyance of information in the presence of ambient noise. Efforts in active noise cancellation and adaptive filtering algorithms provide attenuation of about 20–30 dB [1,2]. This may not be sufficient for optimal communication and voice pickup in environments with high noise levels. Various higher-order microphones have been developed for improved directionality, but many higher-order microphones also have high noise sensitivity [3].

A recently developed electrostatic transducer has the potential to reduce high noise levels while picking up sounds. The sensor's elastomer layer is impedance-matched to the skin, the medium of interest [4,5]. By attaching the device to the skin, the medium of air is bypassed, so the transducer passively rejects airborne noise while reducing the loss of signal energy [5]. The impedance-matched sensor has been implemented in a wide range of settings such as musical acoustics [6] and body sound monitoring [5]. When the transducer is placed on areas with high vocal vibration, such as under the chin or on the cheek, it can

be used as a wearable sensor with high noise-cancellation abilities for voice pickup. This paper focuses on enhancing the speech-pickup abilities of the acoustic impedance-matched transducer and comparing it to more widely used microphones to demonstrate the sensor's potential in vocal applications.

## 2. Materials and Methods

### 2.1. Impedance-Matched Transducer

The electrostatic transducer was created with a tuned elastomer layer with coated microstructures and a charged fluorinated ethylene propylene (FEP) film, as seen in Figure 1. Corona charging was used to charge the FEP film, and the layers were encased with shielding to create a thin shape (Figure 2a,b).

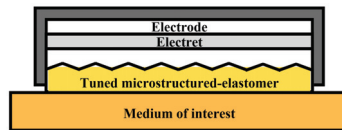


Figure 1. Inner layers of transducer.

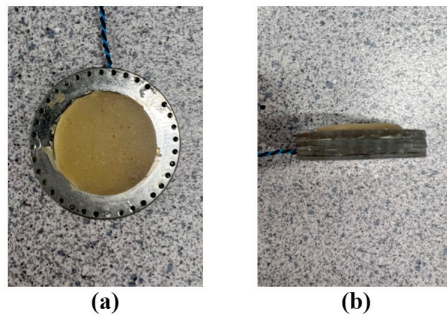


Figure 2. (a) Bottom view of the transducer. (b) Side view of the transducer.

### 2.2. Experimental Setup

Medical tape (3M Tegaderm™) was used to adhere the device to the cheek and under the chin at positions shown in Figure 3. For comparison, three conventionally used microphones were selected: a cardioid lapel microphone (AT898 Lavalier Mic, Audio-Technica, Tokyo, Japan), a cardioid dynamic microphone (e835 Dynamic Mic, Sennheiser, Wedemark, Germany), and an omnidirectional condenser microphone (Yeti Pro Mic, Blue Microphones, China; on omnidirectional mode). A Focusrite Scarlett 2i4 Audio Interface collected the output of the transducer and microphones, and Audacity was used to record the audio. Phantom power of 48 V was supplied by the audio interface for all recordings, and the gain was adjusted to avoid clipping.

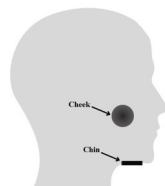


Figure 3. Position of the transducer when taped to the cheek and under the chin on the subject.

The microphones were positioned based on polar patterns. The cardioid dynamic mic was placed on a tabletop microphone holder at a 45-degree angle downward and about



1 inch away from the subject's mouth to ensure maximum pickup. The omnidirectional condenser mic is best placed 4–10 inches away from the source, so it was propped upward and placed 8 inches away from the subject's mouth. The cardioid lapel mic was attached facing upward to the upper chest area of the subject with a magnetic clip.

### 2.3. Speech Quality

To measure the quality of the speech recorded by the transducer, the first list in the Harvard sentences was used [7]. Each list in the Harvard sentences is phonetically balanced and widely used for speech quality measurements. The subject recorded all 10 sentences from List 1, and additional samples included a tongue-twister and counting from 1–10 (Table 1). The transducer, lapel, and omnidirectional mic were each simultaneously recorded with the dynamic mic, which was set as the reference because of its robustness.

**Table 1.** Sentences recorded for speech quality experiment.

Type	Sentence
Counting	One, two, three, four, five, six, seven, eight, nine, ten.
Tongue-twister	She sells seashells by the seashore.
Harvard sentences List 1	<ol style="list-style-type: none"> <li>1. The birch canoe slid on the smooth planks.</li> <li>2. Glue the sheet to the dark blue background.</li> <li>3. It's easy to tell the depth of a well.</li> <li>4. These days a chicken leg is a rare dish.</li> <li>5. Rice is often served in round bowls.</li> <li>6. The juice of lemons makes fine punch.</li> <li>7. The box was thrown beside the parked truck.</li> <li>8. The hogs were fed chopped corn and garbage.</li> <li>9. Four hours of steady work faced us.</li> <li>10. A large size in stockings is hard to sell.</li> </ol>

#### 2.3.1. Post-Processing

Key phonetic features exist in the frequency range up to 6–8 kHz, and higher frequencies can also add spectral information [8]. The acoustic transducer is sensitive to lower frequencies below 500 Hz, so post-processing was needed to enhance the speech recordings. Lowpass filtering at 40 Hz was performed to remove unwanted noise from the impedance-matched transducer recordings. The recordings from the transducer were then amplified by 8 dB to match the volume of the other microphones.

To flatten the frequency response of the transducer's output, commercial equalization software (Logic Pro 10.7.9) was used to match the frequency response of the transducer recording to that of the dynamic mic recording. Equalization had a cutoff frequency at around 1300 Hz for the cheek-positioned recordings and a cutoff frequency at around 1900 Hz for the chin-positioned recordings to minimize high-frequency noise. These cutoffs were determined by maximizing the perceptual evaluation of speech quality (PESQ) [9].

#### 2.3.2. Speech Quality Measurement

To quantify the quality of the speech, the PESQ score was calculated. PESQ takes into consideration noise and audio distortion [9]. The scores range from −0.5 to 4.5 with scores between 2 and 3 needing moderate effort to understand, and scores 3 and above needing less effort to understand.

### 2.4. Noise Cancellation

A noise field was created using two speakers (Yamaha HS8) placed at two opposing corners of a sound booth. White noise generated in Audacity was played through both speakers synchronously, and the decibel level was measured using a sound level meter (Martel 322). The decibel levels were measured in dBA with the meter placed at the site of the recording equipment. The subject sat between the two speakers with the transducers,

and the microphones were positioned similarly to the description above (Figure 4). An '/a/' sound was recorded at noise levels of 60 dB to 85 dB in 5 dB increments, and a reference recording was made without noise.

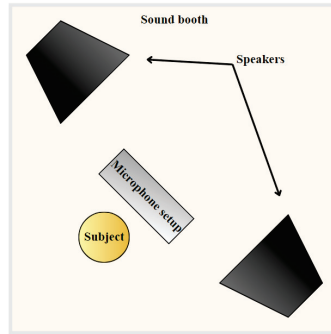


Figure 4. Sound booth set up for noise cancellation experiment.

### 3. Results

The speech quality and noise cancellation results are summarized below.

#### 3.1. Speech Quality

Table 2 presents the PESQ scores of the impedance-matched transducer and comparison microphones. The PESQ score increased for all sentences after post-processing for the acoustic transducer. The average post-processed transducer score is about 2.59 and about 0.5 less than the average score of the other two microphones. Despite containing more artifacts, such as buzzing, the cheek position had a slightly higher post-processed PESQ score than of the chin position.

Table 2. Table of PESQ scores for each transducer position and microphone. The dynamic mic was used as the reference.

Sentence	Transducer (Cheek) Original	Transducer (Chin) Original	Transducer (Cheek) Post-Processed	Transducer (Chin) Post-Processed	Lapel Mic	Omnidirectional Mic
Counting	1.4783	2.1966	3.0238	3.0599	3.4527	3.4018
Tongue-Twister	1.8844	2.0097	2.3804	2.2728	3.1010	2.9669
1 *	1.6549	1.4344	2.6274	2.4440	3.1259	3.0640
2	1.4278	1.3410	2.2930	2.9153	3.2753	3.2726
3	1.8041	1.6775	2.8402	2.6124	3.0955	3.0113
4	1.6774	1.7726	2.3861	2.6759	3.1076	3.0472
5	1.6883	1.6720	2.3723	2.3198	3.0204	2.9092
6	1.8740	1.5036	2.8963	2.3081	3.0204	2.9929
7	1.7565	1.8316	2.6523	2.4899	3.2521	3.0875
8	1.8423	2.1095	2.9682	2.6612	3.2204	3.0691
9	1.7113	1.6813	2.5233	2.4539	3.2069	3.2400
10	1.8941	1.8283	2.5802	2.4474	3.1858	2.8575
Average	1.7245	1.7548	2.6286	2.5551	3.1720	3.0676

\* All numbered sentences are from List 1 of the Harvard Sentences.

#### 3.2. Noise Cancellation

Spectrograms of the signals (Figure 5) show reduced noise in the transducer recordings compared to the other microphones. The white noise visibly appears throughout the frequency range in the audio signals for the comparison microphones at 85 dB. The transducer audio signals have very little visible white noise, and they are similar throughout

different noise-level environments. The white noise is also audibly significant in the three microphone recordings compared to the transducer recordings.

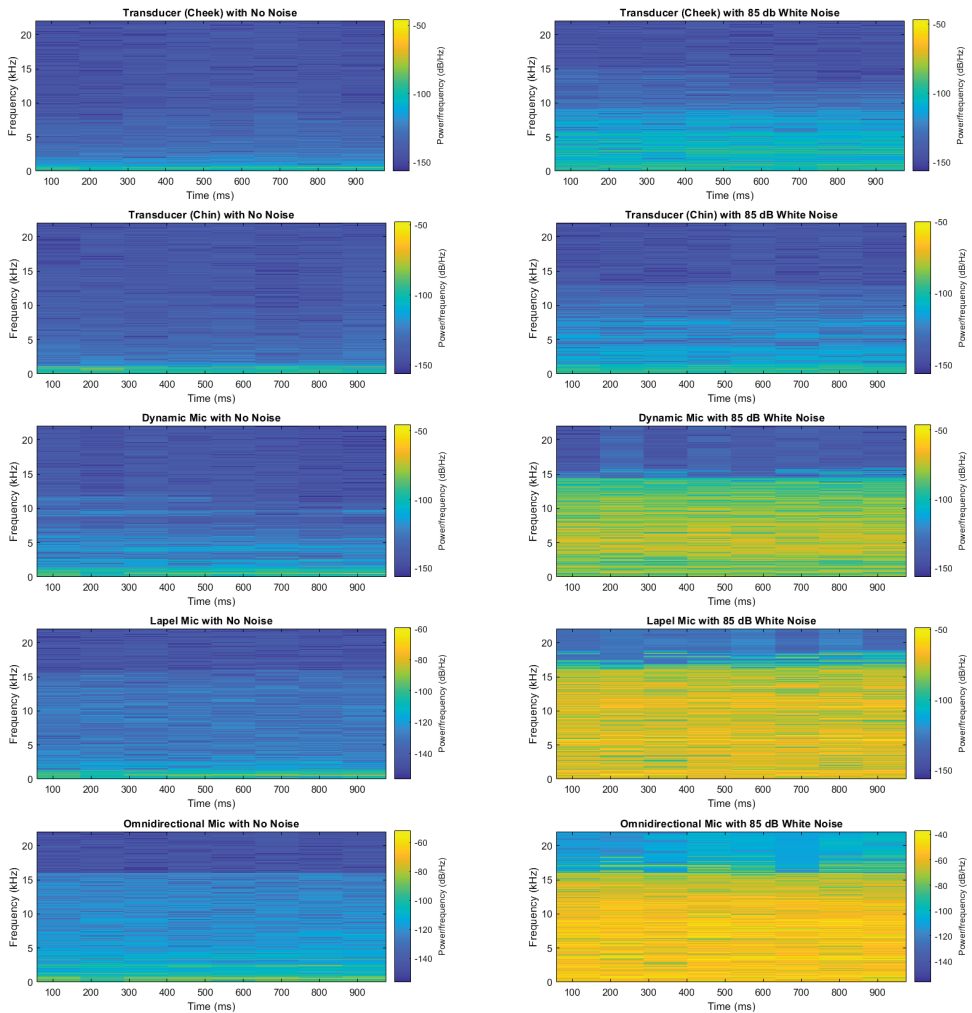


**Figure 5.** Spectrograms of the recordings at no noise and 85 dB noise using Hamming window and 50% overlap.

#### 4. Conclusions

The current paper provides preliminary results on the vocal pickup abilities of an acoustic impedance-matched transducer. The transducer captured similar audio quality at the cheek and chin positions. Equalization improved the speech quality of the transducer recordings, increasing the PESQ score to an intelligible level of 2.6 from the original 1.7. The speech quality may reach a similar standing to other microphones if post-processing methods and additional transducer tuning techniques are further investigated. For noise cancellation, the transducer proved to have superior noise reduction capabilities in comparison to three different microphones. Little noise was detected even at loud noise levels of 85 dB. Future comparison with contact microphones such as throat microphones may prove to be helpful. The impedance-matched sensor demonstrates potential as a wearable

noise-canceling contact microphone in vocal applications, particularly for extreme noise conditions.

**Author Contributions:** Conceptualization, H.Y.S. and H.H.; methodology, H.Y.S. and H.H.; software, H.Y.S.; validation, H.Y.S.; formal analysis, H.Y.S.; investigation, H.Y.S. and H.H.; resources, J.W.; data curation, H.Y.S.; writing—original draft preparation, H.Y.S.; writing—review and editing, H.Y.S. and H.H.; visualization, H.Y.S.; supervision, J.W.; project administration, J.W.; funding acquisition, J.W. All authors have read and agreed to the published version of the manuscript.

**Funding:** This research received no external funding.

**Institutional Review Board Statement:** Not applicable.

**Informed Consent Statement:** Not applicable.

**Data Availability Statement:** The raw data supporting the conclusions of this article will be made available by the authors on request.

**Conflicts of Interest:** The authors declare no conflicts of interest.

## References

1. Boll, S.; Pulsipher, D. Suppression of acoustic noise in speech using two microphone adaptive noise cancellation. *IEEE Trans. Acoust. Speech Signal Process.* **1980**, *28*, 752–753. [CrossRef]
2. Dixit, S.; Nagaria, D. LMS Adaptive Filters for Noise Cancellation: A Review. *Int. J. Electr. Comput. Eng. (IJECE)* **2017**, *7*, 2520–2529. [CrossRef]
3. De Sena, E.; Hacıhabiboglu, H.; Cvetkovic, Z. On the Design and Implementation of Higher Order Differential Microphones. *IEEE Trans. Audio Speech Language Process.* **2012**, *20*, 162–174. [CrossRef]
4. Rennoll, V.; McLane, I.M.; Eisape, A.; Elhilali, M.; West, J. Evaluating the impact of acoustic impedance matching on the airborne noise rejection and sensitivity of an electrostatic transducer. *J. Acoust. Soc. Am.* **2021**, *149*, A23. [CrossRef]
5. Rennoll, V.; McLane, I.M.; Eisape, A.; Grant, D.; Hahn, H.; Elhilali, M.; West, J. Electrostatic Acoustic Sensor with an Impedance-Matched Diaphragm Characterized for Body Sound Monitoring. *ACS Appl. Bio Mater.* **2023**, *6*, 3241–3256. [CrossRef] [PubMed]
6. Rennoll, V.; McLane, I.M.; Eisape, A.; Grant, D.; Betz, C.; Chen, X.; Gebhart, M.; Hahn, H.; Kartub, S.; Lehr, B.; et al. Project-based learning through sensor characterization in a musical acoustics course. *J. Acoust. Soc. Am.* **2022**, *152*, 1932–1941. [CrossRef] [PubMed]
7. Rothausser, E.H. IEEE Recommended Practice for Speech Quality Measurements. *IEEE Trans. Audio Electroacoust.* **1969**, *17*, 225–246. [CrossRef]
8. Trine, A.; Monson, B.B. Extended High Frequencies Provide Both Spectral and Temporal Information to Improve Speech-in-Speech Recognition. *Trends Hear.* **2024**, *24*. [CrossRef] [PubMed]
9. Rix, A.W.; Beerends, J.G.; Hollier, M.P.; Hekstra, A.P. Perceptual evaluation of speech quality (PESQ)-a new method for speech quality assessment of telephone networks and codecs. In Proceedings of the 2001 IEEE International Conference on Acoustics, Speech, and Signal, Salt Lake City, UT, USA, 7–11 May 2001; Volume 2, pp. 749–752. [CrossRef]

**Disclaimer/Publisher’s Note:** The statements, opinions and data contained in all publications are solely those of the individual author(s) and contributor(s) and not of MDPI and/or the editor(s). MDPI and/or the editor(s) disclaim responsibility for any injury to people or property resulting from any ideas, methods, instructions or products referred to in the content.

# Electrospun Nano- and Microfiber Mesh-Based Transducer for Electrochemical Biosensing Applications <sup>†</sup>

Alexander M. Lloyd <sup>1,\*</sup>, Willem J. Perold <sup>1</sup> and Pieter R. Fourie <sup>2</sup>

<sup>1</sup> Department of Electrical and Electronic Engineering, Faculty of Engineering, Stellenbosch University, Stellenbosch 7600, South Africa; wjperold@sun.ac.za

<sup>2</sup> Phagoflux (PTY) LTD, Stellenbosch University, Stellenbosch 7600, South Africa; pieter@stix.co.za

\* Correspondence: amlloyd@sun.ac.za

<sup>†</sup> Presented at the 10th International Electronic Conference on Sensors and Applications (ECSA-10), 15–30 November 2023; Available online: <https://ecsa-10.sciforum.net/>.

**Abstract:** Biosensors hold great promise as diagnostic devices that gain the information needed to discern between different types and severities of infection. Accurate diagnostic information allows for appropriate antimicrobial usage, thereby benefiting patient welfare and curbing the development of antimicrobial resistance. With these aims in mind, a nano- and microfiber mesh-based transducer platform for use in aqueous media was developed. When used in an electrochemical cell, this transducer is able to distinguish between different concentrations of phosphate-buffered saline in deionized water using electrochemical impedance spectroscopy. This transducer, when coupled with a biorecognition element, could serve as a new biosensor platform, to be employed as a diagnostic device that could be applied to various biological targets.

**Keywords:** biosensors; electrospinning; nanofibers; electrochemical impedance spectroscopy

## 1. Introduction

Accurate diagnostic data are crucial to improving patient welfare. Further, the development of antimicrobial resistance (AMR) has been linked to inappropriate antimicrobial prescription practices, including the overreliance on broad-spectrum antibiotics in the absence of diagnostic information [1–3]. Given the challenges that hinder the development of new classes of antibiotics [4–8], and the rapidity with which AMR develops [1,4,9], a crucial avenue is the development of biosensors that provide the diagnostic information required to ensure appropriate antimicrobial usage [1,2]. With this in mind, a novel transducer for use in electrochemical cells was developed by electrospinning a polymer blend onto IDEs to create a conductive nano- and microfiber mesh. The appeal of this substrate stems from its increased surface area as compared to thin-films, which increases the number of potential binding/reaction sites. This transducer was developed to serve as a backbone for further biosensor development. In this work, the transducer shows its potential for this purpose by acting as a sensor to determine concentration changes in a buffer solution. This was achieved by developing predictive models from the observed data.

## 2. Materials and Methods

A custom polymer blend was developed to produce the nano- and microfiber mesh substrate. Using blends by Bessaire et al. [10] and Lloyd [11] as a point of departure, this blend consisted of 0.015 g poly (vinyl alcohol) (PVA)(MW 89,000–98,000) (obtained from Merck), 0.065 g polyethylene oxide (PEO) (MW 1,000,000, obtained from Merck), 2.56 g poly (3,4-ethylenedioxythiophene) polystyrene sulfonate (PEDOT:PSS)(Clevis PH1000, obtained from Ossila) and 0.345 g N,N-Dimethylformamide (DMF) (obtained from Merck). The polymer blend was placed in a glass vial and mixed using a magnetic stirrer and hot-plate for 15 min, with the hot-plate heating the blend to approximately 95 °C. The

**Citation:** Lloyd, A.M.; Perold, W.J.; Fourie, P.R. Electrospun Nano- and Microfiber Mesh-Based Transducer for Electrochemical Biosensing Applications. *Eng. Proc.* **2023**, *58*, 100. <https://doi.org/10.3390/ecsa-10-16217>

Academic Editor: Stefano Mariani

Published: 15 November 2023



**Copyright:** © 2023 by the authors. Licensee MDPI, Basel, Switzerland. This article is an open access article distributed under the terms and conditions of the Creative Commons Attribution (CC BY) license (<https://creativecommons.org/licenses/by/4.0/>).

blend was heated so as to increase the solubility of the PVA, thereby allowing for a shorter mixing duration. It was important to ensure that the temperature did not exceed 100 °C so as to avoid boiling, as this would change the properties of the polymer blend through the removal of water. After mixing, the polymer blend was allowed to cool.

Two electrode interdigitated electrodes (IDEs) with finger spacings of 130 µm were produced on an FR-4 substrate using ICAPE TRAX. The chosen electrode material was electroless nickel immersion gold (ENIG) owing to its chemical resistance. This is necessary as chemical reactions occurring at the electrode would affect the observed response. The electrodes were then placed in a spin-coater and covered with (3-Glycidyloxypropyl)trimethoxysilane (GOPS) at 1000 rpm for 40 s. The purpose of the GOPS is to bind the PEDOT:PSS nano- and microfibers to the IDE substrate. GOPS has been shown to significantly improve the water resilience of PEDOT:PSS [12]. After spin-coating, the electrodes were baked on a hot-plate at 100 °C for 30 min to allow for binding between the GOPS and the IDE substrate.

Once the polymer blend had cooled, it could be electrospun. An enclosure was prepared in which the relative humidity (RH) could be controlled using a heater. This is important as the RH affects the rate of solvent dissipation during the electrospinning process. The RH was set to 10–15% and the ambient temperature was 41.8 °C. The polymer was loaded into a syringe, which was placed into a syringe pump. A 22 G blunt-tipped needle was placed onto the syringe. The prepared electrodes were mounted to a custom octagonal-barrel rotating collector.

The purpose of the octagonal barrel was to provide flat faces to which the rigid electrodes could be mounted. The distance between the blunt needle-tip and a face of the barrel was set to 10 cm. The needle was connected to a high-voltage (HV) supply at 15 kV, and the syringe pump was set to depress the syringe at 2 mL/h. The barrel was set to rotate at 1200 rpm, which translates to a surface velocity of 12.566 m/s. This electrospinning operation was set to run for 30 min, after which the electrodes were removed from the collector. The electrodes, onto which nano- and microfibers were deposited during electrospinning, were then rinsed with ethanol and baked dry using a hot-plate at 100 °C for 1 min. The electrodes were then left to cure overnight. Once cured, 33 electrodes were selected, all with DC resistance measurements of under 2 Ω. The 33 electrodes accounted for 3 electrodes per concentration of PBS in DI water. The produced nano- and microfiber mesh can be seen in Figure 1.

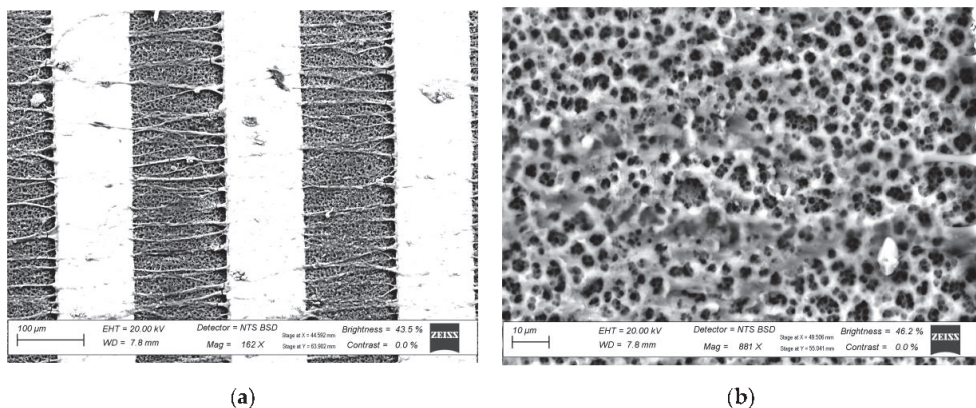


**Figure 1.** The electrospun fibers. (a) Overview of the fibers between the fingers of an IDE; (b) close-up of the mesh.

In order to expose the electrodes to aqueous media, it was necessary to produce reservoirs that could contain the liquid. Custom wells were laser-cut from 5 mm thick plexiglass, and were then mounted directly to the nano- and microfiber transducers.

The next phase of the process involved exposure of the produced transducers to the series of PBS in DI water dilutions. A total of 50  $\mu\text{L}$  of each concentration of PBS in DI water (ranging from 0% to 100%) was placed on the electrodes in triplicate. The electrodes were allowed to soak for 1 h, after which the impedance was measured over a broad frequency band using a Digilent Analog Discovery 2 and the accompanying Impedance Analyzer. Five sets of measurements were taken per electrode.

### 3. Results and Discussion

The frequency band of 100 Hz to 1 MHz was inspected. In order to account for variations in the base values of the electrodes, the data sets were normalized with respect to the impedance observed at 100 Hz. In order to account for noise in the system, a Savitzky–Golay (SavGol) filter was applied to the raw data with a window length of 31 and a polynomial order of 1. Taking the average of the 15 filtered data sets per concentration produced the graphs shown in Figure 2.

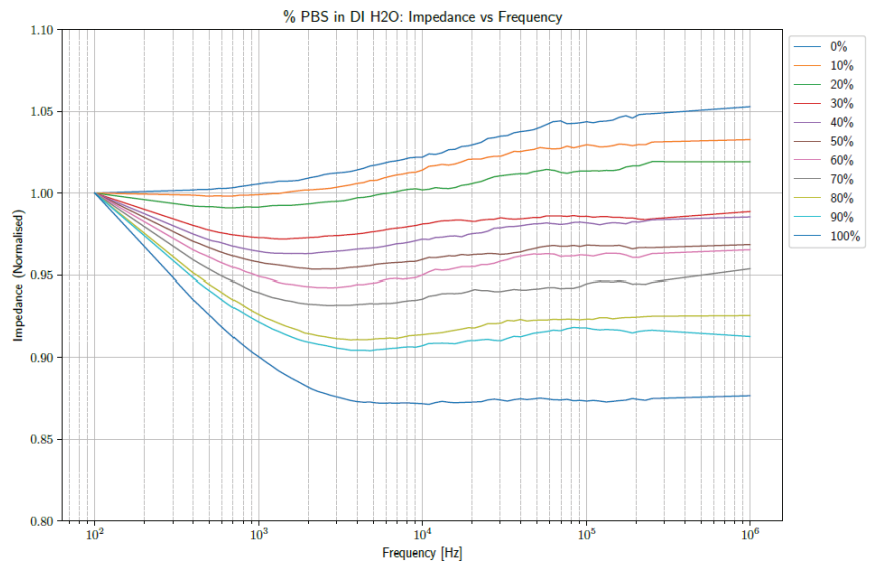


**Figure 2.** The normalized averages of the impedances observed over the frequency band of 100 Hz to 1 MHz.

From the figure above, it is clear that increasing the concentrations of PBS affects the shape of the observed impedance over the selected frequency band. Further investigation into the effect at specific frequencies could provide insight into using the data as a diagnostic tool. Consequently, the data were inspected at 1 kHz and 10 kHz. Box plots of the normalized impedance as a function of PBS concentration are shown in Figures 3 and 4 at frequencies of 1 kHz and 10 kHz, respectively.

From the figures, a distinct linear trend in the data sets can be observed, whereby the impedance changes as the concentration of PBS in DI water increases. This makes sense as the introduction of PBS into the DI water necessarily denotes an increase in the number of conductive species present in the electrochemical cell. The maximum concentration of PBS in DI water is 100%. It must be noted that 1X PBS was used. Increasing the concentration of PBS is expected to produce further changes in impedance. However, this requires further study, as 1X PBS is a standard buffer solution and is therefore the focus of this study. When taking the median of the data points, so as to gain an indication of the trend of the data whilst accounting for outliers, it is possible to draw a line of best fit. These fits can be seen in Figures 5 and 6 at frequencies of 1 kHz and 10 kHz, respectively.

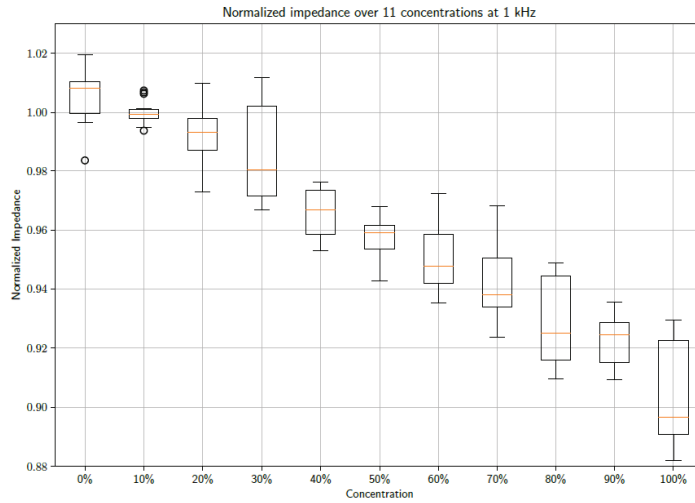


**Figure 3.** A box plot showing the unfiltered data sets of 15 measurements at each concentration sampled at 1 kHz.

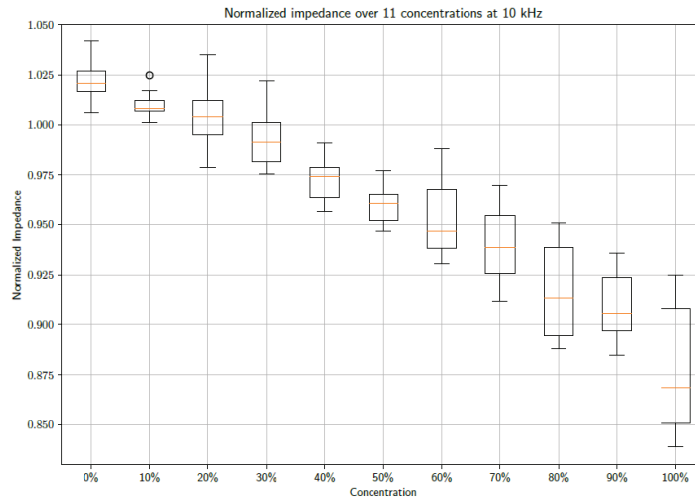


**Figure 4.** A box plot showing the unfiltered data sets of 15 measurements at each concentration sampled at 10 kHz.

The fits follow a linear progression, i.e., the form  $y = ax + b$ . The parameters for the lines of best fit are as follows:

1 kHz

- $a = -0.001058$ ;  $b = 1.011$ .
  - o Goodness of fit: R-squared: 0.9857; adjusted R-squared: 0.9841.
  - o RMSE: 0.004454.

10 kHz

- $a = -0.001434$ ;  $b = 1.029$ .
- Goodness of fit:
  - o R-squared: 0.9737; adjusted R-squared: 0.9708.



o RMSE: 0.008239.

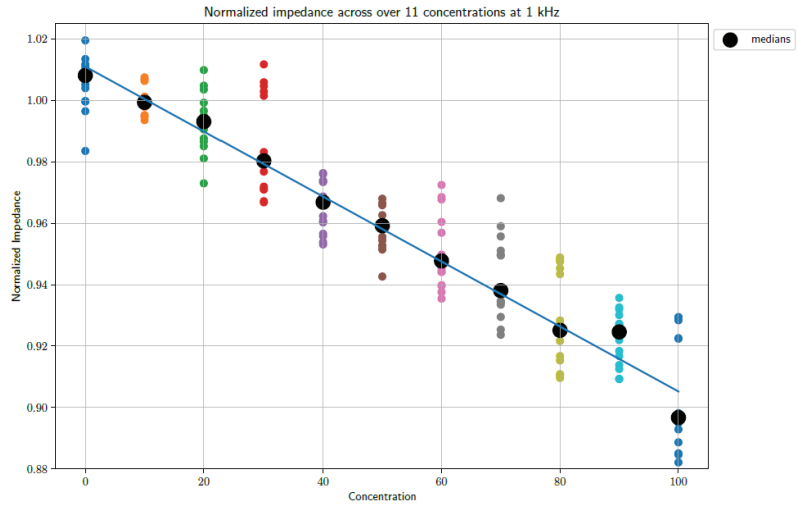


**Figure 5.** A plot showing the unfiltered data sets as well as a trend line based on the medians of the data sets sampled at 1 kHz.

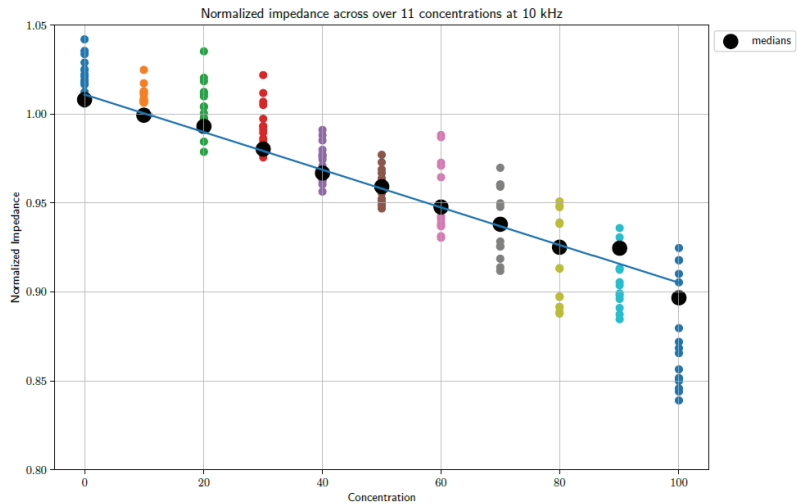


**Figure 6.** A plot showing the unfiltered data sets as well as a trend line based on the medians of the data sets sampled at 10 kHz.

#### 4. Conclusions

The data show a direct link between the concentration of PBS in DI water and the observed conductivity to the extent that linear regressions could be generated to act as predictive models for determining the concentration of unknown blends of PBS in DI water. This shows that the transducers produced can act as sensors, and can serve as the backbone of further sensor developments, specifically in the field of biosensors.

**Author Contributions:** Conceptualization, A.M.L. and W.J.P.; methodology, A.M.L.; formal analysis, A.M.L.; investigation, A.M.L.; resources, W.J.P.; data curation, A.M.L.; writing—original draft preparation, A.M.L.; writing—review and editing, A.M.L., W.J.P. and P.R.F.; supervision, W.J.P. and P.R.F.; project administration, W.J.P. All authors have read and agreed to the published version of the manuscript.

**Funding:** This research received no external funding.

**Data Availability Statement:** The data presented in this study are available on request from the corresponding author.

**Acknowledgments:** The authors would like to acknowledge the contributions of Wessel Croukamp, Wynand van Eeden and Marié Booyens.

**Conflicts of Interest:** Author Pieter R. Fourie was employed by the company Phagoflux (PTY) LTD. The remaining authors declare that the research was conducted in the absence of any commercial or financial relationships that could be construed as a potential conflict of interest.

## References

1. World Health Organization. *Global Action Plan on Antimicrobial Resistance*; World Health Organization: Geneva, Switzerland, 2015; pp. 1–19.
2. Dittrich, S.; Tadesse, B.T.; Moussy, F.; Chua, A.; Zorzet, A.; Tängdén, T.; Dolinger, D.L.; Page, A.; Crump, J.A.; D’Acremont, V.; et al. Target product profile for a diagnostic assay to differentiate between bacterial and non-bacterial infections and reduce antimicrobial overuse in resource-limited settings: An expert consensus. *PLoS ONE* **2016**, *11*, e0161721. [CrossRef] [PubMed]
3. Dittrich, S. *Meeting of Experts on Biomarkers to Discriminate Bacterial from Other Infectious Causes of Acute Fever*; World Health Organization: Geneva, Switzerland, 2015; pp. 5–23.
4. National Research Council (US) Committee on New Directions in the Study of Antimicrobial Therapeutics: New Classes of Antimicrobials; National Research Council (US) Committee on New Directions in the Study of Antimicrobial Therapeutics: Immunomodulation. *Treating Infectious Diseases in a Microbial World: Report of Two Workshops on Novel Antimicrobial Therapeutics*; The National Academies Press (US): Washington, DC, USA, 2006; pp. 7–59.
5. Gaynes, R. Antibiotic resistance in ICUs: A multifaceted problem requiring a multifaceted solution. *Infect. Control Hosp. Epidemiol.* **1995**, *16*, 328–330. [CrossRef] [PubMed]
6. World Health Organization. *Antibacterial Agents in Clinical Development*; World Health Organization: Geneva, Switzerland, 2017; pp. 8–37.
7. Spellberg, B.; Powers, J.H.; Brass, E.P.; Miller, L.J.; Edwards, J.E. Trends in antimicrobial drug development: Implications for the future. *Clin. Infect. Dis.* **2004**, *38*, 1279–1286. [CrossRef] [PubMed]
8. Smolinski, M.S.; Hamburg, M.A.; Lederberg, J. *Microbial Threats to Health: Emergence, Detection, and Response*; The National Academies Press: Washington, DC, USA, 2003; pp. 13–18.
9. Hamilton-Miller, J.M. Antibiotic resistance from two perspectives: Man and microbe. *Int. J. Antimicrob. Agents* **2004**, *23*, 209–212. [CrossRef] [PubMed]
10. Bessaire, B.; Mathieu, M.; Salles, V.; Yeghoyan, T.; Celle, C.; Simonato, J.; Brioude, A. Synthesis of continuous conductive PEDOT:PSS nanofibers by electrospinning: A conformal coating for optoelectronics. *ACS Appl. Mater. Interfaces* **2016**, *9*, 950–957. [CrossRef] [PubMed]
11. Lloyd, A.M. Quantification of CD4+ Cell Count via a Nanofibre-Based Biosensor. Master’s Thesis, Stellenbosch University, Stellenbosch, South Africa, 2019.
12. Håkansson, A.; Han, S.; Wang, S.; Lu, J.; Braun, S.; Fahlman, M.; Berggren, M.; Crispin, X.; Fabiano, S. Effect of (3-Glycidyloxypropyl)Trimethoxysilane (GOPS) on the electrical properties of PEDOT:PSS films. *J. Polym. Sci.* **2017**, *55*, 814–820. [CrossRef]

**Disclaimer/Publisher’s Note:** The statements, opinions and data contained in all publications are solely those of the individual author(s) and contributor(s) and not of MDPI and/or the editor(s). MDPI and/or the editor(s) disclaim responsibility for any injury to people or property resulting from any ideas, methods, instructions or products referred to in the content.

Proceeding Paper

# The Synthesis of Anisotropic 3D Nanomagnets for Magnetic Actuation and Sensing in Piezoelectric Polyvinylidene Fluoride towards Magnetic Nanogenerator Device Fabrication <sup>†</sup>

Ojodomo J. Achadu <sup>1,\*</sup>, Gideon L. Elizur <sup>2</sup> and Owolabi M. Bankole <sup>3</sup>

<sup>1</sup> School of Health and Life Sciences, National Horizon Centre, Teesside University, Middlesbrough TS1 3BA, UK

<sup>2</sup> Institute of Pharmacy and Biomedical Sciences, University of Strathclyde, Glasgow G4 0RE, UK; gideon.elizur.2021@uni.strath.ac.uk

<sup>3</sup> Department of Chemical Sciences, Adekunle Ajasin University, Akungba 0901, Nigeria; bankolemutolib@yahoo.com

\* Correspondence: o.achadu@tees.ac.uk

<sup>†</sup> Presented at the 10th International Electronic Conference on Sensors and Applications (ECSA-10), 15–30 November 2023; Available online: <https://ecsa-10.sciforum.net/>.

**Abstract:** The geometry and anisotropic properties of 3D magnetic nanostructures have a direct impact on their magnetization properties and functionalities due to the presence of spatial coordinates. This has stimulated the exploration and synthesis of various types of nanosized magnetic materials for use in magnetic energy-harvesting technology. Herein, anisotropic 3D nanomagnets with cubic, spherical, and mixed truncated cubic/rod-like morphologies were prepared and embedded in a polyvinylidene fluoride (PVDF) polymer matrix to derive 3D nanomagnet–PDVF composites. The 3D nanomagnet–PDVF composites were found to exhibit the highly electroactive  $\beta$ -phase of PVDF, indicative of enhanced piezoelectric properties. Furthermore, the thin films of the 3D nanomagnet–PDVF composites displayed remarkable magnetic responsiveness and actuation capacity in the presence of a magnetic force. This work highlights the potential of the prepared 3D nanomagnet–PDVF composites as a magnetic sensing and actuator system towards the design of magnetic nanogenerators for harvesting ambient low-frequency magnetic noise.

**Keywords:** 3D nanomagnets; nanomagnet–PDVF composites; magnetic actuation and sensing; magnetic nanogenerators; energy harvesting

**Citation:** Achadu, O.J.; Elizur, G.L.; Bankole, O.M. The Synthesis of Anisotropic 3D Nanomagnets for Magnetic Actuation and Sensing in Piezoelectric Polyvinylidene Fluoride towards Magnetic Nanogenerator Device Fabrication. *Eng. Proc.* **2023**, *58*, 101. <https://doi.org/10.3390/ecsa-10-16228>

Academic Editor: Stefano Mariani

Published: 15 November 2023



**Copyright:** © 2023 by the authors. Licensee MDPI, Basel, Switzerland. This article is an open access article distributed under the terms and conditions of the Creative Commons Attribution (CC BY) license (<https://creativecommons.org/licenses/by/4.0/>).

## 1. Introduction

Magnetic noise from various electrical systems and electronic devices is a plentiful source of energy that is ubiquitous in the environment but rarely utilised. Like sunlight and wind energy, magnetic noise can be renewably harvested and converted into useful electricity using magnetic energy harvesters or generators [1–3]. However, this has not been sustainably feasible and/or achievable due to the technical limitations around the harvesting of ubiquitous magnetic noise with very low frequency in the region of 50/60 Hz [1–3]. This is coupled with the bulky nature of traditional magnetic generator systems [1,4]. State-of-the-art magnetic energy harvesting technology utilises laminated magnetolectric ceramic composites to convert low-frequency magnetic noise into electricity to power wireless sensors and minimise the dependence on batteries [5–8]. Meanwhile, ceramic-based magnetic energy generators are bulky (with heavy magnets used as cantilevers) and mechanically fragile with low power output [9,10]. To address these drawbacks, soft and flexible magnetic generators based on the combination of novel nanostructured magnetic materials with piezoelectric and/or magnetoactive polymers are required. This will not only make it easier to fabricate compact devices but will also result in low-cost and efficient

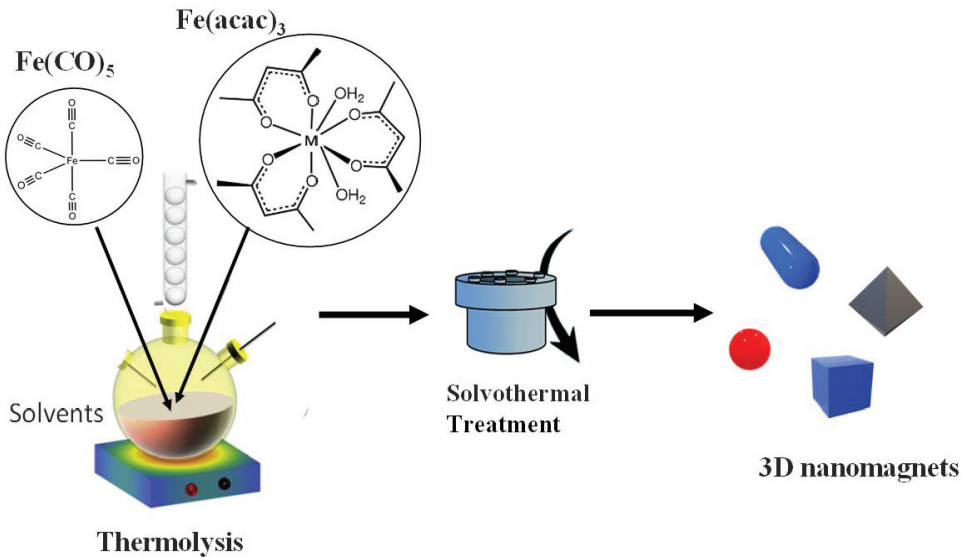
magnetic energy harvesting and conversion. Our hypothesis is that nanostructured magnetic materials that can respond to low-frequency magnetic fields [1,11] will be ideal for enabling high magnetoelectric responsiveness in piezoelectric and/or magnetoactive polymers for the magneto-mechano (piezo)-electric (MME) energy conversion of low-frequency magnetic noise. In this light, 3D nanomagnets are expected to outperform conventional bulk magnets and magnetic nanoparticles with a significant increase in magneto-electric performance due to the special magnetism induced by the 3D spatial coordinates [11–13].

In this work, we demonstrate the proof-of-concept of the magnetic actuation and sensing performance of novel anisotropic 3D nanomagnets when incorporated into piezoelectric polymers such as polyvinylidene fluoride (PVDF). The prepared magnetic nanostructures with different morphologies (mixed truncated cubic/rod-like shapes and cubic and spherical shapes) were characterised using high-resolution transmission electron microscopy (HR-TEM) and superconducting quantum interference device (SQUID) magnetometry. The 3D nanomagnets were subsequently embedded in a PVDF crystalline matrix for the fabrication of magnetic responsive and actuating thin films. The presence of the 3D magnetic nanostructures in the PVDF matrix induced the electroactive  $\beta$ -phase of the PVDF as well as imparting magnetic actuation of the 3D nanomagnet–PVDF composite thin films. We are currently developing propriety magneto-mechanical (piezo)-electric (MME) nanogenerators to realise magnetic energy to electric conversion using the prepared flexible 3D nanomagnet–PVDF composite thin films presented herein. The 3D nanomagnet–PVDF composites will reinforce magneto-restriction in the thin films, thus enlarging the magneto-mechanical coupling, which may lead to a higher magnetoelectric voltage coupling coefficient. With this system, an output voltage will be produced through a direct magnetoelectric electret effect. This paper highlights the exciting possibilities of 3D nanomagnet–PVDF composite thin films to serve as an alternative class of magnetic materials for constructing low-cost and compact magnetic nanogenerators as an upgrade over bulky ceramic-based and traditional magnetic energy harvesting technologies. The real-world applications of magnetic nanogenerator-based energy harvesting systems include providing an unlimited energy supply by recycling untapped magnetic energy for use in powering wearables, portable healthcare devices, and lighting up homes. This has the potential to change how low-power electronic devices, such as wireless sensors and smartphones, are operated and utilised in the future.

## 2. Materials and Methods

### 2.1. Synthesis of 3D Nanomagnets

The synthesis of the 3D nanomagnets with various morphologies ranging from cubic-, spherical-, and truncated cubic/rod-shaped was achieved by means of thermolysis–heterogeneous nucleation and the growth of precursor materials (Scheme 1). In a typical manner, iron (III) acetylacetonate,  $\text{Fe}(\text{acac})_3$  (1.3 mmol) or iron pentacarbonyl,  $\text{Fe}(\text{CO})_5$ , 98%, and oleic acid (3 mL, 90%) (for the synthesis of cubic and truncated cubic/rod-shaped 3D nanomagnets) were mixed with oleylamine (0.956 g, 3 mmol) and 1-octadecene (5 mL) and then heated up to 310 °C for 1.5 h under nitrogen gas protection in a Schlenk line. The resulting nanomagnetic precursors were treated with triethylamine (5 mL, 99%) and poly(styrene-*co*-maleic anhydride), cumene-terminated, *PScMA* ( $M_n = 1900$  g/mol) as a binder, followed by solvothermal heating in a Teflon-lined stainless steel autoclave at 150, 220, and 280 °C for 20 h. The products were cooled to room temperature and purified/collected by means of magnetic separation, followed by annealing at 500 °C to obtain solid 3D magnetic nanostructures.



**Scheme 1.** Synthetic routes for the 3D nanomagnetic materials with different morphologies.

### 2.2. Preparation of 3D Nanomagnet–PVDF Composites and Thin Films

The nanocomposites of 3D nanomagnet–PVDF were prepared by adding 0.1 g of the 3D nanomagnets to 10 mL of 15 wt % (*w/v*) PVDF-dimethyl formamide (DMF) solution. The mixture was mechanically stirred for 5 h. Thin films were prepared by means of a solution casting process on clean glass substrates and dried in vacuo at 70 °C for 10 h to obtain free-standing flexible films.

### 2.3. Morphological and Magnetic Characterisations

The as-synthesised 3D nanomagnets were characterised using high-resolution transmission electron microscopy (HRTEM)/selected area electron diffraction (SAED).

The magnetisation (*M* vs. *H*) and susceptibility ( $\chi$  vs. *T*) of the 3D nanomagnets and PVDF composites/thin films were measured using a Quantum Design MPMS SQUID magnetometer. Fourier-transform infrared (FTIR) spectroscopy was used to elucidate the crystalline phase transformation and piezoelectric properties of the 3D nanomagnet–PVDF composites/thin films.

## 3. Results and Discussion

The synthesis process for the 3D nanomagnets is illustrated in Scheme 1. The adopted synthesis approach typically comprises thermal decomposition and a solvothermal process, which offers better-quality magnetic nanostructures in terms of size and morphology. The synthesis strategy was based on the choice of the precursors and most importantly the solvothermal reaction time and temperatures used to achieve both the size and anisotropic morphologies of the magnetic nanostructures [14]. The controlled synthesis to obtain anisotropic cubic and mixed truncated cubic/rod-like shapes was specifically dictated using  $\text{Fe}(\text{CO})_5$  as a precursor in the presence of oleic acid [15], which resulted in the formation of the mixed truncated cubic/rod-like and purely cubic morphologies.  $\text{Fe}(\text{acac})_3$  was used as the precursor for the spherical-shaped 3D nanomagnets in the absence of oleic acid. The 3D geometry of the nanomagnets was systematically engineered by the solvothermal clustering protocol [16] in the presence of the amphiphilic polymeric PScMA which was a factor that not only allowed for geometrical clustering but also the fine-tuning of the size.

Structural and morphological characterisation were carried out to evaluate the size and shapes of the synthesised nanomagnets. As shown by the HRTEM micrographs in Figure 1a,b, the cubic- and spherical-shaped nanomagnets were non-uniformly distributed, with sizes ranging between 20–30 nm and 15–25 nm, respectively. The HRTEM images also clearly revealed the distinctive adjacent crystal planes of (220) and (311) for the cubic morphology and (100), (111), (311), and (400) for the spherical nanomagnets. The various lattice fringes correspond to the typical magnetite crystalline phases of magnetic nanostructures [17]. The mixed truncated cubic/rod-like nanomagnets exhibited quite heterogeneous compositions with bigger size distributions and diameters in the range of 15–50 nm (Figure 1c).

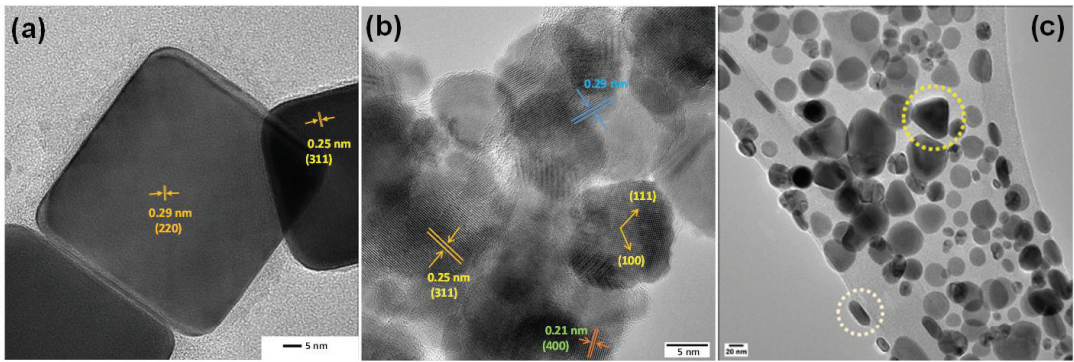


**Figure 1.** HRTEM images of the 3D nanomagnets showing cubic (a), spherical (b), and mixed truncated cubic/rod-like (c) morphologies. The crystalline planes of the cubic and spherical morphologies are shown in (a,b).

Furthermore, the various 3D nanomagnets were dispersed in commodity PVDF polymer to derive magnetically induced piezoelectric composites. Solution-processed 3D-nanomagnet-PVDF films were obtained with free standing, folding, and bending features, as shown in Figure 2a–c. PVDF film without incorporating the 3D nanomagnets was also prepared for comparison in terms of magnetic and piezoelectric susceptibility. The thin films were further characterised using scanning electron microscopy (SEM) to elucidate the structural differences between the 3D nanomagnets embedded and the neat PVDF films. The SEM images (Figure 2d,e) clearly show a difference in their surface morphologies (roughness) which may be ascribed to the encapsulation of the 3D nanomagnets into the PVDF polymer matrix. It is expected that the change in the surface morphology confirmed by SEM will equally result in a change in the surface, structural, and chemical properties of the PVDF such as its crystallinity and piezoelectric properties. It was envisaged that 3D nanomagnets would likely act as an agent for inducing the electroactive  $\beta$ -phase nucleation by aligning the  $-\text{CH}_2/-\text{CF}_2$  molecular dipoles of PVDF [18]. This helps to achieve a high piezoelectric coefficient and sensitivity in addition to the magnetic responsiveness of the films.

To ascertain whether the produced films possess the desired magneto-piezoelectric properties towards MME nanogenerator fabrication, magnetic characterisation such as saturation magnetisation analysis of both the 3D nanomagnets and their PVDF films was carried out. Figure 3a,b shows the M-H hysteresis curve for the 3D nanomagnets (with the cubic shape shown as an example) and the 3D nanomagnet–PVDF film. The 3D nanomagnets generally exhibit very strong magnetic moments at 300 K with a ferromagnetic behaviour. Meanwhile, symmetric hysteresis and saturation magnetisation was observed in both the nanomagnets and their thin films, with saturation magnetisation values of  $\sim 80$  and  $45 \text{ emu/g}$ , respectively. Importantly, for the thin films, saturation magnetisation and remanent magnetization can be observed, which is one of the desired properties as

evident from the displayed remarkable magnetic responsiveness and actuation capacity in the presence of a magnetic force.

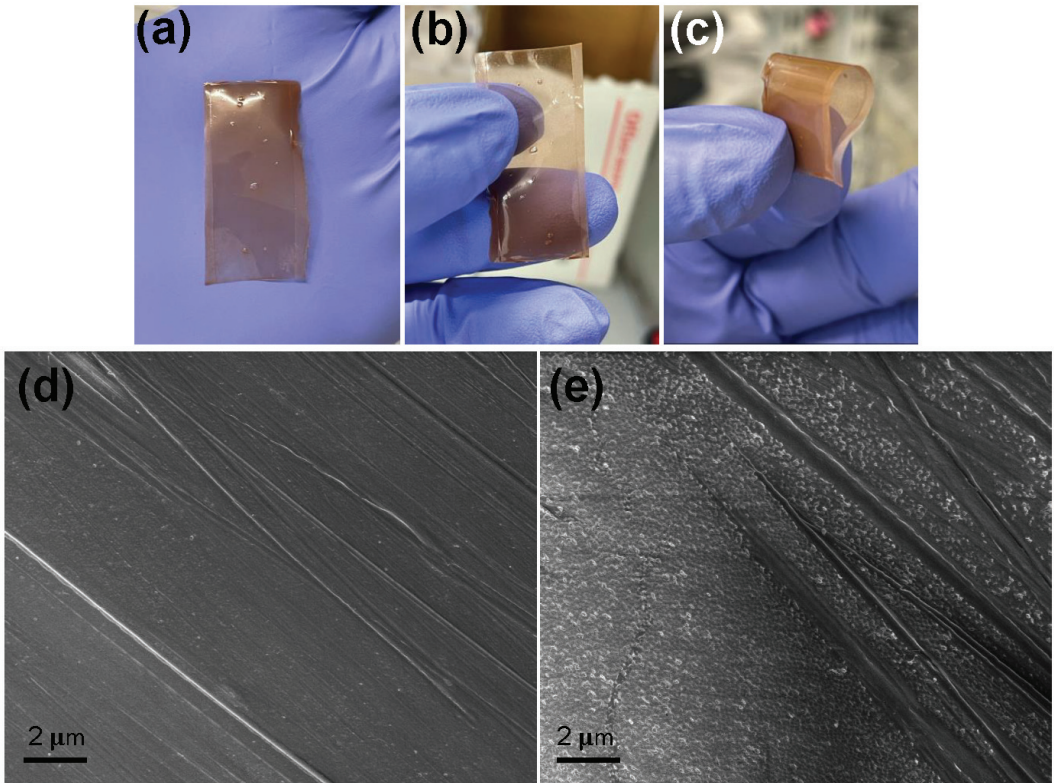


**Figure 2.** Thin films of the cubic-shaped 3D nanomagnet–PVDF composites displaying freestanding, stretching, and bending features (a–c). SEM images of the PVDF (d) and cubic-shaped 3D nanomagnet–PVDF (e) films.

FTIR spectroscopy was used to confirm the PVDF piezoelectric-favored  $-\text{CH}_2/-\text{CF}_2$  dipolar alignments in the presence of the 3D nanomagnets. In Figure 3c, the FTIR results clearly show the induction of the extensive polar  $\beta$ -phase in the 3D nanomagnet–PVDF films. This is evident from the appearance of the intense vibrational peak at  $\sim 1190 \text{ cm}^{-1}$ , which is non-existent in the pristine PVDF films [18]. The dual characteristic peaks at  $705 \text{ cm}^{-1}$  and  $520 \text{ cm}^{-1}$  correspond to the  $\beta$ - and  $\gamma$ -phases, which is an indication of the  $\beta$ -phase [18], suggesting that its induction is the result of the 3D nanomagnets. Similar characterisation trends and results were observed for all of the synthesised anisotropic 3D nanomagnets. However, the cubic morphology of the 3D nanomagnets exhibited superior magnetic properties alone and in the PVDF thin films. The results of all the characterisations illustrate the remarkable properties and motivation for using 3D nanomagnet–PVDF films as an MME generator component.

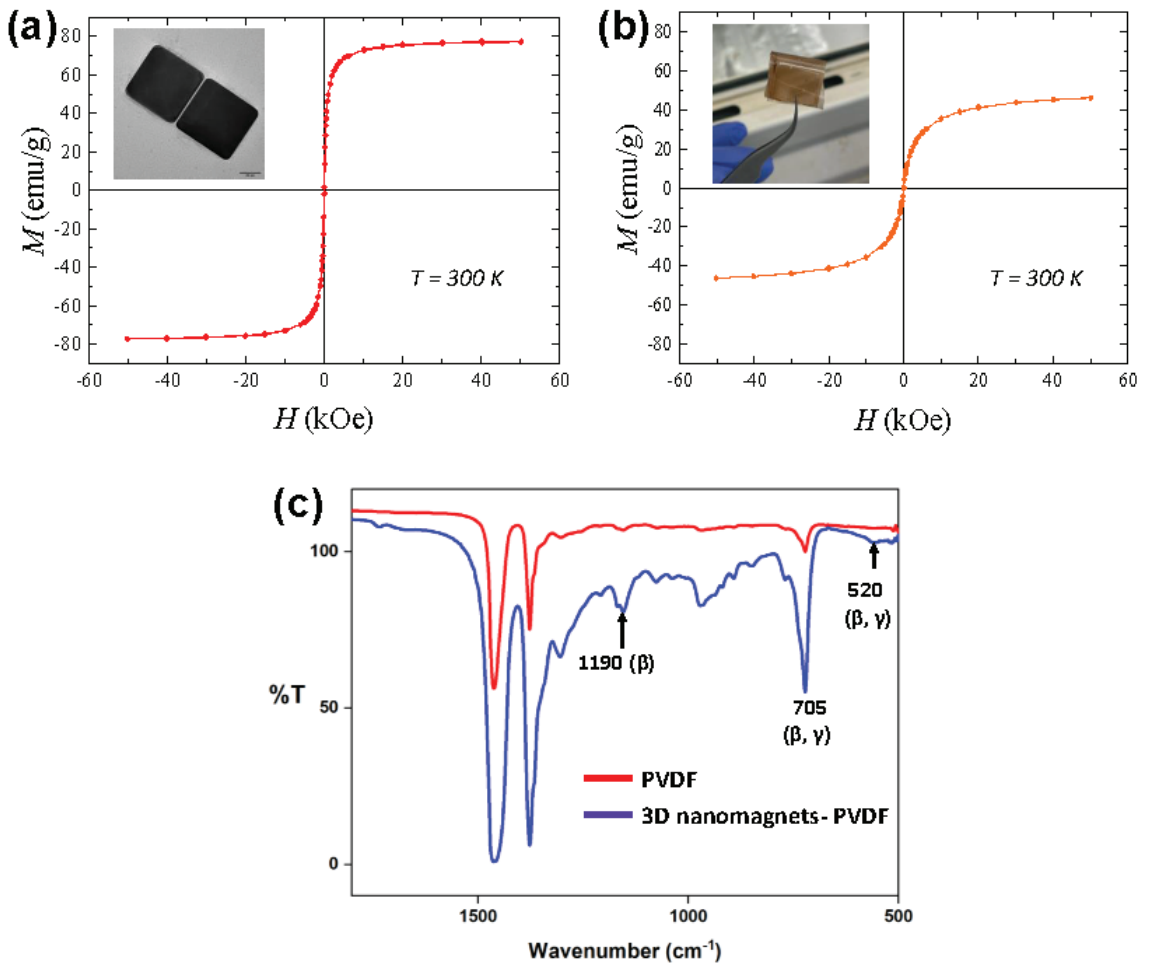


**Figure 3.** Magnetometry plots (hysteresis curves) for the cubic-shaped 3D nanomagnets (a) and their PVDF thin films (3D nanomagnets–PVDF) (b). FTIR spectra of the thin films of PVDF (pristine) and 3D nanomagnets–PVDF (c).

#### 4. Conclusions

In summary, advanced 3D magnetic nanostructures with distinctive anisotropic features such as cubic, spherical, and mixed truncated cubic/rod-like morphologies have been prepared and subsequently embedded in the polymeric matrix of piezoelectric PVDF to induce an electrically active  $\beta$  phase of the PVDF. The fabricated thin films displayed excellent formability features with better adaptability. The flexible films of 3D nanomagnet–PVDF composites with their attractive properties in terms of cost-effectiveness and excellent electroactive properties, as well as the induced large spontaneous polarizability, piezoelectricity, and magnetic responsiveness by incorporating 3D nanomagnets, make them innovative materials for not just magnetic nanogenerator device fabrication but also various magnetic applications such as sensing and actuation. This will facilitate the development of self-powered and portable wireless communication systems and medical and diagnostic devices by harvesting the ambient waste stray magnetic noise and minimising the dependence on batteries, benefitting the fast-growing industry automation and the Internet of Things (IoT).



**Author Contributions:** O.J.A.: conceptualization, methodology, validation, execution of experiments, and manuscript preparation; G.L.E. and O.M.B.: validation, data curation, review, and editing. All authors have read and agreed to the published version of the manuscript.

**Funding:** Funding support from the European Union's Horizon 2020 research and innovation program under the Marie Skłodowska-Curie grant agreement no. 945380 for the project to develop sustainable magnetic nanogenerators is gratefully acknowledged.

**Institutional Review Board Statement:** Not applicable.

**Informed Consent Statement:** Not applicable.

**Data Availability Statement:** The authors can be contacted for further details. The datasets presented in this article are not public due to privacy restrictions and funders specific.

**Conflicts of Interest:** The authors declare no conflict of interest.

## References

1. Annapureddy, V.; Palneedi, H.; Hwang, G.T.; Peddigari, M.; Jeong, D.Y.; Yoon, W.H.; Kim, K.H.; Ryu, J. Magnetic energy harvesting with magnetoelectrics: An emerging technology for self-powered autonomous systems. *Sustain. Energy Fuels* **2017**, *1*, 2039–2052. [CrossRef]
2. Ryu, J.; Kang, J.E.; Zhou, Y.; Choi, S.Y.; Yoon, W.H.; Park, D.S.; Choi, J.J.; Hahn, B.D.; Ahn, C.W.; Kim, J.W.; et al. Ubiquitous magneto-mechano-electric generator. *Energy Environ. Sci.* **2015**, *8*, 2402–2408. [CrossRef]
3. Lee, H.; Sriramdas, R.; Kumar, P.; Sanghadasa, M.; Kang, M.G.; Priya, S. Maximizing power generation from ambient stray magnetic fields around smart infrastructures enabling self-powered wireless devices. *Energy Environ. Sci.* **2020**, *13*, 1462–1472. [CrossRef]
4. Dai, X.; Wen, Y.; Li, P.; Yang, J.; Li, M. Energy harvesting from mechanical vibrations using multiple magnetostrictive/piezoelectric composite transducers. *Sens. Actuators A Phys.* **2011**, *166*, 94–101. [CrossRef]
5. Hu, X. Increased effective piezoelectric response of structurally modulated P(VDF-TrFE) film devices for effective energy harvesters. *Mater. Des.* **2020**, *192*, 108700. [CrossRef]
6. Annapureddy, V.; Na, S.M.; Hwang, G.T.; Kang, M.G.; Sriramdas, R.; Palneedi, H.; Yoon, W.H.; Hahn, B.D.; Kim, J.W.; Ahn, C.W.; et al. Exceeding milli-watt powering magneto-mechano-electric generator for standalone-powered electronics. *Energy Environ. Sci.* **2018**, *11*, 818–829. [CrossRef]
7. Lim, K.W.; Peddigari, M.; Park, C.H.; Lee, H.Y.; Min, Y.; Kim, J.W.; Ahn, C.W.; Choi, J.J.; Hahn, B.D.; Choi, J.H.; et al. A high output magneto-mechano-triboelectric generator enabled by accelerated water-soluble nano-bullets for powering a wireless indoor positioning system. *Energy Environ. Sci.* **2019**, *12*, 666–674. [CrossRef]
8. Al-Ashtari, W.; Hunstig, M.; Hemsell, T.; Sextro, W. Frequency Tuning of Piezoelectric Energy Harvesters by Magnetic Force. *Smart Mater. Struct.* **2012**, *21*, 035019. [CrossRef]
9. Narita, F.; Fox, M. A review on piezoelectric, magnetostrictive, and magnetoelectric materials and device technologies for energy harvesting applications. *Adv. Eng. Mater.* **2018**, *20*, 1700743. [CrossRef]
10. Ahn, C.-W.; Choi, C.-H.; Park, H.-Y.; Nahm, S.; Priya, S. Dielectric and Piezoelectric Properties of  $(1-x)(\text{Na}_{0.5}\text{K}_{0.5})\text{NbO}_3$ - $x\text{BaTiO}_3$  Ceramics. *J. Mater. Sci.* **2008**, *43*, 6784–6797. [CrossRef]
11. Fernández-Pacheco, A.; Streubel, R.; Fruchart, O.; Hertel, R.; Fischer, P.; Cowburn, R.P. Three-dimensional nanomagnetism. *Nat. Commun.* **2017**, *8*, 15756. [CrossRef] [PubMed]
12. Faure, B.; Wetterskog, E.; Gunnarsson, K.; Josten, E.; Hermann, R.P.; Brückel, T.; Andreasen, J.W.; Meneau, F.; Meyer, M.; Lyubartsev, A.; et al. 2D to 3D crossover of the magnetic properties in ordered arrays of iron oxide nanocrystals. *Nanoscale* **2013**, *5*, 953–960. [CrossRef] [PubMed]
13. Anagnostopoulou, E.; Grindi, B.; Lacroix, L.M.; Ott, F.; Panagiotopoulos, I.; Viau, G. Dense arrays of cobalt nanorods as rare-earth free permanent magnets. *Nanoscale* **2016**, *8*, 4020–4029. [CrossRef] [PubMed]
14. Ma, Z.; Mohapatra, J.; Wei, K.; Liu, J.P.; Sun, S. Magnetic Nanoparticles: Synthesis, Anisotropy, and Applications. *Chem. Rev.* **2023**, *123*, 3904–3943. [CrossRef]
15. Soran-Erdem, Z.; Sharma, V.K.; Hernandez-Martinez, P.L.; Demir, H.V. Tailored Synthesis of Iron Oxide Nanocrystals for Formation of Cuboid Mesocrystals. *ACS Omega* **2021**, *6*, 20351–20360. [CrossRef]
16. Niculaes, D.; Lak, A.; Anyfantis, G.C.; Marras, S.; Laslett, O.; Avugadda, S.K.; Cassani, M.; Serantes, D.; Hovorka, O.; Chantrell, R.; et al. Asymmetric assembling of iron oxide nanocubes for improving magnetic hyperthermia performance. *ACS Nano* **2017**, *11*, 12121–12133. [CrossRef]

17. Achadu, O.J.; Nwaji, N.; Lee, D.; Lee, J.; Akinoglu, E.M.; Giersig, M.; Park, E.Y. 3D hierarchically porous magnetic molybdenum trioxide@gold nanospheres as a nanogap-enhanced Raman scattering biosensor for SARS-CoV-2. *Nanoscale Adv.* **2022**, *4*, 871–883. [CrossRef] [PubMed]
18. Tamang, A.; Ghosh, S.K.; Garain, S.; Alam, M.M.; Haeberle, J.; Henkel, K.; Schmeisser, D.; Mandal, D. DNA-Assisted  $\beta$ -phase Nucleation and Alignment of Molecular Dipoles in PVDF Film: A Realization of Self-Poled Bioinspired Flexible Polymer Nanogenerator for Portable Electronic Devices. *ACS Appl. Mater. Interfaces* **2015**, *7*, 16143. [CrossRef]

**Disclaimer/Publisher's Note:** The statements, opinions and data contained in all publications are solely those of the individual author(s) and contributor(s) and not of MDPI and/or the editor(s). MDPI and/or the editor(s) disclaim responsibility for any injury to people or property resulting from any ideas, methods, instructions or products referred to in the content.



Proceeding Paper

# Bridging the Gap: Challenges and Opportunities of IoT and Wireless Sensor Networks in Marine Environmental Monitoring <sup>†</sup>

Hamid Errachdi, Ivan Felis <sup>\*</sup>, Eduardo Madrid and Rosa Martínez

Centro Tecnológico Naval y del Mar, 30320 Fuente Álamo, Spain; hamiderrachdi@ctnaval.com (H.E.); eduardomadrid@ctnaval.com (E.M.); rosamartinez@ctnaval.com (R.M.)

<sup>\*</sup> Correspondence: ivanfelis@ctnaval.com; Tel.: +34-968-197-521

<sup>†</sup> Presented at the 10th International Electronic Conference on Sensors and Applications (ECSA-10), 15–30 November 2023; Available online: <https://ecsa-10.sciforum.net/>.

**Abstract:** Marine environmental monitoring is increasingly vital due to climate change and the emerging Blue Economy. Advanced Information and Communication Technologies (ICTs) have been applied to develop marine monitoring systems, with the Internet of Things (IoT) playing a growing role. Wireless Sensor Networks (WSNs) are crucial for IoT implementation in the marine realm but face challenges like modeling, energy supply, and limited deployment compared to land-based applications. This paper explores various communication technologies, considering factors like coverage, cost, energy use, and stability. It highlights the potential of wireless technology in marine conservation and activities like port operations, aquaculture, and renewable energy, offering insights from real-world testing in the Region of Murcia.

**Keywords:** marine environmental monitoring; marine internet of things (MIoT); wireless sensor networks (WSNs); communication technologies in marine environment; blue economy

## 1. Introduction

Marine environmental monitoring has garnered increasing attention due to mounting concerns regarding climate change and the burgeoning Blue Economy, which acknowledges oceans and seas as economic drivers. Over the past two decades, advanced Information and Communication Technologies (ICTs) have been applied to develop monitoring systems for the marine environment and its anthropogenic activities. In this context, the Internet of Things (IoT) is progressively demonstrating its role. The IoT offers data processing capabilities, enabling intelligent object control and the agile development of applications aligning with biodiversity conservation and economic growth.

A pivotal technology for IoT implementation is Wireless Sensor Networks (WSNs), comprising autonomous devices distributed across an area of interest to monitor physical or environmental parameters. However, the application of the IoT in the marine environment remains distant from realization, and the utilization of WSNs in this context is constrained by issues like modeling, energy supply, range, and bandwidth. In fact, deployments of these technologies in the marine environment lag significantly behind their terrestrial counterparts. Furthermore, a comprehensive and contextualized examination of wireless communication technologies in the marine environment is still lacking.

Hence, this text presents an exploration of various communication technologies (Bluetooth, ZigBee, WiFi, WiMax, LoRa, LoRaWAN, SigmaFox, GSM, 3G, 4G, etc.), considering spatial coverage, deployment and maintenance costs, energy consumption, stability, data throughput, and more. This study, utilizing the coastal telecom stations in the Region of Murcia (Spain) as a pilot application area, focuses on the opportunities wireless technologies offer for marine conservation and the sustainable development of activities such as port operations, aquaculture, fishing, offshore renewable energy, and autonomous risk mitigation vehicles.

**Citation:** Errachdi, H.; Felis, I.; Madrid, E.; Martínez, R. Bridging the Gap: Challenges and Opportunities of IoT and Wireless Sensor Networks in Marine Environmental Monitoring. *Eng. Proc.* **2023**, *58*, 102. <https://doi.org/10.3390/ecsa-10-16158>

Academic Editor: Stefano Mariani

Published: 15 November 2023



**Copyright:** © 2023 by the authors. Licensee MDPI, Basel, Switzerland. This article is an open access article distributed under the terms and conditions of the Creative Commons Attribution (CC BY) license (<https://creativecommons.org/licenses/by/4.0/>).

Additionally, the project conducts systematic tests of these communications by deploying WSN nodes at various distances and data rates to simulate real marine activities, employing advanced data compression techniques to enhance data transmission. The results provide invaluable insights for the future deployment of wireless communication technologies in the marine environment, promoting both environmental preservation and the sustainable advancement of marine-related activities.

## 2. Challenges and State of the Art

### 2.1. Challenges of WSNs in the Marine Environment

In recent decades, there has been an increase in the number of technological solutions based on Wireless Sensor Networks (WSNs), which have a series of advantages in monitoring the environment, its biodiversity, and the activities that take place in it, such as autonomous operation, real-time supervision (reducing effort and staff hours), and relatively low cost [1]. In fact, the costs derived from the use of these monitoring technologies are being reduced, thus making them cost-effective tools compared to traditional forms of monitoring [2].

However, the current protocols and design specifications of land-based WSNs must be adapted to the requirements of the marine environment [3], making their deployment in the marine environment a challenge [4]. In this sense, the development of WSNs in the marine environment presents obstacles related, on the one hand, to the capacity and time needed to store, share, and analyze the large volumes of data that must be managed through communication networks and, on the other hand, the limited resources that we find in the marine context itself, in particular, self-sufficient power supply, data storage capacity, and communication bandwidth [5]. These obstacles are considered one of the largest challenges in the design of automated stations for monitoring the marine environment.

Regarding the large volume of data in the marine environment, it should be noted that, in addition, marine traffic has been growing considerably in recent years [6], as well as the number of monitoring systems necessary for the navigation and monitoring of vessels, which means that the data obtained have increased to the same extent and are susceptible to integration into a network [7].

Regarding the challenges posed by the marine context itself, we find different studies focused, among others, on energy storage beyond conventional batteries that require a high level of replacement [8], renewable energy supplies adapted to WSNs [9], the impact of sea waves on the propagation of communications and the quality of the communications link [10], and the effect of the ocean environment for cellular IoT [11,12].

For all these reasons, new techniques and algorithms must be addressed to achieve this goal, from the scope of the sensors and nodes of the network, and the network architecture itself, to the protocols and network technology used [13].

### 2.2. Application of Existing WSNs to the Marine Environment

An IoT-based protection and monitoring system is composed of five layers [14]: the perception and execution layer, the transmission layer, the data preprocessing layer, the application layer, and the business layer.

The network/transmission layer is the most important layer in IoT architecture, as a variety of devices (switches, hubs, compute performance, gateways, etc.) and different communication technologies (ZigBee, Bluetooth, LTE, 5G, 6LoWPAN, Wi-Fi, etc.) are combined in this layer [15]. The network layer must provide data to or from different objects or applications, through gateways or interfaces between heterogeneous networks, and use different communication technologies and protocols.

The application of these technologies depends on the distance to be considered and the volume of data to be transmitted. For example, to exchange data in a communication at a short distance (~100 m), NFC, ZigBee, and Bluetooth could be a good choice; for medium-distance communication (~0.1–1 km), we could use WiFi; while for long distance (>1 km), the most promising technologies would be LTE, LTE-A, WiMAX, and LoRaWan (LoRa).

Near the coast and in port environments, 3G, 4G, and, in the near-future, 5G coverage is excellent thanks to the proximity of the antennas. Likewise, there are protocols such as NB-IoT (Narrowband Internet of Things) specifically designed to interconnect IoT devices on LTE technologies.

In order to give as complete a picture as possible of the efforts made to date in the implementation of communication networks in the marine environment, a bibliographic search has been carried out, from which two key characteristics can be extracted: name of the technology and protocol, distance between transmitting and receiving antenna, and communication data throughput, as well as other relevant information such as consumption, frequency, and ultimate application.

In this search, 72 articles have been found that address this problem from an empirical point of view. Most of the 72 articles collected were extracted from two reviews by Xu et al. and Sung-Woong [16]. The rest have been obtained by carrying out alternative and specific searches. However, from all these articles, we cannot extract all the key data defined above. This circumstance leads to the fact that this information is not easily found, and even less so in a technology-specific way, in the same article. However, they do give us a global idea of which technologies are most tested in the marine environment.

Of these 72 articles, we can see that 13 articles use radio-based communication technology, 7 use ZigBee technology, 7 use Wi-Fi communication protocols but applied to other technologies such as LTE to achieve greater range, 4 use 4G technology, 6 use 2G technologies, and the rest of the technologies have been used much less. It should be noted that, for technologies such as 3G or SigFox, no studies have been found applied in the marine environment where the flow and range are empirically verified and specified. On the other hand, 21 articles do not specify enough information about the communication technology that has been installed to collect the data in the current state of the art.

However, only 20 relevant applications are extracted from the tested wireless communications, in which we find explicit information regarding the flow and range of the communication. The following shows the feature set of these 20 experiments (Table 1):

**Table 1.** List of technologies tested at sea according to the bibliographic search, in which we find explicit information regarding the flow and range of communication.

Author	Year	Country	Technology	Range (m)	Caudal (kbps)	Cost
Singapore Gov. [17]	2007	Singapore	WiMAX	15,000	5000	Middle
Mi.-T. Zhou et al. [18]	2013	Japan	WiMAX	14,200	6000	Middle
M.-T. Zhou et al. [18]	2013	Japan	WiMAX	8660	6000	Middle
H.-J. Kim et al. [19]	2015	Korea	LTE	10,000	7600	Middle
H.-J. Kim et al. [19]	2015	Korea	WLAN	20,000	4700	Middle
J. M. Almeida et al. [20]	2016	Portugal	LTE	30,000	5000	Middle
J. M. Almeida et al. [20]	2016	Portugal	Wi-Fi	60,000	3200	Middle
Sethuraman et al. [21]	2018	India	LR Wi-Fi	52,000	3000	Low
Sethuraman et al. [21]	2018	India	LR Wi-Fi	22,600	3000	Low
M. Höyhtyä [22]	2017	Finland	Wi-Fi	900	27,000	-
S-W, Jo [16]	2019	Corea	LTE	107,000	12,000	-
G. Kazdaridis [23]	2017	Serbia	LoRa	21,000	50	-
C. De Marziani et al. [24]	2011	Spain	ZigBee	1200	250	-
Silva L.G. [25]	2013	Argentina	WiFi	16,000	64,000	-
S. Jiang et al. [26]	2015	China	MF/HF	463,000	0.1	-
S. Jiang et al. [26]	2015	China	VHF	120,000	1.2	-
S. Jiang et al. [26]	2015	China	VHF	120,000	9.6	-

Table 1. Cont.

Author	Year	Country	Technology	Range (m)	Caudal (kbps)	Cost
S. Jiang et al. [26]	2015	China	MF	556,000	18	-
S. Jiang et al. [26]	2015	China	VHF	120,000	307	-
Marlaski et al. [27]	2018	Denmark	NB-IoT	3439	66.7	-

The following graph shows the scope of the communications used in these publications, taking into account both the distance and the data throughput tested in the different experiments.

It is observed that radio frequency is one of the most used technologies as it has a range well above the average, exceeding 100 km, but with a somewhat limited capacity to transmit data, and whose implementation cost will depend on the base stations that exist. However, there are studies where 4G technology has been implemented for the same distances, but with a substantially higher throughput. On the other hand, there is an area where the use of technologies such as WiFi (but combined with other technologies to achieve these long ranges), WiMAX, LTE (4G), and RF converge for a range of more than 10 km with a data flow between 103 and 104 kbps. Finally, although there are not much data on the range and flow used with ZigBee technology, its use is widespread and, based on the experimental data collected, it can be seen that it has a considerable range, although the data flow would be low, not exceeding 102 kbps at such distances.

With this, the present work aims to test different technologies that allow communications between coastal activities, resource extraction activities, and off-shore renewable energy platforms, among other land-based activities using communication technologies in Figure 1, covering areas that have not been covered in this graph both in bandwidth and distance.

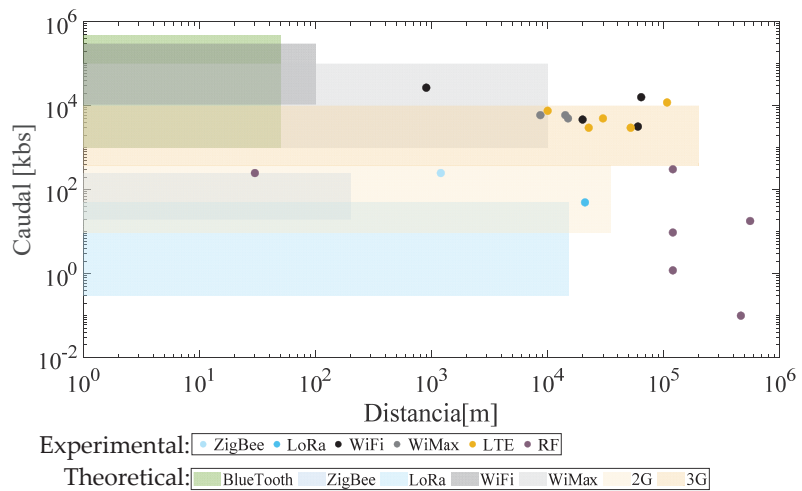


Figure 1. Comparison between distance and expected data throughput for different communications (shading) with respect to experimental results from the literature (points) (authors' own creation).

### 3. Materials and Methods

This research aims to investigate the limitations of existing wireless communication technologies for the development of Wireless Sensor Networks (WSNs) in the marine environment. This study encompasses both theoretical analysis and experimental deployment, focusing on supporting strategies for the sustainable conservation and exploitation of oceans and seas. The coastal regions of the Region of Murcia serve as the practical

application area for this research endeavor. In order to achieve this objective, the following specific methods are outlined:

- To compare different electromagnetic communication propagation simulation techniques that account for the specific circumstances and scenarios in the marine environment.
- To test the development and deployment of different communication technologies at varying distances from the coast, data throughput rates, and consumption requirements, addressing real needs in marine contexts and activities.

To fulfill these specific objectives, a combination of theoretical work, involving a literature review within this report and previous experience from the CTN, and experimental work for technological development and technology deployment in the marine environment is conducted.

### 3.1. Electromagnetic Propagation Simulation in Marine Environments

In this section, we delve into the theoretical study of modeling propagation losses associated with the transmission of electromagnetic waves at typical frequencies used in radiocommunications. Based on this, algorithms of varying complexity are implemented to enable the exploration of more realistic studies.

#### 3.1.1. One-Ray Model (Free-Space Propagation Model)

This model considers a characteristic free-space propagation model, which does not take into account any form of reflection, refraction, or any other scattering mechanism of the beam. It is analogous to a ray model, representing the direct path between the transmitter and receiver, making it the simplest model to consider. This model, also known as the Friis model, considers only losses due to the divergence of the wavefront, as reflected in its mathematical expression:

$$P_R/P_T = G_T G_R \left( \frac{c}{4\pi fl} \right)^2 \tag{1}$$

where  $G_T$  and  $G_R$  ( $P_R$  and  $P_T$ ) are the gains (powers) of the transmitting and receiving antennas in the direction of the vector connecting them, respectively, separated by a distance  $l$ , and where  $f$  is the frequency of the electromagnetic wave considered (with  $c$  representing the speed of light).

More conveniently, in logarithmic scale, the propagation losses can be expressed as

$$L = 10\log_{10}(P_T/P_R) = 20\log_{10}(fl) - 10\log_{10}(G_R G_T) + 20\log_{10}(4\pi/c) \tag{2}$$

#### 3.1.2. Two-Ray Model

In most cases, the previous model proves to be overly simplistic as it does not account for contributions from reflected rays. The two-ray model precisely takes into consideration the ray that, after being reflected by the ground (or another obstacle), also reaches the target, adding a contribution to the received field at the receiving antenna, as illustrated in Figure 2.

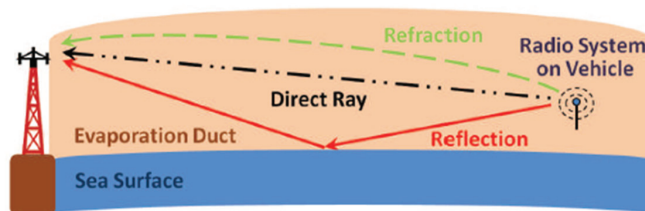


Figure 2. Raytracing corresponding to the different-number ray model.

This model extends the previous one by incorporating an additional term corresponding to the field generated by the reflected ray. In this case, the propagation losses are:

$$L = -20\log_{10}\left(\frac{c}{4\pi f}\right) \left| \frac{e^{-ikl}}{l} \sqrt{G_T^d G_R^d} + R \frac{e^{-ikr_r}}{r_r} \sqrt{G_T^r G_R^r} \right| \quad (3)$$

where  $k$  is the wave number,  $r_r$  is the total distance covered by the reflected ray, and the superscript on the gain denotes the associated ray ( $d$ : direct;  $r$ : reflected).  $R$  is the reflection coefficient of the reflected ray, which depends on the angle of incidence, wave polarization, and electromagnetic characteristics of the involved media (air and water in this application).

In the literature, it is common to make the approximation of very small incidence angles, in which case the expression simplifies significantly. In particular, assuming a vertically polarized wave, it is obtained that the reflection coefficient  $R = -1$  (phase changes by 180 degrees), which will be the default case in our scenario. However, we will continue to use this expression to account for the possible “roughness” of the sea, which will be discussed in more detail in Section 5, although its effects, given the long propagation distances and typical low antenna height(s), will be correspondingly minimal.

### 3.1.3. Three-Ray Model

The two-ray model is a good approximation to the problem at hand for short distances and under the specified conditions. However, it is widely recognized that for longer distances and depending on atmospheric conditions, there are discrepancies between what is observed and the analytical model. The main reason for this is the existence of a propagation channel formed by the presence of water vapor in the first few meters of air above the sea surface, which occurs under certain circumstances. In detail, when this vapor layer exists, it creates a minimum in the profile of the speed of light at altitude, causing the refraction of the beam and leading to a third ray reaching the target, as depicted in Figure 2. According to the literature, this effect appears in channels spanning distances greater than 5 or 6 km. The significance of this effect is that it causes “valleys” of losses and significant “peaks” in gain from distances of this order of magnitude onward.

Although the refracted ray is not reflected at any point, for analytical simplicity, it is assumed to behave as if it were reflected, at a certain effective height approximated as the duct height. In conclusion, the three-ray model follows the following equation:

$$L = -20\log_{10}\left(\frac{c}{4\pi f}\right) \left| \frac{e^{-ikl}}{l} \sqrt{G_T^d G_R^d} + R \frac{e^{-ikr_r}}{r_r} \sqrt{G_T^r G_R^r} + \frac{e^{-ikr_{rf}}}{r_{rf}} \sqrt{G_T^{rf} G_R^{rf}} \right| \quad (4)$$

where  $r_{rf}$  is the distance traveled by the refracted ray, which can be calculated using the following expression:

$$r_{rf} = r_{rf1} + r_{rf2} = \sqrt{(h_e - h_t)^2 + (h_t \tan(\theta))^2} + \sqrt{(h_e - h_r)^2 + (h_r \tan(\theta))^2} \quad (5)$$

where  $\theta$  is the angle of incidence,  $h_e$  is the effective duct height,  $h_r$  is the height of the receiving antenna, and  $h_t$  is the height of the transmitting antenna. On the other hand,  $G_T^{rf}$  and  $G_R^{rf}$  are the gains of the transmitting and receiving antennas in the direction of the refracted ray, respectively. The duct height  $h_e$  can be determined using specific models. In this study, the Paulus–Jeske model [28] was implemented, which is the most referenced analytical model in the literature. This model uses air temperature, water surface temperature, relative humidity, and wind speed as input parameters to estimate the height of the evaporation duct.

### 3.1.4. Specific Models for Rough Seas

As seen earlier in the two- and three-ray models, one of the contributions to the (total) field at the receiving antenna comes from a ray reflected by the sea. While reflection can



normally be assumed with an almost zero angle of incidence ( $\theta$ ), resulting in a reflection coefficient of  $-1$  for vertically polarized waves, significantly simplifying the approach, in the general case, it must be included in the calculation.

There are generalizations beyond the ideal case of specular reflection, where the associated reflection coefficient can be described by the following equation:

$$R = \frac{\sin\theta - Z}{\sin\theta + Z} \tag{6}$$

where  $Z$  is the characteristic impedance of the reflecting medium (water in our case):

$$Z = \begin{cases} \frac{1}{\tilde{\epsilon}_r} \sqrt{\tilde{\epsilon}_r - \cos^2 \theta} \\ \sqrt{\tilde{\epsilon}_r - \cos^2 \theta} \end{cases} \tag{7}$$

with  $\tilde{\epsilon}_r$  representing the complex relative permittivity of the medium.

In this context, when considering a rough surface rather than a smooth one, where reflections are more complicated to determine, it is common to use statistical models that characterize the surface in question and obtain, on average, an effective reflection coefficient. Thus, two different approaches have been implemented, each attributing different statistical properties to the sea surface height profile: the Ament approach and the Miller–Brown approach [29].

The Ament approach assumes that the heights of the sea surface are normally distributed such that

$$P_A(\xi; h_{rms}) = \frac{1}{\sqrt{2\pi}h_{rms}} e^{-\xi^2/2h_{rms}^2} \tag{8}$$

where  $h_{rms}$  is the root-mean-square deviation of sea surface height (of waves).

On the other hand, the more complex Miller–Brown approach considers the sea surface as a collection of sinusoidal waves with a uniform phase distribution, the expression of which is omitted here for brevity.

In summary, the roughness reduction factor is calculated as

$$\rho(k, \theta) = \int_{-\infty}^{\infty} e^{2ik\xi\sin\theta} P(\xi) d\xi \tag{9}$$

When multiplied by the standard reflection coefficient, it yields the effective reflection coefficient ( $R' = \rho R$ ).

Therefore, by introducing the expressions of Ament and Miller–Brown into this equation, we ultimately obtain the expressions for the effective reflection coefficients for the sea surface, which will need to be correspondingly included in the propagation loss equations.

### 3.2. Testing Communication Technologies for Coastal and Marine Needs

Different communication technologies can be used depending on the application. Two communication technologies used in this work are highlighted in green within the context of the wide range of existing technologies: LoRa for long-distance transmission with low bandwidth, and WiFi for transmitting data with higher bandwidth over short distances.

#### 3.2.1. Test of the LoRa System

To ensure that the data reach the location where the gateway will be installed, tests were conducted around the boat’s departure port days before conducting tests on the boat. In the map shown in Figure 3, the positions where coverage tests were conducted have been marked. In the yellow-marked positions (1 and 2), the data reached the gateway without any issues, while in the position marked in blue (position 4), there was no coverage, due to the presence of hills between the transmitter and the LoRa gateway.



**Figure 3.** Tested LoRa coverage positions: (a) gateway position and remote points.; (b) photograph of the device at position 2.

### 3.2.2. Test of the WiFi System

On the one hand, a subsea noise node was deployed near the Faro de la Curra, at the entrance of the port, with an autonomous data acquisition system specifically implemented for signal recording, allowing for the modification of the recording time as needed. The WiFi transmitting antenna, OmniTIK 5ac, was connected to this system via an Ethernet cable. On the other hand, a receiving antenna with the same characteristics was placed at various distances from the transmitter, along the same dock, at distances from 100 to 500 m. Figure 4 shows the positions of the transmitter and receiver on the left and the receiving station with the receiving antenna and a recording PC on the right.

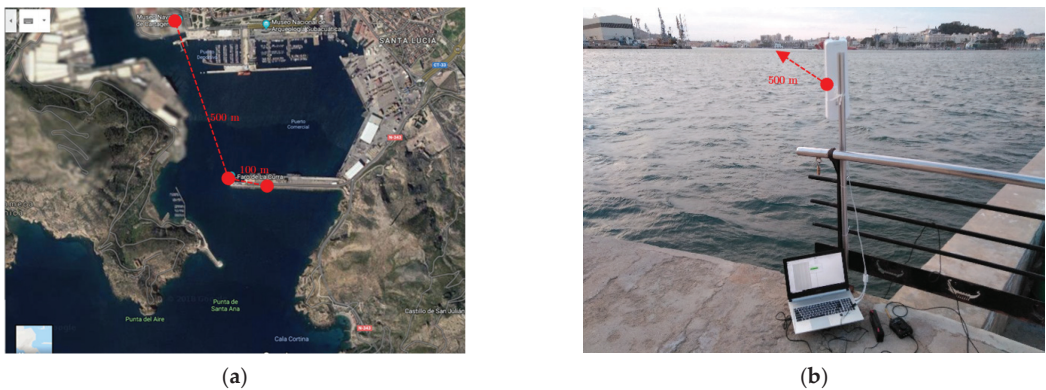


**Figure 4.** Tested LoRa coverage positions: (a) gateway position and remote points; (b) photograph of the device at position 2.

### 3.2.3. Deployment of Lora and WiFi Systems in Real Off-Shore Marine Environment

The technologies (Wimax, Lora, and GSM) are employed to establish communications between a moving vessel and a terrestrial location, with the aim of maintaining seamless and continuous communication between these two points. Receiving antennas will be positioned on the coastline, while the vessel will follow a straight-line trajectory to ensure that the receiving antennas remain consistently within the same range as the transmitting antennas.

The initial deployment was carried out from the following location, with each technology's receivers prepared to receive data. In this deployment, the receiving equipment was

positioned at a height of 6 m above sea level, with maximum effort dedicated to alignment and ensuring that it remained within the same range as the transmitters situated on the vessel. Testing is conducted until all technologies reach their maximum range.

The second deployment, at the subsequent location, is executed from a higher vantage point at 20 m above sea level to ensure a clear line of sight and minimize interference from the water's surface. The transmitter on the sea must be securely located and well mounted on the exterior of the vessel. Testing is conducted within a 20 km range for all three technologies (WiMAX, Lora, and GSM).

To carry out measurements in real environments, a boat trip was conducted in the waters of the Port of Cartagena.

## 4. Results

### 4.1. Theoretical Electromagnetic Propagation Simulation in Marine Environments

In this section, a comparison is made between the results provided by established tools from generic software and the models developed and described in the previous sections. Specifically, a test was conducted using Ubiquiti Networks' AirLink software for a hypothetical transect in the port of Cartagena.

The numerical comparison is shown in Figure 5, where good correspondence is observed between Ubiquiti Networks' software and the models implemented by the CTN. The largest discrepancy is noted with the three-ray model, which was expected as the tool does not account for the evaporation duct.

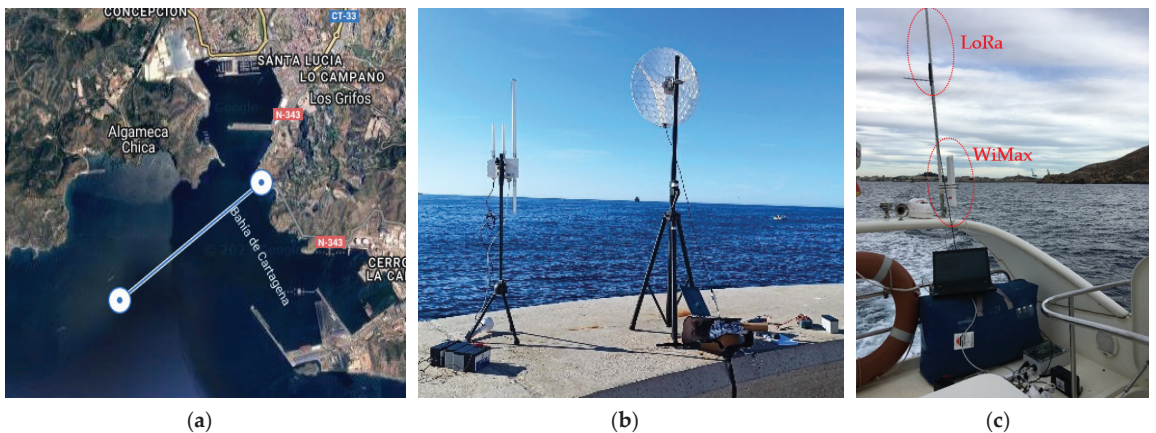


**Figure 5.** (a) Trajectory followed in the pilot study; (b) receiving antennas in this pilot; (c) transmitter antennas in this pilot.

Furthermore, in Figure 6, the results associated with a test using a higher height for the transmitting–receiving antenna (20 m) are provided. In this case, the correspondence between models and software is not as good as in the previous test, with discrepancies in parts of the simulation distance range (the best-matched zone is between 3 and 6 km). The slope of the curves from the ray models, particularly the two-ray model, aligns well with that produced by the reference software, although there is a slight offset between the two.

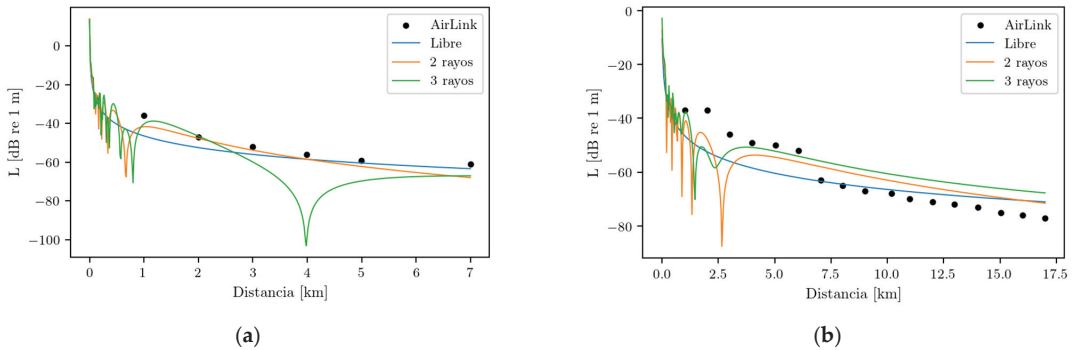


**Figure 6.** Comparison of results between propagation loss models and AirLink software for (a) first test; (b) second test.

4.2. Comparing Measures and Theoretical Propagation

In the first deployment, regarding WIMAX, it had achieved a straight-line range of 5000 m out to sea. Signal quality could have been further improved by deploying the receiving antenna at a higher point. Since the transmitting antenna on the vessel sent the WIMAX signal to the ground-based station, it was crucial to ensure that the antenna was stable and correctly oriented towards the base station. Any movement or change in the orientation of the transmitting antenna could have affected the signal quality sent and, consequently, the performance of the WIMAX connection.

In the second deployment, significant improvements in results were achieved, with a longer-range connection than in the first deployment. At this time, the receiving equipment was positioned at a higher location, providing greater visibility, reduced interference, and no obstacles in the environment that could have affected the signal. When testing for communication, the vessel was aligned as closely as possible with the receiver to remain within range and achieve a connection with a good transmission speed. In this test, the range of WIMAX was a success, reaching up to 14 km in a maritime environment.

In order to establish reliable data communication between the PC-powered Lopy1 device on a constantly transmitting vessel and the ground-based RAK724 receiving gateway at varying altitudes during the conducted deployments, continuous system monitoring was performed to ensure signal quality and reliability as each kilometer was advanced.

LoRa achieved a straight-line range of 6000 m out to sea, both in the initial deployment and in the subsequent one. Communication and range could be further enhanced by positioning the LoRa gateway at a higher point in the sea, increasing the effective transmitter height. This would enable the signal to reach greater distances while reducing the potential for interference and obstacles that could attenuate the signal. In general, elevating the antennas at both ends of the connection is considered the most effective means of improving range and signal quality.

As said, the experimental data were derived from the two campaigns conducted at sea, as detailed in the previous section. Specifically, data from the second sea campaign on 29 March 2023 were utilized. Figure 7 displays the results of this comparison.

As can be observed in Figure 7, there is a relatively good correspondence with the experimental data, especially concerning the two-ray model. Although it exhibits a difference of approximately 5 dB in the first 2 km, it closely replicates the data for longer distances. On the other hand, the free-space loss model underestimates losses for distances above approximately 8 km. Lastly, the three-ray model, which is more sensitive to input variables and exhibits more peaks and valleys, appears unsuitable for this case. One possible cause of this discrepancy may also be the low data resolution. If the data had been sampled more frequently, they might have captured those interference peaks and valleys in signal reception. This suggestion for improvement should be considered for future testing.

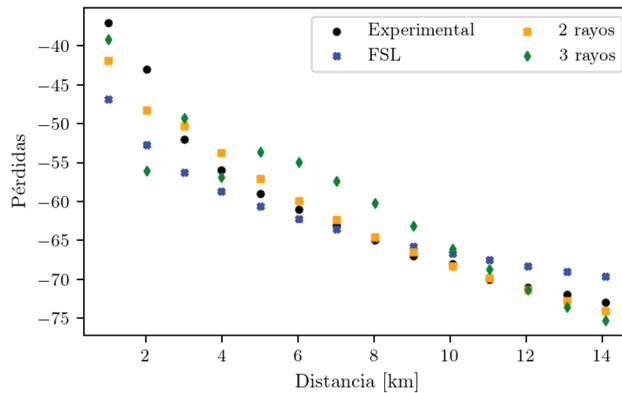


**Figure 7.** Comparison between experimental data (black circles) and those provided by the analytical models (remaining data).

## 5. Discussion

This study has addressed a set of significant challenges related to the implementation of wireless communication technologies in maritime environments, with a particular focus on the development of WSNs. We have thoroughly examined both the theoretical aspects and field tests in a real marine environment. Below, we discuss the findings and implications of this study.

One of the key highlights of this study is the identification and discussion of the major challenges faced in implementing WSNs in maritime environments. These challenges encompass the management of large volumes of data, the provision of sustainable power to sensor nodes, the limited data storage capacity, and the communication bandwidth. It is essential to note that these challenges are not merely technical but also logistical and economic in nature. The rising maritime traffic and the need to monitor and manage a variety of maritime activities such as navigation, fishing, and aquaculture demand effective solutions for data collection, transmission, and analysis. Our study underscores the significance of addressing these challenges as we move towards increased use of WSN technologies in the maritime domain.

We conducted a comprehensive evaluation of several wireless communication technologies in the maritime environment. This included technologies such as WiMAX and LoRa, with a focus on their range and data-carrying capacity. The results from our field tests demonstrated that different technologies have specific applications based on the distance and volume of data they need to transmit.

For instance, WiMAX tests revealed a range of up to 14 km in a maritime setting, making it a viable option for long-range communication in this context. LoRa, on the other hand, showed a range of up to 6 km, which is suitable for shorter-range applications but with adequate data capacity. These findings are valuable for making informed decisions on the selection of communication technologies in specific maritime projects.

A fundamental aspect of this study was the comparison between the results from our field tests and theoretical models of electromagnetic propagation. The models used included the free-space propagation model, the two-ray model, and the three-ray model. We observed that, in general, theoretical models provided a good match with experimental data, although significant discrepancies were noted at both short and long distances.

The two-ray and free-space models proved to be the most effective in describing the propagation conditions in our maritime environment. However, the three-ray model, which takes into account the effect of the water vapor layer on wave propagation, exhibited notable disparities. This suggests that, under certain conditions, this effect may not be as relevant as initially thought in our test environment. Data resolution and sampling

frequency may have contributed to these discrepancies and could be subjects for future research improvements.

## 6. Conclusions

In this text, different deployments of radio signal transmission and reception have been documented, both in relevant environments (near the coast) and in real-world settings (farther from the coast), characterizing various communication scenarios and technologies.

In the marine environment, diverse technologies have been deployed for a range of applications, including long-distance communication and sensor data transmission. This deliverable has documented tests conducted at the laboratory level and deployments in a long-distance marine environment, from various locations, focusing on the previously selected technologies. Each of them exhibited varying ranges, but all achieved successful communications. GSM stood out with the greatest range, reaching 20 km, followed by Wimax at 14 km, and finally, LoRa at 6 km. The choice of which technology to deploy in the marine environment will depend on the specific use case and communication requirements of each project. It is essential to select the appropriate technology, considering factors such as range, speed, reliability, and cost.

Regarding the validation of electromagnetic wave propagation loss models developed in the first work package of the project for marine environments, campaigns were conducted to collect experimental data in marine settings, which could then be compared with the expected results from these models. The comparative analysis indicates that the most robust model appears to be the two-ray model. On the one hand, the free-space loss model partially underestimates the measured losses, and on the other hand, the three-ray model, due to its sensitivity to the height of the evaporation duct, is more complex to accurately adjust. Furthermore, as an improvement for future tests, it is suggested to increase the data sampling resolution in signal reception to capture fine details of spatial loss dependencies.

The use of technologies like WiMAX, LoRa, and others identified in this study can enhance communication in these activities and, ultimately, contribute to a more sustainable exploitation of marine resources. The ability to collect real-time, accurate data and transmit them efficiently is essential for informed decision making and the preservation of marine biodiversity.

**Author Contributions:** Conceptualization, I.F.; methodology, I.F. and H.E.; validation, H.E. and R.M.; formal analysis, I.F. and E.M.; data curation, R.M.; writing—original draft preparation, H.E. and I.F.; writing—review and editing, I.F. and R.M. All authors have read and agreed to the published version of the manuscript.

**Funding:** This research was funded by the Instituto de Fomento de la Región de Murcia (INFO) under the Program of grants aimed at Technological Centers of the Region of Murcia for the realization of non-economic R&D activities. Modality 1: Independent R&D Projects, with File No.: 2022.08.CT01.000041, and titled “MODEM. Investigación de múltiples tecnologías de comunicación para la mejora de redes de sensores inalámbricos en la monitorización del medio marino”.

**Institutional Review Board Statement:** Not applicable.

**Informed Consent Statement:** Not applicable.

**Data Availability Statement:** Data are available on request due to restrictions (e.g., privacy, legal or ethical reasons).

**Conflicts of Interest:** The authors declare no conflicts of interest.

## References

1. Xu, G.; He, W.; Li, S. Internet of Things in Industries: A Survey. *IEEE Trans. Ind. Inform.* **2014**, *10*, 2233–2243. [CrossRef]
2. Stephenson, P.J. Technological advances in biodiversity monitoring: Applicability, opportunities and challenges. *Curr. Opin. Environ. Sustain.* **2020**, *45*, 36–41. [CrossRef]
3. Cui, J.H.; Kong, J.; Gerla, M.; Zhou, S. The Challenges of Building Scalable Mobile Underwater Wireless Sensor Networks for Aquatic Applications. *IEEE Netw.* **2006**, *0890–8044*, 12–17.

4. Vasilescu, I.; Kotay, K.; Rus, D. Krill: An Exploration in Underwater Sensor Networks. In Proceedings of the Second IEEE Workshop on Embedded Networked Sensors, Sydney, Australia, 31 May 2005.
5. Wägele, J.W.; Bodesheim, P.; Bourlat, S.J.; Denzler, J.; Diepenbroek, M.; Fonseca, V.; Frommolt, K.H.; Geiger, M.F.; Gemeinholzer, B.; Glöckner, F.O.; et al. Towards a multisensor station for automated biodiversity monitoring. *Basic Appl. Ecol.* **2022**, *59*, 105–138. [CrossRef]
6. Eurostat. Maritime Ports Freight and Passenger Statistics. 2017. Available online: [https://ec.europa.eu/eurostat/statistics-explained/index.php?title=Maritime\\_ports\\_freight\\_and\\_passenger\\_statistics&oldid=218671](https://ec.europa.eu/eurostat/statistics-explained/index.php?title=Maritime_ports_freight_and_passenger_statistics&oldid=218671) (accessed on 1 November 2023).
7. Addison, P.F.E.; Collins, D.J.; Trebilco, R.; Howe, S.; Bax, N.; Hedge, P.; Jones, G.; Miloslavich, P.; Roelfsema, C.; Sams, M.; et al. A new wave of marine evidence-based management: Emerging challenges and solutions to transform monitoring, evaluating, and reporting. *ICES J. Mar. Sci.* **2017**, *75*, 941–952. [CrossRef]
8. Knight, C.; Davidson, J.; Behrens, S. Energy options for wireless sensor nodes. *Sensors* **2008**, *8*, 8037–8066. [CrossRef] [PubMed]
9. Javaid, N.; Sher, A.; Nasir, H.; Guizani, N. Intelligence in IoT-based 5G networks: Opportunities and challenges. *IEEE Commun. Mag.* **2018**, *56*, 94–100. [CrossRef]
10. Huo, Y.; Dong, X.; Beatty, S. Cellular Communications in Ocean Waves for Maritime Internet of Things. *IEEE Internet Things J.* **2020**, *7*, 9965–9979. [CrossRef]
11. Helmi, A.H.M.A.; Hafiz, M.M.; Rizam, M.S.B.S. Mobile buoy for real time monitoring and assessment of water quality. In Proceedings of the 2014 IEEE Conference on Systems, Process and Control, Kuala Lumpur, Malaysia, 12–14 December 2014; pp. 19–23.
12. Vengatesan, G.; Muthiah, M.A.; Upadhyay, J.S.; Sundaravivelu, N.; Sundar, R.; Venkatesan, R. Real time, low power, high data rate and cost-effective transmission scheme for coastal buoy system. In Proceedings of the International Symposium on Ocean Electronics, SYMPOL, Kochi, India, 23–25 October 2013; pp. 236–241.
13. Mahdy, A.M. Marine Wireless Sensor Networks: Challenges and Applications. In Proceedings of the Seventh International Conference on Networking, Cancun, Mexico, 13–18 April 2008; pp. 530–535.
14. Xu, G.; Shen, W.; Wang, X. Marine environment monitoring using wireless sensor networks: A systematic review. In Proceedings of the 2014 IEEE International Conference on Systems, Man and Cybernetics, San Diego, CA, USA, 5–8 October 2014.
15. Kamolov, A.; Park, S. An iot-based ship berthing method using a set of ultrasonic sensors. *Sensors* **2019**, *19*, 5181. [CrossRef] [PubMed]
16. Jo, S.W.; Shim, W.S. LTE-Maritime: High-Speed Maritime Wireless Communication Based on LTE Technology. *IEEE Access* **2019**, *7*, 53172–53181. [CrossRef]
17. Government of Singapore. Factsheet WISEPORT 2007. Available online: [https://www.imda.gov.sg/-/media/imda/files/inner/archive/news-and-events/news\\_and\\_events\\_level2/20080306142631/factsheetwiseport.pdf](https://www.imda.gov.sg/-/media/imda/files/inner/archive/news-and-events/news_and_events_level2/20080306142631/factsheetwiseport.pdf) (accessed on 1 November 2023).
18. Zhou, M.T.; Hoang, V.D.; Harada, H.; Pathmasuntharam, J.S.; Wang, H.; Kong, P.Y.; Ang, C.W.; Ge, Y.; Wen, S. TRITON: High-speed maritime wireless mesh network. *IEEE Wirel. Commun.* **2013**, *20*, 134–142. [CrossRef]
19. Kim, H.J.; Choi, J.K.; Yoo, D.S.; Jang, B.T.; Chong, K.T. Implementation of MariComm bridge for LTE-WLAN maritime heterogeneous relay network. In Proceedings of the International Conference on Advanced Communication Technology, ICACT 2015, Pyeongchang, Republic of Korea, 1–3 July 2015; pp. 230–234.
20. Campos, R.; Oliveira, T.; Cruz, N.; Matos, A.; Almeida, J.M. BLUECOM+: Cost-effective broadband communications at remote ocean areas. In Proceedings of the MTS/IEEE OCEANS'16 Conference, Shanghai, China, 10–13 April 2016.
21. Rao, S.N.; Raj, D.; Parthasarathy, V.; Aiswarya, S.; Ramesh, M.V.; Rangan, V. A novel solution for high speed internet over the oceans. In Proceedings of the INFOCOM 2018—IEEE Conference on Computer Communications Workshops, Honolulu, HI, USA, 15–19 April 2018; pp. 906–912.
22. Höyhtyä, M.; Huusko, J.; Kiviranta, M.; Solberg, K.; Rokka, J. Connectivity for autonomous ships: Architecture, use cases, and research challenges. In Proceedings of the International Conference on Information and Communication Technology Convergence: ICT Convergence Technologies Leading the Fourth Industrial Revolution, ICTC 2017, Jeju, Republic of Korea, 18–20 October 2017; pp. 345–350.
23. Kazdaridis, G.; Symeonidis, P.; Zographopoulos, I.; Korakis, T.; Klun, K.; Kovac, N. On the development of energy-efficient communications for marine monitoring deployments. In Proceedings of the 2017 13th International Conference on Advanced Technologies, Systems and Services in Telecommunications, TELSIKS 2017, Nis, Serbia, 18–20 October 2017; pp. 271–274.
24. De Marziani, C.; Alcoleas, R.; Colombo, F.; Costa, N.; Pujana, F.; Colombo, A.; Aparicio, J.; Alvarez, F.J.; Jimenez, A.; Urena, J.; et al. A low cost reconfigurable sensor network for coastal monitoring. In Proceedings of the IEEE Conference on OCEANS, Santander, Spain, 6–9 June 2011.
25. Jorge, L.; Santos, S. Wi-Fi Maritime Communications using TV White Spaces. 2013. Available online: [https://paginas.fe.up.pt/~ee08251/tese/wp-content/uploads/2013/03/pdi\\_ee08251.pdf](https://paginas.fe.up.pt/~ee08251/tese/wp-content/uploads/2013/03/pdi_ee08251.pdf) (accessed on 1 November 2023).
26. Jiang, S.; Chen, H. A Possible Development of Marine Internet: A Large Scale Cooperative Heterogeneous Wireless Network. *J. Commun. Comput.* **2015**, *12*, 199–211.
27. Malarski, K.M.; Bardram, A.; Larsen, M.D.; Thrane, J.; Petersen, M.N.; Moeller, L.; Ruepp, S. Demonstration of NB-IoT for Maritime Use Cases. In Proceedings of the 2018 9th International Conference on the Network of the Future, NOF 2018, Poznań, Poland, 19–21 November 2018; pp. 106–108.

28. Paulus, W.L. Specification for Environmental Measurements to Assess Radar Sensors. 1989. Available online: <https://apps.dtic.mil/sti/citations/ADA219127> (accessed on 1 November 2023).
29. Freund, D.E.; Woods, N.E.; Ku, H.-C.; Awadallah, R.S. Forward Radar propagation over a rough sea surface: A numerical assessment of the Miller-brown approximation using a horizontally polarized 3-GHz line source. *IEEE Trans. Antennas Propag.* **2006**, *54*, 1292–1304. [CrossRef]

**Disclaimer/Publisher's Note:** The statements, opinions and data contained in all publications are solely those of the individual author(s) and contributor(s) and not of MDPI and/or the editor(s). MDPI and/or the editor(s) disclaim responsibility for any injury to people or property resulting from any ideas, methods, instructions or products referred to in the content.



Proceeding Paper

# Forecasting Vital Signs in Human–Robot Collaboration Using Sequence-to-Sequence Models with Bidirectional LSTM: A Comparative Analysis of Uni- and Multi-Variate Approaches <sup>†</sup>

Oliver Chojnowski \*, Dario Luipers, Caterina Neef and Anja Richert

Cologne Cobots Lab, TH Köln—University of Applied Sciences, Betzdorfer Str. 2, 50679 Köln, Germany; dario.luipers@th-koeln.de (D.L.); caterina.neef@th-koeln.de (C.N.); anja.richert@th-koeln.de (A.R.)

\* Correspondence: oliver.chojnowski@th-koeln.de

<sup>†</sup> Presented at the 10th International Electronic Conference on Sensors and Applications (ECSA-10), 15–30 November 2023; Available online: <https://ecsa-10.sciforum.net/>.

**Abstract:** Our research investigates an approach to forecasting human vital signs by formulating the problem as a sequence-to-sequence (seq2seq) task, utilizing bidirectional long short-term memory models (BiLSTM). The study aims to compare the forecasting accuracy of uni- and multivariate modeling strategies over different forecasting horizons ranging from 1 s to 10 s. The dataset comprises sensor data collected during a lab study in which thirteen participants engaged in a collaborative assembly scenario with a robot. Our results show that univariate models outperform multivariate ones in terms of forecasting accuracy, offering valuable insights into accurate forecasting of human physiological parameters, with potential implications for human-robot collaboration, personalized medical monitoring, and healthcare applications.

**Keywords:** human-robot collaboration; forecasting; vital signs; deep learning; collaborative assembly

## 1. Introduction

In the dynamic realm of human–robot collaboration (HRC), a significant challenge lies in equipping robotic systems with the ability to seamlessly adapt to users' internal states, such as stress or relaxation. Ongoing research in this field has shown that stress can be indirectly assessed through the integration of diverse sensors that monitor various physiological indicators, including electrocardiograph (ECG), pupil dilation (PD), electromyograph (EMG), electroencephalograph (EEG), heart rate variation (HRV), skin temperature, respiratory rate and electrodermal activity (EDA), or galvanic skin response (GSR) [1–4]. Machine learning classification techniques have made noteworthy advancements in stress detection [5–8]. In diverse environments, such as academic, driving, or office-like settings, accuracy rates exceeding 90% have been achieved [5]. By going beyond simply recognizing emotions in real-time, to anticipatory modeling, robotic systems can adjust their behavior proactively, leading to more natural, productive collaborations. However, despite the promising developments in stress detection, the exploration of forecasting future states remains limited. Some research has been conducted on forecasting vital signs in intensive care patients [9], postoperative complications [10], or in health monitoring [11]. In [11], the authors compared different models, evaluating their accuracy in univariate forecasts of pulse, oxygen level percentage (SpO<sub>2</sub>), and blood pressure. Notably, deep learning models such as long short-term memory (LSTM) and gated recurrent unit (GRU) outperformed classical forecasting strategies like autoregressive (AR) and autoregressive integrated moving average (ARIMA) models, with GRUs performing the best. Earlier work also revealed in different use cases that Bidirectional Long Short-Term Memory (BiLSTM) models lead to a significant improvement in average time series prediction accuracy of 37.78% [12] compared to classical LSTMs. It was observed that training the

**Citation:** Chojnowski, O.; Luipers, D.; Neef, C.; Richert, A. Forecasting Vital Signs in Human–Robot Collaboration Using Sequence-to-Sequence Models with Bidirectional LSTM: A Comparative Analysis of Uni- and Multi-Variate Approaches. *Eng. Proc.* **2023**, *58*, 103. <https://doi.org/10.3390/ecsa-10-16190>

Academic Editor: Francisco Falcone

Published: 15 November 2023



**Copyright:** © 2023 by the authors. Licensee MDPI, Basel, Switzerland. This article is an open access article distributed under the terms and conditions of the Creative Commons Attribution (CC BY) license (<https://creativecommons.org/licenses/by/4.0/>).

bidirectional variant was slower, suggesting that it extracts unique features inaccessible to other models [13]. In the field of mental state and vital sign forecasting the performance of BiLSTMs is unknown. Given the current state of the research, an intriguing avenue for further investigation pertains to the exploration of the intricate interplay between diverse sensor modalities, which may hold the potential to enhance vital sign forecasting. Specifically, there is an opportunity to explore whether the simultaneous utilization of multiple modalities in a multivariate forecasting framework can yield improved forecasting accuracies by leveraging information that remains latent in univariate models. This study significantly contributes by highlighting the impacts of multivariate forecasting strategies versus univariate approaches. It also provides insights into vital sign forecasting, particularly through the integration of BiLSTMs with collaborative robotics, thus advancing the existing knowledge in this field.

## 2. Materials and Methods

### 2.1. Dataset

The dataset used in this study consists of vital signs from 13 subjects recorded in the context of a collaborative assembly. In this assembly, a human worker collaboratively assembles a component with a collaborative robot (cobot). To capture the influence of the cobot on the human's vital signs, six different scenarios, differing in various factors such as the degree of collaboration or the working speed of the robot, were executed. Between every configuration, the recording was stopped. As a result, each of the 13 subjects contributes 6 individual sequences, each lasting approximately 2 min, culminating in a total of 76 sequences. The utilized sensor modalities are the Interbeat Intervals of the heart (IBI) measured via ECG and the EDA of the skin, both using the BiTalino (r)evolution Plugged Kit BLE/BT (PLUX Wireless Biosignals, Portugal) as well as the Pupil Dilation (PD), measured with pupil core eye tracking glasses (Pupil Labs, Berlin, Germany).

### 2.2. Bidirectional Long Short-Term Memory Model

Bidirectional long short-term memory networks (BiLSTM) are a type of recurrent neural network (RNN) architecture used in natural language processing and sequential data tasks, like time series data. Introduced to overcome the limitations of regular RNN they enhance traditional LSTMs by processing input data in both forward and backward directions, capturing context from both past and future [14]. BiLSTMs were introduced to address the vanishing gradient problem and improve the modeling of long-range dependencies in sequential data.

### 2.3. Preprocessing

The data preprocessing involved three steps. First, each modality was handled independently. For IBI, no direct measures were needed. For PD, blink removal was essential using the procedure outlined in [15,16]. EDA-Signal involves extracting the skin conductance response, as described in [17]. In the second step, all modalities underwent uniform processing, which included resampling, smoothing, and data normalization to enhance quality and ensure consistency. In the final phase, individual modalities were synchronized to create a multivariate dataset. Extensive feature engineering was then performed on this dataset, yielding both static features (e.g., means, minimums, and maximums of time series) and dynamic features (e.g., moving averages and lag features).

### 2.4. Stationarity

Stationarity signifies that statistical parameters such as the mean and variance exhibit relative constancy throughout the observed time span [18]. This property holds significant importance, particularly in forecasting applications. To assess stationarity, we employed the augmented Dickey–Fuller test (ADF-Test), which is one of the most commonly used measures of stationarity [19–21]. To induce stationarity a differentiation procedure was implemented, resulting in stationarity in 99% of all sequences.

### 2.5. Sequence-to-Sequence Modeling

In the context of time series forecasting, sequence-to-sequence modeling is a technique wherein a learner maps a sequence of past values to a sequence of future values [22]. To adapt the dataset into a format suitable for input and output sequences, we employed the sliding window method presented in [23]. Three variations of each dataset were created for one-second, five-second, and ten-second forecasting horizons, with consistent look-back window lengths.

### 2.6. Measures of Evaluation

To assess the forecasting accuracy of the models, we employ the Symmetric Mean Absolute Percentage Error (sMAPE). The formula for calculating sMAPE is presented below [24].

$$\text{sMAPE} = \left( \frac{2}{n} \sum_1^n \frac{|y_t - \hat{y}_t|}{|y_t| + |\hat{y}_t|} \right) * 100\% \quad (1)$$

To establish a baseline for assessing the model's performance and to ensure the robustness of our results, we employ a simple benchmark known as the Naïve Forecast as recommended by [25]. In this approach, the prediction for the next time step is generated by using the value from the previous time step, which makes it simple to calculate but nonetheless an effective benchmark method. This basic forecasting method is mathematically represented by Equation (2) [26].

$$\hat{y}_{t+k} = y_t \quad (2)$$

## 3. Results

### 3.1. Univariate Forecast

Table 1 illustrates the superior performance of the BiLSTM model compared to the baseline across all forecasting horizons for univariate IBI.

**Table 1.** sMAPE of the univariate forecast of the interbeat intervals.

Forecasting Horizon	Naïve Forecast	BiLSTM
1 s	123.79%	2.1%
5 s	144.79%	16.01%
10 s	146.37%	17.36%

Table 2 displays results for univariate PD forecasting. The Naïve Method consistently shows higher prediction errors than the BiLSTM model across all horizons.

**Table 2.** sMAPE of the univariate forecast of the pupil dilation.

Forecasting Horizon	Naïve Forecast	BiLSTM
1 s	142.92%	2.07%
5 s	154.14%	5.39%
10 s	157.00%	5.66%

Particularly noteworthy is the fact that when extending the forecasting horizon from 1 to 5 s, a marked increase in sMAPE is observed, amounting to 13.91% for univariate IBI and 3.32% for univariate PD. In contrast, extending the forecasting horizon from 5 to 10 s only results in an increase of 1.35% for univariate IBI and 0.27% for univariate PD.

### 3.2. Multivariate Forecast

Table 3 compares forecasting accuracy for univariate and multivariate models across different horizons. The multivariate approach consistently yields slightly higher sMAPE, outperforming univariate IBI by just 0.24% at the 5-s horizon.

**Table 3.** sMAPE of the multivariate compared to the univariate forecasts.

Forecasting Horizon	Univariate IBI	Univariate PD	Multivariate
1 s	2.1%	2.07%	16.12%
5 s	16.01%	5.39%	15.77%
10 s	17.36%	5.66%	22.48%

#### 4. Discussion

The results presented in this work reveal a substantial disparity in performance between univariate and multivariate models. Despite the potential for multivariate models to leverage relationships among individual parameters, generated features, and additional skin conductance data, the incorporation of this supplementary input does not yield an improvement in forecasting accuracy. Several possible explanations for this phenomenon can be considered. Firstly, no meaningful relationships may exist among the various parameters under investigation. This lack of inherent correlations may limit the capacity of multivariate models to extract valuable predictive insights, rendering the inclusion of additional input variables ineffective. Secondly, the quality of the supplementary skin conductance data may be a contributing factor. It is conceivable that these data introduce noise into the prediction process, thereby diminishing overall accuracy. Further investigation into the reliability and relevance of the additional data may clarify its impact on model performance. Thirdly, the selected features for the multivariate models may either have no significant influence on the prediction accuracy or, in some cases, exert a detrimental effect. The inclusion of irrelevant or potentially confounding features can hinder the model's ability to discern meaningful patterns in the data, leading to suboptimal forecasting outcomes. These findings underscore the importance of a thorough understanding of the underlying relationships within the data and the potential consequences of incorporating additional variables.

#### 5. Conclusions

The research findings presented in this study shed light on the predictive performance of univariate versus multivariate deep learning models in the context of forecasting vital signs. Notably, the univariate prediction of IBI and pupil diameter yields superior results when compared to the multivariate approach, which incorporates additional variables such as skin conductance and generated features. This suggests that the univariate models excel in capturing the intricate patterns and relationships within these physiological signals. Interestingly, as the forecasting horizon increases from one to five seconds, a significant decrease in accuracy is observed. However, this decline in accuracy remains relatively stable when extending the forecasting horizon from five to ten seconds. These findings have important implications for predictive modeling in physiological signal analysis where high precision is required, such as assessing cognitive load or attention levels. The observed stability in forecasting accuracy for longer horizons indicates that the univariate approach may offer a reliable foundation for longer-term physiological forecasting tasks. This work contributes valuable insights into the selection of modeling approaches for vital sign forecasting, underscoring the significance of considering the specific predictive goals and horizons in such applications. Future research in this domain should explore alternative feature engineering strategies, data preprocessing techniques, and model architectures to unlock the latent predictive potential of multivariate approaches. Overall, this study contributes valuable insights into the complexities of multivariate modeling in physiological signal analysis and paves the way for further advancements in this field.

**Author Contributions:** Conceptualization, O.C. and D.L.; methodology, O.C., D.L. and C.N.; software, O.C.; validation, O.C.; formal analysis, O.C.; investigation, O.C.; resources, A.R.; data curation, D.L.; writing—original draft preparation, O.C.; writing—review and editing, C.N., D.L. and A.R.; visualization, O.C.; supervision, A.R.; project administration, A.R.; funding acquisition, A.R. and D.L. All authors have read and agreed to the published version of the manuscript.

**Funding:** This research was funded by the Ministry of Innovation, Science and Research of North Rhine-Westphalia Germany.

**Institutional Review Board Statement:** Institutional Review Board approval was not sought for this study as the data utilized in our research originated from a pre-existing dataset. Furthermore, all data employed in our analysis had been anonymized to protect the privacy and confidentiality of the individuals involved. This rigorous anonymization process ensured that no personally identifiable information was accessible or discernible in the dataset, thereby mitigating any ethical concerns associated with the use of human subjects' data. Consequently, the research conducted in this study adheres to established ethical guidelines and does not require additional IRB approval.

**Informed Consent Statement:** Informed consent was obtained from all the subjects involved in the study.

**Data Availability Statement:** The data presented in this study are available on request from the corresponding author. The data are not publicly available due to privacy reasons.

**Acknowledgments:** The authors would like to thank all the subjects that participated in the study.

**Conflicts of Interest:** The authors declare no conflict of interest.

## References

- Villani, V.; Sabattini, L.; Secchi, C.; Fantuzzi, C. A Framework for Affect-Based Natural Human-Robot Interaction. In Proceedings of the 2018 27th IEEE International Symposium on Robot and Human Interactive Communication (RO-MAN), Nanjing, China, 27–31 August 2018; pp. 1038–1044. [CrossRef]
- Arai, T.; Kato, R.; Fujita, M. Assessment of operator stress induced by robot collaboration in assembly. *CIRP Ann.* **2010**, *59*, 5–8. [CrossRef]
- Lu, L.; Xie, Z.; Wang, H.; Li, L.; Xu, X. Mental stress and safety awareness during human-robot collaboration—Review. *Appl. Ergon.* **2022**, *105*, 103832. [CrossRef]
- Peternel, L.; Tzagarakis, N.; Caldwell, D.; Ajoudani, A. Robot adaptation to human physical fatigue in human–robot co-manipulation. *Auton. Robot.* **2018**, *42*, 1011–1021. [CrossRef]
- Gedam, S.; Paul, S. A Review on Mental Stress Detection Using Wearable Sensors and Machine Learning Techniques. *IEEE Access* **2021**, *9*, 84045–84066. [CrossRef]
- Iqbal, T.; Elahi, A.; Shahzad, A.; Wijns, W. Review on Classification Techniques used in Biophysiological Stress Monitoring. *arXiv* **2022**, arXiv:2210.16040. [CrossRef]
- Baltaci, S.; Gokcay, D. Stress Detection in Human–Computer Interaction: Fusion of Pupil Dilation and Facial Temperature Features. *Int. J. Hum. Comput. Interact.* **2016**, *32*, 956–966. [CrossRef]
- TuerxunWaili; Alshehly, Y. S.; Sidek, K.A.; Johar, M.G.M. Stress recognition using Electroencephalogram (EEG) signal. *J. Phys. Conf. Ser.* **2020**, *1502*, 012052. [CrossRef]
- Phetrattikun, R.; Suvirat, K.; Pattalung, T.N.; Kongkamol, C.; Ingviya, T.; Chaichulee, S. Temporal Fusion Transformer for forecasting vital sign trajectories in intensive care patients. In Proceedings of the 2021 13th Biomedical Engineering International Conference (BMEiCON), Ayutthaya, Thailand, 19–21 November 2021; pp. 1–5. [CrossRef]
- Fritz, B.A.; Chen, Y.; Murray-Torres, T.M.; Gregory, S.; Ben Abdallah, A.; Kronzer, A.; McKinnon, S.L.; Budelier, T.; Helsten, D.L.; Wildes, T.S.; et al. Using machine learning techniques to develop forecasting algorithms for postoperative complications: Protocol for a retrospective study. *BMJ Open* **2018**, *8*, e020124. [CrossRef]
- Bhavani, T.; VamseeKrishna, P.; Chakraborty, C.; Dwivedi, P. Stress Classification and Vital Signs Forecasting for IoT-Health Monitoring. *IEEE/ACM Trans. Computat. Biol. Bioinform.* **2022**, 1–8. [CrossRef]
- Siami-Namini, S.; Tavakoli, N.; Namin, A.S. The Performance of LSTM and BiLSTM in Forecasting Time Series. In Proceedings of the 2019 IEEE International Conference on Big Data (Big Data), Los Angeles, CA, USA, 9–12 December 2019; pp. 3285–3292. [CrossRef]
- Jia, M.; Huang, J.; Pang, L.; Zhao, Q. Analysis and Research on Stock Price of LSTM and Bidirectional LSTM Neural Network. In Proceedings of the 3rd International Conference on Computer Engineering, Information Science & Application Technology (ICCIA 2019), Chongqing, China, 30–31 May 2019; Atlantis Press: Amsterdam, The Netherlands, 2019; pp. 467–473. [CrossRef]
- Schuster, M.; Paliwal, K.K. Bidirectional recurrent neural networks. *IEEE Trans. Signal Process.* **1997**, *45*, 2673–2681. [CrossRef]
- Pedrotti, M.; Lei, S.; Dzaack, J.; Rötting, M. A data-driven algorithm for offline pupil signal preprocessing and eyeblink detection in low-speed eye-tracking protocols. *Behav. Res.* **2011**, *43*, 372–383. [CrossRef]
- Pedrotti, M.; Mirzaei, M.A.; Tedesco, A.; Chardonnet, J.-R.; Merienne, F.; Benedetto, S.; Baccino, T. Automatic Stress Classification With Pupil Diameter Analysis. *Int. J. Hum. Comput. Interact.* **2014**, *30*, 220–236. [CrossRef]
- Zangróniz, R.; Martínez-Rodrigo, A.; Pastor, J.M.; López, M.T.; Fernández-Caballero, A. Electrodermal Activity Sensor for Classification of Calm/Distress Condition. *Sensors* **2017**, *17*, 10. [CrossRef]

18. Livieris, I.E.; Stavroyiannis, S.; Iliadis, L.; Pintelas, P. Smoothing and stationarity enforcement framework for deep learning time-series forecasting. *Neural Comput. Appl.* **2021**, *33*, 14021–14035. [CrossRef]
19. Worden, K.; Iakovidis, I.; Cross, E.J. On Stationarity and the Interpretation of the ADF Statistic. In *Dynamics of Civil Structures, Volume 2*; Pakzad, S., Ed.; Conference Proceedings of the Society for Experimental Mechanics Series; Springer International Publishing: Cham, Switzerland, 2019; pp. 29–38. [CrossRef]
20. Dickey, D.A.; Fuller, W.A. Distribution of the Estimators for Autoregressive Time Series with a Unit Root. *J. Am. Stat. Assoc.* **1979**, *74*, 427–431. [CrossRef]
21. Dickey, D.A.; Fuller, W.A. Likelihood Ratio Statistics for Autoregressive Time Series with a Unit Root. *Econometrica* **1981**, *49*, 1057–1072. [CrossRef]
22. Mariet, Z.; Kuznetsov, V. Foundations of Sequence-to-Sequence Modeling for Time Series. In Proceedings of the Twenty-Second International Conference on Artificial Intelligence and Statistics, Naha, Japan, 16–18 April 2019; pp. 408–417. Available online: <https://proceedings.mlr.press/v89/mariet19a.html> (accessed on 22 September 2023).
23. Shi, J.; Jain, M.; Narasimhan, G. Time Series Forecasting (TSF) Using Various Deep Learning Models. *arXiv* **2022**, arXiv:2204.11115. [CrossRef]
24. Abbasimehr, H.; Paki, R. Improving time series forecasting using LSTM and attention models. *J. Ambient. Intell. Hum. Human. Comput.* **2022**, *13*, 673–691. [CrossRef]
25. Dhakal, C. A Naïve Approach for Comparing a Forecast Model. August 2018. Available online: [https://www.researchgate.net/publication/326972994\\_A\\_Naive\\_Approach\\_for\\_Comparing\\_a\\_Forecast\\_Model](https://www.researchgate.net/publication/326972994_A_Naive_Approach_for_Comparing_a_Forecast_Model) (accessed on 22 September 2023).
26. Hyndman, R.J.; Athanasopoulos, G. *Forecasting: Principles and Practice*, 3rd ed.; OTexts: Melbourne, Australia, 2018. Available online: <https://otexts.com/fpp3/index.html> (accessed on 22 September 2023).

**Disclaimer/Publisher’s Note:** The statements, opinions and data contained in all publications are solely those of the individual author(s) and contributor(s) and not of MDPI and/or the editor(s). MDPI and/or the editor(s) disclaim responsibility for any injury to people or property resulting from any ideas, methods, instructions or products referred to in the content.

Proceeding Paper

# Enhancing Insider Malware Detection Accuracy with Machine Learning Algorithms <sup>†</sup>

Md. Humayun Kabir \*, Arif Hasnat, Ahmed Jaser Mahdi, Mohammad Nadib Hasan, Jaber Ahmed Chowdhury and Istiak Mohammad Fahim

Department of Computer and Communication Engineering, International Islamic University Chittagong, Kumira Chattogram 4318, Bangladesh; arifhasnat83@gmail.com (A.H.); jasermahdi@gmail.com (A.J.M.); nadibhasan.gtu.in@gmail.com (M.N.H.); jaberahmediuc@gmail.com (J.A.C.); istiakfahim94@gmail.com (I.M.F.)

\* Correspondence: mdhkrrabby@gmail.com; Tel.: +880-151-528-6984

<sup>†</sup> Presented at the 10th International Electronic Conference on Sensors and Applications (ECSA-10), 15–30 November 2023; Available online: <https://ecsa-10.sciforum.net/>.

**Abstract:** One of the biggest cybersecurity challenges in recent years has been the risk that insiders pose. Internet consumers are susceptible to exploitation due to the exponential growth of network usage. Malware attacks are a major concern in the digital world. The potential occurrence of this threat necessitates specialized detection techniques and equipment, including the capacity to facilitate the precise and rapid detection of an insider threat. In this research, we propose a machine learning algorithm using a neural network to enhance malware detection accuracy in response to insider threats. A feature extraction, anomaly detection, and classification workflow are also proposed. We use the CERT4.2 dataset and preprocess the data by encoding text strings and differentiating threat and non-threat records. Our developed machine learning model incorporates numerous dense layers, ReLU activation functions, and dropout layers for regularization. The model attempts to detect and classify internal threats in the dataset with precision. We employed random forest, naive Bayes, KNN, SVM, decision tree, logical regression, and the gradient boosting algorithm to compare our proposed model with other classification techniques. Based on the results of the experiments, the proposed method functions properly and can detect malware more effectively and with 100% accuracy.

**Keywords:** cybersecurity; insider threat; malware detection; machine learning

**Citation:** Kabir, M.H.; Hasnat, A.; Mahdi, A.J.; Hasan, M.N.; Chowdhury, J.A.; Fahim, I.M. Enhancing Insider Malware Detection Accuracy with Machine Learning Algorithms. *Eng. Proc.* **2023**, *58*, 104. <https://doi.org/10.3390/ecsa-10-16234>

Academic Editor: Francisco Falcone

Published: 15 November 2023



**Copyright:** © 2023 by the authors. Licensee MDPI, Basel, Switzerland. This article is an open access article distributed under the terms and conditions of the Creative Commons Attribution (CC BY) license (<https://creativecommons.org/licenses/by/4.0/>).

## 1. Introduction

Information is one of today's most precious but vulnerable resources. Most organizations and people in the modern world manage and safeguard their digital content via computer networks and information technologies. As a consequence, there is a rise in cybersecurity threats such as identity theft, hacking, and malware attacks. Malware is used in many of these attacks [1]. Malware, also known as malicious software, consists of programming (code, scripting, dynamic content, and other applications) intended to obstruct or prevent operation, gather data that might be used for exploitation or compromise privacy, obtain illegal access to system resources, or engage in other malicious acts [2]. Infrastructure is always in danger of serious harm from sophisticated malware that is always changing [3]. Threats nowadays are conducted utilizing modern technologies which makes them difficult to identify. Therefore, it is obvious that the need for an intelligent system that can recognize new malware by analyzing the structure of system operations produced by malware as well as a suitable mechanism to recognize infected files is essential. Traditional methods of identifying insider malware frequently fail to precisely identify malicious activities carried out by authorized users. The growing environment of cybersecurity necessitates sophisticated techniques that are capable of recognizing unusual user behavior and differentiating it from authorized actions taken by users. In previous related works, researchers used several techniques such as DCNN [4,5], static malware-analysis [6],

CNN [7], autoencoder network with a grey-scale image representation [8], Visual-AT [9], etc., to identify malware.

This study aims to investigate and evaluate various machine learning algorithms to enhance the precision of insider malware detection. By employing multiple machine learning techniques, anomaly detection, and datasets, including system logs and user behavior data, we intend to develop a robust and scalable solution capable of identifying malicious insider activities. In the present research, we propose a neural network-based machine learning algorithm to improve malware detection accuracy. First, we normalized the CERT 4.2 dataset. Then we designed a neural network model with dense layers and optimizers to identify malware. The effectiveness of our proposed method was then evaluated by comparing it to methods from recent research.

To summarize, we contribute the following in this paper:

1. We propose a reliable and effective machine learning-based method for enhancing the accuracy of infiltrator malware identification.
2. We developed a neural network model with dense layers and optimizers to detect malware.
3. For the purpose of evaluating the efficacy of our proposed method, we contrasted our suggested method with methods used in recent research.

The remaining sections of the paper are organized as follows. In Section 2, a summary of current insider threat detection methodologies is provided. In Section 3, we present our suggested malware detection method. Finally, Section 4 is allocated to the analysis of the results obtained from the proposed approach.

## 2. Research Background

As described previously in this paper, malware is one of the most significant security risks on the Internet right now. Researchers have developed numerous methods for detecting malware. A hierarchical paradigm was suggested by [3] to find security risks or events in real time. This study examined the challenges faced by basic, statistical analysis, conventional machine learning, and deep learning methods. The authors of [4] provided a framework to quickly identify a user's good and bad behavior. In their ensemble learning-based system for detecting insider threats, they recommend over bootstrap sampling, which reduces overfitting caused by sample imbalance. The authors used employee resource access patterns from a benchmark dataset in [5]. They transformed them into 1-D feature vector grayscale images and used DCNN to identify malicious insiders by seeing odd patterns. The idea of determining an executable's maliciousness using a brief overview of behavioral data is presented in [6]. They used static malware analysis. The authors of [7] used a convolutional neural network to identify and classify images by automatically extracting the characteristics of the malware images. The authors of [8] proposed identifying malware using a deep learning autoencoder network and a grey-scale image of the program. Niket et al. [9] used trained deep learning image recognition models to classify malware binaries as images; their results showed that that DL models generalize data better than k-NN. The authors introduced Visual-AT, the first general machine learning (ML)-based visualization technique, to identify malware and its variants [9]. It uses two ML algorithms and transformed picture data to identify and analyze difficult-to-identify malware and variants using AT. The authors of [10] suggested an image-based insider threat detector through geometric transformation (IGT), which turns unsupervised anomaly identification into supervised image classification. Many malware detection models were examined neural network malware detection is more efficient and accurate than other methods, according to the findings.

## 3. Methodology

This paper explores neural network classification techniques for insider threat detection in order to generate new cybersecurity solutions. The CERT4.2 dataset is simulated event log records that represent activities in an organization's computer system. Our work



focuses on this dataset in order to gain insights into computer behaviors and enhance security measurements. Here, we develop an innovative machine learning model to protect against potential threats.

To be inclusive in the neural network model we develop, we extract and process the information in a way that organizes it with the variables we need as “features”. We ensure that all text strings are encoded into integers. The distinction between insider threat and non-threat rows (true positives and true negatives) must also be made. We used the pre-processing techniques to extract the records of true negatives from three complementary CSV files. We first added all the relevant records and then chose a few non-threat true-negative recordings from the R1 dataset. We now had a combined CSV file containing our threats and non-threat baseline. We added a new column representing a binary representation of true or false, 1 or 0, to distinguish between true and false occurrences.

We also manually converted the date and time provided field into Unix epoch time as part of the dataset preparation stage; a manual conversion method was used to determine the Unix epoch time from the supplied date and time values. This demonstration was done to show how the date field might be converted into a big integer, creating a new column for Unix epoch time. A new column was generated in the original spreadsheet by referencing the “scratch” sheet in order to get the intended result. The formula used in this context is expressed as follows:

$$NC = (C2 - DATE(1970,1,1)) * 86400$$

Spreadsheet software, such as Microsoft Excel and Google Sheets, uses the formula to estimate the total number of seconds that have elapsed since 1 January 1970, with respect to a specified date. This approach is in accordance with established norms for managing timestamps in the world of computing. Following up, we encoded the vector column and feature set column mapping; in our last manual pre-processing tasks, we format the CSV into “categorize” by label encoding the data. We mapped the discrete set of vectors for the record of interest in Excel (the value for HTTP is 0, the value for email is 1, and the value for the device is 2). In conclusion, we manually performed label encoding in Excel for a finite set of vectors for the vector column and feature set column map. From the CMU CERT4.2 dataset, the user data usually falls under two categories: malicious and legitimate users. The following illustrates the feature set applied in the proposed method.

Figure 1 shows the suggested insider threat machine learning model feature set. Several features improve the model’s ability to detect hostile behaviors in an organization.

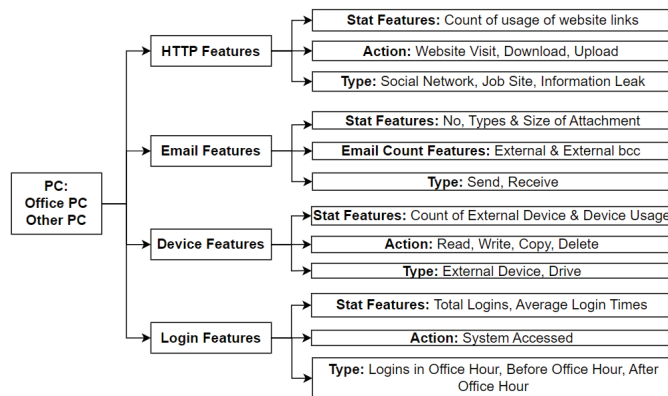


Figure 1. Feature set of the proposed method.

Our technique required splitting the preprocessed CMU CERT4.2 dataset into training and testing subsets. A two-pronged approach is needed for training, testing, and assess-

ment. Machine learning begins with training models on the training set, a carefully selected collection of data to introduce the model. This phase teaches the model to identify data patterns, correlations, and features that signal malware presence or absence. After training, the models are tested on a separate dataset reserved for assessment. This testing set was separated from the training set to expose the models to new conditions.

#### 4. Model Evaluation

We built a neural network classification model for detecting and classifying insider threat from the dataset. In our model, the input layer receives the dataset’s features, and each feature corresponds to a node in the input layer. Then, in the hidden layer section, we add a dense layer to the model. First, we have selected the dense layer as 32. To avoid the vanishing gradients issue and inject non-linearity into our model, we employed the rectified linear unit (ReLU) activation function. Figure 2 presents a concise overview of a sequential Keras model. The model consists of three dense layers, each with 32, 16, and 8 units correspondingly. This is followed by a dropout layer and a final dense layer with a single unit. The model has a cumulative count of 109,089 parameters that are eligible for training.

```

Model: "sequential_1"
-----
Layer (type)                 Output Shape         Param #
-----
dense (Dense)                 (None, 32)           108416
dropout (Dropout)             (None, 32)           0
dense_1 (Dense)               (None, 16)           528
dropout_1 (Dropout)           (None, 16)           0
dense_2 (Dense)               (None, 8)            136
dropout_2 (Dropout)           (None, 8)            0
dense_3 (Dense)               (None, 1)            9
-----
Total params: 109,089
Trainable params: 109,089
Non-trainable params: 0
    
```

Figure 2. Summary of our proposed model.

In order to address the problem of overfitting, a technique known as dropout is used during the training phase. This technique involves randomly setting a portion of the neuron outputs in the hidden layer to zero. The dropout parameter, which is set to 0.5 in this case, signifies that 50% of the inputs will be randomly assigned a value of zero during training. Subsequently, two more dense layers were included in the model, consisting of 16 and 8 neurons, using the rectified linear unit (ReLU) activation function. The ultimate dense layer comprises a solitary neuron, serving the purpose of discerning between malicious and benign samples in a binary classification test. To do this, the sigmoid activation function is used. In brief, the model consists of many densely connected layers that use rectified linear unit (ReLU) activation functions, which are alternated with dropout layers to enforce regularization. The activation function used in the output layer for binary classification is sigmoid.

Figure 3 describes the sequential operations included in the machine learning model suggested for detecting insider threats. The following procedural stages delineate the systematic methodology by which the model evaluates data and formulates educated choices about possible insider threats.

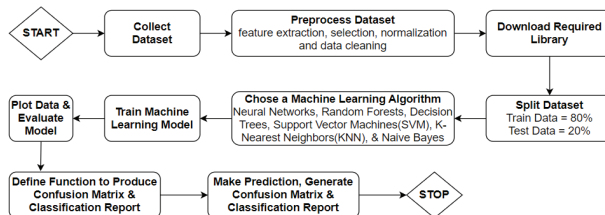


Figure 3. Procedures of the proposed model.

### 5. Results and Discussion

Table 1 displays the outcomes of applying our proposed neural network model, random forest, naive Bayes, gradient boosting, KNN, SVM, decision tree, and the logical regression algorithm to the CERT4.2 dataset.

$$Accuracy(A) = \frac{TP + TN}{TP + FP + FN + TN} \quad Precesion(P) = \frac{TP}{TP + FP}$$

$$Recall(R) = \frac{TP}{TP + FN} \quad F1\ Score(F1) = \frac{2 \times Recall \times Precesion}{Recall + Precesion}$$

**Table 1.** The results of classification techniques.

Classifier	Training (75%)				Training (80%)			
	A	P	R	F1	A	P	R	F1
Our Proposed Method (neural network using Adam optimizer)	100	100	100	100	100	100	100	100
Neural Network (using Adagrad optimizer)	90	91	90	89	99	99	99	99
Random Forest	99.64	99.63	99.65	99.64	99.73	99.74	99.75	99.74
Naive Bayes	61.42	61.42	100	76.10	61.66	61.71	100	76.87
Gradient Boosting	99.01	99.11	99.74	99.99	99.2	99.19	99.79	99.17
KNN	99.45	99.17	99.17	99.10	99.59	99.29	99.29	99.40
SVM	99	99	99	99	99.10	99	98	99
Decision Tree	99.08	99.06	98.67	99.01	99.15	99.09	98.97	99.19
Logistic Regression	61	61	94.5	76	61	61	96.18	76

As per Table 1, the performance of the proposed model is superior to that of the other machine learning algorithms. Compared to the other algorithms, the proposed neural network model provides significantly improved precision and recall while maintaining an accuracy level of 100%. The AUC score of 1.00 that our proposed method achieved is excellent. The categorization outputs derived from several machine learning algorithms and methodologies were used to detect insider threats.

The visual representation depicts the disparities in performance seen across different methods, hence facilitating the identification of the most productive way for properly discerning between normal actions and actions of malintent.

Figure 4 visually represents the confusion matrix related to the suggested machine learning approach for detecting insider threats.

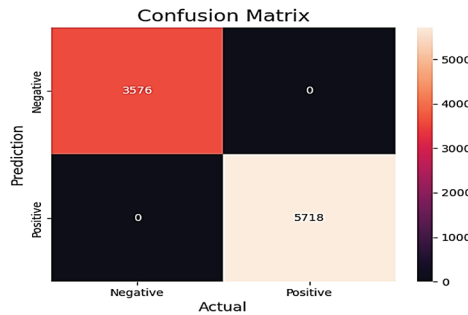


**Figure 4.** Confusion matrix of our proposed model.

Figure 5 illustrates the fluctuating patterns of accuracy and loss during the training phase of our proposed machine learning model designed to detect insider threats. The neural network model that we suggested has shown remarkable performance across various critical criteria, demonstrating its durability and dependability in the context of identifying insider threats.

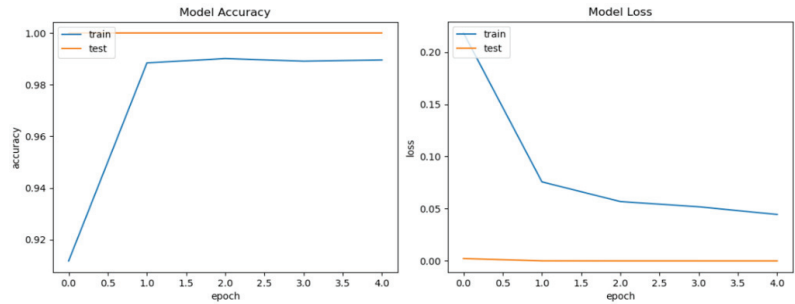


Figure 5. Our proposed model’s accuracy and loss.

Number of training samples: 14,868 for test-size 20%. Table 2 depicts the training hyperparameters associated with the proposed methodology. The model is trained using the Adam optimizer, which is a commonly used choice for developing deep learning models. The batch size is specified as 32, suggesting that the model is updated after processing every 32 training instances. The learning rate used in this study is purposely fixed at 0.001 to address the potential issue of overfitting the training data. The use of a momentum coefficient of 0.9 enhances the expeditious convergence of the model towards an ideal solution. The model undergoes training for a standard duration of five epochs, which aligns with the conventional practice in the training of neural networks.

Table 2. The training hyperparameters for the suggested approach.

Hyperparameter	Values
Optimizer	Adam
Batch Size	32
Rate of Learning	0.001
Momentum	0.9
Epoch	5
Training Steps	2325
Activation Function	Sigmoid, ReLu

The performance assessment of existing approaches using CERT 4.2 is shown in Table 3. Our model for detecting internal threats outperforms all others. Our model has a validation accuracy of 100% and a training accuracy of 99%, versus 94% for the DCNN model [5], and it performs better than the 99.2% accuracy of ensemble learning (Bootstrap) [4] with a validation accuracy of 100%. Our model’s 100% validation accuracy outperforms the 90% random forest model [6]. Our method detects and classifies insider threats considerably more precisely.

**Table 3.** Performance evaluation concerning current methods using CERT 4.2.

Model	Accuracy
DCNN [5]	94%
Ensemble Learning (Bootstrap) [4]	99.2%
Random Forest [6]	90%
Our Proposed Method	100%

## 6. Conclusions

In conclusion, this paper proposed a neural network-based machine learning algorithm to enhance the detection accuracy of infiltrator malware. Using the CERT4.2 dataset, the research effectively demonstrated the efficacy of the proposed method. Other classification techniques such as random forest, naive Bayes, KNN, SVM, decision tree, logical regression, and gradient boosting were outperformed by the proposed algorithm's 100% accuracy in detecting insider threats. A neural network-based approach, multiple dense layers, ReLU activation functions, dropout layers, feature extraction, anomaly detection, and classification workflow contribute to the algorithm's high accuracy and efficacy. The algorithm obtains a greater comprehension of internal malware patterns by encapsulating text sequences and preprocessing the data.

**Author Contributions:** Conceptualization: M.H.K.; methodology: M.H.K., A.H. and A.J.M.; software: A.H., A.J.M. and I.M.F.; formal analysis: M.H.K., M.N.H., A.H. and A.J.M.; writing—original draft preparation: A.H., A.J.M., J.A.C. and I.M.F.; writing—review and editing: M.H.K., A.H., A.J.M., J.A.C. and M.N.H.; supervision: M.H.K. and M.N.H. All authors have read and agreed to the published version of the manuscript.

**Funding:** This research received no external funding.

**Institutional Review Board Statement:** Not applicable.

**Informed Consent Statement:** Not applicable.

**Data Availability Statement:** Not applicable.

**Conflicts of Interest:** The authors declare no conflict of interest.

## References

1. Baset, M. Machine Learning for Malware Detection. Ph.D. Dissertation, Heriot Watt University, Edinburgh, UK, 2016.
2. Virus and Malware Removal—Wickenburg Computers—Fixing Your Computer Problems. (n.d.). Available online: <https://www.wickenburgcomputers.com/services/virus-and-malware-removal> (accessed on 1 October 2023).
3. Tayyab, U.-e.-H.; Khan, F.B.; Durad, M.H.; Khan, A.; Lee, Y.S. A Survey of the Recent Trends in Deep Learning Based Malware Detection. *J. Cybersecur. Priv.* **2022**, *2*, 800–829. [CrossRef]
4. Zhang, C.; Wang, S.; Zhan, D.; Yu, T.; Wang, T.; Yin, M. Detecting Insider Threat from Behavioral Logs Based on Ensemble and Self-Supervised Learning. *Secur. Commun. Netw.* **2021**, *2021*, 4148441. [CrossRef]
5. Gayathri, R.G.; Sajjanhar, A.; Xiang, Y. Image-Based Feature Representation for Insider Threat Classification. *Appl. Sci.* **2020**, *10*, 4945. [CrossRef]
6. Noever, D. Classifier Suites for Insider Threat Detection. *arXiv* **2019**, arXiv:1901.10948.
7. Rhode, M.; Burnap, P.; Jones, K. Early-stage malware prediction using recurrent neural networks. *Comput. Secur.* **2018**, *77*, 578–594. [CrossRef]
8. Cui, Z.; Xue, F.; Cai, X.; Cao, Y.; Wang, G.; Chen, J. Detection of Malicious Code Variants Based on Deep Learning. *IEEE Trans. Ind. Inform.* **2018**, *14*, 3187–3196. [CrossRef]
9. Xing, X.; Jin, X.; Elahi, H.; Jiang, H.; Wang, G. A Malware Detection Approach Using Autoencoder in Deep Learning. *IEEE Access* **2022**, *10*, 25696–25706. [CrossRef]
10. Liu, X.; Lin, Y.; Li, H.; Zhang, J. A Novel Method for Malware Detection on ML-based Visualization Technique. *Comput. Secur.* **2019**, *89*, 101682. [CrossRef]

**Disclaimer/Publisher's Note:** The statements, opinions and data contained in all publications are solely those of the individual author(s) and contributor(s) and not of MDPI and/or the editor(s). MDPI and/or the editor(s) disclaim responsibility for any injury to people or property resulting from any ideas, methods, instructions or products referred to in the content.



Proceeding Paper

# Full-Field Modal Analysis Using Video Measurements and a Blind Source Separation Methodology <sup>†</sup>

Samira Azizi <sup>1,2,\*</sup>, Kaveh Karami <sup>1</sup> and Stefano Mariani <sup>2</sup>

<sup>1</sup> Department of Civil Engineering, University of Kurdistan, Sanandaj 6617715175, Iran; ka.karami@uok.ac.ir

<sup>2</sup> Department of Civil and Environmental Engineering, Politecnico di Milano, 20133 Milano, Italy; stefano.mariani@polimi.it

\* Correspondence: samira.azizi@polimi.it

<sup>†</sup> Presented at the 10th International Electronic Conference on Sensors and Applications (ECSA-10), 15–30 November 2023; Available online: <https://ecsa-10.sciforum.net/>.

**Abstract:** The adoption of wireless sensor networks has brought a significant breakthrough in structural health monitoring, providing an effective alternative to the challenges associated with traditional cable-based sensors. In recent years, a growing interest in developing contactless, vision-based vibration sensors like video cameras has led to advancements, potentially alleviating the previously mentioned drawbacks. In this study, a video of a vibrating frame is converted into a set of frames, so that local phase information can be extracted. The motion matrix is then derived from the phase information; since the number of measuring points is usually greater than the number of the excited modes of the system, the problem can become over-determined. Therefore, by applying dimensionality reduction techniques, the dimension of the motion matrix is significantly reduced. Finally, by exploiting an output-only identification technique, modal parameters are computed. The proposed approach is proven to accurately identify the structural frequencies and mode shapes.

**Keywords:** structural health monitoring; digital cameras; modal analysis; non-negative matrix factorization

## 1. Introduction

Modal analysis can be used to extract parameters that characterize the dynamic response of structures to external excitations [1]. This process can rely upon both input and output data or output data only. As the modal parameters depend on the inherent properties of the structure and are supposed to be unaffected by the external loads, they can be used for the assessment of the health of the monitored structures [2,3].

Typically, experimental and operational modal analyses involve the use of wired or wireless sensor networks, featuring optimized placement and/or cost [4–6], to observe the structural response [7,8]. Such sensors can provide measurements at sparse locations, often resulting in poor spatial resolution. In recent years, the capabilities of high-speed video measurements have significantly increased so that vision-based measurements can be effectively utilized in a wide range of applications in civil engineering, see, e.g., [9]. Estimating the optical flow by assuming a constant intensity between frames is a widely used technique; the equation imposing the invariant condition can be solved using different methods [10]. For instance, Chen et al. [11] identified the modes of cantilever beams and pipes by using phase-based motion magnification. Yang et al. [12,13] extracted the displacement of a three-story structure by combining phase-based optical flow and deep learning [14], while Dasari et al. [15,16] addressed the extraction of mode shapes and frequencies in the case of non-ideal rigid body motion. Martinez et al. [17] investigated the combination of compressed sensing sampling with system identification through images.

In the process of identification through video-based methods, due to the substantial dimensions of data, dimension reduction is necessary to reduce the dimensionality of the

**Citation:** Azizi, S.; Karami, K.; Mariani, S. Full-Field Modal Analysis Using Video Measurements and a Blind Source Separation Methodology. *Eng. Proc.* **2023**, *58*, 105. <https://doi.org/10.3390/ecsa-10-16199>

Academic Editor: Stefan Bosse

Published: 15 November 2023



**Copyright:** © 2023 by the authors. Licensee MDPI, Basel, Switzerland. This article is an open access article distributed under the terms and conditions of the Creative Commons Attribution (CC BY) license (<https://creativecommons.org/licenses/by/4.0/>).

motion matrix to the number of excited modes. This issue represents one of the main challenges within the field of vision-based identification.

In this study, we attack the problem of dimensionality reduction in two ways: first, full-field identification is achieved by handling a few pixels in the images; second, the dimensionality of said matrix is reduced to match the number of excited modes and, simultaneously, denoise the information. After having extracted the phase and amplitude from all of the frames of a video by applying the Gabor filter, pixels are selected by means of two criteria: a customarily adopted one, based on the amplitude, and a newly proposed one, based on the amplitude coupled with a Canny edge detection method. A motion matrix representing the time history of the pixel phase is then extracted and, via non-negative matrix factorization (NMF), the dimension of the data is reduced. Finally, the dimension of the phase matrix is reduced, and by means of complexity pursuit (CP), the full-field mode shapes and the vibration frequencies are obtained. The accuracy of the results is assessed with an example related to a three-story building.

### 2. Phase Extraction with the Gabor Filter

Phase information has been proven to be more correlated with structural motion than the amplitude and intensity value of the image [11]. In Fourier analysis, time delay in a signal corresponds to phase variations in the frequency domain; similarly, in two-dimensional signals (images), the spatial motion results in a phase change. In this context, we refer to the local phase corresponding to a pixel in a specific coordinate system, which can be extracted using the Gabor filter. This filter type, which is a complex quadrature filter, is the product of the Gaussian kernel and a complex sinusoidal function; due to article length constraints, additional details are omitted herein and readers are referred to [18]. The real and imaginary part of this filter in two directions is represented in Figure 1.

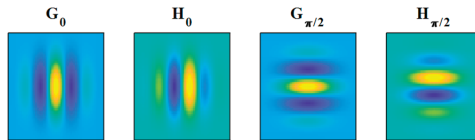


**Figure 1.** A pair of filters with a 90-degree phase difference, oriented horizontally and vertically in the image.

Assuming that  $I(x, y, t_0)$  is the intensity of the image at time  $t_0$  and at the location  $(x, y)$  in the frame, the local phase ( $\Phi_\theta$ ) and local amplitude ( $A_\theta$ ) in the  $\theta$  direction are obtained by convolving the filter ( $G_\theta + iH_\theta$ ) with the image as:

$$A_\theta(x, y, t_0)e^{i\Phi_\theta(x,y,t_0)} = (G_\theta + iH_\theta) \otimes I(x, y, t_0) \tag{1}$$

In the phase-based method, it is assumed that the local phase contour remains constant. The mathematical representation of this concept is given by:

$$\Phi_\theta(x, y, t_0) = C \tag{2}$$

This equation can be used to determine the displacement field.

### 3. Full-Field Identification

By applying the Gabor filter to the frames of a video of a vibrating structure, the local phase  $\Phi(x, y, t)$  is obtained to capture the structural vibrations  $d(x, y, t)$  provided as a linear combination of modal responses:

$$d(x, y, t) = \sum_{i=1}^n \varphi_i(x, y)q_i(t) \tag{3}$$



where  $n$  is the number of excited modes;  $\phi \in \mathbb{R}^{N \times n}$  is the matrix of the mode shapes, with  $\phi_i$  being the  $i$ -th vibration mode;  $N$  is the number of pixels in one frame; and  $q(t) \in \mathbb{R}^{n \times T}$  is the vector of modal coordinates, with  $T$  being the number of handled frames.

Within blind source separation (BSS) methodologies aimed at modal identification, modal responses and vibration frequencies are extracted from the measured output without prior knowledge of the mixing matrix that represents the mode shapes. This is accomplished via the measured output by extracting phase information from the frames. Given that the number of image pixels is significantly higher than the number of typically excited modes, namely given that  $N \gg n$ , the problem becomes characterized by a large amount of data leading to high computational costs. Consequently, the direct application of BSS methods is not feasible for modal identification; dimensionality reduction techniques must be employed to reduce the dimensionality of the time-series matrix.

### 3.1. Non-Negative Matrix Factorization

Non-negative matrix factorization was introduced in [15]. Assuming the matrix  $V \in \mathbb{R}^{n \times m}$  to comprise the phase time history of pixels (motion matrix), reduced to rank  $r$ , its non-negative factorization involves the two matrices  $W \in \mathbb{R}^{n \times r}$  and  $H \in \mathbb{R}^{r \times m}$  such that  $V \approx WH$ . This is achieved by minimizing the Euclidean distance between  $V$  and  $WH$ , according to:

$$\min \|V - WH\| \text{ subjected to } W \geq 0, H \geq 0 \tag{4}$$

NMF relies upon non-convex optimization during its iterative process, potentially resulting in different solutions based on the initialization values of  $W$  and  $H$ . The initialization procedure adopted in this paper is as follows: the eigenvectors corresponding to the largest eigenvalues (larger than 1% of the maximum one), as a result of PCA on the pseudo inverse of the motion matrix, are retained in the analysis;  $W$  is obtained by applying ICA on the whitened matrix of step 1;  $H$  is obtained by means of the motion matrix. Not only can different initialization procedures to set  $W$  and  $H$  affect the accuracy of the identified modes but also the reduced dimension of the problem can be modified; this is a rather common challenge in vision-based identification problems. A comparison between the adopted method and others available in the literature is beyond the scope of this conference paper.

### 3.2. Complexity Pursuit

By applying NMF on the extracted phase matrix, the reduced one  $W$  can be obtained. Assuming that  $W'$ , where the prime stands for transpose, can be decoupled into modal coordinate  $q$  according to:

$$q = LW' \tag{5}$$

The de-mixing matrix  $L^{r \times r}$  has to be acquired through the use of CP [19]. The mode shape matrix, see Equation (3), is then computed with:

$$\phi = H'L^{-1} \tag{6}$$

## 4. Numerical Example

In this study, we assess the capability of the procedure outlined in Section 3, by means of an on-purpose generated video of a three-story structure with mass  $m = [12 \ 10 \ 5] \times 10^3$  kg, stiffness  $k = [45 \ 40 \ 23] \times 10^6$  N/m, and damping proportional to the mass, subject to free vibrations. The phase matrix is obtained by applying the Gabor filter to all of the frames. To effectively handle the data volume and to prove the feasibility of obtaining mode shapes using a reduced number of pixels, the procedure reads as follows: pixels are selected on the basis of the amplitude in the initial frame; Canny edge detection is employed in conjunction with the amplitude information; and NMF and CP are applied to the phase matrix. The entire procedure is sketched out in Figure 2.

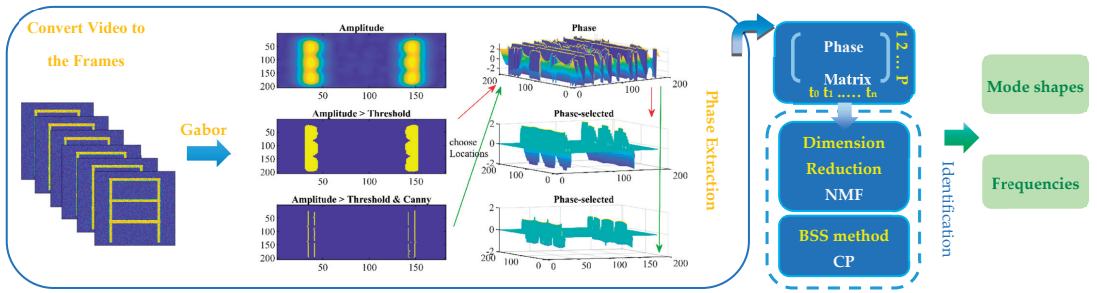


**Figure 2.** Schematic diagram of the proposed NMF–CP based procedure.

As previously mentioned, one of the inherent challenges within vision-based identification methodology pertains to dimension reduction. At this stage, obtaining a matrix with dimensions matching the number of excited modes of a vibrating structure is not straightforward. To illustrate this issue, we refer to the approach employed in [20] for a three-story structure, whose motion to catch the vibrations can be affected by noise, see Figure 3a. A singular value decomposition (SVD) of the covariance matrix derived from the phase matrix is adopted. The dimension reduction is based on the selection of the eigenvalues exceeding 1% of the largest one, as depicted in Figure 3b. If noise is present, the number of eigenvalues exceeding this threshold turns out to be three.

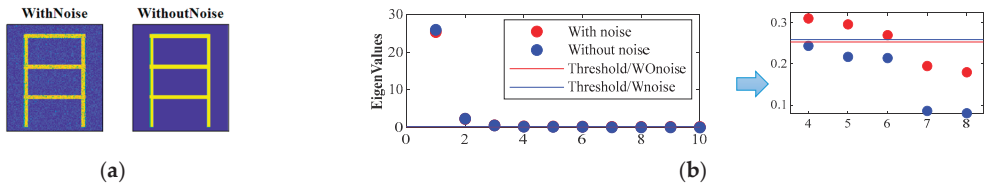


**Figure 3.** (a) A frame of the video with and without noise; (b) eigenvalues of the covariance of the phase matrix.

Upon the adoption of CP for the phase matrix, the number of identified modes may be larger than the actual number of excited modes, thereby needing a post-processing step. While it is relatively straightforward to visually select the correct modes in structures with a simple geometry, it may become prohibitively difficult for structures characterized by a complex shape.

By applying the procedure illustrated in Figure 2 to the noisy video, the phase matrix is obtained using two distinct phase selection methods. The dimension of the phase matrix obtained by employing the Canny edge detection in combination with the amplitude information results in it being smaller than the one obtained by solely using the amplitude data. Figure 4 shows that the identified mode shapes are identical in the two cases.

In Figure 5, a comparison between the identified mode shapes extracted from the video and the mode shapes used to generate the video is provided. It is evident that the first and second modes closely align with the real mode shapes of the structure at story height. However, the third mode shows some disparities at the first story. Upon comparison with the actual values obtained using the modal assurance criterion, it can be observed that the identified vibration frequencies exhibit a high degree of similarity with the real ones, amounting to at least 98.2%.

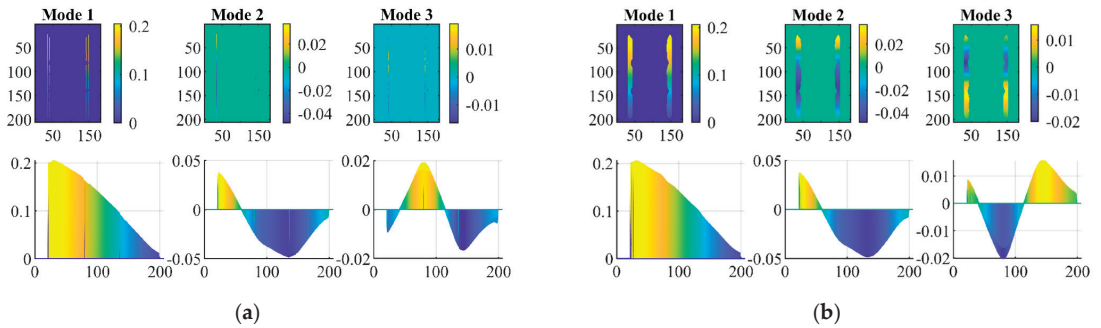


**Figure 4.** Identified mode shapes using: (a) the Canny and amplitude technique and (b) the amplitude technique only.

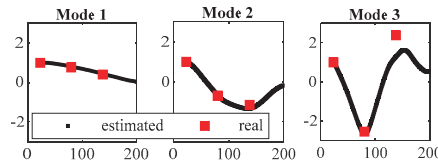


**Figure 5.** Identified mode shapes.

### 5. Conclusions

This study has focused on the identification of the mode shapes and frequencies of vibrating structures. Given the substantial dimensionality of the data to handle such aspects in the analysis, we implemented a two-step pixel selection procedure by applying a threshold to the pixel amplitude obtained by way of the Canny edge detection method. Next, we applied NMF to reduce the dimensionality of the phase matrix and to also denoise the phase time-series. In fact, it has been demonstrated that noisy data can significantly impact the eigenvalue selection phase, potentially leading to the identification of incorrect mode shapes. Subsequently, CP was employed for the identification process.

The results show that this approach can be an accurate and reliable method to identify vibration frequencies and mode shapes, at least for problems related to the vibrations of shear-type buildings. The denoising procedure in fact resulted in the accurate identification of mode shapes. In future research, we aim to investigate the impact of the initialization method of NMF and to refine the process of selecting the rank for NMF dimension reduction.

**Author Contributions:** Conceptualization, S.A., S.M. and K.K.; methodology, S.A. and K.K.; validation, S.A., S.M. and K.K.; formal analysis, S.A.; resources, K.K.; data curation, S.A.; writing—original draft preparation, S.A.; writing—review and editing, S.M.; visualization, S.M.; supervision, S.M. All authors have read and agreed to the published version of the manuscript.

**Funding:** This research received no external funding.

**Institutional Review Board Statement:** Not applicable.

**Informed Consent Statement:** Not applicable.

**Data Availability Statement:** The data presented in this study are available on request from the corresponding author.

**Conflicts of Interest:** The authors declare no conflict of interest.

## References

1. Fu, Z.-F.; He, J. *Modal Analysis*; Elsevier: Amsterdam, The Netherlands, 2001.
2. Torzoni, M.; Rosafalco, L.; Manzoni, A.; Mariani, S.; Corigliano, A. SHM under varying environmental conditions: An approach based on model order reduction and deep learning. *Comput. Struct.* **2022**, *266*, 106790. [CrossRef]
3. Azizi, S.; Karami, K.; Nagarajaiah, S. Developing a semi-active adjustable stiffness device using integrated damage tracking and adaptive stiffness mechanism. *Eng. Struct.* **2021**, *238*, 112036. [CrossRef]
4. Capellari, G.; Chatzi, E.; Mariani, S.; Azam, S.E. Optimal design of sensor networks for damage detection. *Procedia Eng.* **2017**, *199*, 1864–1869. [CrossRef]
5. Bruggi, M.; Mariani, S. Optimization of sensor placement to detect damage in flexible plates. *Eng. Optim.* **2013**, *45*, 659–676. [CrossRef]
6. Capellari, G.; Chatzi, E.; Mariani, S. Cost-benefit optimization of sensor networks for SHM applications. *Proceedings* **2018**, *2*, 132.
7. Liu, Y.; Bao, Y. Real-time remote measurement of distance using ultra-wideband (UWB) sensors. *Autom. Constr.* **2023**, *150*, 104849. [CrossRef]
8. Liu, Y.; Liu, L.; Yang, L.; Hao, L.; Bao, Y. Measuring distance using ultra-wideband radio technology enhanced by extreme gradient boosting decision tree (XGBoost). *Autom. Constr.* **2021**, *126*, 103678. [CrossRef]
9. Spencer, B.F., Jr.; Hoskere, V.; Narazaki, Y. Advances in computer vision-based civil infrastructure inspection and monitoring. *Engineering* **2019**, *5*, 199–222. [CrossRef]
10. Chen, J.G.; Adams, T.; Sun, H.; Bel, E.S.; Büyüköztürk, O. Camera-based vibration measurement of the world war I memorial bridge in Portsmouth, New Hampshire. *J. Struct. Eng.* **2018**, *144*, 04018207. [CrossRef]
11. Chen, J.G.; Davis, A.; Wadhwa, N.; Durand, F.; Freeman, W.; Büyüköztürk, O. Video camera-based vibration measurement for civil infrastructure applications. *J. Infrastruct. Syst.* **2017**, *23*, B4016013. [CrossRef]
12. Fleet, D.J. *Measurement of Image Velocity*; Springer Science & Business Media: Berlin, Germany, 2012; Volume 169.
13. Chen, J.G.; Davis, A.; Wadhwa, N.; Cha, Y.-J.; Durand, F.; Freeman, W.T.; Buyukozturk, O. Modal identification of simple structures with high-speed video using motion magnification. *J. Sound Vib.* **2015**, *345*, 58–71. [CrossRef]
14. Luan, L.; Zheng, J.; Wang, M.L.; Yang, Y.; Rizzo, P.; Sun, H. Extracting full-field subpixel structural displacements from videos via deep learning. *J. Sound Vib.* **2021**, *505*, 116142. [CrossRef]
15. Silva, M.; Martinez, B.; Figueiredo, E.; Costa, J.C.; Yang, Y.; Mascareñas, D. Nonnegative matrix factorization-based blind source separation for full-field and high-resolution modal identification from video. *J. Sound Vib.* **2020**, *487*, 115586. [CrossRef]
16. Dasari, S.; Dorn, C.; Yang, Y.; Larson, A.; Mascarenas, D. A framework for the identification of full-field structural dynamics using sequences of images in the presence of non-ideal operating conditions. *J. Intell. Mater. Syst. Struct.* **2018**, *29*, 3456–3481. [CrossRef]
17. Martinez, B.; Green, A.; Silva, M.F.; Yang, Y.; Mascareñas, D. Sparse and random sampling techniques for high-resolution, full-field, bss-based structural dynamics identification from video. *Sensors* **2020**, *20*, 3526. [CrossRef] [PubMed]
18. Freeman, W.T.; Adelson, E.H. The design and use of steerable filters. *IEEE Trans. Pattern Anal. Mach. Intell.* **1991**, *13*, 891–906. [CrossRef]
19. Yang, Y.; Nagarajaiah, S. Blind modal identification of output-only structures in time-domain based on complexity pursuit. *Earthq. Eng. Struct. Dyn.* **2013**, *42*, 1885–1905. [CrossRef]
20. Yang, Y.; Dorn, C.; Mancini, T.; Talken, Z.; Kenyon, G.; Farrar, C.; Mascareñas, D. Blind identification of full-field vibration modes from video measurements with phase-based video motion magnification. *Mech. Syst. Signal Process.* **2017**, *85*, 567–590. [CrossRef]

**Disclaimer/Publisher’s Note:** The statements, opinions and data contained in all publications are solely those of the individual author(s) and contributor(s) and not of MDPI and/or the editor(s). MDPI and/or the editor(s) disclaim responsibility for any injury to people or property resulting from any ideas, methods, instructions or products referred to in the content.

# The Internet of Things for Smart Farming: Measuring Productivity and Effectiveness <sup>†</sup>

Muhammad Bilal <sup>1,\*</sup>, Muhammad Tayyab <sup>1</sup>, Ali Hamza <sup>1</sup>, Kiran Shahzadi <sup>2</sup> and Farva Rubab <sup>3</sup>

<sup>1</sup> Department of Agriculture, Forestry and Range Management, Bahauddin Zakariya University, Multan 66000, Pakistan; tayyabsultan.pak@gmail.com (M.T.); alihamza29100@gmail.com (A.H.)

<sup>2</sup> Department of Zoology, Education University of Lahore Multan Campus, Multan 66000, Pakistan; bsf2005078@ue.edu.pk

<sup>3</sup> Institute of Botany, Bahauddin Zakariya University, Multan 66000, Pakistan; farvarubab9@gmail.com

\* Correspondence: bilal679.edu@gmail.com

<sup>†</sup> Presented at the 10th International Electronic Conference on Sensors and Applications (ECSA-10), 15–30 November 2023; Available online: <https://ecsa-10.sciforum.net/>.

**Abstract:** The Internet of Things (IoT) has been developed using the current Internet architecture. The IoT concept aims to increase productivity, accuracy, and financial gains. The purpose of this study is to evaluate how well the agricultural sector is using the Internet of Things (IoT). In this study, descriptive analysis approaches are used with qualitative methods. Reviews of the literature from numerous credible national and international periodicals are used in the data collection process. This study found that it is now possible to remotely monitor agricultural development, soil moisture, and crop risk thanks to the growth of the Internet of Things and the digital transformation of rural areas. The efficiency of agriculture and farming processes can be increased by automating human intervention, especially when using the Internet of Things.

**Keywords:** Internet of Things; effectiveness; agricultural sector

## 1. Introduction

The system of interconnected computers, people with unique IDs, and other objects with the ability to interact over an Internet lacking human touch is called the Internet of Things (IoT). The Internet of Things (IoT) aims to integrate the physical and digital worlds through communication and data exchange over the Internet, which includes linked sectors, smart towns, smart houses, and smart energy. Therefore, energy-linked autos, smart farming, linked architecture and buildings, hospitals, and transport are a few instances of places where IoT can be used [1]. In the current world, technological breakthroughs have altered nearly every industry, but especially agriculture. Similar to this, sensors, Internet of Things (IoT) advancements, and smart agriculture [2] are used by the more risk-averse agriculture industry [3]. It is profitable, improves the ecology of the land, protects water supplies, slows down the decomposition of the soil, and ensures a healthy and diverse habitat [4]. Also, all fields of agriculture have distinct critical characteristics to be individually assessed with respect to quantity and quality with regard to a certain crop, such as the type of soil, drainage flow, accessibility of nutrients, and insect susceptibility. Farming optimization in the same location requires geographic variations, rotating crops, and a yearly growth development period [5]. In accordance with estimators made by the United Nations, the global population will exceed 9.8 billion people by 2050 and 11.2 billion people after 70 to 80 years [6]. The projected 2-billion-person increase in the global population is also anticipated to have experienced most of the consequences of population expansion [7]. Among the more significant industries in the economy is agriculture, which also contributes significantly to a nation's financial development. In

**Citation:** Bilal, M.; Tayyab, M.; Hamza, A.; Shahzadi, K.; Rubab, F. The Internet of Things for Smart Farming: Measuring Productivity and Effectiveness. *Eng. Proc.* **2023**, *58*, 106. <https://doi.org/10.3390/ecsa-10-16012>

Academic Editor: Stefano Mariani

Published: 15 November 2023



**Copyright:** © 2023 by the authors. Licensee MDPI, Basel, Switzerland. This article is an open access article distributed under the terms and conditions of the Creative Commons Attribution (CC BY) license (<https://creativecommons.org/licenses/by/4.0/>).

order to meet demand, the Food and Agriculture Organization (FAO) of the United Nations thinks that world food output must increase by 70% by 2050 [8].

Smart farming, sometimes referred to as smart agriculture, is a farming technique that employs sustainable techniques to fulfill the rising food demands of the population while avoiding adverse impacts. The whole world has accepted it and is behind it. This strategy's primary concept is to reduce costs across the board for all operations related to the agriculture sector while efficiently utilizing the resources available for sustainable production [9]. For the rise in production to occur, cultivation techniques must be improved, and various technologies must be adaptable to deliver vital information about the agricultural fields so that necessary measures may be taken. Smart farming or precision farming is the use of cutting-edge technologies in the fields to achieve an optimum irrigation operation [10,11]. Sowing through crop harvest, storage, and transportation all involve the use of sophisticated machinery and tools in modern agriculture. The system is intelligent and cost-effective due to its accurate tracking capacity and timely analysis utilizing a range of sensors. There are now automated drones, cultivators, tractors, satellites, and robots besides conventional agricultural technology. Sensors may begin collecting data right away after installation, which is then available for online analysis right away. Accurate data gathering at each place is made possible by electronic sensors, allowing site- and crop-specific farming [12]. The agricultural crop production industry has access to effective solutions to support farmers and researchers thanks to the Internet of Things. Additionally, it facilitates decision-making by providing numerous easily accessible data sources on soil [13], water [14], pesticides [15], fertilizers [16], and manures [17]. Precision farming has the potential to further mitigate the consequences of global warming by addressing runoff problems, pollutants, and the use of fewer pesticides and fertilizers on agricultural products [18,19].

The Internet of Things may be utilized to control agricultural sensors and connect them to cloud infrastructure, for example, to enable the deployment of precision agriculture [20]. Some of the farming uses for IoT include managing farms, animal monitoring, water control, greenhouse control, drones, and automated farm machinery. All of these contribute to agrarian automation. They will also need more assistance to ensure the longevity of the farmed food sector. To meet these demands, agricultural output forecasts, crop protection, and land assessment are crucial for global food production [21].

## 2. Materials and Method

The architecture of our suggested IoT-based smart farming monitoring system (SFMS) for crop farming is covered in this section. The Internet of Things, cloud computing power, and the advancement of mobile and communication technologies may lead to the creation of low-cost smart agricultural applications and solutions. The design of our suggested SFMS system comprises sensors that collect data regarding air humidity, light intensity, and temperature. Through a gateway, the unprocessed data are sent to a cloud platform so they may be analyzed. After that, the farmer receives notification via email, short messaging service (SMS), or mobile app to take any necessary precautions. The three levels of generic architecture of the Internet of Things are the layers of perception, network, and application, as illustrated in Figure 1 [22]. At the perception layer, often referred to as the "sensing layer", events in the actual world are acquired via a variety of sensors, etc. The network layer uses gateways, routing and switching functions, Wi-Fi and Bluetooth, and other technologies to route data across the Internet. The application layer communicates with the user directly. Using the services that they have identified, each of these tiers carries out certain duties and activities [23].

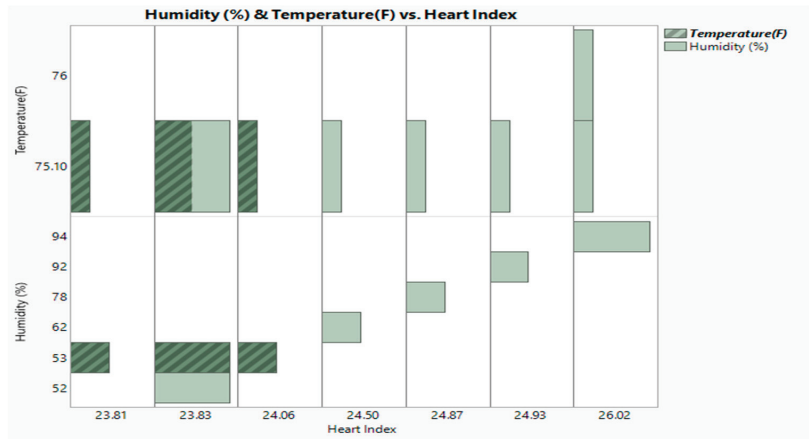


Figure 1. Temperature and humidity by Heart Index.

Traditional farming uses very little, if any, technology and is solely dependent on the expertise of the farmers. Information on environmental factors and their influence on crop growth, health, and productivity is lacking, as are data analysis and prediction systems. Our goal is to close the technology gap and use contemporary technical solutions for improved crop production and cultivation, as well as for the mitigation of crop-related issues. IoT-based farming has the potential to overcome the drawbacks of traditional farming. IoT-based solutions have the potential to improve crop quantity and quality, increase productivity, and manage diseases.

Figure 2 describes the three layers of internet of things for improvement in agriculture production. The whole process is interlinked with each other factors affecting the production. The application layer in which report of things, application and monitoring of things have been done. Then these things go through the process of internet of things [22].

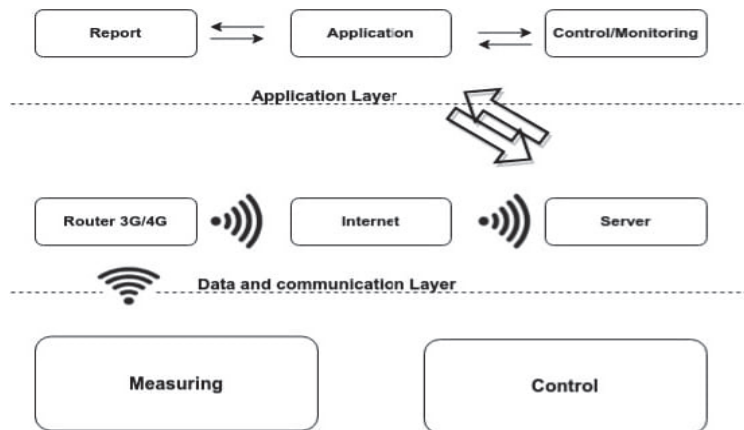


Figure 2. Three layers of Internet of Things [22].

### 3. Results

Adopting innovative techniques based on sensor and IoT technology increased crop output more than using traditional agricultural practices. The improvement of produce quality and output is greatly helped by the regulated use of novel, cutting-edge sensor-based technologies. One of the first smart farming techniques, the cultivation of plants in a

regulated setting, became popular in the nineteenth century. In nations that experienced extreme weather, these practices intensified over the 20th century. Indoor agriculture produces crops that are less impacted by the environment. As a consequence, crops that were previously produced under ideal conditions are now cultivated anytime, anyplace, thanks to the usage of sensors and communication tools. Crop production under regulated conditions depends on a number of variables, including shed constructions and wind-effect-controlling materials, aeration systems, the precision of monitoring parameters, decision-support systems, etc. The exact monitoring of environmental factors is one of the biggest obstacles in greenhouses; as a result, it takes a number of measuring units to forecast the many parameters needed to regulate and maintain the regional weather. Sensors are utilized in a greenhouse powered by IoT to detect and keep track of interior characteristics, including humidity, temperature, light, and pressure. In addition to shielding plants from hail, winds, UV radiation, and bug and pest assaults, the smart greenhouse has assisted farmers in automating field labor without manual inspection. Utilizing lighting, temperature, and air humidity sensors, hibiscus plants are cultivated with the necessary wavelength at night. Research has found that the need for water was reduced by 70–79%, and the IoT makes it feasible for farmers to communicate directly with consumers to increase farming efficiency and profitability. For researchers and designers, creating viable precision farming systems for smallholder farmers still poses testing and design challenges. The use of GPS and position information to direct machinery to specified locations within the farm, increasing agricultural production in comparison to human-driven equipment, is another advantage of data analytics in smart agriculture. Time, gasoline, and operating costs will all be saved as a result of this.

Table 1 shows the different tools, their role in agricultural application and the advantages these tools and their application for improvement of smart farming. The functions and monitoring of these tools with specific output is also described in the table.

**Table 1.** IoT use in agricultural improvement.

Using IoT	Agriculture Applications	Advantages of Agriculture
Wireless Sensor Network (WSNs)	Combining sensors to track a range of physical characteristics.	Sensor’s data can be easily managed and collected.
Cloud Computing	Availability of an on-demand computer resource pool as well as personal computers and other devices.	Making the maps of agriculture field.
Massive Data Analysis	Various type of data is accessible.	Get about market behavior and customer desires.
Embedded system	The system works efficiently on various processes and controlled over them.	Production cost can be reduced and profit can be increased.
Communication protocols	Data sharing made possible through these network.	Simple management of massive data.

Table 2 below displays digital values associated with the graphical outputs of all sensors. The Internet server hosted by Ubidots is utilized to facilitate the execution and oversight of several experimental data grabs. As previously stated, sensor data are saved on a cloud server and updated every five seconds. The table below displays only 11 random experimental values. To demonstrate the operation of the suggested system in various environmental settings, these values are included as an example.



**Table 2.** Sensor-based assessment and tracking benefits of intelligent agriculture.

Sr. No	Temperature (F)	Humidity (%)	Heart Index	Flame Detection	Soil (%)	Pres (Hg)
1	75.10	52	23.83	Peace	85	35.81
2	75.10	53	23.81	Peace	85	32
3	75.10	53	23.83	Peace	85	35.81
4	75.10	52	23.83	Peace	85	34.6
5	75.10	53	23.83	Peace	85	39.8
6	75.10	53	24.06	Peace	85	31
7	75.10	62	24.50	Peace	76	35.81
8	75.10	78	24.87	Fire-367	72	33
9	75.10	92	24.93	Fire-382	72	35.81
10	75.10	94	26.02	Fire-377	82	35.40
11	76	94	26.02	Fire-372	76	35.81

Industrial agricultural farming techniques degrade soil quality more quickly than nature can rebuild it. Arable land has decreased due to the alarming pace of erosion and agricultural use of fresh water, adding to the strain on existing water troughs. With vertical farming (VF), it is possible to maintain the plants in a highly controlled environment, considerably lessening the use of resources while simultaneously boosting output at various periods; based on the number of stacks, just a percentage of the ground surface is required. When compared to conventional farming, VF is also quite good at raising yields and decreasing the usage of water. The goal of IoT-based phenotyping is to assess the crop and associated traits and provide resources for crop breeding and digital agriculture. The links between genotypes, phenotypes, and their growth conditions are determined by the trait analysis methods and modeling tools.

#### 4. Discussion

Lately, the IoT has had a significant impact on the agriculture business, with a wide variety of sensors being used for various smart agricultural aims. IoT applications are linking a growing number of networked devices, including various sensors, drivers, and intelligent objects, to mobile devices over the Internet on an annual basis. As a consequence of the extensive use of wireless remote data collecting, IoT services include information exchange and smart controlling and solutions for making decisions. These skills may support the smart agriculture sector by facilitating productive output. Developing modernized farming while researching an IoT area of interest in the agricultural sector is the conventional approach to agriculture. IoT growth has greatly benefited all industries over the past 10 years [24]. IoT has a tendency to be a vital technology in integrating different approaches to offer clever remedies for all of the recognized issues. It facilitates easy communication between people and things. IoT has helped to solve issues in many other industries, but it is especially important in the agriculture sector [25]. By installing connected sensors across the farm, which provide immediate data, farmers can make decisions and execute actions to boost crop yields. Information on cultivation and wireless sensor networks (WSNs) with GPS capabilities are constantly updating topographic information. Recent advancements in computerized visuals and data processing have expanded WSN capabilities and made it possible to evaluate crop quality and health precisely.

#### 5. Conclusions

The development of IoT technology in recent years has largely helped the farming sector, especially because of its connecting infrastructure. This includes the cloud-based advanced analysis and decision-making process, the network of remote data collection, smart objects, the use of vehicles and sensors accessible through mobile devices and the Internet, and the automation of agricultural processes. Farmers will obtain insight into how to conduct precise and useful agriculture to resolve field concerns through the use of remote sensors, such as those for temperature, humidity, soil moisture, water level

sensors, and pH values. By developing efficient tactics, this development can enable agricultural management systems to manage farm data in an organized manner and expand the agribusiness.

**Author Contributions:** Conceptualization, M.B.; data curation: M.T.; formal analysis: M.B.; methodology, M.T. and A.H.; validation; K.S. and F.R.; writing—original draft: M.B.; writing—review and editing, M.T., A.H., K.S. and F.R. All authors have read and agreed to the published version of the manuscript.

**Funding:** This research received no external funding.

**Institutional Review Board Statement:** Not applicable.

**Informed Consent Statement:** Not applicable.

**Data Availability Statement:** The data are available on suitable demand.

**Conflicts of Interest:** The authors declare no conflicts of interest.

## References

- Mukhtar, H.; Khan, M.Z.; Khan, M.U.G.; Saba, T.; Latif, R. Wheat plant counting using UAV images based on semi-supervised semantic segmentation. In Proceedings of the 2021 1st International Conference on Artificial Intelligence and Data Analytics (CAIDA), Riyad, Saudi Arabia, 6–7 April 2021; pp. 257–261.
- Rehman, A.; Saba, T.; Kashif, M.; Fati, S.M.; Bahaj, S.A.; Chaudhry, H. A revisit of internet of things technologies for monitoring and control strategies in smart agriculture. *Agronomy* **2022**, *12*, 127. [CrossRef]
- Komarek, A.M.; De Pinto, A.; Smith, V.H. A review of types of risks in agriculture: What we know and what we need to know. *Agric. Syst.* **2020**, *178*, 102738. [CrossRef]
- Brodt, S.; Six, J.; Feenstra, G.; Ingels, C.; Campbell, D. Sustainable agriculture. *Nat. Educ. Knowl.* **2011**, *3*, 1.
- Hernández-Ochoa, I.M.; Gaiser, T.; Kersebaum, K.-C.; Webber, H.; Seidel, S.J.; Grahmann, K.; Ewert, F. Model-based design of crop diversification through new field arrangements in spatially heterogeneous landscapes. A review. *Agron. Sustain. Dev.* **2022**, *42*, 74. [CrossRef]
- Report of the United Nations Scientific Committee on the Effects of Atomic Radiation (11–14 June 2018), UNITED Nation, New York. Available online: <https://www.unscear.org/docs/GAreports/2018/A-73-46-e-V1804724.pdf> (accessed on 19 December 2023).
- Kumar, P.; Gupta, G.P.; Tripathi, R. PEFL: Deep privacy-encoding-based federated learning framework for smart agriculture. *IEEE Micro* **2021**, *42*, 33–40. [CrossRef]
- Yang, X.; Shu, L.; Chen, J.; Ferrag, M.A.; Wu, J.; Nurellari, E.; Huang, K. A survey on smart agriculture: Development modes, technologies, and security and privacy challenges. *IEEE/CAA J. Autom. Sin.* **2020**, *8*, 273–302. [CrossRef]
- Buckley, C.; Carney, P. The potential to reduce the risk of diffuse pollution from agriculture while improving economic performance at farm level. *Environ. Sci. Policy* **2013**, *25*, 118–126. [CrossRef]
- Alsoufi, M.A.; Razak, S.; Siraj, M.M.; Nafea, I.; Ghaleb, F.A.; Saeed, F.; Nasser, M. Anomaly-based intrusion detection systems in iot using deep learning: A systematic literature review. *Appl. Sci.* **2021**, *11*, 8383. [CrossRef]
- Cicioğlu, M.; Çalhan, A. Smart agriculture with internet of things in cornfields. *Comput. Electr. Eng.* **2021**, *90*, 106982. [CrossRef]
- Friha, O.; Ferrag, M.A.; Shu, L.; Maglaras, L.; Wang, X. Internet of things for the future of smart agriculture: A comprehensive survey of emerging technologies. *IEEE/CAA J. Autom. Sin.* **2021**, *8*, 718–752. [CrossRef]
- Menne, D.; Hübner, C.; Trebbels, D.; Willenbacher, N. Robust Soil Water Potential Sensor to Optimize Irrigation in Agriculture. *Sensors* **2022**, *22*, 4465. [CrossRef]
- Kamienski, C.; Soininen, J.P.; Taumberger, M.; Dantas, R.; Toscano, A.; Salmon Cinotti, T.; Filev Maia, R.; Torre Neto, A. Smart water management platform: IoT-based precision irrigation for agriculture. *Sensors* **2019**, *19*, 276. [CrossRef] [PubMed]
- Kanuru, L.; Tyagi, A.K.; Aswathy, S.U.; Fernandez, T.F.; Sreenath, N.; Mishra, S. Prediction of pesticides and fertilizers using machine learning and Internet of Things. In Proceedings of the 2021 International Conference on Computer Communication and Informatics (ICCCI), Coimbatore, India, 27–29 January 2021; pp. 1–6.
- Hegedus, P.B.; Maxwell, B.D.; Mieno, T. Assessing performance of empirical models for forecasting crop responses to variable fertilizer rates using on-farm precision experimentation. *Precis. Agric.* **2022**, *24*, 677–704. [CrossRef]
- Ather, D.; Madan, S.; Nayak, M.; Tripathi, R.; Kant, R.; Kshatri, S.S.; Jain, R. Selection of smart manure composition for smart farming using artificial intelligence technique. *J. Food Qual.* **2022**, *2022*, 4351825. [CrossRef]
- Walter, A.; Finger, R.; Huber, R.; Buchmann, N. Smart farming is key to developing sustainable agriculture. *Proc. Natl. Acad. Sci. USA* **2017**, *114*, 6148–6150. [CrossRef] [PubMed]
- Wong, S. Decentralised, off-grid solar pump irrigation systems in developing countries—Are they pro-poor, pro-environment and pro-women. In *Climate Change-Resilient Agriculture and Agroforestry*; Springer: Cham, Switzerland, 2019; pp. 367–382. [CrossRef]
- Piccione, M.; Fuhrmann, S. Using Esri CityEngine. 2016, 38–43. Available online: <https://www.esri.com/about/newsroom/wp-content/uploads/2018/09/creating-a-3d-campus-scene.pdf> (accessed on 19 December 2023).

21. Zhang, L.; Dabipi, I.K.; Brown, W.L., Jr. Internet of Things applications for agriculture. In *Internet of Things A to Z: Technologies and Applications*; John Wiley & Sons, Inc.: Hoboken, NJ, USA, 2018; pp. 507–528. [CrossRef]
22. Muangprathub, J.; Boonnam, N.; Kajornkasirat, S.; Lekbangpong, N.; Wanichsombat, A.; Nillaor, P. IoT and agriculture data analysis for smart farm. *Comput. Electron. Agric.* **2019**, *156*, 467–474. [CrossRef]
23. Ray, P.P. A survey on Internet of Things architectures. *J. King Saud Univ. Comput. Inf. Sci.* **2018**, *30*, 291–319.
24. Suma, D.V. Internet of Things (IoT) based smart agriculture in India: An overview. *J. IoT Soc. Mob. Anal. Cloud* **2021**, *3*, 1–15.
25. Shrivastava, A.; Rajesh, M. Automatic irrigation system with data log creation. In Proceedings of the 2018 Second International Conference on Inventive Communication and Computational Technologies (ICICCT), Coimbatore, India, 20–21 April 2018; pp. 632–635.

**Disclaimer/Publisher’s Note:** The statements, opinions and data contained in all publications are solely those of the individual author(s) and contributor(s) and not of MDPI and/or the editor(s). MDPI and/or the editor(s) disclaim responsibility for any injury to people or property resulting from any ideas, methods, instructions or products referred to in the content.

Proceeding Paper

# Carbon Allotrope-Based Textile Biosensors: A Patent Landscape Analysis <sup>†</sup>

Massimo Barbieri <sup>1,\*</sup> and Giuseppe Andreoni <sup>2,3</sup>

<sup>1</sup> Politecnico di Milano, Technology Transfer Office (TTO), 20133 Milan, Italy

<sup>2</sup> Politecnico di Milano, Dipartimento di Design, 20158 Milan, Italy; giuseppe.andreoni@polimi.it

<sup>3</sup> Bioengineering Laboratory, Scientific Institute IRCCS “E.Medea”, Bosisio Parini, 23842 Lecco, Italy

\* Correspondence: massimo.barbieri@polimi.it; Tel.: +39-0223999233

<sup>†</sup> Presented at the 10th International Electronic Conference on Sensors and Applications (ECSA-10), 15–30 November 2023; Available online: <https://ecsa-10.sciforum.net/>.

**Abstract:** This report aims to provide a patent landscape analysis on carbon allotrope-based textile electrodes and biosensors to measure biosignals and detect several parameters. Espacenet, a free-of-charge patent database provided by the EPO (European Patent Office) and containing data on more than 140 million patent publications from over 100 countries, was used as the reference database. The patent search was carried out by combining keywords and classification symbols. Both classification schemes (IPC–International Patent Classification and CPC–Cooperative Patent Classification) were used. As a result of this study, a total of 227 patent documents were found between 2002 and 2023. The first patent application claiming a fabric electrode arrangement with carbon black as conductive material was filed in 2002 (and published in 2004) by Philips. 2021 was the year with the highest number of published patent applications, with 36 documents. The United States was ranked first with 126 patent documents. Carbon nanotubes and graphene are the most patented carbon allotrope materials, while body temperature, motion, and heart rate measurements are the main disclosed applications. We also analyzed the Orbit database obtaining 288 patent documents (vs. 227) with only 238 still active records (148 granted and 90 pending applications): the first application by Philips on an electrode arrangement is confirmed, and the patent distribution shows a peak in the period 2016–2020 (146 records available), while today it seems to be stable or even decreasing (“only” 52 records in the half period January 2021–June 2023). This outcome suggests that this material and related technology has reached its maximum exploitation or has not demonstrated a disruptive output.

**Keywords:** textile sensors; textile electrodes; patent landscape; IPR; innovation

**Citation:** Barbieri, M.; Andreoni, G.

Carbon Allotrope-Based Textile Biosensors: A Patent Landscape Analysis. *Eng. Proc.* **2023**, *58*, 107. <https://doi.org/10.3390/ecsa-10-16216>

Academic Editor: Stefano Mariani

Published: 15 November 2023



**Copyright:** © 2023 by the authors. Licensee MDPI, Basel, Switzerland. This article is an open access article distributed under the terms and conditions of the Creative Commons Attribution (CC BY) license (<https://creativecommons.org/licenses/by/4.0/>).

## 1. Introduction

Patent surveys and related content are deemed to be of great value for identifying R&D trends and improvements; thus, a patent landscape analysis (PLA) is a very useful tool able to provide an overview of a specific technology field and its exploitation status. PLA is a retrospective study because (almost) all patent applications are published eighteen months (or at least three months) after filing. However, since novel inventions are protected for a considerable time before related products/devices enter the market, patents can be seen as an early indicator of upcoming technologies and related systems and/or services [1].

In recent years, wearable systems and smart textiles for monitoring several biomedical parameters have been the most evolving and diffusing technologies. In this field, together with conductive fibers and fabric, another very promising material is carbon, in the form of fibers, nanotubes, or graphene layers. Its exploration and study are still under development, and no integrated surveys about this material and its application in biomedical sensing were found. This study aims to provide a PLA in the field of carbon allotrope-based textile sensors/electrodes useful for monitoring physiological signals such as heart rate (HR), SpO<sub>2</sub>, body temperature, and other bioelectrical or mechanical parameters.

## 2. Resources and Methods

Espacenet and Orbit databases were used to retrieve patent information. Espacenet (<https://worldwide.espacenet.com>) is a free-of-charge patent database provided by the European Patent Office (EPO) and contains data on more than 140 million patent documents from over 90 countries. Orbit Intelligence (<https://www.orbit.com>) is a platform managed by Questel that offers access to patent information through three patent databases (FamPat, FullPat, and FullText). The coverage of the above-mentioned tools is quite similar, in terms of the number of documents, available full text, and updates. The patent search was carried out through a combination of specific keywords and classification symbols. Both the International Patent Classification (IPC) [2] and the Cooperative Patent Classification (CPC) [3] were used.

These systems share the same hierarchical structure, but the CPC is characterized by more subdivisions (250,000 vs. 80,000). While the IPC is adopted by more than 120 patent offices around the world to classify patent applications, only 30 Offices are participating in the CPC [4]. CPC is limited to a narrow circle of countries [5]. Therefore, both systems have to be used to obtain comprehensive research [6,7]. This statement can be explained using the main group A61B 5/00 (measuring for diagnostic purposes), which is the reference classification symbol for biosensors.

This query was used on Espacenet (accessed on 7 August 2023) to obtain patents classified with IPC symbols only: `ipc = "A61B5/00" NOT (cpc = "A" OR cpc = "B" OR cpc = "C" OR cpc = "D" OR cpc = "E" OR cpc = "F" OR cpc = "G" OR cpc = "H")`.

A total of 48,428 patent documents do not have any CPC code (see Figure 1).

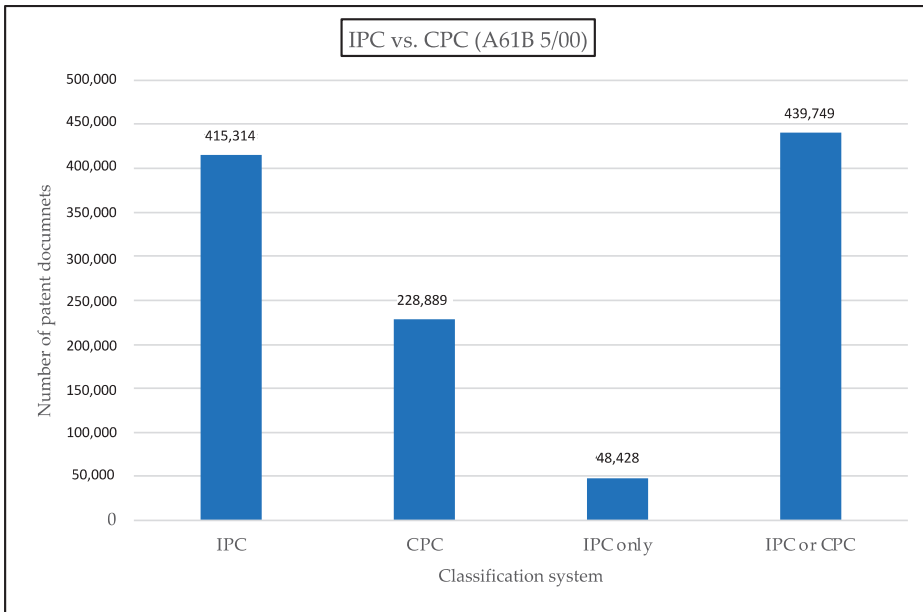


**Figure 1.** Comparison of patent classification systems (IPC vs. CPC).

Therefore, the exclusion of the IPC would lead to a limited patent search.

The classification and indexing codes (and the corresponding definitions) used for carrying out the patent searches are listed in Table 1.

**Table 1.** List of classification symbols (IPC/CPC) used in patent searches.

Classification Code	Classification System	Definition
A61B 5	IPC/CPC	Measuring for diagnostic purposes
D03D 1/0088	CPC	Fabrics having an electronic function
A41D 1/002	CPC	Garments with embedded cable or connector
G06F 1/163	CPC	Wearable computers
H01L 23/5387	CPC	Flexible insulating substrates
H05K 1/038	CPC	Printed circuits-textiles
A41D 13/1281	CPC	Garments with incorporated means for medical monitoring
A61B 2562	CPC (orthogonal indexing)	Details of sensors
A63B 2230	CPC (orthogonal indexing)	Measuring the physiological parameters of the user
H05K 2201	CPC	Printed circuits
D06M	IPC/CPC	Treatment of fibers, yarns, fabrics
C01B 32/00	IPC/CPC	Carbon compounds
C01B 2204/00	CPC	Structure or properties of graphene
B82Y	IPC/CPC	Specific uses or applications of nanostructures
C08K 3/042	CPC	Uses of inorganic substances as compounding ingredients-Graphene or derivatives
C08K 3/041	CPC	Uses of inorganic substances as compounding ingredients-Carbon nanotubes
C01B 32/158	IPC/CPC	Carbon nanotubes
C01B 32/182	IPC/CPC	Graphene
C01B 32/198	IPC/CPC	Graphene oxide
C01P 2004/13	CPC (orthogonal indexing)	Particle morphology-Nanotubes

Classification codes are used to classify inventive or additional information, while indexing codes are helpful to categorize additional information only and to specify aspects not covered by the classification scheme. Moreover, codes are assigned according to the structure, or the function/application of the subject matter claimed in a patent.

Codes referred to function/application are the following: A61B5, D03D 1/0088, A41D 13/1281, A63B 2230, D06M, B82Y, C08K 3/042, C08K 3/041.

The classification and indexing codes listed in Table 1 were retrieved using a simple query [ftxt = ("textile" prox/distance < 3 "electrode?") OR ftxt = ("textile " prox/distance < 3 "sensor?")] on Espacenet and analyzing the results through the function "Filters".

A patent search can be carried out on one or more patent databases. Usually, the collected results are different, and this depends on the specific coverage and search engine of the database.

The following query on Espacenet (accessed on 8 August 2023) (ctxt = ("textile" prox/distance < 3 "electrode?") OR ctxt = ("textile" prox/distance < 3 "sensor?")) AND ftxt = ("carbon" prox/ordered "nanotube?") yielded 110 results. The same search query on Orbit (see Figure 2) produced 154 results.

```

(C)QUESTEL
Base : FAMPAT
SEARCH STRATEGY
-----
SS Results
3      154      1 AND 2
2      242213  (CARBON 1D NANOTUBE?)/TI/AB/CLMS/DESC/ODES/ICLM
1      1501    ((TEXTILE 3D SENSOR?)/TI/AB/CLMS/ICLM OR (TEXTILE 3D ELECTRODE?)/TI/AB/CLMS/ICLM)

```

**Figure 2.** Simple search queries on the Orbit platform (FamPat database).

Therefore, a patent landscape analysis should be conducted on more than one database to obtain a more complete retrieval of documents.

### 3. Results

Data were acquired by Espacenet and the Orbit Intelligence platform (FamPat database). The latter is provided with a comprehensive suite for searching and analyzing patent documents [8].

#### 3.1. Espacenet Results

The following search query was carried out on Espacenet (accessed on 16 July 2023) using keywords and classification symbols (listed in Table 1) in the Title/Abstract/Claims and Full-text fields for data mining of carbon-allotrope based textile sensors and electrodes:

```

cl any "A61B5" AND ctxt = ("textile" prox/distance < 3 "sensor?") OR (cl any
"A61B5" AND ctxt = ("textile" prox/distance < 3 "electrode?")) OR (cpc any
"D03D1/0088" AND (ftxt = ("textile" prox/distance < 3 "electrode?") OR ftxt =
("textile" prox/distance < 3 "sensor?")) OR (cpc any "A41D1/002" AND (ftxt
= ("textile" prox/distance < 3 "electrode?") OR ftxt = ("textile" prox/distance <
3 "sensor?")) OR (cpc any "G06F1/163" AND (ftxt = ("textile" prox/distance <
3 "electrode?") OR ftxt = ("textile" prox/distance < 3 "sensor?")) OR (cpc any
"H01L23/5387" AND (ftxt = ("textile" prox/distance < 3 "electrode?") OR ftxt =
("textile" prox/distance < 3 "sensor?")) OR (cpc any "H05K1/038" AND (ftxt =
("textile" prox/distance < 3 "electrode?") OR ftxt = ("textile" prox/distance < 3
"sensor?")) OR (cpc any "A41D13/1281" AND (ftxt = ("textile" prox/distance <
3 "electrode?") OR ftxt = ("textile" prox/distance < 3 "sensor?")) OR (cpc any
"A61B2562" AND (ftxt = ("textile" prox/distance < 3 "electrode?") OR ftxt =
("textile" prox/distance < 3 "sensor?")) OR (cpc any "A63B2230" AND (ftxt =
("textile" prox/distance<3 "electrode?") OR ftxt = ("textile" prox/distance < 3
"sensor?")) OR (cpc any "H05K2201" AND (ftxt = ("textile" prox/distance <
3 "electrode?") OR ftxt = ("textile" prox/distance < 3 "sensor?")) OR (cl any
"D06M" AND (ftxt = ("textile" prox/distance < 3 "electrode?") OR ftxt = ("textile"
prox/distance < 3 "sensor?")) AND (ftxt all "graphene" OR ftxt all "carbon nano-
tube?" OR ftxt all "carbon black" OR ftxt all "CNTs" OR ftxt all "SWCNTs" OR
ftxt all "MWCNTs" OR ftxt all "graphene oxide" OR ftxt all "reduced graphene
oxide" OR ftxt all "graphene nanosheet?" OR ftxt all "carbon allotrope?" OR cl
=/low "C01B32/00" OR cpc =/low "C01B2204/00" OR cl =/low "B82Y").

```

[Query 1]

As a result of this study, a total of 227 patent documents were found between 2002 and 2023 (see Supplementary File Spreadsheet S1). The first patent application claiming a fabric electrode arrangement with carbon black as conductive material was filed in 2002 (and published in 2004) by Philips. 2021 was the year with the highest number of published patent applications, with 36 documents. The maximum number of patent applications

filed was in 2019 with 32 documents. The United States was ranked first with 126 patent documents, followed by China and Europe (see Figure 3). Carbon nanotubes and graphene are the most patented carbon allotrope materials (Figure 4), while body temperature, motion, and heart rate measurements are the main disclosed applications (Figure 5).

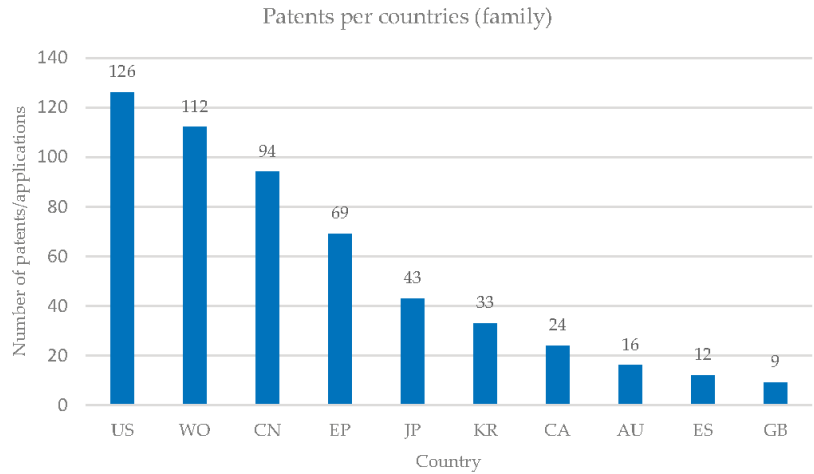


**Figure 3.** Top ten countries per number of published patent documents.

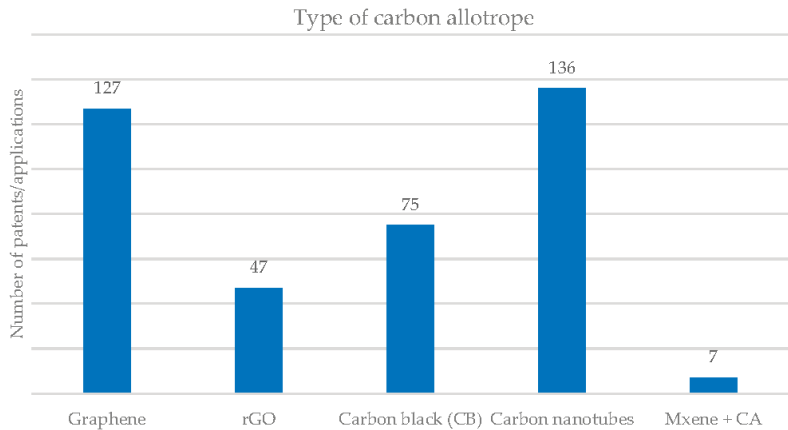


**Figure 4.** Number of patent documents per type of carbon allotrope claimed.

Carbon nanotubes are the main (claimed and described) electrically conductive materials, followed by graphene, carbon black, reduced graphene oxide, and Mxenes (a group of two-dimensional transition metal carbides, nitrides, or carbonitrides with a composition of  $M_{n+1}X_nT_x$ , where M is a transition metal (Ti, V, Nb, etc.), X is nitrogen or carbon, and T is surface functional groups (-OH, -F, -O-, -Cl) [9].

The top ten applicants are reported in Figure 6.



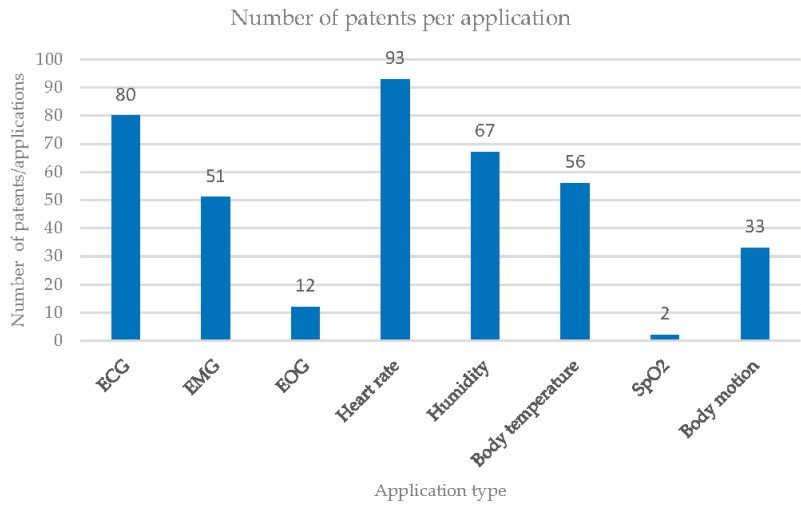


**Figure 5.** Number of patent documents per type of application.

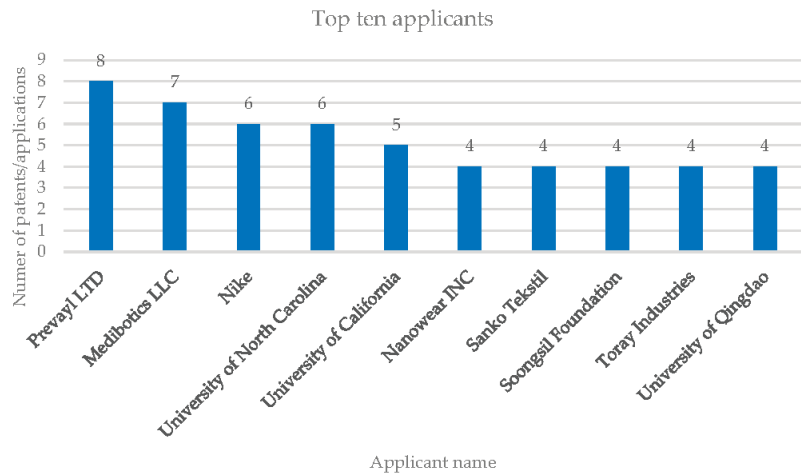


**Figure 6.** The top ten applicants per number of published patent documents.

Both companies and universities are listed as leading applicants per the number of published patent applications. Prevayl is ranked as the first owner, which has recorded eight patent documents. In second place, the company Medibotics has filed seven patent applications. The third place is shared between Nike and the University of North Carolina.

### 3.2. Orbit Results

The patent strategy used on the FamPat database is reported in Table 2. The patent search gave a total of 288 results, of which 238 are active patents (148 granted and 90 pending patent families, see Supplementary File Spreadsheet S2). Four patent families were litigated and nine were subjected to an opposition procedure at the EPO.

**Table 2.** List of search queries used on FamPat (Orbit Intelligence) [Query 2].

Query No.	Results	Query
1	435	((TEXTILE 3D SENSOR?)/TI/AB/CLMS/ICLM OR (TEXTILE 3D ELECTRODE?)/TI/AB/CLMS/ICLM) AND (A61B-005+)/IPC/CPC)
2	122	((TEXTILE 3D SENSOR?)/TI/AB/CLMS/DESC/ODES/ICLM OR (TEXTILE 3D ELECTRODE?)/TI/AB/CLMS/DESC/ODES/ICLM) AND (D03D-001/0088)/CPC)
3	139	((TEXTILE 3D SENSOR?)/TI/AB/CLMS/DESC/ODES/ICLM OR (TEXTILE 3D ELECTRODE?)/TI/AB/CLMS/DESC/ODES/ICLM) AND (A41D-001/002)/CPC)
4	49	((TEXTILE 3D SENSOR?)/TI/AB/CLMS/DESC/ODES/ICLM OR (TEXTILE 3D ELECTRODE?)/TI/AB/CLMS/DESC/ODES/ICLM) AND (G06F-001/163)/CPC)
5	3	((TEXTILE 3D SENSOR?)/TI/AB/CLMS/DESC/ODES/ICLM OR (TEXTILE 3D ELECTRODE?)/TI/AB/CLMS/DESC/ODES/ICLM) AND (H01L-023/5387)/CPC)
6	70	((TEXTILE 3D SENSOR?)/TI/AB/CLMS/DESC/ODES/ICLM OR (TEXTILE 3D ELECTRODE?)/TI/AB/CLMS/DESC/ODES/ICLM) AND (H05K-001/038)/CPC)
7	86	((TEXTILE 3D SENSOR?)/TI/AB/CLMS/DESC/ODES/ICLM OR (TEXTILE 3D ELECTRODE?)/TI/AB/CLMS/DESC/ODES/ICLM) AND (A41D-013/1281)/CPC)
8	444	((TEXTILE 3D SENSOR?)/TI/AB/CLMS/DESC/ODES/ICLM OR (TEXTILE 3D ELECTRODE?)/TI/AB/CLMS/DESC/ODES/ICLM) AND (A61B-2562+)/CPC)
9	18	((TEXTILE 3D SENSOR?)/TI/AB/CLMS/DESC/ODES/ICLM OR (TEXTILE 3D ELECTRODE?)/TI/AB/CLMS/DESC/ODES/ICLM) AND (A63B-2230+)/CPC)
10	69	((TEXTILE 3D SENSOR?)/TI/AB/CLMS/DESC/ODES/ICLM OR (TEXTILE 3D ELECTRODE?)/TI/AB/CLMS/DESC/ODES/ICLM) AND (H05K-2201+)/CPC)
11	233	((TEXTILE 3D SENSOR?)/TI/AB/CLMS/DESC/ODES/ICLM OR (TEXTILE 3D ELECTRODE?)/TI/AB/CLMS/DESC/ODES/ICLM) AND (D06M+)/IPC/CPC)
12	1167	1 OR 2 OR 3 OR 4 OR 5 OR 6 OR 7 OR 8 OR 9 OR 10 OR 11 (((GRAPHENE)/TI/AB/CLMS/DESC/ODES/ICLM OR (CARBON 1D NANOTUBE?)/TI/AB/CLMS/DESC/ODES/ICLM OR (CARBON 1D BLACK)/TI/AB/CLMS/DESC/ODES/ICLM OR (CNTS)/TI/AB/CLMS/DESC/ODES/ICLM OR (SWCNTS)/TI/AB/CLMS/DESC/ODES/ICLM OR (MWCNTS)/TI/AB/CLMS/DESC/ODES/ICLM OR (GRAPHENE 1D OXIDE)/TI/AB/CLMS/DESC/ODES/ICLM OR (REDUCED 1D GRAPHENE 1D OXIDE)/TI/AB/CLMS/DESC/ODES/ICLM OR (GRAPHENE 1D NANOSHEET?)/TI/AB/CLMS/DESC/ODES/ICLM OR (CARBON 1D ALLOTROPE?)/TI/AB/CLMS/DESC/ODES/ICLM) OR ((C01B-032+)/IPC/CPC OR (C01B-2204/00)/CPC OR (B83Y+)/IPC/CPC OR (C08K-003+)/IPC/CPC OR (C01P-2004+)/CPC))
13	1,378,171	12 AND 13
14	288	14 AND STATE/ACT=ALIVE
15	238	

The evolution of patent filings by the first application year, first publication year, and first priority year are shown in Figure 7.

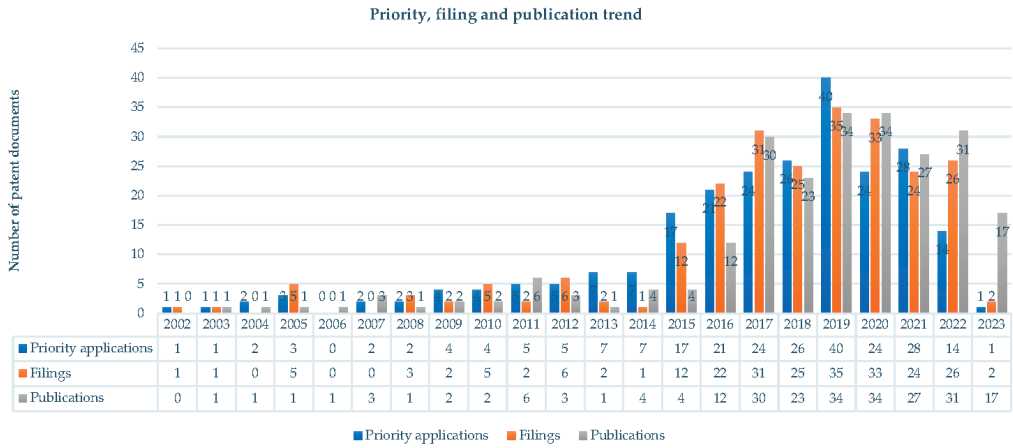


**Figure 7.** Trend of patent priorities, filings, and publications between 2002 and 2023.

Patents are assembled in families. A patent family is a group of patent publications on a single invention, filed by the same applicant or joint applicants in one or more countries [10].

The first application by Philips on an electrode arrangement is confirmed, and the patents distribution shows a peak in the period 2016–2020 (146 records available), while today it seems to be stable or even decreasing (“only” 52 records in the half period January 2021–June 2023).

The year 2019 has seen the maximum patent activity in priority applications filed and published patent applications.

This growing trend has been confirmed in a scientific literature search published in a recent review [11] on carbon-based textile sensors.

The patent protection, publication, and priority trends by country are reported in Figure 8. Patent families by protection country means the number of alive patents protected in the various national offices.

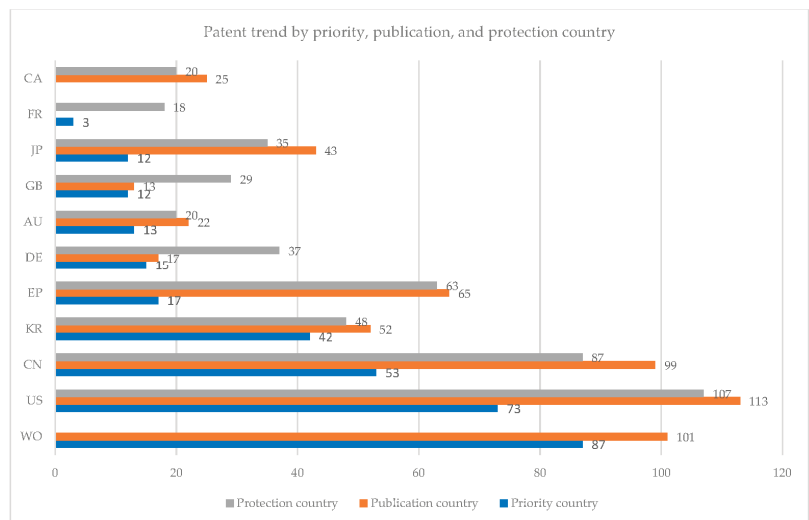
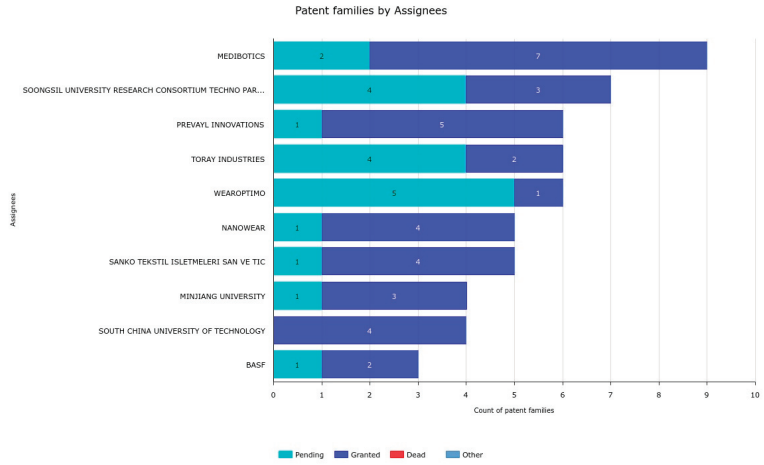


**Figure 8.** Patent filings trend by protection/publication/priority country.

The PCT (Patent Cooperation Treaty) procedure is the preferred solution for filing priority applications, followed by the US and China.

The top ten applicants list is reported in Figure 9.



© Questel 2023

**Figure 9.** The top ten applicants per number of patents.

Medibotics ranks first with nine patent documents (7 granted and 2 pending applications), followed by a Korean foundation and Prevayl Innovations Ltd, a British company. The top ten cited patents are listed in Table 3.

**Table 3.** List of the top ten cited patents (see Supplementary File Spreadsheet S3).

Patent Number	Filing Year of the Earliest Priority	Geographical Scope of Protection	Forward Citations	Applicant
EP2404148	2008	14	8	PatienTech
EP1578482	2002	9	7	Philips
EP3116395	2015	4	6	L.I.F.E.
US11300551	2004	1 (US)	6	Rondevoo Technologies
EP2866596	2013	22	4	Smart Solutions Technologies
EP3202317	2012	7	4	Nippon T&T
WO2011103808	2010	2	4	Hong Kong Institute of Textile and Apparel
EP1814713	2004	7	3	University of Texas
US10321873	2013	1	3	Medibotics
US8191433	2008	2	3	Hong Kong Polytechnic University

Considering the geographical scope of protection, the number of forward citations, and the expiration dates, the most valuable patents are EP2404148 (“Elastically stretchable fabric force sensor arrays and methods of making”), EP3116395 (“Physiological monitoring garments”) and EP2866596 (“Electronic textile assembly”).

#### 4. Conclusions

Patent documents are a valuable source of technical information that is often not available elsewhere since many companies disclose their research and development results only in patents.

Patent landscape analysis can be used to guide R&D work, to find out the most recent inventions, and to study the development of a particular technology.

Results obtained with Espacenet and Orbit are slightly different, and this is due to the different search engines of these databases.

The patenting trend since 2002 shows an increase in filing numbers starting from 2015 until 2019, with a decline in 2020 and an upswing in 2021.

Global patenting is led by the US and China, while the more promising applications are dedicated to electronic textiles applied to biomedical parameter monitoring (with particular relevance to bioelectric signals like ECG and EMG) and mechanical measurements (force monitoring through stretchable fabrics).

**Supplementary Materials:** The following supporting information can be downloaded at: <https://www.mdpi.com/article/10.3390/ecsa-10-16216/s1>, Spreadsheet S1: Espacenet search results.xls; Spreadsheet S2: Orbit search results.xls, Spreadsheet S3: List of top patent cited.xls, Spreadsheet.

**Author Contributions:** Conceptualization, methodology, data curation, writing—original draft preparation, M.B.; supervision, writing—review and editing, G.A. All authors have read and agreed to the published version of the manuscript.

**Funding:** This study was supported by the funds for biomedical research, in particular for the project “5x1000/2023—Sviluppo di nuovi protocolli di valutazione funzionale multifattoriale e relativi indici per l’età pediatrica” awarded to Prof. Giuseppe Andreoni, and by the Italian Ministry of Health (Ricerca Corrente 2023 to Dr.Eng. E. Biffi).

**Institutional Review Board Statement:** Not applicable.

**Informed Consent Statement:** Not applicable.

**Data Availability Statement:** Data are available.

**Conflicts of Interest:** The authors declare no conflict of interest. The authors have no relevant affiliations or financial involvement with any organization or entity with a financial interest in or financial conflict with the subject matter or materials discussed in this article.

#### References

1. Van Rijn, T.; Timmis, J.K. Patent landscape analysis—Contributing to the identification of technology trends and informing research and innovation funding policy. *Microb. Biotechnol.* **2023**, *16*, 683–696. [CrossRef] [PubMed]
2. WIPO IPC Publication. Available online: <https://ipcpub.wipo.int> (accessed on 7 August 2023).
3. Cooperative Patent Classification. Available online: <https://www.cooperativepatentclassification.org/home> (accessed on 7 August 2023).
4. EPO-USPTO Presentation—CPC Status Update. Available online: <https://www.cooperativepatentclassification.org/sites/default/files/attachments/970c93f0-c03f-4cde-a88a-a72bac6b7c2c/CPC+Annual+meeting+with+industry+users+29+March+2021.pdf> (accessed on 7 August 2023).
5. Blokhina, Y.V.; Ilin, A.S. Use of Patent Classification in Searching for Biomedical Information. *Russ. J. Bioorg. Chem.* **2021**, *47*, 1225–1230. [CrossRef]
6. Degroote, B.; Held, P. Analysis of the patent documentation coverage of the CPC in comparison with the IPC with a focus on Asian documentation. *World Pat. Inf.* **2018**, *54*, S78–S84. [CrossRef]
7. Barbieri, M. Patent Prior Art Searches: Basic Principles and Strategies. *Preprints* **2022**, 2022050054. [CrossRef]
8. Machuca-Martinez, F.; Camargo Amado, R.; Gutierrez, O. Coronaviruses: A patent dataset report for research and development (R&D) analysis. *Data Brief* **2020**, *30*, 105551. [CrossRef] [PubMed]
9. Shen, X.; Zheng, Q.; Kim, J.K. Rational design of two-dimensional nanofillers for polymer nanocomposites toward multifunctional applications. *Prog. Mater. Sci.* **2021**, *115*, 100708. [CrossRef]

10. Simmons, E.S. Black sheep in the patent family. *World Pat. Inf.* **2009**, *31*, 11–18. [CrossRef]
11. Shao, W.; Cui, T.; Li, D.; Jian, J.; Li, Z.; Ji, S.; Cheng, A.; Li, X.; Liu, K.; Liu, H.; et al. Carbon-Based Textile Sensors for Physiological-Signal Monitoring. *Materials* **2023**, *16*, 3932. [CrossRef] [PubMed]

**Disclaimer/Publisher’s Note:** The statements, opinions and data contained in all publications are solely those of the individual author(s) and contributor(s) and not of MDPI and/or the editor(s). MDPI and/or the editor(s) disclaim responsibility for any injury to people or property resulting from any ideas, methods, instructions or products referred to in the content.

Proceeding Paper

# Wearable Two-Channel PPG Optical Sensor with Integrated Thermometers for Contact Measurement of Skin Temperature <sup>†</sup>

Jiří Přibil \*, Anna Přibilová and Ivan Frollo

Institute of Measurement Science, Slovak Academy of Sciences, 841 04 Bratislava, Slovakia;  
anna.pribilova@savba.sk (A.P.); ivan.frollo@savba.sk (I.F.)

\* Correspondence: jiri.pribil@savba.sk; Tel.: +421-2-59104543

<sup>†</sup> Presented at the 10th International Electronic Conference on Sensors and Applications (ECSA-10),  
15–30 November 2023; Available online: <https://ecsa-10.sciforum.net/>.

**Abstract:** Many factors affect photoplethysmography (PPG) signal quality, one of them being the actual temperature of the skin surface. This paper describes the process of design, realization, and testing of a special wearable PPG sensor prototype with the contact thermometer measuring in detail the skin temperature in the place where the optical part of the PPG sensor touches a finger/wrist. Performed experiments confirm continual increase of temperature at the place of worn PPG sensors during the whole measurement, influencing mainly the PPG signal range. Other parameters seem to be temperature-independent or influenced by other factors—blood pressure, heart rate, etc.

**Keywords:** photoplethysmography optical sensor; wearable sensor; PPG wave features; contact skin temperature measurement

## 1. Introduction

At present, cardiovascular magnetic resonance imaging (MRI) is an important imaging technique used for investigation of the heart structure and its function. However, in this type of non-invasive examining device, the pulsating current in the gradient coil system generates mechanical vibration and acoustic noise [1]. Such a vibration is often accompanied by a local heating effect which can be measured by a contactless method using a thermal imaging camera [2]. The shape of the peripheral pulse wave of the photoplethysmography (PPG) signal reflects the current state of a human cardiovascular system, including changes in arterial stiffness, blood pressure (BP), and heart rate (HR) [3]. These parameters can also be used for detection of the stress effect [4,5] during examination in an MRI device working with a low magnetic field [6], which is our final long-term research aim.

The quality of the sensed PPG signals and the determined PPG wave features depend also on the actual state of the skin at the position of the optical sensor. Age and gender as well as skin color and the temperature of the skin surface can have an influence on the PPG signal, too. Our previous solution of wearable PPG sensors [7] does not allow direct temperature measurement by any contact thermo-element during the PPG signal sensing. For precise determination of PPG wave parameters, the current temperature should be measured at the same time as the PPG signal is sensed. According to the reactions of the tested persons, we know that the majority of them gradually felt pressing and thermal effect on a finger (wrist) at the contact of the sensor with the skin. While the time duration of the PPG signal sensing was about 1 min, the total time of wearing the optical sensor was about 15 min (including the initial time for basic manipulation during sensor mounting, creation of BT connection with a control laptop, calibration, and testing of the obtained PPG signals in the real-time monitoring mode).

The motivation of the current work was to confirm or reject this subjective feeling of local warming by practical measuring experiments, using a special prototype of the

**Citation:** Přibil, J.; Přibilová, A.; Frollo, I. Wearable Two-Channel PPG Optical Sensor with Integrated Thermometers for Contact Measurement of Skin Temperature. *Eng. Proc.* **2023**, *58*, 108. <https://doi.org/10.3390/ecsa-10-16249>

Academic Editor: Stefano Mariani

Published: 15 November 2023



**Copyright:** © 2023 by the authors. Licensee MDPI, Basel, Switzerland. This article is an open access article distributed under the terms and conditions of the Creative Commons Attribution (CC BY) license (<https://creativecommons.org/licenses/by/4.0/>).

multi-channel wearable PPG sensor with integrated thermometers. In addition, we try to formulate a recommendation about a proper arrangement and timing of PPG signal sensing to obtain the desired PPG parameters with a sufficient accuracy. Described first-step experiments were realized in normal laboratory conditions, with planned further application for measurements inside a running low-field MRI device [7,8].

This paper describes the process of design, realization, and testing of a special prototype of a two-channel wearable PPG sensor with contact thermometers to carry out a detailed measurement of the skin temperature at the point where the optical part of the PPG sensor touches a finger/wrist. Received data (PPG signal/temperature values) are next processed and analyzed statistically. Obtained partial and summary results for all tested persons are presented separately, using graphical as well as numerical forms depending on the type of the processed data. Performed measurements confirm continual increase of temperature at the place of worn PPG sensors during the whole measurement experiment, with the main influence being on the PPG signal range. Other parameters seem to be temperature-independent or affected by other factors—BP, HR, etc.

## 2. Methods

### *Determination of PPG Wave Properties and Analysis of Temperature Value Sequences*

To describe the signal properties of the sensed PPG waves, the energetic, temporal, and statistical parameters can be determined. The currently used methodology of the PPG wave properties, including heart rate determination from the PPG wave, was described in more detail in [8]. The smoothing and de-trending operations must be applied on the sensed raw PPG signal in the frame of pre-processing. All systolic peaks  $P_{SYS}$  are located, and their min/max levels ( $Lp_{MIN}/Lp_{MAX}$ ) and the PPG signal offset level ( $L_{OFS}$ ) are determined, as shown in Figure 1a. The mean signal offset value  $\mu L_{OFS}$  is then used to calculate the relative percentage PPG signal range  $S_{RANGE}$  as:

$$S_{RANGE} = ((Lp_{MAX} + Lp_{MIN})/2 - \mu L_{OFS})/AD_{RES} \times 100 \text{ [%]}, \quad (1)$$

where  $AD_{RES}$  is the resolution of the analog-to-digital converter used to digitize the analog signal output of the PPG optical sensor. Next, the modulation (ripple) of heart pulses as a percentage is calculated as:

$$HP_{RIPP} = (Lp_{MAX} - Lp_{MIN})/Lp_{MAX} \times 100 \text{ [%]}. \quad (2)$$

The peak positions  $P_{SYS}$  are next applied to determine the heart cycle periods  $T_{CP}$ , and using the sampling frequency  $f_S$  [Hz] the heart rate is evaluated as  $HR = 60/(T_{CP} \times f_S)$  (bpm)—see Figure 1b. The two-channel PPG parallel signal ( $PPG_A$ ,  $PPG_B$  waves) can be used to determine the distances between  $P_{SYS}$  positions in samples ( $\Delta P_{SYS}$ ). These values are applicable for calculation of relative percentage parameter  $rPTT$ , invariant on the current  $HR$  value:

$$rPTT = (PTT/T_{CP}) \times 100 \text{ [%]}. \quad (3)$$

where  $PTT$  represents the pulse transmission time defined as a time difference between two systolic peaks measured in parallel by sensors located at a known distance [9], calculated as  $PTT = \Delta P_{SYS}/f_S$ —see Figure 1c,d.

To describe temperature changes during the measurement with the time duration  $t_{DUR}$ , the linear trend is calculated by the least squares fitting technique of linear regression. For practical use, the difference  $\Delta T$  between the temperature values estimated at the start and the end of measurement ( $\Delta T = T_{END} - T_{START}$ ) is determined. Next, the gradient parameter  $T_{GRAD}$  is calculated as the ratio:

$$T_{GRAD} = (\Delta T/t_{DUR}) \text{ [}^\circ\text{C/s]}, \quad (4)$$

Positive  $\Delta T$  and  $T_{GRAD}$  values show the rising temperature trend, and negative ones represent the falling trend. During the current experiments, we have obtained sequences



of  $T_1$ ,  $T_2$  temperature values measured in parallel by two thermometers. From these sequences, the differential parameter  $T_{12\text{DIFF}}$  was determined from the values at  $T_{\text{END}}$  positions. For summary comparison, the variability  $(HR_{\text{VAR}}, T_{\text{VAR}})$  was next calculated as a ratio between the mean  $\mu$  and the standard deviation  $\sigma$  of an input sequence  $X$  ( $HR$  or  $T$ ) as  $X_{\text{VAR}} = (\sigma X / \mu X)$ . Thus, in the final numerical comparison, the temperature parameters of  $T_{\text{VAR}}$ ,  $\Delta T$ ,  $T_{\text{GRAD}}$ , and  $T_{12\text{DIFF}}$  were used. In the case of PPG signal properties, the differential values  $(\Delta HR_{\text{VAR}}, \Delta S_{\text{RANGE}}, \Delta HP_{\text{RIPP}}$ , and  $\Delta r\text{PTT}$ ) were calculated separately for each PPG wave  $(\text{PPG}_{\text{A,B}})$ .

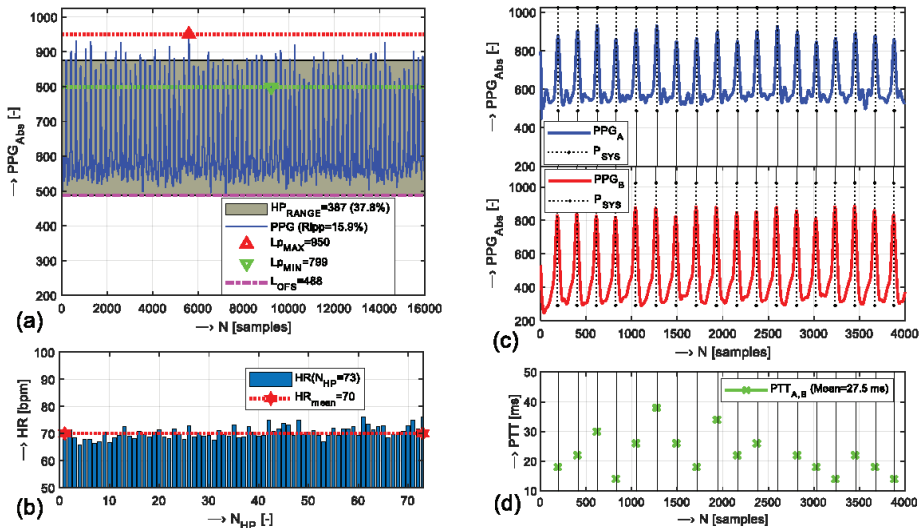


**Figure 1.** Example of determination of temporal and pulse transmission time parameters: (a) 15 k sample two-channel PPG signal ( $\text{PPG}_A$  wave) with determined  $L_{p\text{MAX}}$ ,  $L_{p\text{MIN}}$ , and  $L_{\text{OFS}}$  values, together with  $HP_{\text{RANGE}}$  and heart ripple parameters; (b) HR values corresponding to pulse periods  $T_{\text{HP}}$  ( $N_{\text{HP}} = 70$ ) and a mean HR; (c) visualization of  $P_{\text{SYS}}$  positions of 4092 sample parts of  $\text{PPG}_A$  and  $\text{PPG}_B$  waves; (d) determined  $PTT$  values with their mean value;  $f_s = 250$  Hz.

### 3. Objects, Experiments and Results

The developed wearable two-channel PPG sensor with two integrated thermometers (below called “PPG-4TP”) consists of:

- the micro-controller board Adafruit Metro Mini 328 (Adafruit 2590) by Adafruit Industries, NY, USA, based on the processor ATmega328 by Atmel Company, working at  $f_{\text{CLK}} = 16$  MHz, with eight 10-bit A/D converters, including also a hardware SPI port, a hardware I2C port and a hardware UART to USB [10];
- the bi-directional communication BT module MLT-BT05 by Technics Ltd., Shenzhen, China, working according to the BT4.0 BLE standard at 2.4 GHz;
- two optical PPG sensors working in a reflectance mode with fully integrated analog interfaces—a Crowtail-Pulse Sensor (ER-CT010712P) by Elecrow Company, Shenzhen, China (below called “OS1”), and a Gravity Heart Rate Sensor (SEN0203) by Zhiwei Robotics Corp., Shanghai, China (below called “OS2”);
- two integrated precision I2C thermometers (“MCP1”, “MCP2”), based on Adafruit MCP9808 temperature sensors [11] by Adafruit Industries, NY, USA.

All sensor components are powered via the USB port by a THAZER 5V power bank (with 2200 mAh capacity). The MCP9808 sensors enable temperature measurement in the range of  $-40$  °C to  $+125$  °C, with a typical accuracy of  $\pm 0.125$  °C [11]. Each sensor includes three address pins, so up to eight sensors can be connected in parallel to a single I2C bus. To enable further measurements in the weak magnetic field environment of an

MRI device, the whole PPG sensor consists of non-ferromagnetic components and all parts are fully shielded by aluminum boxes against radiofrequency disturbance. The currently realized PPG-4TP sensor prototype enables: (1) real-time monitoring and displaying of PPG signals picked up currently from optical PPG sensors and thermometers, and (2) continuous real-time two-channel PPG signal measurement with selected sampling frequency  $f_s = \{125, 250, 500, \text{ and } 1000 \text{ Hz}\}$  in data blocks of  $N_{MEAS} = \{1k, 4k, 16k, 32k, \text{ and } 64k\}$  samples. In parallel, the temperature values from two MPC9808 sensors can be taken in time intervals  $T_{INT} = \{0.2, 1, 2, 4, \text{ and } 10 \text{ s}\}$ .

The developed PPG sensor was tested in two steps: after checking of functionality, including the BT data transmission to the control device and verification of quality of real-time two-channel PPG signals and temperature T1, T2 values from thermo-sensors MCP1, MCP2, practical measuring experiments in normal laboratory conditions were carried out. They consisted of real-time sensing of two PPG waves and temperature values from two thermometers simultaneously with parallel control measurement of BP and heart rate values ( $HR_{BPM}$ ) by a BPM device. In this case, the tested person was sitting with both hands laid on a table located in a quiet office room; no visual or acoustic stimuli were present during the measurement (no conversation, no drinking, etc.).

Measuring experiments started with the reference phase (MF0), during which a 10 s record of temperature T1,2<sub>REF</sub> values were measured with both MCP sensors freely laid on the desk. Within the initialization phase, optical PPG sensors OS1 and OS2 were mounted on the person's left/right hand and the pressure cuff of a portable BPM device was worn on the other arm of the tested person. Then, in the monitoring mode, the quality of sensed PPG signals was verified before the start of the practical measurements in three main phases (MF1–3). In the frame of MF1, MF3 phases, two-channel PPG signals were recorded together with measured temperatures T1, T2.

The first optical PPG sensor OS1 with the thermo-sensor MCP1 was placed on the wrist artery (W), and the OS2 sensor with MCP2 thermo-sensor was worn successively on the index finger (F4), as demonstrated by the arrangement photo in Figure 2a. In parallel, the BP and  $HR_{BPM}$  values were measured manually on the opposite hand using the portable BPM device Microlife BP A150-30 AFIB by Microlife AG, Widnau, Switzerland. In phase MF2, with a time duration of 10 min (600 s), the values from thermo-sensors MPC1, MPC2 were received and stored to an output file without PPG signal sensing. The total time duration of whole experiments was approx. 15 ÷ 20 min (depending on the length of the initialization part—see the time schedule in Figure 2b). In the MF0 phase, the temperature values were taken in the intervals of  $T_{INT} = 1 \text{ s}$ , during the MF1 and MF3 phases  $T_{INT} = 0.2 \text{ s}$  was applied, and for measurement in the MF2 phase  $T_{INT} = 4 \text{ s}$  was used.

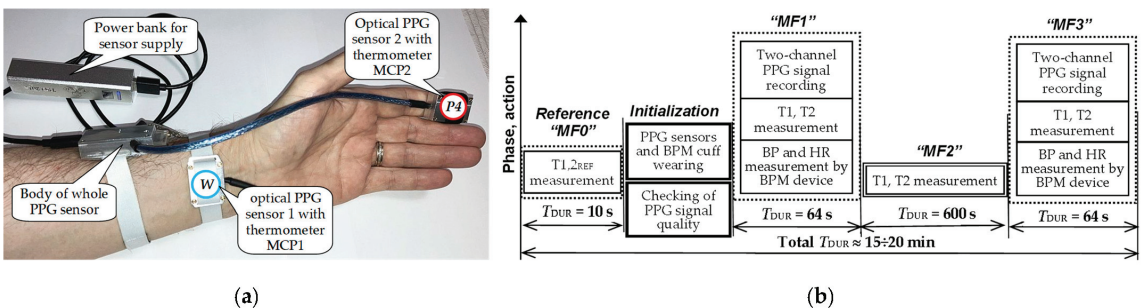
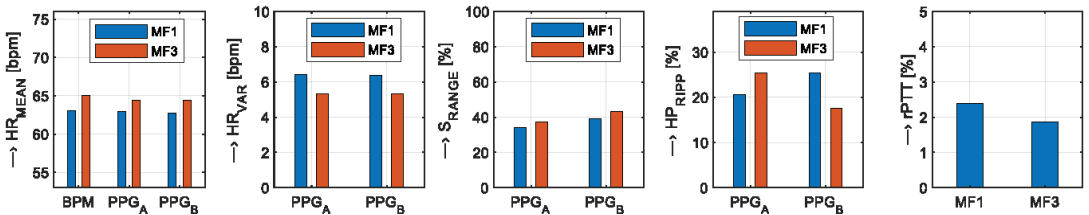


Figure 2. Arrangement of PPG and temperature measurement experiments: (a) principal photo; (b) experimental and time schedule used.

The currently collected corpus of two-channel PPG signals and temperature sequences consists of records taken from eight non-smoker volunteers—six males (P1-6<sub>M</sub>) and two females (P1-2<sub>F</sub>)—with a mean age of 50 years. Each database record includes: (1) two PPG wave files (containing PPG signals and T1, T2 sequences sensed in parallel during the MF1 and MF3 phases), accompanied by two files with BP and HR values measured manually by the external BPM device; (2) two separate files with temperature and time values recorded during the MF0 and MF2 phases.

Partial and summary results obtained for all tested persons are evaluated separately depending on the processed signal type. Partial results of signal parameters determined from PPG waves taken within the MF1 and MF3 measurement phases for one person are shown in Figure 3; summary numerical values of the investigated differential parameters for all tested subjects are enumerated in Table 1. The demonstration example of concatenated temperature sequences from the MF0–3 phases for the MCP1, MCP2 thermo-sensors can be seen in Figure 4; visualization of corresponding statistical parameters is shown in the graphs in Figure 5. Summary temperature differential and statistical parameters separately for the MCP1, MCP2 thermo-sensors for all tested persons are presented in Table 2.



**Figure 3.** Partial results of PPG signal properties taken in the MF1 and MF3 phases for person P4<sub>M</sub> (from left to right): mean HR values, HR variations, PPG signal range and HP ripple, and relative PTT values.

**Table 1.** Summary mean differential parameters together with their std (in parentheses) determined separately for PPG<sub>A</sub> and PPG<sub>B</sub> waves within the MF1, MF3 phases for all tested persons.

PPG Signal	$\Delta HR_{VAR}$ [%]	$\Delta S_{RANGE}$ [%]	$\Delta HP_{RIPPLE}$ [%]	$\Delta rPTT$ [%]
PPG <sub>A</sub>	−2.70 (1.51)	7.10 (3.35)	1.33 (1.35)	−0.496 (0.86)
PPG <sub>B</sub>	−3.32 (1.59)	3.19 (2.35)	−6.15 (1.46)	

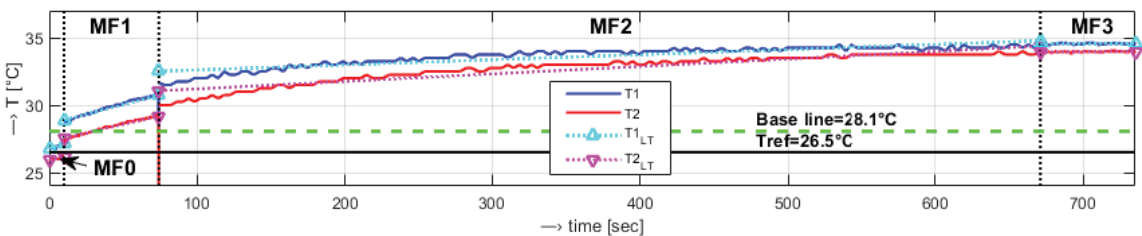


**Figure 4.** Concatenated sequences from thermo-sensors MCP1, MCP2 together with fitted linear regressions  $T_{1,2,LT}$ , calculated mean, and  $\Delta T$  values; concatenated for measuring phases MF0–3.  $T_{REF} = 26.5$  °C, baseline for MF1–3 measurements is 28.1 °C,  $t_{DUR} = 738$  s, person P1<sub>M</sub>.

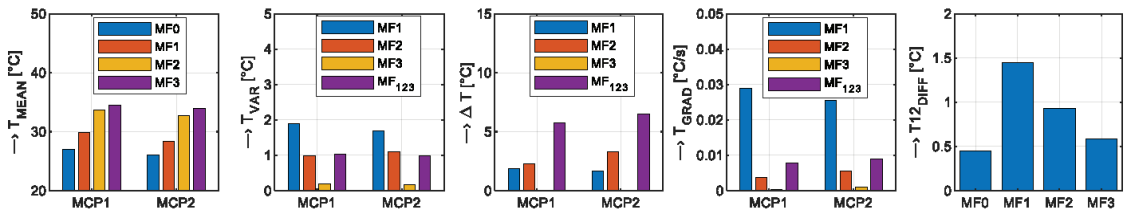


**Figure 5.** Statistical parameters determined from temperature sequences T1, T2 from thermo-sensors MCP1, MCP2 introduced in Figure 4 (from left to right): mean values, relative variations,  $\Delta T$  values, gradients, and differential T12 values between MCP1s and MCP2s for each of three measurement phases (MF1–3); final values MF123 determined for whole measurement.

**Table 2.** Summary temperature mean parameters, together with their std (in parentheses), determined inMF0–3 phases separately for MCP1, MCP2 thermo-sensors, for all tested persons.

Phase	$T_{VAR}$ [°C]		$\Delta T$ [°C]		$T_{GRAD}$ [°C/s]		$T12_{DIFF}$ [°C]
	MCP1	MCP2	MCP1	MCP2	MCP1	MCP2	
MF0	—	—	—	—	—	—	0.11 (0.2)
MF1	0.47 (0.63)	0.49 (0.54)	1.3 (0.72)	1.1 (0.66)	0.0208 (0.0113)	0.0175 (0.0103)	1.37 (0.8)
MF2	0.67 (0.2)	0.68 (0.23)	1.9 (1.50)	2.4 (1.51)	0.0031 (0.0024)	0.0041 (0.0025)	1.08 (0.9)
MF3	0.19 (0.02)	0.24 (0.08)	0.04(0.04)	0.04 (0.03)	0.0006 (0.0007)	0.0006 (0.0005)	0.93 (0.8)
$\Sigma$ MF1–3	0.45 (0.3)	0.47 (0.2)	4.3 (2.1)	4.1 (2.1)	0.0058 (0.0021)	0.0056 (0.0030)	0.87 (0.5)
Final	0.46 (0.019)		4.20 (0.087)		0.0057 (0.0002)		—

#### 4. Discussion and Conclusions

The performed experiments demonstrated a continually raised temperature during all 12-min measurements consisting of phases MF1–3. It was caused partially by internal heating from powered analogue parts of optical sensors but mainly by contact warming from the skin of the hand (wrist and finger) of the tested person. Next, it was found that the temperature increase depends heavily on the placement of the PPG sensors: higher  $\Delta T$  values were obtained from the thermo-sensor MCP1 located on the wrist, but the final increase of T2 values taken from the index finger by the MCP2 thermo-sensor was always lower. While the difference between T1 and T2 values obtained in the reference phase MF0 was minimal (typically given by a chosen precision of the used thermo-sensors), the maximum  $T12_{DIFF}$  was detected usually at the end of the MF1 phase, and it was practically constant until the end of the whole experiment. The same trend was observed for the  $T_{GRAD}$  parameter, but the variability of T1, T2 values was slightly higher in the frame of the MF2 phase, as documented the summary values in Table 2.

Temperature changes also influence the parameters of PPG signals sensed in the M1 and MF3 phases—compare the summary values in Table 1. Two-channel PPG signals (PPG<sub>A</sub> and PPG<sub>B</sub> waves) taken in the MF3 phases always have a higher  $S_{RANGE}$  in comparison with the one sensed in the MF1 phase, during which the temperatures T1 and T2 are lower. In the case of the HP ripple, this trend was not finally confirmed—so these values are practically temperature-independent. Higher relative variation of HR values determined from PPG waves in the MF1 phase are directly related to a lower PPG signal range (generally similar to the signal-to noise ratio in the signal processing area). Finally, slight (although not important) changes detected in the  $rPTT$  parameter can be affected by other factors—mainly by the blood pressure.

The final recommendation following from the experiments performed currently is to keep the optical PPG sensors worn on the tested fingers (wrist) ca 5–10 min before the start of the PPG signal sensing to obtain proper PPG waves with sufficient signal range and pronounced systolic peaks. It is important to obtain subsequently determined parameters with the proper accuracy.

**Author Contributions:** Conceptualization and methodology, J.P., A.P. and I.F.; data collection, processing, and visualization, J.P.; writing—original draft preparation, J.P. and A.P.; writing—review and editing, A.P.; project administration, J.P.; funding acquisition, J.P. All authors have read and agreed to the published version of the manuscript.

**Funding:** This work was funded by the Slovak Scientific Grant Agency project VEGA2/0004/23.

**Institutional Review Board Statement:** Institutional review board statement was waived for this study, due to testing authors themselves and colleagues from IMS SAS. No personal data were saved; only PPG signals and skin temperature sensed on wrist/finger and blood pressure values were used in this research.

**Informed Consent Statement:** Not applicable.

**Data Availability Statement:** The data supporting reported results are not readily available because they can be used only for research purposes and our paper must be cited where our data are used. Requests to access the data should be directed to the corresponding author Dr. Jiří Přibil.

**Acknowledgments:** We would like to thank all our colleagues who participated in the PPG signal recording and temperature measurement experiments.

**Conflicts of Interest:** The authors declare no conflicts of interest.

## References

1. Moelker, A.; Wielopolski, P.A.; Pattynama, P.M.T. Relationship between magnetic field strength and magnetic-resonance-related acoustic noise levels. *Magn. Reson. Mater. Phys. Biol. Med.* **2003**, *16*, 52–55. [CrossRef] [PubMed]
2. Glowacz, A. Thermographic fault diagnosis of electrical faults of commutator and induction motors. *Eng. Appl. Artif. Intell.* **2023**, *121*, 105962. [CrossRef]
3. Nitzan, M.; Ovadia-Blechman, Z. Physical and physiological interpretations of the PPG signal. In *Photoplethysmography: Technology, Signal Analysis, and Applications*; Kyriacou, P.A., Allen, J., Eds.; Elsevier: London, UK, 2022; pp. 319–339, ISBN 978-0-12-823374-0.
4. Celka, P.; Charlton, P.H.; Farukh, B.; Chowienczyk, P.; Alastruey, J. Influence of mental stress on the pulse wave features of photoplethysmograms. *Heal. Technol. Lett.* **2020**, *7*, 7–12. [CrossRef] [PubMed]
5. Steckner, M.C. A review of MRI acoustic noise and its potential impact on patient and worker health. *eMagRes* **2020**, *9*, 21–38. [CrossRef]
6. Marques, J.P.; Simons, F.J.; Webb, A.G. Low-field MRI: An MR physics perspective. *J. Magn. Reson. Imaging* **2019**, *49*, 1528–1542. [CrossRef] [PubMed]
7. Přibil, J.; Přibilová, A.; Frollo, I. Comparison of three prototypes of PPG sensors for continual real-time measurement in weak magnetic field. *Sensors* **2022**, *22*, 3769. [CrossRef] [PubMed]
8. Přibil, J.; Přibilová, A.; Frollo, I. First-step PPG signal analysis for evaluation of stress induced during scanning in the open-air MRI device. *Sensors* **2020**, *20*, 3532. [CrossRef] [PubMed]
9. Zhang, M.; Wei, P.F.; Li, Y. A LabVIEW based measure system for pulse wave transit time. In Proceedings of the International Conference on Information Technology and Applications in Biomedicine, ITAB 2008, Shenzhen, China, 30–31 May 2008.
10. Adafruit Metro Mini 328 V2—Arduino-Compatible—5V 16 MHz—STEMMA QT/Qwiic. Available online: <https://www.adafruit.com/product/2590> (accessed on 6 January 2023).
11. Adafruit MCP9808 Precision I2C Temperature Sensor Guide. Available online: <https://cdn-learn.adafruit.com/downloads/pdf/adafruit-mcp9808-precision-i2c-temperature-sensor-guide.pdf> (accessed on 6 January 2023).

**Disclaimer/Publisher’s Note:** The statements, opinions and data contained in all publications are solely those of the individual author(s) and contributor(s) and not of MDPI and/or the editor(s). MDPI and/or the editor(s) disclaim responsibility for any injury to people or property resulting from any ideas, methods, instructions or products referred to in the content.



Proceeding Paper

# Damage Detection in Machining Tools Using Acoustic Emission, Signal Processing, and Feature Extraction <sup>†</sup>

Lucas Pires Bernardes <sup>1,\*</sup>, Pedro Oliveira Conceição Júnior <sup>1</sup>, Fabio Romano Lofrano Dotto <sup>1</sup>,  
Alessandro Roger Rodrigues <sup>2</sup> and Marcio Marques Silva <sup>3</sup>

<sup>1</sup> Department of Electrical and Computer Engineering, Sao Carlos School of Engineering (EESC), University of Sao Paulo (USP), Sao Carlos 13566-590, Sao Paulo, Brazil; pedro.oliveiracrj@usp.br (P.O.C.J.); fabio.dotto@usp.br (F.R.L.D.)

<sup>2</sup> Department of Mechanical Engineering, Sao Carlos School of Engineering (EESC), University of Sao Paulo (USP), Sao Carlos 13566-590, Sao Paulo, Brazil; roger@sc.usp.br

<sup>3</sup> The National Industrial Training Service (SENAI), Sao Carlos 13574-320, Sao Paulo, Brazil; marciomsil@gmail.com

\* Correspondence: lucasbernardes@usp.br

<sup>†</sup> Presented at the 10th International Electronic Conference on Sensors and Applications (ECSA-10), 15–30 November 2023; Available online: <https://ecsa-10.sciforum.net/>.

**Abstract:** The wear of tools in machining is one of the primary issues in manufacturing industries. Direct measurements of tool wear, such as microscopic observation, lead to increased machine downtime and reduced production rates. To improve this situation, real-time tool condition monitoring systems (TCMs) are needed, which utilize indirect measurement of tool wear through sensors and signal processing. This project focuses on the use of acoustic emission (AE) sensors for experimental analysis of tool damage under various milling conditions. The proposed approach involves designing condition indicators to quantify this damage by implementing infinite impulse response (IIR) digital filters, specifically Butterworth filters, and fast Fourier transform (FFT), in addition to root mean square (RMS), using different frequency bands of the acoustic signals collected during the process. The results from implementing this study show promise for optimizing the process through an alternative TCM system in manufacturing operations, avoiding the drawbacks of the direct method, and extending the equipment's lifespan and efficiency. It's worth noting that this document presents partial results of this implementation, which is still in progress.

**Keywords:** tool condition monitoring; acoustic emission; feature extraction; industrial automation

**Citation:** Bernardes, L.P.; Júnior, P.O.C.; Dotto, F.R.L.; Rodrigues, A.R.; Silva, M.M. Damage Detection in Machining Tools Using Acoustic Emission, Signal Processing, and Feature Extraction. *Eng. Proc.* **2023**, *58*, 109. <https://doi.org/10.3390/ecsa-10-16258>

Academic Editor: Francisco Falcone

Published: 15 November 2023



**Copyright:** © 2023 by the authors. Licensee MDPI, Basel, Switzerland. This article is an open access article distributed under the terms and conditions of the Creative Commons Attribution (CC BY) license (<https://creativecommons.org/licenses/by/4.0/>).

## 1. Introduction

The degradation of the quality of industrial assets due to wear and the increased product cost due to frequent tool replacement is the primary issue in high-speed machining (HSM). The deformation or damage of the cutting edge of a tool during machining due to interactions between the tool and the workpiece is referred to as tool wear. In manufacturing industries, maintenance costs and downtime increase, and production rates decrease due to the failure of cutting tools [1].

Tool condition monitoring systems (TCMs) are useful for these industries as they reduce downtime and increase productivity. The monitoring process helps prevent tool and workpiece damage, improves the productivity and quality of the machined product, and predicts tool wear [2]. According to Quintana and Ciurana [3], the early identification of regenerative vibration (when vibration has just begun and has not fully developed) is essential to minimize its negative effects, such as catastrophic damage to the tool and workpiece. These researchers have chosen vibration recognition strategies in processes as a key line of investigation regarding vibration, emphasizing the importance of obtaining relevant and useful signals and finding efficient signal processing algorithms.

Furthermore, Jantunem [4] extensively studied signal sources (motor spindle currents, acoustic emissions, vibrations, and sounds) as well as TCM analysis methods for drilling, emphasizing that the tool life could not be satisfactorily achieved without TCM due to variations in the actual tool life.

This study was validated through experimental analysis conducted in the milling process, a machining process involving the removal of material from the surface of a workpiece using a rotating cutting tool, called a milling cutter. This tool features multiple cutters or cutting edges, enabling precise cutting and the creation of various shapes and features on the workpiece. The wear of this milling cutter is a gradual damage that occurs over operations, directly affecting dimensional accuracy and surface finish quality. Thus, TCMs become essential. The proposed system in this paper utilizes wireless technologies to collect and transmit acoustic signals generated during milling, which is a key aspect that differs from previous contributions based on traditional acoustic emission systems [5,6]. This approach involves the design of condition indicators that quantify the damage incurred through the implementation of Butterworth-type digital filters, FFT, and the RMS, to quantify the tool wear and validate the effectiveness of the acoustic emission strategy.

The study was conducted by testing different frequency bands of the acoustic signals collected during the process through FFT calculations. The results of this research are significant for increasing productivity, reducing manufacturing costs and material waste, optimizing the life of the milling cutter, reducing the risks of higher-order damage in the process, and taking quick actions when damage occurs. These findings are relevant for the optimization of the manufacturing process.

## 2. Materials and Methods

### 2.1. Experiments

For the study, a machining tool, machine tool, acoustic frequency pickup sensor, carbon plate, and three devices for fixing the carbon plates were used, made of resin, steel, and aluminum. The data acquisition system was composed of a wireless piezoelectric AE sensor, which was responsible for detecting information relating to the condition of the tool and which was expressed through electrical signals digitized on a computer using an acquisition board at sampling rates of the order of 250 kHz. In total, 18 tests were carried out, but only from the seventh signal onwards was it possible to capture them correctly, resulting in 12 useful signals. The milling process diagram is shown in Figure 1.

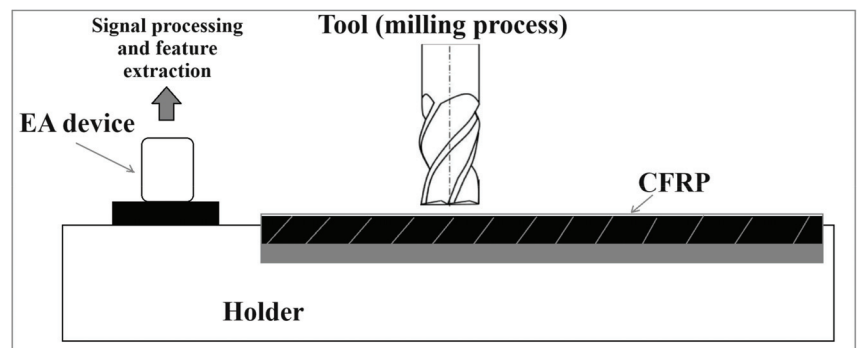


**Figure 1.** Schematic of the milling process and data collection by the sensor.

### 2.2. Feature Extraction

The signals were pre-processed and consolidated for data processing and analysis using the proposed methodology, which involved preprocessing to prepare, filter, and eliminate noise. The generated dataset was labeled for use in digital processing routines through MATLAB® software (version 9.13/2022b).

After collecting the signals in the time domain and importing them into MATLAB®, the FFT was calculated for the most relevant signals (avoiding redundant support) using an 8192-point Hanning window. Subsequently, four frequency ranges were selected, which proved to be relevant for the study as they had the highest magnitudes, excluding very low frequencies, as these are highly susceptible to noise, such as electromagnetic noise from the 60 Hz electrical network and thermal noise. One of these specific ranges is a high-frequency range, which was chosen to determine if high frequencies are relevant for the analysis of milling cutter wear.

To calculate the mean of the RMS signals, the signals were first filtered in the time domain within specific chosen frequency bands to isolate certain signal ranges and identify patterns. This was done using a 5th-order Butterworth digital IIR bandpass filter. Subsequently, the mean RMS of these signals was calculated to analyze their behavior at different frequencies.

### 3. Results and Discussion

The analysis of the results was carried out by observing the most relevant characteristics related to the tool condition extracted using the proposed method. This was based on the comparison of the different levels of damage with their reference (the tool condition before the start of the experiment). Repetitions of the analyses were also performed to ensure reliability in the acquisition of information.

#### 3.1. Tool Wear Analysis

During the experiments, it was observed that the tool exhibited rapid wear due to the abrasiveness of the composite material throughout the drilling process. Figure 2 illustrates a microscopic image of the tool after the experimental tests. It can be observed that the edges experienced wear, resulting in a loss of cutting ability and consequently affecting the accuracy of the drilling operation. In addition, the edge showed a slight rounding, making the cutting inefficient and increasing the delamination effect in composite material.

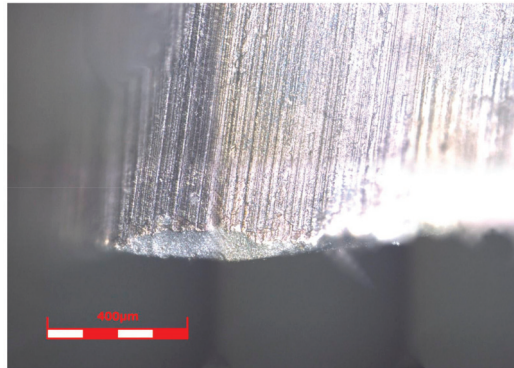


**Figure 2.** Tool wear analysis.

#### 3.2. Time Domain

Figure 3 shows the raw (unprocessed) signals in the time domain on the resin, aluminum, and steel supports. As expected, it can be observed that the behavior of AE (acoustic emission) from the milling cutter changed according to the support material. It is noticeable that the amplitudes (in volts) on the steel and aluminum supports were higher than on the resin support, which was expected, as resin, due to its mechanical properties, tends to dampen vibrations (which generate acoustic emissions), which is not the case with steel and aluminum. However, in the time domain, it can be difficult to discern differences



between signals from the same support, making frequency domain analysis necessary for studying milling cutter wear.

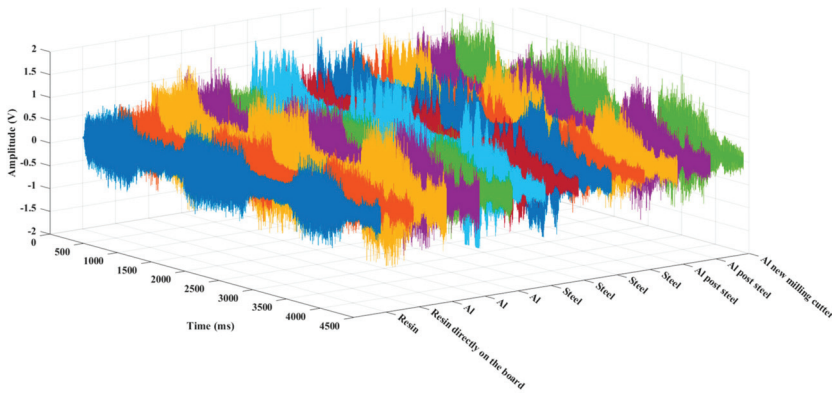


**Figure 3.** All 12 relevant signals are plotted side by side, on their respective supports, in the time domain.

### 3.3. Frequency Domain

In Figure 4, the FFTs of some signals, considered the most relevant (avoiding repetition of support), are presented. Initially, there are significant amplitudes at low frequencies, near 0 Hz, but this range was disregarded for analysis due to the presence of a lot of electromagnetic noise from the 60 Hz power grid, as well as thermal noise. Therefore, frequency ranges from 40 to 80 kHz, 10 to 20 kHz, and 20 to 40 kHz were identified in decreasing order of relevance, based on their significant magnitudes in the signals. Finally, the range from 140 to 170 kHz was chosen to examine the signal behavior at high-frequency ranges and determine its relevance for the analysis.

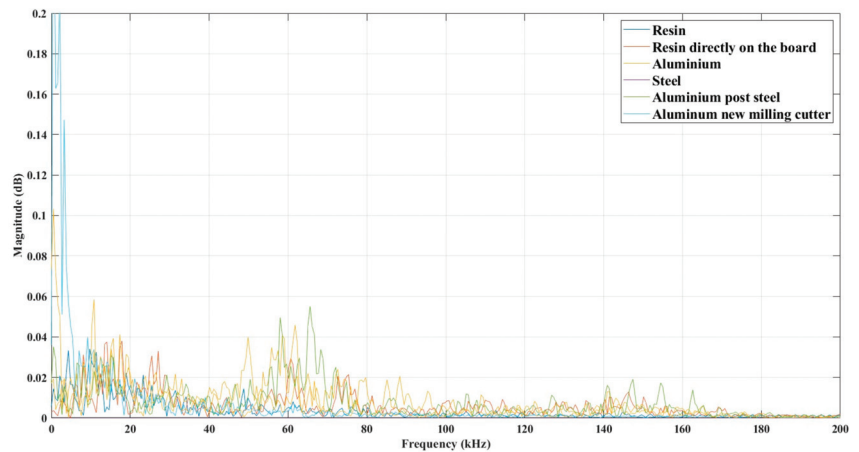


**Figure 4.** FFT of the main AE signals studied, in the range from 0 to 200 kHz.

### 3.4. RMS Signals

In Figure 5, you can see the averages of the bandpass-filtered RMS signals in the chosen frequency ranges. Firstly, the range from 40 to 80 kHz proved to be the most important for the TCM (tool condition monitoring) study, as it showed the highest magnitudes of acoustic emission between passes and supports, as well as greater variations. This allows

for the derivation of values that indicate wear, breakage, or fractures in the milling cutter. Additionally, the range from 10 to 20 kHz was also significant, exhibiting considerable amplitude variations, especially for the aluminum support, which varied significantly between passes. Furthermore, the range from 20 to 40 kHz also yielded good results, though it was of lesser importance compared to the other two treated ranges.

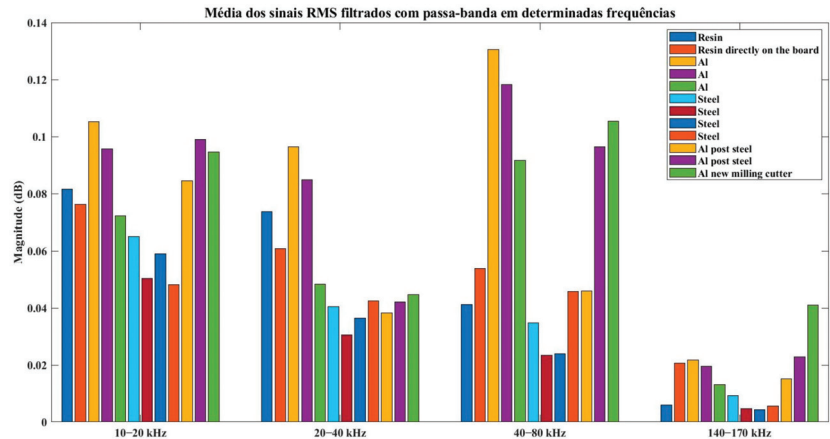


**Figure 5.** Mean of the 12 bandpass-filtered RMS signals in the chosen frequency ranges.

Lastly, the range from 140 to 170 kHz was deemed irrelevant for the study of milling cutter wear, as its magnitudes were much lower compared to the other selected ranges. This suggests that a significant portion of these magnitudes is noise rather than essential signals for TCM, indicating that high-frequency ranges are not relevant for predicting tool life in milling using acoustic emission.

#### 4. Conclusions

To ensure the quality of precision large-scale components while enhancing productivity, this study presents an alternative TCM technique to prevent tool failures and obtain comprehensive information about its state during milling through a wireless data acquisition system. It was found that AE signals contain relevant information that, with proper signal processing, enables the extraction of features that can prevent failures in the milling process. After obtaining the acoustic signals using a piezoelectric AE sensor and using MATLAB<sup>®</sup> to process these signals and extract features, applying FFT and RMS, it was concluded that the frequency ranges of 40 to 80 kHz, 10 to 20 kHz, and 20 to 40 kHz are, in that order, the most important for analyzing milling cutter wear. Additionally, it was concluded that high frequencies are of little importance for wear analysis in the process using AE sensors. In conclusion, the results of this research are significant for increasing productivity, reducing manufacturing costs, optimizing tool life, reducing the risks of higher-order damage in the milling process, and taking swift actions when needed.

**Author Contributions:** Conceptualization, P.O.C.J.; methodology, P.O.C.J., F.R.L.D., A.R.R. and M.M.S.; software, L.P.B.; validation, L.P.B.; formal analysis, L.P.B.; investigation, L.P.B.; resources, P.O.C.J., F.R.L.D., A.R.R. and M.M.S.; data curation, P.O.C.J.; writing—original draft preparation, L.P.B.; writing—review and editing, L.P.B.; visualization, P.O.C.J.; supervision, P.O.C.J.; project administration, P.O.C.J.; funding acquisition, P.O.C.J. All authors have read and agreed to the published version of the manuscript.

**Funding:** Pro-Rectorate of Research and Innovation of the University of São Paulo under grant #22.1.09345.01.2, and the São Paulo Research Foundation, under grant #2023/02413.

**Institutional Review Board Statement:** Not applicable.

**Informed Consent Statement:** Not applicable.

**Data Availability Statement:** Dataset available on request from the authors.

**Acknowledgments:** The authors would like the University of São Paulo (USP), The National Industrial Training Service (SENAI) and the São Paulo Research Foundation (FAPESP) for the opportunity to carry out and publish the research.

**Conflicts of Interest:** The authors declare no conflicts of interest.

## References

1. Dimla, D.E.; Lister, P.M. On-line metal cutting tool condition monitoring.: I: Force and vibration analyses. *Int. J. Mach. Tools Manuf.* **2000**, *40*, 739–768. [CrossRef]
2. Mohanraj, T.; Shankar, S.; Rajasekar, R.; Sakthivel, N.R.; Pramanik, A. Tool condition monitoring techniques in milling process—A review. *J. Mater. Res. Technol.* **2020**, *9*, 1032–1042. [CrossRef]
3. Quintana, G.; Ciurana, J. Chatter in machining processes: A review. *Int. J. Mach. Tools Manuf.* **2011**, *51*, 363–376. [CrossRef]
4. Jantunen, E. A summary of methods applied to tool condition monitoring in drilling. *Int. J. Mach. Tools Manuf.* **2002**, *42*, 997–1010. [CrossRef]
5. Dotto, F.R.L.; Aguiar, P.R.; Alexandre, F.A.; Lopes, W.N.; Bianchi, E.C. In-Dressing Acoustic Map by Low-Cost Piezoelectric Transducer. *IEEE Trans. Ind. Electron.* **2020**, *67*, 6927–6936. [CrossRef]
6. Viera, M.A.A.; Götz, R.; de Aguiar, P.R.; Alexandre, F.A.; Fernandez, B.O.; Junior, P.O. A Low-Cost Acoustic Emission Sensor Based on Piezoelectric Diaphragm. *IEEE Sens. J.* **2020**, *20*, 9377–9384. [CrossRef]

**Disclaimer/Publisher’s Note:** The statements, opinions and data contained in all publications are solely those of the individual author(s) and contributor(s) and not of MDPI and/or the editor(s). MDPI and/or the editor(s) disclaim responsibility for any injury to people or property resulting from any ideas, methods, instructions or products referred to in the content.



# Measurement of Soil Moisture Using Microwave Sensors Based on BSF Coupled Lines <sup>†</sup>

Warakorn Karasaeng, Jitjark Nualkham, Chuthong Summatta and Somchat Sonasang \*

Faculty of Industrial Technology, Nakhon Phanom University, Nakhon Phanom 48000, Thailand; warakorn1991air@npu.ac.th (W.K.); 667030210021@npu.ac.th (J.N.); chuthong@npu.ac.th (C.S.)

\* Correspondence: somchat.s@npu.ac.th; Tel.: +66-91949-8425

<sup>†</sup> Presented at the 10th International Electronic Conference on Sensors and Applications (ECSA-10), 15–30 November 2023; Available online: <https://ecsa-10.sciforum.net/>.

**Abstract:** This research introduces the conceptualization and examination of a microwave sensor incorporated with a microstrip band stop filter. The microwave sensor's design and assessment are based on the microstrip's parallel coupled lines, employing a band stop filter configuration at 2.45 GHz on an FR4 substrate. This study encompasses the evaluation of soil moisture spanning from 20 to 80%. The measurement procedure involved a network analyzer, specifically the KEYSIGHT model E5063A, operating within the frequency range of 100 kHz to 4.5 GHz. This investigation centers around scrutinizing the frequency response of the insertion loss ( $S_{21}$ ) across this spectrum. The outcomes of the experimentation unveiled notable disparities in frequency shifts. The resultant frequency values, labeled as  $(f_0-f_1)$ , manifested at 0, 18, 60, 89, 145, and 200 MHz, sequentially. Remarkably, the correlation between the percentage representation of the frequency shift in the transmission coefficient and the frequency itself emerged distinctly, even as the range of tested samples was finetuned.

**Keywords:** soil moisture; microwave sensors; BSF coupled lines

## 1. Introduction

Recent advancements in wireless and mobile communication technologies, driven by the escalating demand for higher transmission rates and lower latency, have ignited widespread interest among researchers [1]. They are actively working on developing sensors capable of collecting data on the electromagnetic characteristics of dielectric materials within communication channels and monitoring soil moisture levels [2]. These sensors play a crucial role in applications related to both communication and agriculture, ensuring efficient communication channels and improved crop management. Furthermore, the ability to measure soil properties, such as moisture content, provides invaluable benefits for agriculture. Accurate soil moisture data enable farmers to make informed irrigation decisions, leading to optimal water usage and healthier crops. This technology also aids in preventing overwatering or underwatering, minimizing the risk of crop yield reduction and water wastage. By integrating communication technology with soil property measurement, these advancements showcase their potential to revolutionize how we communicate and how we cultivate land and manage our vital resources.

Using microwaves to measure material properties involves employing microwave waves for material inspection and analysis. It finds applications in the following:

dielectric properties, measuring electrical characteristics and microwave signal transmission by passing waves through materials; moisture measurement, detecting moisture changes in materials through microwave wave frequency shifts; distance measurement, gauging distances by measuring wave travel time between a transmitter and receiver; and material thickness, measuring material thickness based on wave penetration and reflection,

**Citation:** Karasaeng, W.; Nualkham, J.; Summatta, C.; Sonasang, S. Measurement of Soil Moisture Using Microwave Sensors Based on BSF Coupled Lines. *Eng. Proc.* **2023**, *58*, 110. <https://doi.org/10.3390/ecsa-10-16029>

Academic Editor: Francisco Falcone

Published: 15 November 2023



**Copyright:** © 2023 by the authors. Licensee MDPI, Basel, Switzerland. This article is an open access article distributed under the terms and conditions of the Creative Commons Attribution (CC BY) license (<https://creativecommons.org/licenses/by/4.0/>).

which is a technique that has broad applications, including material testing, food moisture assessment, microwave temperature control, and more.

Ref. [1] presents a compact sensor utilizing a complementary split-ring resonator (CSRR) structure to assess relative permittivity in various dielectric materials and determine soil water content (SWC). The sensor consists of a circular microstrip patch antenna supporting a 3D printed cylindrical container made from ABS filament. The operational principle relies on changes in two antenna-resonant frequencies due to variations in the relative permittivity of the material under test (MUT). Simulations informed the development of an empirical model, and the sensor's sensitivity was examined through the characterization of typical dielectric materials. The sensor was versatile and applied to estimate water content in different soil types. Prototypes have been fabricated and compared with other research to validate effectiveness. Additionally, the sensor accurately determines water concentration in quartz sand and red clay samples.

Ref. [3] developed a compact microwave sensor using a circular microstrip patch antenna with two slotted complementary split-ring resonators (CSRRs). This sensor accurately characterizes the relative permittivity of different dielectric materials and measures water concentrations in various soil types. Its operating principle relies on comparing resonant frequencies with and without the MUT. The sensor exhibits high sensitivity, requires minimal MUT samples, and is cost-effective, lightweight, and easy to produce. The authors also established an empirical model linking resonant frequency to MUT permittivity, demonstrating strong results for known materials. The sensor's versatility extends to medical, agricultural, and chemical applications due to its sensitivity, low profile, compact size, and planar design.

Ref. [4] used passive microwave sensors to estimate soil moisture using brightness temperatures at low microwave frequencies, with the vegetation optical depth as a key factor. Retrieval algorithms aim to concurrently determine vegetation optical depth (VOD) and soil moisture (SM). However, these algorithms, often based on  $\tau$ - $\omega$  models, which consist of two third-order polynomial equations, can yield multiple solutions due to structural uncertainty. This structural uncertainty significantly affects VOD and SM retrievals, emphasizing the need to address it in soil moisture estimation algorithms.

Ref. [5] presents machine learning models for accurate soil moisture estimation using a short-range radar sensor operating at 3–10 GHz. The sensor measures volumetric water content by analyzing reflected signals. Input features extracted from these signals train various machine learning models, including neural networks, support vector machines, linear regression, and k-nearest neighbors. Model performance was assessed using metrics like the root mean square error (RMSE), coefficient of determination (R<sup>2</sup>), and mean absolute error (MAE). Among the models, neural networks achieved the best performance with an R<sup>2</sup> value of 0.9894. The research aimed to offer cost-effective solutions, particularly for agriculturists, to enhance soil moisture monitoring accuracy.

Ref. [6] presents a corrosion-resistant, embeddable, open-ended, coaxial cable soil moisture sensor. It utilizes a microwave resonator with two key components along the coaxial line: a metal post at the signal input end and a metal plate parallel to the open end, separated by a moisture-sensitive polyvinyl alcohol (PVA) film. The sensor's resonance frequency is highly sensitive to fringe capacitance, which varies with soil moisture levels. Monitoring these frequency changes allows precise tracking of soil moisture fluctuations. The article included a detailed mathematical model for the embeddable open-ended microwave coaxial cable resonator (EOE-MCCR) and demonstrated its effectiveness in soil moisture measurement. In experiments covering soil moisture levels from 4% to 24%, the prototype sensor exhibited impressive sensitivity: 0.76 MHz/% for soil moisture between 4% and 10% and 1.44 MHz/% for soil moisture between 10% and 24%. This sensor is durable, cost-effective, corrosion-resistant, and suitable for long-term and potential industrial applications.

Ref. [7] focused on soil moisture sensors for long-term monitoring of moisture levels in highway subgrades and similar applications. Two microwave sensor designs, operating in

a 4 to 6 GHz range, were studied. The first design uses a low-loss dielectric slab waveguide with a relative dielectric constant of 25. It provided high-resolution measurements for finely divided soils like bentonite clay, covering moisture levels from 10 to 50% by dry weight within effective sample volumes of 20 to 40 cm<sup>2</sup>. A model based on the index of refraction offered effective dielectric constant values that reasonably matched the experimental results when considering ionic conduction effects. The second sensor design is better suited for coarser materials like crushed limestone aggregate. It launches waves from a tapered dielectric slab and can handle aggregate particles passing through a 0.63 cm mesh sieve. It offered satisfactory resolution for moisture levels ranging from 0 to 10% by dry weight. These sensor designs have the potential for effective and long-term soil moisture monitoring in various applications, including highway subgrades.

Finally, Ref. [8] conducted observations using a dual-frequency radiometer (operating at 1.4 and 2.65 GHz) over both bare soil and corn fields for extended periods in 1994. When comparing emissivity and volumetric soil moisture at four different depths for bare soils, we found a clear correlation between the 1 cm soil moisture and the 2.65 GHz emissivity, as well as between the 3–5 cm soil moisture and the 1.4 GHz emissivity. These findings validate previous research. Our observations during drying and rainfall events revealed that these data provide valuable and novel insights for hydrologic and energy balance studies. Recent advancements in wireless and mobile communication technologies have led researchers to develop various sensors for measuring soil moisture and dielectric properties. While existing methods have made significant contributions to the field, they often face limitations in terms of accuracy, cost-effectiveness, and ease of implementation. In this context, our research introduces a novel microwave sensor design incorporating a microstrip band stop filter, aimed at addressing the shortcomings of traditional methods. By utilizing a microstrip's parallel coupled lines with a band stop filter configuration at 2.45 GHz on an FR4 substrate, our approach offers improved precision in measuring soil moisture. This paper aims to present the benefits and unique characteristics of our proposed sensor, highlighting its advantages over existing techniques. This paper presents the design and analysis of a microwave sensor for the measurement of soil moisture using an FR4 substrate and a microstrip's parallel coupled lines, as illustrated in Figure 1. The measurements were conducted using the KEYSIGHT model E5063A network analyzer. The paper is structured as follows: Section 2 covers the design and analysis of the computational band-stop filter based on microstrip parallel coupled lines and sample test. Section 3 presents the results and discusses their implications. Finally, Section 4 provides the conclusion.

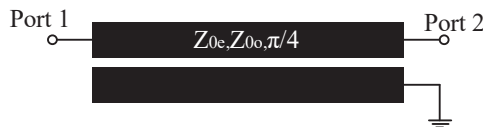


**Figure 1.** The band stop filter based on a microstrip's parallel coupled lines for the microwave sensor.

## 2. Methods

### 2.1. Design and Analysis

The proposed design involves a structure consisting of a microstrip's parallel coupled lines. These signal transmission lines were implemented using a dielectric substrate with a constant dielectric permittivity, while the upper sides of both signal transmission lines are in contact with air and have constant dielectric permittivity. Additionally, a plastic frame was created to house the experimental samples. Below the dielectric substrate, a metal plane serves as the ground plane. Typically, the length of the parallel-coupled microstrip lines is approximately equal to the wavelength of the transmission lines. This occurs because these lines are situated on an inhomogeneous medium, leading to certain effects when these transmission lines are utilized in circuits or devices operating in the microwave frequency range. The characteristic impedance of both the even and odd modes ( $Z_{0e}$ ,  $Z_{0o}$ ) can be

expressed through simple equations, as depicted in Equations (1) and (2), respectively, and based on  $Z_0 = \sqrt{Z_{0e}Z_{0o}}$ .

$$Z_{0e} = Z_0 \sqrt{\frac{1-C}{1+C}}, \quad (1)$$

$$Z_{0o} = Z_0 \sqrt{\frac{1+C}{1-C}} \quad (2)$$

In Figure 1, the microwave sensor, based on a microstrip's parallel coupled lines, was employed for assessing the characteristics of various solutions and their electrical properties within the microwave frequency range. We took into account the parametric impedance equations [9] that define a circuit representing a microwave sensor with parallel coupled lines [9]. Thus, we replaced the impedance parameters with the given values to determine the S-parameters of a 2-port network where  $S_{11}$  represents the return loss (dB) and  $S_{21}$  represents the insertion loss (dB).

$$S_{11} = \frac{(Z_{11T}^2 - Z_0^2) - Z_{12T}Z_{21T}}{(Z_{11T} + Z_0)(Z_{22T} + Z_0) - Z_{12T}Z_{21T}} \quad (3)$$

$$S_{21} = \frac{2Z_0Z_{21T}}{(Z_{11T} + Z_0)^2 - Z_{12T}Z_{21T}} \quad (4)$$

Figure 2a shows the proposed physical dimensions and Figure 2b depicts the simulated outcomes of the proposed band stop filter, presenting the  $S_{11}$  and  $S_{21}$  S-parameters. The frequency response simulations spanned from 500 MHz to 4.5 GHz, based on laboratory measurements utilizing the available equipment. A comparison was drawn between the ideal simulation and the practical implementation of the microstrip under real operating conditions. In these simulation results,  $S_{11}$  represents the return loss, indicating the reflection coefficient, while  $S_{21}$  represents the insertion loss, indicating the transmission coefficient. The power transmission from port 1 to port 4, denoted by  $S_{21}$ , with the same interpretation was illustrated. Notably, there was an enhanced power performance at 2.45 GHz and the subsequent frequencies in the ideal scenario. The physical structure of the prototype corresponds to a microwave microstrip line sensor.

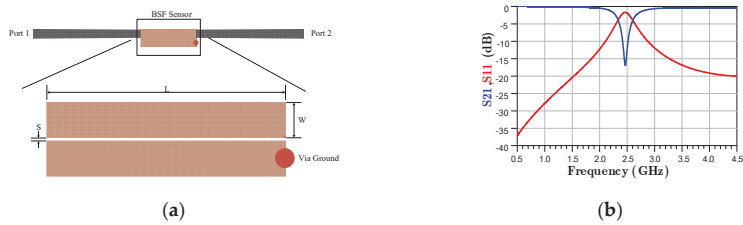


**Figure 2.** (a) The physical dimension; (b) the simulated outcomes of the suggested band-stop filter [3]. This paper aims to design and analyze a microwave sensor for soil moisture measurement, utilizing an FR4 substrate with a microstrip’s parallel coupled lines, as depicted in Figure 1. The measurements were carried out using the KEYSIGHT model E5063A network analyzer. We are currently in the process of developing a sensor that employs a microstrip’s parallel coupled lines, operating at a frequency of 2.45 GHz, and constructed with FR4 material. Concurrently, we are building a prototype for soil moisture measurement. It is crucial to consider the following key parameters: a relative dielectric constant ( $\epsilon_r$ ) of 4.55, a base material height (h) of 1.6 mm, and a loss tangent ( $\tan \delta$ ) of 0.02, as shown in Figure 3. These parameter values are crucial for determining the dimensions of the microstrip’s transmission line required to achieve our desired frequency. Our design encompasses a microstrip band stop filter characterized by a width (W) of 2.45 mm, a spacing (S) of 0.2 mm, and a length (L) of 17.06 mm, as shown in Figure 3. Within this length, there is a designated region for conducting measurements. Furthermore, we integrated an SMA connector into the sensor structure using a parallel microstrip configuration operating at 2.45 GHz.

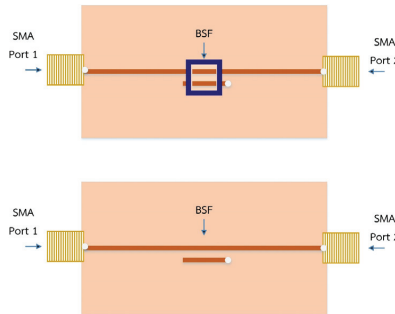


**Figure 3.** The prototype of the band stop filter for the measurement of soil.

### 2.2. The Samples of Soil Moisture Levels

In the experimental setup involving various soil moisture measurement methods, the test samples employed in this experiment underwent a production process to determine soil moisture content. For the samples of interest, soil moisture intensity was assessed using a common method involving a soil moisture meter. The device utilized is depicted in Figure 4a. Furthermore, distinct soil moisture meter values can be derived from this relationship, enabling the measurement of soil moisture content expressed in volume or %soil moisture by volume (SMBV). In this research, soil moisture intensity measurements are presented on a scale ranging from 0% to 100% in 20% increments, corresponding to different soil moisture concentrations. The mixtures were prepared by commencing with a specific soil moisture level and subsequently adding distilled water in proportionate amounts using concentration equipment, as shown in Figure 4b. The frequency response of  $S_{21}$  was measured using the KEYSIGHT model E5063A (ENA Series Network Analyzer), which operates in the frequency range of 100 MHz to 4.5 GHz, employing the proposed BSF based on the microstrip’s parallel coupled line sensor prototype.





**Figure 4.** The experimental setup; (a) involves various methods for measuring soil moisture; (b) measurement setup.

**3. Results and Discussion**

The results of the microwave sensor measurement with the microstrip BSF prototype were obtained using the KEYSIGHT brand E5063A (ENA Series Network Analyzer) within the frequency range of 100 MHz to 4.5 GHz. In Figure 5a, the results of the insertion loss ( $S_{21}$ ) experiment were measured on samples tested at different soil moisture levels, including 0% (air), 20%, 40%, 60%, 80%, and 100%. The measurement result for the insertion loss ( $S_{21}$ ) efficiency with air at a frequency operation of 2.45 GHz was  $-15.12$  dB, the soil moisture at 20% was  $-14.92$  at 2.432 GHz, the soil moisture at 40% was  $-14.85$  at 2.390 GHz, the soil moisture at 60% was  $-15.01$  at 2.361 GHz, the soil moisture at 80% was  $-15.02$  at 2.305 GHz, and the soil moisture at 100% was  $-15.01$  at 2.250 GHz. The frequency decreased accordingly with 0 MHz, 18 MHz, 60 MHz, 89 MHz, 145 MHz, and 200 MHz. The percentage change refers to the relative difference between two values, expressed as a percentage. It is often used to measure the increase or decrease in a quantity over time or between two different states—the formula used to calculate the percentage change as in Figure 5b shows the analysis of the correlation of soil moisture with the frequency shifted according to the soil moisture from 0–100%, respectively. The percentage differences were 0.00, 0.735, 2.449, 3.633, 5.918, and 8.163% between frequency increases with the soil moisture level. The experimental results show a linear relationship between the soil moisture level and BSF microstrip sensor.

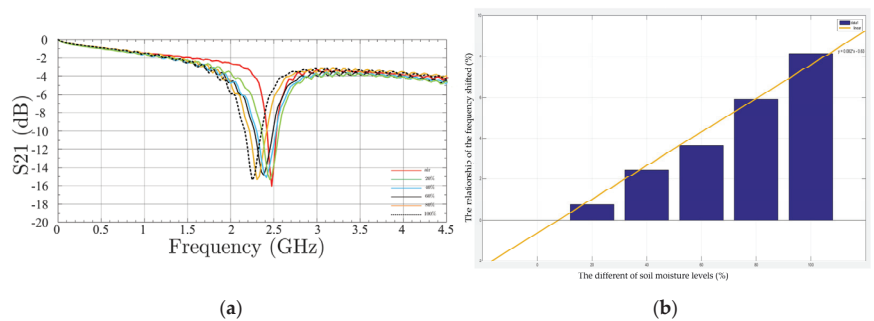


**Figure 5.** The measurement results (a) of insertion loss ( $S_{21}$ ) at different soil moisture levels and (b) the relationships between the frequency shifts.

**4. Conclusions**

In conclusion, our study demonstrates the efficacy of the microwave sensor design based on a microstrip’s parallel coupled lines with a band stop filter for accurate soil moisture measurement. The experimental results consistently show a strong correlation between the frequency shifts and varying soil moisture levels, underscoring the reliability and precision of our proposed approach. Compared to traditional methods, our sensor offers distinct advantages in terms of cost-effectiveness, accuracy, and ease of implementation, making it a valuable tool for agricultural and environmental applications. As our research

contributes to the ongoing advancements in soil moisture measurement technology, future studies could focus on integrating this approach into broader environmental monitoring systems and precision agriculture practices.

**Author Contributions:** Conceptualization, S.S. and J.N.; methodology, J.N.; software, J.N.; validation, W.K.; formal analysis, W.K. and J.N.; investigation, J.N. and W.K.; resources, C.S. and S.S.; writing—original draft preparation, S.S.; writing—review and editing, S.S., J.N. and S.S. All authors have read and agreed to the published version of the manuscript.

**Funding:** This research received no external funding.

**Institutional Review Board Statement:** Not applicable.

**Informed Consent Statement:** Not applicable.

**Data Availability Statement:** Data are contained within the article.

**Acknowledgments:** The authors would like to demonstrate gratitude toward the Department of Electronic Technology, Faculty of Industrial Technology, Nakhon Phanom University, for their research time, research grant, and instrumentation.

**Conflicts of Interest:** The authors declare no conflicts of interest.

## References

1. Oliveira, J.G.D.; Pinto, E.N.M.G.; Silva Neto, V.P.; D'Assunção, A.G. CSRR-Based Microwave Sensor for Dielectric Materials Characterization Applied to Soil Water Content Determination. *Sensors* **2020**, *20*, 255. [CrossRef]
2. Hardie, M. Review of Novel and Emerging Proximal Soil Moisture Sensors for Use in Agriculture. *Sensors* **2020**, *20*, 6934. [CrossRef] [PubMed]
3. Joler, M. An Efficient and Frequency-Scalable Algorithm for the Evaluation of Relative Permittivity Based on a Reference Data Set and a Microstrip Ring Resonator. *Sensors* **2022**, *22*, 5591. [CrossRef] [PubMed]
4. Karthikeyan, L.; Pan, M.; Nagesh Kumar, D.; Wood, E.F. Effect of Structural Uncertainty in Passive Microwave Soil Moisture Retrieval Algorithm. *Sensors* **2020**, *20*, 1225. [CrossRef] [PubMed]
5. Uthayakumar, A.; Mohan, M.P.; Khoo, E.H.; Jimeno, J.; Siyal, M.Y.; Karim, M.F. Machine Learning Models for Enhanced Estimation of Soil Moisture Using Wideband Radar Sensor. *Sensors* **2022**, *22*, 5810. [CrossRef] [PubMed]
6. Guo, J.; Tang, Y.; Wu, Y.; Zhu, C.; Huang, J. Embeddable Soil Moisture Content Sensor Based on Open-End Microwave Coaxial Cable Resonator. *IEEE Sens. J.* **2023**, *23*, 13575–13584. [CrossRef]
7. Birchak, J.R.; Gardner, C.G.; Hipp, J.E.; Victor, J.M. High dielectric constant microwave probes for sensing soil moisture. *Proc. IEEE* **1974**, *62*, 93–98. [CrossRef]
8. Jackson, T.J.; O'Neill, P.E.; Swift, C.T. Passive microwave observation of diurnal surface soil moisture. *IEEE Trans. Geosci. Remote Sens.* **1997**, *35*, 1210–1222. [CrossRef]
9. Phromloungsri, R.; Sonasang, S. Design and Implementation of a Wilkinson Power Divider with Integrated Band Stop Filters Based Parallel-Coupled Lines. *Appl. Comput. Electromagn. Soc. J. (ACES)* **2023**, *38*, 208–213. [CrossRef]

**Disclaimer/Publisher's Note:** The statements, opinions and data contained in all publications are solely those of the individual author(s) and contributor(s) and not of MDPI and/or the editor(s). MDPI and/or the editor(s) disclaim responsibility for any injury to people or property resulting from any ideas, methods, instructions or products referred to in the content.

# Prototyping Bespoke Sensor Industrial Internet-of-Things (IIoT) Systems for Small and Medium Enterprises (SMEs) <sup>†</sup>

Nikolay G. Petrov <sup>1</sup>, Tim J. Mulroy <sup>2</sup> and Alexander N. Kalashnikov <sup>2,\*</sup>

<sup>1</sup> Department of Data Science and Technical Services, Safefood360, Suite 10560, 26/27 Pembroke Street Upper, D02 X36 Dublin, Ireland; npetrov.ie@gmail.com

<sup>2</sup> Department of Engineering and Maths, Sheffield Hallam University, Sheffield S1 1WB, UK; t.j.mulroy@shu.ac.uk

\* Correspondence: a.kalashnikov@shu.ac.uk

<sup>†</sup> Presented at the 10th International Electronic Conference on Sensors and Applications (ECSA-10), 15–30 November 2023; Available online: <https://ecsa-10.sciforum.net/>.

**Abstract:** This paper aims to share our experiences gained from working on multiple industrial-academic collaborative projects within the Digital Innovation for Growth (DIG) regional programme. This initiative provided academic expertise to low-resource SMEs. The projects primarily revolved around measuring various process or structural health variables. The subsequent wireless reporting of these results to an online dashboard and generating alert messages when variables exceeded pre-defined thresholds were central to our work. Due to the diverse nature of our partners' requirements, there was no one-size-fits-all solution for the considered use cases. We will delve into our utilization and insights regarding various IoT-related tools and technologies. These include ESP32 WiFi-enabled microcontrollers, WiFi Manager, NTP time service, watchdog timers, Adafruit IO dashboards and the Twilio SMS gateway, as well as LoRa modules and networks such as TNT and Helium. By effectively combining these tools and technologies, we successfully completed prototypes that enabled testing of the devices on-site.

**Keywords:** sensor IIoT; IIoT prototyping; IIoT for SMEs; IIoT low power; IIoT SMS alerts; IIoT LoRa communication; IIoT reliability

**Citation:** Petrov, N.G.; Mulroy, T.J.; Kalashnikov, A.N. Prototyping Bespoke Sensor Industrial Internet-of-Things (IIoT) Systems for Small and Medium Enterprises (SMEs). *Eng. Proc.* **2023**, *58*, 111. <https://doi.org/10.3390/ecsa-10-16000>

Academic Editor: Stefano Mariani

Published: 15 November 2023



**Copyright:** © 2023 by the authors. Licensee MDPI, Basel, Switzerland. This article is an open access article distributed under the terms and conditions of the Creative Commons Attribution (CC BY) license (<https://creativecommons.org/licenses/by/4.0/>).

## 1. Introduction

Advancements in low-cost WiFi-enabled microcontrollers (MCUs) and cloud infrastructure have generated a growing interest in the Industrial Internet of Things (IIoT) among SMEs. This interest primarily stems from the potential benefits of storing and visualizing sensor data in the cloud, thereby eliminating the need to maintain and transfer data from local data loggers.

However, many SMEs lack the capability to independently develop an IIoT system and are uncertain about the financial feasibility of funding an external development. In such cases, collaborative projects between industry and academia, supported by government or regional sources, emerge as a viable option for prototyping IIoT systems.

This paper presents our observations and findings based on several sensor IIoT prototyping projects, *i.a.*, conducted under the auspices of the Digital Innovation for Growth (DIG) programme [1]. Two projects were concerned with temperature sensing and one with sensing impacts.

IIoT technology has garnered significant interest from industrial partners, who have shown a willingness to engage in basic maintenance tasks for their sensor-based IIoT systems, such as on site commissioning and Arduino script uploads. Their main priorities include cost predictability for both the initial implementation and ongoing maintenance, the utilization of readily available off-the-shelf components for spares and replacements and the suitability of the prototype for operation within their industrial environment.

Developers, on the other hand, emphasize the importance of having access to highly functional components that can be easily assembled. They also seek low-cost or free options for related services, accompanied by example projects, application notes and similar resources to aid in their development process.

In Section 2, we delve into the fundamental setup that proved to be adequate for all three projects. Section 3 highlights firmware features added for usability and reliability. The utilization of text messages to deliver alerts and alarms to users is addressed in Section 4. Section 5 focuses on achieving operation-off WiFi. Finally, Section 6 provides the summary and conclusion of the paper.

## 2. The Basic Sensor IIoT System Design

An IIoT sensor system can be seen as a convenient alternative to a conventional data logger. Instead of simply recording measurements at set time intervals and storing them in non-volatile memory to prevent data loss during power outages or accidental shutdowns, this system transmits each data point to the cloud. This enables reliable long-term storage and archiving of the data, as well as instant access from any connected device for checking or trend analysis, assuming that server-side visualization is available. By utilizing this use case, it becomes possible to significantly reduce power consumption by allowing the sensor and communication link to enter a sleep mode after processing each newly acquired data point.

From a hardware perspective, it is essential for a prototype of this system to be enclosed in a secure casing with robust connections and the necessary IP rating for ingress protection. To simplify the process of commissioning, maintenance and relocation, it is generally preferable for the prototype to be powered by a battery. For battery-powered prototypes, it is important to utilize the deep sleep MCU mode, which has certain restrictions compared to the light sleep mode more suitable for mains-powered devices. Additionally, the devices should have built-in battery charging and protection circuits. An ideal prototyping ecosystem should also offer a wide range of well-documented link and sensor modules that can be easily attached or detached. However, off-the-shelf ecosystems with such capabilities are limited in availability. In our case, we developed the prototypes using the M5StickC ESP-32-based device, which features a built-in 120 mAh battery in the standard configuration, the option to add an additional 186,50 2200 mAh battery and a selection of dedicated HAT and general-purpose Grove-interfaced modules [2]. This hardware only operates in the 2.4 GHz WiFi band, but this was not an issue for our projects (Figure 1).

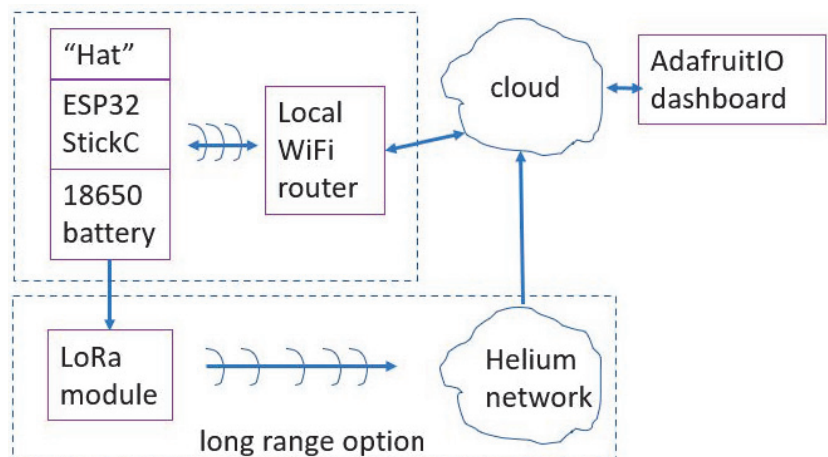


**Figure 1.** Block diagram of the hardware setup and wireless connections that were fully prototyped.

To complete the WiFi-capable hardware setup, it is necessary to integrate a cloud back-end. The small and medium-sized enterprises (SMEs) we collaborated with did not find dedicated company servers or large-scale IoT servers designed for diverse, high-volume industrial clients appealing. These servers often require configuration and administration and lack user-friendly dashboard builders. After careful evaluation, we opted for AdafruitIO [3] as our cloud provider. AdafruitIO stood out due to its transparent pricing structure, extensive documentation and the availability of a free tier for experimentation. An example of the developed user front end (dashboard) and developer’s back end (feed) are presented side-to-side in Figure 2. Additional factors influencing our decision were discussed in [4], Section 5, where another dashboard is presented.

In summary, the prototyped sensor IIoT systems follow a measure–communicate–sleep cycle using the M5Stick ecosystem and leverage the AdafruitIO cloud server. Considering that the estimated current consumption of the M5Stick in deep sleep mode is around 2–3 mA [5], line 36, it has the estimated capability to run on a fully charged additional 18650 battery for around one month. This assumes that the measurement–communication phase of the cycle, which consumes more than 100 mA, occurs infrequently, such as once per hour for a very short period of time.

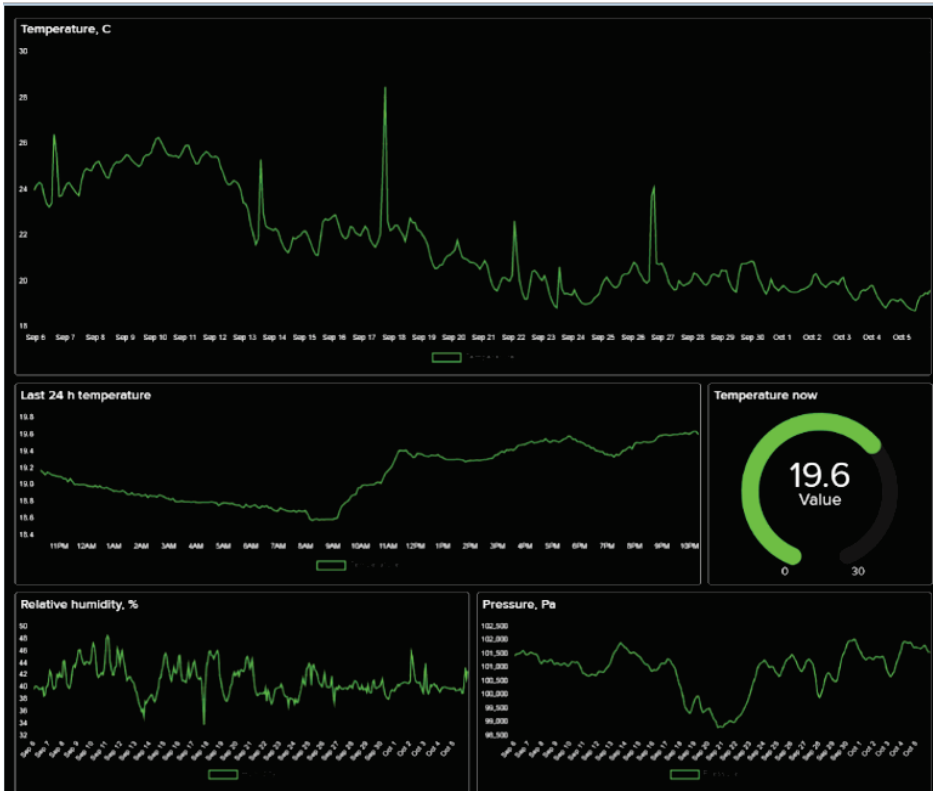


Figure 2. Cont.



**Figure 2.** An example of a dashboard (user’s front end, **above**) and a feed (developer’s back end, **below**) on Adafruit IO.

### 3. Firmware Features Added for Usability and Reliability

The initial development of the firmware involved using the Arduino IDE and AdafruitIO library [6]. However, at a later stage, the library ceased to function, leading to the development and sharing of a POST-based workaround [7]. This workaround was implemented in all three projects, and we encountered no data loss or communication issues.

Occasionally, the MCU would hang up when connecting to the WiFi access point, but due to the intermittent nature of this fault, we chose not to fully investigate it. Instead, we implemented a watchdog timer that resets the MCU after a set time. If the connection after a watchdog reset is re-established, the code proceeds to the loop function, where the watchdog timer is cleared.

To improve user-friendliness, several significant additions were deemed highly beneficial:

- The use of a WiFi manager [8] was implemented to eliminate the necessity for embedding WiFi credentials into the code. This approach offers flexibility during installation, streamlines the process of reconnecting in case of password changes and permits the use of devices at different locations without requiring reprogramming.
- It was observed that the device’s built-in timer, responsible for awakening it from sleep mode, exhibited an inaccuracy on the order of approximately 4 min over a 24 h period, which proved to be unsatisfactory for our partners. To address this issue, we implemented a solution involving the calculation of the time remaining until the next wake-up event, following the acquisition of precise time readings from the network

time protocol (NTP) server. Subsequent to this adjustment, the readings were obtained with an acceptable margin of uncertainty, typically within a few seconds.

- Welcome messages and connection status notifications were presented to assure users of the system’s correct functioning, particularly given that the screen was subsequently powered off to conserve energy while in sleep mode.

#### 4. Communicating Alarms/Alerts

While transitioning data logging to an online platform is valuable, it is important to note that, in the context of two out of three IIoT systems, generating distinct messages was necessary when readings fell outside of the predefined limits. Adafruit IO offers a notification service for account holders, allowing them to receive alerts via either email (accessible for trial accounts) or SMS (requires an AdafruitIO+ paid account), as depicted in Figure 3.

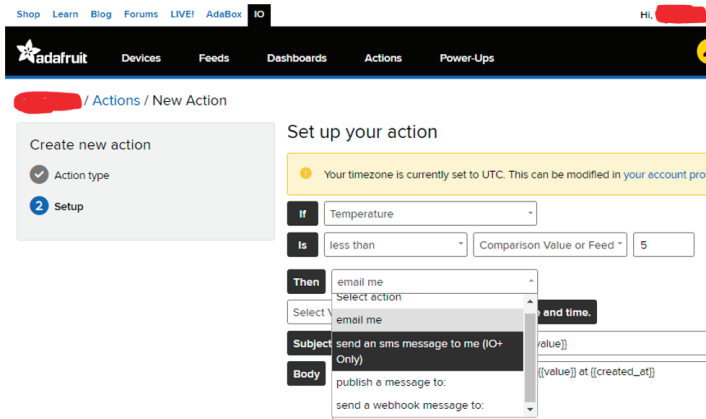


Figure 3. Setting notifications for a reading, getting out of set bounds on AdafruitIO.

Email messages can also be sent using the Arduino reference library EmailSender [9].

Another possibility of notifying the end user of something requiring attention is by sending an SMS to their phone number. There are several internet-to-SMS service providers available; we used Twilio in our developments because of their international availability, good number of examples for various programming languages and a possibility to try it for free using sign-up credit. We used an Arduino library [10] following a detailed tutorial [11]. The Twilio messages were reliably delivered inside both the UK and Ireland, but we could not manage operating it cross-border. Figure 4 presents a console’s output and some of the messages received using this service.

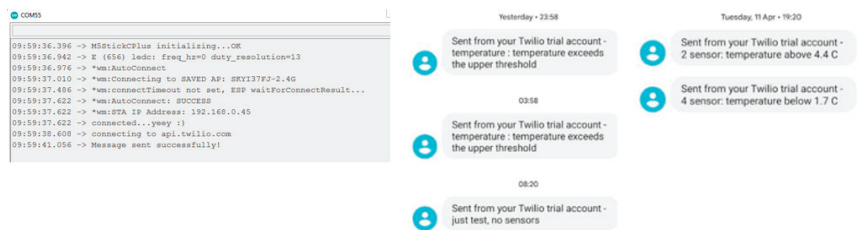


Figure 4. Operating SMS using Arduino library (console output on the left, examples of received messages on the right).

### 5. Operating IoT Devices off WiFi

While WiFi networks are prevalent at most sites, certain end users might not have access to them or may be reluctant to share their login information due to the associated inconvenience and security considerations. An alternative approach involves the use of wireless modem modules to connect to existing mobile networks with extensive coverage. However, fully featured LTE modems tend to be relatively expensive and power-hungry, making them less suitable for IIoT purposes. On the other hand, NB-IoT modems, better suited for these applications, are not yet widely supported, with only one UK provider offering them at the time of writing. Additionally, managing SIM cards (acquisition, registration, billing, security, etc.) poses additional burdens.

Consequently, we initiated an exploration of commercially available radio modules engineered for extended-range communication. Despite the seemingly favourable specifications evident in datasheets and select online demonstrations, we confronted formidable challenges when striving to achieve communication distances surpassing 100 m within a lightly urbanized setting. This was particularly pronounced during our utilization of peer-to-peer module configurations, inclusive of both nRF24L01 + modules, with and without RF amplification, and some LoRa modules.

An effective approach entailed establishing connections with a publicly available network characterized by extensive coverage. Our evaluation encompassed both the LoRa-based The Things Network (TTN), which offers open access, and the subscription-based Helium. It is noteworthy that both of these networks adhere to a decentralized model, relying on nodes privately procured and managed by network associates. Helium was further explored by us because of substantially wider coverage at reasonable cost.

To investigate this possibility, we employed an Arduino library tailored for the LoRa-E5 Grove-connected modules [12] in accordance with a comprehensive tutorial [13]. During our coverage and reliability assessment, the module was woken up and transmitted data through three train rides and two taxi journeys. It transmitted two bytes, deliberately incremented by five at each wake-up cycle. While the data flow from the Helium console to a Google spreadsheet exhibited occasional interruptions and resets, it ultimately affirmed the network’s overall resilience as shown in Figure 5.

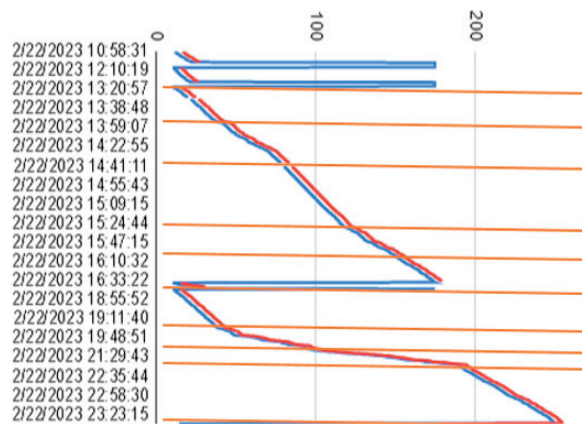


**Figure 5.** A visual depiction of the data captured through the Helium user console during the LoRa transmitter’s engagement in three train rides and two taxi journeys.

The Helium network functions on a package-oriented data transmission system, where users are billed according to the volume of packages received by the network’s gateways. Quite often, the very same data packet is captured simultaneously by multiple gateways. Thanks to reasonably low packet charges, the resulting redundancy does not place a substantial financial burden on users. However, it is important to note that the network



enforces a limitation on packet size, capping it at a maximum of 24 bytes. While this constraint might seem restrictive, it is, in fact, a suitable fit for many IIoT applications.

## 6. Summary and Conclusions

We have elucidated the diverse methods employed in the successful prototyping of customized IIoT sensor systems tailored to resource-constrained small and medium enterprises (SMEs). Our choice of the M5Stick hardware ecosystem, renowned for its modularity, the presence of enclosed displays and efficient battery and charging circuits, proved instrumental. In order to assess the data reporting capabilities over extended distances, we conducted an evaluation of LoRa-E5 within the decentralized Helium network, thereby affirming the network's extensive coverage and dependable performance.

Additionally, the Arduino software ecosystem played a pivotal role by facilitating rapid integration and evaluation of diverse firmware options. This process contributed significantly to the enhancement in both reliability and usability of the prototypes. It is important to note that many of the lessons we have learned and reported hold universal relevance and can be applied to the development of similar IIoT systems with confidence.

**Author Contributions:** Conceptualization, N.G.P. and A.N.K.; methodology, N.G.P. and A.N.K.; software, A.N.K.; validation, N.G.P.; formal analysis, N.G.P.; investigation, T.J.M.; resources, N.G.P.; data curation, N.G.P.; writing—original draft preparation, A.N.K.; writing—review and editing, N.G.P., T.J.M. and A.N.K.; visualization, A.N.K.; supervision, N.G.P. and T.J.M.; project administration, N.G.P. and T.J.M. All authors have read and agreed to the published version of the manuscript.

**Funding:** This research received no external funding.

**Institutional Review Board Statement:** Not applicable.

**Informed Consent Statement:** Not applicable.

**Data Availability Statement:** We did not upload the obtained data to a public repository because of the amount of work involved in properly describing and labelling these. However, we are happy to supply the reported data on request.

**Acknowledgments:** The authors gratefully acknowledge support from the Digital Innovation for Growth (DIfG) programme.

**Conflicts of Interest:** The authors declare no conflicts of interest.

## References

1. Digital Innovation for Growth Welcome Page. Available online: <https://www.shu.ac.uk/business/start-your-business/digital-innovation-for-growth> (accessed on 30 September 2023).
2. M5Stick Product Page. Available online: <https://shop.m5stack.com/products/stick-c> (accessed on 30 September 2023).
3. AdafruitIO. Available online: <https://learn.adafruit.com/welcome-to-adafruit-io> (accessed on 30 September 2023).
4. Elyounsi, A.; Kalashnikov, A.N. Predictive IoT Temperature Sensor. *Eng. Proc.* **2022**, *27*, 55. [CrossRef]
5. Example Code for Sleep Modes on M5Stick. Available online: <https://github.com/m5stack/M5StickC/blob/master/examples/Advanced/AXP192/sleep/sleep.ino> (accessed on 30 September 2023).
6. Adafruit IO Arduino Library. Available online: [https://github.com/adafruit/Adafruit\\_IO\\_Arduino](https://github.com/adafruit/Adafruit_IO_Arduino) (accessed on 30 September 2023).
7. Using POST to Add Data Points to a Feed. Available online: <https://forums.adafruit.com/viewtopic.php?f=56&t=177055> (accessed on 30 September 2023).
8. WiFiManager Code Page. Available online: <https://github.com/tzapu/WiFiManager> (accessed on 30 September 2023).
9. EmailSender, Arduino Reference Library. Available online: <https://www.arduino.cc/reference/en/libraries/emailsender/> (accessed on 30 September 2023).
10. Demuri, A. Twilio-esp32-client. Available online: <https://github.com/ademuri/twilio-esp32-client> (accessed on 30 September 2023).
11. Send SMS with the ESP32 (Twilio). Available online: <https://randomnerdtutorials.com/send-sms-esp32-twilio/> (accessed on 30 September 2023).

12. Helium-E5-DHT22. Available online: <https://gist.github.com/NorHairil/808ec64b1d4eac3f4b6f286a9392abce> (accessed on 30 September 2023).
13. Mutalib, H. Sending Data to Helium Console using Grove LoRa-E5. Available online: <https://www.cytron.io/tutorial/sending-data-to-helium-console-using-grove-lora-e5> (accessed on 30 September 2023).

**Disclaimer/Publisher's Note:** The statements, opinions and data contained in all publications are solely those of the individual author(s) and contributor(s) and not of MDPI and/or the editor(s). MDPI and/or the editor(s) disclaim responsibility for any injury to people or property resulting from any ideas, methods, instructions or products referred to in the content.



# Multipurpose Smart Shoe for Various Communities <sup>†</sup>

Vijayaraja Loganathan <sup>1,\*</sup>, Dhanasekar Ravikumar <sup>1</sup>, Gokul Raj Kusala Kumar <sup>1</sup>, Sarath Sasikumar <sup>1</sup>,  
Theerthvasan Maruthappan <sup>1</sup> and Rupa Kesavan <sup>2</sup>

<sup>1</sup> Department of Electrical and Electronics Engineering, Sri Sairam Institute of Technology, Chennai 600044, Tamilnadu, India; dhanasekar.eee@sairamit.edu.in (D.R.); sit21ee008@sairamtap.edu.in (G.R.K.K.); sit21ee048@sairamtap.edu.in (S.S.); sitl22ee02@sairamtap.edu.in (T.M.)

<sup>2</sup> Department of Computer Science and Engineering, Sri Venkateswara College of Engineering, Sriperumbudur 602117, Tamilnadu, India; rupakesavan@svce.ac.in

\* Correspondence: vijayaraja.eee@sairamit.edu.in

<sup>†</sup> Presented at the 10th International Electronic Conference on Sensors and Applications (ECSA-10), 15–30 November 2023; Available online: <https://ecsa-10.sciforum.net/>.

**Abstract:** A recent survey depicts that across the globe there are nearly 36 million visually impaired people facing serious issues in accessibility, education, navigating public spaces, safety concerns, and mental health. In recent times, the evolutions of obstacle detectors for blind people have been from peoples' use of sticks, smart glasses, and smart shoes. Among the above, the major problem faced by all blind people is to walk independently to every place, so to make them feel independent while they walk, herein is a proposal for an intelligent shoe. The proposed intelligent shoe consists of a controller connected with an ultrasonic sensor, voice alert system (VAS), vibration patterns, GPS navigation, connectivity with a smart phone or smart-watch, voice assistance, feedback on gait and posture, and emergency features that are embedded with each other to communicate the presence of obstacles in the directions of the path of the blind. The sensor identifies an obstacle in the direction present then it passes the signal to the controller that activates the VAS and the vibration patterns present in that direction. Therefore, by the proposed concept of vibration sense and VAS with GPS navigation, connectivity with a smart phone or smart-watch means the system provides easy access for the blind to identify obstacles present in their way and help them toward social inclusion.

**Keywords:** Arduino board; ultrasonic sensor; vibrator; voice alert system (VAS)

**Citation:** Loganathan, V.; Ravikumar, D.; Kusala Kumar, G.R.; Sasikumar, S.; Maruthappan, T.; Kesavan, R. Multipurpose Smart Shoe for Various Communities. *Eng. Proc.* **2023**, *58*, 112. <https://doi.org/10.3390/ecsa-10-16284>

Academic Editor: Stefano Mariani

Published: 16 November 2023



**Copyright:** © 2023 by the authors. Licensee MDPI, Basel, Switzerland. This article is an open access article distributed under the terms and conditions of the Creative Commons Attribution (CC BY) license (<https://creativecommons.org/licenses/by/4.0/>).

## 1. Introduction

Blindness is a defect that is divided into two types: one is caused by hormones inherited from the previous generation, which is labeled as permanent blindness, and the other one is caused by higher usage of radiation, which is called temporary blindness to humans. The system of network connections that is present in-between electronic components and humans is represented as the Internet of Things (IoT), where the electronic components transmit signals to humans by means of data. The detection of an obstacle, pothole, or slippery surface, as well as health tracking and heat sensing, is performed using an Arduino board. This work includes GPS-GSM navigation and location tracking, as well as providing an emergency SOS facility to assist blind people [1]. A hardware component [2] is incorporated in the IOT technology to help people with vision deficiency to solve the issues they face every day. A smart shoe for the blind is proposed in [3] which conveys the presence of obstacles in vibrational form through the use of vibrators. Here, the shoe [4] not only conveys the presence of an obstacle but also notifies the wearer of the presence of underground holes in the form of an audio message. In [5], the designed shoe has two modules, namely shoe and phone modules: the shoe module consists of a controller and sensors, whereas the phone module is linked to a GPS system. The controller is embedded with a Bluetooth transceiver which is linked to a smart phone app that uses Google maps to direct the blind to the required destination by audio message.

In [6], the system embedded in the shoe detects the presence of an obstacle present at a certain distance and conveys the information either through a vibrator or audio message, and through the use of an alarm sound, the blind can detect the presence of an obstacle. An assistance system proposed in [7] uses computer vision algorithms which are written with certain functions such as obstacle detection, avoidance, and navigation. Here, the obstacle detection is performed by sensors present, and the presence is conveyed using smart phone audio which gives haptic feedback to the blind. In [8], an intelligent shoe is embedded with sensors, a buzzer, and a microcontroller. After the detection of an object, the buzzer indicates the presence of an obstacle, and for better accuracy, smart glass is used. In [9], three pairs of ultrasonic sensors placed on the medial, central, and lateral part of the shoe are used to detect the presence of holes and pits; the study includes the usage of piezoelectric transducers for recharging the battery while walking. A wearable shoe in [10] is used to detect the presence of obstacles, wet floors, and patient falls by using voice alarms. An additional method is to prevent accidents, falling, and getting lost in some areas unknown to the visually impaired by communicating this information to the care-taker via a mobile application. With respect to the above studies, some feasible solutions have been presented for blind people all around the world. There is the usage of detection in either audio or vibration form for the transmission of messages relating to the detection of obstacles:

- (i) The usage of a GPS module to communicate the location of the visually impaired person.
- (ii) The usage of smart glass for the further detection of obstacles.

In connection with this, herein is a design of an intelligent shoe that transmits the detection of obstacles in both vibration and audio form that is embedded within the microcontroller. Upon the detection of an obstacle, the alert mode, either by voice or vibration, is passed to the blind to avoid the upcoming obstacle. Further, the design is embedded with a GPS module which locates the blind, so as to transmit the location to the care-taker in emergency situations.

## 2. Design of Smart Shoe Model

By the usage of an ultrasonic sensor combined with a pre-programmed Arduino controller, it is easy to detect the object present before visually impaired ones. The Arduino controller is coded in such a way that after detection of an object, the controller passes the message to the vibrator and VAS. After receiving the command from controller, the object detection is represented by means of vibration through a vibrational motor and voice alert through a speaker attached to it. Using IoT technology in the shoe that is being worn by the visually impaired gives them the independence to walk wherever they like. This paper describes the proposal of a smart shoe for the blind that indicates obstacles in the directions such as in the front, left, right, and upper part of the visually impaired making them more independent to walk along the path without depending on others. There is also an ultrasonic sensor present in the upper part of the breadboard/shoe which is used to detect the obstacle that is present in the upper view of the blind and allows those visually challenged to realize that there is obstacle. The components used for the making of this model are a battery, motor, ultrasonic sensor, Arduino board, vibrator, and a breadboard/shoe. If there is any detection of obstacles in the fixed path of the ultrasonic sensor, then the ultrasonic sensor passes the received signal to the Arduino board. After receiving the signal feedback from the ultrasonic sensor, the pre-programmed Arduino sends or transmits the signals to the vibrator and VAS. The received signal from the Arduino board makes the vibrator vibrate and instructs the VAS to interact with the user and inform about the obstacle. By this method, it is easy to help the blind to detect where the object is and avoid it so that he/she can walk freely in the road. By using the GPS module along with the shoe, the location of the blind person can be shared with the care-taker in emergency conditions. By using the CNN algorithm in the camera module of the shoe, the name of the upcoming obstacle can be mentioned to the blind person, and the distance between them

and the obstacle can be accurately determined. Figure 1 represents the block diagram of the smart shoe. Figure 2 shows the simulation model in the OFF state whereby if the distance of the ultrasonic sensor is less than the fixed range, the light source is turned OFF. Figure 3 shows the simulation model in the ON state whereby if the distance of the ultrasonic sensor is greater than the fixed range, the light source is turned ON to indicate the presence of an obstacle. In the ON state, the ultrasonic sensors work based on the following order:

- (i) If the obstacle is identified in the first ultrasonic sensor, then the vibrational motor on the right side glows up (turns on) and vice versa.
- (ii) If the obstacle is identified in the second ultrasonic sensor, then the vibrational motor present at the second position on the right side glows up (turns on).
- (iii) If the obstacle is detected in the third ultrasonic sensor, then the vibrational motor present at the second position on the left side glows up (turns on).
- (iv) Finally, if an obstacle is detected at the the fourth ultrasonic sensor, then the vibrational motor present on the left side glows on (turns on).

This is how the stimulation model works, so based on this functionality, the obstacle present at each direction can be identified, and based on the vibration caused by the vibrational motor, the object detection can be performed.

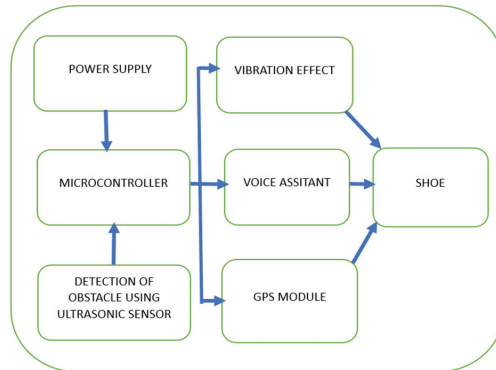


Figure 1. Block diagram of smart shoe.

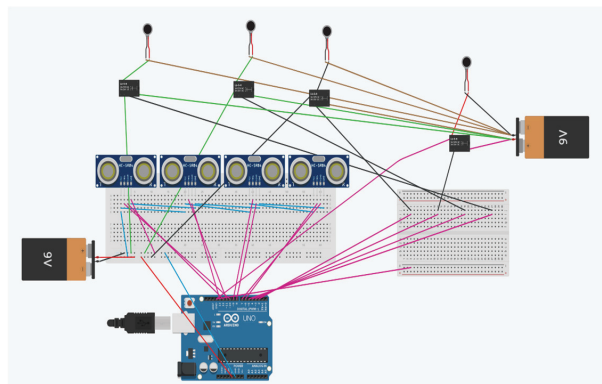


Figure 2. Simulation in OFF state.

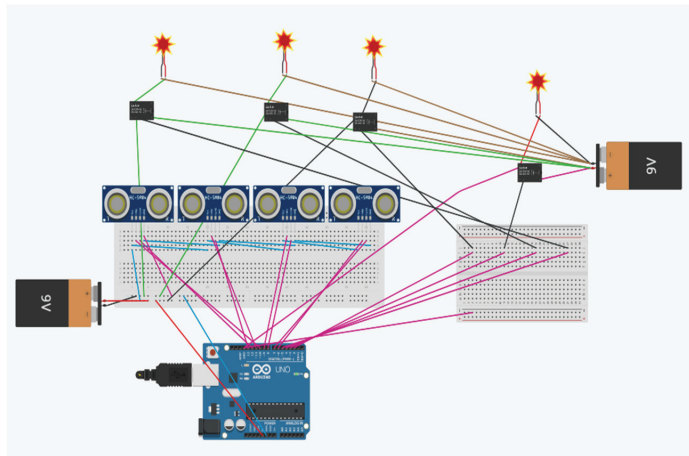


Figure 3. Simulation in ON state.

### 3. Prototype of Smart Shoe

The schematic diagram Figure 4a is sketched for the circuit connection of the prototype model, and for the proceeding of the prototype model, the workflow diagram shown in Figure 4b is designed. The prototype model is shown in Figure 5 and consists of four ultrasonic sensors with a range of distance coverage between 2 cm and 300 cm. Here, the four ultrasonic sensors are used to detect the presence of obstacles in the directions such as the following: in the right, left, straight, and upward direction of the blind person, four vibrators, four speakers, and the process of obstacle detection will take place in the following pattern: As shown in Figure 6a, if the obstacle is identified in the first ultrasonic sensor which is present in the forward direction, then the vibrational motor on the front side vibrates, and also, the VAS present on the front side produces an alert which indicates the presence of an obstacle.

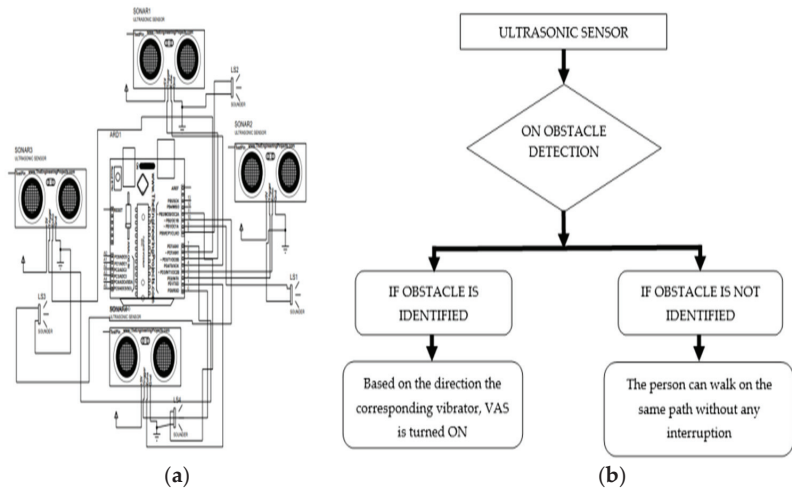


Figure 4. (a,b) Schematic of sensor placement in proposed smart shoe; workflow of obstacle detection by proposed smart shoe.

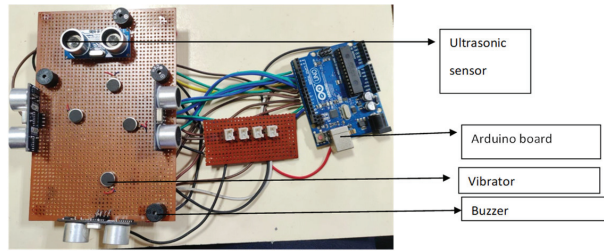


Figure 5. Hardware model.

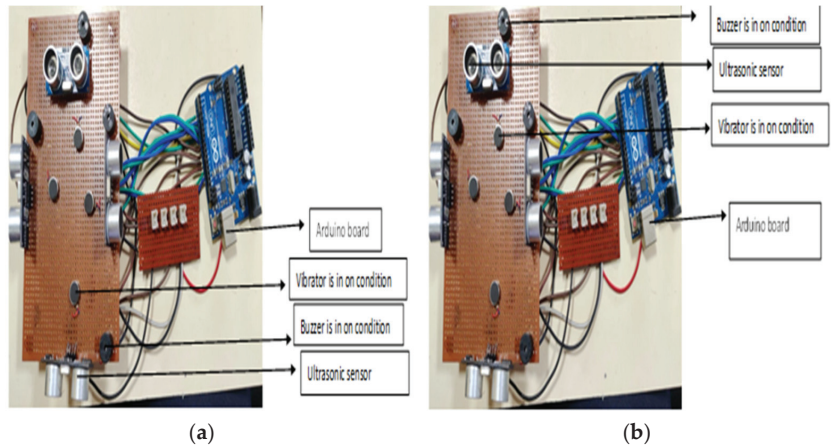
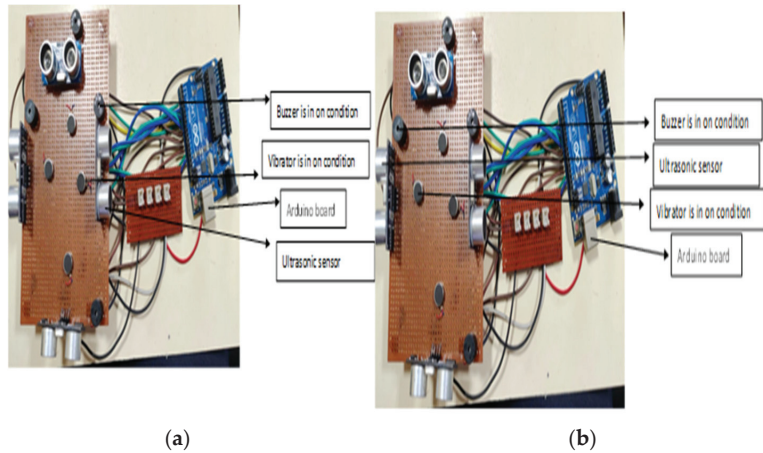


Figure 6. (a,b) Obstacle in forward direction; obstacle in above direction.

As shown in Figure 6b, if the obstacle is identified in the second ultrasonic sensor present on the upside, then the vibrational motor present at the upside position vibrates, and the VAS present on the upside produces an alert sound indicating the presence of an obstacle in the upside direction. As shown in Figure 7a, if the obstacle is detected in the third ultrasonic sensor present on the right side, then the vibrational motor present on the right side vibrates, and also, the VAS present on the right produces an alert which indicates the presence of an obstacle on the right side.



**Figure 7.** (a,b) Obstacle in right direction; obstacle in left direction.

As shown in Figure 7b, if an obstacle is detected at the fourth ultrasonic sensor present on the left side of the blind, then the vibrational motor present on the left side vibrates, and also, the VAS present on the left side produces an alert which indicates the presence of an obstacle in the left direction.

Thus, the entire working model of the smart shoe is explained here, so based on this, the presence of an obstacle in either direction mentioned can be identified, and based on the vibration caused by the vibrational motor and the alert from the VAS, the message can be conveyed to the visually impaired person. As shown in Figure 8, the prototype model is embedded with the GPS module in order to pass the location of the blind person in emergency conditions. Here, the SPI protocol is used with the Arduino board for communicating the location of the blind person to the care-taker.

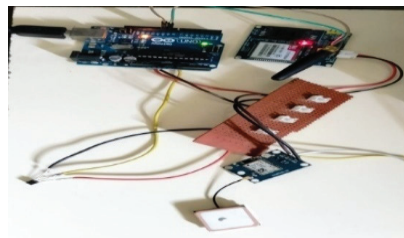


**Figure 8.** GPS module.

Once the location of the blind person is transmitted to the care-taker, the output of the location will be as shown in Figure 9. The location of the blind person is communicated with the care-taker in emergency conditions (i.e., the blind will be provided with a switch to transmit the location with the care-taker) in order to make them feel free and to monitor the current location of the blind person without being with them.



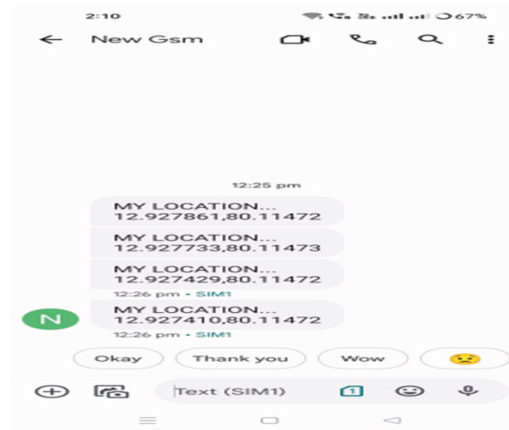


Figure 9. GPS location prediction.

#### 4. Conclusions

In the olden days, blind people suffered from the problem of walking independently in roads, which brought about the invention of the walking stick, which was used for the detection of objects. However, as it could not sense the presence of an obstacle, there came the invention of an additional ultrasonic sensor to detect the presence of an object, but this was not as effective as first thought because the stick could not be used in every location where the blind travel. So, in order to solve this problem, presented here is IOT-based technology used in the shoe of a blind person which will help to them to walk independently in roads and help them to feel independent without depending on the help of others to walk. This helps blind people effectively as there are four ultrasonic sensors combined with the vibrators and VAS which can predetermine the presence of object in all directions when a blind person walks in the road. In this solution, there is the usage of both the VAS and vibrators, because if the blind person also has a hearing impairment, then the vibration is enough for him to detect the location of an obstacle present. By the usage of a GPS module, the blind person's location is transmitted to the care-taker for reasons of safety in emergency situations. The placement of the ultrasonic sensors on the shoe will be as follows: two ultrasonic sensors on the right shoe to detect obstacles on the right side and in the forward direction, and two ultrasonic sensors in the left shoe for the detection of obstacles in the upward and left directions of the blind person. The prototype model is to be installed on the shoe in order to make the product more efficient for the blind to use, but due to size compactness, the model is to be reduced to a smaller size and developed within the shoe in the future.

**Author Contributions:** Conceptualization, V.L. and D.R.; methodology, G.R.K.K., S.S. and T.M.; software, G.R.K.K.; validation, V.L., G.R.K.K. and R.K.; investigation, R.K.; writing—original draft preparation, V.L. and G.R.K.K.; writing—review and editing, supervision, V.L., G.R.K.K., S.S. and T.M. All authors have read and agreed to the published version of the manuscript.

**Funding:** This research received no external funding.

**Institutional Review Board Statement:** Not applicable.

**Informed Consent Statement:** Not applicable.

**Data Availability Statement:** Not applicable.

**Conflicts of Interest:** The authors declare no conflicts of interest.

## References

1. Bhongade, P.; Girhay, S.; Sheikh, A.M.; Ghata, R.; Ambadkar, S.; Dusane, C. Internet of Things—Enabled Smart Shoes for Blind People. In Proceedings of the IEEE Delhi Section Conference (DELCON), New Delhi, India, 11–13 February 2022; pp. 1–9.
2. Durgadevi, S.; Komathi, C.; ThirupuraSundari, K.; Hareesh, S.S.; Harishanker, A.K.R. IOT Based Assistive System for Visually Impaired and Aged People. In Proceedings of the 2nd International Conference on Power Electronics & IoT Applications in Renewable Energy and its Control (PARC), Mathura, India, 21–22 January 2022; pp. 1–4.
3. Mishra, R.; Pippal, S.K.; Asif; Kumar, A.; Singh, D.; Singh, A. Clear Vision—Obstacle detection using Bat Algorithm Optimization Technique. In Proceedings of the 9th International Conference on Reliability, Infocom Technologies and Optimization (Trends and Future Directions) (ICRITO), Noida, India, 3–4 September 2021; pp. 1–5.
4. Nandalal, V.; Kumar, V.A.; Sujitha, A.; Sumitha, G.; Sureka, A.S. Intelligent Multi-Utility Shoe for Visually Impaired Persons. In Proceedings of the 2nd International Conference on Smart Electronics and Communication (ICOSEC), Trichy, India, 7–9 October 2021; pp. 1102–1108.
5. Kumar, P.; Inchara, K.M.; Lekhashree, S.; Likhith, C.N.; Pavan, U. Real Time Assistive Shoe for Visually Impaired People. In Proceedings of the 6th International Conference for Convergence in Technology (I2CT), Maharashtra, India, 2–4 April 2021; pp. 1–5.
6. Anisha, M.; Kirthika, S.; Harline, D.J.; Thenmozhi, P.; Rubala, R.; Pragathi, T.G.; Benisha, M.; Elliot, C.J. Low-Cost Smart Shoe for Visually Impaired. In Proceedings of the Third International Conference on Intelligent Communication Technologies and Virtual Mobile Networks (ICICV), Tirunelveli, India, 4–6 February 2021; pp. 1108–1111.
7. Rao, S.; Singh, V.M. Computer Vision and Iot Based Smart System for Visually Impaired People. In Proceedings of the 11th International Conference on Cloud Computing, Data Science & Engineering (Confluence), Noida, India, 28–29 January 2021; pp. 552–556.
8. Chava, T.; Srinivas, A.T.; Sai, A.L.; Rachapudi, V. IoT based Smart Shoe for the Blind. In Proceedings of the 6th International Conference on Inventive Computation Technologies (ICICT), Coimbatore, India, 20–22 January 2021; pp. 220–223.
9. Maheshwari, B.U.; Subashini, P.R. Sneak-Sight Shoes for the Visually Challenged. In Proceedings of the International Conference on Power, Energy, Control and Transmission Systems (ICPECTS), Chennai, India, 10–11 December 2020; pp. 1–3.
10. Daou, R.A.Z.; Chehade, J.; Haydar, G.A.; Hayek, A.; Boercsoek, J.; Olmedo, J.J.S. Design and Implementation of Smart Shoes for Blind and Visually Impaired People for More Secure Movements. In Proceedings of the 32nd International Conference on Microelectronics (ICM), Aqaba, Jordan, 14–17 December 2020; pp. 1–6.

**Disclaimer/Publisher’s Note:** The statements, opinions and data contained in all publications are solely those of the individual author(s) and contributor(s) and not of MDPI and/or the editor(s). MDPI and/or the editor(s) disclaim responsibility for any injury to people or property resulting from any ideas, methods, instructions or products referred to in the content.

Proceeding Paper

# QoS Performance Evaluation for Wireless Sensor Networks: The AQUASENSE Approach <sup>†</sup>

Sofia Batsi <sup>‡</sup> and Stefano Tennina <sup>\*‡</sup>

Wireless Embedded Systems Technologies L'Aquila Srl, SS17 snc c/o Tecnopolo d'Abruzzo, 67100 L'Aquila, Italy; sofia.mpatsi@westaquila.com

\* Correspondence: stefano.tennina@westaquila.com

<sup>†</sup> Presented at the 10th International Electronic Conference on Sensors and Applications (ECSA-10), 15–30 November 2023; Available online: <https://ecsa-10.sciforum.net/>.

<sup>‡</sup> These authors contributed equally to this work.

**Abstract:** The AQUASENSE project is a multi-site Innovative Training Network (ITN) that focuses on water and food quality monitoring by using Internet of Things (IoT) technologies. This paper presents the communication system suitable for supporting the pollution scenarios examined in the AQUASENSE project. The proposed system is designed and developed in the SimuLTE/OMNeT++ simulation for simulating an LTE network infrastructure connecting the Wireless Sensors Network (WSN) with a remote server, where data are collected. In this frame, two network topologies are studied: Scenario A, a single-hop (one-tier) network, which represents a multi-cell network where multiple sensors are associated with different base stations, sending water measurements to the remote server through them, and Scenario B, a two-tier network, which is again a multi-cell network, but this time, multiple sensors are associated to local aggregators, which first collect and aggregate the measurements and then send them to the remote server through the LTE base stations. For these topologies, from the network perspective, delay and goodput parameters are studied as representative performance indices in two conditions: (i) periodic monitoring, where the data are transmitted to the server at larger intervals (every 1 or 2 s), and (ii) alarm monitoring, where the data are transmitted more often (every 0.5 or 1 s); and by varying the number of sensors to demonstrate the scalability of the different approaches.

**Keywords:** wireless sensor network; water quality monitoring; simulation

**Citation:** Batsi, S.; Tennina, S. QoS Performance Evaluation for Wireless Sensor Networks: The AQUASENSE Approach. *Eng. Proc.* **2023**, *58*, 113. <https://doi.org/10.3390/ecsa-10-16181>

Academic Editor: Stefano Mariani

Published: 15 November 2023



**Copyright:** © 2023 by the authors. Licensee MDPI, Basel, Switzerland. This article is an open access article distributed under the terms and conditions of the Creative Commons Attribution (CC BY) license (<https://creativecommons.org/licenses/by/4.0/>).

## 1. Introduction

Water is considered one of the scarcest natural resources on our planet [1]. It directly impacts our lives, as it is vital to humankind, animals, and plants [2]. Thus, the alteration of water quality caused by, for example, industrial waste or climatic changes, is a significant concern. Its quality might be a source of life or death [3]. Promptly detecting the pollution and locating its source is vital in environmental protection. Considering the multiple advantages offered by the technology, the Wireless Sensor Network (WSN) is adopted in pollution-monitoring works. WSNs are suitable for monitoring the physical and chemical characteristics of water remotely [4–7]. In this paper, we describe our contribution to the AQUASENSE project in designing and assessing the performance of a WSN-based end-to-end system for water quality monitoring through computer simulations.

In such a context, a simulation framework built in SimuLTE/INET/OMNeT++ [8–10] is developed, tailored to two scenarios to evaluate the performance of a remote pollution monitoring service through a 4G/LTE-enabled WSN. The first scenario builds on a multi-cell network architecture, in which multiple sensors are associated with different LTE base stations (eNBs) and transmit their water quality measurements directly to the remote server. The second scenario still builds on the multi-cell network architecture. Still, multiple sensors are associated with local aggregators and communicate using short-range technology

(e.g., Wi-Fi or ZigBee). The aggregators coordinate their local network of sensors, collect and aggregate their water measurements, and transmit them to the remote server through LTE base stations (eNBs), with which every aggregator is associated. For the above scenarios, we provide valuable performance results regarding the network's Quality of Service (QoS) under different conditions.

## 2. Previous Work

Our main goal was to design a good quality model that evaluates our project best. Accordingly, following the indications of the most referenced network architectures reviewed by Farmanullah Jan et al. ([11] and the references therein), who provided an in-depth literature review on Water Quality Monitoring Systems based on Internet-of-Things (IoT-WQMS), in [12], we already developed a performance comparison of the most suitable communication technologies.

In our previous work, with the help of the WinProp software simulation framework [13], we compared the performance of three long-range communications technologies to support an IoT-based network reporting data from the sensing devices spread along rivers of the Abruzzo region in Italy to a remote central station, where they are collected and analyzed. More in detail, we jointly assessed the radio signal coverage and the maximum achievable data rate for (i) 4G/LTE, (ii) NB-IoT, and (iii) LoRa communications technologies. In particular, the transmitting antennas' were placed at different heights above the ground or the river's water level.

Our results demonstrated that 4G/LTE outperforms the other two technologies since it achieves the highest throughput and allows adding value services, such as video surveillance over simple data chunks reporting. Nevertheless, 4G/LTE is limited in coverage: the best performance results are achieved near the base stations, i.e., in urban/suburban areas, while the rural regions need more radio signal quality. On the contrary, the LoRa and NB-IoT technologies achieve outstanding connectivity for large regions far from the base stations. However, this performance is paid with a reduced capacity of the medium to support the mentioned added value service.

Considering all the above, we believe, in this paper, that the most exciting scenarios to study are identifying pollutants in urban and suburban areas, i.e., where most people live. Accordingly, the suitable solution for our project is to focus on the 4G/LTE communication technology [14] due to its maturity, its overall coverage, i.e., the availability of base stations, and in general its capacity in terms of guaranteeing radio connections of good quality (low packet loss rate and latency, and generally high throughput). We then assess the system's performance to support different network topologies.

## 3. The Study

### 3.1. System Level Simulator

The simulator builds upon INET/SimuLTE over the OMNeT++ Discrete Event Network Simulator. OMNeT++ is an extensible, modular, component-based C++ simulation library and framework primarily developed for building network simulators.

SimuLTE is an innovative simulation tool enabling complex performance evaluation at the system level for LTE and LTE Advanced networks in the OMNeT++ framework. It simulates the data plane of the LTE/LTE-A Radio Access Network and Evolved Packet Core. SimuLTE implements eNBs and User Equipment (UE) as OMNET++ compound modules. These can be connected with other nodes (e.g., routers and applications) to compose networks, as shown, e.g., in Figure 1.

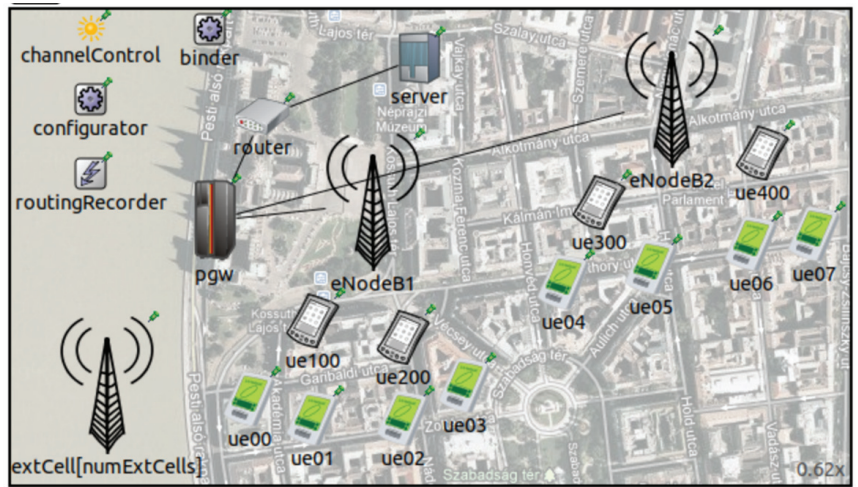


**Figure 1.** Design mode of the NED file in the OMNeT++ environment represents a system with four sensors and two aggregators (6 UEs) attached to an eNB each.

### 3.2. The Scenarios

The first scenario is a one-tier network architecture including communication between two parties, the sensors, and the server as is shown in Figure 2(left). The sensors are deployed along a river; each is assigned to a base station and communicates with the server through the LTE network. The challenges in this scenario are to measure the propagation of a pollutant in a river and the reaction (alarm) on the server side, taking into consideration the QoS of the network in two conditions: periodic monitoring and alarm reaction. In systematic monitoring, each sensor sends the river’s water measurements at a specific time interval. The server continuously checks the measurements, i.e., it compares them against some given thresholds, and when this comparison indicates the presence of a pollutant, it enters into the alarm condition by sending back a command to all the sensors to start sending their data more often (i.e., lowering their sampling and sending time interval) to track the pollutant appropriately while it flows along the water.

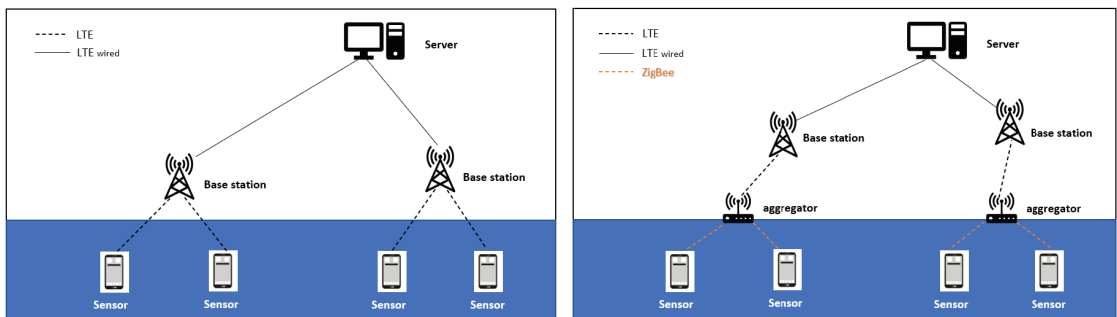


**Figure 2.** (left) Scenario A, one-tier architecture: the sensors are connected directly to the server through the base stations. (right) Scenario B, two-tier architecture: the sensors are connected to an aggregator, and the aggregators are connected to the server through base stations.

The second scenario is a two-tier network architecture including communication between three parties, (i) the sensors, (ii) the aggregators, and (iii) the server, as Figure 2(right) shows. The aggregators collect all the data from the sensors transmitted through ZigBee, aggregate them, and then send them to the server, again through LTE. In this case, we

simulate pollution through a river to investigate the server's reaction considering the QoS of the network, again in the two conditions as before. The difference with the previous scenario is that when the server detects anomalies in the measurements, it cannot reach the sensors directly; instead, it sends a message to the aggregators, which coordinate their group of sensors to lower their sampling and transmission interval.

### 3.3. Pollution Simulation

The primary goal is to simulate the effect of a pollutant on the sensors' measurements and then its propagation along the river. In our simulation, we adopted a simple U-shape model in which the presence of the pollutant leads to a temporary decrease in the  $pH$  measurement of the sensor while the pollutant flows along the river. We imagine placing and ordering the sensors toward the water flow. Accordingly, as the pollutant flows along the river, the sensor  $s_1$  will start reporting a reduction in its  $pH$  measurements to the server at time  $t = T_1$ . At time  $t = T_1 + \Delta T$ , UE2 starts sensing the reduction in its measurements too. The interval  $\Delta T > 0$  depends on the river water's speed (assumed as constant, for the sake of simplicity) and the distance between the sensors. To make the simulation more realistic, we adopt a model of the  $pH$  sensor based on which the value of a sensor reading is assumed to be affected by an error (Equation (1)):

$$pH_{read} = pH_{ideal} + N(0, \sigma) \quad (1)$$

where  $pH_{read}$  is the reading value of the WSN node which will be transmitted,  $pH_{ideal}$  is the value generated according to our U-shape model of the pollutant as described above, and  $N(0, \sigma)$  represents the error as a random value according to a Gaussian distribution having 0 mean and standard deviation  $\sigma$  (e.g.,  $\sigma = 0.01$ ).

### 3.4. Scenarios Implementation

#### 3.4.1. Network A: One-Tier Architecture

In this scenario, the involved entities are  $S$  sensors in the water,  $E$  eNodeB cell towers of the LTE network, and the server. The sensors monitor the river water's  $pH$  and periodically sends the information to the server. In the alarm condition, when the server starts receiving data indicating pollution from a sensor  $s_i$ , it notifies all the subsequent ones ( $s_j$ ,  $j = i + 1, \dots, S$ ) to begin transmitting more often for better tracking the pollutant.

#### 3.4.2. Network B: Two-Tier Architecture

In this scenario, the  $S$  sensors in the water are organized in  $G$  groups, each coordinated by an aggregator. The aggregators are connected to  $E$  eNodeB cell towers of the LTE network, and the server. As before, the sensors monitor the water's  $pH$ , then they transmit the measurements to the aggregator. The aggregator collects the data, aggregates them into a report containing the average, the standard deviation, and the maximum and minimum values of such measurements, and transmits them to the server. In this scenario, the alarm condition involves the server sending commands to aggregators to increase how often they transmit when an alteration in the data is detected. At the same time, the server requests a change in the format of the aggregators' packets from sending aggregated statistics to sending all the (node ID,  $pH$  value)-pairs for each node that the aggregator coordinates.

### 3.5. Simulation Setup

The parameters for the networks A and B mainly consist of the following:

- Network A:  $E = 2$  eNBs and  $S = 6$  sensors. The sensors are equally distributed to the eNBs and directly transmit packets to the server every  $t_{per}^A = 1$  s in the periodic and  $t_{ala}^A = 0.5$  s in the alarm conditions.
- Network B:  $E = 2$  eNBs,  $G = 2$  aggregators and  $S = 6$  sensors (equally distributed between the aggregators). The sensors always transmit data to the aggregator every 1 s.

In the periodic condition, the aggregators communicate to the server every  $t_{per}^B = 2$  s, while in the alarm condition, they transmit to the server every  $t_{ala}^B = 1$  s.

Then, we simulated two scenarios for each network and conditions: (i) varying the number of sensors, i.e.,  $S = \{3; 6; 10; 40; 50\}$ , each generating packets at the application layer with a fixed size of  $P = 40$  B, and the number of aggregators  $G = \{1; 2; 2; 4; 5\}$  for the network B, respectively, and (ii) varying the packet's size  $P$ , i.e.,  $P = \{40; 80; 120; 400; 800; 1000; 2000\}$  bytes, with the number of sensors referred in the two networks above.

The performance indices considered in these simulations are the End-to-End (E2E) delay (from the sensor to the server) and the goodput, i.e., the valuable sensor's measurement data that reach the collector application on the server in the unit of time. For those two indices, we computed their average over all the packets received by the server.

Finally, the default simulation run lasts five minutes.

### 4. Results

Figure 3 shows the resulting E2E delay and goodput in all the simulated cases. In agreement with the LTE protocol and network architecture, which grants to the communicating nodes some so-called resource blocks available in a shared way, the trends we obtained from these results confirm our expectations. Nevertheless, from this figure, a couple of conclusions can be drawn: (i) the LTE network supports well the alarm condition since its end-to-end delay is lower than the periodic condition for all the cases of  $S$  and  $P$ ; (ii) network B scales much better than network A, particularly as a function of  $P$ , where the mean E2E delay stabilizes at values less than 15 ms for the periodic condition and around 10 ms for the alarm condition as the packet size increases above 400 B, as compared with network A cases, whose trend keep increasing; and (iii) when either the number of sensors or the packet size grows, the goodput increases with a pretty stable linear trend. The results suggest that a WSN network, where multiple nodes transmit data to a sink node that sends only the aggregated report to the server, is much more reliable and predictable regarding LTE network performance results.

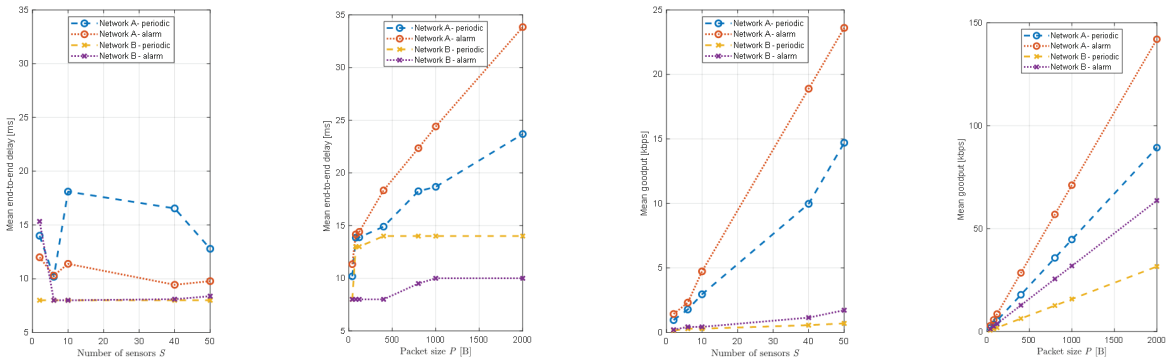


**Figure 3.** Mean end-to-end delay and goodput. From (left) to (right): E2E delay against  $S$ ; E2E delay against  $P$ ; goodput against  $S$ ; and goodput against  $P$ .

The figure also presents an unexpected trend in the delay for network A for both periodic and alarm cases. For instance, we found a mean E2E delay of 18 ms for ten sensors in the periodic case, but for fifty sensors, we obtained only 12 ms, even though the expected network load in the second case is five times higher than in the former. The reason for this is that while we increased the number of sensors  $S$ , we were forced to also increase  $E$ , i.e., the number of the eNBs. Accordingly, the fewer sensors each eNB serves, the lower the E2E delay and, consequently, the lower the network load. To make this more evident, we ran the same experiment with ten sensors two times, the first time, with  $E = 2$  eNBs and

five sensors each, and the second time with  $E = 3$  eNBs and three, three, and four sensors, respectively. The results are shown in Table 1.

**Table 1.** Network A: Mean E2E delay for periodic case as compared to the number of eNBs and different distribution of sensors.

$E$	$S$	Mean E2E Delay [ms]
2	(5 + 5)	18.10
3	(3 + 3 + 4)	13.68

Overall, comparing the alarm results with the periodic conditions, the absolute values show an increase of roughly 40% and 60% in the maximum E2E and goodput, respectively. This is due to the increased traffic generated by the sensor nodes, which flows through the LTE network. Once again, these results confirm that the LTE resources support well the traffic generated by the AQUASENSE WSN, and thus, the expectations already anticipated in our previous work [12] are met.

## 5. Conclusions

This paper gave an overview of the work conducted in the frame of the AQUASENSE project concerning the design, development, and analysis of a communication system. These communication systems are evaluated through computer simulations using SimuLTE for simulating an LTE network infrastructure connecting the WSN with a remote server, where data are collected. In this frame, two network topologies are studied: (i) network A, which represents a multi-cell network, where multiple sensors are associated with different base stations, sending water measurements to the server, and (ii) network B, which is again a multi-cell network, but this time multiple sensors are associated to local aggregators, which collect and aggregate the measurements and send them to the remote server through LTE base stations. For these topologies, the end-to-end delay and the goodput are evaluated as representative performance indices in two conditions: (i) periodic monitoring, where the data are transmitted to the server at larger intervals; and (ii) alarm monitoring, where the data are transmitted more often. The performance of the two scenarios described above demonstrates that when we use the aggregators to collect the data from the sensors, the network's QoS is higher. In particular, an intelligent implementation of how the aggregators provide the information to the server in normal and alarm conditions dramatically helps achieve efficient monitoring and accurate pollution event detection.

**Author Contributions:** Conceptualization, S.B. and S.T.; methodology, S.T.; software, S.B.; validation, S.B. and S.T.; formal analysis, S.T.; investigation, S.T.; resources, S.B.; data curation, S.B.; writing—original draft preparation, S.B.; writing—review and editing, S.T.; visualization, S.T.; supervision, S.T.; project administration, S.T.; funding acquisition, S.T. All authors have read and agreed to the published version of the manuscript.

**Funding:** The European Commission supported the work through AQUASENSE (H2020-MSCA-ITN-2018-813680).

**Institutional Review Board Statement:** Not applicable.

**Informed Consent Statement:** Not applicable.

**Data Availability Statement:** No new data were created or analyzed in this study. Data are contained within the article.

**Conflicts of Interest:** The authors declare no conflicts of interest. The funders had no role in the design of the study; in the collection, analyses, or interpretation of data; in the writing of the manuscript; or in the decision to publish the results.



## References

1. Bakker, K. Water security: Research challenges and opportunities. *Science* **2012**, *337*, 914–915. [CrossRef] [PubMed]
2. Adu-Manu, K.S.; Tapparelo, C.; Heinzelman, W.; Katsriku, F.A.; Abdulai, J.-D. Water quality monitoring using wireless sensor networks: Current trends and future research directions. *Acm Trans. Sens. Netw. TOSN* **2017**, *13*, 4. [CrossRef]
3. Storey, M.V.; van der Gaag, B.; Burns, B.P. Advances in on-line drinking water quality monitoring and early warning systems. *Water Res.* **2011**, *45*, 741–747. [CrossRef] [PubMed]
4. Andersson, K.; Hossain, M.S. Smart Risk Assessment Systems using Belief-rule-based DSS and WSN Technologies. In Proceedings of the 2014 4th International Conference on Wireless Communications, Vehicular Technology, Information Theory and Aerospace and Electronic Systems, VITAE 2014: Co-located with Global Wireless Summit, Aalborg, Denmark, 11–14 May 2014.
5. Thombre, S.; Islam, R.U.; Andersson, K.; Hossain, M.S. IP based Wireless Sensor Networks: Performance Analysis using Simulations and Experiments. *J. Wirel. Mob. Netw. Ubiquitous Comput. Dependable Appl.* **2016**, *7*, 53–76.
6. Andersson, K.; Hossain, M.S. Heterogeneous Wireless Sensor Networks for Flood Prediction Decision Support Systems. In Proceedings of the in 2015 IEEE Conference on Computer Communications Workshops (INFOCOM WKSHPS): 6th IEEE INFOCOM International Workshop on Mobility Management in the Networks of the Future World, Hong Kong, China, 26 April–1 May 2015; pp. 133–137.
7. Thombre, S.; Islam, R.U.; Andersson, K.; Hossain, M.S. Performance Analysis of an IP based Protocol Stack for WSNs. In Proceedings of the 2016 IEEE Conference on Computer Communications Workshops (INFOCOM WKSHPS), San Francisco, CA, USA, 10–14 April 2016; pp. 691–696.
8. Varga, A. (03/10). INET Framework—An Open-Source OMNeT++ Model Suite for Wired, Wireless and Mobile Networks. Available online: <https://inet.omnetpp.org> (accessed on 11 January 2024).
9. Varga, A.; Hornig, R. An overview of the OMNeT++ simulation environment. In Proceedings of the 1st International Conference on Simulation Tools and Techniques for Communications, Networks and Systems & Workshops, Marseille, France, 3–7 March 2008.
10. Virdis, A.; Stea, G.; Nardini, G. Simulating LTE/LTE-Advanced Networks with SimuLTE. In *Simulation and Modeling Methodologies, Technologies and Applications*; Springer: Berlin/Heidelberg, Germany, 2015; pp. 83–105.
11. Jan, F.; Min-Allah, N.; Düşteğör, D. Iot-based smart water quality monitoring: Recent techniques, trends and challenges for domestic applications. *Water* **2021**, *13*, 1729. [CrossRef]
12. Batsi, S.; Tennina, S. Wireless Technologies and Network Planning for Water Quality Monitoring: The AQUASENSE Approach. In Proceedings of the 14th International Conference on Emerging Ubiquitous Systems and Pervasive Networks (Accepted to EUSPN 2023), Almaty, Kazakhstan, 7–9 November 2023.
13. Altair Feko and WinProp Applications. Available online: <https://altair.com/feko-applications> (accessed on 11 January 2024).
14. 3GPP LTE Advanced. Available online: <https://www.3gpp.org/specifications-technologies/releases/release-10> (accessed on 11 January 2024).

**Disclaimer/Publisher’s Note:** The statements, opinions and data contained in all publications are solely those of the individual author(s) and contributor(s) and not of MDPI and/or the editor(s). MDPI and/or the editor(s) disclaim responsibility for any injury to people or property resulting from any ideas, methods, instructions or products referred to in the content.

# Experimental Measurement of Air Temperature in an Enclosure Using Ultrasonic Oscillating Temperature Sensors (Uotses)<sup>†</sup>

Ali Elyounsi<sup>1</sup>, Tim J. Mulroy<sup>2</sup> and Alexander N. Kalashnikov<sup>2,\*</sup>

<sup>1</sup> Industry and Innovation Research Institute, Sheffield Hallam University, Sheffield S1 1WB, UK; a8013965@exchange.shu.ac.uk

<sup>2</sup> Department Engineering and Maths, Sheffield Hallam University, Sheffield S1 1WB, UK; t.j.mulroy@shu.ac.uk

\* Correspondence: a.kalashnikov@shu.ac.uk

<sup>†</sup> Presented at the 10th International Electronic Conference on Sensors and Applications (ECSA-10), 15–30 November 2023; Available online: <https://ecsa-10.sciforum.net/>.

**Abstract:** In this paper, we present experimental findings related to the measurement of air temperature within an enclosure. We utilized both a conventional temperature sensor and a UOTS (ultra-sensitive oscillating temperature sensor) for this purpose. The UOTS's output frequency was measured using a microcontroller's timer and direct memory access. In one experiment, we subjected the air inside the enclosure to rapid heating to evaluate the responsiveness of both sensors. In another experiment, the air temperature was indirectly increased through the laboratory's heating system. The initial experiment reaffirmed the superior responsiveness of the UOTS, as observed in previous tests. The second experiment, conducted over a duration of more than 20 h, allowed us to establish a frequency-temperature curve for the UOTS. It also enabled us to determine that the UOTS exhibits sensitivity at approximately 45 Hz per degree Celsius. This assessment provided valuable insights into temperature underestimation by the conventional temperature sensor, revealing a discrepancy of 9 °C during the rapid heating experiment. This quantified the significant advantage offered by the UOTS in terms of accuracy and responsiveness.

**Keywords:** temperature measurement; temperature monitoring; ultrasonic oscillating temperature sensor; UOTS; frequency measurement

**Citation:** Elyounsi, A.; Mulroy, T.J.; Kalashnikov, A.N. Experimental Measurement of Air Temperature in an Enclosure Using Ultrasonic Oscillating Temperature Sensors (Uotses). *Eng. Proc.* **2023**, *58*, 114. <https://doi.org/10.3390/ecsa-10-16001>

Academic Editor: Stefano Mariani

Published: 15 November 2023



**Copyright:** © 2023 by the authors. Licensee MDPI, Basel, Switzerland. This article is an open access article distributed under the terms and conditions of the Creative Commons Attribution (CC BY) license (<https://creativecommons.org/licenses/by/4.0/>).

## 1. Introduction

Measuring air temperature is crucial for a wide range of human activities, from maintaining comfortable living conditions to preserving food and other materials. Different types of temperature sensors are available, such as resistance temperature detectors (RTDs) known for their high accuracy [1], thermocouples designed for a wider temperature range [2], thermistors that are cost-effective [3], and semiconductor sensors suitable for easy integration with microcontrollers (MCUs) [4]. Conventional contact sensors can only measure the temperature in the immediate vicinity and require time to reach thermal equilibrium before sensing any changes in their environment. In addition to these conventional options, non-contact temperature sensors like infrared sensors are utilized to measure the temperature of objects located at a distance. The global market size for temperature sensors was valued at \$6.3 billion in 2020 and was projected to grow at an annual rate of 4.8% until 2027 [5].

Ultrasonic oscillating temperature sensors (UOTS) offer a compelling alternative to conventional temperature sensors as they can measure temperature across the entire ultrasound pathway, responding rapidly to changes in temperature. UOTS are made up of two ultrasonic transducers, a receiver and transmitter, and an electronic amplifier that compensates for acoustic and electrical losses in the signal loop, allowing the oscillations to continue. The medium between the transducers, where the ultrasound propagates,

acts as the body of the sensor, as the speed of ultrasound is dependent on the medium’s temperature. The relative merits of the various air temperature sensors are presented in Table 1.

**Table 1.** Advantages and disadvantages of various air temperature sensors.

Title 1	Thermistors	Thermocouples	RTDs	Semiconductor	UOTsEs
Advantages	Cost	Measurement range	Accuracy	Ease of interfacing	Aggregate measurement Instant response
Dis-advantages	Accuracy	Sensitivity Thermal inertia and single point measurement	Cost	Cost	Hysteresis of readings Experimental only

Over the years, our research group developed various UOTsEs for use in water and demonstrated that their advantages were achieved at a considerably lower cost compared to the direct measurement of the ultrasonic time of flight. Recently, we started developing UOTsEs for air temperature measurements [6].

Section 2 of this paper describes the instrumentation and experimental procedures used in our study. Section 3 presents the data recorded by a conventional temperature sensor and the UOTS for a rapid heating test of the air inside an enclosure. The measurement results, recorded for 22 h in an open office environment, are presented in Section 4. Section 5 summarizes and concludes the paper.

## 2. Instrumentation and Experimental Procedures

We employed the experimental arrangement and equipment described in a previous article [6] with an important enhancement for the frequency measurement reported in [7]. The distance between the transducers was set at 150 mm. The UOTS output frequency was measured for 4000 periods using a clock frequency of 10 MHz. The measurement time was around 0.1 s (4000/40,000 Hz). The number of the counted clock pulses was approximately 1,000,000 (0.1 s × 10,000,000 Hz), resulting in a counting error of up to one pulse out of 1,000,000 or roughly 0.04 Hz frequency measurement error (40 kHz/1,000,000). After each measurement, there was a 0.1-s delay before the next measurement began.

The temperature readings were taken every second from the BMP280 sensor and stored on an SD card with a time stamp provided by a real-time clock.

Two experiments were carried out. The first one involved a rapid heating test in which a hairdryer was used to quickly increase the temperature inside the enclosure to record readings from both the conventional temperature sensor and the UOTS, as performed previously [6]. After switching the hairdryer on, some time was taken for the heater and fan to operate at full power, and then it was directed inside the enclosure.

The second experiment involved taking measurements over extended periods of time in an open office environment, where the heating was turned on for several hours in the afternoon. The sensors were placed inside the enclosure to minimize the influence of air circulation on the UOTS readings. It should be noted that enclosing conventional sensors also helps reduce the scatter of their readings.

## 3. Assessing Responsiveness of the Sensors to a (Nearly) Step Change in Air Temperature

We use a cardboard box to house both sensors and created a step change by using a hairdryer as it was shown in Figure 6 [5]. Upon initiating the recording of both temperature and UOTS output frequency, the hairdryer was removed from the enclosure, directed away from it, and switched on for a period of time to allow its heating element to reach the desired temperature. Subsequently, the hairdryer was directed inside the enclosure for a brief duration. To minimize air exchange with the environment, the enclosure flap was closed. This sequence was repeated five times, as illustrated in Figure 1a. Figure 1b

provides a closer view of the recorded data, highlighting that the frequency of the UOTS decreased more rapidly compared to the readings from the conventional temperature sensor when the hairdryer was turned off.

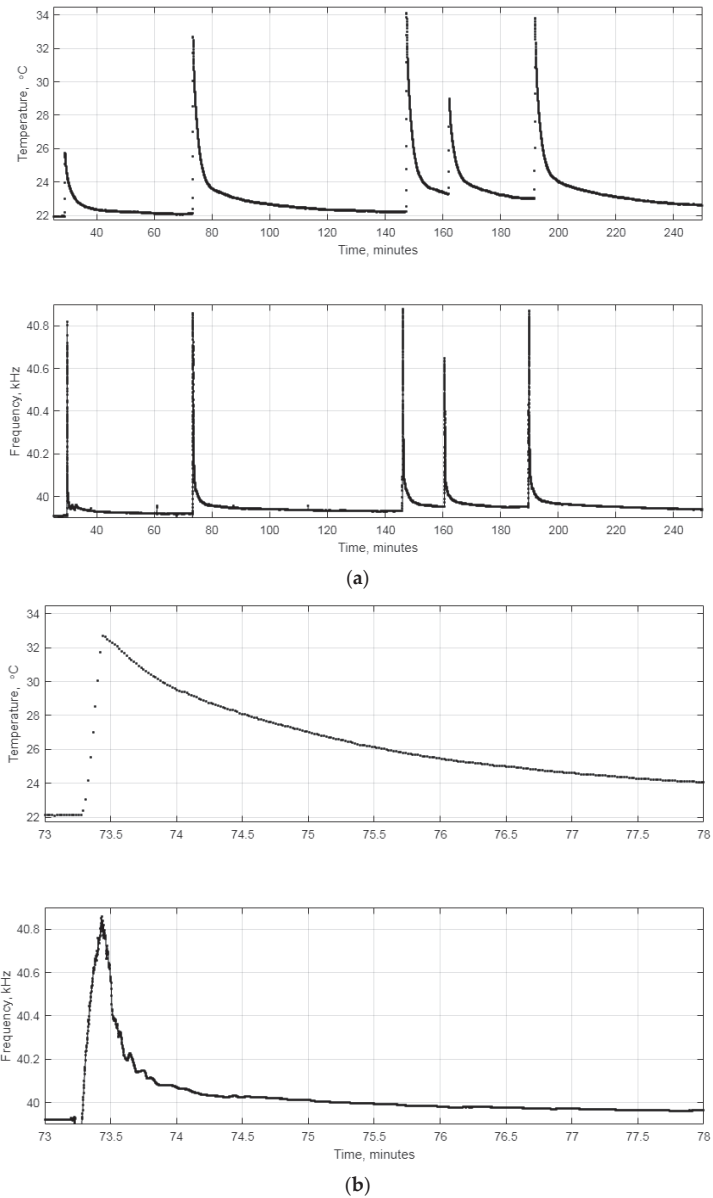


**Figure 1.** Experimental records for the rapid heating test (0.1 s measurement time). (a) Five subsequent heating cycles. (b) A section of the complete recording (second heating instance) viewed at a closer scale.

The test conducted successfully showcased the significantly quicker response time of the air UOTS in comparison to conventional temperature sensors, confirming previous findings as reported in references [6].

#### 4. Continuous Monitoring of the Temperature inside the Enclosure

An UOTS detects temperature by responding to changes in the speed of sound, which is approximately  $0.6 \text{ m/s}/^\circ\text{C}$  [8]. Additionally, this speed is influenced by relative humidity (around  $0.2 \text{ m/s}$  per 10%) and the speed of axial wind if present. To evaluate the feasibility of the UOTS as low-cost temperature sensors, we placed the sensor inside a cardboard box to minimize air movement and humidity fluctuations compared to the surrounding environment.

Figure 2a illustrates the temperature and UOTS frequency recorded over a 22-h period in an open-plan office environment during the night, with the heating being activated roughly 5.5 h after the start of the recording. These curves demonstrate a remarkable visual similarity when appropriately scaled. However, the UOTS frequency curve exhibited spikes resembling those observed earlier when the UOTS was operated in liquids.

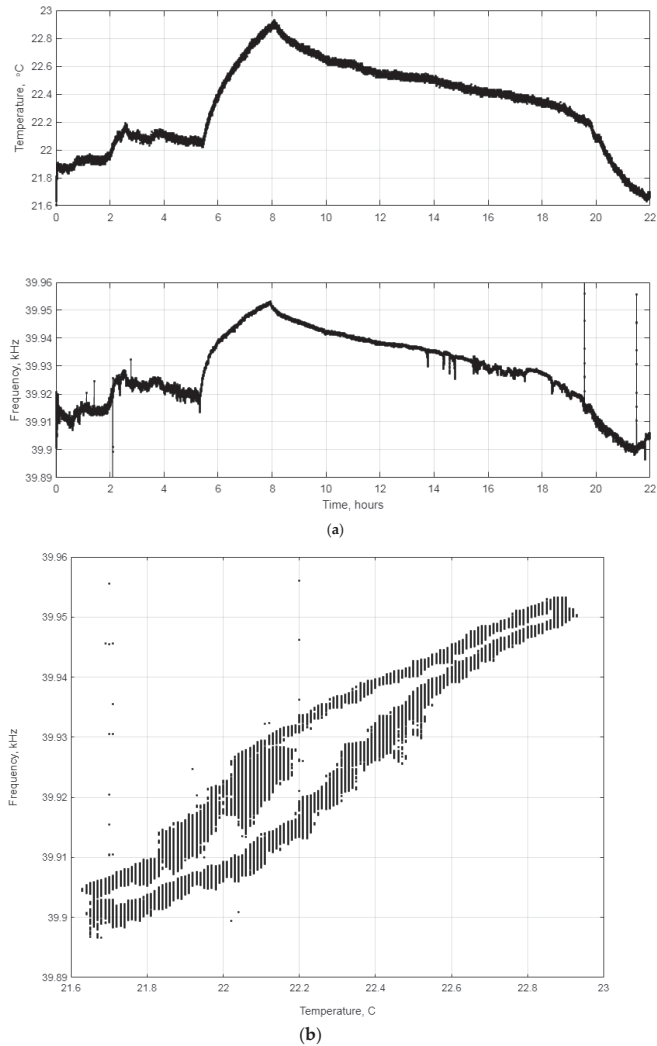


**Figure 2.** Records obtained from an experiment monitoring the air temperature overnight inside a container (0.1 s measurement time). (a) Overall recordings. (b) Temperature–frequency relationship showing hysteresis.

Figure 2b presents a scatter diagram depicting the temperature-frequency readings, interpolated to correspond to the same time instances. If the plot resembled a narrow straight line, it would have been convenient to convert the UOTS readings directly into the temperature values recorded by the temperature sensor. However, this was unlikely because the conventional contact sensor had a greater thermal inertia, as demonstrated in Figure 1, and it did not capture the entire space between the transducers. Consequently, since the UOTS was not calibrated at this stage, we utilized the readings from the conventional temperature sensor as the best estimate available for the temperature between the transducers.

The scatter plot reveals some hysteresis in the frequency of the UOTS, as evidenced by the different frequency values at the same temperature. The slope of the graph indicates the sensitivity of the UOTS frequency to temperature, which we roughly estimated to be 45 Hz/°C within the temperature range of 21.8 °C to 22.8 °C. As the variation in UOTS frequencies at the same temperature did not exceed 20 Hz, we can conclude that the uncertainty of the UOTS output frequency in representing the readings of the conventional temperature sensor was within  $\pm 10$  Hz/45 Hz/°C, approximately  $\pm 0.22$  °C. For the current unoptimized prototype, this level of uncertainty was deemed acceptable.

This sensitivity value allows us to assess temperature increases when hot air from a hairdryer is introduced into the enclosure (Figure 1b). Since the frequency increased by up to 900 Hz, we can estimate that the air temperature rose by approximately 900 Hz/45 Hz/°C, which amounts to around 20 °C. This increase was considerably higher than the reported increment by the conventional temperature sensor, which was approximately 11 °C from the 22 °C baseline.

## 5. Summary and Conclusions

This paper presents experimental temperature data collected using both a conventional temperature sensor and a UOTS for measuring air temperature within an enclosure, employing most of the setups previously detailed [6]. The primary distinction in this study was related to the UOTS's output frequency measurement method [7], which allowed for measurements to be taken every 0.1 s using an economical general-purpose microcontroller synchronized by a standard crystal oscillator. This represented a significant cost reduction compared to specialized microcontrollers that required oven-controlled crystal oscillators, as used in prior studies.

These sensors were positioned within a cardboard enclosure and subjected to two scenarios: rapid heating of the enclosed air and continuous temperature monitoring over a full day. The initial experiment affirmed the UOTS's superior responsiveness, consistent with previous findings [6]. However, the second experiment demonstrated the UOTS's suitability for long-term temperature monitoring, enabling the creation of a frequency-temperature diagram, which yielded an estimated UOTS sensitivity of 45 Hz per degree Celsius. Using this value, we calculated a temperature increase of 20 °C during the first experiment, whereas the conventional temperature sensor reported an increase of only 11 °C from the initial 22 °C baseline.

These developments and experimental outcomes open the possibility of constructing cost-effective ultrasonic temperature sensors capable of providing reliable and prolonged temperature readings that closely correspond to those of conventional sensors. The advantages of UOTS devices include enhanced responsiveness and the ability to measure temperature throughout the entire path between the transducers. The subsequent phase of UOTS development involves evaluating their performance in open spaces at various distances between the transducers.

**Author Contributions:** Conceptualization, A.N.K.; methodology, A.N.K.; software, A.N.K.; validation, A.E.; formal analysis, A.E.; investigation, A.E.; resources, A.E.; data curation, A.E.; writing—original draft preparation, A.N.K.; writing—review and editing, A.N.K.; visualization, A.E.; supervision, A.N.K. and T.J.M.; project administration, A.E. and T.J.M.; funding acquisition, A.E. All authors have read and agreed to the published version of the manuscript.

**Funding:** This research received no external funding.

**Institutional Review Board Statement:** Not applicable.

**Informed Consent Statement:** Not applicable.

**Data Availability Statement:** We did not upload the obtained data to a public repository because of the amount of work involved in properly describing and labeling these. However, we are happy to supply the reported data upon request.

**Acknowledgments:** Ali Elyounsi gratefully acknowledges support for his PhD studies from the Libyan Embassy (UK).

**Conflicts of Interest:** The authors declare no conflict of interest.

## References

1. The Fundamentals of RTD Temperature Sensors, PR Electronics. Available online: <https://www.prelectronics.com/the-fundamentals-of-rtd-temperature-sensors/> (accessed on 3 January 2023).
2. Webster, E. A critical review of the common thermocouple reference functions. *Metrologia* **2021**, *58*, 025004. [CrossRef]
3. Wang, H. Experimental Research on the Stability of Negative Temperature Coefficient Thermistors. *IEEE Instr. Meas. Mag.* **2023**, *26*, 42–47. [CrossRef]
4. Designing with Semiconductor Temperature Sensors, Sensor Tips. Available online: <https://www.sensortips.com/temperature/designing-with-semiconductor-temperature-sensors/> (accessed on 3 January 2023).
5. Temperature Sensor Market by Product Type (Thermocouples, RTDs, Thermistors, Temperature Sensor ICs, Bimetallic, Infrared, and Fiber Optic Temperature Sensors), Output, End-User Industry, and Region—Global Forecast to 2027, MarketsandMarkets, March 2020, Online Summary. Available online: <https://www.marketsandmarkets.com/Market-Reports/temperature-sensor-market-522.html> (accessed on 3 January 2023).
6. Elyounsi, A.; Kalashnikov, A.N. Ultrasonic Oscillating Temperature Sensor for Operation in Air. *Eng. Proc.* **2021**, *10*, 62. [CrossRef]
7. Elyounsi, A.; Kalashnikov, A.N. Continuous Rapid Accurate Measurement of the Output Frequency of Ultrasonic Oscillating Temperature Sensors. *Eng. Proc.* **2022**, *27*, 56. [CrossRef]
8. Kaye and Laby, Tables of Physical and Chemical Constants, Table for Speed of Sound in Air. Available online: <https://tinyurl.com/3ajpxh67> (accessed on 3 January 2023).

**Disclaimer/Publisher’s Note:** The statements, opinions and data contained in all publications are solely those of the individual author(s) and contributor(s) and not of MDPI and/or the editor(s). MDPI and/or the editor(s) disclaim responsibility for any injury to people or property resulting from any ideas, methods, instructions or products referred to in the content.

Proceeding Paper

# Interaction of the Fluorescent Cell-Labeling Dye Rhodamine 6G with Low-Molecular-Weight Compounds: A Comparative QCM Study of Adsorption Capacity of Rh6G for Gaseous Analytes <sup>†</sup>

Ivanna Kruglenko <sup>\*</sup>, Julia Burlachenko and Borys Snopok

Department of Optoelectronics, V.E. Lashkaryov Institute of Semiconductor Physics, National Academy of Sciences of Ukraine, 41 Pr. Nauki, 03028 Kyiv, Ukraine; burlachenko@isp.kiev.ua (J.B.); snopok@isp.kiev.ua (B.S.)

<sup>\*</sup> Correspondence: kruglen@isp.kiev.ua

<sup>†</sup> Presented at the 10th International Electronic Conference on Sensors and Applications (ECSA-10), 15–30 November 2023; Available online: <https://ecsa-10.sciforum.net/>.

**Abstract:** Rhodamine 6G is widely used in biochemistry and cell imaging as a sensitive layer of chemical sensors. At the same time, the features of the interaction of Rh6G with low-molecular-weight analytes present in most biochemical preparations have not been studied. In this study, the interaction of Rh6G thin films with water vapor, acetic acid, ethyl alcohol, ammonia, benzene, pyridine, nitrobenzene, acetone, and acetonitrile in the gas phase was studied. The kinetic features and adsorption capacity of the sensitive layer were compared with those of other sensitive layer materials (macrocyclic dibenzotetraazaanulenes, phthalocyanines, and their metal complexes). The response values of the Rh6G-based sensor significantly exceed the responses of other sensors, regardless of the type of analyte. This means that this material is promising for multivariate sensor arrays, where the issue of cross-selectivity is a prerequisite. However, when developing selective sensors or when using Rhodamine 6G for analytical analysis in biochemistry, the ability of Rh6G to interact with a wide range of low-molecular-weight analytes must be taken into account.

**Keywords:** QCM sensor; Rhodamine 6G; adsorption; absorbance; low-molecular-weight analytes

**Citation:** Kruglenko, I.; Burlachenko, J.; Snopok, B. Interaction of the Fluorescent Cell-Labeling Dye Rhodamine 6G with Low-Molecular-Weight Compounds: A Comparative QCM Study of Adsorption Capacity of Rh6G for Gaseous Analytes. *Eng. Proc.* **2023**, *58*, 115. <https://doi.org/10.3390/ecsa-10-16200>

Academic Editor: Stefano Mariani

Published: 15 November 2023



**Copyright:** © 2023 by the authors. Licensee MDPI, Basel, Switzerland. This article is an open access article distributed under the terms and conditions of the Creative Commons Attribution (CC BY) license (<https://creativecommons.org/licenses/by/4.0/>).

## 1. Introduction

Chemosensors based on rhodamine and its derivatives are potentially attractive tools for analytical chemistry, biology, medicine, and environmental protection. Such sensor systems play an important role as they are simple, fast, effective, and low-cost monitoring and diagnostic tools. High biocompatibility and fluorescence in the near-infrared range of rhodamine derivatives make them an excellent choice for the creation of biosensors.

Rhodamine 6G is a highly effective luminescent xanthene dye of the rhodamine family. The building blocks common to all rhodamines are a dibenzopyrene chromophore (xanthene) and a derivative of the benzoic acid molecule (carboxyphenyl group) (Figure 1). Rhodamines are singly charged positive ions with a size of *c.a.*  $0.7 \times 1.4$  nm; the positive charge is mainly located on two amino groups (due to the tautomerism of two energetically equivalent states with the rearrangement of the aromatic ring and a  $-C=N^+$  double bond). An interesting feature of its molecular structure is the perpendicularity of the plane of the xanthene chromophore and that of the aromatic carboxyphenyl group.

In recent years, there has been a consistent development of classical rhodamine-based sensor systems; at the same time, researchers are showing an increasing interest in new devices that use non-standard analytical approaches [1]. In particular, the use of rhodamine-based luminescent chemosensors that emit in the near-infrared range (NIR) is considered for the detection of metal ions such as Al(III), Cu(II), Hg(II), Co(II), Fe(III), Au(III), and Cr(III) [2].



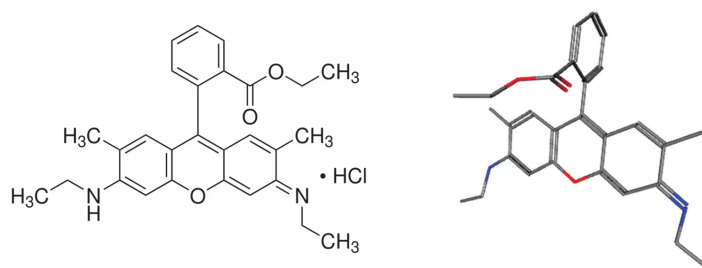


**Figure 1.** Chemical structure (left) and the 3D conformation (right) of Rhodamine 6G molecule. The spatial structure is presented according to PubChem modeling data (<https://pubchem.ncbi.nlm.nih.gov/compound/Rhodamine-6G#section=Names-and-Identifiers> (accessed on 17 January 2024)).

Sensors based on Rhodamine 6G can be used for water vapor detection, as hydrogel sensors capable of detecting  $\text{Hg}^{2+}$  in flowing or stagnant water [3], to detect the physiologically important ions of transition metals, such as Cu(II) and Fe(III) [4]. The idea of detecting heavy and transition metal ions using different characteristics of the same Rh6G sensors in living organisms is particularly attractive [5,6].

Rhodamine 6G is also widely used for labeling oligonucleotides in biochemistry as well as cell imaging. Despite the widespread use of this compound for various analytical purposes, the features of the interaction of Rh6G with low-molecular-weight analytes present in most biochemical preparations have not been studied. This is important not only for understanding the possibility of the influence of non-target components on the analytical signal during analysis, but also it is of great practical importance since it allows the development of (bio)chemical sensors for specific applications. In this study, we studied the features of the interaction of Rh6G thin films with a number of low-molecular-weight analytes in the gas phase (to exclude cross-interaction, etc.), namely, water vapor, acetic acid, ethyl alcohol, ammonia, benzene, pyridine, nitrobenzene, acetone, and acetonitrile. The kinetic features and the adsorption capacity of the sensitive layer were compared with those for other classical sensitive layer materials (macrocyclic dibenzotetraazaanulenes, phthalocyanines, and their metal complexes).

## 2. Materials and Methods

$\text{H}_2\text{TAA}$ , its derivative (EGTAA), and their metal complexes with copper were kindly provided by Prof. Lampeka Ya.D. Phthalocyanine, its metal complexes with copper and lead, and Rhodamine 6G were obtained from Sigma-Aldrich Inc. and were used without additional purification (Figure 2). Planar molecules of  $\text{H}_2\text{TAA}$  and its metal complexes with copper form dimers in the crystalline state;  $\text{H}_2\text{EGTAA}$  molecules and their metal complexes lose their planar conformation due to the steric effects of peripheral substituents. Phthalocyanines do not form dimers, both in the case of planar ( $\text{H}_2\text{Pc}$  CuPc) and structures distorted by the large size of the cation (PbPc). Thus, these compounds demonstrate quite diverse binding centers on the surface of their films for molecules from the gas phase.

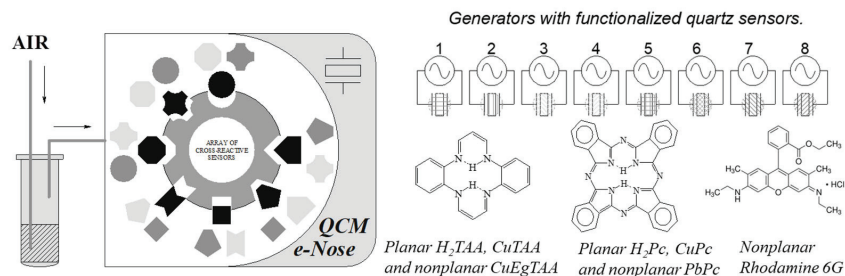


**Figure 2.** Illustration of the measurement procedure using an “electronic nose”-type system based on quartz microbalance transducers with the sensitive layers of organic molecular crystals.

Thin oriented films of all compounds used as sensitive layers in this study were obtained using thermal sputtering in vacuum (VUP-5M, pressure of  $5 \times 10^{-4}$  Pa, growth rate of *c.a.* 0.1 nm/min) at a temperature of  $297 \pm 2$  °K. Furthermore, 100 nm thick films were deposited on one side of metal electrodes of quartz piezoelectric resonators (quartz crystal microbalance, QCM) of RK169 type with a resonant frequency of 10 MHz.

To prepare the samples, we used double-distilled water and chemically pure acetic acid, ethyl alcohol, ammonia, benzene, pyridine, nitrobenzene, and acetone acids obtained from the Khimlaborreaktiv (UA) and Makrokhim (UA) companies. Liquids (5 mL) were collected immediately before measurements. To form a sample (headspace), the gas phase formed above the surface of a liquid due to bubbling was mixed with a flow (60 mL/min) of carrier gas (argon) at a constant temperature ( $297 \pm 2$  °K) (Figure 2).

The measurement procedure included (i) the stabilization of the baseline in an argon flow (frequency deviation:  $\pm 2$  Hz), (ii) an exposure to a gas sample of analyte vapor in carrier gas (10–25 min) under the constant flow rate, and (iii) subsequent purging with a carrier gas. To minimize the influence of previous experiments, a break of at least 4–5 h was taken between individual experiments, during which the sensor array was in an atmosphere of dried argon.

The equipment and software developed in the V. Lashkaryov Institute of Semiconductor Physics NAS of Ukraine were used for QCM oscillation excitation and for the measurements of their frequency shifts, which is proportional to the change in mass due to the adsorption of analyte's molecules (Figure 2) [7].

### 3. Results and Discussion

#### 3.1. Features of the Optical Characteristics of Thin Films of Rhodamine 6G

Despite the widespread use of Rh6G as a material for many optical devices (the active medium of tunable lasers, waveguide substrates, etc.), many features of its absorption spectrum remain unclear (Figure 3). Indeed, the lowest energy absorption band consists of a large peak (*c.a.* 545 nm, the bathochromic shift relative to the 520 nm position in solution is due to an interaction between molecules in a solid [8]) with the smaller peak at 514 nm (*c.a.* 498 nm in solution) and shoulder around 475 nm. According to the results of quantum chemical calculations, the absorption in this region is due to  $\pi$ - $\pi$  transition (HOMO-LUMO), whose electron density is localized predominantly in the xantheno ring of Rh6G [9]. A characteristic feature of this transition is a vibronic structure as a shoulder at smaller wavelengths [10] due to electron–vibrational interaction (for example, in planar dibenzotetraazaannulene and its complexes). The results of spectral analysis in the gas phase [11], where the formation of intermolecular aggregates is unlikely, confirm the presence of a shoulder on the short-wavelength side of the main transition. This allows us to conclude that for Rh6G, there is a process of interaction between the lower electronic transition and the intramolecular vibration.

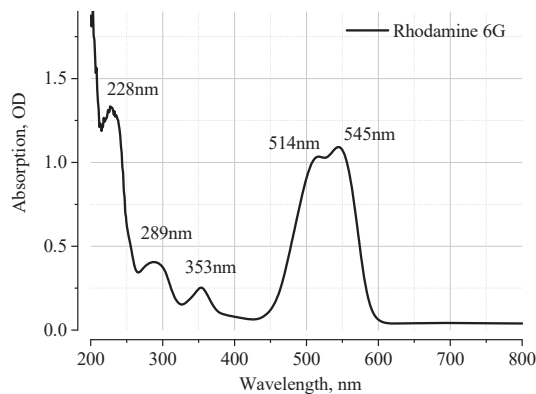


**Figure 3.** The absorption spectrum of the 100 nm thick Rhodamine 6G film on a glass substrate obtained with thermal sputtering in vacuum.

At the same time, the numerous results of experimental studies show that upon transition from the gas phase to a solvent environment, Rh6G molecules form stable dimeric structures (H-dimers, which form in the ground state), and the equilibrium of these structures with single molecules depends on their concentration in the solution and on the type of solvent [12]. The absorption band of the dimer practically coincides with the position of the first vibronic band of the monomer, which makes their separation difficult. Theoretical calculations confirm the possibility of self-assembly of this kind of Rh6G aggregates [13]: calculation results predict the substantial redshifts or blueshifts of the optical absorption spectra of Rh6G dye molecules after aggregation in J or H dimers, respectively. Experimental results confirm theoretical expectations. For example, in thin films, dimers are credited with making the main contribution to high-luminescence quantum yields [14]. Despite some ambiguity in the interpretation of the role of Rh6G dimers in different aggregative states, there is an undoubtable need to take into account the characteristic features of excimer aggregates (the dimers of the same compound formed in the ground state) when considering the effects with their participation.

The absorption spectrum of the Rhodamine 6G film, presented in Figure 3, demonstrates not only the typical bathochromic shift of the spectrum of organic molecular crystals upon transition to a solid but also shows changes in the shape of the spectrum compared to the spectrum in solution [15]. Taking into account the short discussion above, it can be assumed that the increase in the band intensity in the 514 nm region is associated with the formation of Rh6G dimeric structures in the solid.

Summarizing all abovementioned facts, it is reasonable to highlight that Rh6G thin films may contain several types of reactive centers, and the properties of which differ due to one of the following local structural organizations: (1) several nucleophilic centers of different nature in the region of different types of side groups with the possibility of rotation and the ability to specifically interact with other molecules (including through the formation of hydrogen bonds); (2) the conjugated parts of molecule suitable for the formation of various configurations with aromatic fragments of other molecules and stacking interactions; (3) centers whose energy is modulated by the vibrational modes of the molecule; (4) dimeric structures with different energy levels due to the local effects of neighboring, closely located molecules; and (5) supramolecular structures caused by the structural feature of Rhodamine 6G due to the specific configuration of the molecule, namely, the perpendicular arrangement of the plane of the central fragment and a separate aromatic ring.

As noted above, in this study, we are interested in analyzing the diversity of binding centers for gaseous molecules in the thin films of Rhodamine 6G. The most promising way of doing so is direct adsorption measurements using the analytes of various natures, which allow the formation of various configurations of the organic adsorbate, and, accordingly, obtaining information about the cross-reactive (low-selective) centers that are present in this system.

### *3.2. The Ratio between the Magnitude of the Responses of QCM Sensors Based on Rhodamine 6G Sensitive Layers and Macrocyclic Heterocycles*

The analysis of the obtained results unambiguously indicates that, among the used sensitive materials mentioned above, Rh6G has the maximum value of response with respect to all studied analytes in the gas phase (Figure 4). Despite the fact that the kinetics of the interaction of Rh6G with analytes significantly depends on the nature of the analyte, the interaction is controlled by the process of physical (ad)sorption and is a completely reversible process.

It should be especially emphasized that the response values for the Rh6G-based sensor significantly exceed the responses of other sensors, regardless of the type of analyte. This means that this material is promising for multivariate sensor arrays, where the issue of cross-selectivity is a prerequisite. However, this is an unacceptable property for selective and, especially, specific sensors, since the surface of the coating based on Rhodamine 6G

has a sufficiently high adsorption capacity for compounds of various natures. Notably, this is applicable to the equilibrium filling of the surface in the presence of an analyte, i.e., reversible processes caused by interactions based on surface binding reactions typically of the physical adsorption type.

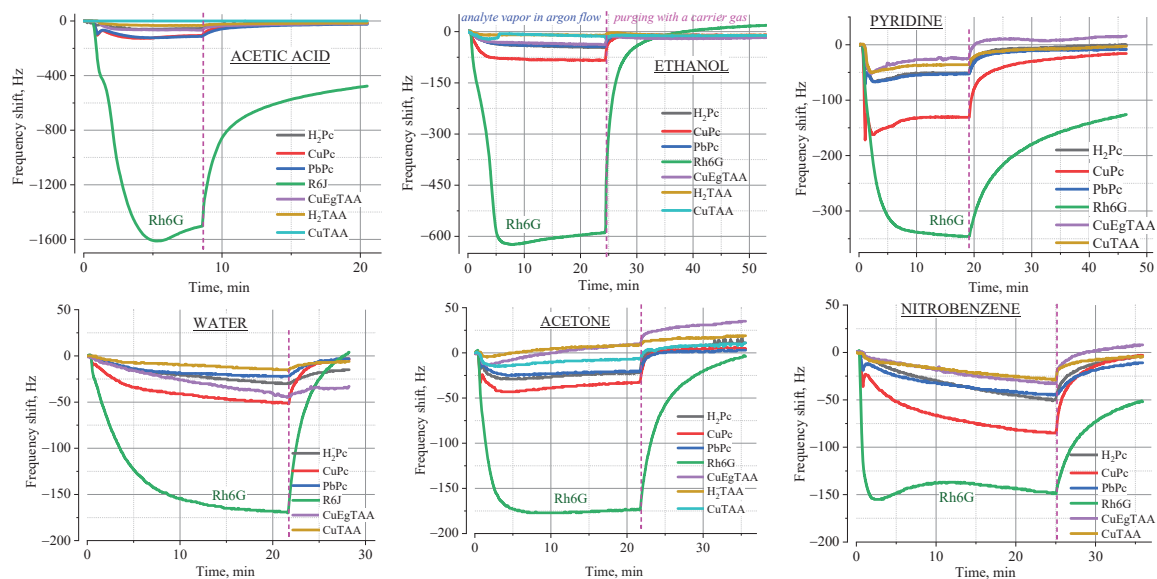


**Figure 4.** Typical adsorption curves for various analytes (acetic acid, ethyl alcohol, pyridine, nitrobenzene, and acetone) for a sensor array with sensitive coatings based on heterocyclic macrocycles (annulenes and phthalocyanines, including their complexes with copper and lead) and Rhodamine 6G.

### 3.3. Features of the Response of a Sensor with a Sensitive Coating Based on Rhodamine 6G in Relation to Analytes of Various Nature

The response of sensors coated by Rhodamine 6G shows that the adsorption of all analytes is characterized by monotonic dependences when reaching a saturation level. The magnitude of the frequency shift is determined by the nature of the analyte (Figure 5). As can be seen from the figure, this coating has the greatest adsorption capacity for acetic acid and ethyl alcohol and the smallest adsorption capacity for acetonitrile, acetone, and nitrobenzene. The rather small response to water (about 200 Hz), in which Rh6G is highly soluble, is apparently due to the short exposure time. Indeed, as can be seen from Figure 4, the adsorption process did not reach a steady state, suggesting a higher adsorption capacity. Moreover, as already observed, in such cases, there are changes in the morphology of the coating and, as a consequence, changes in the selectivity profile of the sensor element. Thus, such sensors are unsuitable for practical use.

Acetonitrile, acetone, and nitrobenzene are similar in their limited ability to form hydrogen bonds, and the interactions in which they participate are usually related to the polar nature of their molecules (large dipole moments, tendency towards nucleophilic reactions, etc.). The small response values for these analytes possibly indicate that, on the surface of Rhodamine 6G, there is a relatively large number of centers capable of forming hydrogen bonds. The response to ethyl alcohol confirms this statement. Moreover, the presence of methyl and hydroxyl fragments in the structure of the ethyl alcohol molecule can facilitate its binding, since similar bi-functional fragments are present in the Rhodamine 6G molecule, its dimers, or more complex aggregates. The same principle of multifunctional coincidence according to the somewhat simplified “guest-host” principle can explain the rather strong difference in the adsorption capacity in relation to the analytes listed above.

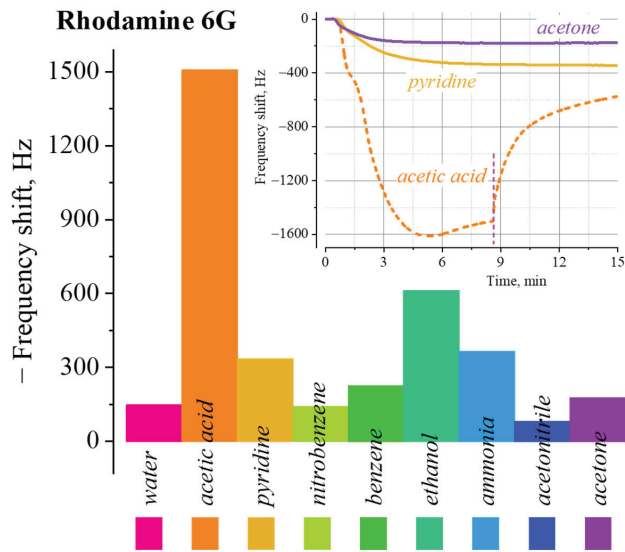


**Figure 5.** The maximum response amplitudes of a QCM sensor with a sensitive Rh6G-based coating on the vapors of different analytes (inset): the kinetic dependences of the frequency change on time during the adsorption of acetic acid, pyridine, and acetone molecules from their vapors in carrier gas (argon) under a constant flow rate.

As can be seen from the presented data, the greatest response is observed for acetic acid vapor. First of all, it should be noted that the response in this case is non-monotonic, i.e., after reaching the minimum frequency value, the response begins to increase. This behavior, in particular, may be associated with an anti-Sauerbrey response, i.e., changes in the mechanical properties of the coating are caused due to swelling, morphological changes, etc. [16]. A similar effect, although to a lesser extent, is observed for alcohol, in which these films can also dissolve.

The highest magnitude of adsorption on the surface of acetic acid molecules may be associated with cooperative solvation effects capable of forming multicomponent surface coatings. However, it is known that, in the gas phase, acetic acid is in the form of a dimer, which, when adsorbed on a surface, breaks down into two acid molecules, forming hydrogen bonds with the surface and with other acid molecules on a surface. In the case of dilute acetic acid, its percentage on the surface decreases due to the presence of water molecules; however, at the same time, conditions are created for the formation of surface networks of a multimolecular coating. According to the classification of solvents, acetic acid belongs to solvents that have acidic properties and are prone to the formation of loosely bound large surface associates.

#### 4. Conclusions

The wide variety of low-energy binding sites for gaseous analytes on the surface of Rhodamine 6G films are due to a number of interrelated reasons at different levels of organization of the sensitive materials:

1. The presence of nucleophilic centers of different natures on side groups with the possibility of forming hydrogen bonds;
2. The ability of forming hydrophobic interactions, including those due to aromatic stacking;
3. Binding centers and their energy is modulated by the vibrational modes of the molecule;
4. The presence of dimeric structures with different energy levels due to the local effects of neighboring, closely located molecules;

### 5. Supramolecular structures that stimulate the cooperative surface binding.

All this leads to an increase in the diversity of analytes capable of binding to the surface of Rhodamine 6G. It is the low selectivity coupled with the differences in responses to various analytes that make this material promising for cross-reactive sensor systems, provided that the selectivity profile is maintained with its long-term use. At the same time, these effects of physically (ad)sorbed compounds must be taken into account when developing selective sensors.

Finally, it is reasonable to emphasize the promise of Rh6G for the development of composite materials, since the combination of Rh6G with various inorganic nanostructured materials (ZnO, metal nanoparticles, etc.) makes it possible to purposefully change the selectivity profile of a sensitive layer. This allows the creation of efficient sensor arrays optimized for specific applications, including environmental monitoring or as a potential bio-sniffer for acute toxicity assays or highly sensitive sensors of the low-molecular-weight biological regulators of vital activity.

**Author Contributions:** Conceptualization, B.S. and I.K.; methodology, B.S., I.K. and J.B.; formal analysis and validation, I.K. and J.B.; investigation, J.B.; data curation, B.S. and J.B.; writing—original draft preparation, B.S.; writing—review and editing, B.S. and I.K.; visualization, J.B. All authors have read and agreed to the published version of the manuscript.

**Funding:** This research received no external funding.

**Institutional Review Board Statement:** Not applicable.

**Informed Consent Statement:** Not applicable.

**Data Availability Statement:** Data are available on request.

**Conflicts of Interest:** The authors declare no conflicts of interest.

## References

1. Wang, Y.; Wang, X.; Ma, W.; Lu, R.; Zhou, W.; Gao, H. Recent Developments in Rhodamine-Based Chemosensors: A Review of the Years 2018–2022. *Chemosensors* **2022**, *10*, 399. [CrossRef]
2. Sarkar, S.; Chatterjee, A.; Biswas, K. A Recent Update on Rhodamine Dye Based Sensor Molecules: A Review. *Crit. Rev. Anal. Chem.* **2023**, *27*, 1–27. [CrossRef] [PubMed]
3. Qu, Z.; Wang, C.; Duan, H.; Chi, L. Highly efficient and selective supramolecular hydrogel sensor based on rhodamine 6G derivatives. *RSC Adv.* **2021**, *11*, 22390–22397. [CrossRef] [PubMed]
4. Sikdar, A.; Panja, S.S.; Biswas, P.; Roy, S. A Rhodamine-Based Dual Chemosensor for Cu(II) and Fe(III). *J. Fluoresc.* **2012**, *22*, 443–450. [CrossRef] [PubMed]
5. Wang, L.; Yan, J.; Qin, W.; Liu, W.; Wang, R. A new rhodamine-based single molecule multianalyte (Cu 2p, Hg 2p) sensor and its application in the biological system. *Dye. Pigment.* **2012**, *92*, 1083–1090. [CrossRef]
6. Suresh, M.; Shrivastav, A.; Mishra, S.; Suresh, E.; Das, A. A Rhodamine-Based Chemosensor that Works in the Biological System. *Org. Lett.* **2008**, *10*, 3013–3016. [CrossRef] [PubMed]
7. Snopok, B.A.; Kruglenko, I.V. Multisensor systems for chemical analysis: State-of-the-art in Electronic Nose technology and new trends in machine olfaction. *Thin Solid Film.* **2002**, *418*, 21–41. [CrossRef]
8. Snopok, B.A.; Lampeka, Y.D. Electron interactions in crystalline dibenzotetraazaannulene. *Theor. Exp. Chem.* **1996**, *32*, 20–23. [CrossRef]
9. Watanabe, H.; Hayazawa, N.; Inouye, Y.; Kawata, S. DFT Vibrational Calculations of Rhodamine 6G Adsorbed on Silver: Analysis of Tip-Enhanced Raman Spectroscopy. *J. Phys. Chem. B* **2005**, *109*, 5012–5020. [CrossRef] [PubMed]
10. Guthmuller, J.; Champagne, B. Resonance Raman Scattering of Rhodamine 6G as Calculated by Time-Dependent Density Functional Theory: Vibronic and Solvent Effects. *J. Phys. Chem. A* **2008**, *112*, 3215–3223. [CrossRef] [PubMed]
11. Forbes, M.W.; Jockusch, R.A. Gas-Phase Fluorescence Excitation and Emission Spectroscopy of Three Xanthene Dyes (Rhodamine 575, Rhodamine 590 and Rhodamine 6G) in a Quadrupole Ion Trap Mass Spectrometer. *J. Am. Soc. Mass Spectrom.* **2011**, *22*, 93–109. [CrossRef] [PubMed]
12. Chapman, M.; Euler, W.B. Rhodamine 6G Structural Changes in Water/Ethanol Mixed Solvent. *J. Fluoresc.* **2018**, *28*, 1431–1437. [CrossRef] [PubMed]
13. Gavrilenko, V.I.; Noginov, M.A. Ab initio study of optical properties of rhodamine 6G molecular dimers. *J. Chem. Phys.* **2006**, *124*, 044301. [CrossRef] [PubMed]

14. Kazakevičius, A.; Peckus, D.; Boiko, O.; Valkunas, L.; Leonenko, E.; Telbiz, G.; Gulbinas, V. Insights into the Mechanism of Enhanced Rhodamine 6G Dimer Fluorescence in Mesoscopic Pluronic-Silica Matrixes. *J. Phys. Chem. C* **2015**, *119*, 19126–19133. [CrossRef]
15. Toptygin, D.; Packard, B.Z.; Brand, L. Resolution of absorption spectra of rhodamine 6G aggregates in aqueous solution using the law of mass action. *Chem. Phys. Lett.* **1997**, *277*, 430–435. [CrossRef]
16. Kruglenko, I.; Kravchenko, S.; Kruglenko, P.; Burlachenko, J.; Krishchenko, I.; Manoilov, E.; Snopok, B. Advanced Quartz Microbalance Sensors for Gas-Phase Applications: Effect of Adsorbate on Shear Bond Stiffness between Physical Transducer and Superlattice of Latex Nanoparticles. *Eng. Proc.* **2022**, *27*, 40. [CrossRef]

**Disclaimer/Publisher’s Note:** The statements, opinions and data contained in all publications are solely those of the individual author(s) and contributor(s) and not of MDPI and/or the editor(s). MDPI and/or the editor(s) disclaim responsibility for any injury to people or property resulting from any ideas, methods, instructions or products referred to in the content.



Proceeding Paper

# On the Use of Muscle Activation Patterns and Artificial Intelligence Methods for the Assessment of the Surgical Skills of Clinicians <sup>†</sup>

Ejay Nsugbe <sup>1,\*</sup>, Halin Buruno <sup>2</sup>, Stephanie Connelly <sup>3</sup>, Oluwarotimi Williams Samuel <sup>4</sup> and Olusayo Obajemu <sup>5</sup>

<sup>1</sup> Nsugbe Research Labs, Swindon SN1 3LG, UK

<sup>2</sup> Medic Minds, Limerick University, V94 T9PX Limerick, Ireland; halin.bruno2021@gmail.com

<sup>3</sup> Hereford County Hospital, Wye Valley NHS Trust, Hereford HR1 2ER, UK; stephconnelly12@gmail.com

<sup>4</sup> School of Computing and Engineering, University of Derby, Derby DE22 1GB, UK; o.samuel@derby.ac

<sup>5</sup> Department of Automatic Control and Systems Engineering, University of Sheffield, Sheffield S10 2TN, UK; olusayoobajemu@gmail.com

\* Correspondence: ennsugbe@yahoo.com

<sup>†</sup> Presented at the 10th International Electronic Conference on Sensors and Applications (ECSA-10), 15–30 November 2023; Available online: <https://ecsa-10.sciforum.net/>.

**Abstract:** The ranking and evaluation of a surgeon's surgical skills is an important factor in order to be able to appropriately assign patient cases according to the necessary level of surgeon competence in addition to helping us in the process of pinpointing the specific clinicians within the surgical cohort who require further developmental training. One of the more frequent means of surgical skills evaluation is through a qualitative assessment of a surgeon's portfolio alongside other supporting pieces of information, a process which is rather subjective. The contribution presented as part of this paper involves the use of a set of Delsys Trigno EMG wearable sensors, which track and record the muscular activation patterns of a surgeon during a surgical procedure, alongside computationally driven artificial intelligence (AI) methods towards the differentiation and ranking of the surgical skills of a clinician in a quantitative fashion. The participants in the research involved novice-level surgeons, intermediate-level surgeons and expert-level surgeons in various simulated surgical cases. A comparison of different signal processing approaches has shown that the proposed approach can prove beneficial in monitoring and differentiating the skillsets of various surgeons for various kinds of surgical cases. The presented method could also be used to track the evolution of the surgical competencies of various trainee surgeons at various stages during their training.

**Keywords:** wearable sensors; surgery; surgical education; artificial intelligence; EMG; machine learning; signal processing

**Citation:** Nsugbe, E.; Buruno, H.; Connelly, S.; Samuel, O.W.; Obajemu, O. On the Use of Muscle Activation Patterns and Artificial Intelligence Methods for the Assessment of the Surgical Skills of Clinicians. *Eng. Proc.* **2023**, *58*, 116. <https://doi.org/10.3390/ecsa-10-16231>

Academic Editor: Stefano Mariani

Published: 15 November 2023



**Copyright:** © 2023 by the authors. Licensee MDPI, Basel, Switzerland. This article is an open access article distributed under the terms and conditions of the Creative Commons Attribution (CC BY) license (<https://creativecommons.org/licenses/by/4.0/>).

## 1. Introduction

The ability to robustly assess and estimate a surgeon's skillset is a core component of surgical training and education and aids towards the identification of the competence level of a particular surgeon [1,2]. The literature suggests that current means used for the assessment of these surgical competence levels mostly involve the review of tapes, which are ultimately interpreted and assessed by a peer reviewer, thereby opening the process up to factors such as bias and subjectivity in addition to being costly [3]. This has given rise to the application of alternate means of skill assessments primarily based around the use of kinematic and virtual reality measures alongside artificial intelligence methods for the classification of surgical competence levels, with the aid of objective and quantitative prediction machines [4–9].



Recent work has also seen the use of wearable sensors—attached to the surgeon’s upper limb—as part of the skill identification process in an attempt to identify movement and contraction patterns using electromyography (EMG) and accelerometers (ACCs). This was notably conducted in the work of Soangra et al. [3] who, as part of their studies, applied both sets of wearable sensors in various anatomical locations to a group comprising novice, intermediate and expert participants in order to distinguish skill and competence levels across a number of simulated surgical tasks. From this, they were also able to identify a number of anatomical “hotspots” whose movements encoded key information regarding the levels of competence during surgical tasks [3,10]. As part of the postprocessing of the acquired signals from the wearable sensors, it can be seen that a concise list of features was extracted from the signals, which happened to be mostly nonlinear features [3,10,11]. Although effective in the characterization of signals, these could be expanded upon and concatenated with other linear features in order to boost the overall modelling accuracy [3,10,11]. In addition to this, the related literature is yet to explore the use of multiresolution and signal decomposition algorithms such as deep wavelet scattering (DWS), linear series decomposition learner (LSDL) and empirical mode decomposition (EMD), to name a few [12–14].

The contributions presented in this work present a first-stage investigation on the use of varied signal processing approaches towards the classification of surgical expertise based on the signals obtained from the EMG sensors in particular. In this paper, expanded signal processing approaches are used to differentiate between surgical skillset and expertise for a specific task based solely on the acquired signals from areas deemed to be anatomical hotspots (as determined by a previous study [3]), which span the deltoid, biceps and extensor carpi ulnaris (ECU). From this, it is immediately hypothesized that the assembled model can form a basis for the evaluation of surgical skills with a much more robust approach, which can be used to rank surgeons based on appropriate levels of expertise for different kinds of surgeries ranging from basic all the way towards minimally invasive and robotic surgeries.

## 2. Materials and Methods

### 2.1. Dataset

The original dataset was acquired from a broad list of subjects of varied surgical expertise at the Department of Urology at the University of California, Irvine, from which all subjects provided written consent to take part in the study [3]. The subjects comprised three expertise classes as follows: novice surgeons who were individuals without surgical experience; intermediate surgeons who were primarily urology residents; and expert surgeons who were urology doctors with over five years’ worth of experience [3]. For the work carried out in this paper, one participant was taken from each class as part of the pilot exercise. Various surgical tasks were performed and conducted, while the pegboard transfer task was the surgical task used as part of the accompanying signal processing work carried out in this paper. The EMG electrode used was the DELSYS Trigno Wireless, Boston, MA, USA (for which data were sampled at 2 KHz), which was attached on a number of anatomical locations determined by the surgical ergonomics identified from prior studies [3]. Specifically, the deltoid was also chosen as a site of interest due to it being an area where laparoscopic surgeons report musculoskeletal pain [3]. Figure 1 is an image of one of the subjects performing the pegboard transfer task.

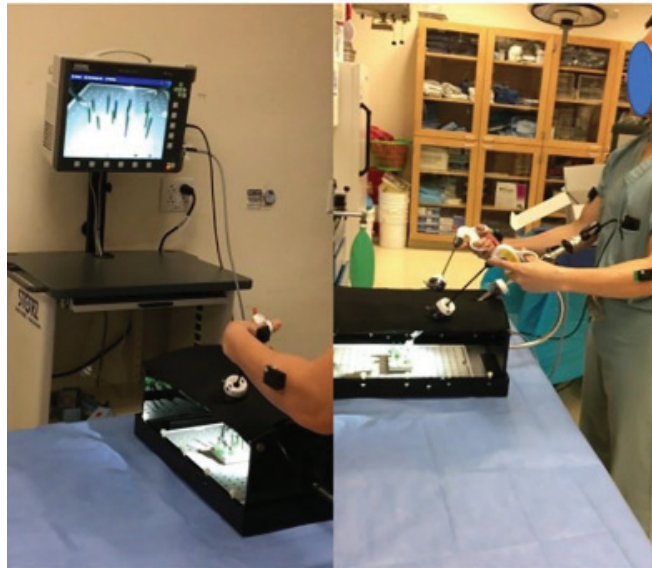


**Figure 1.** A subject performing the pegboard transfer task [3].

## 2.2. DWS

DWS is an unsupervised feature extraction approach that is capable of extracting features which are robust, continuous and a factor of a fused ensemble between the wavelet decomposition and the convolutional neural network (CNN) [15]. For the DWS, both the wavelets and filters are set at fixed values to prevent any form of iterative computations of these values, and it is able to work well with a small set of samples [15]. As mentioned, the mathematical formalism of the method can be seen in the published work of Andén and Mallat [15]. As part of the computational implementation, the DWS works with a CNN, which works in an iterative sense whilst performing convolutions through the wavelets and nonlinear modules with an average scaling function [15].

The implementation of the CNN in this work involved the use of the Gabor wavelet as the mother wavelet with a scale invariance of 1 s, with the filter banks of eight wavelets per octave in the first filter bank being followed by one wavelet per octave in the second set of filter banks.

## 2.3. Feature Extraction and Machine Learning Models

Prior to feature extraction, the EMG signals were windowed using a series of windows of 10,000 samples each, of which 10 windowed segments among these were used. The following features were extracted from the EMG signals which comprised a concatenation of both linear and nonlinear features: mean, waveform length, slope sign change, root mean squared, cepstrum, maximum fractal length, median frequency, simple square integral, variance, 4th order autoregressive coefficient, Higuchi fractal dimension, detrended fluctuation analysis, peak frequency, and sum of peaks [10,11].

The following machine learning models were used as part of this paper: decision tree (DT), linear discriminant analysis (LDA), linear support vector machine (LSVM), quadratic support vector machine (QSVM), cubic support vector machine (CSVM), fine Gaussian support vector machine (FGSVM) and K-nearest neighbors (KNN). The K-fold cross-validation approach was utilized for the validation of all models, where K was chosen as 10.

### 3. Results

Table 1 shows the results for the various scenarios investigated using the raw signal as well the DWS, with various models using different configurations. For the case of the raw signal, it can be seen that the results benefitted from a more complex model with a nonlinear architecture. It can be seen that the models with linear decision boundaries produced a dampened classification accuracy, which was seen to be improved upon by being trained with models with nonlinear decision boundaries. The DWS produced an improved classification accuracy across the majority of the models when compared with the raw signal results. The classification accuracy is seen to be improved through the use of the decomposition algorithm which provides unsupervised features and therein shows that the concept of decomposing the signal is beneficial in this case study. The machine learning models with nonlinear decision boundaries were also seen to be the best performing in this case.

**Table 1.** Classification accuracies of the various models for the raw signal and DWS.

Model	Raw Signal/Handcrafted Features (%)	DWS (%)
DT	87	92
LDA	83	86
LSVM	76	90
QSVM	90	97
CSVM	93	99
FGSVM	95	92
KNN	95	99

This shows that the proposed model and methods in this paper could serve towards enhancing the recognition accuracy of the use of wearable sensors for the classification and assessment of surgical skills expertise.

### 4. Conclusions and Future Work

The use of wearable sensors has gained momentum for the characterization of muscular activation patterns as a means towards differentiating between the skillsets of various surgeons for competency purposes. In this paper, we have attempted to use an expanded feature extraction method, alongside the DWS, towards further analysis of the EMG signal from a group of subjects, in order to investigate the extent to which these methods aid towards differentiating various surgical skillsets. This exercise was conducted for the pegboard transfer task and for three subjects, i.e., one from each skill class. The results show that the DWS is capable of differentiating between the various classes to a greater degree than the raw signal.

Subsequent work in this area would involve the use of a broader sample set comprising more subject participants and a variety of surgical tasks, including tasks involving the use surgical robots, along with data from accelerometers to serve as a basis of comparison with the EMG. In addition, preprocessing of the data through the use of the LSDL signal decomposition algorithm, which has been seen to help boost the predictive performance of machine learning algorithms, would also be performed [16,17].

To conclude, these interim results suggest that the use of wearable sensors does indeed carry appeal for non-subjective interpretations of the skillsets and competencies of clinical surgeons.

**Author Contributions:** All authors contributed equally to the article. All authors have read and agreed to the published version of the manuscript.

**Funding:** This research received no external funding.

**Institutional Review Board Statement:** The data used as part of this paper was taken from an opensource database which has been cited within the manuscript itself.

**Informed Consent Statement:** Informed consent was obtained from all subjects involved in the study.

**Data Availability Statement:** The data are available from a cited repository within the manuscript.

**Acknowledgments:** The authors would like to thank Brian Kerr for proofreading the manuscript.

**Conflicts of Interest:** The authors declare no conflicts of interest.

## References

1. Birkmeyer, J.D.; Finks, J.F.; O'Reilly, A.; Oerline, M.; Carlin, A.M.; Nunn, A.R.; Dimick, J.; Banerjee, M.; Birkmeyer, N.J.O. Surgical Skill and Complication Rates after Bariatric Surgery. *N. Engl. J. Med.* **2013**, *369*, 1434–1442. [CrossRef] [PubMed]
2. Fonseca, A.L.; Reddy, V.; Longo, W.E.; Gusberg, R.J. Graduating General Surgery Resident Operative Confidence: Perspective from a National Survey. *J. Surg. Res.* **2014**, *190*, 419–428. [CrossRef] [PubMed]
3. Soangra, R.; Sivakumar, R.; Anirudh, E.R.; Reddy, Y., S.V.; John, E.B. Evaluation of Surgical Skill Using Machine Learning with Optimal Wearable Sensor Locations. *PLoS ONE* **2022**, *17*, e0267936. [CrossRef] [PubMed]
4. Ismail Fawaz, H.; Forestier, G.; Weber, J.; Idoumghar, L.; Muller, P.-A. Evaluating Surgical Skills from Kinematic Data Using Convolutional Neural Networks. In Proceedings of the Medical Image Computing and Computer Assisted Intervention–MICCAI 2018, Granada, Spain, 16–20 September 2018; Frangi, A.F., Schnabel, J.A., Davatzikos, C., Alberola-López, C., Fichtinger, G., Eds.; Springer International Publishing: Cham, Switzerland, 2018; pp. 214–221.
5. Yanik, E.; Intes, X.; Kruger, U.; Yan, P.; Diller, D.; Van Voorst, B.; Makled, B.; Norfleet, J.; De, S. Deep Neural Networks for the Assessment of Surgical Skills: A Systematic Review. *J. Def. Model. Simul.* **2022**, *19*, 159–171. [CrossRef]
6. Bissonnette, V.; Mirchi, N.; Ledwos, N.; Alsidieri, G.; Winkler-Schwartz, A.; Del Maestro, R.F.; on behalf of the Neurosurgical Simulation & Artificial Intelligence Learning Centre. Artificial Intelligence Distinguishes Surgical Training Levels in a Virtual Reality Spinal Task. *J. Bone Jt. Surg.* **2019**, *101*, e127. [CrossRef] [PubMed]
7. Lee, D.; Yu, H.W.; Kwon, H.; Kong, H.-J.; Lee, K.E.; Kim, H.C. Evaluation of Surgical Skills during Robotic Surgery by Deep Learning-Based Multiple Surgical Instrument Tracking in Training and Actual Operations. *J. Clin. Med.* **2020**, *9*, 1964. [CrossRef] [PubMed]
8. Lavanchy, J.L.; Zindel, J.; Kirtac, K.; Twick, I.; Hosgor, E.; Candinas, D.; Beldi, G. Automation of Surgical Skill Assessment Using a Three-Stage Machine Learning Algorithm. *Sci. Rep.* **2021**, *11*, 5197. [CrossRef] [PubMed]
9. Davids, J.; Makariou, S.-G.; Ashrafian, H.; Darzi, A.; Marcus, H.J.; Giannarou, S. Automated Vision-Based Microsurgical Skill Analysis in Neurosurgery Using Deep Learning: Development and Preclinical Validation. *World Neurosurg.* **2021**, *149*, e669–e686. [CrossRef] [PubMed]
10. Nsugbe, E.; Phillips, C.; Fraser, M.; McIntosh, J. Gesture Recognition for Transhumeral Prosthesis Control Using EMG and NIR. *IET Cyber-Syst. Robot.* **2020**, *2*, 122–131. [CrossRef]
11. Nsugbe, E.; Samuel, O.W.; Asogbon, M.G.; Li, G. Phantom Motion Intent Decoding for Transhumeral Prosthesis Control with Fused Neuromuscular and Brain Wave Signals. *IET Cyber-Syst. Robot.* **2021**, *3*, 77–88. [CrossRef]
12. Nsugbe, E.; Connelly, S. Multiscale Depth of Anaesthesia Prediction for Surgery Using Frontal Cortex Electroencephalography. *Healthc. Technol. Lett.* **2022**, *9*, 43–53. [CrossRef]
13. Nsugbe, E. Particle Size Distribution Estimation of a Powder Agglomeration Process Using Acoustic Emissions. Ph.D. Thesis, Cranfield University, Cranfield, UK, 2017.
14. Nsugbe, E.; Starr, A.; Foote, P.; Ruiz-Carcel, C.; Jennions, I. Size Differentiation of a Continuous Stream of Particles Using Acoustic Emissions. *IOP Conf. Ser. Mater. Sci. Eng.* **2016**, *161*, 012090. [CrossRef]
15. Andén, J.; Mallat, S. Deep Scattering Spectrum. *IEEE Trans. Signal Process.* **2014**, *62*, 4114–4128. [CrossRef]
16. Nsugbe, E.; Williams Samuel, O.; Asogbon, M.G.; Li, G. Contrast of Multi-Resolution Analysis Approach to Transhumeral Phantom Motion Decoding. *CAA Trans. Intell. Technol.* **2021**, *6*, 360–375. [CrossRef]
17. Nsugbe, E.; Ruiz-Carcel, C.; Starr, A.; Jennions, I. Estimation of Fine and Oversize Particle Ratio in a Heterogeneous Compound with Acoustic Emissions. *Sensors* **2018**, *18*, 851. [CrossRef] [PubMed]

**Disclaimer/Publisher's Note:** The statements, opinions and data contained in all publications are solely those of the individual author(s) and contributor(s) and not of MDPI and/or the editor(s). MDPI and/or the editor(s) disclaim responsibility for any injury to people or property resulting from any ideas, methods, instructions or products referred to in the content.

Proceeding Paper

# Statistical Analysis of Gyroscopic Data to Determine Machine Health in Additive Manufacturing <sup>†</sup>

Alexander Isiani <sup>1</sup>, Leland Weiss <sup>1</sup> and Kelly Crittenden <sup>2,\*</sup>

<sup>1</sup> Institute for Micromanufacturing, Louisiana Tech University, Ruston, LA 71272, USA; aci004@latech.edu (A.I.); lweiss@latech.edu (L.W.)

<sup>2</sup> Mechanical Engineering, College of Engineering and Science, Louisiana Tech University, Ruston, LA 71272, USA

\* Correspondence: kellyc@latech.edu

<sup>†</sup> Presented at the 10th International Electronic Conference on Sensors and Applications (ECSA-10), 15–30 November 2023; Available online: <https://ecsa-10.sciforum.net/>.

**Abstract:** Additive manufacturing, commonly known as 3D printing, has significantly advanced component production across multiple industry sectors. Despite its numerous benefits, including reduced lead times and the ability to produce complex geometries, a few obstacles still prevent widespread adoption. Current research efforts have predominantly focused on in situ monitoring and investigating the mechanical properties of 3D-printed materials, with limited attention given to the sources of skewness in the fabricated products. To address this gap, our study aims to explore the factors contributing to skewness in 3D-printed objects. Specifically, we examine the influence of the belt and carriage wheel conditions within the 3D printer on the shape of the fabricated products, resulting from potential distortions in the orientation of the print head carriage during the printing process. A comprehensive analysis was employed, utilizing One-Way ANOVA, Tukey’s test, the Fisher Least Significant Difference Method, and the Friedman Rank Test, to establish statistically significant evidence supporting the notion that the mechanical components, namely the belt and wheel, have a substantial impact on the orientation of the print head, consequently leading to skewness in the final 3D-printed products.

**Keywords:** print head carriage; gyroscope; skewness; additive manufacturing

**Citation:** Isiani, A.; Weiss, L.; Crittenden, K. Statistical Analysis of Gyroscopic Data to Determine Machine Health in Additive Manufacturing. *Eng. Proc.* **2023**, *58*, 117. <https://doi.org/10.3390/ecsa-10-16218>

Academic Editor: Stefano Mariani

Published: 15 November 2023



**Copyright:** © 2023 by the authors. Licensee MDPI, Basel, Switzerland. This article is an open access article distributed under the terms and conditions of the Creative Commons Attribution (CC BY) license (<https://creativecommons.org/licenses/by/4.0/>).

## 1. Introduction

Additive manufacturing (AM), also known as 3D printing, is an innovative and transformative technology that has the potential to disrupt traditional design and manufacturing practices developed over the past two centuries [1,2]. AM has been implemented in the fields of optics [3], construction [4], medicine [5,6], food processing [7], dental [8,9], biotechnology [10], mechanical systems [11–14], aerospace [15], automobile [16–18], electrical [19,20], electronic [21–23], and fashion [24,25]. Although 3D printing offers various advantages, such as decreased lead times and the ability to produce intricate geometries, several barriers remain to hinder its widespread adoption. Extensive research efforts have been undertaken to characterize the mechanical properties [26–31] and thermal properties [32–36] and establish reliable quantification methods for 3D-printed components [37–41].

Researchers have conducted extensive investigations into using various sensors, including accelerometers [42–44], cameras [45,46], acoustic emission sensors [47,48], and thermocouples [49–52], for in situ monitoring. Through these studies, it has been consistently observed that employing in situ monitoring techniques enables the prediction of the health condition of 3D printers and facilitates the detection of defects in the quality of the printed products. Sensing systems are crucial for the effectiveness of in situ monitoring systems; however, their capability to accurately attribute a signal to a specific fault source

is constrained by their signals' limited "uniqueness" [53]. Researchers have investigated the mechanical properties of 3D-printed components, specifically examining factors such as tensile strength [54], nozzle temperature [55], infill orientation [56], printing speed, and feed rate [57]. The findings of this study revealed that the upright infill orientation demonstrated the lowest mechanical properties, whereas the on-edge and flat infill orientations exhibited the highest levels of mechanical strength [12].

The literature reviewed above encompasses recent endeavors to investigate in situ monitoring techniques and the mechanical properties of structures produced through Fused Filament Fabrication (FFF) 3D printing technologies. While substantial efforts have been devoted to evaluating material properties, a noticeable gap exists in understanding the influence of print head orientation during fabrication. Furthermore, research regarding the effects of different belt and wheel parameters on the performance of 3D printers has been scarce up to this point.

This study undertakes an experimental endeavor to assess the print head orientation and carriage condition of a 3D printer. Additionally, it investigates the impact of belt and wheel parameters. The findings of this research offer valuable insights into understanding the influence of these factors on the overall performance of the 3D printing process.

This article is structured as follows: Section 2 presents an overview of the experimental setup utilized in this study. Section 3 provides a detailed explanation of the experimental design techniques employed. The findings and discussions derived from the experiments are presented in Section 4. Finally, Section 5 concludes the article with a summary of the key outcomes and provides concluding remarks based on the current work.

## 2. Experimental Setup

Figure 1 illustrates the experimental setup employed for the statistical analysis. A Bowden-tube-style Fused Filament Fabrication (3D printing) machine manufactured by Creality (the Ender 3) was utilized to observe the movement of the print head carriage. A 3-axis MPU6050 Accelerometer/Gyroscope sensor was mounted on the carriage of the printer to capture the angular velocity and acceleration data as the print head traversed the y-axis of the machine. The sensor was connected to an Arduino Uno microcontroller for data acquisition. To ensure data integrity, an SD shield and a laptop were employed to record and save the collected data. The recorded data comprised different angular velocities corresponding to belt and carriage wheel conditions. A statistical analysis was conducted to evaluate the significance of these recorded angular velocities.

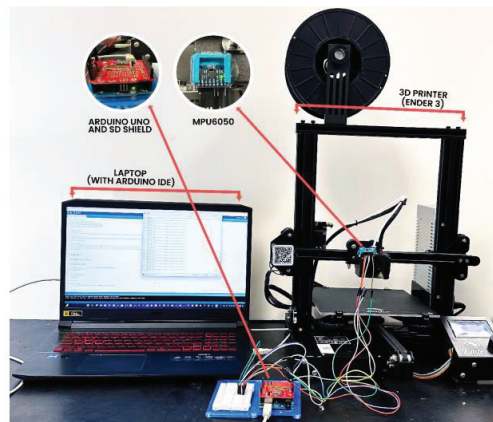
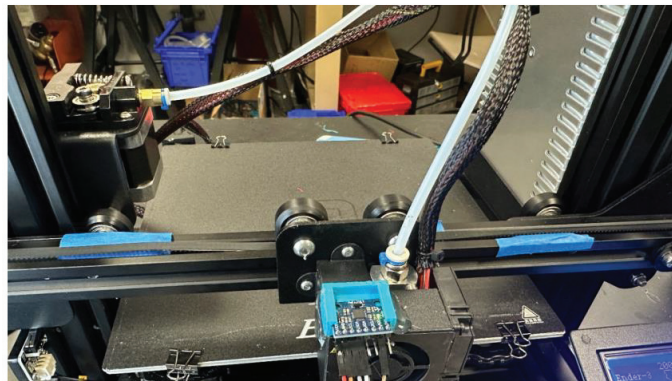


**Figure 1.** Experimental setup used for checking for the factors contributing to skewness in 3D-printed samples.

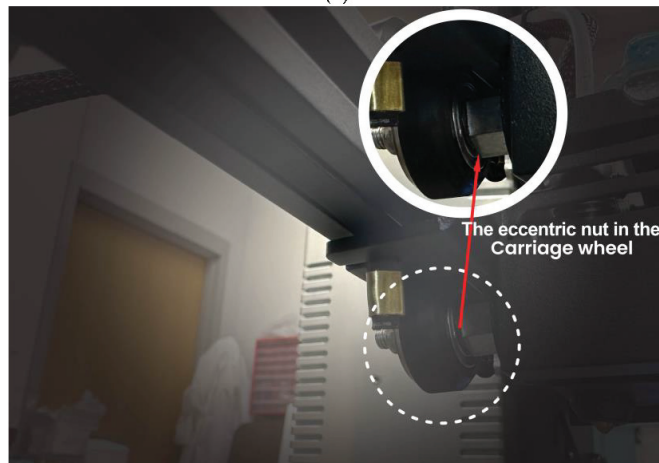
### 3. Experimental Design

The experimental setup depicted in Figure 1 was utilized with minor modifications applied to the belt and carriage wheel configurations, as shown in Figure 2. These variations allowed for examining the print head carriage under different conditions, aiding in a comprehensive assessment of its performance. These conditions are stated as follows:

- a. **Leveled Belt–Tight Wheel:** This is the state desired for the 3D printer to maintain as it fabricates products. This condition ensures stable orientation of the printer carriage head as it moves from one point to the other in the x, y, and z directions. In addition, the eccentric nut holding the wheel, which drives the carriage, is well-tightened while the belt is leveled;
- b. **Unleveled Belt–Tight Wheel:** this condition is achieved by creating bumps along the belt path to observe what happens when the carriage is slightly misoriented;
- c. **Leveled Belt–Loose Wheel:** this condition makes the carriage head tilt and generates an inconsistent orientation as it moves along the reel because of loosed wheels, although the belt is leveled;
- d. **Unleveled Belt–Loose Wheel:** this is an extreme case where the belt and wheels are unstable.



(a)



(b)

**Figure 2.** (a). The print head carriage with the integration of an MPU6050 sensor and blue tapes placed to interrupt the belt path. (b). The eccentric nut in the carriage wheel, which was intentionally varied during the course of the experiment.

This study analyzed the conditions based solely on the recorded angular velocity data obtained from the MPU6050 sensor. The focus was primarily on the changes in the orientation of the print head carriage. By utilizing the angular velocity data, much insight would be gained through the rotational motion of the carriage during different experimental conditions. This approach allowed the examination of how variations in orientation affected the performance and behavior of the print head carriage. The analysis of the recorded angular velocity data served as a valuable tool in understanding the dynamics and characteristics of the print head carriage in relation to its orientation changes.

The data collection process commenced immediately after the default calibration routine, which involved a 15 nd pause on the print head carriage to calibrate its orientation. Subsequently, the carriage was driven back and forth along the x-axis of the reel, covering a distance of 100 mm. The speed of this movement was set at 1000 mm/min for a duration of one minute and thirty seconds. Throughout this motion, a total of 1500 data points were recorded and saved in the laptop’s storage for subsequent analysis. The recorded data points captured the relevant variables (x, y, and z angular velocity) necessary for evaluating the performance and behavior of the print head carriage during the specified movement scenario. These data points will be subjected to thorough analysis and examination to extract meaningful insights and draw valid conclusions regarding the carriage’s orientation and motion characteristics. The equations employed for checking statistical evidence and determining significance will be elaborated in Appendix A.

**4. Result and Discussion**

The analysis in this study involved reducing the initial dataset of 1500 data points into 30 data points. This reduction was achieved by segmenting the collected data into sections of 50 data points each. This reduction aimed to streamline the dataset for further analysis and interpretation. Firstly, the correlation matrix in Figure 3 presented a comprehensive overview of the correlations between the root mean square (RMS) values of the different explore conditions, allowing for determining the degree of correlation. By examining the correlation coefficients, we can evaluate whether the variables exhibit perfect, strong, or weak correlations with each other.

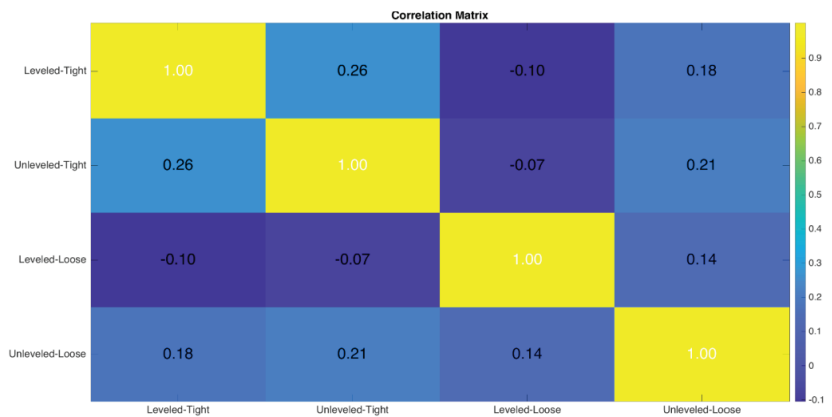


**Figure 3.** The correlation matrix for the Leveled Belt-Tight Wheel condition, the Unleveled Belt-Tight Wheel condition, the Leveled Belt-Loose Wheel condition, and the Unleveled Belt-Loose Wheel condition.

The correlation matrix analysis revealed that either uncorrelated or weak correlations were observed among the data collected for each condition. This finding suggests that variations in the condition of the belt and wheel of the 3D printer directly corresponded to changes in the orientation of the print head carriage. The lack of strong correlations or the presence of weak correlations between the collected data indicates that alterations in the belt



and wheel conditions had a noticeable influence on the orientation of the print head carriage. As the condition of the belt and wheel changed, the orientation of the carriage exhibited corresponding adjustments. These results highlight the direct relationship between the belt and wheel conditions and the orientation of the print head carriage.

Figure 4 presents the normality test graphs generated using Minitab 21 software. These graphs are based on the reduced data points corresponding to the four different conditions examined in the study. The normality test determines the distributional characteristics of the data, thereby facilitating the selection of appropriate parametric or non-parametric statistical tests for further analysis. Table 1 provides descriptive statistics for each of the conditions investigated. The combination of the normality test graphs from Figure 3 and the descriptive statistics presented in Table 1 assists in elucidating the nature of the collected data and determining the appropriate statistical methods for subsequent analyses.

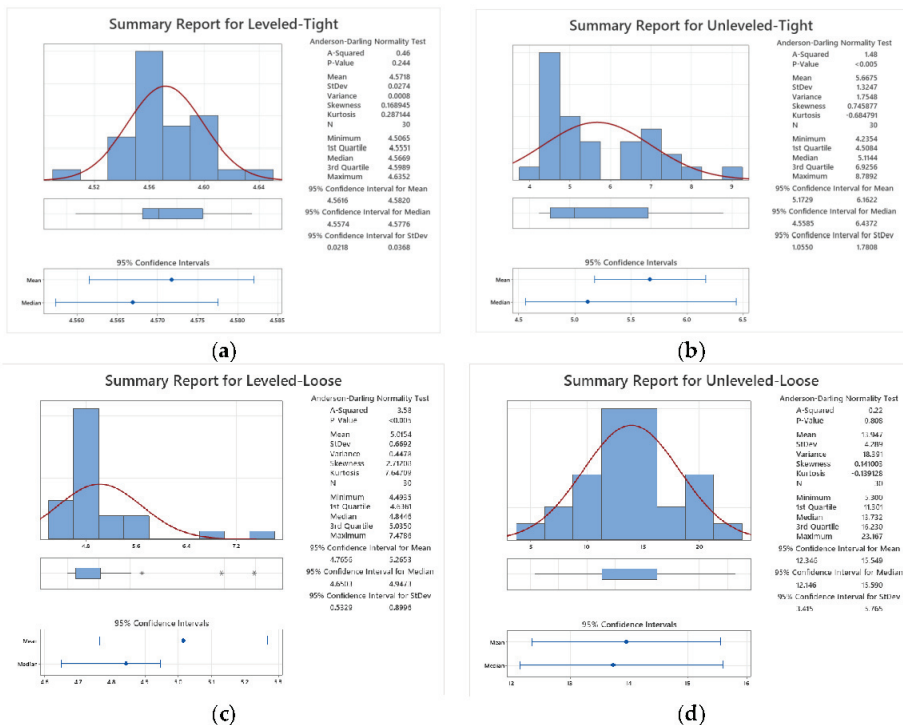


**Figure 4.** The descriptive statistics summary report and normality plot for (a) the Leveled Belt-Tight Wheel condition; (b) the Unleveled Belt-Tight Wheel condition; (c) the Leveled Belt-Loose Wheel condition; and (d) the Unleveled Belt-Loose Wheel condition.

**Table 1.** The descriptive statistics with the p-value of the condition.

Conditions	Mean	Std. Dev.	Variance	p-Value
Leveled Belt-Tight Wheel	4.572	0.027	0.00075	0.244
Unleveled Belt-Tight Wheel	5.668	1.325	1.755	<0.005
Leveled Belt-Loose Wheel	5.015	0.669	0.448	<0.005
Unleveled Belt-Loose Wheel	13.947	4.289	18.391	0.808

The normality plots generated from the analysis indicate that the data for the conditions “Leveled Belt-Tight Wheel” and “Unleveled Belt-Loose Wheel” exhibit a normal distribution. The p-values associated with these conditions are 0.244 and 0.808, respectively. Conversely, the distribution of data for the other two conditions remains unknown.

Based on these findings, the subsequent analysis can be conducted using parametric and non-parametric tests while considering a type 1 error,  $\alpha$ , of 0.05. Since the data for the “Leveled Belt–Tight Wheel” and “Unleveled Belt–Loose Wheel” conditions follow a normal distribution, parametric tests such as One-Way Analysis of Variance (ANOVA), Tukey Pairwise Comparison, and Fisher Least Significant Difference (LSD) methods were applied.

Table 2 illustrates the hypothesis and the significance level used for the parametric analysis. The One-way ANOVA result presented in Table 3 demonstrates the influence of the belt and wheel conditions on the orientation of the print head, consequently affecting the shape of fabricated products. The obtained p-value of zero suggests rejecting the null hypothesis, indicating significant evidence supporting the assertion that a meaningful difference exists in the print head’s mean root mean square (RMS) orientation based on the varying belt and carriage wheel conditions. These findings highlight the impact of the experimental conditions on the overall performance and behavior of the print head. By rejecting the null hypothesis, it can be inferred that the belt and carriage wheel conditions play a significant role in determining the orientation of the print head during the fabrication process. This observation underscores the importance of carefully selecting and optimizing the belt and wheel configurations to ensure consistent and accurate fabrication results.

**Table 2.** The hypothesis and type 1 error significance level.

Null hypothesis	All means are equal
Alternative hypothesis	Not all means are equal
Significance level	$\alpha = 0.05$

**Table 3.** Results from One-Way Analysis of Variance for the parametric machine conditions (“Leveled Belt–Tight Wheel” and “Unleveled Belt–Loosed Wheel”).

Source	DF	Adj SS	Adj MS	F-Value	p-Value
Machine Condition	1	1318.5	1318.46	143.37	0.000
Error	58	533.4	9.20		
Total	59	1851.8			

Tables 4–7 present the comparison results obtained using the Tukey Pairwise Comparison and Fisher Least Significant Difference (LSD) methods. These methods were employed to analyze and compare the grouping information of the two parametric conditions under investigation. The primary objective of employing these statistical methods was to identify significant differences between the various groups formed by the parametric conditions. Tukey Pairwise Comparison and Fisher LSD methods are widely recognized and utilized in statistical analysis for conducting multiple pairwise comparisons between means.

Using Tukey’s and LSD methods, similar results were obtained, indicating that the grouping information derived from the two machine conditions (“Leveled Belt–Tight Wheel” and “Unleveled Belt–Loose Wheel”) is significantly distinct. These findings strongly imply that the state of the belt and gear components indeed influences the orientation of the print head carriage. The observed distinctions in grouping information suggest that there is evidence that variations in the state of the belt and gear have a notable impact on the orientation of the print head carriage.

**Table 4.** Grouping information using the Tukey method and 95% confidence interval (CI).

Machine Condition	N	Mean	Grouping
Unleveled–Loose	30	13.947	A
Leveled–Tight	30	4.57180	B

**Table 5.** Tukey simultaneous tests for differences of means.

Difference of Levels	Difference of Means	SE of Difference	95% CI	T-Value	Adjusted p-Value
Unleveled Belt–Loose Wheel and Leveled Belt–Tight Wheel	9.375	0.783	(7.808, 10.943)	11.97	0.000

**Table 6.** Grouping information using the LSD method and 95% confidence interval (CI).

Machine Condition	N	Mean	Grouping
Unleveled–Loose	30	13.947	A
Leveled–Tight	30	4.57180	B

**Table 7.** Fisher individual tests for differences of means.

Difference of Levels	Difference of Means	SE of Difference	95% CI	T-Value	Adjusted p-Value
Unleveled Belt–Loose Wheel and Leveled Belt–Tight Wheel	9.375	0.783	(7.808, 10.943)	11.97	0.000

However, a non-parametric analysis was conducted on the entire set of conditions using the Friedman Rank Test due to the unknown distribution of the “Unleveled Belt–Tight Wheel” and “Leveled Belt–Loose Wheel” conditions. This test is equivalent to a repeated measures ANOVA and is suitable for analyzing data when parametric assumptions are unmet. Tables 8 and 9 provide the descriptive statistics and test results obtained from the Friedman Rank Test. These tables offer valuable insights into the data and the outcomes of the statistical analysis. The results of the Friedman Rank Test revealed a significant rejection of the null hypothesis, as indicated by a *p*-value of zero. This finding indicates the presence of statistically significant evidence to support the assertion that the mean difference in the orientation of the carriages is indeed influenced by the gear and wheel conditions under investigation. These results further emphasize the importance of considering the gear and wheel components’ condition when examining the carriages’ orientation. By rejecting the null hypothesis, the analysis affirms that the gear and wheel conditions play a significant role in affecting the orientation of the carriages during the experimental procedures.

**Table 8.** The descriptive statistics from the Friedman Rank Test.

Machine Condition	N	Median	Sum of Ranks
Leveled–Loose	30	4.9493	70.0
Leveled–Tight	30	4.5211	41.0
Unleveled–Loose	30	13.3443	119.0
Unleveled–Tight	30	5.2660	70.0
Overall	120	7.0202	

**Table 9.** Hypothesis test and results from the Friedman Rank Test.

Null hypothesis	H <sub>0</sub> : All treatment effects are zero		
Alternative hypothesis	H <sub>1</sub> : Not all treatment effects are zero		
<b>DF</b>	<b>Chi-Square</b>	<b>p-Value</b>	
3	62.84	0.000	

Thus, based on the analysis conducted, it becomes evident that optimizing and fine-tuning the belt and wheel conditions is of utmost importance. This optimization is essential to achieving precise and accurate print head orientations, which, in turn, minimizes skewness in the 3D-fabricated products. By focusing on enhancing the precision and accuracy

of the print head orientation, the overall quality and reliability of the 3D printing process can be significantly improved. The findings from this study highlight the direct impact of the belt and wheel conditions on the orientation of the print head carriage. By carefully adjusting and optimizing these mechanical components, it becomes possible to minimize deviations and inaccuracies in the print head's movements. This, in turn, translates into improved outcomes in the final fabricated products, reducing any skewness that may occur during the printing process. Ultimately, by achieving precise print head orientations, manufacturers can ensure the production of high-quality and accurate 3D-printed objects, meeting the desired specifications and minimizing any imperfections or inconsistencies.

## 5. Conclusions

Researchers have predominantly concentrated on studying the mechanical characteristics of 3D-printed objects and monitoring them in real time. This is due to the increasing prevalence of additively manufactured structures in dynamic applications. Consequently, it is crucial to identify the factors that contribute to irregularities in 3D-printed products.

The primary objective of this study was to explore and understand the factors that contribute to skewness in 3D-printed structures. In order to achieve this, the MPU6050 gyroscope was employed as a means to quantify the extent of variation in the root mean square orientation of the print head carriage during the fabrication process. Through rigorous analysis and experimentation, the findings of this study indicate that the condition of the belt and the wheel play a pivotal role in influencing skewness. This conclusion was derived from both parametric and non-parametric statistical analyses, which further underscore the significance of these factors. Overall, these results shed light on the key contributors to skewness in 3D-printed products, providing valuable insights for improving such components' dynamic reliability and structural integrity. Further research and development in this area can help in developing innovative strategies and targeted interventions to mitigate skewness effectively, thereby resulting in a marked enhancement of the real-time quality of additively manufactured structures. By harnessing deeper insights into the underlying mechanisms, researchers and practitioners can collaboratively contribute to the establishment of a more refined and reliable additive manufacturing process. This, in turn, will pave the way for the creation of intricate, flawless, and precisely engineered components across various applications. Furthermore, future studies will delve extensively into the influence of the rheological and mechanical properties of the material during the fabrication process. This investigation is paramount, as the printability of the material hinges significantly on the interplay between these two essential properties.

**Author Contributions:** Conceptualization, K.C. and A.I.; methodology, K.C. and A.I.; software, A.I.; validation, A.I., K.C. and L.W.; formal analysis, A.I.; investigation, A.I.; resources, K.C. and A.I.; data curation, A.I.; writing—original draft preparation, A.I.; writing—review and editing, K.C. and L.W.; visualization, A.I.; supervision, K.C.; project administration, K.C. All authors have read and agreed to the published version of the manuscript.

**Funding:** This research received no external funding.

**Institutional Review Board Statement:** Not applicable.

**Informed Consent Statement:** Not applicable.

**Data Availability Statement:** The data are available in a publicly accessible repository. The data presented in this study are openly available at [https://figshare.com/articles/dataset/Data\\_files\\_for\\_Statistical\\_Analysis\\_of\\_Gyroscope/24987000](https://figshare.com/articles/dataset/Data_files_for_Statistical_Analysis_of_Gyroscope/24987000).

**Conflicts of Interest:** The authors declare no conflicts of interest.

### Appendix A

$$\text{Mean, } \bar{x} = \frac{\sum_{i=1}^n x_i}{n}$$

$$\text{Variance, } s^2 = \frac{\sum_{i=1}^n (x_i - \bar{x})^2}{n-1}$$

$$\text{Standard Deviation, } s = \sqrt{\frac{\sum_{i=1}^n (x_i - \bar{x})^2}{n-1}}$$

#### Parametric Test:

One-Way ANOVA assumes the following:

1. Completely randomized design and observations are mutually independent;
2. Model errors are normally and independently distributed random variables;
3. Variance is constant for all levels of the factor.

#### Sum of Squares (SS)

$$SS_{\text{Total}} = \sum_{i=1}^a \sum_{j=1}^n (x_{ij} - \bar{x}_{..})^2$$

$$SS_{\text{Observations}} = \frac{1}{n} \sum_{i=1}^a x_i^2 - \frac{x_{..}^2}{N}$$

$$SS_{\text{Error}} = SS_{\text{Total}} - SS_{\text{Observations}}$$

where  $x_{..}$  = grand total of all observations and  $\bar{x}_{..}$  = grand average of all observations.

#### Degree of Freedom (DF)

$$DF_{\text{Total}} = a(n) - 1$$

$$DF_{\text{Observations}} = a - 1$$

$$DF_{\text{Error}} = a(n - 1)$$

#### Mean Square (MS)

$$MS_{\text{Observations}} = \frac{SS_{\text{Observation}}}{a - 1}$$

$$MS_{\text{Error}} = \frac{SS_{\text{Error}}}{a(n - 1)}$$

$$F - \text{Value} = \frac{MS_{\text{Observations}}}{MS_{\text{Error}}}$$

#### Comparison of Observation Means

Tukey's Test:

$$q = \frac{\bar{x}_{\text{max}} - \bar{x}_{\text{min}}}{\sqrt{\frac{MS_{\text{Error}}}{n}}}$$

Confidence Interval (CI):

$$\bar{x}_i - \bar{x}_j - q(a, f) \sqrt{\frac{MS_{\text{Error}}}{n}} \leq \mu_i - \mu_j \leq \bar{x}_i - \bar{x}_j + q(a, f) \sqrt{\frac{MS_{\text{Error}}}{n}}$$

Fisher Least Significant Difference (LSD) method:

$$t_0 = \frac{\bar{x}_i - \bar{x}_j}{\sqrt{MS_{\text{Error}} \left( \frac{1}{n_i} + \frac{1}{n_j} \right)}}$$

Confidence Interval (CI):

$$\bar{x}_i - \bar{x}_j - t_{\frac{\alpha}{2}, N-a} \sqrt{MS_{Error} \left( \frac{1}{n_i} + \frac{1}{n_j} \right)} \leq \mu_i - \mu_j \leq \bar{x}_i - \bar{x}_j + t_{\frac{\alpha}{2}, N-a} \sqrt{MS_{Error} \left( \frac{1}{n_i} + \frac{1}{n_j} \right)}$$

#### Non-Parametric Test:

Friedman Rank Test:

$$Q = \left[ \frac{12}{n(k)(k+1)} \left( \sum R_j^2 \right) - 3n(k+1) \right]$$

Critical value  $(k - 1, \alpha)$ .

#### References

- Dickinson, H. The Next Industrial Revolution? The Role of Public Administration in Supporting Government to Oversee 3D Printing Technologies. *Public Adm. Rev.* **2018**, *78*, 922–925. [CrossRef]
- Gokhare, V.G.; Raut, D.N.; Shinde, D.K. A Review Paper on 3D-Printing Aspects and Various Processes Used in the 3D-Printing. Available online: [www.ijert.org](http://www.ijert.org) (accessed on 20 May 2023).
- Schubert, C.; Van Langeveld, M.C.; A Donoso, L. Innovations in 3D printing: A 3D overview from optics to organs. *Br. J. Ophthalmol.* **2013**, *98*, 159–161. [CrossRef]
- Tay, Y.W.D.; Panda, B.; Paul, S.C.; Mohamed, N.A.N.; Tan, M.J.; Leong, K.F. 3D printing trends in building and construction industry: A review. *Virtual Phys. Prototyp.* **2017**, *12*, 261–276. [CrossRef]
- Lafeber, I.; Ruijgrok, E.J.; Guchelaar, H.-J.; Schimmel, K.J.M. 3D Printing of Pediatric Medication: The End of Bad Tasting Oral Liquids?—A Scoping Review. *Pharmaceutics* **2022**, *14*, 416. [CrossRef] [PubMed]
- Yan, Q.; Dong, H.; Su, J.; Han, J.; Song, B.; Wei, Q.; Shi, Y. A Review of 3D Printing Technology for Medical Applications. *Engineering* **2018**, *4*, 729–742. [CrossRef]
- Brunner, T.A.; Delley, M.; Denkel, C. Consumers' attitudes and change of attitude toward 3D-printed food. *Food Qual. Preference* **2018**, *68*, 389–396. [CrossRef]
- Dawood, A.; Marti, B.M.; Sauret-Jackson, V.; Darwood, A. 3D printing in dentistry. *Br. Dent. J.* **2015**, *219*, 521–529. [CrossRef]
- Barone, S.; Neri, P.; Paoli, A.; Razionale, A.V.; Tamburrino, F. Development of a DLP 3D printer for orthodontic applications. In *Procedia Manufacturing*; Elsevier: Amsterdam, The Netherlands, 2019; pp. 1017–1025. [CrossRef]
- Gross, B.C.; Erkal, J.L.; Lockwood, S.Y.; Chen, C.; Spence, D.M. Evaluation of 3D Printing and Its Potential Impact on Biotechnology and the Chemical Sciences. *Anal. Chem.* **2014**, *86*, 3240–3253. [CrossRef] [PubMed]
- Štaffová, M.; Ondreáš, F.; Svatík, J.; Zbončák, M.; Jančář, J.; Lepcio, P. 3D printing and post-curing optimization of photopolymerized structures: Basic concepts and effective tools for improved thermomechanical properties. *Polym. Test.* **2022**, *108*, 107499. [CrossRef]
- Nguyen, H.T.; Crittenden, K.; Weiss, L.; Bardaweel, H. Experimental Modal Analysis and Characterization of Additively Manufactured Polymers. *Polymers* **2022**, *14*, 2071. [CrossRef]
- Gardan, J.; Makke, A.; Recho, N. A Method to Improve the Fracture Toughness Using 3D Printing by Extrusion Deposition. In *Procedia Structural Integrity*; Elsevier: Amsterdam, The Netherlands, 2016; pp. 144–151. [CrossRef]
- Chen, Z.; Li, Z.; Li, J.; Liu, C.; Lao, C.; Fu, Y.; Liu, C.; Li, Y.; Wang, P.; He, Y. 3D printing of ceramics: A review. *J. Eur. Ceram. Soc.* **2018**, *39*, 661–687. [CrossRef]
- Shahrubudin, N.; Lee, T.; Ramlan, R. An Overview on 3D Printing Technology: Technological, Materials, and Applications. *Procedia Manuf.* **2019**, *35*, 1286–1296. [CrossRef]
- Prabhu, S.R.; Ilangkumaran, M.; Mohanraj, T. 3D Printing of automobile spoilers using MCDM techniques. *Mater. Test.* **2020**, *62*, 1121–1125. [CrossRef]
- Janeková, J.; Pelle, S.; Onofrejová, D.; Pekarčíková, M. The 3D printing implementation in manufacturing of automobile components. *Acta Technol* **2019**, *5*, 17–21. [CrossRef]
- Elakkad, A.S. 3D Technology in the Automotive Industry. Available online: [www.ijert.org](http://www.ijert.org) (accessed on 9 June 2023).
- Zare, Y.; Rhee, K.Y.; Park, S.-J. A developed equation for electrical conductivity of polymer carbon nanotubes (CNT) nanocomposites based on Halpin-Tsai model. *Results Phys.* **2019**, *14*, 102406. [CrossRef]
- Szabó, L.; Fodor, D. The Key Role of 3D Printing Technologies in the Further Development of Electrical Machines. *Machines* **2022**, *10*, 330. [CrossRef]
- Park, Y.; Yun, I.; Chung, W.G.; Park, W.; Lee, D.H.; Park, J. High-Resolution 3D Printing for Electronics. *Adv. Sci.* **2022**, *9*, 2104623. [CrossRef]
- Espera, A.H.; Dizon, J.R.C.; Chen, Q.; Advincula, R.C. 3D-printing and advanced manufacturing for electronics. *Prog. Addit. Manuf.* **2019**, *4*, 245–267. [CrossRef]
- Leigh, S.J.; Bradley, R.J.; Purssell, C.P.; Billson, D.R.; Hutchins, D.A. A Simple, Low-Cost Conductive Composite Material for 3D Printing of Electronic Sensors. *PLoS ONE* **2012**, *7*, e49365. [CrossRef]

24. Sun, L.; Zhao, L. Envisioning the era of 3D printing: A conceptual model for the fashion industry. *Fash. Text.* **2017**, *4*, 25. [CrossRef]
25. Wang, B.Z.; Chen, Y. The Effect of 3D Printing Technology on the Future Fashion Design and Manufacturing. *Appl. Mech. Mater.* **2014**, *496*, 2687–2691. [CrossRef]
26. Cantrell, J.T.; Rohde, S.; Damiani, D.; Gurnani, R.; DiSandro, L.; Anton, J.; Young, A.; Jerez, A.; Steinbach, D.; Kroese, C.; et al. Experimental Characterization of the Mechanical Properties of 3D-Printed ABS and Polycarbonate Parts. In *Advancement of Optical Methods in Experimental Mechanics*; Springer: Cham, Switzerland, 2017; Volume 3. [CrossRef]
27. Wittbrodt, B.; Pearce, J.M. The effects of PLA color on material properties of 3-D printed components. *Addit. Manuf.* **2015**, *8*, 110–116. [CrossRef]
28. Galeta, T.; Raos, P.; Stojšić, J.; Pakši, I. Influence of Structure on Mechanical Properties of 3D Printed Objects. *Procedia Eng.* **2016**, *149*, 100–104. [CrossRef]
29. Lederle, F.; Meyer, F.; Brunotte, G.-P.; Kaldun, C.; Hübner, E.G. Improved mechanical properties of 3D-printed parts by fused deposition modeling processed under the exclusion of oxygen. *Prog. Addit. Manuf.* **2016**, *1*, 3–7. [CrossRef]
30. Chadha, A.; Haq, M.I.U.; Raina, A.; Singh, R.R.; Penumarti, N.B.; Bishnoi, M.S. Effect of fused deposition modelling process parameters on mechanical properties of 3D printed parts. *World J. Eng.* **2019**, *16*, 550–559. [CrossRef]
31. Al Khawaja, H.; Mansour, A.; Alabdouli, H.; Ahmed, W.; Alqaydi, H.; Al Jassmi, H. Investigating the Mechanical Properties of 3D Printed Components. In Proceedings of the Advances in Science and Engineering Technology International Conferences (ASET), Dubai, United Arab Emirates, 4 February–9 April 2020. [CrossRef]
32. Shemelya, C.; De La Rosa, A.; Torrado, A.R.; Yu, K.; Domanowski, J.; Bonacuse, P.J.; Martin, R.E.; Juhasz, M.; Hurwitz, F.; Wicker, R.B.; et al. Anisotropy of thermal conductivity in 3D printed polymer matrix composites for space based cube satellites. *Addit. Manuf.* **2017**, *16*, 186–196. [CrossRef]
33. Laureto, J.; Tomasi, J.; King, J.A.; Pearce, J.M. Thermal properties of 3-D printed polylactic acid-metal composites. *Prog. Addit. Manuf.* **2017**, *2*, 57–71. [CrossRef]
34. Blanco, I.; Cicala, G.; Recca, G.; Tosto, C. Specific Heat Capacity and Thermal Conductivity Measurements of PLA-Based 3D-Printed Parts with Milled Carbon Fiber Reinforcement. *Entropy* **2022**, *24*, 654. [CrossRef]
35. Rahim, T.N.A.T.; Abdullah, A.M.; Akil, H.M.; Mohamad, D.; Rajion, Z.A. The improvement of mechanical and thermal properties of polyamide 12 3D printed parts by fused deposition modelling. *Express Polym. Lett.* **2017**, *11*, 963–982. [CrossRef]
36. Pascual-González, C.; Martín, P.S.; Lizarralde, I.; Fernández, A.; León, A.; Lopes, C.; Fernández-Blázquez, J. Post-processing effects on microstructure, interlaminar and thermal properties of 3D printed continuous carbon fibre composites. *Compos. Part B: Eng.* **2021**, *210*, 108652. [CrossRef]
37. Rynio, P.; Wojtuń, M.; Wójcik, Ł.; Kawa, M.; Falkowski, A.; Gutowski, P.; Kazimierzczak, A. The accuracy and reliability of 3D printed aortic templates: A comprehensive three-dimensional analysis. *Quant. Imaging Med. Surg.* **2022**, *12*, 1385–1396. [CrossRef]
38. Siraj, I.; Bharti, P.S. Reliability analysis of a 3D Printing process. *Procedia Comput. Sci.* **2020**, *173*, 191–200. [CrossRef]
39. Keleş, Ö.; Blevins, C.W.; Bowman, K.J. Effect of build orientation on the mechanical reliability of 3D printed ABS. *Rapid Prototyp. J.* **2017**, *23*, 320–328. [CrossRef]
40. Goh, G.D.; Sing, S.L.; Yeong, W.Y. A review on machine learning in 3D printing: Applications, potential, and challenges. *Artif. Intell. Rev.* **2021**, *54*, 63–94. [CrossRef]
41. Wu, H.-C.; Chen, T.-C.T. Quality control issues in 3D-printing manufacturing: A review. *Rapid Prototyp. J.* **2018**, *24*, 607–614. [CrossRef]
42. Song, X.; Liu, H.; Fang, Y.; Zhao, C.; Qu, Z.; Wang, Q.; Tu, L.-C. An Integrated Gold-Film Temperature Sensor for In Situ Temperature Measurement of a High-Precision MEMS Accelerometer. *Sensors* **2020**, *20*, 3652. [CrossRef] [PubMed]
43. Li, Y.; Zhao, W.; Li, Q.; Wang, T.; Wang, G. In-Situ Monitoring and Diagnosing for Fused Filament Fabrication Process Based on Vibration Sensors. *Sensors* **2019**, *19*, 2589. [CrossRef]
44. Noda, T.; Kawabata, Y.; Arai, N.; Mitamura, H.; Watanabe, S. Animal-Mounted Gyroscope/Accelerometer/Magnetometer: In Situ Measurement of the Movement Performance of Fast-Start Behaviour in Fish. 2013. Available online: <http://www.elsevier.com/open-access/userlicense/1.0/http://www.elsevier.com/open-access/userlicense/1.0> (accessed on 29 April 2023).
45. Schleier, M.; Adelman, B.; Esen, C.; Hellmann, R. Image Processing Algorithm for In Situ Monitoring Fiber Laser Remote Cutting by a High-Speed Camera. *Sensors* **2022**, *22*, 2863. [CrossRef]
46. Grasso, M.; Colosimo, B.M. Process defects and *in situ* monitoring methods in metal powder bed fusion: A review. *Meas. Sci. Technol.* **2017**, *28*, 044005. [CrossRef]
47. Wu, H.; Wang, Y.; Yu, Z. In situ monitoring of FDM machine condition via acoustic emission. *Int. J. Adv. Manuf. Technol.* **2016**, *84*, 1483–1495. [CrossRef]
48. De Rosa, I.M.; Sarasini, F. Use of PVDF as acoustic emission sensor for in situ monitoring of mechanical behaviour of glass/epoxy laminates. *Polym. Test.* **2010**, *29*, 749–758. [CrossRef]
49. Nam, J.; Jo, N.; Kim, J.S.; Lee, S.W. Development of a health monitoring and diagnosis framework for fused deposition modeling process based on a machine learning algorithm. *Proc. Inst. Mech. Eng. Part B J. Eng. Manuf.* **2019**, *234*, 324–332. [CrossRef]
50. Chang, T.; Mukherjee, S.; Watkins, N.N.; Stobbe, D.M.; Mays, O.; Baluyot, E.V.; Pascall, A.J.; Tringe, J.W. In-situ monitoring for liquid metal jetting using a millimeter-wave impedance diagnostic. *Sci. Rep.* **2020**, *10*, 22325. [CrossRef] [PubMed]

51. Dressler, M.; Röllig, M.; Schmidt, M.; Maturilli, A.; Helbert, J. Temperature distribution in powder beds during 3D printing. *Rapid Prototyp. J.* **2010**, *16*, 328–336. [CrossRef]
52. Woszczyński, M.; Rogala-Rojek, J.; Bartoszek, S.; Gaiceanu, M.; Filipowicz, K.; Kotwica, K. In Situ Tests of the Monitoring and Diagnostic System for Individual Photovoltaic Panels. *Energies* **2021**, *14*, 1770. [CrossRef]
53. Fu, Y.; Downey, A.; Yuan, L.; Pratt, A.; Balogun, Y. In situ monitoring for fused filament fabrication process: A review. *Addit. Manuf.* **2021**, *38*, 101749. [CrossRef]
54. Dawoud, M.; Taha, I.; Ebeid, S.J. Mechanical behaviour of ABS: An experimental study using FDM and injection moulding techniques. *J. Manuf. Process.* **2016**, *21*, 39–45. [CrossRef]
55. Yousefi, A.A. Effects of 3D Printer Nozzle Head Temperature on the Physical and Mechanical Properties of PLA Based Product. 2016. Available online: <https://www.researchgate.net/publication/309721923> (accessed on 15 May 2023).
56. Rankouhi, B.; Javadpour, S.; Delfanian, F.; Letcher, T. Failure Analysis and Mechanical Characterization of 3D Printed ABS With Respect to Layer Thickness and Orientation. *J. Fail. Anal. Prev.* **2016**, *16*, 467–481. [CrossRef]
57. Christiyan, K.G.J.; Chandrasekhar, U.; Venkateswarlu, K. A study on the influence of process parameters on the Mechanical Properties of 3D printed ABS composite. In Proceedings of the IOP Conference Series: Materials Science and Engineering, Bali, Indonesia, 19–20 March 2016. [CrossRef]

**Disclaimer/Publisher’s Note:** The statements, opinions and data contained in all publications are solely those of the individual author(s) and contributor(s) and not of MDPI and/or the editor(s). MDPI and/or the editor(s) disclaim responsibility for any injury to people or property resulting from any ideas, methods, instructions or products referred to in the content.



Proceeding Paper

# Cow Milk Quality Determination Using a Near-Infrared Spectroscopic Sensing System for Smart Dairy Farming <sup>†</sup>

Patricia Iweka <sup>1,\*</sup>, Shuso Kawamura <sup>1</sup>, Tomohiro Mitani <sup>2,\*</sup> and Takashi Kawaguchi <sup>3</sup>

<sup>1</sup> Graduate School of Agricultural Science, Hokkaido University, Sapporo 060-8589, Japan; shusokawamura@gmail.com

<sup>2</sup> Field Science for Northern Biosphere, Hokkaido University, Sapporo 060-0811, Japan

<sup>3</sup> Orion Machinery Co., Ltd., Nagano 382-8502, Japan; kawaguchi-takashi@orionkikai.co.jp

\* Correspondence: patricia.iweka.agric@gmail.com (P.I.); tmitani@agr.hokudai.ac.jp (T.M.)

<sup>†</sup> Presented at the 10th International Electronic Conference on Sensors and Applications (ECSA-10), 15–30 November 2023; Available online: <https://ecsa-10.sciforum.net/>.

**Abstract:** This study investigated the accuracy of a near-infrared spectroscopic sensing system for predicting milk quality indicators in cow milk. The system determined three major milk quality indicators (milk fat, protein, and lactose), milk urea nitrogen (MUN), and somatic cell count (SCC) of two Holstein cows at the Hokkaido University dairy farm. The results showed excellent accuracy for milk fat and protein contents, while sufficient accuracy was found for lactose, MUN, and SCC. This suggests that the NIR spectroscopic sensing system could be used for online real-time milk quality determination, aiding dairy farmers in effective individual cow management and smart dairy farming.

**Keywords:** near-infrared spectroscopy; sensing system; calibration models; milk quality; milk urea nitrogen; somatic cell count; smart dairy farming

## 1. Introduction

Smart dairy farming technologies are used to continually and in real time determine cattle milk and health quality indicators in order to maximize nutrition and productivity and to discover health problems at an early stage [1–4]. The ability to determine the three major milk quality indicators, such as milk fat, protein, and lactose; milk urea nitrogen (MUN), which is the nutritional indicator; and somatic cell count (SCC), which is the mastitis disease indicator, from milk samples taken during milking using near-infrared spectroscopy (NIRS) has grown in popularity [5–7].

NIRS is an appropriate technology for assessing milk quality during the milking process due to its non-invasive, quick, user-friendly, time-saving, and pretreatment-free characteristics [8]. NIRS has been utilized to determine agricultural items such as rice, wheat, pomegranate, and other vegetables and to offer qualitative and quantitative information [9–12]. In Japan, NIRS has been used to determine rice quality [9].

Numerous studies have been carried out on the development of online near-infrared (NIR) sensing systems that could help dairy farmers navigate the challenges that come with individual cow management, but there has been difficulty in developing an efficient and sustainable NIR sensing system [13–16]. According to Iweka et al. [17,18], the developed NIR spectroscopic sensing system might be utilized to accurately and precisely measure the quality of the milk of individual cows while milking in real-time. Nevertheless, the actual application of the NIR sensing system for real-time online identification of each cow's milk quality while milking has yet to be realized. One of the major reasons is the measurement accuracy of the sensing system [19].

Therefore, we developed an experimental online NIR spectroscopic sensing system for milk quality determination of individual cows during milking. The goal of this study

**Citation:** Iweka, P.; Kawamura, S.; Mitani, T.; Kawaguchi, T. Cow Milk Quality Determination Using a Near-Infrared Spectroscopic Sensing System for Smart Dairy Farming. *Eng. Proc.* **2023**, *58*, 118. <https://doi.org/10.3390/ecsa-10-16020>

Academic Editor: Stefano Mariani

Published: 15 November 2023



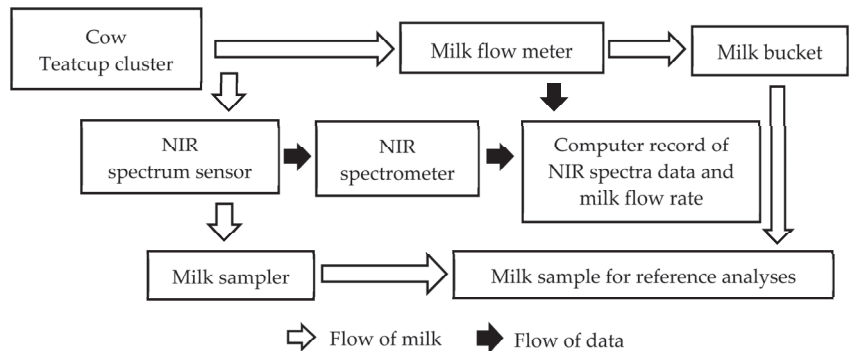
**Copyright:** © 2023 by the authors. Licensee MDPI, Basel, Switzerland. This article is an open access article distributed under the terms and conditions of the Creative Commons Attribution (CC BY) license (<https://creativecommons.org/licenses/by/4.0/>).

was to assess both the precision and accuracy of the developed novel NIR spectroscopic sensing system in our study for individual cow milk quality determination every 20 s during milking.

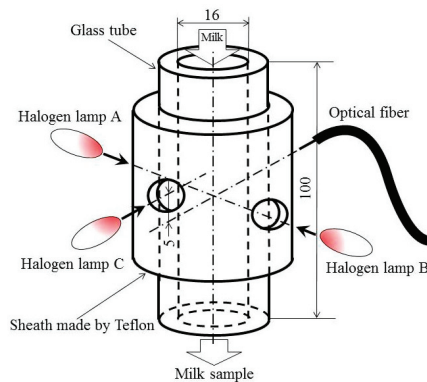
## 2. Materials and Methods

### 2.1. Description of the Near-Infrared Spectroscopic Sensing System

To determine the quality of each cow’s milk during milking, an experimentally based online NIR spectroscopic sensing system was created. The system included an NIR spectrum sensor, an NIR spectrometer, a milk flowmeter, a sampler, and a laptop computer (Figure 1). The system was linked between a teatcup cluster and the milking system’s milking bucket. Through a bypass, raw milk from the teatcup cluster was constantly flowing into the milk chamber (sample cell) of the NIR spectrum sensor. The extra milk flowed down a line tube past the milk flowmeter and into the bucket (Figure 1). The volume of the milk in the NIR milk chamber is about 30 mL (Table 1). The optical axes of halogen lamps A and B were positioned at the same height as the optical fiber, whereas the optical axes of halogen lamp C were set 5 mm higher (Figures 2–4). The milk chamber of the NIR spectrum sensor has a path length of 100 mm and a diameter of 16 mm (Figure 2). The NIR spectrum sensor collected absorbance spectra via the milk. During milking, the spectra were taken at 1 nm intervals every 20 s in the 700 nm to 1050 nm range. The milk flow rate was also recorded on the laptop computer.



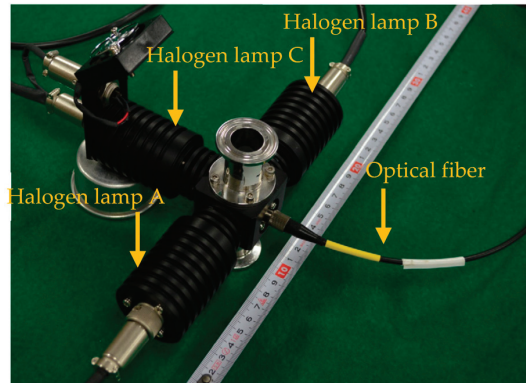
**Figure 1.** Flow chart of an on-line real-time near-infrared spectroscopic sensing system for determining milk quality indicators during milking. Adapted from [18] with permission from Environmental Control in Biology, 2020.



**Figure 2.** Schematic of the optical system of the NIR spectrum sensor’s milk chamber. Adapted from [20] with permission from MDPI, 2023.

**Table 1.** Specifications of the near-infrared (NIR) spectroscopic instrument.

Devices	Specifications
NIR spectrum sensor	Absorbance spectrum sensor
Light source	Three halogen lamps
Optical fiber	Quartz Fiber
Milk chamber surface	Glass
Volume of milk sample	Approx. 30 mL
Distance between optical axis and milk level	55 mm
NIR spectrometer	Diffraction grating spectrometer
Optical density	Absorbance
Wavelength range	700–1050 nm, 1 nm internal
Wavelength resolution	Approx. 6.4 nm
Photocell	CMOS linear array, 512 pixels
Thermal controller	Heater and cooling fan
Data processing computer	Windows 7
A/D converter	16 bit
Spectrum data acquisition	Every 20 s

**Figure 3.** Original NIR spectrum sensor.

### 2.2. Holstein Cows and Milk Samples

In this study, we used two Holstein cows belonging to the Hokkaido University dairy barn in Japan. The lactation phases of these cows varied. During the experiment, the measurements were taken during two consecutive milkings, one in the evening and one in the morning. On the Hokkaido University dairy farm, cows were milked using a pipeline milking system. Milk spectra and flow data were collected, and raw milk samples were drawn from the milk sampler every 20 s during milking.

### 2.3. Reference Analysis

The MilkoScan device was used to determine the three primary milk quality indices and MUN, while the Fossomatic device was utilized for estimating SCC. The two devices are from Foss Electric, Hillerod, Denmark. The reference analyses involved 142 milk samples.

### 2.4. Chemometric Analysis

Statistical investigations were conducted to generate calibration models for each milk quality indicator and to validate the model's accuracy as well as precision. The analyses were carried out utilizing the spectra data analysis technique, the Unscrambler ver. 10.3 from Camo AS Trondheim, Norway. The total data from the reference analyses were used to develop calibration using the full cross-validation method. The calibration models

were built using the partial least squares regression (PLSR) method from the absorbance spectra and reference data. No data pretreatment method was used for this analysis.

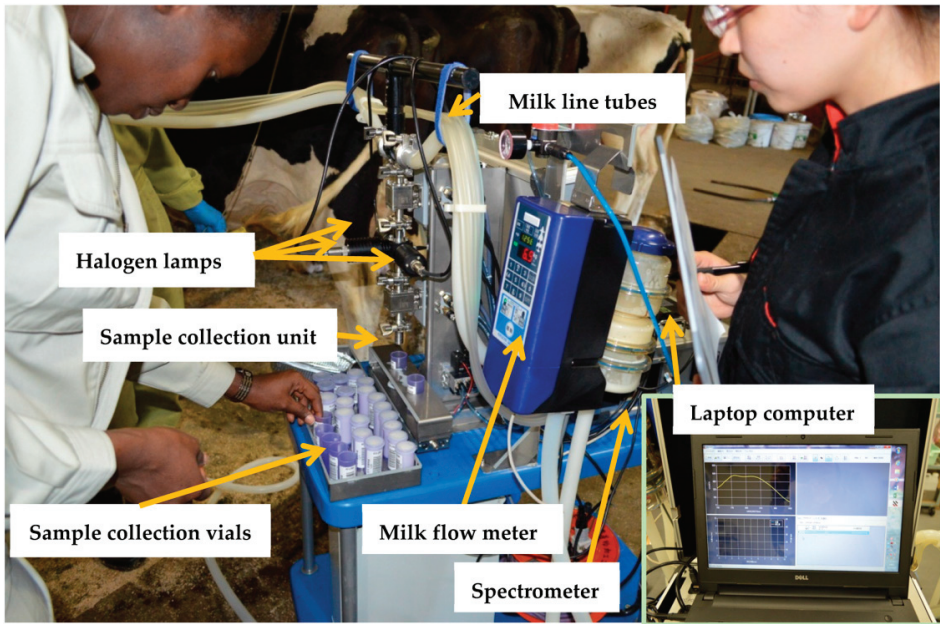


Figure 4. Overview of the NIR spectroscopic sensing system.

### 3. Results and Discussion

#### 3.1. Near-Infrared Spectra

Figure 5 shows the original raw milk spectra. The NIR spectra indicated a pair of bands, having peaks at 740 and 840 nm, respectively. These peaks represent overtone absorptions by the C-H and C-C bands, which are associated with the different absorption bands of milk components such as fat, protein, and lactose. The O-H functional groups found in water exhibited an elevated absorption peak, distinguishing the spectra band at about 960 nm [15].

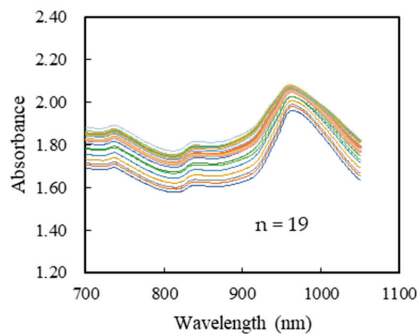


Figure 5. The original spectra of raw milk from cow number 1256 during milking.

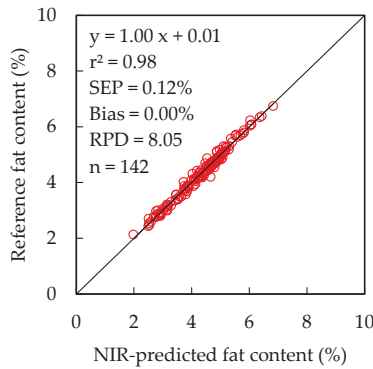
#### 3.2. Calibration Models' Precision and Accuracy

Table 2 summarizes the validation results of the NIR spectroscopic sensing system utilized to determine milk quality indicators. The relationships between the reference and NIR-predicted values of the milk fat content and SCC are shown in Figures 6 and 7, respectively.

**Table 2.** Validation statistics of the near-infrared sensing system for milk quality determination.

Milk Quality Indicators	n	Range	R <sup>2</sup>	SEP	Bias	RPD	Regression Line
Fat (%)	142	2.1–6.8	0.98	0.12	0.00	8.05	$y = 1.00x + 0.01$
Protein (%)	142	3.3–3.8	0.92	0.03	0.00	3.58	$y = 0.99x + 0.04$
Lactose (%)	142	3.9–4.7	0.70	0.09	0.00	1.83	$y = 0.96x + 0.18$
MUN (mg/dL)	142	8.9–13.8	0.45	0.60	0.00	1.35	$y = 0.92x + 0.97$
SCC (log SCCmL <sup>-1</sup> )	142	5.2–6.8	0.60	0.22	0.00	1.58	$y = 0.94x + 0.36$

n: number of validation samples. R<sup>2</sup>: coefficient of determination value of validation set. SEP: standard error of prediction. RPD: ratio of SEP to standard deviation of reference data. Regression line: regression line from predicted value (x) to reference value (y). MUN: milk urea nitrogen. SCC: Somatic cell count.



**Figure 6.** Correlation between reference fat content and NIRS-predicted fat content.

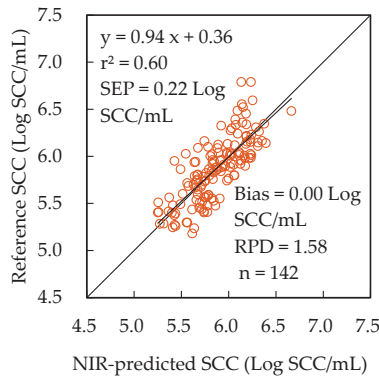


**Figure 7.** Correlation between reference SCC and NIRS-predicted SCC.

For predicting milk fat, protein, lactose, MUN, and SCC, the coefficient of determination ( $r^2$ ), standard error prediction (SEP), and bias were 0.98, 0.12%, and 0.00% for milk fat content; 0.92, 0.03%, and 0.00% for milk protein content; 0.70, 0.03%, and 0.00% for milk lactose; 0.45, 0.60%, and 0.00 mg/dL for MUN; and 0.60, 0.22 log SCC/mL, and 0.00 log SCC/mL, respectively. The high  $r^2$  values and low SEP and bias values were indicative of high levels of precision and accuracy. The calibration model for milk fat worked quite well. The carbon–hydrogen strings of triacylglycerol were adequately represented in the NIR spectra, allowing for extraordinarily high precision. These findings suggested that the NIR could be used to determine the three major milk quality indicators of raw milk and the MUN and SCC of each cow during milking. The level of precision and accuracy for predicting SCC was adequate. SCC is a globally recognized indicator of cow subclinical

mastitis disease, and the calibration model created for SCC could be used to diagnose subclinical mastitis.

### 3.3. Near-Infrared Sensing System

The accuracy for determining the three major milk quality indicators, MUN, and SCC was very good, especially for milk fat and protein, as compared to the accuracy of the previous NIR sensing system [6]. The cylindrical structure of the NIR spectrum sensor contributed to its high accuracy by reducing the effect of air bubbles and fluctuations in milk flow. Another explanation is that the NIR spectroscopic sensing system used in our work has three halogen lamps that were used as near-infrared light sources to irradiate the milk samples from three directions with an exposure length of 200 ms, which was repeated ten times in one experimental run. It was discovered that our NIR sensor, which is comprised of three halogen lamps, accurately collected the near-infrared light by fat content, as opposed to the prior study's single halogen lamp [6]. As a result, a strong signal was produced. The exposure time ensured that the important bright part of the captured spectra was not lost, resulting in a reduction in various random and fixed pattern noises.

This indicates that the NIR sensing system might provide dairy farmers and vets with useful information on each cow's physiological state and milk quality, providing evaluation control for better dairy farm management. By deploying the data from each cow, dairy farm management might proceed to the next step of smart dairy farming by using this NIR sensing technology.

## 4. Conclusions

The NIR spectroscopic sensing system created in this study might be utilized to determine the three major milk quality indices, MUN and SCC, of each cow during milking in real time. Further research should be undertaken to improve the precision and accuracy of the proposed calibration models, allowing for the practical implementation of this NIR sensing technology, resulting in smart dairy farming.

**Author Contributions:** Conceptualization, S.K. and P.I.; methodology, S.K., P.I., T.M., and T.K.; software, S.K. and P.I.; validation, P.I. and S.K.; formal analysis, P.I., S.K., and T.M.; investigation, P.I., S.K., T.M., and T.K.; data curation, P.I. and S.K.; writing—original draft preparation, P.I., writing—review and editing, S.K., T.M., and P.I. All authors have read and agreed to the published version of the manuscript.

**Funding:** This study was funded by a grant from the National Agriculture and Food Research Organization (NARO) of Japan named Project for Development of New Practical Technology.

**Institutional Review Board Statement:** Not applicable.

**Informed Consent Statement:** Not applicable.

**Data Availability Statement:** The content of this paper summarizes all the new data obtained in this study.

**Conflicts of Interest:** The author Takashi Kawaguchi works for Orion Company in Nagano, Japan. He worked in collaboration with the authors from Hokkaido University, Japan. The remaining authors declare that the research was conducted in the absence of any commercial or financial relationships that could be construed as a potential conflict of interest.

## References

1. Evangelista, C.; Basirico, L.; Bernabucci, U. An Overview on the Use of Near Infrared Spectroscopy (NIRS) on Farms for the Management of Dairy Cows. *Agriculture* **2021**, *11*, 296. [CrossRef]
2. Diaz-Olivares, J.A.; Adriaens, I.; Stevens, E.; Saeys, W.; Aernouts, B. Online Milk Composition Analysis with an On-farm Near-infrared Sensor. *Comput. Electron. Agric.* **2020**, *178*, 105734. [CrossRef]
3. Zhu, Z.; Lin, B.; Zhu, X.; Guo, W. A Rapid Method of Identifying Mastitis Degree of Bovines Based on Dielectric Spectra of Raw milk. *Food Qual. Saf.* **2023**, *7*, fyad014. [CrossRef]

4. Iweka, P.; Kawamura, S.; Mitani, T.; Yamaguchi, T.; Koseki, S. Near-infrared Spectroscopic Sensing System for Online Real-time Milk Quality Evaluation in an Automatic Milking System. In Proceedings of the Seventh Asian NIR Symposium (ANS 2020), Khonkaen, Thailand, 12–15 February 2020.
5. Tsenkova, R.; Atanassova, S.; Morita, H.; Ikuta, K.; Toyoda, K.; Iordanova, K.I.; Hakogi, E. Near Infrared Spectra of Cows' Milk for Milk Quality Evaluation: Disease Diagnosis and Pathogen Identification. *J. Near Infrared Spectrosc.* **2006**, *14*, 363–370. [CrossRef]
6. Kawasaki, M.; Kawamura, S.; Tsukahara, M.; Morita, S.; Komiyama, M.; Natsuga, M. Near-infrared spectroscopic sensing system for on-line milk quality assessment in a milking robot. *Comput. Electron. Agric.* **2008**, *63*, 22–27. [CrossRef]
7. Iweka, P.; Kawamura, S.; Mitani, T.; Yokoe, M.; Okatani, T. Effect of Milking Season on the Accuracy of Calibration Models for Milk Quality Determination using Near-infrared Spectroscopic Sensing System during Milking. In Proceedings of the 5th Asian NIR Symposium, Kagoshima, Japan, 30 November–3 December 2016.
8. Iweka, P.N. Development of Near-Infrared Spectroscopic Sensing System for Online Real-Time Monitoring of Milk Quality during Milking. Ph.D. Thesis, Hokkaido University, Sapporo, Japan, 25 September 2019. Available online: [https://eprints.lib.hokudai.ac.jp/dspace/bitstream/2115/75864/1/Iweka\\_Patricia\\_Nneka](https://eprints.lib.hokudai.ac.jp/dspace/bitstream/2115/75864/1/Iweka_Patricia_Nneka). (accessed on 15 October 2023).
9. Ohtsubo, K.; Kobayashi, A.; Shimizu, H. Quality evaluation of rice in Japan. *JARQ* **1993**, *27*, 95–101.
10. Du, Z.; Tian, W.; Tilley, M.; Wang, D.; Zhang, G.; Li, Y. Quantitative assessment of wheat quality using near-infrared spectroscopy: A comprehensive review. *Compr. Rev. Food Sci Food Saf.* **2022**, *21*, 2956–3009. [CrossRef] [PubMed]
11. Opara, U.L.; Arendse, E. Near-Infrared Spectroscopy for Pomegranate Quality Measurement and Prediction. In *Nondestructive Quality Assessment Techniques for Fresh Fruits and Vegetables*; Pathare, P.B., Rahman, M.S., Eds.; Springer: Singapore, 2022; pp. 211–232. [CrossRef]
12. Nicolai, B.M.; Defraeye, T.; Ketelaere, B.; Herremans, E.; Hertog, M.L.; Saeys, W.; Torricelli, A.; Vandendriessche, T.; Verboven, P. Nondestructive measurement of fruit and vegetable quality. *Annu. Rev. Food. Sci. Technol.* **2014**, *5*, 285–312. [CrossRef] [PubMed]
13. Tsenkova, R.; Atanassova, S.; Kawano, S.; Toyoda, K. Somatic cell count determination in cow's milk by near-infrared spectroscopy: A new diagnostic tool. *J. Anim Sci.* **2001**, *79*, 2550–2557. [CrossRef] [PubMed]
14. Iweka, P.; Kawamura, S.; Mitani, T.; Koseki, S. Non-destructive determination of bovine milk progesterone concentration during milking using near-infrared spectroscopy. *CIGR J.* **2020**, *22*, 171–178.
15. Ozaki, Y.; McClure, W.F.; Christy, A.A. *Near-Infrared Spectroscopy in Food Science and Technology*, 1st ed.; Wiley: Hoboken, NJ, USA, 2006. [CrossRef]
16. Sato, T.; Yoshino, M.; Furukawa, S.; Someya, Y.; Yano, N.; Uozumi, J.; Iwamoto, M. Analysis of Near Infrared Milk Constituents by the Spectrophotometric Method. *Jpn. J. Zootech. Sci.* **1987**, *58*, 698–706.
17. Iweka, P.; Kawamura, S.; Mitani, T.; Kawaguchi, T.; Koseki, S. Cow Milk Progesterone Concentration Assessment during Milking Using Near-infrared Spectroscopy. *EAEF* **2021**, *14*, 30–36. [CrossRef] [PubMed]
18. Iweka, P.; Kawamura, S.; Mitani, T.; Kawaguchi, T.; Koseki, S. Online Milk Quality Assessment during Milking Using Near-infrared Spectroscopic Sensing System. *Environ. Control Biol.* **2020**, *58*, 1–6. [CrossRef]
19. Iweka, P.; Kawamura, S.; Mitani, T.; Koseki, S. Effect of cow individuality and calving times on accuracy of near-infrared spectroscopic sensing system for milk quality determination during milking. In Proceedings of the 33rd NIR Forum JCNIR, Tsukuba, Japan, 15–17 November 2017; p. 83.
20. Iweka, P.; Kawamura, S.; Mitani, T.; Kawaguchi, T. Online near-infrared spectroscopy for the measurement of cow milk quality in an automatic milking system. *Eng. Proc.* **2023**, *56*, 145. [CrossRef]

**Disclaimer/Publisher's Note:** The statements, opinions and data contained in all publications are solely those of the individual author(s) and contributor(s) and not of MDPI and/or the editor(s). MDPI and/or the editor(s) disclaim responsibility for any injury to people or property resulting from any ideas, methods, instructions or products referred to in the content.



Proceeding Paper

# Design and Simulation of AI-Enabled Digital Twin Model for Smart Industry 4.0<sup>†</sup>

Md. Humayun Kabir \*, Jaber Ahmed Chowdhury, Istiak Mohammad Fahim, Mohammad Nadib Hasan, Arif Hasnat and Ahmed Jaser Mahdi

Department of Computer and Communication Engineering, International Islamic University Chittagong, Kumira Chattogram 4318, Bangladesh; jaberahmediuc@gmail.com (J.A.C.); istiakfahim94@gmail.com (I.M.F.); nadibhasan.gtu.in@gmail.com (M.N.H.); arifhasnat83@gmail.com (A.H.); jasermahdi@gmail.com (A.J.M.)

\* Correspondence: mdhkrrabby@gmail.com; Tel.: +880-151-528-6984

<sup>†</sup> Presented at the 10th International Electronic Conference on Sensors and Applications (ECSA-10), 15–30 November 2023; Available online: <https://ecsa-10.sciforum.net/>.

**Abstract:** One of the core ideas of Industry 4.0 has been the use of digital twin networks (DTNs). A DTN facilitates the co-evolution of real and virtual things through the use of DT modelling, interactions, computation, and information analysis systems. A DT simulates product lifecycles to forecast and optimize manufacturing systems and component behavior. Industry and Academia have been developing digital twin (DT) technology for real-time remote monitoring and control, transport risk assessment, and intelligent scheduling in the smart industry. This study aims to design and simulate a comprehensive digital twin model connecting three factories to a single server. It incorporates remote network control, IoT integration, advanced networking protocols, and security measures. The model utilizes the Open Shortest Path First (OSPF) routing protocol for seamless network connectivity within the interconnected factories. The Access Control List (ACL) and authentication, authorization, and accounting (AAA) mechanisms ensure secure access and prevent unauthorized entry. The digital twin model is simulated using Cisco Packet Tracer, validating its functionality in network connectivity, security, remote control, and motor efficiency monitoring. The results demonstrate the successful integration and operation of the model in smart industries. The networked factories exhibit improved operational efficiency, enhanced security, and proactive maintenance.

**Keywords:** industry 4.0; digital twin; internet of things; artificial intelligence; network requirements

**Citation:** Kabir, M.H.; Chowdhury, J.A.; Fahim, I.M.; Hasan, M.N.; Hasnat, A.; Mahdi, A.J. Design and Simulation of AI-Enabled Digital Twin Model for Smart Industry 4.0. *Eng. Proc.* **2023**, *58*, 119. <https://doi.org/10.3390/ecsa-10-16235>

Academic Editor: Stefano Mariani

Published: 15 November 2023



**Copyright:** © 2023 by the authors. Licensee MDPI, Basel, Switzerland. This article is an open access article distributed under the terms and conditions of the Creative Commons Attribution (CC BY) license (<https://creativecommons.org/licenses/by/4.0/>).

## 1. Introduction

A digital twin network is a computer simulation model of a communication network, including the environment in which it operates and the application traffic it carries. It uses the Internet of Things (IoT) to enhance decision making in complicated systems by facilitating learning and reasoning. According to a study, adopting DT and IoT technologies is projected to generate economic benefits ranging from USD 5.5 trillion to USD 12.6 trillion worldwide by 2030. The smart manufacturing industry is predicted to expand from USD 214.7 billion in 2020 to USD 384.8 billion in 2025, with a CAGR of 12.4% [1]. Despite smart manufacturing's many advantages, including integrated components and digitization, maintenance remains a significant obstacle. Maintenance is a pivotal determinant that exerts a significant economic impact on the sector, garnering notable emphasis in the era of digitalization. The entire manufacturing cost is projected to include maintenance expenses ranging from around 15% to 40% [2]. Based on the U.S. Department of Energy findings, it has been shown that predictive maintenance offers cost savings of around 8–12% compared to preventive maintenance and can yield savings of up to 40% compared to reactive maintenance [3]. The adoption rate of predictive maintenance experienced a modest increase from 47% to 51% from 2017 to 2018. This implementation of predictive maintenance



strategies reduced equipment failure rates from 61% to 57% [4]. Hence, the maintenance process exerts a direct impact on the economic aspects of the industry. Furthermore, in the contemporary era of Industry 4.0, the utilization of intelligent maintenance techniques incorporating digital twin (DT) technology has the potential to yield substantial advantages compared to existing maintenance methodologies [5].

Therefore, it is imperative to comprehend the concept of a digital twin and the potential of digital twin technology in facilitating an organization’s digital transformation. A digital twin refers to a computer-generated model replicating a tangible object’s characteristics and behavior or a procedural operation. Digital twins undergo dynamic transformations throughout the life cycles of entities and processes, facilitated by utilizing real-time IoT data. Novel network applications have emerged as a result of society and industry being digitally transformed [6]. The complex requirements for these applications make it difficult for them to be managed by conventional network management techniques like network overprovisioning or admission control. For instance, cutting-edge communication technologies like holographic telepresence and augmented reality/virtual reality demand extremely low deterministic latency, yet modern industrial advancements like vehicular networks demand real-time network topology adaptation. The behavior of current networks is very dynamic and heterogeneous due to the rapid increase in linked devices. Modern communication networks have become so sophisticated and expensive to manage as a result. The DT paradigm has lately been adopted by other industrial sectors to describe complex and dynamic systems [7]. A DT’s primary strength is in its ability to accurately replicate a complex system, eliminating the need for costly, time-consuming human interaction. A DT enables Industry 4.0 general network architecture, as shown in Figure 1.

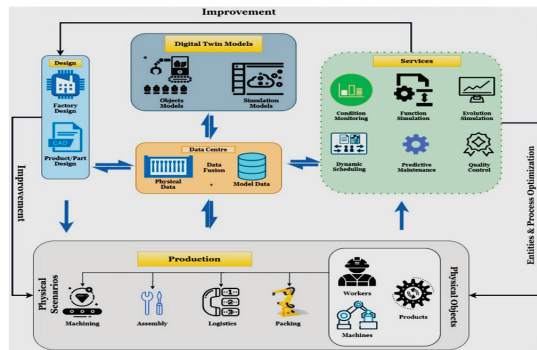


Figure 1. Digital twin general network architecture [2].

To examine various situations and forecast decision outcomes, computer simulations are performed. Digital twins vary and are updated frequently to mirror changes in their physical counterparts for timely engagement [8,9]. Artificial intelligence algorithms and network setups, which are at the heart of modern technologies, are made possible by necessary techniques trained on large volumes of data obtained from numerous connected sensors on physical objects [10]. In addition to raising significant issues for their organizations and procedures, this drives up the expenses for manufacturing businesses. Because of this, it is expected that AI-driven DT technology will be able to successfully assist decision making in multi-objective issues by adapting traditional model-based methodologies to shifting boundary circumstances and providing a demand-oriented, real-time assessment foundation. Many studies have previously provided descriptions and definitions of DTs from the standpoint of broad ideas and technological frameworks [11]. Not only that, but product design, simulation, and modeling would not be able to take advantage of their own unique enabler, artificial intelligence diagnostics and prognostics for faults [12]. The industrial technology revolution has brought attention to manufacturing concepts like personalized and distributed manufacturing. These new manufacturing paradigms and

the Industrial Internet of Things (IIoT) make connected microsmart factories in factory-as-a-service systems inefficient in cost and production [13]. A digital twin, which employs a digital version of a process with identical manufacturing elements, synchronized information, and functional units, was created to tackle these issues. The digital twin leverages up-to-date information from the Internet to collect data from IIoT devices and operates in many applications. It also generates the components of a detailed digital twin application design and defines procedures. This study could help managers organize the benefits of digital twin utilization through a hierarchy by providing real-time monitoring, tracking information, and operational decision-making support [14]. The proposed application also effectively mitigates cost and production inefficiencies, leading to the optimal functioning of a manufacturing system. We explore the problem in several phases:

**Technical complexity:** from functional requirement selection and architecture planning to the integration and verification of the final (digital) models.

**Data Incompatibility:** we address how physical components exchange real-time information with DTs, as well as experimental platforms, to build DTs (including protocols and standards).

**Security Risks:** interoperability between different systems and devices can increase the risk of security breaches, as it creates more opportunities for hackers to exploit vulnerabilities.

In this paper, we aim to design a digital twin model for smart industries that are AI-enabled. The paper's primary contributions include the following:

1. We focus on the construction of a DT network model.
2. More specifically, we focus on determining (methodologically) how to design, create, and connect physical objects with their virtual counterparts, which will improve interoperability, resilience, and security in smart manufacturing systems.
3. We implement an Access Control List (ACL) and an authentication, authorization, and accounting (AAA) system to judiciously manage access to computer resources, enforce rules, audit usage, and deliver the data required to charge for services.
4. The proposed digital twin network model incorporates remote access capabilities.

The remainder of the article is organized as follows: Section 2 introduces the digital twin frameworks for development. Section 3 discusses the simulation result. Finally, Section 4 summarizes the main findings of this work.

## 2. Digital Twin Frameworks for Development

Digital transformation encompasses a convergence of various cutting-edge technologies, including Big Data, cloud computing, the Internet of Things, the Industrial Internet of Things, sensors, artificial intelligence (AI), machine learning, and numerous more. These technologies are undergoing continuous evolution. Therefore, it is postulated that digital transformation (DT) constantly evolves alongside these technologies. The technological advancement of digital twin applications in industrial processes has experienced substantial progress over the past forty years. The adoption of digital twins for the real-time monitoring and improvement of processes has been made possible by the recent technological developments in sensing, monitoring, and decision-making tools within the context of Industry 4.0. A design for digital twins ensures that devices with virtual copies work well together in the cyber-physical domain and that data and information can flow easily between digital twins, physical twins, and the outside world. The architectural framework encompasses diverse tangible devices, sensors, and data-gathering systems inside the physical realm. These components facilitate data transfer, processing, collecting, calculating, and sharing within the virtual environment.

This research aims to design and simulate a digital twin model for smart industries that unites three separate factories on a single server. The study aims to examine the viability, effectiveness, and practical effects of creating a digital twin model that uses the OSPF routing protocol, an ACL, an AAA, connected IoT materials, remote network control, and motor efficiency monitoring made possible by artificial intelligence. Cisco Packet Tracer is used as a simulation tool to investigate these components' integration further. The

design of a digital twin simulation model and the setup of the virtual network environment, including routers, switches, IoT devices, and network security features using the Cisco Packet Tracer network simulation tool, are shown in Figure 2. For this simulation, we implement OSPF routing protocol for network routing, Extended ACL rules for network access, and AAA authentication process for network authentication.

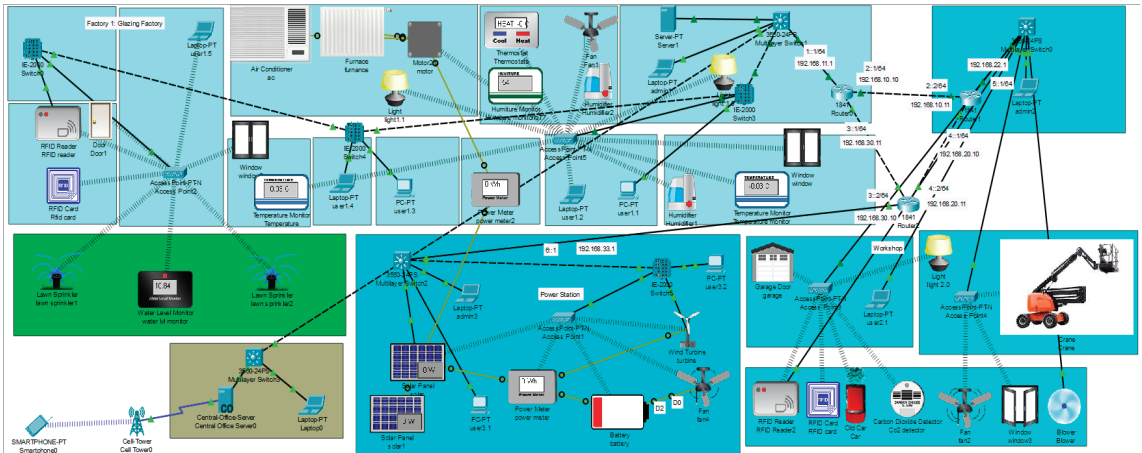


Figure 2. Proposed simulation of digital twin model for smart industries.

Figure 3 shows the working conditions of IoT devices that integrate with the proposed smart factory network topology. The working conditions will be automated and updated based on real-time sensor data.

Actions	Enabled	Name	Condition	Actions
Edit Remove	Yes	RFID valid	RFID reader Card ID = 1001	Set RFID reader Status to Valid
Edit Remove	Yes	RFID invalid	RFID reader Card ID != 1001	Set RFID reader Status to Invalid
Edit Remove	Yes	door unlock	RFID reader Status is Valid	Set Door1 Lock to Unlock
Edit Remove	Yes	door lock	RFID reader Status is Invalid	Set Door1 Lock to Lock
Edit Remove	Yes	Fan on	Match all: • Temperature monitor Temperature >= 22.0 °C • Temperature monitor Temperature > 28.0 °C	Set Fan1 Status to Low Set Fan1 Status to High
Edit Remove	Yes	Humidifier	Humidure monitorIo7 Humitor >= 60	Set Humidifier1 Status to true
Edit Remove	Yes	window open	Temperature monitor Temperature > 20.0 °C	Set window On to true Set window2 On to true
Edit Remove	Yes	window close	Temperature monitor Temperature <= 20.0 °C	Set window On to false Set window2 On to false
Edit Remove	Yes	Fan off	Temperature monitor Temperature <= 22.0 °C	Set Fan1 Status to Off
Edit Remove	Yes	RFID2	RFID Reader2 Card ID = 1001	Set RFID Reader2 Status to Valid
Edit Remove	Yes	RFID2 off	RFID Reader2 Card ID != 1001	Set RFID Reader2 Status to Invalid
Edit Remove	Yes	garage on	RFID Reader2 Status is Valid	Set garage On to true
Edit Remove	Yes	garage off	RFID Reader2 Status is Invalid	Set garage On to false
Edit Remove	Yes	blower+fan+window on	Co2 detector Level >= 0.02	Set Blower Status to High Set fan2 Status to High Set window3 On to true
Edit Remove	Yes	blower+fan low	Co2 detector Level <= 0.019	Set Blower Status to Low Set fan2 Status to Low
Edit Remove	Yes	blower off	Co2 detector Level <= 0.008	Set Blower Status to Off Set fan2 Status to Off

Figure 3. AI condition of IoT device used smart industries.

Figure 4 shows the multi-area OSPF configuration in the proposed network. The OSPF protocol actively receives and processes link-state data from neighboring routers, utilizing this information to construct a comprehensive topology map encompassing all routers inside the network. ACLs can control network access, prevent attacks, and maximize bandwidth. This is achieved by carefully identifying network message flow and working with other technologies. ACLs are essential for network security and service quality. All networks require user management for security. The configuration of Extended ACL rules for proposed network access shown in Figure 5. The AAA framework provides security to provide particular users access to designated resources and document their

operational activity. This technology is popular because it scales well and centralizes user data. Most practical AAA implementations use the Remote Authentication Dial-in User Service (RADIUS). In Figure 6 show the AAA authentication configuration of proposed network authentication.

<pre>router ospf 1 router-id 1.1.1.1 passive-interface GigabitEthernet0/0 network 192.168.72.1 0.0.0.0 area 0 network 192.168.95.1 0.0.0.0 area 0 network 192.168.127.1 0.0.0.0 area 1 auto-cost reference-bandwidth 10000</pre>	<pre>router ospf 1 router-id 2.2.2.2 passive-interface GigabitEthernet0/0 network 192.168.80.1 0.0.0.0 area 0 network 192.168.95.2 0.0.0.0 area 0 auto-cost reference-bandwidth 10000</pre>	<pre>router ospf 1 router-id 3.3.3.3 passive-interface GigabitEthernet0/0 network 192.168.104.1 0.0.0.0 area 1 network 192.168.127.2 0.0.0.0 area 1 auto-cost reference-bandwidth 10000</pre>
--	---	---

Figure 4. OSPF configuration in multi-area factory router.

<pre>Admin-1: Router-0 Router(config)#access-list 100 deny ip 192.168.11.11.0.0.0 192.168.22.12.0.0.0 Router(config)#access-list 100 deny ip 192.168.11.11.0.0.0 192.168.33.3.0.0.0 Router(config)#access-list 100 deny ip 192.168.11.11.0.0.0 192.168.33.3.0.0.0 Router(config)#access-list 100 permit ip any any Router(config)#exit Router(config)#ip access-group 100 in Router(config)#end Router#</pre>	<pre>Admin-3: Router-2 Router(config)#access-list 102 deny ip 192.168.33.11.0.0.0 192.168.11.13.0.0.0 Router(config)#access-list 102 deny ip 192.168.33.11.0.0.0 192.168.11.3.0.0.0 Router(config)#access-list 102 deny ip 192.168.33.11.0.0.0 192.168.11.14.0.0.0 Router(config)#access-list 102 deny ip 192.168.33.11.0.0.0 192.168.11.32.0.0.0 Router(config)#access-list 102 deny ip 192.168.33.11.0.0.0 192.168.11.29.0.0.0 Router(config)#access-list 102 deny ip 192.168.33.11.0.0.0 192.168.22.12.0.0.0 Router(config)#access-list 102 deny ip 192.168.33.0.0.0.0 192.168.11.13.0.0.0 Router(config)#access-list 102 deny ip 192.168.33.0.0.0.0 192.168.11.3.0.0.0 Router(config)#access-list 102 deny ip 192.168.33.0.0.0.0 192.168.11.14.0.0.0 Router(config)#access-list 102 deny ip 192.168.33.0.0.0.0 192.168.11.32.0.0.0 Router(config)#access-list 102 deny ip 192.168.33.0.0.0.0 192.168.11.29.0.0.0 Router(config)#access-list 102 deny ip 192.168.33.0.0.0.0 192.168.11.3.0.0.0 Router(config)#access-list 102 deny ip 192.168.33.0.0.0.0 192.168.11.14.0.0.0 Router(config)#access-list 102 deny ip 192.168.33.0.0.0.0 192.168.22.12.0.0.0 Router(config)#access-list 102 permit ip any any Router(config)#ip access-group 102 in Router(config)#end</pre>
---	---

Figure 5. ACL configuration in network.

<pre>Router(config)#username admin1 secret admin@R35 Router(config)#hostname Router0 Router(config)#radius-server host 192.168.11.101 Router(config)#aaa new-model Router(config)#aaa authentication login default group radius local Router(config)#line console 0 Router(config-line)#login authentication default Router(config-line)#end Router#</pre>	<pre>Router(config)#username admin1 secret admin@R35 Router(config)#aaa new-model Router(config)#aaa authentication login default local Router(config)#line console 0 Router(config-line)#login authentication default Router(config)#ip domain name cncassecurity.com Router(config)#radius key generate rsa Router(config)#aaa authentication login SSH_LOGIN local Router(config)#line vty 4 Router(config-line)#transport input ssh Router(config-line)#login authentication SSH_LOGIN</pre>	<pre>Router(config)#username admin1 secret admin@R35 Router(config)#aaa authentication login default local Router(config)#line console 0 Router(config-line)#login authentication default Router(config)#ip domain name cncassecurity.com Router(config)#radius key generate rsa Router2(config)#aaa authentication login SSH_LOGIN local Router2(config)#line vty 0 4 Router2(config-line)#transport input ssh Router2(config-line)#login authentication SSH_LOGIN</pre>
--	--	---

Figure 6. AAA configuration in network.

### 3. Results and Discussion

The entrance door opens automatically when a valid RFID card is presented to the RFID reader. A lawn sprinkler will automatically explode when the garden water level drops. The fan rotates slowly if the room temperature is >22.0 °C and quickly if it is >28.0 °C. A light turns on when the motor efficiency decreases to by less than 35%. However, if the motor efficiency drops below 20%, a light will blink and be seen in a workplace by blinking another light. The motor runs on solar electricity. The device continually monitors the water levels using smart sensors. The system activates lawn sprinklers when the water level dips, optimizing watering and conserving water. An automatic humidity management system uses a hygrometer and humidifier to maintain appropriate air moisture levels. The humidifier produces water vapor or steam when the hygrometer detects humidity above 60%, increasing the surrounding moisture. The device controls the fan speed by monitoring the ambient temperature. The fan slows at 22.0 °C or above. If the temperature exceeds 28.0 °C, the fan speed rises, aiding temperature regulation, as shown in Figure 7a.

The garage door opens automatically when a valid RFID card is scanned in front of the RFID reader. The blower fan will spin swiftly and open the window if the vehicle smokes. Blinking lights alert the workshop when Factory 1 motor efficiency drops. Raw materials will then be delivered from the workshop to Factory 1. The system evaluates the motor efficiency and activates lights at specified levels. A light turns on when the motor efficiency drops below 35%. The light blinks, and a similar light in the workplace (Factory 2) blinks to inform personnel if the efficiency drops below 20%. The gadget detects vehicle smoke using CO<sub>2</sub> levels. Smoke extraction and ventilation are improved by activating a high-speed blower fan and opening the window when the CO<sub>2</sub> levels climb by 0.02%. Every authorized person receives an RFID card. A microprocessor on these cards/tags stores identifying numbers and access credentials. Presenting a valid RFID card to the RFID reader opens the door, as shown in Figure 7b. Power meters display and quantify the

power absorption. Solar and wind turbines will generate energy and directly supply to the center power grid. The battery provides backup power in case of emergencies. A power meter monitors the absorbed power, a power station gathers energy from solar panels and wind turbines, and a battery backup ensures power delivery in unexpected circumstances, as shown in Figure 7c.

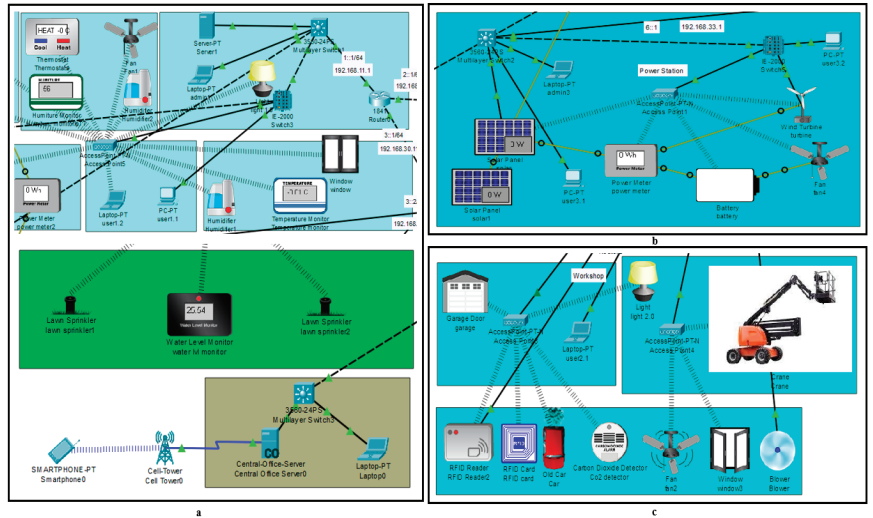


**Figure 7.** (a) Sensor output of Factory 1, (b) sensor output of Factory 2, and (c) sensor output of Factory 3.

**4. Conclusions**

Digital twins (DTs) offer novel opportunities for the optimization, monitoring, simulation, prediction, diagnosis, and control of physical processes. These resources provide valuable insights for developing novel business models and decision support systems, as well as enhancing operational efficiency. This paper comprehensively analyzed the most current scholarly works, concentrating on the DT factory. As documented in the contemporary scientific literature, the methodological techniques utilized for constructing decision trees have been thoroughly examined and briefly explained. Based on the abovementioned findings, a comprehensive examination has been conducted to ascertain the requisite procedures for systematically constructing a DT. This process encompasses many stages, including design, modeling, and execution. It has been determined that the expansion of digital technologies (DTs) will rely on the integration of complementary technologies, including artificial intelligence (AI), the Internet of Things (IoT), and big data analysis. The significance of network connectivity is elevated as it facilitates the transmission of data from the tangible entity to be analyzed by its digital equivalent. In this study, we examine the development of secure DTs intended to enhance the safeguarding of sensed data. Our objective is to establish dependable systems well suited for essential operations by examining viable methods of fortifying data protection.

**Author Contributions:** Conceptualization, M.H.K. and M.N.H.; methodology, M.H.K., J.A.C., I.M.F., A.H. and A.J.M.; software, J.A.C., I.M.F. and A.H.; formal analysis, M.H.K., M.N.H., J.A.C. and I.M.F.; writing—original draft preparation, J.A.C. and I.M.F.; writing—review and editing, M.H.K., M.N.H., J.A.C. and A.J.M.; supervision, M.H.K. and M.N.H. All authors have read and agreed to the published version of the manuscript.

**Funding:** This research received no external funding.

**Institutional Review Board Statement:** Not applicable.

**Informed Consent Statement:** Not applicable.

**Data Availability Statement:** Data are contained within the article.

**Conflicts of Interest:** The authors declare no conflicts of interest.

## References

1. Javaid, M.; Haleem, A. Digital Twin applications toward Industry 4.0: A Review. *Cogn. Robot.* **2023**, *3*, 71–92. [CrossRef]
2. Warke, V.; Kumar, S.; Bongale, A.; Kotecha, K. Sustainable Development of Smart Manufacturing Driven by the Digital Twin Framework: A Statistical Analysis. *Sustainability* **2021**, *13*, 10139. [CrossRef]
3. Benotsmane, R.; Kovács, G.; Dudás, L. Economic, social impacts and operation of smart factories in Industry 4.0 focusing on simulation and artificial intelligence of collaborating robots. *Soc. Sci.* **2019**, *8*, 143. [CrossRef]
4. Segovia, M.; Garcia-Alfaro, J. Design, Modeling and Implementation of Digital Twins. *Sensors* **2022**, *22*, 5396. [CrossRef] [PubMed]
5. Wu, Y.; Zhang, K.; Zhang, Y. Digital twin networks: A survey. *IEEE Internet Things J.* **2021**, *8*, 13789–13804. [CrossRef]
6. Tsaramirsis, G.; Kantaros, A.; Aldarraj, I.; Piriomalis, D.; Apostolopoulos, C.; Pavlopoulou, A.; Alrammal, M.; Ismail, Z.; Buhari, S.; Stojmenovic, M.; et al. A Modern Approach towards an Industry 4.0 Model: From Driving Technologies to Management. *J. Sens.* **2022**, *2022*, 5023011. [CrossRef]
7. Fuller, A.; Fan, Z.; Day, C.; Barlow, C. Digital twin: Enabling technologies, challenges and open research. *IEEE Access* **2020**, *8*, 108952–108971. [CrossRef]
8. Mozo, A.; Karamchandani, A.; Gómez-Canaval, S.; Sanz, M.; Moreno, J.I.; Pastor, A. B5GEMINI: AI-Driven Network Digital Twin. *Sensors* **2022**, *22*, 4106. [CrossRef] [PubMed]
9. Zhou, C.; Yang, H.; Duan, X.; Lopez, D.; Pastor, A.; Wu, Q.; Boucadair, M.; Jacquenet, C. *Digital Twin Network: Concepts and Reference Architecture*; Internet Engineering Task Force: Fremont, CA, USA, 2021.
10. Rathore, M.M.; Shah, S.A.; Shukla, D.; Bentafat, E.; Bakiras, S. The role of ai, machine learning, and big data in digital twinning: A systematic literature review, challenges, and opportunities. *IEEE Access* **2021**, *9*, 32030–32052. [CrossRef]
11. Kabir, M.H.; Kabir, M.A.; Islam, M.S.; Mortuza, M.G.; Mohiuddin, M. Performance Analysis of Mesh Based Enterprise Network Using RIP, EIGRP and OSPF Routing Protocols. *Eng. Proc.* **2021**, *10*, 47. [CrossRef]
12. Biller, B.; Biller, S. Implementing Digital Twins That Learn: AI and Simulation Are at the Core. *Machines* **2023**, *11*, 425. [CrossRef]
13. Thelen, A.; Zhang, X.; Fink, O.; Lu, Y.; Ghosh, S.; Youn, B.D.; Todd, M.D.; Mahadevan, S.; Hu, C.; Hu, Z. A comprehensive review of digital twin—Part 1: Modeling and twinning enabling technologies. *Struct. Multidiscip. Optim.* **2022**, *65*, 354. [CrossRef]
14. Park, K.T.; Nam, Y.W.; Lee, H.S.; Im, S.J.; Noh, S.D.; Son, J.Y.; Kim, H. Design and implementation of a digital twin application for a connected micro smart factory. *Int. J. Comput. Integr. Manuf.* **2019**, *32*, 596–614. [CrossRef]

**Disclaimer/Publisher’s Note:** The statements, opinions and data contained in all publications are solely those of the individual author(s) and contributor(s) and not of MDPI and/or the editor(s). MDPI and/or the editor(s) disclaim responsibility for any injury to people or property resulting from any ideas, methods, instructions or products referred to in the content.



Proceeding Paper

# IOTA and Smart Contract Based IoT Oxygen Monitoring System for the Traceability and Audit of Confined Spaces in the Shipbuilding Industry <sup>†</sup>

Ángel Niebla-Montero <sup>1,2,\*</sup>, Iván Froiz-Míguez <sup>1,2</sup>, José Varela-Barbeito <sup>3</sup>, Paula Fraga-Lamas <sup>1,2,\*</sup> and Tiago M. Fernández-Caramés <sup>1,2</sup>

<sup>1</sup> Centro Mixto de Investigación UDC-Navantia, Universidade da Coruña, Edificio de Batallones, s/n, 15403 Ferrol, Spain; ivan.froiz@udc.es (I.F.-M.); tiago.fernandez@udc.es (T.M.F.-C.)

<sup>2</sup> Department of Computer Engineering, Faculty of Computer Science, Universidade da Coruña, 15071 A Coruña, Spain

<sup>3</sup> Navantia S. A., Unidad de Producción de Ferrol, Taxonera, 15403 Ferrol, Spain; jvarelaba@navantia.es

\* Correspondence: angel.niebla@udc.es (Á.N.-M.); paula.fraga@udc.es (P.F.-L.); Tel.: +34-981167000 (ext. 6051) (P.F.-L.)

<sup>†</sup> Presented at the 10th International Electronic Conference on Sensors and Applications (ECSA-10), 15–30 November 2023; Available online: <https://ecsa-10.sciforum.net/>.

**Abstract:** Security presents significant challenges due to the exponential growth in the number of Internet of Things (IoT) devices that generate and collect data over the network. It is crucial to ensure the integrity and security of IoT devices, as well as to address issues such as interoperability and trust in data sources. In the proposed article, we present a novel architecture together with its implementation as a proof-of-concept of a traceability and auditing IoT system based on Distributed Ledger Technology (DLT). To demonstrate the applicability of the proposed solution, a smart contract-based system for occupational risk prevention (ORP) has been developed to monitor oxygen concentration in confined spaces that exist in ships and shipyards. The system has been devised for the operators that weld inside the ships of the Spanish shipbuilding company Navantia, which is one of the largest shipbuilders in the world. Specifically, the IOTA network has been used, which benefits the system through its decentralized, secure, and scalable data structure. In addition, the integration of smart contracts allows for establishing predefined rules and conditions, ensuring the execution of logic in a reliable and automated manner. To demonstrate the viability of the system, it has been tested locally and in the IOTA testing environment. Despite the challenges in deploying smart contracts with IOTA, the developed system is considered useful for the traceability and auditing of the oxygen concentrations without the need for any human intervention. Furthermore, it establishes the groundwork for future advancements in IoT traceability and auditing in industrial ORP scenarios.

**Keywords:** IoT; IOTA; smart contract; Industry 5.0; occupational risk prevention

**Citation:** Niebla-Montero, Á.; Froiz-Míguez, I.; Varela-Barbeito, J.; Fraga-Lamas, P.; Fernández-Caramés, T.M. IOTA and Smart Contract Based IoT Oxygen Monitoring System for the Traceability and Audit of Confined Spaces in the Shipbuilding Industry. *Eng. Proc.* **2023**, *58*, 120. <https://doi.org/10.3390/ecsa-10-16226>

Academic Editor: Stefano Mariani

Published: 15 November 2023



**Copyright:** © 2023 by the authors. Licensee MDPI, Basel, Switzerland. This article is an open access article distributed under the terms and conditions of the Creative Commons Attribution (CC BY) license (<https://creativecommons.org/licenses/by/4.0/>).

## 1. Introduction

In a traditional database audit, the auditor must physically visit the servers to thoroughly analyze them. This is because, in a client/server architecture, there is no way to know the internal server operations, requiring a thorough examination of its internal workings. On the contrary, the use of Distributed Ledger Technology (DLT) systems provides a significant advantage in terms of transparency [1]. The ability to execute smart contracts in these systems allows any entity involved in the construction of a ship or in its maintenance processes to be fully aware of the actions carried out during the smart contract execution.

The objective of this paper is to describe an Internet of Things (IoT) system for traceability and occupational risk prevention (ORP) auditing that has been developed for the Spanish shipbuilder Navantia. The proposed system is designed for the monitoring and

control of oxygen concentrations in the confined spaces found on ships and shipyards, where operators perform welding tasks.

In the proposed system, initially, the involved parties sign a smart contract in which the terms of use are accepted and the audited database is created. Then, any participating entity will be able to automatically carry out the audit of the agreed-upon database by downloading it via another smart contract. Specifically, the IOTA [2] network has been used to implement a smart contract that, when deployed, creates an OrbitDB [3] database where the data of the monitored parameters will be stored.

The choice of IOTA over other blockchain-based systems is related to the fact that IOTA nodes only perform basic operations that do not require a lot of computational power (for example, operations like storing transactions on a shared ledger, or validating such transactions). As a result, its application in IoT projects is really promising. At this point, it is important to note that IOTA does not use a blockchain, but a Distributed Ledger Technology (DLT) that makes use of Direct Acyclic Graphs (DAGs).

Specifically, the development described in this paper has the following features:

- Smart contract-based. At the first stage, all involved parties sign a contract that outlines the specific terms and conditions for the creation of the database, which will be audited and shared among them.
- Decentralized storage. The database is distributed across multiple nodes using a decentralized storage approach. Each node keeps an immutable copy of the content.
- Traceability for audits. If one of the involved entities wants to validate or audit the stored data, it can easily access the database by executing a specific smart contract. Such an action allows for downloading the latest stored content.

## 2. Communications Architecture

The proposed communications architecture is divided into two basic layers, each serving a specific purpose:

- Low-Level Layer: This layer, shown in Figure 1, is responsible for managing communications between nodes, represented as Raspberry Pi (RPI) devices, through Bluetooth Low-Energy (BLE) connections. A client-server connection is established via a BLE interface, for connection to Low Power Node (LPN) nodes, and libp2p, an essential component of Interplanetary File System (IPFS) [4], is used for transport layer to ensure data security between peers. Libp2p ensures that each peer has a unique identifier known as a PeerId, which allows any entity to retrieve the public key of the node with which it communicates. This guarantees peer identity and protects the data from unauthorized access or manipulation by third parties.
- High-Level Layer: The IOTA network is established in this layer via the data network known as the Tangle [5]. The Tangle network is a decentralized structure that records data exchanges in an immutable way, ensuring the reliability and integrity of the stored data. One of the key differences between IOTA and other blockchain-based technologies is that there is no distinction between miners and users. All IOTA network nodes can participate in the consensus process, thus promoting the decentralization and scalability of the system. This layer is illustrated in Figure 2.

The definition of a consensus layer, which determines the validity of transactions through mutual approval, is at the heart of consensus in IOTA. Transactions gain more consensus as more subsequent transactions validate them. The proposed architecture includes IOTA nodes, called “Wasps”, that are in charge of executing smart contracts in the Tangle. A critical node known as “GoShimmer” [6] is also deployed to provide network access to the other Wasp nodes. A committee of randomly selected Wasp nodes runs a chain where smart contracts are deployed. The committee’s primary goal is to ensure a smooth transition from one state to the next one, thus enabling distributed, fault-tolerant, and leaderless operations. The IOTA Smart Contracts Protocol (ISCP) enables the private execution of smart contract chains, which are validated by a committee of nodes. Unlike



traditional systems, IOTA smart contracts do not need the execution of all contracts by all nodes in the network, providing greater flexibility and significantly reducing energy consumption and cost [7].

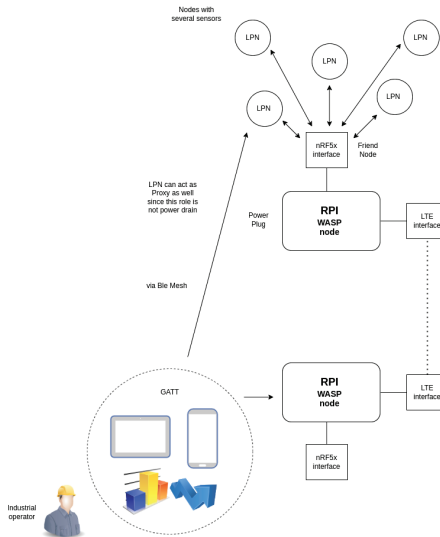


Figure 1. Low-level layer of the communications architecture.

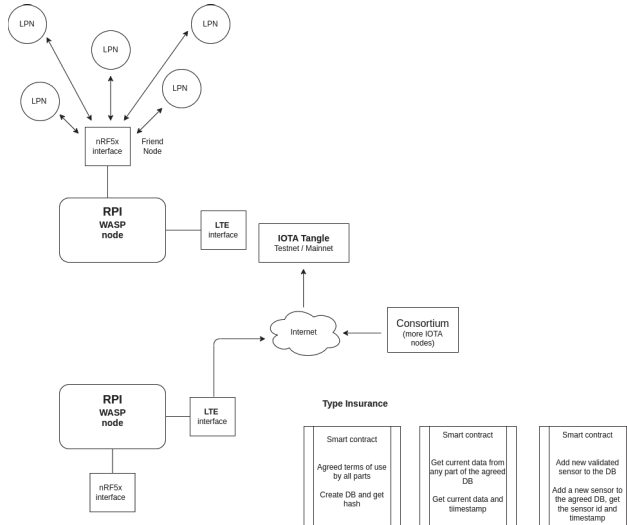


Figure 2. High-level layer of the communications architecture.

### 3. Implementation

The high-level layer of the architecture is the focus of this paper. The high-level layer includes a locally implementable IOTA private network that can later be integrated into the nodes that constitute the oxygen monitoring system (one such node is shown in Figure 3). The implementation consists of a GoShimmer node for messaging and a Wasp node that runs smart contracts. The proposed architecture is deployed in a series of steps that configure and activate the key elements in an IOTA 2.0 private network.

First, the GoShimmer node (version 0.7.5) is installed, which serves as a central component for network messaging. The client wallet is then downloaded and initialized,

producing a seed that will be used to allocate the required funds. The IOTA network wallet is a must-have tool for token access, transfer and management. It provides a solution for storing secret keys and using them to control tokens in the network. The lack of transaction fees is a distinguishing feature of IOTA [8]. For each transaction, the amount deducted from the sender's wallet equals the amount added to the recipient's wallet.

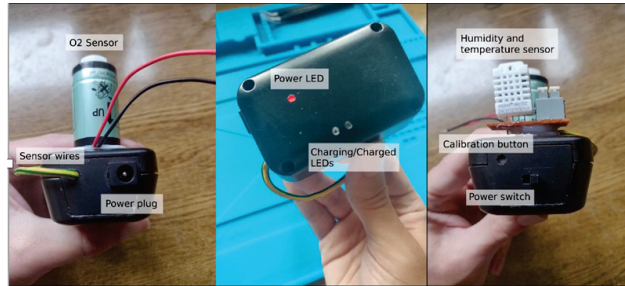


**Figure 3.** Oxygen level monitoring node.

The next step is to create a custom Genesis snapshot, which includes a transaction that directs funds to the newly initialized wallet. After the GoShimmer node is up and running, the Wasp node is installed, which is critical for executing smart contracts on the Tangle.

The smart contract is created using the Go programming language. A contract is created, and a Processor is established to allow the contract to be initialized with the necessary functions, such as “initialize” (used during contract deployment) and “getOxygen” (providing database values). The “initialize” function receives a value that can be provided as a parameter during contract deployment, and the database is initialized in the system and the received value is added via the “initOrbit” function. The code for the three functions mentioned above can be found in [9].

Following that, the smart contract is imported into the Wasp node and executed when the node boots. After starting the Wasp node, funds are transferred to the Wasp node wallet using the address obtained when starting the node.

Finally, to deploy the smart contract, a chain with a single Wasp node is first built. The funds are then deposited in this chain, allowing the smart contract to be executed later. Finally, the smart contract is deployed in the chain, completing the implementation process of the proposed architecture.

#### 4. Initial Experiments

To verify the proper operation of the proposed system, tests took place in a real-life scenario at Navantia's shipyard in Ferrol. Specifically, one of the previously mentioned nodes (whose main hardware components are displayed in Figure 3) was placed inside a tank of a gas carrier (as shown in Figure 4a,b), since such a scenario is an example where dangerous soldering works can be performed. Data on the percentage of oxygen inside the gas carrier was obtained and stored in the database during these tests, resulting in the creation of a smart contract.

The use of an off-chain environment, such as the one described in Section 3, allows for more agile development when implementing the system. However, once a preliminary version of the system has been developed, it is recommended that it should be tested in a more realistic environment. In this case, IOTA provides a Tangle Devnet environment. To use the IOTA devnet, it must first be deployed the GoShimmer node. Such a node must have a fixed or dynamic public IP address that is not Carrier Grade (this is the primary requirement for synchronization with the Tangle). A GoShimmer node can involve multiple Wasp nodes, implying that multiple committee nodes can use the same GoShimmer node to connect to the Tangle. The Wasp nodes, which can be deployed in any type of network, must be linked to the GoShimmer node for proper operation in the IOTA devnet. To run Smart

Contracts on a GoShimmer node, several plugins must be enabled (remotelog, networkdelay, spammer, prometheus, faucet, and txstream) and TCP port 5000 must be exposed.



**Figure 4.** Gas carrier where the system was tested (a) and ORP IoT device placed inside a tank of the gas carrier (b).

Then, the GoShimmer node must synchronize its state with the rest of the network when it boots up for the first time. This step is critical because, without it, it will be impossible to request funds, which are required to carry out any operation in the chain. It should be noted that only the most recent version of the GoShimmer node will be synchronized. Once synchronized, internal operations will be performed for load testing and for measuring response times, but they have nothing to do with the use of smart contracts. Figure 5 depicts the synchronized GoShimmer node dashboard [10], showing its performance in operation in terms of messages per second (the amount of messages issued to the network every second) and current tips (transactions that have not yet been approved). The latter is related to the fact that, when a transaction is added to the tangle, it must reference two other transactions (tips) that are already in the Tangle: if the current tips parameter is less than two, the transaction has to wait.

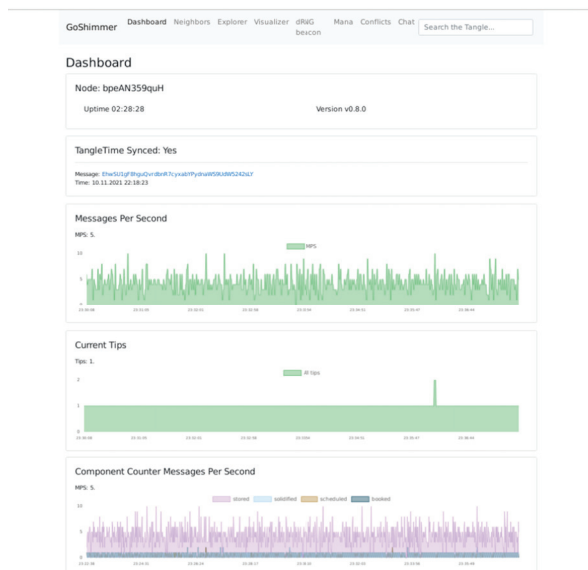


**Figure 5.** Synchronized GoShimmer node dashboard.

## 5. Conclusions

This paper presented a novel architecture, together with its implementation, as a proof-of-concept of a traceability and auditing IoT system for monitoring oxygen concentration in confined spaces. Specifically, the paper described a smart contract-based system for occupational risk prevention for monitoring oxygen concentration in confined spaces found in ships and shipyards.

A smart contract was successfully implemented both locally and in the IOTA test environment, and the overall system was tested in a real-world scenario (inside a gas carrier). Given the technology's current state of development, both the environment configuration and smart contract development were performed in IOTA's native language. The initial tests demonstrated the viability of the proposed approach in real shipbuilding scenarios, like inside a tank of a gas carrier.

In conclusion, this project has laid the basis for a more comprehensive and robust solution in the field of IoT traceability and auditing, and it is expected to contribute to future developments and improvements in the IOTA infrastructure, as well as the deployment and operation of smart contracts.

**Author Contributions:** conceptualization, T.M.F.-C., J.V.-B.; methodology, P.F.-L. and T.M.F.-C.; investigation, A.N.-M., I.F.-M., P.F.-L. and T.M.F.-C.; writing—original draft preparation, A.N.-M., I.F.-M. and T.M.F.-C.; writing—review and editing, A.N.-M., I.F.-M., P.F.-L. and T.M.F.-C.; supervision, T.M.F.-C., J.V.-B.; project administration, T.M.F.-C.; funding acquisition, T.M.F.-C. All authors have read and agreed to the published version of the manuscript.

**Funding:** This work has been supported by Centro Mixto de Investigación UDC-NAVANTIA (IN853C 2022/01), funded by GAIN (Xunta de Galicia) and ERDF Galicia 2021-2027. In addition, this work has been funded by the Xunta de Galicia (by grant ED431C 2020/15), and by grant PID2020-118857RA-100 (ORBALLO) funded by MCIN/AEI/10.13039/501100011033.

**Institutional Review Board Statement:** Not applicable.

**Informed Consent Statement:** Not applicable.

**Data Availability Statement:** Data sharing is not applicable due to privacy.

**Conflicts of Interest:** The authors declare no conflicts of interest.

## References

1. Fernández-Caramés, T.M.; Fraga-Lamas, P. Design of a fog computing, blockchain and IoT-based continuous glucose monitoring system for crowdsourcing mHealth. In Proceedings of the 5th International Electronic Conference on Sensors and Applications, Online, 15–30 November 2018.
2. IOTA Wiki. Available online: <https://wiki.iota.org/learn/about-iota/an-introduction-to-iota/> (accessed on 27 September 2023).
3. OrbitDB GitHub Repository. Available online: <https://github.com/orbitdb/orbitdb> (accessed on 27 September 2023).
4. Official IPFS Website. Available online: <https://ipfs.io/> (accessed on 27 September 2023).
5. Popov, S. The tangle. *White Pap.* **2018**, *1*, 30.
6. IOTA Wiki. Setting Up a GoShimmer Node. Available online: <https://wiki.iota.org/goshimmer/tutorials/setup/> (accessed on 27 September 2023).
7. IOTA Wiki. Energy Efficiency. Available online: <https://wiki.iota.org/learn/about-iota/energy-efficiency/> (accessed on 27 September 2023).
8. Popov, S.; Lu, Q. IOTA: Feeless and free. *IEEE Blockchain Tech. Briefs* **2019**. Available online: <https://blockchain.ieee.org/technicalbriefs/january-2019/iota-feeless-and-free/> (accessed on 27 September 2023).
9. Repository with the Code of the Smart Contracts of the Project. Available online: <https://git.armriot.com/umi/autoid/blockchain> (accessed on 27 September 2023).
10. IOTA Wiki. GoShimmer Analysis Dashboard. Available online: [https://wiki.iota.org/goshimmer/teamresources/analysis\\_dashboard](https://wiki.iota.org/goshimmer/teamresources/analysis_dashboard) (accessed on 27 September 2023).

**Disclaimer/Publisher's Note:** The statements, opinions and data contained in all publications are solely those of the individual author(s) and contributor(s) and not of MDPI and/or the editor(s). MDPI and/or the editor(s) disclaim responsibility for any injury to people or property resulting from any ideas, methods, instructions or products referred to in the content.

Proceeding Paper

# Automated Damage and Defect Detection with Low-Cost X-ray Radiography Using Data-Driven Predictor Models and Data Augmentation by X-ray Simulation <sup>†</sup>

Stefan Bosse

Department of Mathematics & Computer Science, University of Bremen, 28359 Bremen, Germany; sbosse@uni-bremen.de

<sup>†</sup> Presented at the 10th International Electronic Conference on Sensors and Applications (ECSA-10), 15–30 November 2023; Available online: <https://ecsa-10.sciforum.net/>.

**Abstract:** The detection of hidden defects in materials using X-ray images is still a challenge. Often, a lot of defects are not directly visible in visual inspection. In this work, a data-driven feature marking model is introduced to perform semantic pixel annotation. Input data are delivered by a standard industrial X-ray instrument and a low-cost self-constructed portable X-ray instrument, which is introduced in detail in this work, too. The technical details of the X-ray instrument are relevant since the quality of the feature detector is compared with respect to noise, contrast, and signal quality. Finally, a simulation of X-ray images is used to provide a ground truth data set for the training of the feature detector. It is shown that this approach is suitable for detecting hidden pores in high-pressure die-casted aluminum plates.

**Keywords:** non-destructive testing; damage diagnostics; X-ray imaging; computer tomography; feature detection; machine learning

## 1. Introduction

It is still difficult to identify and detect hidden faults or impurities in multi-layered composites like fiber-metal laminates (FML), as well as in homogeneous materials, e.g., high-pressure die-casted aluminum materials, even using advanced X-ray Computer Tomography (CT). For example, an impact damage can be nearly invisible using a frontal X-ray projection, although the deformation can be seen and detected manually by hand perception. Hidden pores in materials can be detected and analyzed by 3D CT volume rendering, but they are hard to identify in single projection images (radiography). Things become worse if a portable low-cost X-ray radiography or semi-tomography machine is used (called a LowQ measuring device), as introduced and described in this work.

It is desirable to detect or mark defects, damages, or impurities using an automated feature marking system directly in the measure images. The impact of image quality can be relevant to the feature detection quality, regardless of the complexity of the model behind [1]. Often, complex neural networks (deep learning models) are used [2]. In this work, a simple pixel classifier is used. Semantic pixel detectors are simple mathematical models that can be used to mark Regions of Interest (ROIs) in an image relating to a specific semantic class. After the image preprocessing and filtering stages, damage and material faults are identified by a pixel anomaly detector, basically an advanced Convolutional Neural Network (CNN) and region proposal R-CNN models. Training pixel classifiers can require the use of only a few images because each pixel region is a sample instance. R-CNN models require an extended sample data base which cannot be acquired only by physical measurements. The training and test data set will always be limited by a limited number of specimens, e.g., with impact damages, and a limited variance in material and damage parameters (e.g., location). For this reason, the data set is extended by synthetic data

**Citation:** Bosse, S. Automated Damage and Defect Detection with Low-Cost X-ray Radiography Using Data-Driven Predictor Models and Data Augmentation by X-ray Simulation. *Eng. Proc.* **2023**, *58*, 121. <https://doi.org/10.3390/ecsa-10-16126>

Academic Editor: Stefano Mariani

Published: 15 November 2023



**Copyright:** © 2023 by the author. Licensee MDPI, Basel, Switzerland. This article is an open access article distributed under the terms and conditions of the Creative Commons Attribution (CC BY) license (<https://creativecommons.org/licenses/by/4.0/>).

augmentation using X-ray simulation. In contrast to other wave measurement principles like Guided Ultrasonic Waves (GUWs), X-ray images can be simulated with high accuracy (compared with physically measured images). We are using the gVirtualXray software library [3,4] and performing X-ray image simulation by using GPU processing only and ray tracing. gVirtualXray is proven in terms of its suitability to produce accurate images as long as the diffraction and reflection of X-rays are neglected. In addition, a novel few projection hidden-damage detection methodology is introduced that can be used in-field with a portable X-ray machine as described above. Preliminary results show a high defect detection rate for a wide range of materials.

An X-ray measuring system (see Figure 1, left) consists of an X-ray source (commonly a cone beam with a specific focal size diameter  $fsd$ ) and an X-ray detector. The X-ray source uses either a cold emission or hot emission (Coolidge) X-ray tube. In cold emission, the electrical field extracts and accelerates electrons from the cathode to the anode; in hot emission, there is a heated free electron source, and the electrical field only accelerates the electron to a target anode material. Cold emission tubes lack independent tube current control (dependent on the tube voltage).

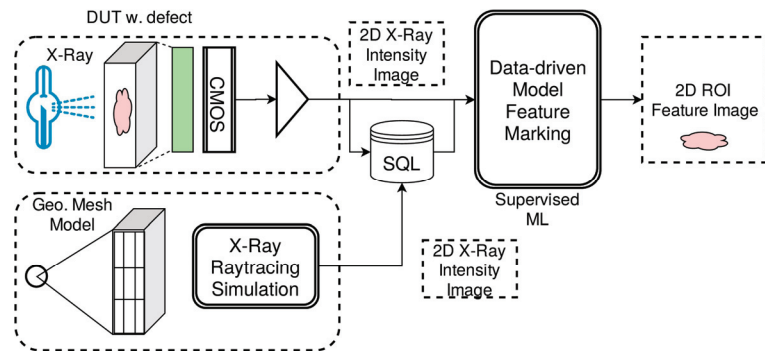


**Figure 1.** The basic framework combining experimental measuring data with simulated data.

The X-ray detector can be a direct or indirect conversion system. In a direct conversion system, the X-ray photons will generate electrons (photo effect) directly in the solid-state device; in an indirect conversion system, a conversion material (scintillator) is required to convert X-ray photons into visible light photons, which are finally converted to electrons in a solid-state detector.

In addition to the X-ray conversion mode, there are direct coupled detectors and imaging systems that map the X-ray converted image from a scintillator onto a solid-state detector. Direct coupled systems require an optical coupling material, commonly a fiber optic plate (FOP) posing high geometric accuracy and low distortion. An indirect imaging system with a lens-based imaging system can introduce optical distortion and yield reduced geometric accuracy, but these types of systems have the advantage of being inexpensive [5].

Solid-state detectors are typically Coupled Charge Devices (CCDs) or CMOS pixel detectors. Despite the fact that when used in an indirect conversion system, they are sensitive to visible light, they are still sensitive to incident X-ray radiation producing shot or popcorn noise.

The X-ray equipment consists of a low-cost X-ray source for dental diagnostics and an X-ray detector consisting of a conventional medical X-ray converter and amplifier foil (Fine 100) backside imaged by a commercially available CMOS monochrome image sensor (back-illuminated Sony IMX290 2 M pixel sensor, described later) and a simple two-lens optics. The optical distortion introduced by the optics increases with increasing distance from the center of the image (“barrel distortion”) and must be corrected, at least for CT 3D volume reconstruction.

The measured X-ray images pose increased gaussian- and non-gaussian distributed noise (compared with high-quality flat panel detectors) and more important randomly located “popcorn” shot noise by avalanche effects in pixels and pixel clusters (islands) due to X-ray radiation exposure (back-illuminated sensors are very sensitive to this noise). The gaussian noise can be reduced by averaging; the shot noise is removed by using multiple images recorded in series and an automated pixel replacement algorithm. The shot noise is a seed threshold phenomenon, i.e., the location and number of white pixels changes from image to image, therefore allowing for the replacement of white pixels in one image from unaltered pixels from another image.

Basically, we can classify X-ray measuring devices and systems into three classes with respect to non-destructive testing (NDT) in engineering, especially for metals and composite materials:

1. HighQ: Micro CT devices with micro focus tubes with optional optical magnification (focal spot diameter below 50  $\mu\text{m}$ ), effective resolution below 100  $\mu\text{m}$ ;
2. MidQ: Industrial systems (standard focal spot diameter above 100  $\mu\text{m}$ , typically 0.8 mm), effective resolution above 100  $\mu\text{m}$ ;
3. LowQ: Low-cost system (standard focal spot diameter above 100  $\mu\text{m}$ , typically 0.8 mm), effective resolution above 30  $\mu\text{m}$ .

The classification quality relies on resolution, contrast, and noise. In the following section, we only distinguish between a low-cost and self-constructed LowQ and an industrial MidQ instrument as a reference with standard focal spot diameters of about 0.8 mm. The low-cost X-ray measuring instrument (<EUR 1000) should be an alternative for laboratory and industrial devices that are much more expensive (>EUR 100,000). The technical and construction details are important for comparing the device classes.

In addition to the description and evaluation of the LowQ X-ray measuring system used for NDT applications (Section 2), we investigate X-ray image simulation, discussed in Section 3, finally used for the training of ML defect detection models (Section 4). The overall framework addressed in this work is shown in Figure 1.

## 2. X-ray Radiography and CT Systems

Two experimental setups, delivering input data for the training and testing of the automated damage feature marking model, are described in this work:

1. MidQ: A laboratory radiography and CT system (Fraunhofer IFAM, Yxlon Y.MU2000-D, Hamamatsu detector), electron beam focus spot diameter—0.75 mm (Wolfram anode material), anode voltage—50–120 kV, tube current up to 10 mA, direct imaging solid-state detector 1000  $\times$  1000 pixels, detector pixel size—200  $\mu\text{m}$ .
2. LowQ: A self-constructed, mobile, low-cost radiography and CT system, electron beam focus spot diameter 0.8 mm (Wolfram anode material), anode voltage 30–70 kV, tube current up to 1 mA, indirect imaged monochrome and back-illuminated CMOS camera sensor (1920  $\times$  1080 pixels), detector pixel size—3  $\mu\text{m}$ , image-scaled virtual detector pixel size—40  $\mu\text{m}$ , X-ray scintillator screen (Ortho Fine 100 foil).

### 2.1. Low-Cost X-ray Device

The first device is only a reference system used to derive material and structure models and to compare with the low-cost system introduced in this work. The architecture and the main components of the proposed low-cost LowQ X-ray measuring device are shown in Figure 2. A low-cost commercial wolfram X-ray tube with a focal spot diameter of 0.8 mm and a typical anode voltage range of 30–80 kV is used. The imaging system consists of a widely used X-ray intensifier screen (Ortho Fine 100) and a commercial CMOS camera with double-lens optics. The entire X-ray measuring device is controlled by an embedded computer (Raspberry Pi 4). The camera and the device controls can be accessed remotely via a Web browser.

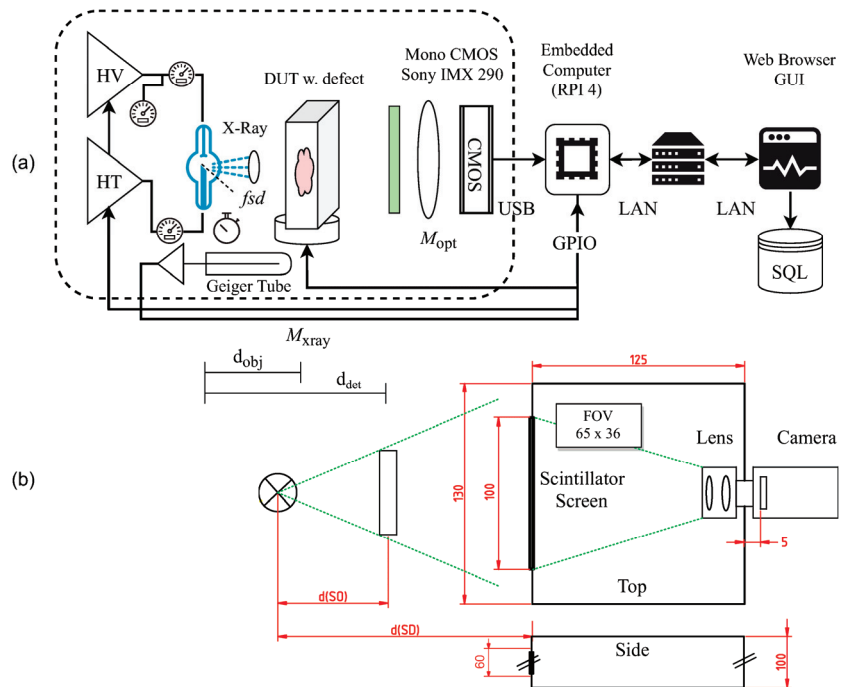


**Figure 2.** Low-cost X-ray radiography and CT instrument: (a) General overview; (b) details of the detector (all dimensions in mm).

The X-ray tube is a KL 27-0.8-70 based on a classical Coolidge principle (hot emission tube). The focal spot diameter is about 0.8 mm, with an opening angle of  $19^\circ$  (i.e., 70 mm spot diameter at 200 mm distance). The X-ray beam current can be controlled by the heater independently from the X-ray anode voltage (maximal tube current is 10 mA). Nearly most of the electrical input power is converted into heat in the tube anode. Even low tube currents of about 1 mA produce a heat power of more than 50 W, raising the temperature of the anode far beyond  $100^\circ\text{C}$  (measured using a thermal camera). The heat must be propagated outside the tube; here, it is propagated by an attached massive Cooper cylinder (see the right side of the tube in Figure 3 for a detailed view of the X-ray source) and a ventilator. With this cooling, the anode temperature can be kept below  $40^\circ\text{C}$  for operating times below one minute.

The camera consists of a commercial monochrome CMOS back-illuminated image sensor (Sony IMX 290, Omegon Kamera Guide 2000 M Mono), providing  $1920 \times 1080$  pixels with  $3\ \mu\text{m} \times 3\ \mu\text{m}$  pixel size. The CMOS sensor supports high exposure times (5 s and longer) by posing low-noise output. The optical imaging system consists of a zoomable double-lens system that maps the backside of the scintillator screen on the image sensor. With the given distance of 125 mm (see Figure 2b) between screen and image sensor, the effective Field of View (FOV) is about  $65 \times 36$  mm (effective image size is  $30\ \mu\text{m}$ ).

The X-ray source unit, the X-ray detector unit, and the optional rotation stage are controlled by an embedded computer (Raspberry Pi 4), which is connected to a LAN. The instrument can be accessed via a Web browser. There is one main application program running on the embedded computer. The program controls the camera (using a vendor SDK, Touptek photonics, <http://www.touptek.com/>) and captures images via USB, the X-ray unit, and a rotation stage stepper motor via a GPIO port. A Geiger counter is used to monitor the X-ray intensity. The remote access is provided via a HTTP service, providing the HTML control page, too (embedded in the software).



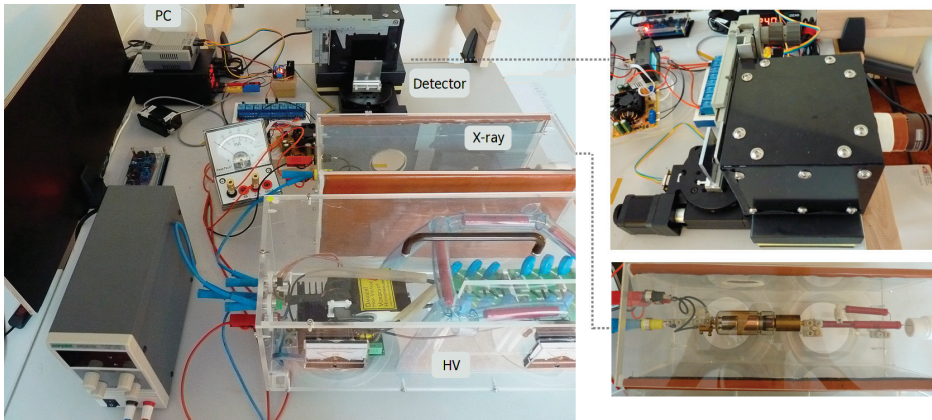


**Figure 3.** Prototype of the low-cost X-ray radiography and CT instrument.

### 2.2. Electronics

An electronic schematic of the X-ray source is shown in Figure 4. The circuit consists of a high-voltage generator, an electron heater constant current supply, and relay switches connected to the embedded computer. The high-voltage generator uses a classical discrete zero voltage switching (ZVS) driver circuit to drive a high-voltage transformer. The input voltage of the ZVS determines the output voltage of transformer T1 (about 40 kHz; input range: 5–12 V; output voltage: 5–12 kV). The output voltage of the high-voltage transformer is multiplied by a six-stage Villard cascade. The HV supply delivers up to 70 kV and 1 mA current (70 W). Neither the voltage nor the tube current is regulated by a feed-back loop, in contrast to industrial devices.

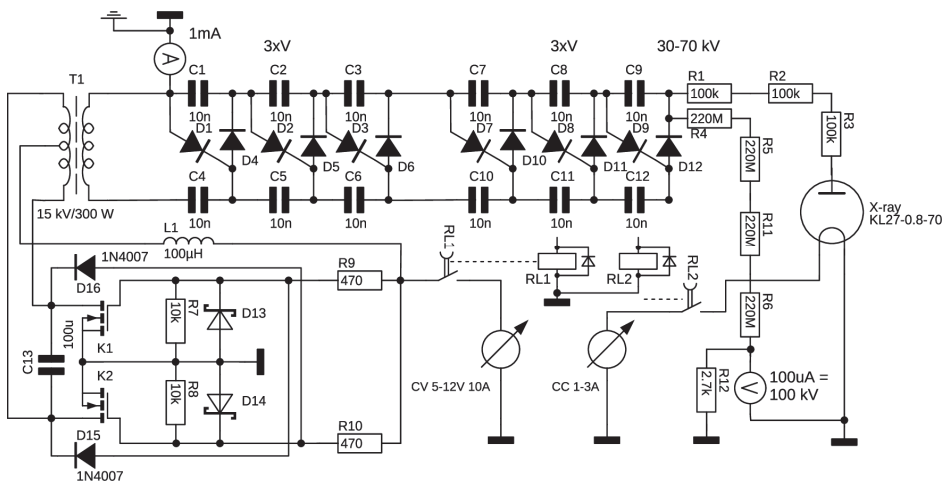


**Figure 4.** Electronic schematic of the low-cost X-ray source (CV: Constant voltage, CC: Constant current source).

### 2.3. Detector

The resolution of an X-ray imaging system is mainly limited by two parameters:

1. Detector pixel size  $d_p$  multiplied by the optical image magnification, i.e.,  $d_p M_{opt}$ ;
2. The X-ray magnification  $M_{xray}$ .

The X-ray magnification is given by the following:

$$M_{xray} = \frac{d_{det,src}}{d_{obj,src}} \tag{1}$$

$$a = (M_{xray} - 1) f_b$$

with  $f_b$  as the focal spot diameter (FSD), resulting in an imaging focus limit of about  $a$  (aperture limit) [6].

The exposure time  $t_x$  defines the noise level and the source-to-noise ratio achievable with the given X-ray power  $P_x$ . The industrial reference Mid-Q system has a pixel area size of about  $40 \mu\text{m}^2$ , whereas the LowQ detector has a pixel area of only  $9 \mu\text{m}^2$ ! The direct imaging MidQ system tightly couples the scintillator to the detector pixels via a FOP, whereas the indirect imaging system poses optical losses in lenses and coupling components. The MidQ system typically requires exposure times in the order of 100 ms (with  $P_x = 200 \text{ W}$ ), whereas the LowQ device requires at least 5000 ms (with  $P_x = 50 \text{ W}$ ).

The camera deployed in the LoWQ device is a USB 2.0 Omegon Guide 2000 M Mono with a back-illuminated monochrome Sony IMX290 sensor. The optical imaging system consists of a CS-Mount double-lens system with 2.8–12 mm focal length and  $f/1.4$  aperture. The IMX290 image sensor uses an integrated 12 Bits ADC (directly accessible by a camera raw format) for image digitalization, while an external 16 Bits ADC is used in the industrial MidQ detector.

The scintillator used in the detector has a normalized conversion factor of 100, providing sufficient amplification and high resolution. The scintillator consists of phosphor materials based upon a mix of rare earths with a high luminous intensity and low graininess. The screen emission matches ideally with the spectral sensitivity of the image sensor, as shown in Figure 5 (relative sensitivity of 0.95 at main emission peak). A limiting resolution up to 10 Line Pairs (LP)/mm with 10% contrast can be achieved. The contrast of the entire low-cost X-ray detector is about 70% at 2 LP/mm and about 25% at 8 LP/mm.

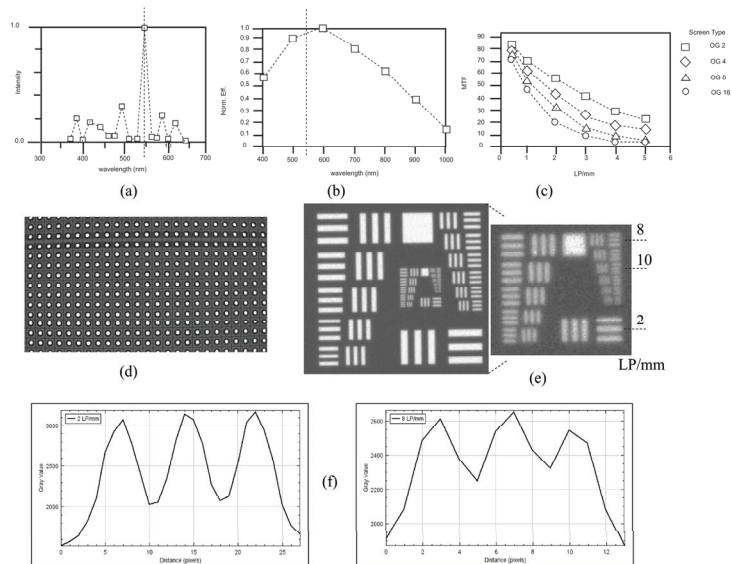


**Figure 5.** (a) Emission spectrum of the scintillator material [7]. (b) Spectral sensitivity of the Sony IMX290 image sensor [8]. (c) Resolution of the scintillator screen independent of the material thickness and amplification factor [7] (OG-2: conversion factor 100, OG-4: 200, and so on). (d) Dot pattern measured using the LowQ X-ray detector. (e) USAF 1951 pattern recorded with 55 kV/0.7 mA/average of four images. (f) Intensity profiles and contrast at 2 and 8 LP/mm from (e).

#### 2.4. Noise

The CMOS image sensor is sensitive to X-ray radiation, not too much to warrant the use of the image sensor directly, but with respect to popcorn and shot noise. Popcorn noise is a random seed phenomena; i.e., in some pixels, there is an electron wall breakthrough, leading to saturated (white) pixels. Fortunately, after the pixels are cleared (before the sampling of the next image), the saturation is eliminated, and two succeeding images will commonly not pose the same flooded pixels.

Commonly, the image device is not directly exposed to the X-ray beam. Instead, a mirror under an angle of  $45^\circ$  is used, and the camera is placed with a  $90^\circ$  angle with respect to the X-ray beam axis (see [5]). We tried the same approach, but we observed the following:

1. An expected reduction in light intensity (mirror reflectivity  $< 1$ ) and more geometric distortions.
2. There is still shot noise (albeit strongly reduced but not totally vanished).

The second observation is a result of the mirror construction. The mirror was a conventional industrial aluminum mirror mounted on an aluminum carrier under the same angle as the mirror. This combination still scatters some X-rays.

Therefore, we placed the camera in the X-ray beam again and used a simple multi-image noise compensation method. This removes shot noise and reduces non-gaussian X-ray and gaussian (electronics) noise, as shown in Alg. 1. Examples and results are shown in Figure 6. Choosing the  $\gamma$  threshold is crucial because not all shot noise pixels reach the maximum camera intensity, and some will only be reduced by averaging if they are below the chosen threshold, as shown in Algorithm 1.

---

**Algorithm 1:** Shot (popcorn) noise removal and image averaging.  $\gamma$  is a noise threshold with respect to the image pixel value range (commonly  $0.9max$ ), and  $\Sigma$  is a set of images. The result of the averaged and noise-corrected image is  $\sigma_0$ .

---

```

 $\sigma_0 := \Sigma[1]$ 
 $\forall (x,y) \in \text{coord}(\sigma_0)$  do
  if  $\sigma_0[x,y] > \gamma$  then
     $\forall \sigma \in \{\Sigma/\sigma_0\}$  do
      if  $\sigma[x,y] < \gamma$  then
         $\sigma_0[x,y] := \sigma[x,y]$ 
        break
      endif
    done
  endif
 $\forall \sigma \in \{\Sigma/\sigma_0\}$  do
  if  $\sigma[x,y] < \gamma$  then
     $\sigma_0[x,y] := \sigma_0[x,y] + \sigma[x,y]$ 
  else
     $\sigma_0[x,y] := \sigma_0[x,y] + \sigma_0[x,y]$ 
  endif
 $\sigma_0[x,y] := \sigma_0[x,y] / |\Sigma|$ 
done

```

---

In addition to the shot noise, there is gaussian electronics and detector noise (not correlated among pixels) and non-gaussian X-ray radiation and source noise, which can pose spatial correlation. In Section 5 and Figure 10, the gaussian noise of the images sampled by the LowQ and MidQ instruments are compared. The industrial MidQ device (including the X-ray source) has an average noise level of  $\text{SNR} = \text{avg}(x) / \sigma = 280$  (the  $2\sigma$  noise interval is about 0.7%), whereas the LowQ device has an  $\text{SNR} = 95$  (the  $2\sigma$  noise interval is about 2%).

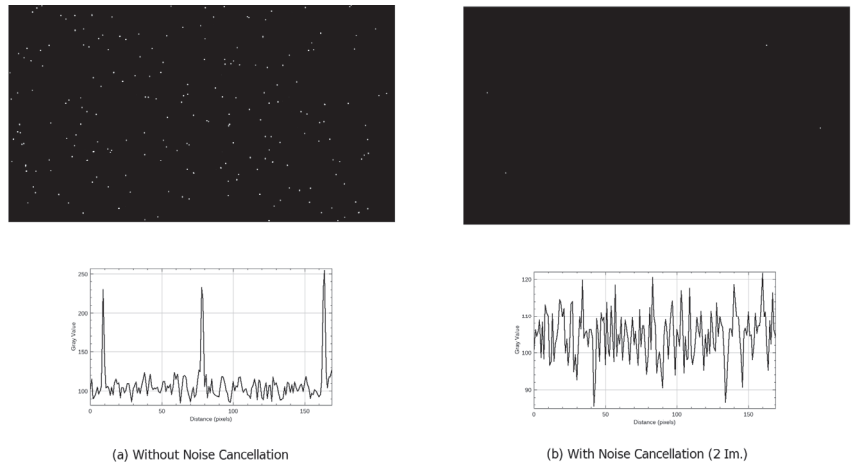


**Figure 6.** Without (a) and with (b) noise cancellation: (top) example image with threshold binarisation; (bottom) example line intensity plots with flooded pixels.

### 3. Simulation

As is common in engineering applications, the data variance of the experiments and specimens is limited. On one hand, specimens with impact damage pose a wide range of different micro and macro damages (e.g., delaminations, cracks, kissing bond defects, and many more). Therefore, the measurement (X-ray image) of one specimen delivers only a few features, and the number of specimens is limited, too. High-pressure die-casted aluminum specimens, on the other hand, contain a high number of gas pores (herein named defects), and the number of specimens can be high. Even if the feature and data variance is sufficient, there is no ground truth in the data, which is specifically required for the accurate labeling of training data for supervised Machine Learning (ML). For this reason, in this work, X-ray images are computed (simulated) numerically from synthetic specimens based on a CAD model and Monte Carlo simulation techniques, as shown in Figure 7. The model is composed of Constructive Solid Geometry operations creating solid materials or defects (pores) by union or difference operations. The OpenSCAD software [9] was used to convert the CSG model into a triangular mesh grid model (STL). This mesh model was finally processed by our own X-ray simulation software [10] based on the `gvxr/gVirtualXray` C++ software library [3] for the computation of X-ray images.

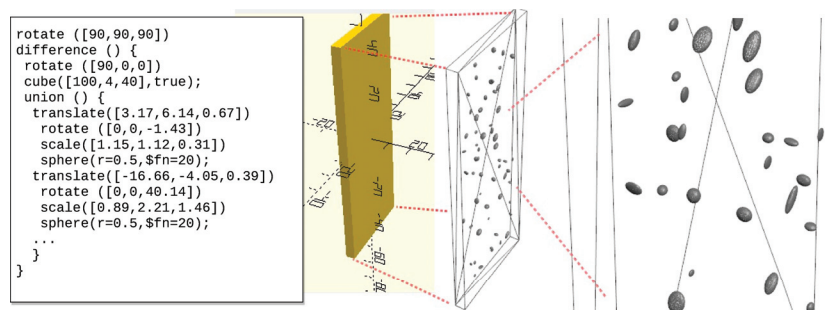


**Figure 7.** The modeling of a die-casted aluminum plate with gas pores using Monte Carlo simulation. Geometric parameters of real measure pores are used to create synthetic pores at random positions. (left) Programmatic CSG model; (right) rendered 3D model with synthetic pores (holes).

The Monte Carlo simulation of the synthetic pores was based on a simple geometric ellipsoid model with a base parameter set derived from real pore analysis using CT reconstruction and projections measured using the MidQ device.

#### 4. Feature Detection Using a Semantic Pixel Classifier

The main objective of this work is to use an automated feature detector and apply it to single projection X-ray images delivered by a Low-Q (low-cost) X-ray instrument to detect hidden defects in materials (which, in the context of this study, are pores in high-pressure die-casted aluminum plates).

The input is an X-ray image; the output is a feature map image that marks pores and provides the geometric parameters and position, as shown in Figure 8. A pixel classifier is commonly implemented with a Convolutional Neural Network (CNN), mostly with only one or two convolution-pooling layer pairs. The input of the CNN is a sub-window masked out from the input image at a specific center position  $(x,y)$ . The output is a class (or a real value in the range  $[0, 1]$  as an indicator level for a class). The neighboring pixels determine the classification result. The window with the CNN application is moved over the entire input image, producing the respective feature output images.

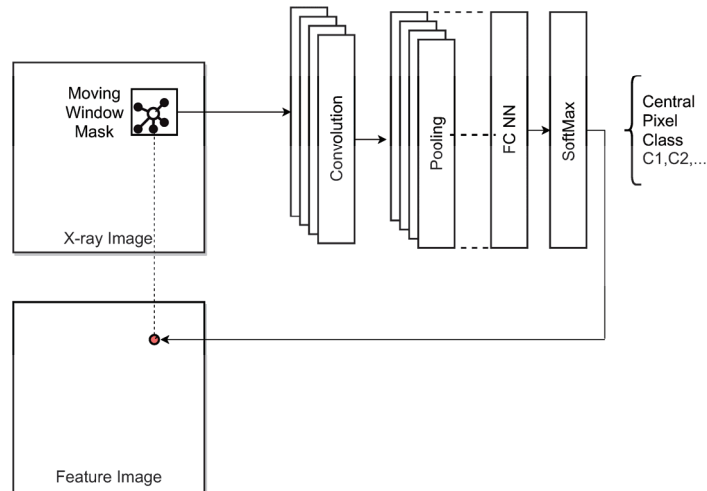


**Figure 8.** Semantic pixel classifier applied to X-ray single projection images to detect and mark hidden defects.

The pixel classifier is trained, while supervised, using labeled regions of pores (i.e., pixels inside a closed polygon path surrounding a pore in the image), as discussed in the following Section 5.

#### 5. Experiments

Experiments were carried out with aluminum die-casted plates ( $150 \text{ mm} \times 40 \text{ mm} \times 3 \text{ mm}$ ) containing process pores. The objective was to find a simple pore feature-marking pixel detector that maps an X-ray single projection image on a feature image, marking all pores. The aluminum die-casted plates, as well as the MidQ reference measurements, were contributed by Dirk Lehmus, Fraunhofer IFAM, Bremen, Germany.

In addition to the feature detection experiments, the low-cost and low-quality X-ray measuring device was compared with the aforementioned commercial device in terms of noise, spatial resolution, contrast, and geometric distortions.

Samples of the original X-ray images are shown in Figure 9. The contrast of the pore peak is  $C(\text{HighQ}) = 1.42$  and  $C(\text{LowQ}) = 1.86$ . The FWHM of the pore peak is

$FWHM(\text{HighQ}) = 7 \text{ px} \approx 0.7 \text{ mm}$  and  $FWHM(\text{LowQ}) = 25 \text{ px} \approx 0.75 \text{ mm}$ , as shown in Figure 10.

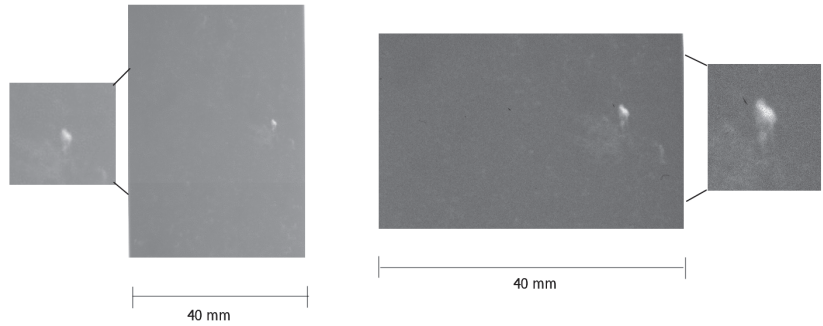


**Figure 9.** X-ray image sections from HighQ (left) and LowQ (right) devices, respectively, of a selected hidden pore in an aluminum high-pressure die-casted plate (pixel scaling: left—100  $\mu\text{m}/\text{pixel}$ ; right—30  $\mu\text{m}/\text{pixel}$ ).

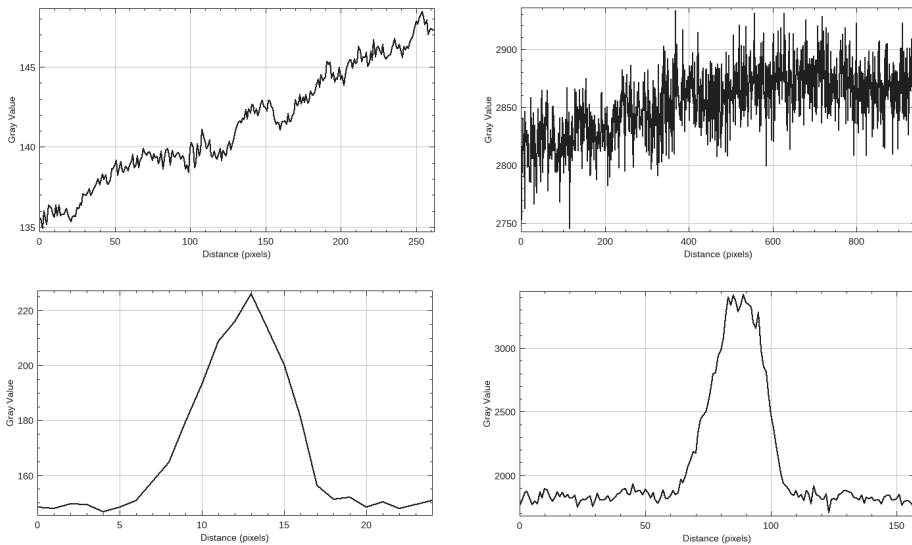


**Figure 10.** Comparison of MidQ (left) and LowQ (right) measurement results from an aluminum die-casted plate with pores. (top) Averaged slice intensity of mostly homogeneous area. (bottom) Averaged slice intensity (vertically averaged over 20/3 pixels) of a strong pore.  $M_{\text{xray}} = 2.0$  (HighQ)/1.0 (LowQ),  $s_{\text{px,eff}} = 100 \mu\text{m}$  (HighQ)/30  $\mu\text{m}$  (LowQ), exposure time  $t = 100 \text{ ms}$  (MidQ)/2  $\times$  5 s (LowQ).

The main objective of this work was to apply a semantic pixel classifier for the feature marking of pores in aluminum die-casted plates using single projection X-ray images sampled using the LowQ device introduced in this paper. Since there is no ground truth in the measured images (i.e., accurate labeling for training is not possible), synthetic images retrieved from the numerical X-ray simulation were used to train the pixel classifier, which was finally applied to X-ray images thereafter.

Figure 11 shows some selected results. There are always image pairs consisting of the X-ray input image (left) and the pore feature-marking image (right), as predicted by the semantic pixel classifier. One of the synthetic images is shown in Figure 11a, as is the prediction of the trained model. Additionally, the feature image shows the ROI

selection and labeling of the input images used for training (red: pore area; blue: selected background regions). The ROIs were automatically created from the CAD model used for simulation. The predictor model was trained with 40 epochs. The CNN architecture consists of two convolution-pooling layer pairs with 8 filters each. The training set consisted of an imbalanced set, with background examples being preferred to suppress false positive predictions rather than false negative. Since there is no ground truth for the measured images, we can only evaluate the results for the synthetic images. The overall accuracy achieved on the test set was 93%, with a class-specific error of 4% background and 11% pore region marking. The F1 score was 0.93. These results sound promising, and examples of the feature marking of the measured images are shown in Figure 11c,d for the low-noise Mid-Q and noisy Low-Q instruments, respectively. It can be seen that there is significantly increased pore feature marking in the LowQ images compared with the MidQ images. To estimate the impact of noise (from detector and radiation source), we tested a pore-free rolled and polished aluminum plate, as shown in Figure 11b, applying the same predictor model and expecting a black image; however, the image did not turn out to be black. This clearly shows the noise sensitivity of the predictor model, which must be suppressed. One approach for discriminating noise from pores in the feature marking of images is to calculate the union of two independent images from the same specimen, as it is expected (and can be shown) that noisy marking are randomly positioned. The geometric distortions of the Low-Q system seem to be irrelevant to the feature marking process.

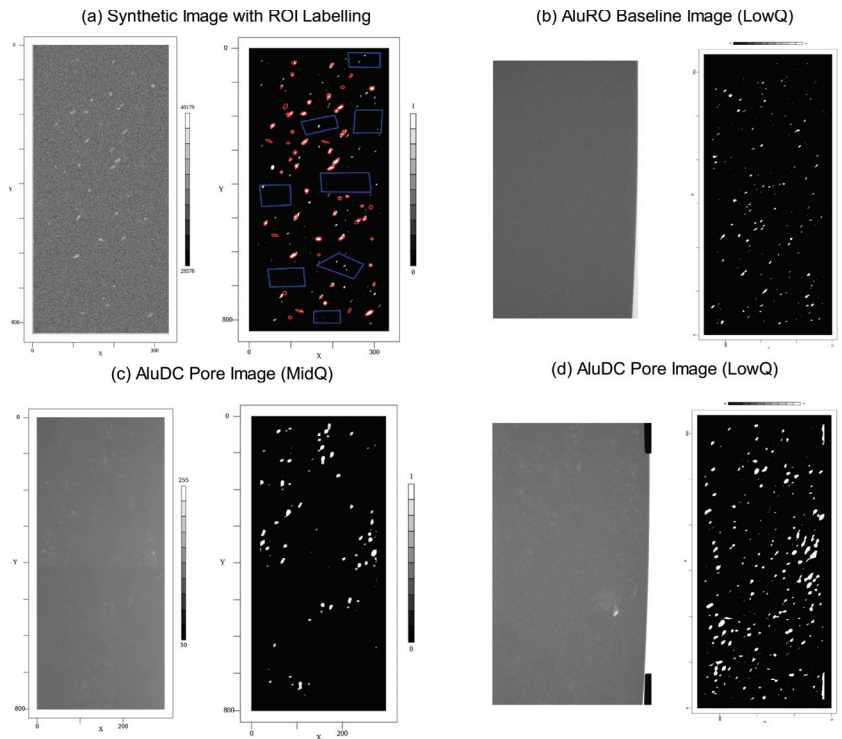


**Figure 11.** Results of the feature marking of different X-ray images using a selected sample plate and two measuring instruments and synthetic images. Note that the LowQ images have a different scaling system and regions compared to the Mid-Q and synthetic X-ray images. aluDC: die-casted aluminum plate with pores; aluRO: rolled and polished aluminum plate without pores.

## 6. Conclusions

One of the main findings of this work is that a low-cost constraint does not necessarily result in low-quality output (this applies to the LowQ device described in this work). With respect to resolution and contrast, the LowQ device outperforms an industrial MidQ device, but when using the LowQ device, the noise is significantly higher due to the lower overall sensitivity and long exposure times not allowing for the extra exposure required to significantly reduce image noise. Additionally, random popcorn/shot noise in the LowQ indirect imaging system requires at least two independent images to substantially remove this noise.

The higher noise of the LowQ instrument compared with the industrial MidQ device has a significant impact on the accuracy and quality of the data-driven, feature-marking model. The geometric distortions of the LowQ system seem to be irrelevant to the feature marking process. It was possible to train the feature-marking detector with pure synthetic X-ray images computed by a numerical simulator using a CAD model of the specimen with randomly created defects.

Future work must involve improving the training data set by overlaying measured noise (especially from the LowQ device) to the simulated X-ray images.

**Funding:** This research was funded by the the German Research Foundation (Deutsche Forschungsgemeinschaft (DFG) Project number: 418311604).

**Institutional Review Board Statement:** Not applicable.

**Informed Consent Statement:** Not applicable.

**Data Availability Statement:** Data is available from the authors on request.

**Acknowledgments:** The aluminum die-casted plates, as well as the MidQ reference measurements, were contributed by Dirk Lehmus, Fraunhofer IFAM, Bremen, Germany.

**Conflicts of Interest:** The authors declare no conflict of interest.

## References

- Hena, B.; Wei, Z.; Castanedo, C.I.; Maldague, X. Deep Learning Neural Network Performance on NDT Digital X-ray Radiography Images: Analyzing the Impact of Image Quality Parameters—An Experimental Study. *Sensors* **2023**, *23*, 4324. [CrossRef] [PubMed]
- Booto Tokime, R.; Maldague, X. *Automatic Defect Detection for X-ray Inspection: Identifying Defects with Deep Convolutional Network*; Canadian Institute for Non-Destructive Evaluation (CINDE): Edmonton, AB, Canada, 2019.
- gVirtualXray. Available online: <https://gvirtualxray.fpvidal.net> (accessed on 24 January 2023).
- Vidal, F.P. Introduction to X-ray simulation on GPU using gVirtualXRay. In Proceedings of the Workshop on Image-Based Simulation for Industry 2021 (IBSim-4i 2020), London, UK, 18–21 October 2021.
- Balasubramanian, S.L.; Krishnamurthi, G. X-ray scintillator lens-coupled with CMOS camera for pre-clinical cardiac vascular imaging—A feasibility study. *PLoS ONE* **2022**, *17*, e0262913. [CrossRef] [PubMed]
- Carl Zeiss. *Resolution of a 3D X-ray Microscope—Defining Meaningful Resolution Parameters for XRM*; Technical note; Carl Zeiss Microscopy GmbH: Oberkochen, Germany, 2013.
- CAWO. Green-Emitting Screens. Available online: <https://www.cawo.com/products/intensifying-screens/green-emitting> (accessed on 13 September 2023).
- FRAMOS. FSM-IMX290 Datasheet. Available online: <https://www.amos.com> (accessed on 13 September 2023).
- OpenSCAD, version 2022.11.06.nightly (git 63b97a0). Available online: <https://openscad.org/> (accessed on 1 November 2023).
- Bosse, S. XraySim. Available online: <https://github.com/bsLab/XraySim> (accessed on 1 November 2023).

**Disclaimer/Publisher's Note:** The statements, opinions and data contained in all publications are solely those of the individual author(s) and contributor(s) and not of MDPI and/or the editor(s). MDPI and/or the editor(s) disclaim responsibility for any injury to people or property resulting from any ideas, methods, instructions or products referred to in the content.



# A Pore Classification System for the Detection of Additive Manufacturing Defects Combining Machine Learning and Numerical Image Analysis <sup>†</sup>

Sahar Mahdie Klim Al-Zaidawi <sup>1,2,\*</sup> and Stefan Bosse <sup>2</sup><sup>1</sup> Leibniz-Institute for Materials Engineering-IWT, Badgasteiner Str. 3, 28359 Bremen, Germany<sup>2</sup> Department of Mathematics and Computer Science, University of Bremen, Bibliothekstr. 5, 28359 Bremen, Germany; sbosse@uni-bremen.de

\* Correspondence: saharimah@uni-bremen.de or saharimahdie@yahoo.com

<sup>†</sup> Presented at the 10th International Electronic Conference on Sensors and Applications (ECSA-10), 15–30 November 2023; Available online: <https://ecsa-10.sciforum.net/>.

**Abstract:** This study aims to enhance additive manufacturing (AM) quality control. AM builds 3D objects layer by layer, potentially causing defects. High-resolution micrograph data capture internal material defects, e.g., pores, which are vital for evaluating material properties, but image acquisition and analysis are time-consuming. This study introduces a hybrid machine learning (ML) approach that combines model-based image processing and data-driven supervised ML to detect and classify different pore types in AM micrograph data. Pixel-based features are extracted using, e.g., Sobel and Gaussian filters on the input micrograph image. Standard image processing algorithms detect pore defects, generating labels based on different features, e.g., area, convexity, aspect ratio, and circularity, and providing an automated feature labeling for training. This approach achieves sufficient accuracy by training a Random Forest as a hybrid-model data-driven classifier, compared with a pure data-driven model such as a CNN.

**Keywords:** additive manufacturing; pore classification; machine learning; numerical image analysis

**Citation:** Al-Zaidawi, S.M.K.; Bosse, S. A Pore Classification System for the Detection of Additive Manufacturing Defects Combining Machine Learning and Numerical Image Analysis. *Eng. Proc.* **2023**, *58*, 122. <https://doi.org/10.3390/ecsa-10-16024>

Academic Editor: Stefano Mariani

Published: 15 November 2023



**Copyright:** © 2023 by the authors. Licensee MDPI, Basel, Switzerland. This article is an open access article distributed under the terms and conditions of the Creative Commons Attribution (CC BY) license (<https://creativecommons.org/licenses/by/4.0/>).

## 1. Introduction

### 1.1. General Motivation

Medical implants have transformed healthcare, yet their production presents significant challenges. Additively manufactured Ti6Al4V implants can develop porosity, influencing their mechanical properties, particularly under dynamic loads. Understanding the relationship between manufacturing parameters and implant quality, especially post-HIP treatment, is crucial. Laser powder bed fusion (LPBF) is an additive manufacturing technique that constructs intricate components with complex shapes layer-by-layer [1]. This technique involves the application of a fine powder layer using a thin blade, followed by localized melting using a laser. These steps are iteratively performed until the components reach their desired final height [2]. A component's mechanical characteristics, similar to powder metallurgy, depend on factors like relative density and defect shapes [3], which are influenced by several variables such as laser power, scanning speed, and particle properties [4]. These factors can lead to defects like cracks and porosity, which are linked to the applied energy density [5]. This research aims to study critical defects in additively manufactured medical implants, offering supervised machine learning methods for feature extraction of metallurgical micrographs to detect and classify different defects. To detect defects, different model- and data-driven approaches are investigated. The major advantage of a model-driven over a pure data-driven approach is the ability to be explained and tractability of the model, i.e., a correlation between classification output and geometric features that are amplified by the selected filter operators.

### 1.2. Related Work

In our investigation of common pore types in additive manufacturing, we have identified several distinct categories. Keyhole pores [6,7], characterized by vapor bubbles trapped in the melt pool during printing and the potential for merge process pores, exhibit dimensions ranging from microscopic to millimeters, featuring keyhole-like voids and channeling. These defects result in reduced mechanical strength, diminished fatigue resistance, and heightened susceptibility to crack initiation. Gas pores [8], closely related to keyhole pores but with slight shape differences (a gas pore is a circular keyhole), share the same vapor bubble characteristics and similar size dimensions. They display an irregular distribution and spherical shapes, contributing to decreased fatigue life, lowered mechanical strength, and compromised surface finish. Lake of Fusion (LOF) pores [8,9], attributed to insufficiently melted material, can vary in size up to millimeters, presenting interlayer gaps and unfused regions that serve as starting points for cracks under stress. Unmelted Particle Pores [8,10,11], a subset of LOF pores, are characterized by the inclusion of unmelted powder within the pore, sharing similar dimensions and geometric features and similarly contributing to crack initiation and growth. Process pores [9], identified by a low packing density of powder, hollow particles, and entrapped inert gas, are typically microscopic to less than 100  $\mu\text{m}$  in size, with an irregular distribution and spherical shapes of a minimal area, exerting a relatively minor impact on material properties. Finally, cracks [3], ranging from microscopic to millimeter dimensions and featuring a large aspect ratio, pose the most significant risk for initiating mechanical failures within the additive manufacturing process, often arising from the presence of other pore types or inherent defects. A detailed summary of these pore types is available in Table A1 in Appendix A for reference.

Most of the work in the classification of defects in additive manufacturing using supervised machine learning focuses on categorizing defects in images. For instance, Mika [9] utilized a Random Forest Tree model to examine the occurrence of pores in binary micrograph images, achieving a classification accuracy of around 95% for keyhole, lack of fusion, and process pores.

Another approach by Zhang et al. [12] involved the use of Support Vector Machines (SVMs) for defect detection in Ti-6Al-4 V additive manufacturing. It involved extracting geometric features from thermal images, resulting in an accuracy of 90.1% for distinguishing porous and non-porous defects. In contrast, Convolutional Neural Networks (CNNs) excelled in handling image-based defect detection problems. Scime et al. [13] applied multi-scale CNNs for in situ defect detection, achieving high accuracy in anomaly detection and differentiation (97%, 85%, and 93%, respectively).

While these models perform well with larger datasets, the challenge of limited data and their annotation (labeling without ground truth) has led to the adoption of semantic segmentation. Semantic segmentation assigns human-interpretable classes to each pixel in an image. Recent research addressed the binary pixel segmentation of additive manufacturing defects in X-ray Computed Tomography (XCT) 3D images. To address issues such as poor contrast, small defect sizes, and appearance variations, a 3D U-Net model was proposed. When applied to an AM dataset, this model achieved a mean Intersection over Union (IOU) value of 88.4% [14].

### 1.3. Contribution of Our Research

In this study, we employ semantic segmentation techniques with reduced training data due to the time-intensive nature of data generation. We introduce a model-driven data-driven approach utilizing a Random Forest (RF) classifier, a supervised machine learning method, for efficient pore classification, which is particularly effective with limited training data. Comparative analysis reveals that conventional purely data-driven models like Convolutional Neural Networks (CNNs) underperform in contrast to our model-driven data-driven model. Our model is primarily designed to predict four distinct pixel classes: background (class 0, trivial class), lack of fusion (LOF) (class 1), gas keyhole pores (class 2), and process pores (class 3).

The next sections proceed with an overview of the used materials and methods, subdivided into subsections describing the dataset, preprocessing, and machine learning classifiers, including Random Forest (RF) and Convolutional Neural Network (CNN). The performance metrics used are also explained. The “Experimental Design” section details the research methodology. “Results and Discussion” presents the experimental outcomes, comparing classifier performance and discussing findings. Finally, the “Conclusion and Future Work” section will summarize our preliminary results and key findings.

## 2. Materials and Methods

### 2.1. Dataset

To facilitate both unsupervised and supervised defect classification modeling, a dedicated data pipeline and database were established for our study. The dataset encompasses diverse manufacturing process parameters for Ti6Al4V, including laser power, layer thickness, hatch distance, and scan speed. The dataset comprises 400 distinct process parameter combinations, printed in Ti6Al4V on an SLM 125 HL (SLM Solutions GmbH, Lübeck, Germany). Specifically, the laser power, scan speed, hatch distance, and layer thickness were systematically varied. Laser power ranged randomly from 152 W to 350 W, scan speed varied randomly between 803 mm/s and 1599 mm/s, and hatch distance was randomly adjusted between 0.07 mm and 0.15 mm. Layer thicknesses were selected in increments of 0.025 mm, encompassing 0.05 mm, 0.075 mm, and 0.1 mm. In the manufacturing process, the parameter combinations were randomly positioned on the build platform. Three process parameter combinations were consistently produced in close proximity to each other, utilizing the skip layer function to enable the construction of all four layer thicknesses in a single process. To minimize heat transfer effects between combined parameter combinations, a small gap was maintained between the three sections, with minimal contact at the bottom. Following the printing process, specimens underwent embedding, grinding, and polishing, culminating in microscopic imaging.

We also created a new dataset of human annotated pores, so we cut the images of different pore types to obtain (see Figure 1) a bunch of images that show three types of pores with a total of 200 pores for each pore type. This dataset was used for statistical computations of the pore characteristics.

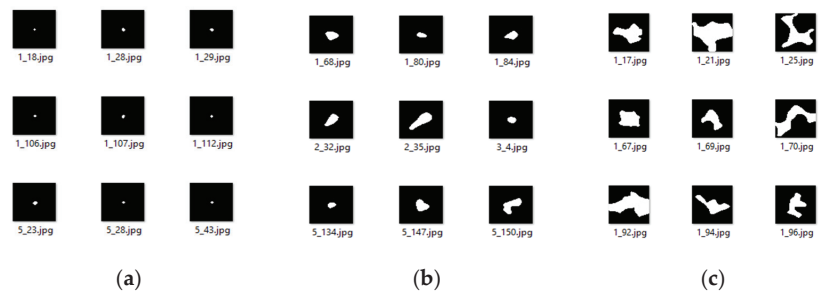


**Figure 1.** The extracted pore types as (a) process pores; (b) keyhole (gas) pores; (c) lack of fusion pores.

### 2.2. Preprocessing and Feature Extraction

The initial data preparation involved vertically slicing specimens to create micrograph image scanning (see Figure 2a,b). Within these micrograph images, discernible porosity defects resulting from the manufacturing process were observed. To analyze various pore types, we initially converted the color images to grayscale, unifying image intensity within a single channel and thus streamlining subsequent image processing and analysis. Subsequently, binary thresholding and post-cropping were applied using the OpenCV library [15] (see Figure 2c). Following this, we employed the same image processing approach to identify pore contours, utilizing an iterative bounding box method based on the algorithm detailed by Satoshi Suzuki and others in [16] (see Figure 2d). These identified

pore contours allowed for the extraction of local features, such as pore area, position, and angle, as well as shape descriptors like solidity, circularity, and convexity (see Figure 2e).

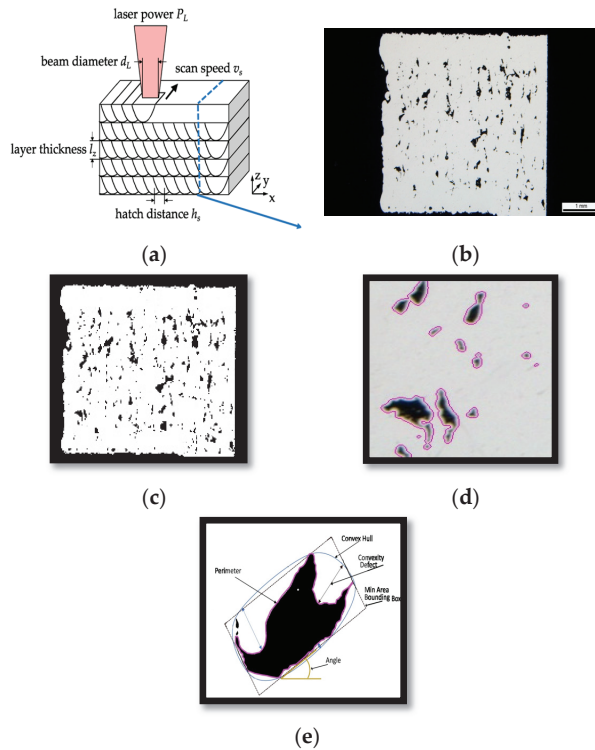


**Figure 2.** Illustration of the preprocessing and feature extraction pipeline (a) SLM; (b) micrograph slicing; (c) image binarization; (d) contour and ROI marking; (e) pore characterization and classification.

### 2.3. Machine Learning Classifiers

ML algorithms that are applied to images commonly perform two tasks: (1) region of interest prediction and geometric feature and contour approximation and (2) classification of ROI areas or the entire image. ML algorithms are typically purely data-driven, requiring a solid database, which in engineering is mostly based on measurements and experiments. In our work, we try to combine data-driven with model-based approaches and to use primarily models with low complexity.

#### 2.3.1. Random Forest Classifier (RF)

The Random Forest (RF) algorithm is a powerful and widely used classification supervised machine learning method [17,18]. RF builds multiple decision trees, combining them as weak classifiers using “bagging” [19]. The RF classifier creates several decision trees, which are combined to improve the outcomes. It uses majority-voting technique to decide the final outcome from the various decision trees. In a Random Forest model, each decision tree relies on values from a randomly selected vector with the same distribution [17]. This classifier has many parameters, e.g., maximum features, n-estimators, minimum samples split, minimum samples leaf, and maximum depth. Most of the parameters were the default algorithmic and model parameters using the scikit-learn software package [20]. Only one selectable parameter was optimized by grid search, which is the number of trees (we used n-estimators = 100). The RF is used in this work as mapping algorithm that maps geometric model-based precomputed latent features on classification features (pore classes). The input feature vectors of the RF model are aggregate variables derived from the micrograph

input image. The kernel-based aggregating filter operators can be freely chosen, e.g., mean, Gaussian blurring, or Sobel filters. A broad set of filters were applied, and the best were selected by feature ranking, mainly edge and shape boundary amplifying detectors.

### 2.3.2. Semantic Pixel Classifier

A pixel classifier is applied to sub-images (mask window) of an image to predict the class of the central pixel of the current mask window, as illustrated in Figure 3. A variant is a segment classifier. The input image is segmented, and the classifier is applied to each segment annotating the entire segment (not suitable for pore annotation). If the window mask is moved over all pixels of the input image, an annotated semantic class feature map output image can be created. The pixel classifier can be implemented by the aforementioned RF or CNN models, introduced in the next sub-section. Semantic pixel classifiers, e.g., based on CNN architectures, were already successfully deployed for image feature segmentation, e.g., for defect detection in X-ray images [21,22].

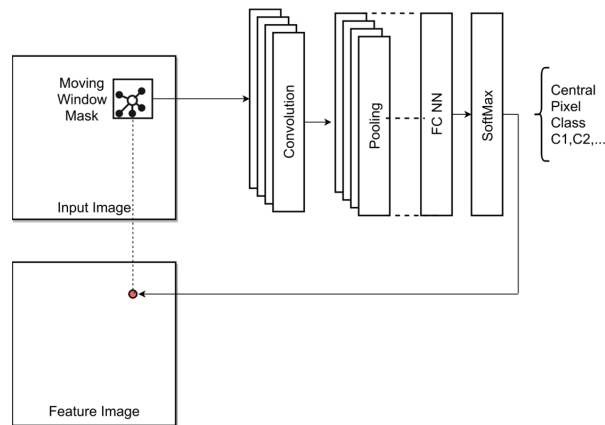


**Figure 3.** Pixel classifier principle using a CNN (alternatively replaced by the proposed RF approach).

### 2.3.3. Convolutional Neural Network (CNN) and U-Shaped Neural Network (U-Net)

Convolutional Neural Networks (CNNs) [23] are widely used models that are deployed in image recognition and feature extraction tasks. CNNs are used for tasks like image classification and object detection. They operate by making predictions at both the image and object levels, focusing on tasks such as assigning labels or bounding boxes to entire images or objects within them.

U-Net, a multi-level and complex CNN architecture with automated embedded or separated ROI proposal algorithms that is often used for automated image segmentation and ROI searches, particularly in medical analysis, features a U-shaped design, with encoding and decoding paths connected via a central bottleneck (based on auto encoder principles). It excels at capturing fine-grained spatial information in images and has proven effective in tasks such as medical image segmentation. Designed by Ronneberger and colleagues in 2015, U-Net specializes in image segmentation, classifying each pixel. It is tailored for scenarios with limited training data and avoids substantial resolution reduction. Importantly, U-Net and similar architectures tackle a significant computer vision challenge by delivering better performance with smaller training datasets. However, if the model complexity increases, the required training data instance volume and their variance must be increased significantly to achieve suitable generalized and robust predictive models. This extended and large database is not available in this work. This capability is especially valuable in scenarios where amassing extensive labeled data is impractical [24]

Hyper-parameters that are tunable in both CNNs and U-Net encompass learning rate, batch size, layer count, filter size, activation functions, pooling size, and loss function, influencing network performance and training progress.

#### 2.4. Performance Metrics

Metrics are used for the assessment of the machine learning model's performance throughout training and testing. The model assessment metrics considered in this work are as follows [25]:

Accuracy quantifies the model's performance by dividing correct predictions by total predictions, averaged either for all classes or for individual classes (1-error). The standard error of the mean (SEM) measures how the sample mean differs from the actual population mean.  $\sigma_{\mu} = \sigma/\sqrt{k}$ , where  $\sigma$  is the standard deviation of the results and  $k$  the number of runs. Precision (Positive Predictive Value) gauges the classifier's bias toward false positives. Recall (sensitivity) indicates the classifier's bias toward false negatives; low recall implies numerous false negatives. F1-Score (F-measure) is a harmonic mean of accuracy and recall, combining precision and recall. The segmentation performance is quantified using Mean Intersection over Union (Mean IoU), which measures the percentage overlap between predicted and true segmentation masks. Traditionally, an IoU value exceeding 0.5 is regarded as indicative of "good" segmentation [26].

### 3. Experimental Design

In this section, we elucidate our machine learning pipeline, illustrated in Figure 4, designed for pore detection and analysis, subsequently leading to the prediction of diverse pore types. The training process utilizes input image(s), from which we extract pixel-based features employing different filters: Canny, Roberts, Sobel, Scharr, Prewitt, Gaussian, Median, and Variance filters. Different kernel sizes employed for these operations were investigated:  $3 \times 3$ ,  $5 \times 5$ ,  $25 \times 25$ , and  $50 \times 50$  pixels. In our supervised machine learning (ML) approach, annotation is essential for distinguishing between various pore types. To accomplish this, we applied classical image processing algorithms, as detailed in Section 2.2 of our study. This tool facilitates the iterative detection of object (pore) contours and then derives different features such as aspect ratio, area, and convexity, as elaborated in Section 2.2. Drawing upon statistical analyses of pore characteristics conducted using the data presented in Figure 1, we formulated criteria for pore classification, an example of which is documented in Table A2 in Appendix B. These criteria are structured as an if-else logic system, enabling the classification of diverse pore types based on their statistical attributes. This classification scheme, as depicted in Appendix B Figure A1, encompasses process pores, gas or pore keyholes, LOFs, and another category. It is worth noting that our dataset lacks information on cracks. Consequently, our RF classifier is configured to predict four classes: 0 for background, 1 for LOF pores, 2 for keyhole pores, and 3 for process pores, aligning with the available data characteristics. Subsequently, following the conditions outlined in Figure A1 in Appendix B, we assign labels to the pores and employ this information to generate a pixel-based mask, effectively attributing each pixel to its corresponding pore. This mask is then input into the RF classifier. Finally, the classifier's performance is assessed with new testing images, yielding the predictive accuracy. In Appendix B, Figure A2 depicts examples of the input image, labeled image, and predicted image, respectively.

The CNN model used in this work employs two or three Conv2D-MaxPooling2D layer pairs for feature extraction and classification, typically with 4–8 filters in each layer using a filter mask size of  $5 \times 5$  pixels. ReLU (Rectified Linear Unit) activation functions are applied throughout the network to introduce amplification of positive features and damping of negative latent features and enhance feature separation capabilities. The objective of this architecture is to classify each pixel in the input images into one of four classes: background, LOF pores, keyhole pores, and process pores, creating a feature map image.

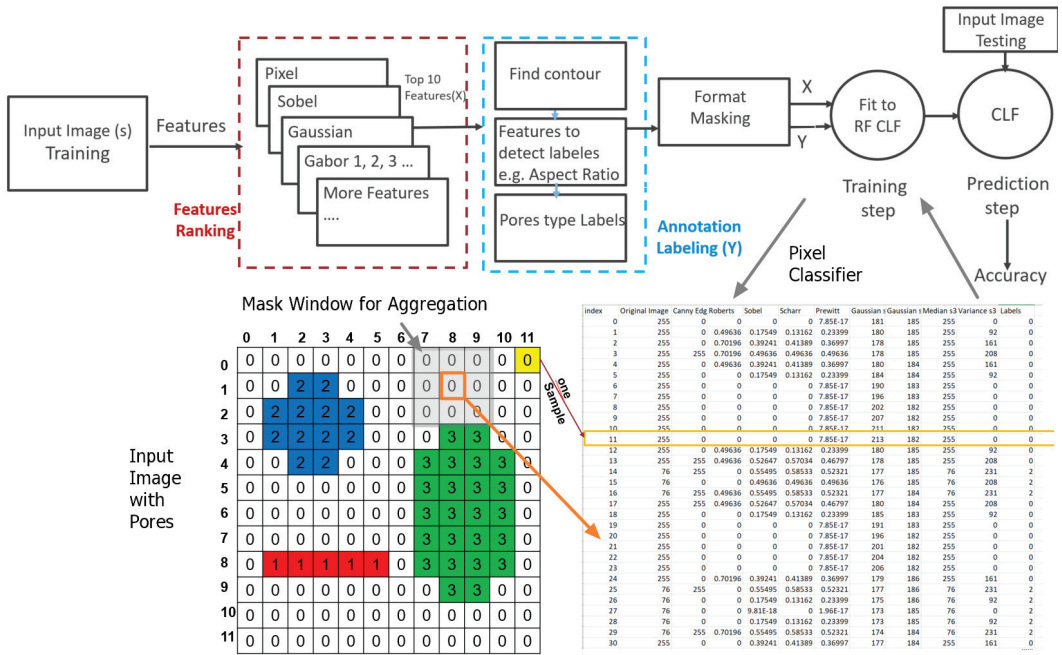


Figure 4. (Top) RF-based model pipeline. Input is a sub-window from the original input image at a specific index position x, y. (Bottom) Feature vector generation and local pixel aggregation.

We also utilized the U-Net architecture, which is designed for pixel-level segmentation tasks, as introduced by Ronneberger et al. in 2015 [25]. U-Net’s distinctive features include an encoder (down-sampling) and decoder (up-sampling) CNN framework (see an example of this model architecture in Appendix C Figure A3), skip connections linking encoder and decoder layers, transposed convolution for up-sampling, and crop-concatenate for contextual information integration, concluding with a 1 × 1 convolution layer. In comparison to standard CNNs with broader applications in computer vision, U-Net specializes in pixel-level image segmentation and ROI detection. Our custom U-Net design incorporates five Conv2D layers for down-sampling (64 × 64, 32 × 32, 16 × 16, 8 × 8, and 4 × 4) and four Conv2DTranspose layers for up-sampling (4 × 4 to 8 × 8, 16 × 16, 32 × 32, and 64 × 64), interconnected through skip connections, culminating in a Conv2DTranspose layer with a 3 × 3 kernel to achieve a 128 × 128 resolution. Loss and activation functions are customizable, with categorical cross-entropy and ReLU often chosen. Our model aims for precise pixel-wise classification.

#### 4. Results and Discussion

In our study, we trained a Random Forest (RF) model using up to 10 million classes of imbalanced training samples (i.e., pixel vectors, but background pixels are the majority), as detailed in Section 3, using a progressive approach where we employed an increasing number of ten images randomly selected from our dataset and tested with all these ten images. This approach was adopted due to the non-normal distribution of the accuracy results, leading us to calculate the standard error of the mean (SEM) as a more robust measure, representing one standard deviation. Training the model with eight images achieved a lower SEM of testing the model. The model’s overall average test accuracy across all classes, along with its SEM, was determined to be 77% ± 1% (refer to Figure 5a). Since the background class is trivial in this use case, the three-class average accuracy is about 76%. Notably, the model achieved a maximum test accuracy of 82% among the

ten tested images. When trained with eight images, the model demonstrated an overall average test precision of 67%, recall of 77%, F1 score of 69%, and an impressive Area Under the Curve (AUC) of 99.7%. The class-specific accuracy is not homogeneous. Only the LOF class, which was the majority class in the initial training sample distribution, can be clearly identified. We repeated the training with a balanced training set, but without significant improvement, concluding that the RF training is insensitive to imbalanced training examples.

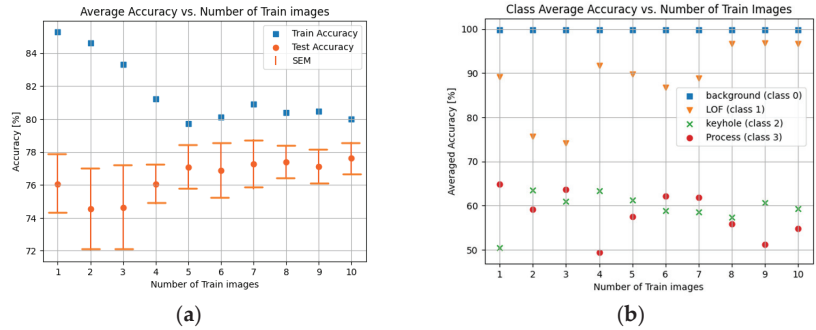


**Figure 5.** Figure 5. (a) Overall averaged accuracy of RF classifier vs. increasing number of training images, (b) each class-averaged accuracy of RF classifier vs. increasing number of training images.

A comprehensive breakdown of individual class training and test accuracies can be found in Figure 5b. Notably, the model excelled in predicting classes with larger pixel counts, such as the LOF pore type, as exemplified in Figure A2c, where a predicted image is showcased. The decrease in the overall model prediction accuracy of the training data and a parallel increase in the test data accuracy with the increasing number of training images, as shown in Figure 5a, is an indicator for the high variance (class distribution and geometric variations) of particular images.

We trained the CNN with a moving input window size of  $20 \times 20$  pixels (with about 10,000 training examples), as well as the RF with eight images, and tested the model with all ten images. The results, as summarized in Table 1, show that the CNN model that is described is not performing well, either. After 30 training epochs with a training rate of  $\alpha = 0.01$ , we obtain a total accuracy on the test set (70% of the entire image segment database consisting of 27,000 segments) of about 80%, but the keyhole and LOF classes pose an individual error of about 30–40% due to misclassification (mostly overlapping classification of these classes). Only the process pore class (with its small geometric size, see Appendix for details) can be detected with a low error (about 6%). The error is an individual pixel classification error without considering neighboring pixel results. After pixel feature classification, a pixel clustering (DBSCAN) can be applied. Spurious misclassification can be suppressed by clustering, resulting in a much lower pore-wise classification error.

**Table 1.** Summarized comparison of the accuracies for the three approaches considered in this work (FC: False classification).

Class \ Method	RF	CNN	U-NET
Process Pore Class	54% (40% Keyhole FC)	93%	50%
LOF Class	99%	60% (25% Keyhole FC)	5%
Keyhole Class	75% (20% Pro FC)	65% (25% LOF FC)	20%
Total	76%	73%	25% (failed)



The RF and CNN models rely on a divide-and-conquer principle posing a low model complexity. For comparison, we employed a complex U-Net model that is also described in Section 3. The training process was not suitable to create a usable model, as shown in Figure A4. The predicted images still look different to the labeled images, as can be seen in Figure A5 (a: input test image, b: labeled image, and c: the predicted labeled image). The model was trained with eight images, resulting in a training and testing dataset accuracy of 54% and 25%, respectively, i.e., the training failed completely, basically due to the limited training dataset size (here, only eight different instances).

As concluded in this section, the RF-based model performed slightly better than both the simple CNN and the U-Net models for our task of predicting different pore types. However, both RF and CNNs can only predict one of the three pore class with high accuracy, while two of three are not clearly distinguishable. The currently unusable U-NET needs to be tuned, and data augmentation is important in order to improve the results. We emphasize the importance of employing data augmentation techniques such as geometric transformations involving random cropping, shifting, and rotation. These strategies hold great promise for enhancing classifier performance and advancing pore classification.

The RF and CNN show different distributions of the per-class accuracy, so they could be combined to create a more robust class-specific classifier model. The misclassification noise, as illustrated in the images in Figure A2c–f, depends on the filter mask sizes. Too small masks reduce the spatial correlation and increase noise significantly, while too large masks increase averaging and extended area misclassification (e.g., by multiple pores inside the mask).

## 5. Conclusions and Future Work

Our research has introduced a hybrid classifier model using model-driven feature selection combined with an RF classifier, a supervised machine learning model that is designed to perform well even with limited training data. Compared with purely data-driven models like CNNs, our RF approach has demonstrated a competitive quality in pore classification, which can be trained with a highly class-imbalanced training set without compromising accuracy. Both RF and CNN approaches used local data models of a low complexity combined with a divide-and-conquer methodology. One major contribution is an automated feature annotation using classical image processing and iterative object search, finally providing shape boundary approximations and elliptical shape fitting. Based on a few characteristic features, the pores can be classified using a simple decision tree. The image processing approach always depends on a global context limiting parallelism, whereas the pixel classifier depends only on bound local data, enabling the usage of parallel Cellular Automata processing architectures. The U-NET approach uses a highly complex and deep functional graph model, which is not suitable for being trained with only a few images as was done in this work.

The major advantage of the model-driven over the purely data-driven approach is the ability to be explained and tractability of the model, i.e., a correlation between the classification output and geometric features that are amplified by the selected filter operators. Finally, the RF approach showed low sensitivity to highly imbalanced datasets with respect to the target class distributions.

Given the challenges in gathering micrograph data, we emphasize the importance of employing data augmentation techniques such as geometric transformations, including random cropping, shifting, and rotation. These strategies hold great promise for enhancing classifier performance and advancing pore classification.

In future work, we aim to:

- Use a semantic pixel clustering based on DBSCAN to improve pore classification by majority decision and to derive ROI boundaries of the pores;
- Enhance the RF- and CNN-based micrograph data classification model, finally fusing these models to create a more robust meta model;
- Develop a forward ML model for predicting mechanical properties;

- Create an inverse ML model for predicting AM process parameters.

**Author Contributions:** Conceptualization, S.M.K.A.-Z. and S.B.; methodology, S.M.K.A.-Z. and S.B.; software, S.M.K.A.-Z.; validation, S.M.K.A.-Z. and S.B.; investigation, S.M.K.A.-Z. and S.B.; writing—original draft preparation, S.M.K.A.-Z. and S.B.; writing—review and editing, S.B.; visualization, S.B.; supervision. All authors have read and agreed to the published version of the manuscript.

**Funding:** This work is funded by the University of Bremen Research Alliance (UBRA) AI Center for Healthcare within the project PORTAL (grant number 40301026).

**Institutional Review Board Statement:** Not applicable.

**Informed Consent Statement:** Not applicable.







**Data Availability Statement:** The data that support the findings of this study are available from the corresponding author upon reasonable request.

**Acknowledgments:** The authors would like to thank Mika Altmann for providing experimental data for the defect classification.

**Conflicts of Interest:** The authors declare no conflicts of interest.

## Appendix A

**Table A1.** Summary of the pore types.

	Defect Type	Characteristics	Geometric Features	Material and Mechanical Properties
	Keyhole pore [6,7]	Vapor bubbles trapped in melt pool during printing and vaporized metal at high local temperatures or merge process pores	Keyhole-like voids, channeling	Reduced mechanical strength, reduced fatigue resistance, susceptibility to crack initiation
	Gas pore (circular keyhole) [8]	Vapor bubbles trapped in melt pool during printing (or merge process pores)	Irregular distribution, spherical	Decreased fatigue life, lowered mechanical strength, compromised surface finish
	Lake of Fusion (LOF) [8,9]	Due to insufficiently melted material	Interlayer gaps, unfused regions, not necessarily spherical	Starting point for cracks which may grow further due to stress
	Unmelted particle (LOF) [8,10,11]	Due to insufficiently melted material (inclusion of unmelted powder)	Same as above but with unmelted powder trapped inside	Starting point for cracks which may grow further due to stress
	Process pore [9]	Low packing density of the powder, hollow powder particles, and entrapped inert gas	Irregular distribution, spherical with smallest area	Less effect on the material
	Crack [3]	Fractures in printed layers or at interfaces or can be caused due to failure induced by other pores	Large aspect ratio	Biggest risk for initiating mechanical failure

Appendix B

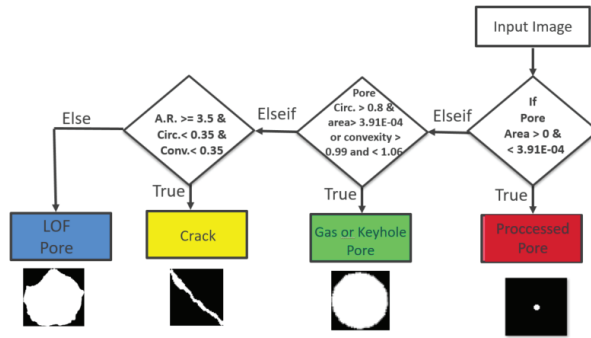


Figure A1. Automatic annotation procedure for the pore type classification.

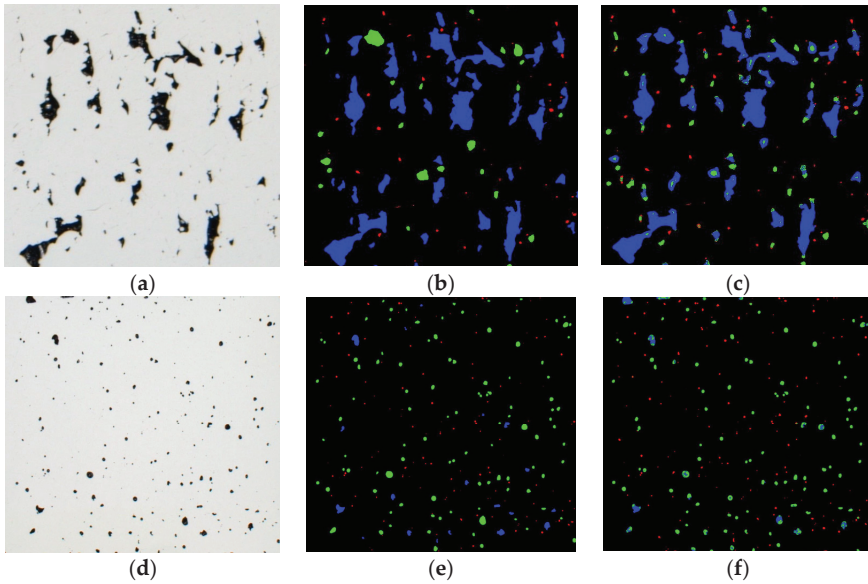
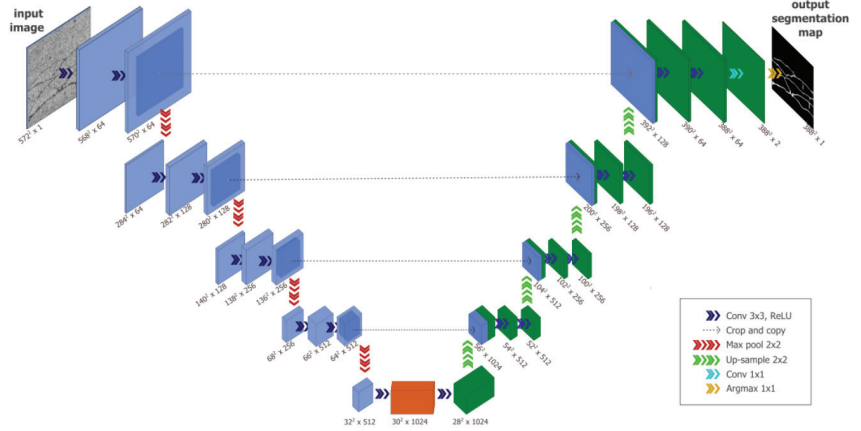


Figure A2. (a) Example of an input micrograph image. (b) Automatically labeled image where blue pixels represent the LOF pore, green keyhole or gas pores, and red is the process pores. (c) Predicted pixel classification by the RF model with a filter operator mask of  $25 \times 25$  pixels. (d) Another example. (e) Automatically labeled image. (f) Prediction using a  $3 \times 3$  filter mask with noisy classification.

Table A2. The mean area, convexity defects, and aspect ratio features of three pore types.

Pore Type	Mean Area mm	Convexity Defects	Aspect Ratio
Process	$8.59 \times 10^{-5}$	1.135	1.397
Keyhole	0.018	23.750	1.211
LOF	0.029	12.517	1.972

Appendix C



**Figure A3.** Example of U-Net architecture. The blue tiles on the left hand side represent the encoder (down-sampling) section of the network, and the green tiles on the right show the decoder (up-sampling) section [24].

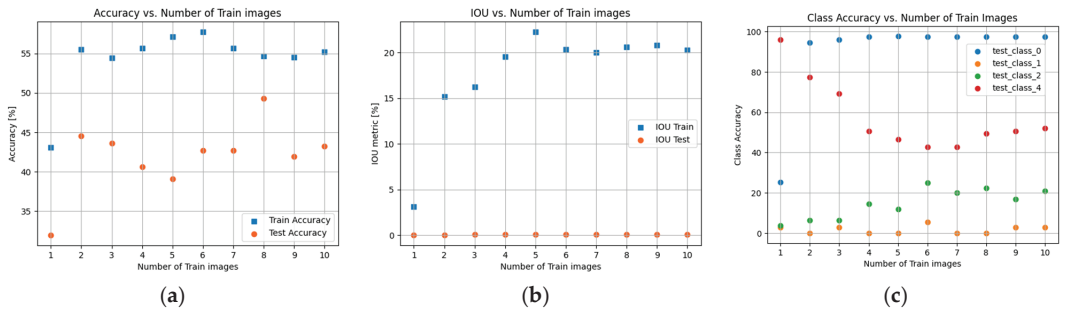


**Figure A4.** Results of using U-Net model (a) accuracy vs. increasing number of training images, (b) IoU vs. increasing number of training images, (c) each class accuracy vs. increasing number of training images.

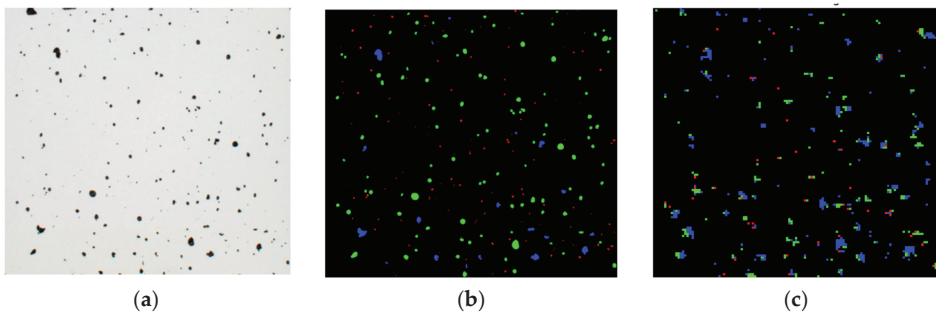


**Figure A5.** Results of U-Net model trained with eight images: (a) test image, (b) labeled test image (c) predicted image.

## References

1. Khorasani, A.; Gibson, I.; Veetil, J.K.; Ghasemi, A.H. A review of technological improvements in laser-based powder bed fusion of metal printers. *Int. J. Adv. Manuf. Technol.* **2020**, *108*, 191. [CrossRef]
2. Kruth, J.-P.; Mercelis, P.; van Vaerenbergh, J.; Froyen, L.; Rombouts, M. Binding mechanisms in selective laser sintering and selective laser melting. *Rapid Prototyp. J.* **2005**, *11*, 26. [CrossRef]
3. Gong, H.; Rafi, K.; Gu, H.; Ram, G.D.J.; Starr, T.; Stucker, B. Influence of defects on mechanical properties of Ti-6Al-4V components produced by selective laser melting and electron beam melting. *Mater. Des.* **2015**, *86*, 545–554. [CrossRef]
4. Keshavarzkermani, A.; Marzbanrad, E.; Esmaeilzadeh, R.; Mahmoodkhani, Y.; Ali, U.; Enrique, P.D.; Zhou, N.Y.; Bonakdar, A.; Toyserkani, E. An investigation into the effect of process parameters on melt pool geometry, cell spacing, and grain refinement during laser powder bed fusion. *Opt. Laser Technol.* **2019**, *116*, 83. [CrossRef]
5. Cepeda-Jiménez, C.M.; Potenza, F.; Magalini, E.; Luchin, V.; Molinari, A.; Pérez-Prado, M.T. Effect of energy density on the microstructure and texture evolution of Ti-6Al-4V manufactured by laser powder bed fusion. *Mater. Charact.* **2020**, *163*, 110238. [CrossRef]
6. Wang, T.; Dai, S.; Liao, H.; Zhu, H. Pores and the formation mechanisms of SLMed AISi10Mg. *Rapid Prototyp. J.* **2020**, *26*, 1657–1664. [CrossRef]
7. Martin, A.A.; Calta, N.P.; Khairallah, S.A.; Wang, J.; Depond, P.J.; Fong, A.Y.; Thampy, V.; Guss, G.M.; Kiss, A.M.; Stone, K.H.; et al. Dynamics of pore formation during laser powder bed fusion additive manufacturing. *Nat. Commun.* **2019**, *10*, 1987. [CrossRef]
8. Ellendt, N.; Fabricius, F.; Toenjes, A. PoreAnalyzer—An Open-Source Framework for the Analysis and Classification of Defects in Additive Manufacturing. *Appl. Sci.* **2021**, *11*, 6086. [CrossRef]
9. Altmann, M.L.; Benthien, T.; Ellendt, N.; Toenjes, A. Defect Classification for Additive Manufacturing with Machine Learning. *Materials* **2023**, *16*, 6242. [CrossRef]
10. Kruth, J.P.; Froyen, L.; Van Vaerenbergh, J.; Mercelis, P.; Rombouts, M.; Lauwers, B. Selective laser melting of iron-based powder. *J. Mater. Process. Technol.* **2004**, *149*, 616–622. [CrossRef]
11. Wang, W.; Ning, J.; Liang, S.Y. Prediction of lack-of-fusion porosity in laser powder-bed fusion considering boundary conditions and sensitivity to laser power absorption. *Int. J. Adv. Manuf. Technol.* **2021**, *112*, 61–70. [CrossRef]
12. Zhang, Y.; Hong, G.S.; Ye, D.; Zhu, K.; Fuh, J.Y. Extraction and evaluation of melt pool, plume and spatter information for powder-bed fusion AM process monitoring. *Mater. Des.* **2018**, *156*, 458–469. [CrossRef]
13. Scime, L.; Beuth, J. Anomaly detection and classification in a laser powder bed additive manufacturing process using a trained computer vision algorithm. *Addit. Manuf.* **2018**, *19*, 114–126. [CrossRef]
14. Wong VW, H.; Ferguson, M.; Law, K.H.; Lee YT, T.; Witherell, P. Automatic volumetric segmentation of additive manufacturing defects with 3D U-Net. *arXiv* **2021**, arXiv:2101.08993.
15. Bradski, G. The openCV library. *Dr. Dobb's J. Softw. Tools Prof. Program.* **2000**, *25*, 120–123.
16. Suzuki, S. Topological structural analysis of digitized binary images by border following. *Comput. Vis. Graph. Image Process.* **1985**, *30*, 32–46. [CrossRef]
17. Breiman, L. Random forests. *Mach. Learn.* **2001**, *45*, 5–32. [CrossRef]
18. Cutler, A.; Cutler, D.R.; Stevens, J.R. Random forests. *Ensemble Mach. Learn. Methods Appl.* **2012**, 157–175. [CrossRef]
19. Breiman, L. Bagging predictors. *Mach. Learn.* **1996**, *24*, 123–140. [CrossRef]
20. Fabian, P.; Gael, V.; Alexandre, G.; Vincent, M.; Bertrand, T.; Olivier, G.; Mathieu, B.; Peter, P.; Ron, W.; Vincent, D.; et al. Scikit-learn: Machine learning in Python. *J. Mach. Learn. Res.* **2011**, *12*, 2825–2830.
21. Bosse, S.; Lehnhus, D. Automated Detection of hidden Damages and Impurities in Aluminum Die Casting Materials and Fibre-Metal Laminates using Low-quality X-ray Radiography, Synthetic X-ray Data Augmentation by Simulation, and Machine Learning. *arXiv* **2023**, arXiv:2311.12041. [CrossRef]
22. Shah, C.; Bosse, S.; von Hehl, A. Taxonomy of Damage Patterns in Composite Materials, Measuring Signals, and Methods for Automated Damage Diagnostics. *Materials* **2022**, *15*, 4645. [CrossRef] [PubMed]
23. Boser, B.; Denker, J.S.; Henderson, D.; Howard, R.E.; Hubbard, W.; Jackel, L.D.; Laboratories, H.Y.L.B.; Zhu, Z.; Cheng, J.; Zhao, Y.; et al. Backpropagation applied to handwritten zip code recognition. *Neural Comput.* **1989**, *1*, 541–551.
24. Jenkins, M.D.; Carr, T.A.; Iglesias, M.I.; Buggy, T.; Morison, G. A deep convolutional neural network for semantic pixel-wise segmentation of road and pavement surface cracks. In Proceedings of the 2018 26th European Signal Processing Conference (EUSIPCO), Rome, Italy, 3–7 September 2018; pp. 2120–2124. [CrossRef]
25. Al-Zaidawi, S.M.K. Machine Learning Classification of User Attributes via Eye Movements. Ph.D. Thesis, Universität Bremen, Bremen, Germany, 2022. [CrossRef]
26. Rezatofghi, H.; Tsoi, N.; Gwak, J.; Sadeghian, A.; Reid, I.; Savarese, S. Generalized intersection over union: A metric and a loss for bounding box regression. In Proceedings of the IEEE/CVF Conference on Computer Vision and Pattern Recognition (CVPR), Long Beach, California, USA, 15–20 June 2019; pp. 658–666.

**Disclaimer/Publisher's Note:** The statements, opinions and data contained in all publications are solely those of the individual author(s) and contributor(s) and not of MDPI and/or the editor(s). MDPI and/or the editor(s) disclaim responsibility for any injury to people or property resulting from any ideas, methods, instructions or products referred to in the content.

Proceeding Paper

# Deep Learning-Enabled Pest Detection System Using Sound Analytics in the Internet of Agricultural Things <sup>†</sup>

Rajesh Kumar Dhanaraj <sup>1</sup> and Md. Akkas Ali <sup>2,3,\*</sup>

<sup>1</sup> Symbiosis Institute of Computer Studies and Research, Symbiosis International (Deemed University), Pune 412115, India; rajesh.dhanaraj@sicsr.ac.in

<sup>2</sup> School of Computing Science and Engineering, Galgotias University, Greater Noida 201310, India

<sup>3</sup> Bangabandhu Sheikh Mujibur Rahman Science and Technology University, Gopalganj 8100, Bangladesh

\* Correspondence: md.21scse3010038@galgotiasuniversity.edu.in

<sup>†</sup> Presented at the 10th International Electronic Conference on Sensors and Applications (ECSA-10), 15–30 November 2023; Available online: <https://ecsa-10.sciforum.net/>.

**Abstract:** Around the globe, agriculture has grown to a point where it is now a financially feasible way to produce more sophisticated cultivation methods. Throughout the long tradition of agriculture, this represents a pivotal moment. The widespread adoption of data and the latest technological advances in the contemporary period allowed this paradigm change. However, pests remain to blame for significant harm done to crops, which has a detrimental impact on finances, the natural world, and society. This highlights the necessity of using automated techniques to apprehend pests before they cause widespread harm. Agriculture-related issues are currently the predominant subject for research that utilizes ML. The overarching aim of this investigation is the development of an economically feasible method for pest detection in vast fields of crops that IoT enables through the use of pest audio sound analytics. The recommended approach incorporates numerous acoustic preparation methods from audio sound analytics. The Chebyshev filter; the Welch method; the non-overlap-add method; FFT, DFT, STFT, and LPC algorithms; acoustic sensors; and PID sensors are among them. Eight hundred pest sounds were examined for features and statistical measurements before being incorporated into Multilayer Perceptron (MLP) for training, testing, and validation. The experiment's outcomes demonstrated that the proposed MLP model triumphed over the currently available DenseNet, VGG-16, YOLOv5, and ResNet-50 approaches alongside an accuracy of 99.78%, a 99.91% sensitivity, a 99.64% specificity, a 99.59% recall, a 99.82% F1 score, and a 99.85% precision. The significance of the findings rests in their potential to proactively identify pests in large agricultural fields. As a result, the cultivation of crops will improve, leading to increased economic prosperity for agricultural producers, the country, and the entire globe.

**Keywords:** Internet of Agricultural Things; deep learning; Multilayer Perceptron; pest detection; sound analytics

**Citation:** Dhanaraj, R.K.; Ali, M.A. Deep Learning-Enabled Pest Detection System Using Sound Analytics in the Internet of Agricultural Things. *Eng. Proc.* **2023**, *58*, 123. <https://doi.org/10.3390/ecsa-10-16205>

Academic Editor: Francisco Falcone

Published: 15 November 2023



**Copyright:** © 2023 by the authors. Licensee MDPI, Basel, Switzerland. This article is an open access article distributed under the terms and conditions of the Creative Commons Attribution (CC BY) license (<https://creativecommons.org/licenses/by/4.0/>).

## 1. Introduction

Intelligent agriculture monitoring systems collect real-time agricultural data via IoT sensor networks [1]. Agriculture's production, efficiency, and sustainability are improved via automation and artificial intelligence. IoT devices use small sensors to measure soil moisture, temperature, humidity, light intensity, air quality, crop health, and water levels. These sensors are deliberately placed across a farm to collect data from multiple places. Internet-connected sensors use Wi-Fi, Lo-RaWAN, cellular, or satellite networks [2]. This link allows data to be easily transmitted to the cloud. IoT sensors are stored, analyzed, and processed in the cloud. Cloud computing features include scalability, real-time data access, and secure storage. The cloud platform discovers machine learning and analytics [3]. Estimates of crop health, appropriate watering regimens, and early disease and pest detection

are examples of these findings. Farmers and agriculturalists can access real-time data via simple smartphone apps and web dashboards [4]. They use these networks to monitor their crops and farms remotely.

Pest management and irrigation systems can be automated using research and ideas. Data-driven farmers save money and resources [5,6]. They improve irrigation, fertilization, and other agricultural practices to boost crop output. Water and the environment are conserved via efficient fertilizer and water use. Early pest and disease detection prevent mega-outbreaks and crop losses. Remote agriculture gives farmers independence. Sustainable farming techniques decrease waste and resource usage [7–9]. This study proposes a real-time pest detection method using MLP and sound analytics. Technology will improve insect monitoring and treatment, making farming more efficient and environmentally friendly [10,11].

## 2. Dataset and Data Pre-Processing

The Agricultural Research Service (ARS) of the United States Department of Agriculture (USDA) is responsible for keeping the sound pest library, which is located at [12]. The sound recordings in this library were gathered using various acoustic sensors to record the sounds produced by various insect species. A network of IoAT devices over large agricultural areas can record pest sounds. The suggested technique analyzed 800 audio recordings of 16 pests, as indicated in Figure 1. The Chebyshev filter denoised pest audio data; the Welch approach reduced audio spectrum leakage; the non-overlap-add method transformed overlapping frames into non-overlapping ones; FFT, DFT, and STFT transferred time to the frequency domain and characterized and analyzed pest audio data for fusing with a recommended deep learning system model; and LPC extracted features from pest audio sound signals. The GMM calculated statistical measurements. In total, 70% of the data were used for training, 20% for testing, and 10% for validation.

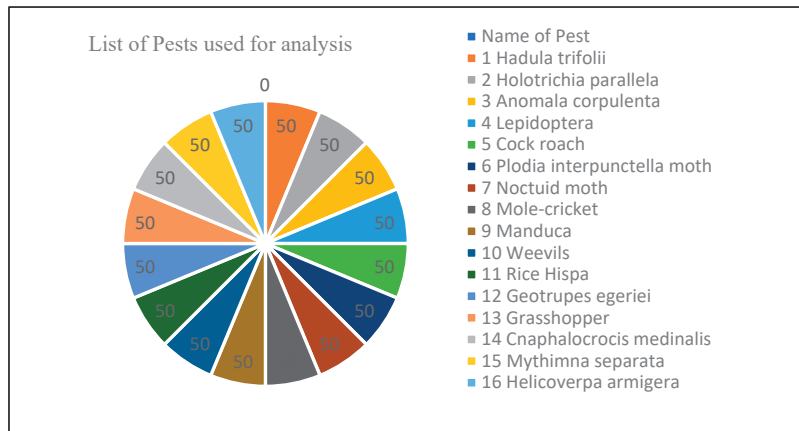


Figure 1. List of pests used for analysis.

## 3. Proposed Methodology

### 3.1. MLP System Model

We have used a fully lined 4-layered MLP as shown in Figure 2. Every computation abstraction layer has a fixed number of neurons. NN learns and weights neurons. The model layer sequence is input, first hidden, second hidden, output. The number of feature dataset input–output neurons create NN input and output layers. Based on identified ideas, inner layers have any number of neurons. The input layer has 20 nodes. It is 20\*1. The improved first hidden layer has 40 neurons and ReLU. This layer’s neurons weigh all input layer neurons. A 20\*40 input-hidden layer connects the weight matrix. The 40-

neuron second hidden layer activates ReLU. Neurons are weighted to all first hidden-layer outputs. The first and second hidden layers' linking weight matrix is 40\*40. The fourth layer, output, contains instantaneous input feature labels in 16 nodes, 1 per class. The output layer activates the sigmoid. Each node has all second hidden-layer neurons with output layer weights. The second hidden and output layers have a 40\*16 linking weight matrix. Equation (1) calculates the output of a neuron  $Z(B_1)$  at the first hidden layer using the weighted average of all inputs and bias  $E_1$  and  $F_1(p)$  from Equation (2).

$$Z(B_1) = F_1(\sum_{i=1}^{20} (A_i M_{i1}) + E_1) \tag{1}$$

$$F_1(p) = \begin{cases} 0, & 0 < p \\ p, & p \geq 0 \end{cases} \tag{2}$$

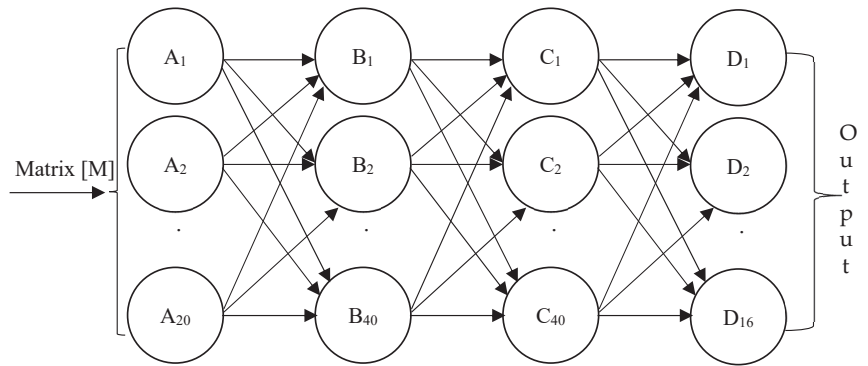


Figure 2. The architecture of the MLP system model.

The outcome of each neuron  $Z(C_1)$  in the second hidden layer is supplied by Equation (3) and computed as the weighted average and  $E_2$ , which is assessed by  $F_1(p)$ , provided via Equation (2).

$$Z(C_1) = F_1(\sum_{j=1}^{40} (Z(B_j) M_{j1}) + E_2) \tag{3}$$

In the end,  $D_1$ , provided via Equation (4), produced second layer outputs and bias  $E_3$ , assessed with  $F_2(p)$ , provided via Equation (5). The prediction output probability changed from 0 to 1.

$$D_1 = F_2(\sum_{k=1}^{40} (Z(C_k) M_{k1}) + E_3) \tag{4}$$

$$F_2(p) = \frac{1}{1 + e^{-p}} \tag{5}$$

### 3.2. Architecture of the Proposed System

In big agricultural fields, it is feasible to identify pests by monitoring the sounds that pests produce and then comparing those sounds to data that have been gathered. This process is known as acoustic analysis. One can examine a sound to detect insects by comparing it with data already known in the database. These data should include sound processing information and should be analyzed with the help of the MLP system model and the sound analysis algorithm. Sending an agricultural pest's sound to the microcontroller analyses it to find the insects. If pests are unwanted, the PID sensor detects changes in their infrared emission (heat). The PID sensor can detect heat up to nine meters from an object above 0 degrees Celsius. The suggested system design is shown in Figure 3. After confirming that the invasive species is present in the field, acoustic sensors that cover the entire field are utilized to record pest sounds. After that, these noises are compared to



a modified insect sound from the database. It uses sound-based technology to identify unwanted animals.

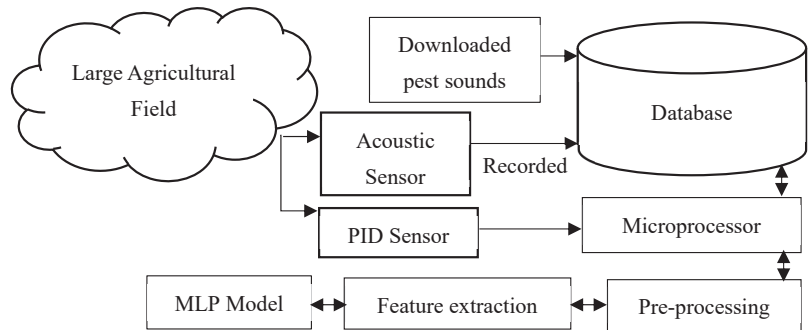


**Figure 3.** The architecture of the proposed system.

#### 4. Experimentation, Results, and Analysis

##### 4.1. Experimental Setup

For experiments, we used a computer with Windows 10, an Intel(R)Core (TM) i5-9300H processor at 2.40 GHz, 64 gigabytes of RAM, and a video card with additional effects. The study used Python 3.8.10 to simplify completion. Throughout the study, PyTorch 1.9.0 helped create the network model. Additionally, GPU acceleration with CUDA 10.2 increased computer graphics’ computation power.

##### 4.2. Performance Parameters

A different arrangement was assessed for general performance. Then, it was compared to the recommended solution, which used multiple methods to attain this goal. “True positive,” “true negative,” “false positive,” and “false negative” were symbolized by their respective words.

$$\text{Accuracy} = \frac{(\text{TrueN} + \text{TrueP})}{(\text{TrueN} + \text{TrueP} + \text{FalseN} + \text{FalseP})} \text{ and Sensitivity} = \frac{\text{TrueP}}{\text{TrueP} + \text{FalseN}} \quad (6)$$

$$\text{Specificity} = \frac{\text{TrueN}}{\text{TrueN} + \text{FalseP}} \text{ and Reca} = \frac{\text{TrueP}}{(\text{FalseN} + \text{TrueP})} \quad (7)$$

$$\text{and Precision} = \frac{\text{TrueP}}{\text{TrueP} + \text{FalseP}} \cdot \text{ and F1 - score} = \frac{\text{Two} * \text{precision} * \text{recall}}{\text{precision} + \text{recall}} \quad (8)$$

$$\text{MSE} = (1/m) * \Sigma (a - f)^2 \quad (9)$$

$$\text{PE} = (a - f) * 100 \quad (10)$$

##### 4.3. Results

Table 1 presents the training, testing, and hypothesis testing data. The respective values of these percentages are 70, 20, and 10 percent.

**Table 1.** Samples were taken from the dataset.

Training Samples 70%	Testing 20%	Validating 10%	Total Samples
560	160	80	800

The accuracy scores, sensitivity scores, specificity scores, recall and precision scores, F1 scores, MSE scores, and PE values were generated by the MLP system model. These findings are presented visually in Figure 4. The presented MLP system model obtained accuracy ratings of 99.78%, 99.63%, and 99.76%, respectively, throughout the training, validation, and testing phases summarized and shown visually in Figure 5. As shown in Figure 6, the recommended MLP system representation had impairments of 0.22, 0.37, and 0.24 throughout training, validation, and testing.

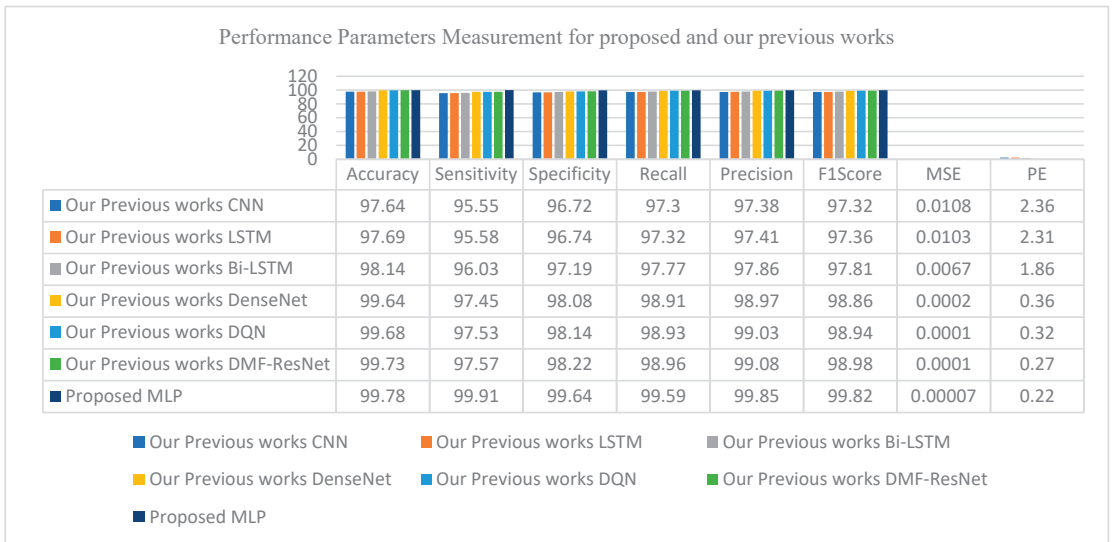


Figure 4. Performance parameter measurement for our proposed and previous works.

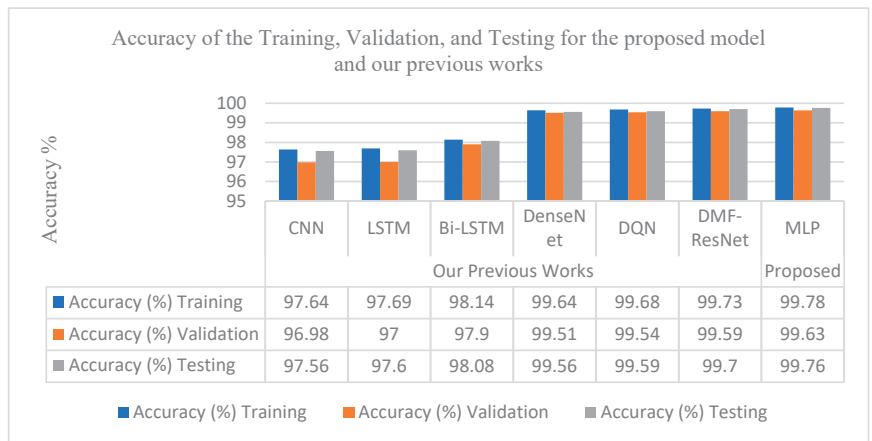


Figure 5. Training, validation, and testing accuracy for our proposed and previous works.

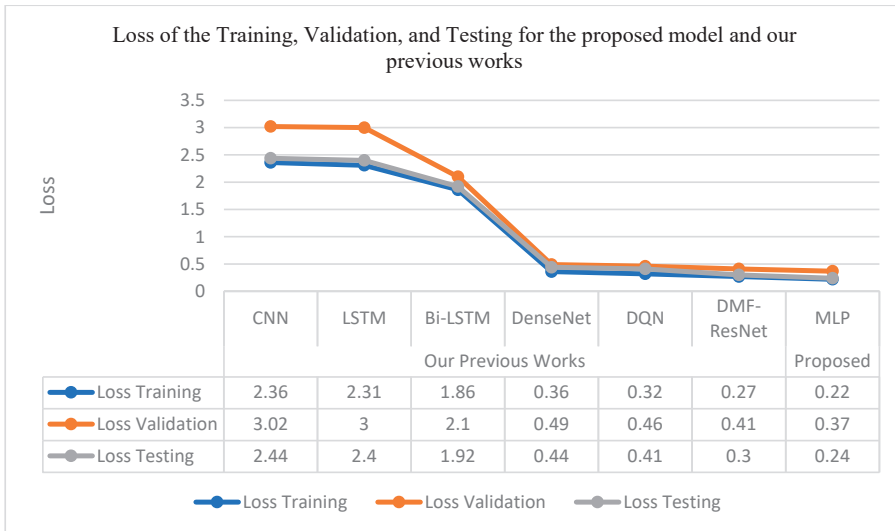


Figure 6. Training, validation, and testing loss for the proposed model and our previous works.

#### 4.4. Performance Comparisons

Figure 7 presents an exposition of what was found in an investigation comparing the currently proposed research initiatives and the state-of-the-art methods.

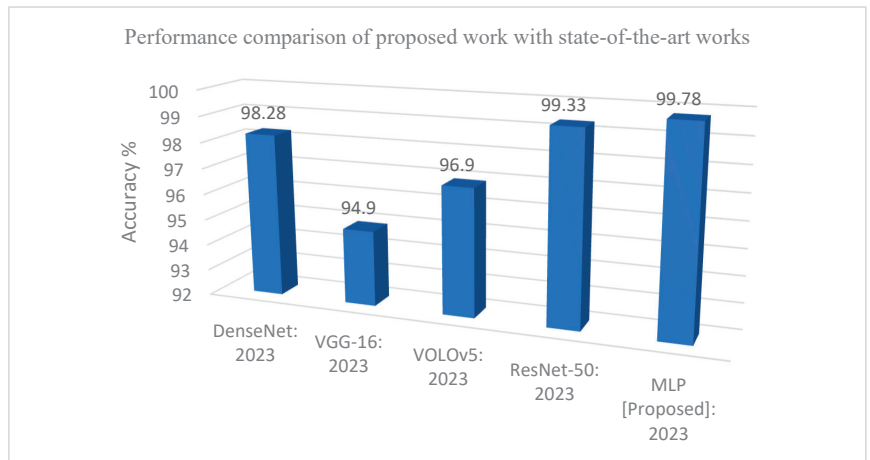


Figure 7. Performance comparison of proposed work with state-of-the-art works.

### 5. Limitations of the Proposed System and Future Scope

The proposed system used only 16 pest species and had a 99.78% detection rate; this is a limitation. With at least 100 pests, the suggested approach is expected to detect 100% soon.

### 6. Conclusions

We present the most data-driven, scientifically sound, and technologically advanced agricultural data ever. Agricultural IoT has made farming wise. This calamity transformed farming and opened doors. The problems farmers encounter limit agricultural productivity. Bugs, mites, and others cost agriculture a lot. Pesticides help farmers control weeds, plant-killing pathogens, and illnesses. Pesticides harm the environment, health, and the economy.

This study built an MLP-based, IoT-based autonomous real-time insect surveillance system. The IoT and sound analytics reduce pesticide use. Sound analytics can establish a pest's field presence by recording its sound.

**Author Contributions:** All authors have equal contributions. All authors have read and agreed to the published version of the manuscript.

**Funding:** This research received no external funding.

**Institutional Review Board Statement:** Not applicable.

**Informed Consent Statement:** Not applicable.

**Data Availability Statement:** Data are contained within the article.

**Conflicts of Interest:** The authors declare no conflict of interest.

## References

1. Gupta, B.; Madan, G.; Md, A.Q. A smart agriculture framework for IoT-based plant decay detection using innovative croft algorithm. *Mater. Today Proc.* **2022**, *4758–4763*. [CrossRef]
2. Siddiquee, K.N.E.A.; Islam, M.S.; Singh, N.; Gunjan, V.K.; Yong, W.H.; Huda, M.N.; Naik, D.B. Development of IoT-based smart agriculture monitoring system algorithms. *Wirel. Commun. Mob. Comput.* **2022**, *2022*, 7372053. [CrossRef]
3. Vangala, A.; Das, A.K.; Chamola, V.; Korotaev, V.; Rodrigues, J.J. Security in IoT-enabled smart agriculture: Architecture, security solutions, and challenges. *Clust. Comput.* **2023**, *26*, 879–902. [CrossRef]
4. Pagano, A.; Croce, D.; Tinnirello, I.; Vitale, G. A Survey on LoRa for Smart Agriculture: Current Trends and Future Perspectives. *IEEE IoT J.* **2022**, *10*, 3664–3679. [CrossRef]
5. Qazi, S.; Khawaja, B.A.; Farooq, Q.U. IoT-equipped and AI-enabled next generation smart agriculture: A critical review, current challenges, and future trends. *IEEE Access* **2022**, *10*, 21219–21235. [CrossRef]
6. Lovesum, J.; Prince, B. A Study on Experimental Analysis of Best Fit Machine Learning Approach for Smart Agriculture. *SN Comput. Sci.* **2023**, *4*, 187. [CrossRef]
7. Shaikh, T.A.; Mir, W.A.; Rasool, T.; Sofi, S. Machine Learning for Smart Agriculture and Precision Farming: Towards Making the Fields Talk. *Arch. Comput. Methods Eng.* **2022**, *29*, 4557–4597. [CrossRef]
8. Gong, H.; Liu, T.; Luo, T.; Guo, J.; Feng, R.; Li, J.; Guo, Y. Based on FCN and DenseNet Framework for the Research of Rice Pest Identification Methods. *Agronomy* **2023**, *13*, 410. [CrossRef]
9. Zhu, D.; Xie, L.; Chen, B.; Tan, J.; Deng, R.; Zheng, Y.; Andrew, W.H. Knowledge graph and deep learning-based pest detection and identification system for fruit quality. *Internet Things* **2023**, *21*, 100649. [CrossRef]
10. Chu, J.; Li, Y.; Feng, H.; Weng, X.; Ruan, Y. Research on Multi-Scale Pest Detection and Identification Method in Granary Based on Improved YOLOv5. *Agriculture* **2023**, *13*, 364. [CrossRef]
11. Hadipour-Rokni, R.; Asli-Ardeh, E.A.; Jahanbakhshi, A.; Sabzi, S. Intelligent detection of citrus fruit pests using a machine vision system and convolutional neural network through transfer learning technique. *Comput. Biol. Med.* **2023**, *155*, 106611. [CrossRef]
12. Available online: <https://data.nal.usda.gov/dataset/bug-bytes-sound-library-stored-product-insect-pest-sounds/resource/ff1b1ed6-5597-4494-be21-7205122dae63> (accessed on 1 January 2023).

**Disclaimer/Publisher's Note:** The statements, opinions and data contained in all publications are solely those of the individual author(s) and contributor(s) and not of MDPI and/or the editor(s). MDPI and/or the editor(s) disclaim responsibility for any injury to people or property resulting from any ideas, methods, instructions or products referred to in the content.

Proceeding Paper

# Sons al Balcó: A Subjective Approach to the WASN-Based $L_{Aeq}$ Measured Values during the COVID-19 Lockdown <sup>†</sup>

Enric Dorca, Daniel Bonet-Solà, Pau Bergadà, Carme Martínez-Suquía and Rosa Ma Alsina-Pagès \*

Human-Environment Research (HER), La Salle-URL, Sant Joan de la Salle, 42, 08022 Barcelona, Spain; enric.dorca@students.salle.url.edu (E.D.); daniel.bonet@salle.url.edu (D.B.-S.); pbergadac@gmail.com (P.B.); carmenjulia.martinez@salle.url.edu (C.M.-S.)

\* Correspondence: rosamaria.alsina@salle.url.edu

<sup>†</sup> Presented at the 10th International Electronic Conference on Sensors and Applications (ECSA-10), 15–30 November 2023; Available online: <https://ecsa-10.sciforum.net/>.

**Abstract:** The lockdown in Spain due to COVID-19 caused a strong decrease in the urban noise levels observed in most cities, clearly followed in the case that these cities had acoustic sensor networks deployed. This fact had an impact on people's lives, who, at that time, were mainly locked at home due to health reasons. In this paper, we present a qualitative analysis of the subjective vision of the citizens participating in a data-collecting campaign during the COVID-19 lockdown in Girona, a Catalan city, named 'Sons al Balcó'. The alignment of the subjective data gathered was too scarce to conduct final conclusions, but already giving a bias of the results indicates that the objective  $L_{Aeq}$  measurements, which showed a clear decrease in noise in the streets during the lockdown, were supported by the fact that new sounds found during the lockdown were not very annoying. Former existing noise sources, such as road traffic noise or leisure noise, are depicted as annoying but their decrease during the lockdown improved the soundscape of many homes. This paper's goal is to show the possibility of gathering both objective and calibrated data with perceptive approximation for the first time in 'Sons al Balcó', and how this supports our conclusions, in survey with a limited number of participants conducted during the 2020 lockdown period in Catalonia.

**Keywords:** lockdown; soundscape;  $L_{Aeq}$ ; annoyance; perception; WASN; Girona; citizen science

**Citation:** Dorca, E.; Bonet-Solà, D.; Bergadà, P.; Martínez-Suquía, C.; Alsina-Pagès, R.M. Sons al Balcó: A Subjective Approach to the WASN-Based  $L_{Aeq}$  Measured Values during the COVID-19 Lockdown. *Eng. Proc.* **2023**, *58*, 124. <https://doi.org/10.3390/ecsa-10-16241>

Academic Editor: Stefan Bosse

Published: 15 November 2023



**Copyright:** © 2023 by the authors. Licensee MDPI, Basel, Switzerland. This article is an open access article distributed under the terms and conditions of the Creative Commons Attribution (CC BY) license (<https://creativecommons.org/licenses/by/4.0/>).

## 1. Introduction

Since the outbreak of COVID-19 at the end of 2019, a number of social changes have impacted almost all countries around the world. First of all, health authorities imposed unprecedented containment measures, whose goal was to reduce the impact of COVID-19 on national health systems. These policies, such as long-period lockdowns, social distancing in public places, and face masks impairing human communication, brought a number of collateral social effects. Among others, man-made noise was considerably diminished in urban scenarios; therefore, many research activities have been carried out to study the effects of lockdown on noise pollution. The aim of this paper is to compare the objective outcomes gathered by a number of noise sensors in the city of Girona (Catalonia), i.e., [1], with the subjective responses gathered by a survey conducted in the aforementioned city. All data and subjective surveys were collected during the COVID lockdown in 2020.

Regarding the relationship between objective and subjective sound pressure level measurements, previous research works, such as [2], studied the accuracy with which individuals may estimate the sound pressure level in their current day life. This research work claims that the reported results indicate that young adults are able to make a reasonable estimate of the noise level of events in their daily lives. This analysis has also been conducted with a wider scope in [3], where the authors study how people reacted to the unexpected situation of the lockdown, coming to the conclusion that people had a positive reaction to the lower noise level.

Other research works, e.g., [4], studied subjective methods of measurement suitable for Active Noise Reduction (ANR) devices. They reported differences between subjective and physical measurements of up to 20 dB at 250 Hz and below when applying pink noise with a maximum noise level of 80 dB SPL (Sound Pressure Level) for a device in which the sound pressure level varied substantially near the ear canal. Since noise annoyance and excessive noise exposure have been linked to adverse physical and mental health issues, some research initiatives, such as [5], investigated the disparities in noise complaints in the city of New York since 2010, including the lockdown period in 2020 and beginning of 2021. The results showed that communities with a high proportion of low-income residents reported a higher number of noise complaints, which increased over time, especially during warmer months.

The only previous work facing subjective answers of citizens, also in this conference and with reference [6], detailed the first stages of the analysis of the questionnaire results, without entering the comparison of the answers by citizens to the place in town where the questionnaire was being uploaded, gathering together all the results in Catalonia. The purpose of this work is to conduct a subjective approach, coming from a group of questionnaire data gathered during the lockdown in Girona, in order to contrast their opinions with the objective measurements already published in [1], which was also performed in Barcelona in [7]. The former works always put the focus on objective data given by sensors and never entered the comparison with what citizens gave us as the perception of their soundscape. In order to be maximally meaningful in results, only the questionnaires filled in by people living at a maximum distance of 1 km from the sensor have been taken into account, assuming that even this situation gives an approximation, especially due to the low number of answers by citizens in the campaign. Nevertheless, and assuming the qualitative approach of the description in this work, the results converge to what objective data were measured and analyzed during (and before, and after) the lockdown, which encourages the team to keep on working on citizen science campaigns in order to increase the number of contributions obtained in each campaign.

This paper is structured as follows. Section 2 details the methodology of data collection used. Section 3 details several sensors in Girona with the comparison of the objective measurements and the subjective results, and Section 4 details the conclusions of this work.

## 2. Data Gathering

Subjective data gathered by citizens have been used in this work as qualitative data. Despite the lack of enough statistical reliability to obtain enough supported conclusions, the methods of data gathering and collection campaign description are detailed in this section, especially taking into account the replicability of the method. In order to carry out the study presented in this paper, data of a diverse nature have been examined. On the one hand, we have analyzed the data obtained through a questionnaire responded to by a representative number of participants. On the other hand, data on equivalent levels measured by sensors deployed in the city of Girona have also been analyzed. Thus, the following quantitative data have been studied: (1) surveys to citizens about their perception of the soundscape both before and during the lockdown, with details about the most annoying sounds and quantifying this annoyance; (2) recordings collected thanks to the citizen science web platform during the lockdown; and (3) equivalent acoustic levels ( $L_{Aeq}$ ) measurements, carried out by sensors calibrated in the city of Girona during the lockdown.

### 2.1. Data Collection Campaign

Three campaigns of data collection were carried out and later on analyzed in this study. A socio-acoustic digital participatory survey was implemented in order to obtain perceptive data representative of all of the citizens of Catalonia. A web service platform allowing an online question-and-answer, with different response formats and even video uploading was set. The LimeSurvey [8] application was selected, which is an open-source online application that offers a web platform to create and edit surveys. Furthermore, their source

code is also available to be deployed in any other server that supports it. Specifically, an Amazon EC2 cloud computing instance running a Bitnami Stack for LimeSurvey 4.2.3-0 on Ubuntu 16.04.6 LTS was chosen. In addition, an Amazon S3 bucket was used to upload the videos directly from the devices of the participants, in order to reduce traffic. Finally, a Fine Uploader library running on EC2 was used to manage and sign requests allowing access to the S3 bucket. The survey included questions on the following topics: sociodemographic data, residential soundscape quality, and individual positive and negative perceptions before and during the closure. In addition, participants could select from different categories of noise sources. See [9] for more details.

## 2.2. Sensors Data

This work has used the Wireless Acoustic Sensor Network (WASN) of the city center of Girona, which was mainly used to conduct a previous work, giving detailed values of variation during the COVID-19 lockdown in Girona [1]. The WASN used to gather the data of Girona has eight sensors deployed in several points (see Figure 1 in [10]). The sensors give detail of  $L_{Aeq}$  with a maximum temporal resolution of 1 min. In this study, we analyzed raw data from these sensors 24 h a day for 7 days a week working at  $L_{Aeq,1min}$ . A detailed description of the locations can be found in [1].

## 3. Comparative Analysis

In this section, we analyze the most relevant sensor data gathered in Girona together with the subjective contribution of the participants in the campaign. Former research papers, i.e., [1,11], analyzed gathered data *only* from the sensors-so, only objective data- in Girona and reached the following conclusions. During the lockdown period, a high decrease in noise level was measured in most of the sensors in Girona, except for those locations where traffic noise was totally predominant since they are the main connection roads. Leisure noise sources almost disappeared, especially during the lockdown and curfew period nights, mainly following the strict regulations set by the government. As the number of respondents in Girona is not statistically relevant, in this section, we are interested in showing whether the perception of citizens shows some kind of coincidence and exhibits a tendency toward the above conclusions. We have chosen three different sensors that correspond to different acoustic realities. Sensor 2 gathers noise from a mixture of leisure and traffic noise in a wide central street, whereas sensor 3 is placed in a narrow street and mainly records leisure noise, and finally, sensor 4 is located in a big drive with heavy traffic noise. The aim is to expose respondents to different noise realities to detect a common pattern or on the contrary, whether there is a particular behavior in each environment.

### 3.1. Sensor 2

This sensor corresponded to a city center location (i.e., Ramon Folch Street) with both heavy traffic and leisure noise sources such as the post office, the city court, a theater, a cinema, and several outdoor restaurants. It is worth mentioning that the railway, uplifted 6 m, crosses this street. Although there were 22 respondents in Girona, only 4 of them were less than 1 km near this sensor. These people were either men or women between the ages of 38 and 42. The respondents were asked to describe their home sound environment before the lockdown and only one of them described it as “Good”. These data stand out from that obtained during the lockdown, in which 3 out of 4 respondents considered their sound environment to be “Very good”. According to the poll, there was a major improvement in the sound quality after the lockdown as all of the respondents described the sound environment of their home after the lockdown as “Very good” or “Good” versus just one that chose those options before the lockdown. As reported in [11], the data from the sensors obtained during the confinement showed that the sound environment was improved during the confinement. During the confinement noise levels were drastically reduced between March and May 2020, due to the reduction in citizen movement and travel within the city. During the lockdown almost three quarters of the respondents, on

average, did not identify the sounds present in the video recording neither as “Exciting” nor “Disturbing”, see Figure 1. Moreover, the adjectives Noisy, Shrill, and Loud appeared not to define the recorded sound environment either. The sounds recorded in sensor #2 could be considered Pleasant, Calming, and Sharp as half of the survey answers selected “Agree” for all these three adjectives. It is interesting that even though sensor #2 is placed in a busy area, the sound environment is considered neither Noisy nor Loud. This matches with the study in [11], in which the  $L_{Aeq}$  decreased throughout the lockdown both during the day, when urban traffic is notorious, and at night, when leisure noise is more frequent. Despite the scarce number of respondents to this sensor, the answers to the poll might show a trend toward a reduction in leisure noise but not a clear reduction in traffic noise.

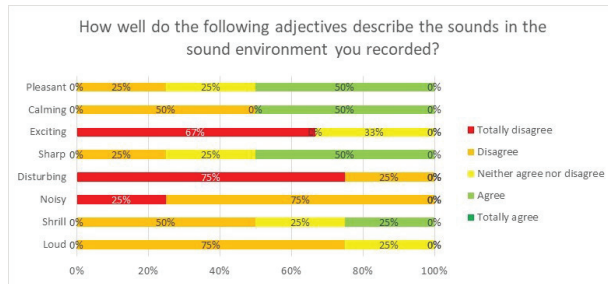


Figure 1. Descriptive assessment of the sound environment from sensor #2.

### 3.2. Sensor 3

Sensor #3 was placed in a narrow street (i.e., Figuerola Street) in the city center where leisure noise dominates. The whole street is full of restaurants and bars that are open until late at night, causing a number of complaints regarding the noise level [11]. Due to its location next to other heavy-traffic streets, cars and urban mobility-related noise are also present. The railway splits the street in half and since sensor #2 is quite near similar results are expected. Of the 22 respondents from Girona, 7 were near enough to the sensor (less than 1 km) to be considered in its scope. They were both men and women from 38 to 50 years old. Regarding the sound environment of sensor #3, it is implied to be better after the lockdown rather than before the lockdown. Before the lockdown, only 29% of the people considered their environment to be “Good”, 43% considered it “Not bad/not good” and the remaining 29% considered it “Bad”. These results differ when asked after the lockdown when it is suggested that the sound environment improved. As plotted in Figure 2, the respondents related their sound environment during the lockdown as Sharp since 43% selected that they “Agree” with this adjective to describe their sound environment. Although it is not the majority of them, 29% selected “Neither agree nor disagree” and the remaining 28% “Disagree” or “Totally disagree”, which makes this adjective the one with greater agreement. The sound environment in sensor #3 is considered neither Exciting nor Disturbing at 62%, on average, “Totally disagree” with these adjectives. The remaining respondents selected the “Disagree” or “Neither agree nor disagree” options for these categories, versus a slight 14% that selected “Agree” in the Disturbing question. It is worth mentioning that even though the location of the sensor is known to be in a noisy place, the volunteers thought that their environment noise was neither Disturbing nor Loud. The tendency of the answers to the poll might show an indication that the global noise was reduced derived from the fact that other noise sources, which were previously squelched, were reported. It could also be suggested that there is some kind of parallelism with sensor 2, as traffic noise is still detected, while the feeling is that leisure noise is reduced.



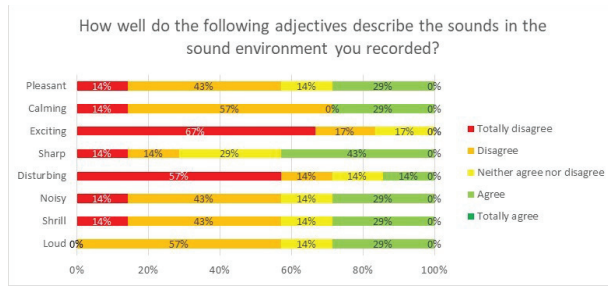


Figure 2. Descriptive assessment of the sound environment from sensor #3.

### 3.3. Sensor 4

Sensor #4 was located on a big avenue with heavy traffic (i.e., Riu Güell Street) all along the river Güell. It has several traffic lanes in both directions that continue to President Josep Tarradellas and Joan Avenue. Both streets cross the entire city from end to end. The sensor is not placed in the center of the city but on the path to multiple big supermarkets with parking lots, a school, some residential areas, and even an auditorium. The sound environment of this sensor is perceived better after lockdown than before the lockdown since 91% of the respondents selected the “Good” and “Very good” answers when asked about their home’s sound environment after the lockdown. Before the lockdown the “Good” and “Not bad/Not good” options were equally selected by 36% of the respondents and only 27% of the answers pointed to “Bad”. The sound environment around sensor #4 is perceived as Sharp by 45% of the respondents. It is the most positive voted adjective followed by Shrill, Calming, and Pleasant with 27% of the “Agree” option selected in each case. These outcomes contrast with the adjectives Exciting and Disturbing, which 81% on average relate to “Totally disagree” and “Disagree” answers. It would be noted that the perception of the adjectives Noisy and Loud spread along all possible options. According to [11], the street was considered to be noisy being traffic the main noise source. However, the most voted answer in both adjectives is “Disagree”, and hence it should not be considered a noisy or loud street during the survey period. It should be pointed out that the “Totally agree” and “Agree” options are also presented by 19% on average but still the “Disagree” and “Totally disagree” options represent a bigger part, with values over 50%, as observed in Figure 3.

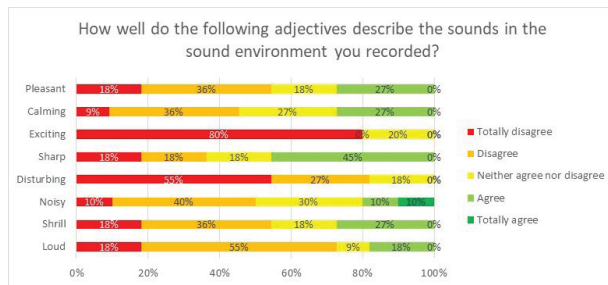


Figure 3. Descriptive assessment of the sound environment from sensor #4.

## 4. Conclusions

In this research work, we have compared data from acoustic sensors scattered in varied acoustic points in a medium-sized city (i.e., Girona, Spain) with the answers reported in a poll conducted around the same points. The authors are aware that the subjective data analyzed is a very small set of information. Nevertheless, it satisfies the goal of opening the door to the possibility of evaluating the soundscape with means of objective and calibrated measurements coming from the administration with citizen science campaigns, opened

to all people, maximizing the participation of a wider number of citizens. The answers reported in the survey, despite being a preliminary analysis with few data, are able to distinguish the sound sources present around a certain sensor and also match those noise sources detected in sensor data analysis. The results presented in this work align the objective measurements related to noise levels with the perception of the volunteers in this study living in the surroundings. There is a coherence between the former analysis [1], when the authors also analyzed the environmental sound before and during the lockdown from all and each of the sensors evaluated. In this work, the noise sources have been contrasted with the opinions of the participants in the campaign, deepening the knowledge of what happened in the soundscape of these two cities during the 2020 lockdown.

**Author Contributions:** Conceptualization, R.M.A.-P. and P.B.; methodology, D.B.-S. and E.D.; validation, R.M.A.-P. and C.M.-S.; resources, R.M.A.-P.; data curation, D.B.-S., C.M.-S. and E.D.; writing—original draft preparation, P.B., D.B.-S. and E.D.; writing—review and editing, C.M.-S. and R.M.A.-P.; supervision, R.M.A.-P.; project administration, R.M.A.-P.; funding acquisition, R.M.A.-P. All authors have read and agreed to the published version of the manuscript.

**Funding:** The research that led to this contribution has been conducted thanks to funding from Secretaria d'Universitats i Recerca from the Departament d'Empresa i Coneixement (Generalitat de Catalunya) and Universitat Ramon Llull, under the grant 2020-URL-Proj-054 (Rosa Ma Alsina-Pagès).

**Institutional Review Board Statement:** Not applicable.

**Informed Consent Statement:** Informed consent was obtained from all subjects in the study.

**Data Availability Statement:** Not applicable.

**Acknowledgments:** The authors would like to thank all the participants of this first data collection campaign of the project *Sons al Balcó*. The authors would also like to thank *Ajuntament de Girona* for the data collection in the Girona monitoring network.

**Conflicts of Interest:** The authors declare no conflicts of interest.

## Abbreviations

The following abbreviations are used in this manuscript:

WHO	World Health Organization
EU	European Union
SPL	Sound Pressure Level
$L_{Aeq}$	A-weighted equivalent sound level

## References

1. Alsina-Pagès, R.; Bergadà, P.; Martínez-Suquía, C. Sounds in Girona during the COVID Lockdown. *J. Acoust. Soc. Am.* **2021**, *149*. [CrossRef] [PubMed]
2. Farrés, J.C.; Novas, J.C. Noise level assessments: Subjective vs objective measures. In Proceedings of the Acoustics 2011, Gold Coast, Australia, 2–4 November 2011; pp. 140–142.
3. Caniato, M.; Bettarello, F.; Gasparella, A. Indoor and outdoor noise changes due to the COVID-19 lockdown and their effects on individuals' expectations and preferences. *Sci. Rep.* **2021**, *11*, 16533. [CrossRef] [PubMed]
4. Zera, J.; Brammer, A.J.; Pan, G.J. Comparison between subjective and objective measures of active hearing protector and communication headset attenuation. *J. Acoust. Soc. Am.* **1997**, *101*, 3486–3497. [CrossRef] [PubMed]
5. Ramphal, B.; Dworkin, J.D.; Pagliaccio, D.; Margolis, A.E. Noise complaint patterns in New York City from January 2010 through February 2021: Socioeconomic disparities and COVID-19 exacerbations. *Environ. Res.* **2022**, *206*, 112254. [CrossRef] [PubMed]
6. Baño, X.; Bergadà, P.; Bonet-Solà, D.; Egea, A.; Foraster, M.; Freixes, M.; Ginovart-Panisello, G.J.; Mallol, R.; Martín, X.; Martínez, A.; et al. Sons al Balcó, a Citizen Science Approach to Map the Soundscape of Catalonia. *Eng. Proc.* **2021**, *10*, 54.
7. Bonet-Solà, D.; Martínez-Suquía, C.; Alsina-Pagès, R.; Bergadà, P. The Soundscape of the COVID-19 Lockdown: Barcelona Noise Monitoring Network Case Study. *Int. J. Environ. Res. Public Health* **2021**, *18*, 5799. [CrossRef] [PubMed]
8. LimeSurvey Online Survey Tool. Available online: <https://www.limesurvey.org/en/> (accessed on 12 October 2020).
9. Alsina-Pagès, R.M.; Orga, F.; Mallol, R.; Freixes, M.; Baño, X.; Foraster, M. Sons al balcó: Soundscape Map of the Confinement in Catalonia. *Eng. Proc.* **2020**, *2*, 77.

10. Alsina-Pages, R.M.; Bergadà, P. *Evaluation of the  $L_{Aeq}$  Levels during the COVID-19 Lockdown Period Using a Static Wireless Acoustic Sensor Network in the City of Girona*; MDPI: Basel, Switzerland, 2021.
11. Martínez-Susquía, C.; Bergadà, P.; Alsina-Pages, R.M. Noise levels evolution before, during and after the COVID19 Lockdown in Girona. *Proc. Euronoise 2021, 2021*, 25–27.

**Disclaimer/Publisher's Note:** The statements, opinions and data contained in all publications are solely those of the individual author(s) and contributor(s) and not of MDPI and/or the editor(s). MDPI and/or the editor(s) disclaim responsibility for any injury to people or property resulting from any ideas, methods, instructions or products referred to in the content.

Proceeding Paper

# Bio-Magneto Sensing and Unsupervised Deep Multiresolution Analysis for Labor Predictions in Term and Preterm Pregnancies <sup>†</sup>

Ejay Nsugbe <sup>1,\*</sup>, Oluwarotimi Williams Samuel <sup>2</sup>, Jose Javier Reyes-Lagos <sup>3</sup>, Dawn Adams <sup>4</sup>  
and Olusayo Obajemu <sup>5</sup>

<sup>1</sup> Nsugbe Research Labs, Swindon SN1 3LG, UK

<sup>2</sup> School of Computing and Engineering, University of Derby, Derby DE22 1GB, UK; o.samuel@derby.ac.uk

<sup>3</sup> School of Medicine, Autonomous University of Mexico State (UAEMéx), Toluca de Lerdo 50180, Mexico; jjreyesl@uaemex.mx

<sup>4</sup> Southern Health and Social Care Trust, Northern Ireland BT63 5QQ, UK; dawn.adams@southerntrust.hscni.net

<sup>5</sup> Department of Automatic Control and Systems Engineering, University of Sheffield, Sheffield S10 2TN, UK; olusayoobajemu@gmail.com

\* Correspondence: ennsugbe@yahoo.com

<sup>†</sup> Presented at the 10th International Electronic Conference on Sensors and Applications (ECSA-10), 15–30 November 2023; Available online: <https://ecsa-10.sciforum.net/>.

**Abstract:** The effective prediction of preterm labor continues to be a topic of interest for research within pregnancy medicine, where uterine muscle contraction signals have shown to be insightful to predict a potential preterm birth. Magnetomyography (MMG) is a physiological-measurement-based tool which measures the orthogonal offset of bioelectrical manifestations from uterine contractions and may serve to predict potential premature deliveries with an enhanced accuracy. The decoding of the physiological signal is an area of substantial research where classical signal processing approaches and metaheuristics optimization routines have been utilized in the postprocessing and decomposition of MMG signals. This work requires a degree of expert knowledge and an understanding of tuning and parameter initialization. As a stride towards creating a more automated clinical decision support platform for predictions of preterm labor, we employ the use of a deep wavelet scattering (DWS) model. This methodology allows for a deep multiresolution analysis alongside unsupervised feature learning for the postprocessing of candidate MMG signals. DWS is combined with select pattern-recognition-based prediction machines in order to assemble a clinical decision pipeline for the prediction of the states of various pregnancies, with a greater degree of machine intelligence. The patient cohort consisted of a multi-ethnic demographic population composed of preterm and term pregnancies, where births occurred both under and over 48 h after labor commenced. Contrasting results were found between the various methods from the literature and DWS using the logistic regression algorithm. It was seen that DWS produced a slightly lower accuracy in comparison, as a trade-off for its streamlined unsupervised feature extraction process. Further work will now involve the application of various other machine learning methods in an attempt to assess and identify the most appropriate machine learning method with DWS that proves to be the most accurate.

**Keywords:** maternal care; signal decomposition; machine learning; signal processing; pregnancy; magneto sensing; electrodynamic; LSDL

**Citation:** Nsugbe, E.; Samuel, O.W.; Reyes-Lagos, J.J.; Adams, D.; Obajemu, O. Bio-Magneto Sensing and Unsupervised Deep Multiresolution Analysis for Labor Predictions in Term and Preterm Pregnancies. *Eng. Proc.* **2023**, *58*, 125. <https://doi.org/10.3390/ecsa-10-16245>

Academic Editor: Stefano Mariani

Published: 15 November 2023



**Copyright:** © 2023 by the authors. Licensee MDPI, Basel, Switzerland. This article is an open access article distributed under the terms and conditions of the Creative Commons Attribution (CC BY) license (<https://creativecommons.org/licenses/by/4.0/>).

## 1. Introduction

Labor is the culmination of pregnancy involving the safe delivery of a fetus from the womb of a female, where different timespans of birth, including preterm births, can occur during this process [1–3]. It is important to identify potential preterm births in order to commence proactive care strategies where necessary [1]. The medical literature and earlier research have shown that uterine contraction signals contain an encoding which

can be utilized in an analytical prediction of potential labor and an inference for a preterm birth [1]. As the uterine wall itself is a muscle, its involuntary contractions take place with ionic current flows, which are electrophysiological manifestations that can be measured from either a bioelectric or biomagnetic perspective [4]. The affordability and relative ease of acquisition of measurements via electrohysterogram (EHG) signals means that the majority of recordings come from a bioelectric perspective [1]. However, the limitations of EHG signals are based around the attenuation of the bioelectrical signals as they steadily travel through tissue from the source contractions to the receivers [1]. Regarding the orthogonal counterpart, the magnetic offset can be acquired with a magnetomyography (MMG) instrument which is robust from the aspect of tissue conductivities [4].

Prior studies into the use of MMG for the prediction of labor imminency has been performed by Eswaran et al. [5], who adopted a high-resolution superconducting quantum interference device array for reproductive assessments (SQUID Array for Reproductive Assessment (SARA)), which comprises 151 MMG channels. The dataset from Eswaran et al.'s [5] work has been utilized by multiple authors for various areas of research relating to this topic, including by the author of this paper alongside various signal processing and machine learning models towards improved predictions of imminent labor cases [6,7]. The majority of the analytics adopted involved the use of classical signal processing and multiresolution analysis, alongside various machine learning methods [7]. It should be noted that the adopted signal processing methods were stringent in their use of "handcrafted" features that relied on expert knowledge as part of their selection and extraction.

The emergence of deep learning has given rise to alternate means of feature extraction methods with the ability to extract deep multiscale features from a candidate signal without the need for any specific expert knowledge, in contrast to handcrafted features [8]. Deep wavelet scattering (DWS) comprises a merger between convolutional neural networks (CNNs) from the deep learning architecture and wavelet decomposition from the multiscale resolution aspect, which together allow multiresolution unsupervised feature extraction and characterization of a signal [8]. This recent approach has encountered an uprise in the literature, with applications spanning across various aspects of clinical medicine due to the appeal of having an automated and unsupervised feature extraction approach.

Thus, as part of this work, the authors aim to adopt the DWS method towards evaluating the extent to which it can differentiate between two sets of labor states based on the MMG dataset, whilst contrasting its performance with the prior related literature.

## 2. Materials and Methods

### 2.1. Materials

The dataset used for this work comes from the publicly available Physionet database, which hosts data from a number of pregnant patients who delivered a mixture of both term and preterm neonates, whilst spanning a range of ethnicities, i.e., Caucasian, Black, and Hispanic. The data contain two class labels, which correspond to patients whose labor was completed within 48 h of the MMG acquisition measurements, and those whose labor lasted over 48 h [9]. The data were initially acquired at an acquisition rate of 250 Hz, which was then subsequently downsampled to 32 Hz. An illustration of MMG data acquisition can be seen in Figure 1. A total of 22 patients' data were utilized for the work performed as part of this study.

A database containing further information on the data acquisition process, ethical approval and patient information consent, can be seen on the Physionet website [9].

### 2.2. Methods

#### 2.2.1. DWS

DWS is capable of extracting unsupervised features that are continuous and mostly robust to translations whilst comprising features of both wavelet decomposition and CNNs [8]. For DWS, the wavelets and filters are preset in order to reduce the overall computational complexity of the method; it also possesses the strength of being able to

work with a constrained number of samples due to its multiscale principle and configuration [8]. A mathematical formalism of the DWS configuration was proposed by Andén and Mallat [8], where the computational interpretation of DWS involves a deep CNN which is responsible for iterations, whilst convolving through the wavelets and nonlinear modules, alongside an average scaling function. For the implementation of DWS, the Gabor wavelet was used as the mother wavelet, while the scale invariance of 1 s was used; the filter banks were set to eight wavelets per octave in the first filter bank, followed by one wavelet per octave in the second filter bank.

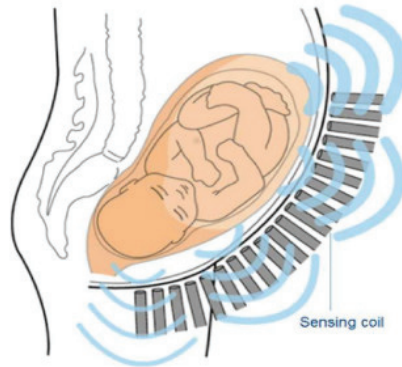


**Figure 1.** Illustration of MMG data acquisition [10].

### 2.2.2. Linear Series Decomposition Learner (LSDL)

In order to benchmark and contrast the performance of DWS, results of the LSDL from the literature were also included. The LSDL is a metaheuristically driven method which is capable of separating a candidate signal into multiple components with a view towards finding the optimal region in a signal that can minimize redundancies and maximize prediction accuracy [11–13]. Its algorithmic formulation is based around artificial-intelligence-based metaheuristic reasoning, which guides towards the systematic separation of a signal using a designated basis function alongside an embedded cost function [11–14].

The inception study for the LSDL was based on a source separation exercise involving a heterogeneous mixture of powders which produced highly variable nonlinear signals, for which the LSDL appeared adept at estimating, the results of which superseded classical wavelet decomposition [11–14]. The LSDL has been adopted in a multitude of other studies in which there exist signals that exhibit similar dynamic behavior to its inception exercise, which has led to applications within clinical medicine in areas spanning obstetric medicine, oncological medicine, surgical anesthesia, rehabilitation, and psychiatry [15–18]. The preprocessing act of the LSDL has been seen to enhance the modelling prowess of the candidate signals in question [15–18].

### 2.2.3. Handcrafted Features and Machine Learning Models

To form a contrastive basis for the results from DWS, the following features were extracted: mean of peaks, waveform length, slope sign change, root mean squared, cepstrum, maximum fractal length, median frequency, simple square integral, variance, fourth order autoregressive coefficient, Higuchi fractal dimension, detrended fluctuation analysis, peak frequency, and sum of peaks [4].

The SMOTE synthetic sample generator was also utilized as a means towards class balancing purposes in order to minimize the effect of decision bias on the classification models. The statistically driven logistic regression model was utilized as the classification model in this study, for which a K-fold cross-validation approach was adopted, where K was chosen as 10.

### 3. Results

The results in Table 1 show the accuracies of the model prediction of labor imminency across the various patients, from which it can be seen that DWS produced an accuracy of 62.7%. This is lower than the other methods, which produced accuracies of 90% and 70%, respectively. This indicates that, unlike previous works, DWS does not appear to be optimal in this application. The reasons for this remain subject to further research, but interim beliefs are based around the dynamics of the MMG signal, which make it unfeasible for effective analytics with DWS. In contrast, the LSDL produced a much better performance. However, there are benefits and positives associated with the use of each method; for example, the DWS does provide the benefit of enabling an unsupervised feature extraction process, which in turn negates the need for expert knowledge within that segment of the signal processing phase.

**Table 1.** Accuracies, merits and demerits of the models in predicting labor imminency.

Method	Accuracy (%)	Merits	Demerits	Reference
DWS	62.7	<ul style="list-style-type: none"> <li>- Unsupervised feature learning</li> <li>- No expert knowledge required</li> </ul>	<ul style="list-style-type: none"> <li>- Relatively low performance accuracy</li> <li>- No feature interpretations</li> </ul>	Present study
LSDL + Handcrafted Features	90	<ul style="list-style-type: none"> <li>- Computationally effective multiresolution decomposition</li> <li>- Optimal for this application as evidenced by accuracy</li> </ul>	<ul style="list-style-type: none"> <li>- Arduous tuning required for parameter initialization for the LSDL</li> <li>- Requires expert knowledge of features</li> </ul>	[7]
Handcrafted Features Only	70	<ul style="list-style-type: none"> <li>- Less processing time</li> <li>- Sparse tuning and parameter setting required</li> </ul>	<ul style="list-style-type: none"> <li>- Requires expert knowledge of features</li> </ul>	[7]

### 4. Conclusions

This work has investigated the notion of utilizing largely uninvestigated and novel means of signal processing in the prediction of labor imminency from a set of MMG signals. DWS was investigated for the first time for unsupervised feature learning and extraction prior to modelling of the signal with the use of a machine learning model. The results of this were contrasted with the LSDL + handcrafted features and handcrafted features only methods, where it was seen that for the LR model used, DWS had a slightly lower accurate classification accuracy score under various modelling conditions, albeit with the caveat of having a more streamlined process due to having an unsupervised component as part of its architecture.

In an attempt to optimize and improve the classification accuracy of DWS's predictions, further work will now involve the application of various other kinds of models to investigate which models provide the best pattern recognition results for DWS.

**Author Contributions:** All authors contributed equally to the article. All authors have read and agreed to the published version of the manuscript.

**Funding:** This research received no external funding.

**Institutional Review Board Statement:** The study did not require ethical approval as the dataset used was taken from an opensource database.

**Informed Consent Statement:** Informed consent was obtained from all subjects involved in the study.

**Data Availability Statement:** The data are available from a repository cited within the manuscript.

**Acknowledgments:** The authors would like to thank Brian Kerr from Kerr Editing for proofreading the manuscript.

**Conflicts of Interest:** The authors declare no conflict of interest.

## References

1. Nsugbe, E. A Cybernetic Framework for Predicting Preterm and Enhancing Care Strategies: A Review. *Biomed. Eng. Adv.* **2021**, *2*, 100024. [CrossRef]
2. World Health Organization Preterm Birth. Available online: <https://www.who.int/news-room/fact-sheets/detail/preterm-birth> (accessed on 25 August 2022).
3. Nsugbe, E.; Obajemu, O.; Samuel, O.W.; Sanusi, I. Enhancing Care Strategies for Preterm Pregnancies by Using a Prediction Machine to Aid Clinical Care Decisions. *Mach. Learn. Appl.* **2021**, *6*, 100110. [CrossRef]
4. Nsugbe, E.; Obajemu, O.; Samuel, O.W.; Sanusi, I. Application of Noninvasive Magnetomyography in Labour Imminency Prediction for Term and Preterm Pregnancies and Ethnicity Specific Labour Prediction. *Mach. Learn. Appl.* **2021**, *5*, 100066. [CrossRef]
5. Eswaran, H.; Preissl, H.; Wilson, J.D.; Murphy, P.; Lowery, C.L. Prediction of Labor in Term and Preterm Pregnancies Using Non-Invasive Magnetomyographic Recordings of Uterine Contractions. *Am. J. Obstet. Gynecol.* **2004**, *190*, 1598–1602; discussion 1602–1603. [CrossRef] [PubMed]
6. Babu, T.A.; Kumar, D. Features Extraction and Classification of Uterine Magnetomyography Signals. *Int. J. Curr. Eng. Sci. Res.* **2018**, *5*.
7. Nsugbe, E.; Sanusi, I. Towards an Affordable Magnetomyography Instrumentation and Low Model Complexity Approach for Labour Imminency Prediction Using a Novel Multiresolution Analysis. *Appl. AI Lett.* **2021**, *2*, e34. [CrossRef]
8. Andén, J.; Mallat, S. Deep Scattering Spectrum. *IEEE Trans. Signal Process.* **2014**, *62*, 4114–4128. [CrossRef]
9. Escalona-Vargas, D.; Govindan, R.B.; Furdea, A.; Murphy, P.; Lowery, C.L.; Eswaran, H. MMG Database 2016.
10. Zhang, M.; Rosa, P.S.L.; Eswaran, H.; Nehorai, A. Estimating Uterine Source Current during Contractions Using Magnetomyography Measurements. *PLoS ONE* **2018**, *13*, e0202184. [CrossRef] [PubMed]
11. Nsugbe, E.; Starr, A.; Ruiz-Carcel, C. Monitoring the Particle Size Distribution of a Powder Mixing Process with Acoustic Emissions: A Review. *Eng. Technol. Ref* **2016**, 1–12. [CrossRef]
12. Nsugbe, E. Particle Size Distribution Estimation of a Powder Agglomeration Process Using Acoustic Emissions. Ph.D. Thesis, Cranfield University, Cranfield, UK, 2017.
13. Nsugbe, E.; Starr, A.; Jennions, I.; Ruiz-Carcel, C. Estimation of Online Particle Size Distribution of a Particle Mixture in Free Fall with Acoustic Emission. *Part. Sci. Technol.* **2019**, *37*, 953–963. [CrossRef]
14. Nsugbe, E.; Williams Samuel, O.; Asogbon, M.G.; Li, G. Contrast of Multi-Resolution Analysis Approach to Transhumeral Phantom Motion Decoding. *CAAI Trans. Intell. Technol.* **2021**, *6*, 360–375. [CrossRef]
15. Nsugbe, E.; Ser, H.-L.; Ong, H.-F.; Ming, L.C.; Goh, K.-W.; Goh, B.-H.; Lee, W.-L. On an Affordable Approach towards the Diagnosis and Care for Prostate Cancer Patients Using Urine, FTIR and Prediction Machines. *Diagnostics* **2022**, *12*, 2099. [CrossRef] [PubMed]
16. Nsugbe, E.; Connelly, S. Multiscale Depth of Anaesthesia Prediction for Surgery Using Frontal Cortex Electroencephalography. *Healthc. Technol. Lett.* **2022**, *9*, 43–53. [CrossRef] [PubMed]
17. Nsugbe, E. On the Application of Metaheuristics and Deep Wavelet Scattering Decompositions for the Prediction of Adolescent Psychosis Using EEG Brain Wave Signals. *Digit. Technol. Res. Appl.* **2022**, *1*, 9–24. [CrossRef]
18. Nsugbe, E.; Phillips, C.; Fraser, M.; McIntosh, J. Gesture Recognition for Transhumeral Prosthesis Control Using EMG and NIR. *IET Cyber-Syst. Robot.* **2020**, *2*, 122–131. [CrossRef]

**Disclaimer/Publisher’s Note:** The statements, opinions and data contained in all publications are solely those of the individual author(s) and contributor(s) and not of MDPI and/or the editor(s). MDPI and/or the editor(s) disclaim responsibility for any injury to people or property resulting from any ideas, methods, instructions or products referred to in the content.



Proceeding Paper

# Computational Feasibility Study for Time-Frequency Analysis of Non-Stationary Vibration Signals Based on Wigner-Ville Distribution <sup>†</sup>

Luis Otávio de Angeles Dias \*, Pedro Oliveira Conceição Junior and Paulo Monteiro de Carvalho Monson

Department of Electrical and Computer Engineering, São Carlos School of Engineering (EESC), University of São Paulo (USP), São Carlos 13566-590, SP, Brazil; pedro.oliveira@usp.br (P.O.C.J.); paulo.monson@usp.br (P.M.d.C.M.)

\* Correspondence: luisotavio1906@usp.br; Tel.: +55-18-99747-1001

<sup>†</sup> Presented at the 10th International Electronic Conference on Sensors and Applications (ECSA-10), 15–30 November 2023; Available online: <https://ecsa-10.sciforum.net/>.

**Abstract:** The time-frequency analysis has garnered attention for research due to its applications in studying non-stationary signals, revealing information often obscured by conventional time or frequency domain analysis. This study aims to reduce the computational cost associated with large dataset analysis using the smoothed pseudo Wigner-Ville distribution (WVD), a valuable time-frequency tool for analyzing various signal data. We used a 9000-sample acoustic signals from a milling machine, sampled at 100 kHz. Three approaches were pursued: the first consisting in calculating the average WVD from equidistant time windows; the second consisting in reducing the sampling rate by a factor of 'k' by creating an array where each 'nth' element corresponds to the 'k\*nth' element of the original signal; and the third consisting in a joint analysis, incorporating a preprocessing routine into the second method. The mean WVD method distorted the time-frequency diagram with middle-range frequencies, while the second approach preserved the WVD, even with significant 'k' factors, reducing analysis time significantly. The Incorporation of the preprocessing routine in the sampling rate reduction process markedly reduces analysis time.

**Keywords:** wigner ville; non stationary; time-frequency analysis

**Citation:** de Angeles Dias, L.O.; Conceição Junior, P.O.; Monson, P.M.d.C. Computational Feasibility Study for Time-Frequency Analysis of Non-Stationary Vibration Signals Based on Wigner-Ville Distribution. *Eng. Proc.* **2023**, *58*, 126. <https://doi.org/10.3390/ecsa-10-16193>

Academic Editor: Stefano Mariani

Published: 15 November 2023



**Copyright:** © 2023 by the authors. Licensee MDPI, Basel, Switzerland. This article is an open access article distributed under the terms and conditions of the Creative Commons Attribution (CC BY) license (<https://creativecommons.org/licenses/by/4.0/>).

## 1. Introduction

Machine learning-based artificial intelligence systems are becoming increasingly important in monitoring conditions in manufacturing processes due to the possibilities of automating manual processes and making real-time decisions based on data generated by sensors. Following new industrial practices and the concept of Industry 4.0, such intervention will ensure a smarter and automated manufacturing process, resulting in improved quality and cost reduction [1–3].

Convolutional neural networks (CNNs) stand out as powerful tools for the tasks mentioned above, particularly for image recognition and processing through deep learning algorithms. These algorithms can be trained to recognize patterns indicating tool wear onset, predict when a tool needs replacement, classify different levels of wear, and estimate remaining useful life. However, technical challenge when using CNNs is related to long sequences, such as those derived from monitoring a manufacturing process, which can become a complex task requiring high computational demand. In the study conducted by Wang and Oates [4], an approach for transforming time series data into images was developed, enabling the extraction of features by CNN in time series analysis. While the strategy of converting time series into images has proven effective, due to the aforementioned challenges, there is a need for tools that can overcome the limitations of training with long sequences and provide greater clarity in interpreting their decisions.

Therefore, the aim of the present study is to assess the feasibility of using time-frequency representations as a feature extraction tool from non-stationary signals, while also providing the ability to correlate the tool condition with changes in the frequency spectrum corresponding to the acoustic signal. The data analyzed in this work corresponds to the study of the milling process. It is employed for the manufacturing of a wide variety of parts, characterized by its ability to remove material from the surface of the work-piece, giving it complex shapes and precise finishing. The machining process of parts inevitably involves the wear of the milling cutter, resulting in a gradual loss of its cutting precision. This degradation can lead to the production of parts with inadequate finishing or damage. Hence, in order to enhance this operation's quality, it is of great ambition to monitor the preceding phenomenon. In this study, time series data based on acoustic emission signals related to the milling tool wear were transformed into images using the Wigner-Ville distribution (WVD), as employed by Scholl [5]. The time-frequency representation will be particularly useful in examining the variable frequency content at different time intervals in the signal, potentially providing additional insights into the level, intensity, and onset of tool wear. Related approaches in the literature have used short-time Fourier transform [6] and wavelet transform [7]. The WVD method serves as an alternative not yet reported within the scope of this study. A scientific gap lies at the computational cost associated with applying WVD to large datasets, limiting its practical utility. This study addresses this challenge by employing methods such as the average spectrum, sampling frequency reduction, and joint signal analysis to overcome the computational cost of WVD, enabling more reliable analysis of non-stationary signals. The results are also expected to contribute to the automation of the manufacturing process and the optimization of tool life in machining operations, specifically focusing on the milling process.

## 2. Material and Methods

Three ways to carry out the diminish of computational cost aforementioned were proposed, which will be detailed in the following subtopics.

### 2.1. Dataset

The dataset taken as reference was obtained from the work of [8], which consists of a MATLAB structure composed of acoustic emission signals with 9000 samples, obtained from a sampling frequency of 100 kHz using the WD 925 sensor for monitoring purposes. The experiments of the dataset were conducted on a milling machine for different speeds, feeds, and depth of cut. The tool wear, VB, was also measured for each test series. For the first two subsequent analysis, the signal was filtered by a band-pass filter at the band 5 to 7 kHz with the objective of easing the analysis.

### 2.2. Methodology of the Resulting Average Spectrum

In this methodology, three sample windows were extracted from the original signal, all of the same size, representing three different instants of the sampling: the beginning, middle, and end of the milling process. From these three sub-signals, a fourth one was generated following the relationship presented in the equation below:

$$a_{mi} = \frac{a_{1i} + a_{2i} + a_{3i}}{3}$$

where  $a_{mi}$ ,  $a_{1i}$ ,  $a_{2i}$ ,  $a_{3i}$  are the  $i$ -th terms, respectively, of the final sub-series and the three time windows taken from the original signal.

### 2.3. Methodology of Reducing the Sampling Frequency

In this approach to mitigate the computational cost of the WVD, a sub-series of the original signal was generated in such a way that:

$$b_i = k \cdot a_i$$

where  $b_i, a_i$  represent, respectively, the  $i$ -th term of the resulting signal and the original signal. In the meantime, the resulting signal is a version of the original signal sampled at a sampling frequency:

$$f_b = \frac{f_a}{k}$$

where  $f_b$  and  $f_a$  are the respective sampling frequencies of the resulting signal and the original, and  $k$  is the sampling frequency division factor.

#### 2.4. Joint Analysis

It was also tracked a joint analysis based on associating the aforesaid method of diminishing the sample frequency with a preprocessing of the signals analysed. The latter was executed in two main steps. First, signal noise was eliminated by applying a low-pass filter with cut frequency of 40 kHz. The selection of this frequency band also better simulates the research conditions, since it represents the overall band of the acoustic emission signal. Then, undesired transient information was eliminated by selecting an interval of the original signal correspondent to the stabilization of the milling process.

As a result of the 40 kHz bandwidth and following the Nyquist Criterion, the new sampling frequency taken was 80 kHz, which means a division factor of:

$$k = 1.25$$

This factor was obtained by discarding every sample whose position was a multiple of five from the original signal.

### 3. Results and Discussion

#### 3.1. Methodology of the Resulting Average Spectrum

For the sake of simplicity, the following methods' results will be shown for only one signal from the dataset mentioned previously. The WVD of the signal, without any prior treatment, is shown in the Figure 1.

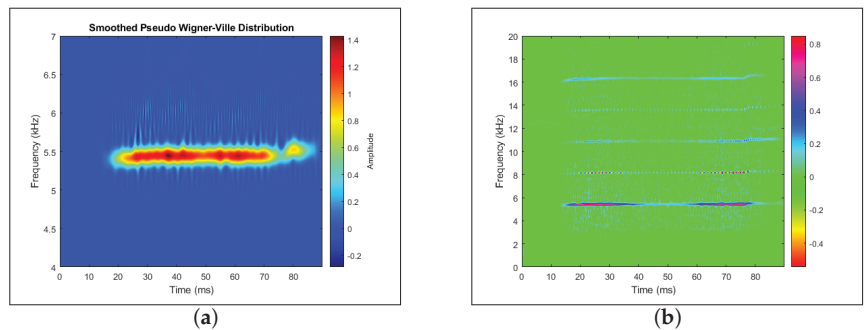


**Figure 1.** WVD of the Signal. (a) For the band 4 kHz to 7 kHz. (b) For the full signal band.

#### 3.2. Methodology of the Resulting Average Spectrum

The analysis of the average spectrum from 2000 and 3000 sample windows based on the WVD is shown in Figure 2 below. In this figure, the horizontal axis represents time in seconds, while the vertical axis represents the signal's component frequency in Hz.

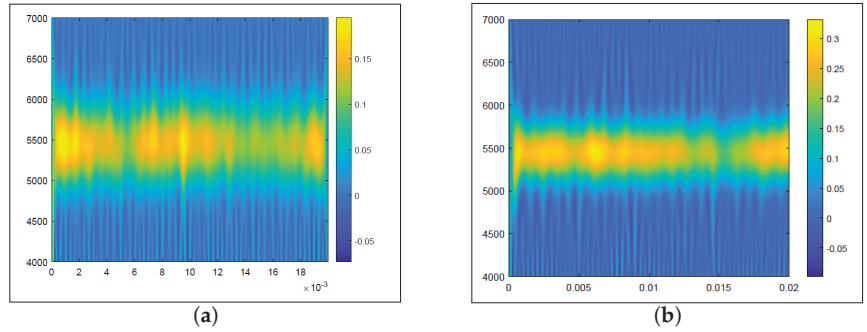


**Figure 2.** Mean spectrum for 2000 and 3000 sample windows. (a) WVD of the average spectrum obtained from 2000 samples of the original signal. (b) WVD of the average spectrum obtained from 3000 samples of the original signal.

Using the methodology of the average spectrum, the compilation time for the observed plot was significantly shorter than that taken to produce Figure 1a. Furthermore, the signal’s spectral density remains close to 5.5 kHz, as in the original plot. However, it is noteworthy that no windowing time adopted was able to faithfully reproduce the original signal’s spectrum. The reason for this mismatch between the spectra presented in Figure 2 and the original spectrum is due to the multidimensional nature of the tool used. The calculation of the average between the spectra of the adopted time windows resulted in the mixing of the energy densities of the spectrum in these analyzed time intervals, resulting in distortions in the final average spectrum that propagate throughout the temporal extension of the WVD.

3.3. Methodology of Reducing the Sampling Frequency

The compilation of spectra for this methodology took significantly less time than that spent on the average spectrum analysis and notably yielded better results compared to the method being compared, maintaining the signal’s spectrum even for a sample size six times smaller than the original signal. However, it can be observed from Figure 3b that the tool loses resolution with high values of  $k$ . This occurs as the sampling frequency division ( $F_a$ ) must still adhere to Nyquist’s Law, which dictates that  $F_a$  must be at least 2 times greater than the signal’s bandwidth. Since the original signal has a bandwidth of 40 kHz, the reduction in sampling frequency could not adopt values of the division factor  $k$  large enough for a useful reduction in computational cost. In this scope, greater changes in time analysis, using this approach, can only be achieved for lower frequency bands of the signal.

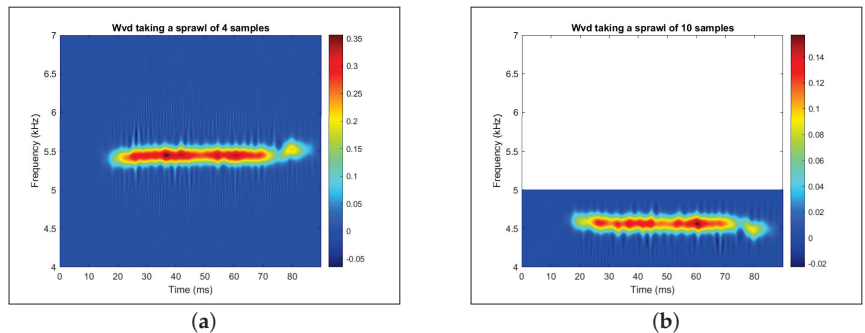


**Figure 3.** WVD obtained for different sampling frequency division factors  $k$ . (a) WVD for  $k = 4$ . (b) WVD for  $k = 10$ .

### 3.4. Joint Analysis

By analyzing the signal time-series plot, it can be observed that the moment where the milling process stabilizes is approximately 20–70 ms. This interval corresponds for samples number 2000 to 7000 of the signal.

Applying the original signal by a band-pass filter from 1–40 kHz, dividing the sample rate by a factor of 1.25 and taking the aforementioned interval of the signal results in Figure 4:

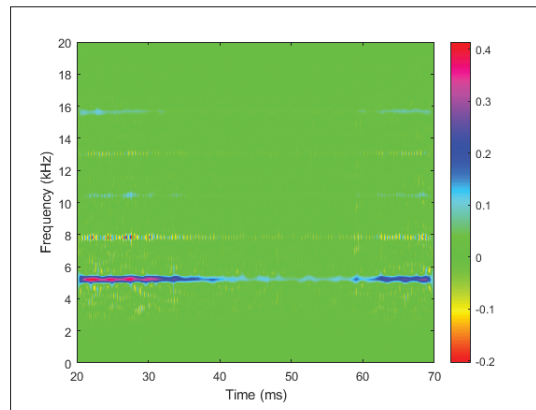


**Figure 4.** WVD of the signal after joint analysis.

Figure 4 is identical to Figure 1b, with the only difference being the time range. The time taken to plot the former was about 5 s, while the latter took 75 s to be prepared. This proves that the approach reported in this subsection is of great efficiency, and enhances significantly the time of analysis without damaging the original information.

## 4. Conclusions

This research delved into the realm of time-frequency analysis, with a specific focus on addressing the computational challenges associated with the analysis of large datasets. The study harnessed the smoothed pseudo Wigner-Ville distribution (WVD) as a potent tool for time-frequency analysis, utilizing a 9000-sample acoustic signal from a milling machine, sampled at 100 kHz, and filtered between 1 kHz to 8 kHz. In essence, this research has showcased the feasibility of employing a joint preprocessing of the signal, consisting in incorporating noise and transient data elimination to the second method formerly presented, as a valuable technique for reducing the computational burden associated with large dataset analysis in the realm of time-frequency analysis. By offering a pragmatic solution that balances computational efficiency with the preservation of analytical fidelity, this study paves the way for more efficient and expedited analysis of non-stationary signals in various applications. The findings of this research can be instrumental in enhancing the practicality and utility of time-frequency analysis for researchers and practitioners working with substantial datasets in diverse fields.

**Author Contributions:** Conceptualization, P.O.C.J., L.O.d.A.D., and P.M.d.C.M.; methodology, P.O.C.J. and L.O.d.A.D.; software, L.O.d.A.D.; validation, P.O.C.J. and L.O.d.A.D.; formal analysis, P.O.C.J., L.O.d.A.D. and P.M.d.C.M.; investigation, L.O.d.A.D.; resources, P.O.C.J.; data curation, P.O.C.J. and L.O.d.A.D.; writing—original draft preparation, L.O.d.A.D.; writing—review and editing, P.O.C.J. and L.O.d.A.D.; visualization, L.O.d.A.D.; supervision, P.O.C.J.; project administration, P.O.C.J.; funding acquisition, P.O.C.J. All authors have read and agreed to the published version of the manuscript.

**Funding:** This research was funded by the São Paulo Research Foundation (FAPESP), under grants: #2023/02413 and #2023/02447-4, and the Pro-Rectorcy of Research and Innovation of the University of São Paulo (USP), under grant: #22.1.09345.01.2.

**Institutional Review Board Statement:** Not applicable.

**Informed Consent Statement:** Not applicable.

**Data Availability Statement:** Publicly available dataset was analyzed in this study. This data can be found here: [<https://www.nasa.gov/intelligent-systems-division/discovery-and-systems-health/pcoe/pcoe-data-set-repository/>]. 3. Milling. (accessed on 5 April 2023).

**Acknowledgments:** The authors would like to thank the São Paulo Research Foundation (FAPESP) and the Pro-Rectorcy of Research and Innovation of the University of São Paulo (USP) for supporting this research work.

**Conflicts of Interest:** The authors declare no conflict of interest.

### Abbreviations

The following abbreviations are used in this manuscript:

WVD Wigner–Ville Distribution  
CNN Convolutional Neural Networks

### References

1. Çınar, Z.M.; Abdussalam Nuhu, A.; Zeeshan, Q.; Korhan, O.; Asmael, M.; Safaei, B. Machine Learning in Predictive Maintenance towards Sustainable Smart Manufacturing in Industry 4.0. *Sustainability* **2020**, *12*, 8211. [CrossRef]
2. Ding, H.; Gao, R.X.; Isaksson, A.J.; Landers, R.G.; Parisini, T.; Yuan, Y. State of AI-Based Monitoring in Smart Manufacturing and Introduction to Focused Section. *IEEE/ASME Trans. Mechatron.* **2020**, *25*, 2143–2154. [CrossRef]
3. Serin, G.; Sener, B.; Ozbayoglu, A.M.; Unver, H.O. Review of tool condition monitoring in machining and opportunities for deep learning. *Int. J. Adv. Manuf. Technol.* **2020**, *109*, 953–974. [CrossRef]
4. Wang, Z.; Oates, T. Imaging Time-Series to Improve Classification and Imputation. *arXiv* **2015**, arXiv:1506.00327. [CrossRef]
5. Scholl, S. Fourier, Gabor, Morlet or Wigner: Comparison of Time-Frequency Transforms. *arXiv* **2021**, arXiv:2101.06707. [CrossRef]
6. Huang, Z.; Zhu, J.; Lei, J.; Li, X.; Tian, F. Tool Wear Monitoring with Vibration Signals Based on Short-Time Fourier Transform and Deep Convolutional Neural Network in Milling. *Math. Probl. Eng.* **2021**, *2021*, 9976939. [CrossRef]
7. Aghazadeh, F.; Tahan, A.; Thomas, M. Tool condition monitoring using spectral subtraction and convolutional neural networks in milling process. *Int. J. Adv. Manuf. Technol.* **2018**, *98*, 3217–3227. [CrossRef]
8. Kai Goebel, A.A. *Documentation for Mill Data Set*; NASA AMES Research Center: Mountain View, CA, USA, 2007.

**Disclaimer/Publisher’s Note:** The statements, opinions and data contained in all publications are solely those of the individual author(s) and contributor(s) and not of MDPI and/or the editor(s). MDPI and/or the editor(s) disclaim responsibility for any injury to people or property resulting from any ideas, methods, instructions or products referred to in the content.



Proceeding Paper

# Machine Learning DFT-Based Approach to Predict the Electrical Properties of Tin Oxide Materials <sup>†</sup>

Hichem Ferhati <sup>1,2</sup>, Tarek Berghout <sup>3</sup>, Abderraouf Benyahia <sup>1</sup> and Faycal Djeflal <sup>1,\*</sup>

<sup>1</sup> Laboratoire Electronique Avancée (LEA), Department of Electronics, University of Batna 2, Batna 05000, Algeria; hichemferhati@gmail.com (H.F.); araoufbenyahia@gmail.com (A.B.)

<sup>2</sup> Institut Sciences Techniques Appliquées (ISTA), University of Larbi Ben M'hidi, Oum El Bouaghi 04000, Algeria

<sup>3</sup> Laboratory of Automation and Manufacturing Engineering, University of Batna 2, Batna 05000, Algeria; t.berghout@univ-batna2.dz

\* Correspondence: faycal.djeflal@univ-batna2.dz

<sup>†</sup> Presented at the 10th International Electronic Conference on Sensors and Applications (ECSA-10), 15–30 November 2023; Available online: <https://ecsa-10.sciforum.net/>.

**Abstract:** The effects of oxygen concentration and growth technique during the deposition process on the electrical properties of tin oxide alloy (SnOx) should be investigated for developing new eco-friendly photosensors and photovoltaic devices. The present work aims to predict the electrical key governing parameters throughout the device developing processes such as the Energy level values and band-gap energy as function of the injected oxygen concentrations. For realization, over 100 data points were collected by modeling the effect of oxygen contents on the SnOx electrical properties using Density Function Theory (DFT). Through extensive Machine Learning (ML) analysis, the impact of the oxygen concentration on the electrical properties and the material type is well predicted, where the applied ML prediction model for band-gap energy showed a good correlation between predicted values and the calculated ones using DFT computations. It is revealed that the combined DFT-ML-based approach can be a powerful tool to study and accelerate the developing of new highly efficient materials for microelectronic applications.

**Keywords:** tin-oxide; DFT; machine learning; prediction; photosensors

**Citation:** Ferhati, H.; Berghout, T.; Benyahia, A.; Djeflal, F. Machine Learning DFT-Based Approach to Predict the Electrical Properties of Tin Oxide Materials. *Eng. Proc.* **2023**, *58*, 127. <https://doi.org/10.3390/ecsa-10-16017>

Academic Editor: Stefano Mariani

Published: 15 November 2023



**Copyright:** © 2023 by the authors. Licensee MDPI, Basel, Switzerland. This article is an open access article distributed under the terms and conditions of the Creative Commons Attribution (CC BY) license (<https://creativecommons.org/licenses/by/4.0/>).

## 1. Introduction

Tin oxide (SnOx) semiconducting alloys have been considered promising candidates for the next generation of microelectronic materials, and have attracted considerable attention in developing high-performance sensing devices (e.g., photodetectors, gas sensors, photocatalysts, photovoltaics, . . . , etc.) because of their scalable elaboration techniques, tunable electrical and optical properties, good light-matter interactions, adjustable electronic energy band structures, and excellent gas-molecules-interaction properties [1–4]. Tuning the electrical and sensing properties of tin-oxide-based alloys can be carried out using deferent experimental approaches such as chemical doping, strain engineering, and changing the elemental composition (i.e., tin and oxide). The latter technique is considered as an effective approach to modulate the optical, electrical, and structural parameters, where it was demonstrated that the sensing properties of the material are significantly affected by the band-gap energy value and the elemental composition ratio in the SnOx alloy. In other words, the oxygen concentration can be varied in the SnOx film, which can modify its electronic and optical properties. Consequently, the impact of oxygen content on the electrical characteristics of SnOx should be investigated to offer new insights in developing eco-friendly and high-performance devices for sensing applications.

In this work, a new modeling framework approach is proposed to predict the electrical key governing parameters throughout the device, developing processes such as the Energy

level values and band-gap energy as function of the injected oxygen concentrations. To do so, over 100 data points were collected by modeling the impact of the oxygen contents on the SnOx electrical properties using Density Function Theory (DFT). Through extensive combined DFT-ML (Machine Learning) analysis, the effect of the oxygen concentrations on the electrical properties and the material type (metal, P-type and N-type) is well predicted, where the applied ML prediction model for band-gap energy showed a good correlation between predicted values and the calculated ones using DFT computations.

## 2. Modeling Frameworks

In this section, multipurpose modeling approaches are considered to predict the electrical properties of SnOx-based alloys based on combined DFT-ML calculations. The first step will be used to build the required database to forecast the electronic properties of SnOx thin-film using DFT computations. Secondly, the ML-based calculations will be employed to predict the impact of the oxygen concentration on the electrical properties and the material type of the tin-oxide materials.

### 2.1. DFT Calculations

In the present work, the DFT-based calculation technique was used to perform the band structure electrical properties of SnO super-cell [4]. The band structure calculations were carried out using generalized gradient approximation (GGA) with the Perdew–Burke–Ernzerhof (PBE) functional and the Heyd–Scuseria–Ernzerhof screened Coulomb (HSE06) hybrid-functional [4]. The experimental lattice constants are used for the initial structure of SnO. Moreover, the tetragonal system of the rutile SnO with stable crystalline phase is considered. In order to study the impact of the oxygen concentration on the SnO structure, additional interstitial oxygen atoms were introduced in the SnO super-cell at its lattice. In addition, the SnO semiconductor type is determined from the Fermi-level position provided by DFT calculations. It is important to note that the SnO semiconductor type obtained from DFT simulations is in good agreement with the experimental results.

### 2.2. ML Algorithm

Machine learning (ML) has been demonstrated to be a powerful tool in overcoming high-cost experimental tests and practice limitations in understanding the parameters affecting material properties and their relationships [5]. Therefore, the use of ML techniques in the development of new materials for sensing applications, including SnOx alloy, is on an upward trajectory. In this work, we explore the use of ML techniques to assess the impact of oxygen concentration on the electrical behavior of SnOx alloy for sensing applications. The ML model has been trained using our DFT-based calculation database. Correlation analysis and machine learning algorithms have been employed to study key parameters affecting material properties and their interactions. DFT-ML predictive approach has been developed to determine the material type and the band-gap energy values associated with oxygen concentration, offering fast and crucial guidance for experimental elaboration of SnOx-based sensing devices.

## 3. Results and Discussion

The obtained band structure of SnO<sub>2</sub> is depicted in Figure 1 using DFT calculations. It can be shown from this figure that the SnO<sub>2</sub> material exhibits a wide band gap of 3.56 eV with a direct transition mechanism at G symmetric point. The obtained results make SnO<sub>2</sub> a potential material for developing Ultra-Violet photodetectors and gas sensors. Moreover, in order to investigate the impact of the oxygen concentration on the material band-gap energy, Figure 2 plots the variation of band-gap energy values as function of oxygen concentrations. It is clearly shown that the introduction of oxygen can induce variations on the bond angle caused by the disorder of octahedra, which leads also to increase the tin oxide band gap values. The tunability of band-gap energy values and the type of material can open up new paths in developing multispectral photodetectors and new devices for gases sensing.



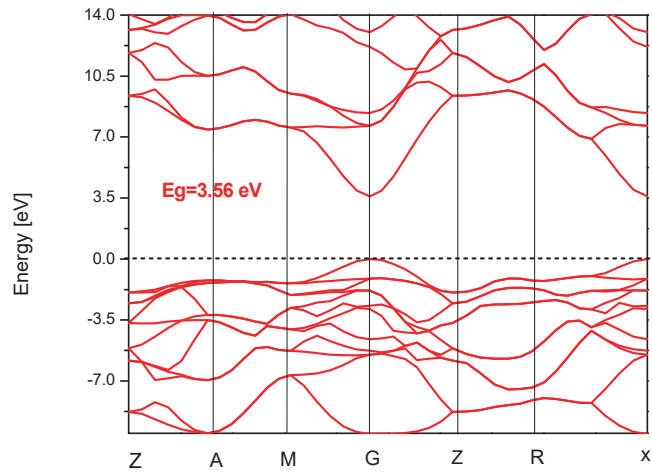


**Figure 1.** Band structure of thin-film SnO<sub>2</sub> based on DFT calculations.

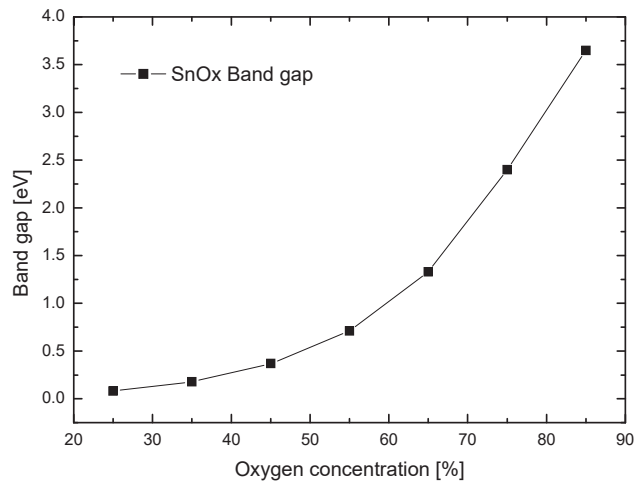


**Figure 2.** Variation of band gap energy as a function of the oxygen concentration for SnO<sub>x</sub> material.

From an ML modeling perspective, these collected data can be visualized as presented in Figure 3 for a better understanding of both data change and complexity, respectively. Figure 3a shows variation of energy gap with respect to oxygen concentration. Likewise, it represents differences in data linked to doping type. Regarding the former's data drift, it is a somewhat exponential variation referring to a rapid change in data characteristics. Meanwhile, the doping type data points are divided into three categories, namely metallic (m), p-type (p), and n-type (n) semiconductors. The obtained data distributions show a kind of data imbalance that is perfectly revealed by class ratio calculation in Figure 3b. In addition, it is worth mentioning that data patterns in this case do not show any signs of noise or outliers in collected measurements, which requires less data processing except for normalization. Under such circumstances, ML modeling requirements face two main challenges, particularly data drift (i.e., continuous change in data characteristics) and data complexity (i.e., class imbalance). To combat such challenges, this work proposed the following contributions [6].

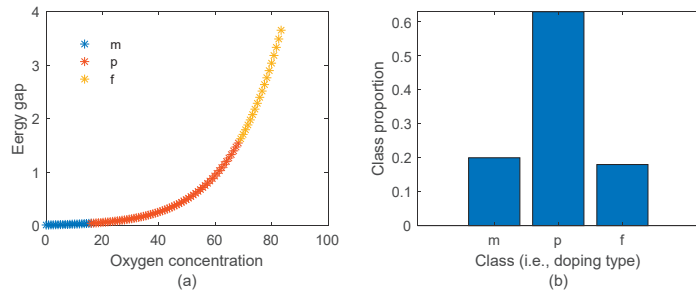


**Figure 3.** Visualizing data from perspective of ML modeling: (a) regression function and class scatters; (b) class proportion.

**Adaptive learning:** Adaptive learning rules of the long-short term memory neural network are involved in this case, while training a single-layer neural network for both energy gap prediction and dope type classification. This ensures that the learning model is kept up-to-date by tracking only upcoming important new data.

**Data sampling:** To solve the class imbalance problem, the synthetic minority over sampling technique is involved in this case [5]. Such a technique helps to overcome this variation in the class proportion ratio by generating synthetic examples of the minority class, thereby enabling fair representations of data points and preventing model bias towards majority class. However, an important issue could arise as a result of this contribution. First, since adaptive learning rules from long-short term memory network experience deeper representations, 100 single-dimensional points are considered a lightweight problem to solve. This can lead to a so-called underfitting problem. Second, generating data using the aforementioned synthetic minority oversampling technique may result in different drawbacks related to increased risk of misclassification due to the difficulty in generating informative samples. Therefore, an additional process of monitoring learning and validating the ML model is urgently needed. Consequently, the cross-validation technique constitutes a third contribution to this work.

**Cross-validation:** cross-validation allows for efficient use of data, thereby increasing the robustness and reliability of performance estimation by dividing data into different folds and performing tests on the entire dataset [6]. In this work, the neural network used is subjected to manual tuning following simple error-trial learning rules. The following Table 1 presents the final parameters achieved for the classification and regression problems.

**Table 1.** Parameters tuning results.

Hyperparameters	Regression	Classification
Maximum number of epochs	50	250
Mini-batch size	10	5
Neurons	20	30
Learning algorithm	Adam optimizer	RMS propagation
Initial learning rate	0.01	0.1
Gradient threshold	1	1
L2 regularization	0.0001	0.0001

Training and evaluation of the discussed ML model goes through a three-fold cross-validation process for both problems. The performance of ML modeling for the regression process is evaluated using well-known metrics, including root mean square error (RMSE), root mean squares (RMS), and mean absolute error (MAE). The expected result of these measurements is to get closer to “zero” for greater accuracy of approximation and generalization. Additionally, the famous  $R^2$  metric is also included, while when its value approaches “one”, it refers to better performance. Similarly, classification performance evaluations involve four different metrics well-used in the literature, including accuracy, F1

score, recall, and precision. The expected result of the classification metrics is to approach the value “one”. In this work, we focused on collecting results from the validation set because they are more important than the training set, because in this case, they make it possible to observe both generalization and approximation capacities at the same time. It is also worth mentioning that such experiments are conducted on an i7 processing unit computing with a power of 16 GB RAM and 12 MB cache memory. Additionally, a MATLAB r2023a library is used as the main programming platform for this application. Table 2 is dedicated to summarizing results obtained from the whole experiment. On the one hand, discussing results obtained on the regression problem, the prediction models behave in a similar way. This means that they have the ability to induce stability even across different datasets/folds. This is proven by the performance evaluation results of RMSE, MSE, and MAE, respectively, in validation folds from 1 to 3. Their mean values and standard deviation also explain the similarity of results obtained. Likewise,  $R^2$  values show the same patterns of prediction stability and similarity between other folds, achieving an excellent performance of 0.71. On the other hand, the averaged values of the classification metrics show impressive results in terms of stability and accuracy, reaching 0.99 for all metrics with a very small standard deviation of 0.008, while most models show 100% prediction performance.

**Table 2.** Summary of obtained results.

Regression				
Cross-validation Folds	RMSE	MSE	MAE	$R^2$
1	0.51	0.26	0.28	0.72
2	0.41	0.17	0.20	0.71
3	0.56	0.31	0.38	0.69
Average	0.49	0.25	0.29	0.71
Standard deviation	0.1341			0.01
Classification				
Crossvalidation folds	Accuracy	F1 score	Recall	Precision
1	1	1	1	1
2	1	1	1	1
3	0.98	0.98	0.98	0.98
Average	0.99	0.99	0.99	0.99
Standard deviation	0.008			

Overall, the obtained results are promising for the application of such modeling process in predicting the electronic, optical, and electrical properties of wide band gap materials, which can be effective for the design of alternative opto-electronic and gas-sensing devices. However, certain points/limitations must be taken into account when generalizing such investigations to real applications. These points can be addressed as follows:

- An amount of 100 data points are somehow too small for results generalizability in terms of regression.
- A total of three different types of classes with different propositions under a too small set of data can create problems of misrepresentation of data when using generative models during data balancing.
- There is a higher probability staking in overfitting when trying further number of cross validation folds.

#### 4. Conclusions

In this paper, the effect of oxygen concentration on the electronic properties of SnOx material is investigated. First-principles calculations are carried out to estimate the band gap of SnOx material for various oxygen levels. It is found that the material band gap increases with the oxygen content increase to reach its highest value of 3.56 eV corresponding to oxygen-rich SnOx. Machine Learning analysis are then performed to predict the electronic

properties and material type of SnOx alloy with varied oxygen containing for photodetectors and gas-sensing applications. Adaptive learning rules of long-term memory under cross-validation techniques are involved during the ML modeling process. Additionally, synthetic minority oversampling techniques are integrated into the classification process. The whole methodology turns out to be very effective for both regression and classification, achieving impressive results, especially for classification. Regarding future opportunities, and consistent with the limitations discussed in Section 3, future opportunities will revolve around: (i) targeting an even more massive and complex dataset; (ii) discussing different ML tools under different adaptive learning algorithms; (iii) discussing other generative modeling and subsampling tools to address class imbalance issues. The obtained results make the proposed approach a power tool for fast and accurate predicting the electrical properties metal oxides for sensing applications.

**Author Contributions:** Conceptualization, H.F., T.B. and F.D.; methodology, F.D.; validation, H.F., T.B. and F.D.; formal analysis, H.F., T.B., A.B. and F.D.; investigation, H.F., T.B., A.B. and F.D.; data curation, H.F., T.B. and F.D.; writing—original draft preparation, F.D. and T.B.; writing—review and editing, H.F., T.B., A.B. and F.D. All authors have read and agreed to the published version of the manuscript.

**Funding:** This research received no external funding.

**Institutional Review Board Statement:** Not applicable.

**Informed Consent Statement:** Not applicable.

**Data Availability Statement:** Data are available in this manuscript.

**Conflicts of Interest:** The authors declare no conflicts of interest.

## References

1. Wang, G.; Lu, W.; Li, J.; Choi, J.; Jeong, Y.; Choi, S.Y.; Park, J.B.; Ryu, M.K.; Lee, K. V-Shaped Tin Oxide Nanostructures Featuring a Broad Photocurrent Signal: An Effective Visible Light-Driven Photocatalyst. *Small* **2006**, *2*, 1436–1439. [CrossRef] [PubMed]
2. Dalapati, G.K.; Sharma, H.; Guchhait, A.; Chakrabarty, N.; Bamola, P.; Liu, Q.; Saianand, G.; Krishna, A.M.; Mukhopadhyay, S.; Dey, A.; et al. Tin oxide for optoelectronic, photovoltaic and energy storage devices: A review. *J. Mater. Chem. A* **2021**, *9*, 16621–16684. [CrossRef]
3. Ferhati, H.; Djeflal, F.; AbdelMalek, F. Towards improved efficiency of SnS solar cells using back grooves and strained-SnO<sub>2</sub> buffer layer: FDTD and DFT calculations. *J. Phys. Chem. Solids* **2023**, *178*, 111353. [CrossRef]
4. Kumar, M.; Askari, S.S.A.; Pandey, P.S.; Singh, Y.; Singh, R.; Raghuvanshi, S.K.; Singh, G.K.; Kumar, S. Experimental Investigation and DFT Study of Tin-Oxide for Its Application as Light Absorber Layer in Optoelectronic Devices. *IEEE Access* **2023**, *11*, 23347–23354. [CrossRef]
5. Dama, F.; Sinoquet, C. Partially Hidden Markov Chain Multivariate Linear Autoregressive model: Inference and forecasting—Application to machine health prognostics. *Mach Learn* **2023**, *112*, 45–97. [CrossRef]
6. Bandaru, N.; Enduri, M.K.; Reddy, C.V.; Kakarla, R.R. Aspects of effectiveness and significance: The use of machine learning methods to study CuIn<sub>1-x</sub>GaxSe<sub>2</sub> solar cells. *Sol. Energy* **2023**, *263*, 111941. [CrossRef]

**Disclaimer/Publisher’s Note:** The statements, opinions and data contained in all publications are solely those of the individual author(s) and contributor(s) and not of MDPI and/or the editor(s). MDPI and/or the editor(s) disclaim responsibility for any injury to people or property resulting from any ideas, methods, instructions or products referred to in the content.

# Photoresponsivity Enhancement of SnS-Based Devices Using Machine Learning and SCAPS Simulations <sup>†</sup>

Abdelhak Maoucha <sup>1</sup>, Faycal Djeflal <sup>1,\*</sup>, Tarek Berghout <sup>2</sup> and Hichem Ferhati <sup>1,3</sup>

<sup>1</sup> Laboratoire Electronique Avancée (LEA), Department of Electronics, University of Batna 2, Batna 05000, Algeria; hakosp82@yahoo.com (A.M.); hichemferhati@gmail.com (H.F.)

<sup>2</sup> Laboratory of Automation and Manufacturing Engineering, University of Batna 2, Batna 05000, Algeria; t.berghout@univ-batna2.dz

<sup>3</sup> Institut Sciences Techniques Appliquées (ISTA), University of Larbi Ben M'hidi, Oum El Bouaghi 04000, Algeria

\* Correspondence: faycal.djeflal@univ-batna2.dz

<sup>†</sup> Presented at the 10th International Electronic Conference on Sensors and Applications (ECSA-10), 15–30 November 2023; Available online: <https://ecsa-10.sciforum.net/>.

**Abstract:** In this work, we propose a novel alternative design technique based on combined SCAPS numerical simulations and Machine Learning (ML) computation to improve the photocurrent performances for efficient eco-friendly optoelectronic applications. In this context, a new SnS absorber structure based on introducing gold (Au) nanoparticles (NPs) is proposed. It is revealed that the proposed design framework can predict the best spatial distribution of Au NPs, allowing for the enhanced optical behavior of SnS absorber film. This can pave the way for the optoelectronic systems designers to identify the geometry and the appropriate material for each layer of the device. Moreover, the results of the proposed SnS-based structure offer an innovative approach for the elaboration of eco-friendly, high-efficiency thin-film optoelectronics devices that is more promising than the previously reported designing techniques.

**Keywords:** photocurrent; photosensing; machine learning; tin sulfide; efficiency

## 1. Introduction

Photodetectors hold a prominent role in optoelectronic devices as they possess the capacity to convert optical signals into electrical signals. They find applications in various fields, including early missile threat detection, optical communication, environmental monitoring, water purification, flame detection, ultraviolet astronomy, environmental surveillance, remote sensing, biomedicine, and photography [1–3]. In these circumstances, various materials like perovskites, monolayers, colloidal quantum dots, and solution-processable substances have been extensively investigated with the goal of addressing the primary challenges associated with conventional photodetectors [3,4]. Particularly, tin sulfide (SnS) stands out as a highly promising material. It is characterized by its non-toxic properties, chemical stability, Earth abundance, high carrier mobility, visible light-absorption ability, low recombination velocity, and a tunable direct bandgap [3,5]. These attributes collectively position SnS as an exceptional candidate for high-performance optoelectronic devices. In addition, tin sulfide encompasses various phases, including SnS, Sn<sub>2</sub>S<sub>3</sub>, SnS<sub>2</sub>, Sn<sub>3</sub>S<sub>4</sub>, and Sn<sub>4</sub>S<sub>5</sub>, each characterized by distinct stoichiometric ratios of tin and sulfur. The synthesis and doping of these diverse SnS phases are achievable through various methods, such as pulse electrodeposition (PED), spray pyrolysis, physical vapor deposition (PVD), plasma-enhanced chemical vapor deposition (PECVD), chemical bath deposition (CBD), electron beam evaporation (EBM), atomic layer deposition (ALD), and RF magnetron sputtering [3–7]. While certain SnS photodetectors have exhibited a noteworthy performance, their achieved results still fall short of expectations. Moreover,

**Citation:** Maoucha, A.; Djeflal, F.; Berghout, T.; Ferhati, H.

Photoresponsivity Enhancement of SnS-Based Devices Using Machine Learning and SCAPS Simulations. *Eng. Proc.* **2023**, *58*, 128. <https://doi.org/10.3390/ecsa-10-16014>

Academic Editor: Jean-marc Laheurte  
Published: 15 November 2023



**Copyright:** © 2023 by the authors. Licensee MDPI, Basel, Switzerland. This article is an open access article distributed under the terms and conditions of the Creative Commons Attribution (CC BY) license (<https://creativecommons.org/licenses/by/4.0/>).

the SnS alloys are not free from disadvantages. One of which is their low resistance to the aggressive influence of environmental factors such as temperature, oxygen, and electromagnetic radiation. With that, there are new different classes of sulfide-based materials with good electronic properties, which have been developed using appropriate experimental facilities [8,9]. To address this challenge, noble metal nanoparticles can be introduced in the SnS absorber layer. This can enhance the photodetector optoelectronic properties through improving light absorption and generating plasmonic effects. Nonetheless, in the domain of thin-film semiconductor devices, a persistent iterative optimization process results in the inefficient utilization of energy and material resources, leading to elevated experimental costs and increased human labor demands. Intuitively, to expedite the experimentation timeline and reduce the overall cost, machine learning (ML) analysis techniques can be a potential solution. The field of machine learning analysis has gained prominence as a powerful tool for addressing these challenges. It resides within the domain of artificial intelligence and is instrumental in uncovering latent insights within datasets. Machine learning can extract a diverse range of authentic material information through computational and data mining methodologies. In this work, employing ML analysis, we accurately predict the plasmonic impact on optoelectronic properties by optimizing the positioning of gold nanoparticles within the SnS layer (top, middle, or bottom) and determining the most suitable nanoparticle radius to achieve optimal performance. The outcomes reveal that our eco-friendly SnS photodetector design, featuring gold nanoparticles, significantly enhances its optoelectronic characteristics, establishing it as a promising choice for the development of cost-effective and environmentally friendly photodetectors.

## 2. Device Structure and Modeling Frameworks

### 2.1. Device Structure

The proposed SnS absorber film consists of introducing Au NPs as shown in Figure 1a. The latter shows a cross sectional view of the investigated SnS absorber and the spatial distribution of the introduced Au NPs is depicted in Figure 1b. From this figure,  $P$  denotes the NPs position from the surface following the  $z$  direction,  $r$  is the nanoparticle radius, and  $S$  refers to the spacing between Au NPs. The proposed SnS absorber film is considered on a glass substrate and the thin-film thickness ( $t_{SnS}$ ) is fixed at 400 nm. It is interesting to note that the chemical stability of the investigated structure including Au NPs has already been investigated and demonstrated by several published works [4,10,11].

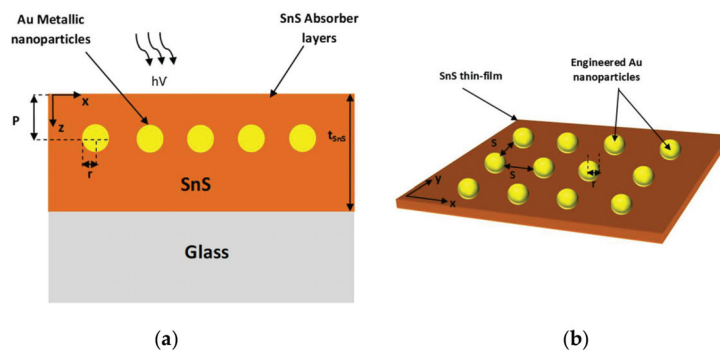


**Figure 1.** (a) Cross-sectional view of plasmonic gold nanoparticles based on the SnS absorber film (b) schematic of SnS surface, decorated with Au NPs.

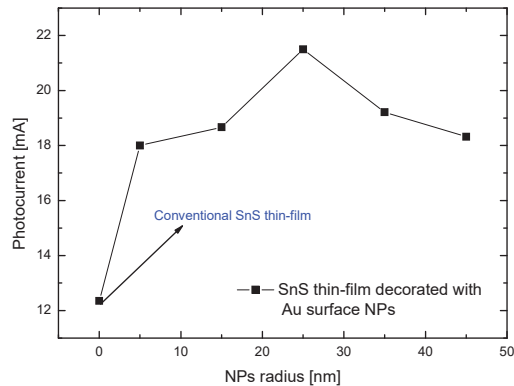
### 2.2. Modeling Frameworks

In the initial phase of our study, we utilize the SCAPS (Solar cell Capacitance Simulator) application to generate an extensive dataset [12]. Before that, the Finite Difference Time Domain method (FDTD) is used to estimate the absorbance of the proposed SnS thin film based on specially distributed Au NPs. The details regarding the optical modeling of the

proposed SnS absorber layer decorated with Au NPs can be found in our previous work [3]. Subsequently, in the second phase, we employ machine learning-based calculations to forecast the influence of the position and radius of gold nanoparticles on the optoelectronic properties of the SnS photodetector. The ML model has been trained using our SCAPS-based calculation database. Correlation analysis and machine learning algorithms have been exploited to investigate the key parameters affecting the optical behavior of the SnS absorber film. A SCAPS-ML predictive approach has been developed to determine the best spatial distribution of Au NPs, offering fast and crucial guidance for the experimental elaboration of SnS-based optoelectronic devices with high-photodetection capabilities.

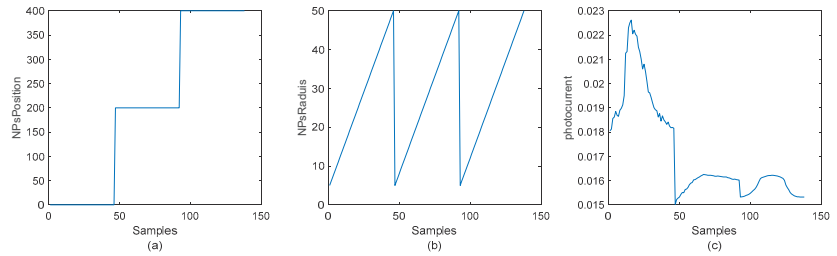
### 3. Results and Discussion

Figure 2 shows the variation of the photocurrent as a function of the NPs' radius for the proposed SnS-based photodetector. It can be seen from this figure that the introduction of Au NPs leads to the enhancement of the device's optical behavior, where an enhanced photocurrent is achieved as compared to the conventional SnS thin film. This improvement can be attributed to the role of introducing Au NPs to enhance light management in the SnS absorber layer through generating plasmonic effects. Additionally, the highest photocurrent ( $I_{ph} = 21$  mA) is achieved for the specific Au NP radius of 25 nm. It can also be revealed from Figure 2 that the use of higher radius values leads to decreasing the device photocurrent. This indicates the complex optical behavior of the SnS absorber film when Au NPs are introduced, where their geometry and spatial distribution can greatly affect the film's optical properties. This opens up new insights for the implementation of ML analysis techniques to study and understand the effect of Au NP plasmons on the photodetection capabilities of SnS photodetectors.



**Figure 2.** Variation of the photocurrent as a function of the Au NPs' radius.

In the context of machine learning modeling, and since the collected data contain observations of 138 samples, which appears to be a light volume feature space, a simple data visualization method will be effective in providing guidance on both feature and model selection. Accordingly, Figure 3 deals with both inputs (Figure 3a,b) and outputs (Figure 3c) of the dataset. First, the photocurrent variation shows a kind of monotonicity in the deterioration by demonstrating a kind of regular degradation behavior over time. Similarly, such patterns can also be distinguished in the NPs' positions. Whereas NPs' radius exhibits a sort of periodicity that corresponds neither to inputs nor outputs. In this case, a first look at the feature selection strongly suggests eliminating these unnecessary features, which definitely lead to model bias. Second, variations in NPs' positions and photocurrent over time show clear behavior of data drift. This means that this type of data are subject to continuous change in its characteristics, making the model generalization out-of-date, if one is not considering such an issue.



**Figure 3.** Dataset features: (a,b) inputs; (c) output.

In this work, suggestions for overcoming these challenges are twofold. First, the data are subjected to a feature selection process including only NPs’ position features. After that, these features are also made subject to a normalization layer via min–max scaling in the range [0,1]. Second, adaptive learning rules are also integrated to ensure that the model is continually updated with new data and overcomes data drift issues. In this case, data drift problems are addressed by involving a neural network with long-short term memory (LSTM) as in [11,12]. It is worth mentioning that the network hyperparameters are manually tuned based on a simple error–trial basis, as in Table 1. Meanwhile, a threefold cross-validation technique is used to ensure the stability and generalizability of the model on the dataset.

**Table 1.** List of obtained hyperparameters.

Hyperparameters	Assigned Values
Maximum number of epochs	300
Mini batch size	30
Neurons	20
Learning algorithm	Adam optimizer
Initial learning rate	0.01
Gradient threshold	1
L2 regularization	0.0001

The model is evaluated according to a robust criterion that includes different estimation error measures, namely root mean squared error (RMSE), root mean of squares (RMS), and mean absolute error (MAE). In addition, the learning model is also subject to another performance evaluation criterion represented by R2. Simply put, the three errors should approach “zero”, while the R<sup>2</sup>, should approach the value of one for a better model performance. It is worth mentioning that the application of these evaluation criteria was carried out based on a validation set for each learning fold. This guarantees both the approximation capacity and the generalizability of the learning models. Additionally, another comparative study between the proposed architect and an ordinary multilayer perceptron (MLP) is also conducted. The comparison conclusions obtained will be very effective in observing the benefits of adaptive learning. An important point to consider in such a case is that the MLP uses the same hyperparameters to ensure a fair comparison.

The obtained results are summarized in Table 2. The cross-validation results of the RMSE, MSE, and MAE show an extremely better stability of LSTM compared to an ordinary MLP. Additionally, the mean values and standard deviation also explain this important information. This performance gap explains the need to use adaptive learning, on the one hand, and also the importance of feature selection, on the other hand. Furthermore, the results obtained regarding R<sup>2</sup> clearly prove the explainability and importance of the predictions obtained.



**Table 2.** Performance evaluation results.

LSTM				
Cross-validation Folds	RMSE	MSE	MAE	R <sup>2</sup>
1	$9.49 \times 10^{-4}$	$9.00 \times 10^{-7}$	$6.85 \times 10^{-4}$	0.72
2	$1.03 \times 10^{-3}$	$1.07 \times 10^{-6}$	$7.10 \times 10^{-4}$	0.75
3	$1.25 \times 10^{-3}$	$1.56 \times 10^{-6}$	$9.16 \times 10^{-4}$	0.65
Average	$1.07 \times 10^{-3}$	$1.18 \times 10^{-6}$	$7.7 \times 10^{-4}$	0.71
Standard deviation		$4.91 \times 10^{-4}$		0.051
MLP				
Cross-validation folds	RMSE	MSE	MAE	R <sup>2</sup>
1	$2.09 \times 10^{-3}$	$4.40 \times 10^{-6}$	$1.63 \times 10^{-3}$	−0.36
2	$1.65 \times 10^{-3}$	$2.74 \times 10^{-6}$	$1.31 \times 10^{-3}$	0.382
3	$1.37 \times 10^{-3}$	$1.89 \times 10^{-6}$	$1.12 \times 10^{-3}$	0.58
Average	$1.71 \times 10^{-3}$	$3.01 \times 10^{-6}$	$1.35 \times 10^{-3}$	0.20
Standard deviation		$8.11 \times 10^{-4}$		0.5003

#### 4. Conclusions

In this paper a new computation framework based on combined SCAPS numerical simulations and machine learning has been developed. The proposed approach can rapidly and accurately predict the photosensitizing ability of SnS-based sensors, including plasmonic effects and the impact of the gold nanoparticles' position and size. Applying LSTM learning rules to such a data drift and complexity problem allows the learning model to be updated based on any changes in the data. This is explained by great performance in approximation metrics such as the RMSE, MSE, and MAE. Meanwhile, R<sup>2</sup> clearly demonstrates the importance of the results from an expandability perspective. As for the prospects, this work will continue to explore such a tool for more complex and massive data, to reach more generalized conclusions in the context of data complexity and drift.

**Author Contributions:** Conceptualization, A.M., F.D., T.B. and H.F.; methodology, F.D.; validation, H.F., T.B. and F.D.; formal analysis, H.F., T.B. and F.D.; investigation, H.F., T.B. and F.D.; data curation, H.F., T.B. and F.D.; writing—original draft preparation, F.D. and T.B.; writing—review and editing, H.F., T.B. and F.D.; All authors have read and agreed to the published version of the manuscript.

**Funding:** This research received no external funding.

**Institutional Review Board Statement:** Not applicable.

**Informed Consent Statement:** Not applicable.

**Data Availability Statement:** Data are available in this manuscript.

**Conflicts of Interest:** The authors declare no conflicts of interest.

#### References

1. Kawamura, F.; Song, Y.; Murata, H.; Tampo, H.; Nagai, T.; Koida, T.; Imura, M.; Yamada, N. Tunability of the bandgap of SnS by variation of the cell volume by alloying with A.E. elements. *Sci. Rep.* **2022**, *12*, 7434. [CrossRef] [PubMed]
2. Zhang, H.; Li, H.; Yu, H.; Wang, F.; Song, X.; Xu, Z.; Wei, D.; Zhang, J.; Dai, Z.; Ren, Y.; et al. High responsivity and broadband photodetector based on SnS<sub>2</sub>/Ag<sub>2</sub>S heterojunction. *Mater. Lett.* **2023**, *330*, 133037. [CrossRef]
3. Dong, W.; Lu, C.; Luo, M.; Liu, Y.; Han, T.; Ge, Y.; Xue, X.; Zhou, Y.; Xu, X. Enhanced UV-Vis photodetector performance by optimizing interfacial charge transportation in the heterostructure by SnS and SnSe<sub>2</sub>. *J. Colloid Interface Sci.* **2022**, *621*, 374–384. [CrossRef] [PubMed]
4. Ye, Z.; Yu, H.; Wei, J.; Xie, Y. Direct observation of kinetic characteristic on SnS-based self-powered photodetection. *J. Lumin* **2023**, *253*, 119473. [CrossRef]
5. Kacha, K.; Djeflal, F.; Ferhati, H.; Foughali, L.; Bendjerad, A.; Benhaya, A.; Saidi, A. Efficiency improvement of CIGS solar cells using RF sputtered TCO/Ag/TCO thin-film as prospective buffer layer. *Ceram. Int.* **2022**, *48*, 20194–20200. [CrossRef]
6. Trukhanov, S.V.; Bodnar, I.V.; Zhafar, M.A. Magnetic and electrical properties of (FeIn<sub>2</sub>S<sub>4</sub>)<sub>1-x</sub>(CuIn<sub>5</sub>S<sub>8</sub>)<sub>x</sub> solid solutions. *J. Magn. Magn. Mater.* **2015**, *379*, 22–27. [CrossRef]

7. Bodnar, I.V.; Jaafar, M.A.; Pauliukavets, S.A.; Trukhanov, S.V.; Victorov, I.A. Growth, optical, magnetic and electrical properties of  $\text{CuFe}_{2.33}\text{In}_{9.67}\text{S}_{17.33}$  single crystal. *Mater. Res. Express* **2015**, *2*, 085901. [CrossRef]
8. Zdorovets, M.V.; Kozlovskiy, A.L.; Shlimas, D.I.; Borgekov, D.B. Phase transformations in  $\text{FeCo—Fe}_2\text{CoO}_4/\text{Co}_3\text{O}_4$ -spinel nanostructures as a result of thermal annealing and their practical application. *J. Mater. Sci. Mater. Electron.* **2021**, *32*, 16694–16705. [CrossRef]
9. Migas, D.B.; Turchenko, V.A.; Rutkauskas, A.V.; Trukhanov, S.V.; Zubar, T.I.; Tishkevich, D.I.; Trukhanov, A.V.; Skorodumova, N.V. Temperature induced structural and polarization features in  $\text{BaFe}_{12}\text{O}_{19}$ . *J. Mater. Chem. C* **2023**, *11*, 12406–12414. [CrossRef]
10. Troyanchuk, I.O.; Trukhanov, S.V.; Szymczak, H.; Baerner, K. Effect of oxygen content on the magnetic and transport properties of  $\text{Pr}_{0.5}\text{Ba}_{0.5}\text{MnO}_{3-\gamma}$ . *J. Phys. Condens. Matter.* **2000**, *12*, L155–L158. [CrossRef]
11. Kozlovskiy, A.; Egizbek, K.; Zdorovets, M.V.; Ibragimova, M.; Shumskaya, A.; Rogachev, A.A.; Ignatovich, Z.V.; Kadyrzhanov, K. Evaluation of the efficiency of detection and capture of manganese in aqueous solutions of  $\text{FeCeO}_x$  nanocomposites doped with  $\text{Nb}_2\text{O}_5$ . *Sensors* **2020**, *20*, 4851. [CrossRef] [PubMed]
12. Berghout, T.; Mouss, M.-D.; Mouss, L.-H.; Benbouzid, M. ProgNet: A Transferable Deep Network for Aircraft Engine Damage Propagation Prognosis under Real Flight Conditions. *Aerospace* **2022**, *10*, 10. [CrossRef]

**Disclaimer/Publisher’s Note:** The statements, opinions and data contained in all publications are solely those of the individual author(s) and contributor(s) and not of MDPI and/or the editor(s). MDPI and/or the editor(s) disclaim responsibility for any injury to people or property resulting from any ideas, methods, instructions or products referred to in the content.



Proceeding Paper

# Internet of Things-Based Smart Helmet with Accident Identification and Logistics Monitoring for Delivery Riders <sup>†</sup>

Alyssa Dainelle T. Alcantara, Ramon Balancer H. Balbuena III, Venlester B. Catapang \*, John Patrick M. Catchillar, Rick Edmond P. De Leon, Steven Niño A. Sanone, Charles G. Juarizo, Carlos C. Sison and Eufemia A. Garcia

Department of Electronics Engineering, Pamantasan ng Lungsod ng Maynila, Manila 1002, Philippines; alcantara.alyssa177@gmail.com (A.D.T.A.); rbbalbuena111@gmail.com (R.B.H.B.III); rickedmondpuno@gmail.com (R.E.P.D.L.); stevenminosanone@gmail.com (S.N.A.S.); cgjuarizo@plm.edu.ph (C.G.J.); ccison@plm.edu.ph (C.C.S.); eagarcia@plm.edu.ph (E.A.G.)

\* Correspondence: vbcatapang.education@gmail.com

<sup>†</sup> Presented at the 10th International Electronic Conference on Sensors and Applications (ECSA-10), 15–30 November 2023; Available online: <https://ecsa-10.sciforum.net/>.

**Abstract:** The study developed a smart helmet prototype that prioritizes delivery rider safety and facilitates logistical communication for small businesses. This was achieved with a smart helmet, utilizing IoT equipped with crash detection and logistics monitoring functions. Various sensors such as an accelerometer and alcohol sensors were calibrated to improve accuracy and minimize errors. A mobile application was introduced to coordinate delivery logistics and track the location of drivers. The system had 90% accuracy in distinguishing real accidents, and it also had drunk driver detection with an accuracy of 88%. An ATTM336H GPS module was used for geolocation tracking, and a mobile application built with Bubble.io and Firebase was integrated into the helmet to send alerts the shop owners of Roger’s Top Silog House who provided delivery drivers as participants for the study, who gave us positive feedback indicating that our smart helmet performed very well and exceeded expectations.

**Keywords:** Bubble.io; crash detection; Firebase; internet of things; logistics monitoring; smart helmet

**Citation:** Alcantara, A.D.T.; Balbuena, R.B.H., III; Catapang, V.B.; Catchillar, J.P.M.; De Leon, R.E.P.; Sanone, S.N.A.; Juarizo, C.G.; Sison, C.C.; Garcia, E.A. Internet of Things-Based Smart Helmet with Accident Identification and Logistics Monitoring for Delivery Riders. *Eng. Proc.* **2023**, *58*, 129. <https://doi.org/10.3390/ecsa-10-16238>

Academic Editor: Jean-marc Laheurte

Published: 15 November 2023



**Copyright:** © 2023 by the authors. Licensee MDPI, Basel, Switzerland. This article is an open access article distributed under the terms and conditions of the Creative Commons Attribution (CC BY) license (<https://creativecommons.org/licenses/by/4.0/>).

## 1. Introduction

The use of commercial transportation, such as motorcycles, for the purpose of collecting, transporting, and delivering documents, parcels, and packages from various sectors (i.e., mail, food, and carrier) has been increasing; this has become a main driver in augmenting the essentials in the delivery industry [1]. However, motorcycle accidents are associated mostly with injuries and fatalities. The cause of these involve behavioral conditions, such as substance abuse, helmet wearing, violations [2], and even road environmental conditions [1]. According to a 2018 WHO Philippines report, 53% of the 11,264 road accident deaths were attributed to two-wheeled and three-wheeled riders and passengers, with 90% of them not wearing helmets. As of December 2020, there were 7,328,116 registered motorcycles, including 1,949,589 new units [3]. In 2018 alone, an average of 86 daily cases of motorcycle-related road crashes were recorded based on the annual report released by the MMARAS (Metro Manila Accident Recording and Analysis System) [4]. In 2021, there were 14,870 persons injured in motorcycle-related crashes, giving an average of 41 individuals per day [5]. In 2022, accidents involving motorcycles alone consisted of 22.59% of the total road accidents in Metro Manila, 31,124 of which were motorcycle accidents, with 17,089 of those resulting in injuries and 313 resulting in fatalities [6]. Even if road accidents are inevitable, humans involved in life-or-death situations rely heavily on the speed of emergency response. The study designs a smart helmet prototype that values the safety of the delivery rider and provides logistical information between the delivery rider and management. Using IOT-based solutions, the objectives of the study consist of the following: (1) design

an IOT smart helmet accident detection system that gathers data from the accelerometer; (2) design a breath analyzer using MQ3 testing for the rider’s drunkenness during the smart helmet’s operation; (3) create a mobile application which notifies management of the delivery history and GPS location status; and (4) assess smart helmet’s operation quality upon usage by the delivery rider. The study only focuses on using a smart helmet with an embedded IoT system and Wi-Fi communication protocol. It enables data transmission through a Firebase IoT cloud server for the backend and utilizes Bubble.io for the frontend. This system notifies management about delivery riders, including crash detection and logistics information.

**2. Methodology**

This section contains an overview of the system’s block diagram as a prototype of an IoT-based smart helmet, with all of the relevant sensors, system design, as well as the processes behind its operation together with its circuit connection and implementation.

*2.1. System Design*

The smart helmet incorporates various sensors such as an accelerometer, vibration, alcohol and pressure resistive sensors, and GPS for point-to-point logistics tracking. Figure 1 shows the flow of operation. The data collected by these sensors are transmitted to the ESP32C3 microcontroller, which then relays it to Firebase as the backend database. This information is reflected in the Bubble.io mobile application for end-users, including administration (admins) who can monitor delivery manpower and potential accidents, delivery riders who use the app to accept deliveries and locate destinations, and customers who can track their deliveries. Figure 2 displays the wiring of the smart helmet.

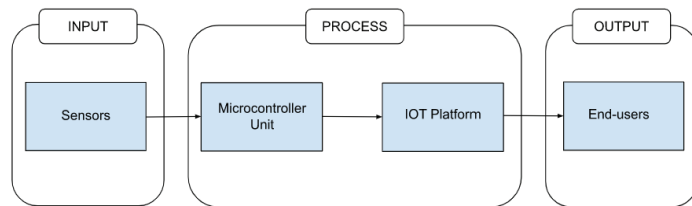


**Figure 1.** General block diagram of the system.

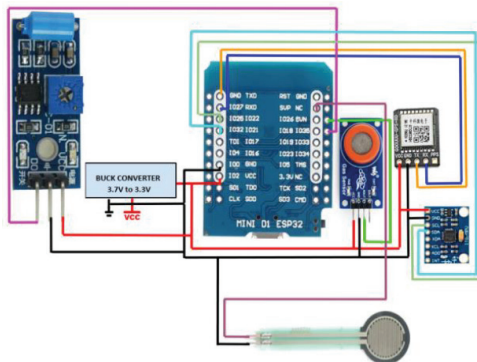


**Figure 2.** Circuit diagram of the embedded system.

*2.2. System Architecture*

This includes a calibration of the two (2) main sensory component systems for the creation of the smart helmet, a crash and alcohol detection system and a GPS system. The primary data that is determined here is sent to Firebase before it reflects any of those

data onto the application. Figure 3 displays the flow of information of the accelerometer, vibration, and alcohol sensor. All data is sent to the MCU to be stored in Firebase. This data is interpreted and is displayed unto the mobile application interface.

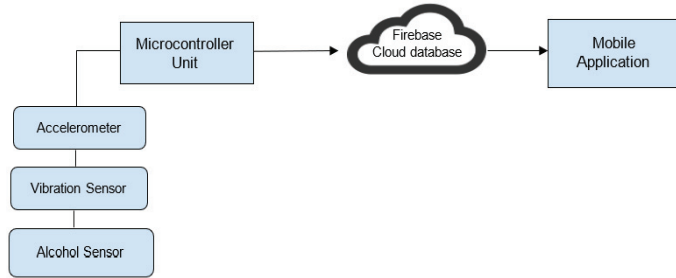


Figure 3. Crash detection system.

Figure 4 shows the communication of the GPS module to the MCU. Data are sent to Firebase to undergo external API map routing in order to be properly displayed on the mobile app, which is then reflected, as shown in Figure 5 below.

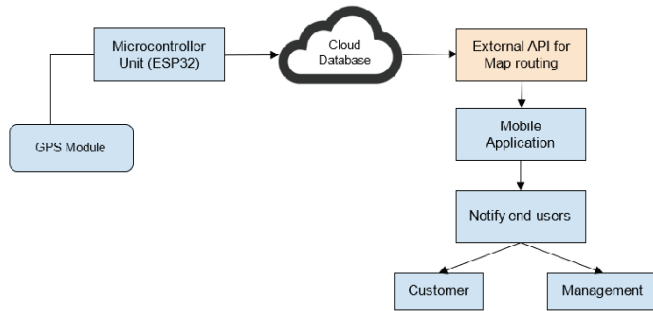


Figure 4. GPS design.

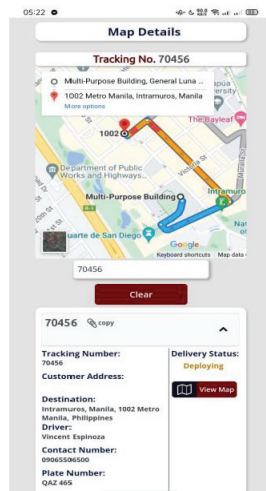


Figure 5. Mobile application for notification system.

### 2.3. Testing Procedure

The steps taken for the implementation of the smart helmet are as follows: (1) The admin and delivery rider create an account and connect the smart helmet via pocket Wi-Fi. (2) The delivery rider wears the helmet to begin the calibration of the accelerometer, vibration and alcohol sensors for initialization. (3) After approximately 2 min of warm-up time for the GPS, the admin can start placing orders for the delivery rider to accept. (4) After the order is accepted for delivery, the alcohol sensor samples the delivery rider's breath. If they are determined to be sober, they can proceed with delivery. If not, the sensors can notify all admins that the delivery rider is drunk. (5) The smart helmet continuously sends all sensor data for potential accidents/crashes and intoxication detection, as well as tracks the location of the delivery using GPS. (6) Once the delivery is confirmed to be successful through the mobile app, the sensors would still run in the background to check for accidents, intoxication, and the location of the delivery rider, ready to notify admin of their logistics.

#### 1. Accelerometer Threshold

An accident is determined via the smart helmet whenever the accelerometer responds with x, y, and z values that go over the threshold of 12G or roughly  $117.6 \text{ m/s}^2$  [7]. It then counterchecks with the vibration sensor's output, determining whether the rider has been involved in an accident or not, as shown in Equation (1) as follows:

$$|a| = \sqrt{(ax^2 + ay^2 + az^2)} \quad (1)$$

where  $|a|$  is the magnitude of linear acceleration and  $a$  = acceleration.

#### 2. Confusion or Error Matrix

To examine the reliability of the accelerometer and vibration sensor in accident detection, the following are calculated: the accuracy, as shown in Equation (2), the precision, as true instances of true positives shown in Equation (3), the recall, as the true positive rate shown in Equation (4), and the F1 score, as the harmonic mean between precision and the recall, shown in Equation (5), in terms of the error matrix of the results recorded from ten trials.

$$\text{Accuracy} = (TP + TN)/(TP + TN + FP + FN) \quad (2)$$

$$\text{Precision} = TP/(TP + FP) \quad (3)$$

$$\text{Recall} = TP/(TP + FN) \quad (4)$$

$$\text{F1 Score} = 2TP/(2TP + FP + FN) \quad (5)$$

where TP = true positive results, FP = false positive results, TN = true negative results and FN = false negative results.

#### 3. Calibration of MQ3 Sensor

To calibrate the MQ3 sensor as a breath analyzer, we extract the analog values from the sensor with a range of 0 to 4095 (with a resolution of 12 for the ESP32C3). R2 is taken from the physical resistor on the sensor, R0 (resistance of the sensor in normal conditions) is taken from the MQ3 datasheet, and Rs (output resistance of the sensor to alcohol) is used to acquire the blood alcohol content (BAC), computed using Equation (6). This value should be less than 0.05% to qualify as "sober".

$$\text{BAC} = ab^{(\text{ratio})} \quad (6)$$

where a is the BAC-intercept and b = slope.

#### 4. Root Mean Square Error

In order to assess the accuracy, the researchers compare the proposed system (smart helmet) over the conventional system (smartphone) and compute the difference between the resulting two values using Equation (7).

$$RMSE = \sqrt{\frac{\sum_{i=1}^n (Conventional_i - Proposed_i)^2}{n}} \tag{7}$$

5. Time Delay, Likert Scale, and Standard Deviation

The time delay from the entirety of the data communication of the proposed system—from the embedded IoT device up to the data that are reflected upon the mobile application—is calculated using Equation (8). The questions are subdivided into three categories: (1) reliability, (2) usability, and (3) functionality, wherein responses follow a scale of 1 to 5, with 1 = strongly disagree and 5 = strongly agree, to undergo a Likert scale evaluation. The standard deviation can be used to provide additional information about the variability or consistency of the data, as shown in Equation (9).

$$\text{Mean time delay} = \text{sum of trials} / \text{number of trials} \tag{8}$$

$$\sigma = \sqrt{\frac{\sum (x_i - \mu)^2}{n - 1}} \tag{9}$$

where  $x_i$  is the individual values from sample,  $\mu$  = sample mean and  $n$  = sample size.

3. Results and Discussions

This section is divided to present the results for each objective of the testing and implementation of the prototype’s system to identify accidents and logistics monitoring.

3.1. Design of an IOT Smart Helmet Accident Detection System That Gathers Data from the Accelerometer

As detailed in Table 1, the crash detection was tested using an accelerometer and a vibration sensor that determined whether the impact was a crash or not attained. This was conducted over 10 trials for situations with expected results, and these were then compared with the obtained results to determine whether the smart helmet succeeded in detecting an accident.

Table 1. Crash Detection from Accelerometer and Vibration Sensor Data.

No. of Trials	Situation of Test	Expected Output	Obtained Output	Interpretation
Trial 1	Helmet dropped 2 m above ground	T	T	Success (TP)
Trial 2	Helmet dropped 2 m above ground	T	T	Success (TP)
Trial 3	Helmet dropped 2 m above ground	T	T	Success (TP)
Trial 4	Helmet placed on the ground	F	F	Success (TP)
Trial 5	Helmet dropped 2 m above ground	T	T	Success (TP)
Trial 6	Helmet placed on the ground	F	T	Failed (FP)
Trial 7	Helmet dropped 2 m above ground	T	T	Success (TP)
Trial 8	Helmet dropped 2 m above ground	T	T	Success (TP)
Trial 9	Helmet placed on the ground	F	F	Success (TP)
Trial 10	Helmet dropped 2 m above ground	T	T	Success (TP)

As shown in Table 2, the accuracy of the system in detecting the situation as a crash yielded 90% while having a precision of 87.5%, a recall of 100%, and an F1 score of 93.3% from drop testing the smart helmet over 10 trials.

**Table 2.** Analysis of crash detection data.

Accuracy	Precision	Recall	F1 Score
0.90	0.875	1.0	0.933

*3.2. Design of a Breath Analyzer Using MQ3 Testing for the Rider’s Drunkenness during the Smart Helmet’s Operation*

As shown in Table 3, the accuracy of the MQ3 sensor to act as a breath analyzer had an accuracy of 89.09% while having a precision of 87.87%, a recall of 96.03%, and an F1 score of 91.78% from testing with different concentrations of alcohol readily available in the market.

**Table 3.** Analysis of alcohol detection.

Accuracy	Precision	Recall	F1 Score
0.890909	0.878787	0.960264	0.917721

*3.3. GPS Location and Status of the Delivery*

As shown in Table 4, the lower the RMSE value, the better the fit. Based on the calculations, the RMSE of the latitude equates to 0.000051274. Meanwhile, the longitude is 0.00017925, implying that the smart helmet is on par with GPS from smartphones. Figure 6 shows the implantation of the smart helmet together with the GPS feature below.

**Table 4.** Comparison of longitude and latitude between GPS.

No. of Trials	GPS from Smart Helmet		GPS from Smartphone	
	Longitude <sub>1</sub>	Latitude <sub>1</sub>	Longitude <sub>2</sub>	Latitude <sub>2</sub>
Trial 1	121.1922234	14.4668264	121.191716	14.4668255
Trial 2	121.1898427	14.4656059	121.1896703	14.4656555
Trial 3	121.1923470	14.4655427	121.1923521	14.4655419
Trial 4	121.1925436	14.4661518	121.1925606	14.4661125
Trial 5	121.1922318	14.465562	121.1922424	14.4655219
Trial 6	121.1936799	14.4655621	121.1936354	14.4655812
Trial 7	121.1908917	14.4654065	121.1908906	14.4653565
Trial 8	121.191133	14.4650616	121.1910309	14.4650906
Trial 9	121.19221	14.4645827	121.1923497	14.4645032
Trial 10	121.193271	14.4641768	121.1932287	14.4640736

RMSE = 0.000051274 (Latitude); 0.00017925 (Longitude)



**Figure 6.** Field implementation of the helmet. (a) Rider receiving order; (b) rider equipping smart helmet; (c) rider confirming delivery.



As shown in Table 5, the mean time delay of the 10 trials is 2.37 s, which is considered real-time.

**Table 5.** Time delay from the helmet to application.

No. of Trials	Data from Helmet to Application (s)	Mean Time Delay (s)
Trial 1	3.764	2.37480108
Trial 2	1.449	
Trial 3	1.66	
Trial 4	2.024	
Trial 5	3.915	
Trial 6	1.256	
Trial 7	2.185	
Trial 8	6.657	
Trial 9	3.059	
Trial 10	1.423	

**3.4. Assess the Smart Helmet’s Operation Quality upon Usage by the Delivery Rider**

As shown in Table 6, the actual mean and S.D. of the reliability of the smart helmet and mobile application are 4.24 and 0.469. The actual mean and S.D. of the usability of the smart helmet and mobile application are 4.12 and 0.561. The actual mean and S.D. of the functionality of the smart helmet and mobile application are 4.36 and 0.570. The smart helmet and mobile application performed greatly for the three categories. Figure 6 displays the actual helmet in use.

**Table 6.** Weighted mean of responses using a 5-point Likert scale.

Category	Questions	Responses	Actual Mean	Standard Deviation	Interpretation
Reliability	5	5	4.24	0.469	Great
Usability	5	5	4.12	0.561	Great
Functionality	5	5	4.36	0.570	Great

**Author Contributions:** Conceptualization, J.P.M.C., R.B.H.B.III and V.B.C.; methodology, A.D.T.A., J.P.M.C., S.N.A.S., R.B.H.B.III, R.E.P.D.L. and V.B.C.; software, J.P.M.C., R.B.H.B.III, R.E.P.D.L. and V.B.C.; validation, A.D.T.A., J.P.M.C., R.B.H.B.III and V.B.C.; formal analysis, J.P.M.C., R.B.H.B.III, R.E.P.D.L. and V.B.C.; investigation, A.D.T.A., J.P.M.C., R.B.H.B.III and V.B.C.; resources, A.D.T.A., J.P.M.C., S.N.A.S., R.B.H.B.III, R.E.P.D.L. and V.B.C.; data curation, A.D.T.A., J.P.M.C., R.B.H.B.III and V.B.C.; writing—original draft preparation, A.D.T.A. and S.N.A.S.; writing—review and editing, C.G.J., C.C.S., J.P.M.C., R.B.H.B.III and V.B.C.; visualization, A.D.T.A., J.P.M.C., S.N.A.S., R.B.H.B.III, R.E.P.D.L. and V.B.C.; supervision, C.C.S., C.G.J., E.A.G., J.P.M.C., R.B.H.B.III. and V.B.C.; project administration, J.P.M.C., R.B.H.B.III and V.B.C. All authors have read and agreed to the published version of the manuscript.

**Funding:** This research received no external funding.

**Institutional Review Board Statement:** Not applicable.

**Informed Consent Statement:** Not applicable.

**Data Availability Statement:** Data are contained within the article.

**Conflicts of Interest:** The authors declare no conflict of interest.

## References

1. Shin, Y.; Van Thai, V.; Grewal, D.; Kim, Y. Do Corporate Sustainable Management Activities Improve Customer Satisfaction, Word of Mouth Intention and Repurchase Intention? Empirical Evidence from the Shipping Industry. *Int. J. Logist. Manag.* **2017**, *28*, 555–570. [CrossRef]
2. Behr, C.J.; Kumar, A.; Hancke, G.P. A smart helmet for air quality and hazardous event detection for the mining industry. In Proceedings of the 2016 IEEE International Conference on Industrial Technology (ICIT), Taipei, Taiwan, 14–17 March 2016; pp. 2026–2031. [CrossRef]
3. Inquirer. Available online: <https://newsinfo.inquirer.net/1392480/lto-estimates-unregistered-motorcycles-in-ph-to-reach-47866> (accessed on 22 October 2022).
4. MMRAS Annual Report 2018. Available online: <https://mmda.gov.ph/images/Home/FOI/MMARAS/MMARAS-Annual-Report-2018.pdf> (accessed on 20 October 2022).
5. MMRAS Annual Report 2021. Available online: [https://mmda.gov.ph/images/Home/FOI/MMARAS/MMARAS\\_Annual\\_Report\\_2021.pdf](https://mmda.gov.ph/images/Home/FOI/MMARAS/MMARAS_Annual_Report_2021.pdf) (accessed on 20 October 2022).
6. MMRAS Annual Report 2022. Available online: [https://mmda.gov.ph/images/Home/FOI/MMARAS/MMARAS\\_Annual\\_Report\\_2022.pdf](https://mmda.gov.ph/images/Home/FOI/MMARAS/MMARAS_Annual_Report_2022.pdf) (accessed on 7 September 2023).
7. Khan, A.; Bibi, F.; Dilshad, M.R.; Ahmed, S.; Ullah, Z.; Ali, H. Accident Detection and Smart Rescue System using Android Smartphone with Real-Time Location Tracking. *Int. J. Adv. Comput. Sci. Appl.* **2018**, *9*, 341–355. [CrossRef]

**Disclaimer/Publisher’s Note:** The statements, opinions and data contained in all publications are solely those of the individual author(s) and contributor(s) and not of MDPI and/or the editor(s). MDPI and/or the editor(s) disclaim responsibility for any injury to people or property resulting from any ideas, methods, instructions or products referred to in the content.



Proceeding Paper

# A Novel Ensemble of Fourier Transform Infrared Spectroscopic Biosensing and Deep Learning Postprocessing for Diagnosis of Endometrial Cancer <sup>†</sup>

Ejay Nsugbe <sup>1,\*</sup>, Dephney Mathebula <sup>2</sup> and Dawn Adams <sup>3</sup>

<sup>1</sup> Nsugbe Research Labs, Swindon SN1 3LG, UK

<sup>2</sup> Department of Decision Sciences, College of Economics and Management Sciences, University of South Africa Muckleneuck, Pretoria 0027, South Africa; mathed2@unisa.ac.za

<sup>3</sup> School of Computing, Ulster University, Antrim BT15 1ED, UK; dawn.adams@southerntrust.hsni.net

\* Correspondence: ennsugbe@yahoo.com

<sup>†</sup> Presented at the 10th International Electronic Conference on Sensors and Applications (ECSA-10), 15–30 November 2023; Available online: <https://ecsa-10.sciforum.net/>.

**Abstract:** Cancers are prevalent worldwide, affecting a substantial amount of the global population, while early and proactive diagnosis of the disease continues to be a global medical challenge. Endometrial cancer represents a gynecological variant which is not only difficult to diagnose but also produces symptoms that are not distinct or exclusive to just the cancer itself. Blood spectroscopy has recently prevailed as a means towards a high-throughput and largely inexpensive method of diagnosing endometrial cancer. Using this method, and with the postprocessing of the accompanying spectra alongside the use of multivariate statistics, an inference can be formed which gives an indication of the presence and extent of the cancer. Previous work in this area has shown that the prediction results for this cancer could be improved with the use of signal decomposition models alongside machine learning prediction models, thus demonstrating the potential appeal of decomposition models in the processing pipeline of the spectroscopy data. As part of this exploratory study, we employ for the first time the use of deep learning, in the form of deep wavelet scattering, for the processing of acquired Fourier transform infrared (FTIR) spectra, which allows for a fully unsupervised decomposition and feature extraction of the resulting spectra, coupled with prediction machines capable of predicting the presence of cancer. The obtained results show that the use of deep learning allows for enhanced predictions of endometrial cancer, whilst allowing for a clinical decision-support platform which carries a greater degree of autonomy and, therein, diagnosis throughput.

**Keywords:** cancer; AI; machine learning; obstetrics; gynecology; FTIR; deep learning

**Citation:** Nsugbe, E.; Mathebula, D.; Adams, D. A Novel Ensemble of Fourier Transform Infrared Spectroscopic Biosensing and Deep Learning Postprocessing for Diagnosis of Endometrial Cancer. *Eng. Proc.* **2023**, *58*, 130. <https://doi.org/10.3390/ecsa-10-16244>

Academic Editor: Stefano Mariani

Published: 15 November 2023



**Copyright:** © 2023 by the authors. Licensee MDPI, Basel, Switzerland. This article is an open access article distributed under the terms and conditions of the Creative Commons Attribution (CC BY) license (<https://creativecommons.org/licenses/by/4.0/>).

## 1. Introduction

Endometrial cancer directly affects the lining of the uterus; it is one of the most diagnosed forms of cancer and is also more prevalent in developing regions [1–5]. The formation of the cancer first involves structural changes within the endometrium due to hormonal variations, where prolonged exposure to certain hormones within the endometrium results in different initial variants of the cancer [1–5]. Risk factors include age, hormonal imbalances, genetic markers, and obesity, to name a few [1–5].

A symptom and direct manifestation of endometrial cancer is unusual uterine bleeding. Some of the more frequently used diagnostic methods include endometrial biopsy processes, alongside transvaginal ultrasound methods [1–5]. Common treatment methods include: hysterectomies and vaginal brachytherapy, as well as medications depending on the overall stage of the cancer, followed by close monitoring of the behavior of the cancerous cells themselves [1–5].

Current means towards diagnosis of the cancer have been shown to carry undesired shortcomings, which has spurred the need for the exploration of other diagnosis mechanisms [1–5]. More effective means of diagnosis carry both cost-saving implications, as well as reducing the need for severe interventions such as significant clinical, pharmacological, and surgical treatments, including hysterectomies [1–5]. Recent work has shown the promise of the use of blood biomarkers, alongside spectroscopic measurements, as a high-throughput means of triage and initial diagnosis, to be followed by invasive observations in the patients [1–5]. An illustration of the endometrial cancer disease can be seen in Figure 1.

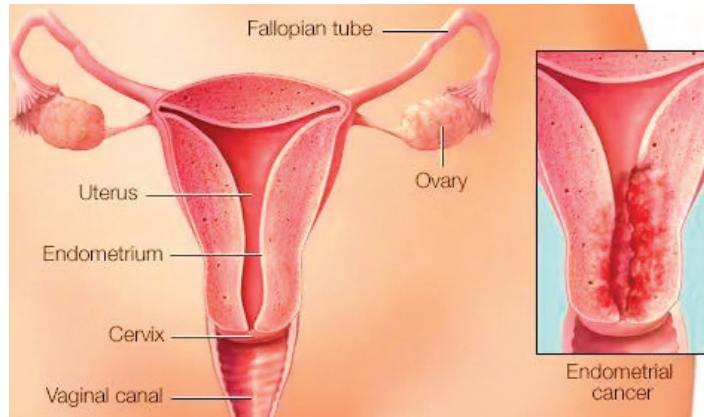


**Figure 1.** Illustration of endometrial cancer [6].

Related work has shown further results in the investigation of this theory; for example, Paraskevaïdi et al. [7] and Nsugbe et al. [5] used a combination of blood biomarkers and FTIR spectra for the classification and recognition of different variants of endometrial cancer infections. Paraskevaïdi et al.'s work utilized primarily multivariate statistics to create various discriminatory-based models, while Nsugbe et al. utilized a novel approach based on spectra decompositions and machine learning to assemble prediction models [5,7–9]. Nsugbe et al.'s work brought to light the potential clinical value of the application of multiresolution and signal decomposition algorithms within the area of spectroscopy postprocessing [5,8,9]. Deep wavelet scattering (DWS) represents a multiresolution-based approach which also allows for unsupervised feature extraction and is structurally an ensemble of both the classical wavelet transform and the deep learning-based convolutional neural network (CNN) [10]. Recent work has seen the application of DWS in various capacities within clinical medicine, which has shown to be beneficial in not requiring any expert knowledge regarding the feature extraction aspect of the process, whilst also being able to perform a decomposition act [11–13]. The majority of this has been carried out primarily on time-series data. In this work, we investigate the use of DWS for the first time on spectroscopic data for the prediction of various kinds of cancers, using Paraskevaïdi et al.'s FTIR spectroscopic data [7,11–13].

From this, it is hypothesized that a combination of blood spectroscopy, FTIR, and DWS, alongside pattern recognition models, can help form a rapid high-throughput means for an initial triage and diagnosis of endometrial cancer which requires minimal expert intervention due to its unsupervised nature.

## 2. Materials and Methods

### 2.1. Dataset

The FTIR data utilized in this study comprised 242 noncancerous patients: 258 with type 1 endometrial cancer and 64 with type 2 endometrial cancer; further insights into the patient cohort can be found in the publication by Paraskevaïdi et al. [7]. The recruitment

of the participants was performed by the Manchester University NHS Foundation Trust, the Salford Royal Foundation Trust, and the Lancashire Teaching Hospital, with ethical approval given and patient consent provided prior to the start of the study. All of the biopsy samples were labelled by certified gynecological pathologists as either normal or a variant of endometrial cancer [7]. The spectra were obtained from the blood samples using the Tensor 27 FTIR spectrometer with a Helios ATR attachment containing a diamond ATR crystal by Bruker Optics Ltd. (Ettlingen, Germany).

## 2.2. DWS

DWS is based around the multiscale extraction of features in an unsupervised fashion, in a way which they are robust and continuous, and its architecture comprises a merger between the wavelet transform and the CNN [10]. In an attempt to minimize the overall computational complexity of the method, preset values of the filters are set, which null the need for iterative estimations and make the method adept at working with a small set of samples due to these multiscale properties [10]. In DWS, the deep CNN is used for iterative applications, whilst the convolution is performed via wavelets and nonlinear modules, as well as an averaging function. The implementation of DWS in this paper involved a Gabor mother wavelet, a scale invariance of 1 s, and filter banks of 8 wavelets per octave in the first filter bank, as well as 1 wavelet per octave in the second filter bank.

## 2.3. Machine Learning Models

The discriminant analysis model, i.e., linear and quadratic (LDA and QDA), was employed, while the K-nearest neighbor was also utilized as part of this work, with K selected as 1 [14]. These models have been specifically chosen largely due to their computational efficiency. All models were validated using the K-fold cross validation approach with K chosen to be 10, while the SMOTE algorithm was utilized for the purpose of class balancing.

## 3. Results

The results for the various machine learning exercises can be seen in Table 1, from which it can be seen that the DWS appears to be producing a better prediction accuracy, with the best performance of 71.6%, when compared with the prior method utilized in a previous publication [15]. This has, thus, provided a degree of statistical evidence showing that DWS can indeed be utilized towards spectra decomposition whilst also performing unsupervised feature extraction, therein negating the need for an expert knowledge-dependent feature extraction process.

**Table 1.** Accuracy of the machine learning exercises.

Model	Postprocessing Method from Nsugbe and Sanusi [15] (without LSDL) (%)	DWS (%)
LDA	57	59.7
QDA	n/a	64.1
KNN	71.3	71.6

Subsequent work to be conducted in this area would involve further optimization exercises in order to determine if the performance of the DWS can be improved, while also training the data on various other machine learning models with nonlinear decision boundaries. The results in Table 1 appear to suggest that these kinds of models are optimal for the case study being investigated.

## 4. Conclusions

Endometrial cancer is an increasingly common cancer variant which ranks as one of the more frequently diagnosed forms of the disease, with symptoms that typically

feature uterine bleeding of various degrees. The use of blood spectroscopy has begun to be investigated in the literature, where FTIR spectroscopy has been used as a means towards the postprocessing of the blood samples acquired from the patients.

This work has investigated the use of DWS for the first time, which is a multiresolution unsupervised feature extraction method for the design of prediction models from FTIR spectra. The interim results from the case study carried out in this paper show the potential and applicability of the approach towards the prediction of endometrial cancer in patients. Further work should involve the use of a broader sample size of patients with the cancer and optimization exercises to tune and improve the performance of the DWS, whilst also training other available machine learning models on the dataset to find a best-fit model for the desired application. Furthermore, the exploration of unsupervised learning pattern recognition/machine learning models should be implemented.

**Author Contributions:** Conceptualization, E.N.; methodology, E.N.; software, E.N.; validation, E.N.; formal analysis, E.N.; investigation, E.N.; resources, E.N.; data curation, E.N.; writing—original draft preparation, E.N.; writing—review and editing, E.N., D.M. and D.A.; visualization, E.N.; supervision, E.N.; project administration, E.N.; funding acquisition, E.N.; E.N., D.M. and D.A. contributed equally to the article. All authors have read and agreed to the published version of the manuscript.

**Funding:** This research received no external funding.

**Institutional Review Board Statement:** The study was conducted within ethical standards, details of which have been included within the manuscript.

**Informed Consent Statement:** Informed consent was obtained from all subjects involved in the study.

**Data Availability Statement:** The data are available from a cited repository within the manuscript.

**Acknowledgments:** The authors would like to thank Brian for proofreading the manuscript.

**Conflicts of Interest:** The authors declare no conflicts of interest.

## References

1. Amant, F.; Moerman, P.; Neven, P.; Timmerman, D.; Van Limbergen, E.; Vergote, I. Endometrial Cancer. *Lancet* **2005**, *366*, 491–505. [CrossRef] [PubMed]
2. Parkin, D.M.; Pisani, P.; Ferlay, J. Global Cancer Statistics. *CA Cancer J. Clin.* **1999**, *49*, 33–64. [CrossRef] [PubMed]
3. Madison, T.; Schottenfeld, D.; James, S.A.; Schwartz, A.G.; Gruber, S.B. Endometrial Cancer: Socioeconomic Status and Racial/Ethnic Differences in Stage at Diagnosis, Treatment, and Survival. *Am. J. Public Health* **2004**, *94*, 2104–2111. [CrossRef] [PubMed]
4. Clement, P.B.; Young, R.H. Endometrioid Carcinoma of the Uterine Corpus: A Review of Its Pathology with Emphasis on Recent Advances and Problematic Aspects. *Adv. Anat. Pathol.* **2002**, *9*, 145–184. [CrossRef] [PubMed]
5. Nsugbe, E. On the Use of Spectroscopy, Prediction Machines and Cybernetics for an Affordable and Proactive Care Approach for Endometrial Cancer. *Biomed. Eng. Adv.* **2022**, *4*, 100057. [CrossRef]
6. O'Hara, J. Mayo Clinic Q&A Podcast: Why Are More People Dying of Uterine Cancer? Available online: <https://newsnetwork.mayoclinic.org/discussion/mayo-clinic-qa-podcast-why-are-more-people-dying-of-uterine-cancer/> (accessed on 28 July 2023).
7. Paraskeva, M.; Morais, C.L.M.; Ashton, K.M.; Stringfellow, H.F.; McVey, R.J.; Ryan, N.A.J.; O'Flynn, H.; Sivalingam, V.N.; Kitson, S.J.; MacKintosh, M.L.; et al. Detecting Endometrial Cancer by Blood Spectroscopy: A Diagnostic Cross-Sectional Study. *Cancers* **2020**, *12*, 1256. [CrossRef] [PubMed]
8. Nsugbe, E. Particle Size Distribution Estimation of a Powder Agglomeration Process Using Acoustic Emissions. Ph.D. Thesis, Cranfield University, Cranfield, UK, 2017.
9. Nsugbe, E.; Williams Samuel, O.; Asogbon, M.G.; Li, G. Contrast of Multi-Resolution Analysis Approach to Transhumeral Phantom Motion Decoding. *CAAI Trans. Intell. Technol.* **2021**, *6*, 360–375. [CrossRef]
10. Andén, J.; Mallat, S. Deep Scattering Spectrum. *IEEE Trans. Signal Process.* **2014**, *62*, 4114–4128. [CrossRef]
11. Nsugbe, E. On the Application of Metaheuristics and Deep Wavelet Scattering Decompositions for the Prediction of Adolescent Psychosis Using EEG Brain Wave Signals. *Digit. Technol. Res. Appl.* **2022**, *1*, 9–24. [CrossRef]
12. Nsugbe, E.; Connelly, S. Multiscale Depth of Anaesthesia Prediction for Surgery Using Frontal Cortex Electroencephalography. *Healthc. Technol. Lett.* **2022**, *9*, 43–53. [CrossRef] [PubMed]
13. Nsugbe, E.; Olorunlambe, K.; Dearn, K. On the Early and Affordable Diagnosis of Joint Pathologies Using Acoustic Emissions, Deep Learning Decompositions and Prediction Machines. *Sensors* **2023**, *23*, 4449. [CrossRef] [PubMed]

14. Nsugbe, E.; Phillips, C.; Fraser, M.; McIntosh, J. Gesture Recognition for Transhumeral Prosthesis Control Using EMG and NIR. *IET Cyber-Syst. Robot.* **2020**, *2*, 122–131. [CrossRef]
15. Nsugbe, E.; Sanusi, I. Towards an Affordable Magnetomyography Instrumentation and Low Model Complexity Approach for Labour Imminency Prediction Using a Novel Multiresolution Analysis. *Appl. AI Lett.* **2021**, *2*, e34. [CrossRef]

**Disclaimer/Publisher’s Note:** The statements, opinions and data contained in all publications are solely those of the individual author(s) and contributor(s) and not of MDPI and/or the editor(s). MDPI and/or the editor(s) disclaim responsibility for any injury to people or property resulting from any ideas, methods, instructions or products referred to in the content.

Proceeding Paper

# On the Clinical Use of Artificial Intelligence and Haematological Measurements for a Rapid Diagnosis and Care of Paediatric Malaria Patients in West Africa <sup>†</sup>

Ejay Nsugbe <sup>1,\*</sup>, Dephney Mathebula <sup>2</sup>, Evi Viza <sup>3</sup>, Oluwarotimi W. Samuel <sup>4</sup>, Stephanie Connelly <sup>5</sup> and Ian Mutanga <sup>6</sup>

<sup>1</sup> Nsugbe Research Labs, Swindon SN1 3LG, UK

<sup>2</sup> Department of Decision Sciences, College of Economics and Management Sciences, University of South Africa Muckleneuck, Pretoria 0027, South Africa; mathed2@unisa.ac.za

<sup>3</sup> School of Computing, Engineering & Physical Sciences, University of the West of Scotland, Paisley PA1 2BE, UK; evi.viza@uws.ac.uk

<sup>4</sup> School of Computing, University of Derby, Derby DE22 1GB, UK; o.samuel@derby.ac.uk

<sup>5</sup> Hereford County Hospital, Wye Valley NHS Trust, Hereford HR1 2BN, UK; stephconnelly12@gmail.com

<sup>6</sup> Hereford Hospitals NHS Trust University of Bristol, Bristol HR1 2BN, UK; ianrodney008@gmail.com

\* Correspondence: ennsugbe@yahoo.com

<sup>†</sup> Presented at the 10th International Electronic Conference on Sensors and Applications (ECSA-10), 15–30 November 2023; Available online: <https://ecsa-10.sciforum.net/>.

**Abstract:** Malaria continues to be a major cause of death worldwide, with a broad range of people spread over 90 countries being at risk of contracting the disease, and a significant cause of death in children under the age of 5. Due to this, there continues to be substantial investment towards not just the treatment of the disease, but also a more rapid and accurate means towards its diagnosis. In this work, we look to explore how measurements obtained from the complete blood count (CBC) technique from patients' blood, alongside artificial intelligence (AI) methods, could form an affordable analytical pipeline that could be adopted in hospital settings in both developed and developing countries. As part of this work, we utilize patient blood measurements acquired from paediatric patients from Ghana, West Africa, alongside various configurations of AI models towards distinguishing between malaria vs. non-malaria cases in a sample set comprising over 2000 patients. Class balancing algorithms are utilized to first balance the classes for the various patient groups, followed by the use of AI algorithms to train machine learning models to differentiate between a malaria vs. a non-malaria patient. The results showcased a generally high prediction accuracy, especially in the case of models with nonlinear decision boundaries, therein showing how the proposed analytic pipeline can serve as a high-throughput approach towards tackling the malaria epidemic from a diagnostics perspective and ultimately enhancing patient care strategies.

**Keywords:** malaria; machine learning; artificial intelligence; epidemiology; paediatrics; haematology; West Africa; diagnosis; decision support

**Citation:** Nsugbe, E.; Mathebula, D.; Viza, E.; Samuel, O.W.; Connelly, S.; Mutanga, I. On the Clinical Use of Artificial Intelligence and Haematological Measurements for a Rapid Diagnosis and Care of Paediatric Malaria Patients in West Africa. *Eng. Proc.* **2023**, *58*, 131. <https://doi.org/10.3390/ecsa-10-16246>

Academic Editor: Stefano Mariani

Published: 15 November 2023



**Copyright:** © 2023 by the authors. Licensee MDPI, Basel, Switzerland. This article is an open access article distributed under the terms and conditions of the Creative Commons Attribution (CC BY) license (<https://creativecommons.org/licenses/by/4.0/>).

## 1. Introduction

Malaria is a widespread disease which is caused by a number of “source” parasites implanted by mosquitos and manifests itself in human beings with an array of symptoms [1]. Although malaria occurs globally, there are certain hotspots where malaria tends to occur more frequently, including sub-Saharan Africa and Southeast Asia [1]. In terms of health statistics, the World Health Organization (WHO) approximated that, in the year 2020, around 241 million cases of malaria were reported, with 627,000 of these resulting in death, and the majority being children in sub-Saharan Africa [1].

The full impact of malaria transcends the death toll since it is also a source of financial burden due to the costs of clinical care for the affected economies [1]. Moreover, this effect



is amplified by the fact that the bulk of these economies are “developing” nations, therein contributing towards the cycle of disease and poverty in these regions [1].

Malaria parasites are only transmitted through bites of female mosquitos of the genus *Anopheles* [1]. The transmission mode first involves the mosquito biting a person who is infected, and then subsequently passing on parasites with its saliva to the next human being when it feeds on their blood [1]. Figure 1 illustrates the malaria infection cycle.

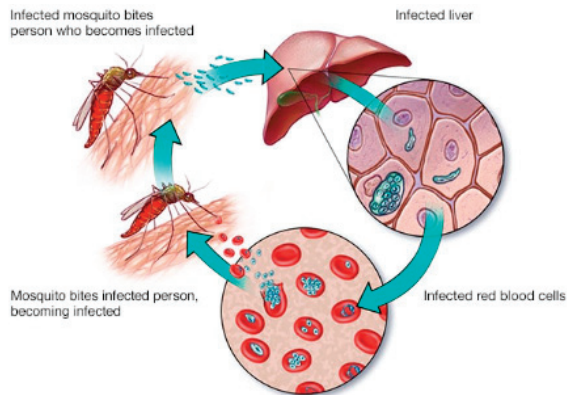


**Figure 1.** The malaria infection cycle [2].

*Plasmodium falciparum* is viewed as the most lethal of the malaria parasites, with a large number of casualties in sub-Saharan Africa in particular, where young children under the age of 5 as well as pregnant women are seen to be the most susceptible cohort [1]. Due to the nature of the disease, the WHO has invested in the order of billions towards the diagnosis, control, and elimination of the global malaria issue, with a substantial amount being devoted towards treatment therapies [3]. Despite this, it has been seen that the effectiveness of the treatment continues to be reliant on the accuracy of the initial diagnosis, where progressive use of an incorrect treatment could lead to wrongful drug resistance and even death in a handful of cases [3–5]. The generalized standard for the diagnosis includes the likes of the electron microscopy method, while recently rapid diagnosis tests (RDTs) have gained a considerable amount of traction due to their ability to be used as a point of care tool [6]. However, the drawbacks of RDTs include poor detection sensitivity when parasitaemia is low [6]. All of this has borne a form of motivation for an improved means towards the diagnosis of the presence of malaria parasites. The complete blood count (CBC) method has become popular in both developed and developing environments, whereby a key correlative factor of the presence of severe malaria includes a decreased count of platelets [7].

Previous related work in this area has sought to combine results from lab-based measurements alongside machine learning methods towards an automated and potential high-throughput mechanism for the diagnosis of malaria [6]. Artificial intelligence and machine learning itself have become staple mechanisms in the area of clinical medicine, with a particular appeal of providing a data-driven pattern recognition in a variety of cases, spanning areas such as oncology, anaesthesia, pregnancy medicine, psychiatry, and rehabilitation, to name a few [8–13]. With respect to this particular work, the related literature applied machine learning in various capacities towards the prediction of malaria, one of which used a sample size of 376 patients for the model build exercises [6,14–17]. This has been critiqued for having an overly concise sample size to converge on meaningful conclusions within the area [6]. Advancement within the research area was achieved by Morang’a et al., who managed to assemble data from a cumulative amount of 2207 patients from a number of regions in Ghana, for which various degrees of malaria were classified as part of their study using purely haematological parameters [6]. The main shortcoming of

this study was that their machine learning models were tuned and optimized using what has been perceived as an unbalanced dataset, which would lead to prediction biases in all inference and prediction actions. With the intention of advancing the body of knowledge in this area, we aim to apply class balancing algorithms towards first balancing the various data classes as a means towards negating the effect of the model, followed by the prediction of whether or not a patient has the malaria illness, and finally a differentiation between the malaria types, i.e., uncomplicated malaria (UM), non-malaria infections (nMI), and severe malaria (SM).

As a first step towards this, we utilize the broad comprehensive malaria dataset from Morang'a et al. of 2207 patients spread across Accra, Kintampo, and Navrongo in Ghana, West Africa [6]. As part of this paper, a combination of the CBC measurements and machine learning models are utilized towards first reaching an overall prediction on whether or not a patient has the malaria parasite.

## 2. Dataset and Methods

### *Dataset*

The dataset used in this research was acquired according to the reporting of diagnostic accuracy studies (STARD) guidelines, by Morang'a et al., where the patient inclusion criteria were as follows [6]:

**SM:** within the ages of 6–59 months with fever within the last 24 h and admitted to the Navrongo War Memorial Hospital, residence within the Navrongo Health and Demographic Surveillance System area, and informed consent [6]. SM is defined as haemoglobin standards of  $<5$  g/dL, or haematocrit  $<15\%$ , for which ethical approval was granted by the Noguchi Memorial Institute of Medical Research (NMIMR) review board, Naval Medical Research Center review board, and Ghana Health Service Ethics Review Committee (GHS-ERC) [6].

**nMI and UM:** patients for this cohort were recruited across a number of hospitals spanning Kintampo North-Municipal Hospital, Kintampo, and Ledzokuku Krowor Municipal Assembly Hospital (LEKMA), Accra [6]. The inclusion criteria were as follows: in the age range of 1–15 years, fever within the last 24 h, and a signed informed consent, with ethical approval also obtained for the study [6]. A case of nMI is defined as a malaria case that is identified as negative, via microscopic validation.

**CBC Measurements:** based around the use of haematological analysis of the cells within blood, which perform a characterization based on population density and morphology, from which the concentration of haemoglobin is estimated from the measurements of the red blood cells [7,18]. Various scholars have provided incremental contributions towards the effectiveness of the technology, which culminated nicely with the Coulter principle, which utilizes electrical impedance properties to perform a blood count purpose and continues to be a method of appeal and application to this very day, although optical measurements methods have now also been steadily introduced [19].

**Sample Collection:** as part of the sample collection process, venous blood was collected with the tourniquet not applied beyond a single minute in order to minimize erroneous measurements [6]. The sample acquisition occurred between 8 a.m. and 12 p.m. daily in order to minimize the influence of external factors such as rehydration and ingestion of food [6]. All samples were typically analysed immediately, and those that were not analysed within 2 h of acquisition were stored in a chamber of 2–8 degrees Celsius in order to stall any haematological changes in the sample sets [6]. It should be noted that no capillary blood samples were acquired as part of the study as they represent variations from venous blood parameters [6]. The CBC analytics was conducted using the automated ABX Micros 60 Hematology Analyzer, which characterizes both white and red blood cell parameters, in addition to platelets, while all data were cross-referenced as a means of validation in order to ensure consistency through the collection procedure [6].

**Features and Machine Learning:** the following CBC features were used as part of the analytics carried out in this paper: white blood cell counts, red blood cell counts,

haemoglobin level, haematocrit, mean cell volume, mean corpuscular haemoglobin, mean cell haemoglobin concentration, platelet count, platelet distribution width, mean platelet volume, neutrophils percent, lymphocytes percent, mixed cells percent, neutrophils count, lymphocytes count, mixed cells count, red blood cells distribution width percent, fever symptom, and temperature [6].

The microscopy readings were utilized as the labels for the data, i.e., malaria vs. no malaria, while the SMOTE algorithm was applied towards serving as class balancing purposes, which resulted in a total number of 2304 samples being utilized for all the subsequent analytics [20].

Machine Learning: the following machine learning models were used as part of the pattern recognition exercises: decision tree (DT), linear discriminant analysis (LDA), logistic regression (LR), support vector machines (SVM), linear-SVM (LSVM), quadratic-SVM (QSVM), cubic-SVM (CSVM), fine Gaussian-SVM (FGSVM), and k-nearest neighbours (KNN) [8]. All classification models were validated with the K-fold validation scheme, with K selected as 10.

### 3. Results

The results in Table 1 show the model-based prediction performance for the classification of malaria vs. non-malaria from the aforementioned CBC measurements. From the results in Table 1, it can be seen that the prediction results are generally high across all the various candidate classification models, of which the QSVM and CSVM (characterized by the nonlinear Kernels) both achieved the best classification performance of 89% accuracy, therein showing that a nonlinear decision boundary is optimal for the separation of the two data classes. Additionally, it can be seen that the fine Gaussian-SVM and the Decision Tree classifiers yielded the least classification performance (84% and 85%) in comparison to the other classification methods. These results reflect a more robust model performance when compared with that of Morang'a et al. whose model build and design was conducted with the use of an unbalanced sample set, which ultimately would probably result in a biased model prediction.

**Table 1.** Model prediction performance for classification of malaria vs. non-malaria from CBC measurements.

Model	Accuracy (%)
DT	85
LDA	86
LR	86
LSVM	87
QSVM	89
CSVM	89
FGSVM	84
KNN	87

The achievement of this would potentially allow for a deployment of a high throughput model pipeline which would allow for a quicker diagnosis of malaria patients from their blood samples, CBC analysis, and model-based predictions. A pipeline of this can be adopted and deployed in both developed and developing economies, due to the nature of the tools and model adopted. An illustration of the proposed flow can be seen in Figure 2.

The pipeline diagram shows a multi-stage model comprising the various sub-processes needed to come together in an ensemble-like fashion to produce the intended outcome of a high-throughput malaria prediction system. This features the lab-based CBC measurements which are used towards the training and optimising of the machine learning model with the intended role to carry out a tier-like prediction scheme. This includes, first, a surface prediction of whether or not the malaria parasite exists within the sample of the patient (focus of this paper), followed by a rating of the class of malaria where possible, i.e., SM or

UM, which would provide key information that would assist in the prioritisation of patient care (area of focus for further work).

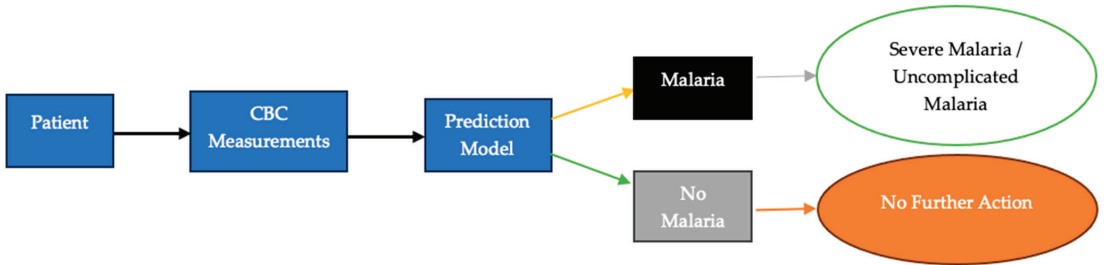


**Figure 2.** Pipeline for quicker diagnosis of malaria from blood samples, CBC analysis, and model-based predictions.

A visualisation of the data using the principal component analysis (PCA) can be seen in Figure 3, where it can be observed that there exists a degree of overlap between the various data classes; hence, the optimal decision boundary appeared to be of a nonlinear nature due to the apparent overlap between the classes. The inclusion of further features within the feature vector would enhance the class separability of the various data classes, a notion which would be explored deeper in subsequent work on this topic.

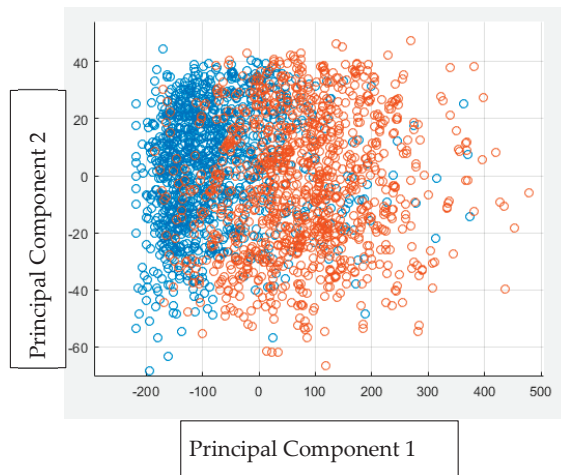


**Figure 3.** Principal component analysis of the data (Where Blue—Malaria and Red—Non-Malaria).

The computational complexity of machine learning models is a pivotal consideration in their practical deployment. Briefly, it encompasses the number of computational resources, time, and memory required to train and deploy these models. The computational complexity of a model depends on various factors, including the size of the dataset, the number of features, the model’s architecture, and parameters of the algorithm. While we have focused on classification accuracy as a metric thus far, it is worth noting that the computational complexity of the models should be further investigated.

#### 4. Conclusions

Malaria is a global disease that has been identified by the WHO as an epidemic, with a large portion of related deaths centring around children in sub-Saharan Africa. The negative effects of malaria within these countries are profound in terms of healthcare and

economics. The CBC represents a measurement technique largely employed in the diagnosis of malaria, which has been adopted in both developed and developing regions. Prior work has adopted the use of artificial intelligence as a means towards pattern recognizing measurements which correlate towards a subsequent malaria diagnosis. The shortcoming of this involved the use of an unbalanced dataset, which would lead to biased predictions by the concurrent prediction machine. The contributions made in this paper involve the use of class balancing algorithms, firstly to the paediatric malaria dataset, alongside the formulation of a multistage pipeline which looks to provide an initial binary diagnosis of whether a patient has the malaria parasite, followed by an associated prediction of the extent of the malaria.

The obtained results showed that the various adopted models have good prowess in the prediction of whether a patient has malaria, where the SVM with a quadratic nonlinear decision boundary was seen to be optimal for differentiating between the two classes of paediatric patients. As a means towards improving this, subsequent work in this area would now involve the potential inclusion of further features within the feature vector to potentially induce class separability with a view towards a higher-class differentiation result. This would be followed by addressing the second portion of the prediction model, aimed around the identification of the extent of the malaria, given a positive malaria diagnosis. Further work in this area would also involve the potential projection of the features in a time-series format, which would enable the use of classical signal processing and signal decomposition toolsets as applied in previous studies [21–23].

**Author Contributions:** Conceptualization, E.N.; methodology, E.N.; software, E.N.; validation, E.N.; formal analysis, E.N.; investigation, E.N.; resources, E.N.; data curation, E.N.; writing—original draft preparation, E.N.; writing—review and editing, E.N., D.M., E.V., O.W.S., S.C. and I.M.; visualization, E.N.; supervision, E.N.; project administration, E.N.; funding acquisition, E.N.; E.N., D.M., E.V., O.W.S., S.C. and I.M. contributed equally to this manuscript. All authors have read and agreed to the published version of the manuscript.

**Funding:** This research received no external funding.

**Institutional Review Board Statement:** The study was conducted within ethical standards, details of which have been included within the manuscript.

**Informed Consent Statement:** Written consent was obtained from all patients.

**Data Availability Statement:** The data used are available via a cited repository within the manuscript.

**Acknowledgments:** The authors would like to thank Brian Kerr from Kerr Editing for proofreading this manuscript.

**Conflicts of Interest:** The authors declare no conflicts of interest.

## References

1. CDC—Centers for Disease Control and Prevention. CDC-Malaria-FAQs. Available online: <https://www.cdc.gov/malaria/about/faqs.html> (accessed on 6 July 2023).
2. Malaria Transmission Cycle. Available online: <https://www.mayoclinic.org/diseases-conditions/malaria/multimedia/malaria-transmission-cycle/img-20006373> (accessed on 6 July 2023).
3. World Health Organization. *World Malaria Report 2018*; World Health Organization: Geneva, Switzerland, 2018; ISBN 978-92-4-156565-3.
4. Watson, O.J.; Sumner, K.M.; Janko, M.; Goel, V.; Winskill, P.; Slater, H.C.; Ghani, A.; Meshnick, S.R.; Parr, J.B. False-Negative Malaria Rapid Diagnostic Test Results and Their Impact on Community-Based Malaria Surveys in Sub-Saharan Africa. *BMJ Glob. Health* **2019**, *4*, e001582. [CrossRef] [PubMed]
5. Mouatcho, J.C.; Goldring, J.P.D. Malaria Rapid Diagnostic Tests: Challenges and Prospects. *J. Med. Microbiol.* **2013**, *62*, 1491–1505. [CrossRef] [PubMed]
6. Morang’a, C.M.; Amenga-Etego, L.; Bah, S.Y.; Appiah, V.; Amuzu, D.S.Y.; Amoako, N.; Abugri, J.; Oduro, A.R.; Cunningham, A.J.; Awandare, G.A.; et al. Machine Learning Approaches Classify Clinical Malaria Outcomes Based on Haematological Parameters. *BMC Med.* **2020**, *18*, 375. [CrossRef] [PubMed]
7. Healthdirect Australia Full Blood Count (FBC)—A Common Blood Test. Available online: <https://www.healthdirect.gov.au/full-blood-count> (accessed on 6 July 2023).

8. Nsugbe, E.; Ser, H.-L.; Ong, H.-F.; Ming, L.C.; Goh, K.-W.; Goh, B.-H.; Lee, W.-L. On an Affordable Approach towards the Diagnosis and Care for Prostate Cancer Patients Using Urine, FTIR and Prediction Machines. *Diagnostics* **2022**, *12*, 2099. [CrossRef] [PubMed]
9. Nsugbe, E.; Connelly, S. Multiscale Depth of Anaesthesia Prediction for Surgery Using Frontal Cortex Electroencephalography. *Healthc. Technol. Lett.* **2022**, *9*, 43–53. [CrossRef] [PubMed]
10. Nsugbe, E.; Obajemu, O.; Samuel, O.W.; Sanusi, I. Application of Noninvasive Magnetomyography in Labour Imminency Prediction for Term and Preterm Pregnancies and Ethnicity Specific Labour Prediction. *Mach. Learn. Appl.* **2021**, *5*, 100066. [CrossRef]
11. Nsugbe, E. On the Application of Metaheuristics and Deep Wavelet Scattering Decompositions for the Prediction of Adolescent Psychosis Using EEG Brain Wave Signals. *Digit. Technol. Res. Appl.* **2022**, *1*, 9–24. [CrossRef]
12. Nsugbe, E.; Williams Samuel, O.; Asogbon, M.G.; Li, G. Contrast of Multi-Resolution Analysis Approach to Transhumeral Phantom Motion Decoding. *CAAI Trans. Intell. Technol.* **2021**, *6*, 360–375. [CrossRef]
13. Nsugbe, E.; Phillips, C.; Fraser, M.; McIntosh, J. Gesture Recognition for Transhumeral Prosthesis Control Using EMG and NIR. *IET Cyber-Syst. Robot.* **2020**, *2*, 122–131. [CrossRef]
14. Poostchi, M.; Silamut, K.; Maude, R.J.; Jaeger, S.; Thoma, G. Image Analysis and Machine Learning for Detecting Malaria. *Transl. Res.* **2018**, *194*, 36–55. [CrossRef] [PubMed]
15. Bediako, Y.; Adams, R.; Reid, A.J.; Valletta, J.J.; Ndungu, F.M.; Sodenkamp, J.; Mwacharo, J.; Ngoi, J.M.; Kimani, D.; Kai, O.; et al. Repeated Clinical Malaria Episodes Are Associated with Modification of the Immune System in Children. *BMC Med.* **2019**, *17*, 60. [CrossRef] [PubMed]
16. KalantarMotamedi, Y.; Eastman, R.T.; Guha, R.; Bender, A. A Systematic and Prospectively Validated Approach for Identifying Synergistic Drug Combinations against Malaria. *Malar. J.* **2018**, *17*, 160. [CrossRef] [PubMed]
17. Shrinet, J.; Nandal, U.K.; Adak, T.; Bhatnagar, R.K.; Sunil, S. Inference of the Oxidative Stress Network in *Anopheles Stephensi* upon Plasmodium Infection. *PLoS ONE* **2014**, *9*, e114461. [CrossRef] [PubMed]
18. Blood Tests for CLL. Available online: <https://www.cancerresearchuk.org/about-cancer/chronic-lymphocytic-leukaemia-ctl/getting-diagnosed/tests/blood-tests> (accessed on 6 July 2023).
19. Graham, M.D. The Coulter Principle: Foundation of an Industry. *JALA J. Assoc. Lab. Autom.* **2003**, *8*, 72–81. [CrossRef]
20. Chawla, N.V.; Bowyer, K.W.; Hall, L.O.; Kegelmeyer, W.P. SMOTE: Synthetic Minority Over-Sampling Technique. *J. Artif. Intell. Res.* **2002**, *16*, 321–357. [CrossRef]
21. Nsugbe, E.; Starr, A.; Ruiz-Carcel, C. Monitoring the Particle Size Distribution of a Powder Mixing Process with Acoustic Emissions: A Review. *Eng. Technol. Ref.* **2016**, *1*, 1–12. [CrossRef]
22. Nsugbe, E. Particle Size Distribution Estimation of a Powder Agglomeration Process Using Acoustic Emissions. Ph.D. Thesis, Cranfield University, Cranfield, UK, 2017.
23. Nsugbe, E.; Ruiz-Carcel, C.; Starr, A.; Jennions, I. Estimation of Fine and Oversize Particle Ratio in a Heterogeneous Compound with Acoustic Emissions. *Sensors* **2018**, *18*, 851. [CrossRef] [PubMed]

**Disclaimer/Publisher’s Note:** The statements, opinions and data contained in all publications are solely those of the individual author(s) and contributor(s) and not of MDPI and/or the editor(s). MDPI and/or the editor(s) disclaim responsibility for any injury to people or property resulting from any ideas, methods, instructions or products referred to in the content.

# Designing Unknown Input Observers for Fault Reconstruction in Disturbed Takagi-Sugeno Fuzzy Systems <sup>†</sup>

Khalida Mimoune \*, Mohamed Yacine Hammoudi and Wail Hamdi

Laboratory of Energy Systems Modeling (LMSE), Department of Electrical Engineering, University of Biskra, BP 145, Biskra 07000, Algeria; my.hammoudi@univ-biskra.dz (M.Y.H.); wail.hamdi@univ-biskra.dz (W.H.)

\* Correspondence: khalida.mimoune@univ-biskra.dz

<sup>†</sup> Presented at the 10th International Electronic Conference on Sensors and Applications (ECSA-10), 15–30 November 2023; Available online: <https://ecsa-10.sciforum.net/>.

**Abstract:** Fault occurrence in practical systems, if not addressed, can cause diminished performance or even system breakdown. Therefore, fault detection has emerged as a crucial challenge in ensuring system safety and reliability. This paper presents a novel fuzzy observer aimed at reconstructing actuator and sensor faults in nonlinear systems, even when subjected to external disturbances. The approach we propose utilizes the Takagi-Sugeno fuzzy model and Lyapunov function. Initially, by filtering the system output, we construct a system where actuator faults correspond to the original actuator and sensor faults. Subsequently, the impact of disturbance on state estimations is minimized by employing the H-infinity performance criteria. We demonstrate that, for non-disturbed systems, these estimations gradually converge to their true values. In designing the observer gains, transformation matrices are derived by solving linear matrix inequalities. Our approach boasts some advantages over existing methods. By assuming that the premise variables are immeasurable, we enhance the usability of our approach. As a proof of concept, we evaluate two practical systems. The simulation results underline the benefits of our proposed method in terms of rapid and accurate fault detection performance.

**Keywords:** Takagi-Sugeno fuzzy system; actuator fault; sensor fault; Lyapunov function; linear matrix inequalities; H<sub>∞</sub> performance

**Citation:** Mimoune, K.; Hammoudi, M.Y.; Hamdi, W. Designing Unknown Input Observers for Fault Reconstruction in Disturbed Takagi-Sugeno Fuzzy Systems. *Eng. Proc.* **2023**, *58*, 132. <https://doi.org/10.3390/ecsa-10-16283>

Academic Editor: Stefano Mariani

Published: 16 November 2023



**Copyright:** © 2023 by the authors. Licensee MDPI, Basel, Switzerland. This article is an open access article distributed under the terms and conditions of the Creative Commons Attribution (CC BY) license (<https://creativecommons.org/licenses/by/4.0/>).

## 1. Introduction

Takagi-Sugeno Fuzzy (TSF) systems, particularly effective in engineering for observer and fault detection, use observers like the Proportional Integral Observer (PIO) and its enhanced version, the Proportional Multi-Integral Observer (PMIO) [1], for complex nonlinear systems such as the Continuous Stirred Tank Reactor (CSTR) in chemical engineering. The CSTR, a multi-input multi-output (MIMO) system, presents control and estimation challenges due to its nonlinear dynamics [2]. Luenberger's observers, initially for linear systems, have been adapted for nonlinear systems, offering cost-effective state estimation solutions [3].

The TS multi-model approach simplifies state estimation in CSTRs by interpolating between linear models for different behaviors [4]. This is crucial in scenarios with simultaneous unknown input actuator and sensor faults, necessitating integrated control and diagnostic systems. For TS models, several state and unknown input estimation methods have been developed. These include PI observers for decoupled Multiple Models [5], UI-PI observers with measurable premise variables [6,7], and a TS multi-model based PI observer for simultaneous state and input estimation [8]. However, PI observers have limitations with time-varying inputs, leading to the development of PMI observers, like the Thau-Luenberger observer [9], capable of assessing all unknown input derivatives. This research aims to refine PMI-based unknown input observers for TS-model systems, focusing on convergence conditions as linear matrix inequalities.

The paper’s structure is as follows: Section 2 introduces the TS fuzzy model and constructs a fictitious system with a fault, with the design of a PMI observer, ensuring estimation error stability and  $H_\infty$  performance. In Section 3, we validate the approach with simulation results. Conclusions are drawn in Section 4.

**2. Problem Statement**

Consider the Takagi-Sugeno model described by the system of equations:

$$\begin{cases} \dot{x}(t) = \sum_{i=1}^Q \mu_i(x(t))(A_i x(t) + B_i u(t) + E_i f_a(t)) + M w(t) \\ y(t) = C x(t) + F f_a + H w(t) \end{cases} \tag{1}$$

Here,  $x(t) \in \mathbb{R}^n$  represents the state vector,  $u(t) \in \mathbb{R}^{n_u}$  is the control input vector,  $f_a(t) \in \mathbb{R}^{n_{f_a}}$  signifies the unknown input vector including actuator and sensors faults,  $w(t)$  is the disturbance, and  $y(t) \in \mathbb{R}^{n_y}$  corresponds to the output vector.

Consider the matrices  $A_i, B_i, E_i, M, C, F,$  and  $H,$  which are constants with appropriate dimensions. The activation functions  $\mu_i(x(t)),$  dependent on the system’s state, adhere to the following convexity properties [10,11]:

$$\begin{cases} \sum_{i=1}^Q \mu_i(x(t)) = 1 \\ \forall i \in \{1, \dots, Q\} \end{cases} \tag{2}$$

The scalar  $Q$  designates the number of local models.

**Hypothesis 1.** *Unknown input  $f_a(t)$  satisfies:*

$$f_a^{(q)}(t) = 0 \tag{3}$$

Generally, the sequences  $f_a^{(1)}(t), f_a^{(2)}(t), \dots, f_a^{(q-1)}(t)$  denote the continuous derivatives of  $f_a(t),$  expressed as:

$$\begin{bmatrix} \dot{f}_a(t) \\ \dot{f}_{a_1}(t) \\ \vdots \\ \dot{f}_{a_{q-1}}(t) \end{bmatrix} = \begin{bmatrix} f_{a_1}(t) \\ f_{a_2}(t) \\ \vdots \\ f_{a_q}(t) \end{bmatrix} \tag{4}$$

System (1) can be expressed as a perturbed system with weighting functions  $\mu_i$  based on the estimated state, where the signals  $u(t), f_a(t),$  and  $w(t)$  are bounded.

$$\begin{cases} \dot{\hat{x}}(t) = \sum_{i=1}^Q \mu_i(\hat{x})(A_i \hat{x} + B_i u + E_i f_a + M w(t) + \delta(t)) \\ y(t) = C x(t) + F f_a + H w(t) \end{cases} \tag{5}$$

where:

$$\delta(t) = \sum_{i=1}^Q (\mu_i(x) - \mu_i(\hat{x}))(A_i x + B_i u + E_i f_a + M w(t))$$

Then, system (1) can be articulated as:

$$\begin{cases} \dot{\hat{x}}_a(t) = \sum_{i=1}^Q \mu_i(\hat{x}(t))(\bar{A}_i \hat{x}_a(t) + \bar{B}_i u(t) + \bar{\sigma}_i \bar{\Omega}(t)) \\ y(t) = \bar{C} \hat{x}_a(t) + F \bar{\Omega}(t) \end{cases} \tag{6}$$



$$x_a = \begin{bmatrix} x \\ f_a \\ f_{a1} \\ \vdots \\ f_{a_{q-1}} \end{bmatrix}, \bar{A}_i = \begin{bmatrix} A_i & E_i & 0 & \dots & 0 & 0 \\ 0 & 0 & I_{n_{fa}} & \dots & 0 & 0 \\ 0 & 0 & 0 & \ddots & 0 & 0 \\ \vdots & \vdots & \vdots & \vdots & \vdots & \vdots \\ 0 & 0 & 0 & \dots & 0 & I_{n_{fa}} \\ 0 & 0 & 0 & \dots & 0 & 0 \end{bmatrix}, \bar{B}_i = \begin{bmatrix} B_i \\ 0 \\ \vdots \\ 0 \\ 0 \\ 0 \end{bmatrix}, \bar{\sigma}_i = \begin{bmatrix} \sigma_i^T \\ 0 \\ \vdots \\ 0 \end{bmatrix}, \quad (7)$$

$$\bar{\Omega}(t) = \begin{bmatrix} \sigma(t) \\ w(t) \end{bmatrix}, \text{ and } \bar{C} = [ C \quad F \quad 0 \quad \dots \quad 0 \quad 0 ] \quad (8)$$

where:  $\sigma_i = [ I_n \quad M ]$ , and  $\bar{F} = [ 0 \quad H ]$ ,

**Hypothesis 2.** The pairs  $(\bar{A}_i, \bar{C})$  are observable for all  $i$ .

The Proportional Multiple Integral (PMI) observer can be described by the Equation (9), and the principle of this observer is presented in Figure 1:

$$\begin{cases} \dot{\hat{x}}(t) = \sum_{i=1}^Q \mu_i(\hat{x}(t)) (A_i \hat{x}(t) + B_i u(t) + E_i \hat{f}_a(t) + L_{Pi}(y(t) - \hat{y}(t))) \\ \dot{\hat{f}}_{a_j}(t) = \sum_{i=1}^Q \mu_i(\hat{x}(t)) (\hat{f}_{a_{j+1}} + L_{ji}^j (y(t) - \hat{y}(t))), \quad j = 1, \dots, q-2 \\ \dot{\hat{f}}_{a_j}(t) = \sum_{i=1}^Q \mu_i(\hat{x}(t)) (L_{li}(y(t) - \hat{y}(t))) \quad j = q-1 \\ \hat{y}(t) = C \hat{x}(t) + F \hat{f}_a \end{cases} \quad (9)$$

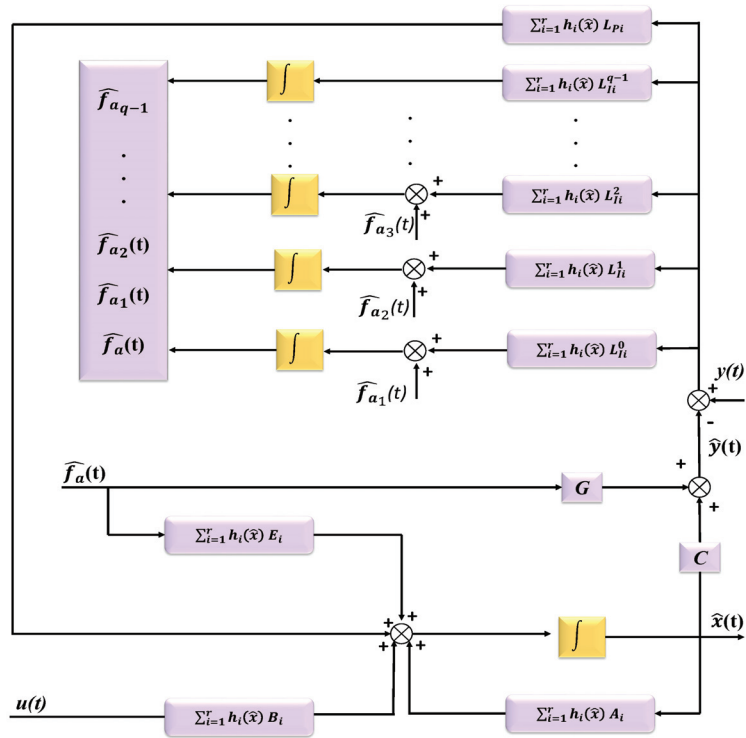


Figure 1. Principle of the PMI Observer.

With the above, the augmented PMI observer that incorporates an output error into its activation functions is articulated.

$$\begin{cases} \hat{x}_a(t) = \sum_{i=1}^Q \mu_i(\hat{x}(t))(\bar{A}_i \hat{x}_a(t) + \bar{B}_i u(t) + \bar{L}_i(y(t) - \hat{y}(t))) \\ \hat{y}(t) = \bar{C} \hat{x}_a(t) \end{cases} \quad (10)$$

where  $\bar{L}_i = \begin{bmatrix} L_{\bar{p}_i}^T & L_{\bar{l}_i}^T & L_{\bar{l}_i}^{1T} & \dots & L_{\bar{l}_i}^{q-2T} & L_{\bar{l}_i}^{q-1T} \end{bmatrix}^T$ .

The dynamic of the state estimation error is presented in the following augmented format:

$$\dot{\bar{e}} = \sum_{i=1}^Q \mu_i(\hat{x})((\bar{A}_i - \bar{L}_i \bar{C})\bar{e} + (\bar{\sigma}_i - \bar{L}_i \bar{F})\bar{\Omega}) \quad (11)$$

**Theorem 1.** *The PMI Observer, as defined by (9), designed to Simultaneously estimate the state and the unknown inputs of the fuzzy system represented in (1). This is achieved while minimizing the  $\mathcal{L}_2$ -gain  $\bar{\gamma}$  from the unknown inputs to the augmented state estimation error  $\bar{e}$ . This can be obtained by determining a positive definite matrix  $P$ , matrices  $M_i$ , and a positive scalar  $\bar{\gamma}$  that satisfy the following LMI constraints for  $i = 1, \dots, r$ :*

$$\begin{bmatrix} \bar{A}_i^T P + P \bar{A}_i - M_i \bar{C} - \bar{C}^T M_i^T + I & P \bar{\sigma}_i - M_i \bar{F} \\ \bar{\sigma}_i^T P - \bar{F}^T M_i^T & -\bar{\gamma} I \end{bmatrix} < 0 \quad (12)$$

where  $\gamma = \sqrt{\bar{\gamma}}$ .

The observer gains:  $\bar{L}_i = P^{-1} M_i$

**Proof.** Where System (1) stands as a paragon of stability and all preceding signals remain bounded, a transformative revelation unfolds. By invoking Lemma of Perturbation attenuation and satisfying the condition  $\|\bar{e}(t)\|_2 < \gamma \|\hat{\omega}(t)\|_2$  yields an enigmatic Linear Matrix Inequality (LMI):

$$\begin{bmatrix} \bar{A}_i^T P + P \bar{A}_i - P L_i \bar{C} - \bar{C}^T L_i^T P + I & P \bar{\sigma}_i - P L_i \bar{F} \\ \bar{\sigma}_i^T P - \bar{F}^T L_i^T P & -\gamma^2 I \end{bmatrix} < 0 \quad (13)$$

The essence of Theorem 1 obtain through variable transformations:

$$M_i = P \bar{K}_i, \quad \bar{\gamma} = \gamma^2$$

□

### 3. Practical Example

As a demonstration of the methodology, we examine a nonlinear CSTR system depicted by a multi-model with unmeasurable premise variables. This multi-model comprises two local models, each with three states [3].

Consider a thoroughly mixed CSTR where the multi-component chemical reaction  $A \rightleftharpoons B \rightarrow C$  takes place. The Schematic of the Continuous Stirred Tank Reactor (CSTR) is shown in Figure 2, illustrating the concentrations of species  $A, B$ , and  $C$  as  $C_A, C_B$ , and  $C_C$  respectively. The reactor temperature is denoted by  $T$ , with  $C_{Af}$  and  $T_f$  representing the feed’s actual concentration and temperature. The flow rate and temperature of the cooling water are indicated by  $q_c$  and  $T_c$ . The system’s nonlinear dynamics can be represented as:

$$\dot{x} = \begin{bmatrix} -4 & 0.8796 & 0 \\ 3 & -3.6388 & 0 \\ 0 & 1.7592 & -1 \end{bmatrix} x + \begin{bmatrix} 0 \\ 1 \\ 0 \end{bmatrix} u + \begin{bmatrix} 0.5x_2^2 \\ -1.5x_2^2 \\ x_2^2 \end{bmatrix}, \quad (14)$$

where  $x = [x_1 \quad x_2 \quad x_3]^T$  denotes the concentrations of species  $A, B$ , and  $C$  respectively.

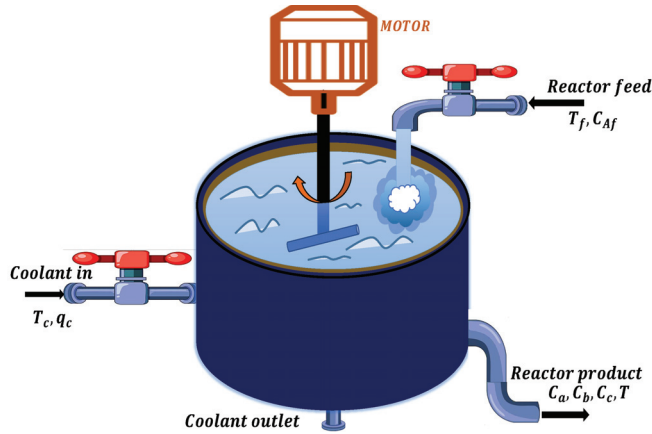


Figure 2. Schematic of CSTR.

To evaluate the effectiveness of our proposed approach, we introduce a fault and disturbance to the dynamics, leading to:

$$\begin{cases} \dot{x} = \begin{bmatrix} -4 & 0.8796 + 0.5x_2 & 0 \\ 3 & -3.6388 - 1.5x_2 & 0 \\ 0 & 1.7592 + x_2 & -1 \end{bmatrix} x + \begin{bmatrix} 0 \\ 1 \\ 0 \end{bmatrix} u + \begin{bmatrix} 1 \\ 0 \\ 0 \end{bmatrix} f_a + \begin{bmatrix} 0.6 \\ 0.05 \\ 0.03 \end{bmatrix} w(t) \\ y = \begin{bmatrix} 1 & 0 & 0 \\ 0 & 1 & 0 \end{bmatrix} x + \begin{bmatrix} 0.01 \\ 0.001 \end{bmatrix} f_a + \begin{bmatrix} 0.01 \\ 0.03 \end{bmatrix} w(t) \end{cases} \quad (15)$$

Assuming the concentration of species B is dimensionless, it is given by  $x_2 \in [-1, 1]$ . This allows the definition of two membership functions using Takagi-Sugeno (TS) rules as:

$$h_1 = \frac{1 - x_2}{2} \quad \text{and} \quad h_2 = \frac{1 + x_2}{2}. \quad (16)$$

With this, the corresponding local linear TS matrices can be established as:

$$A_1 = \begin{bmatrix} -4 & 0.8796 - 0.5 & 0 \\ 3 & -3.6388 + 1.5 & 0 \\ 0 & 1.7592 - 1 & -1 \end{bmatrix}, \quad A_2 = \begin{bmatrix} -4 & 0.8796 + 0.5 & 0 \\ 3 & -3.6388 - 1.5 & 0 \\ 0 & 1.7592 + 1 & -1 \end{bmatrix}, \quad B_1 = B_2 = \begin{bmatrix} 0 \\ 1 \\ 0 \end{bmatrix},$$

$$E_1 = E_2 = \begin{bmatrix} 1 \\ 0 \\ 0 \end{bmatrix}, \quad \text{and} \quad F = \begin{bmatrix} 0.01 \\ 0.001 \end{bmatrix} \quad (17)$$

Given that these TS fuzzy system matrices comply with all the preconditions, the TS fuzzy observer (9) is constructible.

For the simulation setup, parameters and input signals were chosen as follows:  $u = \sin(t)$ , with initial conditions  $x_0 = [0.15 \ 0.2 \ 0.1]^T$  and  $\hat{x}_0 = [0.15 \ 1 \ 3]^T$ . The disturbance profile depicted in Figure 3.

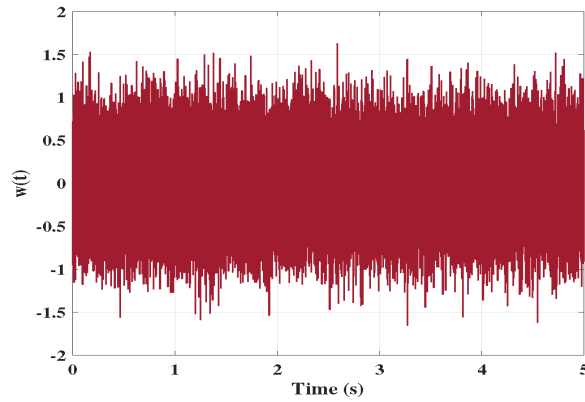


Figure 3. Disturbance  $w(t)$ .

The Linear Matrix Inequality (LMI) outlined in the provided theorem is addressed using the Matlab Yalmip toolbox, leading to the determination of the observer’s gains. The results of state and fault estimation are visually depicted in Figures 4 and 5.

In Figure 4, it is evident that the estimated states converge rapidly to their true signals right from the beginning. Figure 5 displays a robust estimation of the fault. These simulation outcomes distinctly demonstrate that the proposed observer not only guarantees accurate state estimation but also effectively handles concurrent fault detection, even in the presence of unknown disturbances.

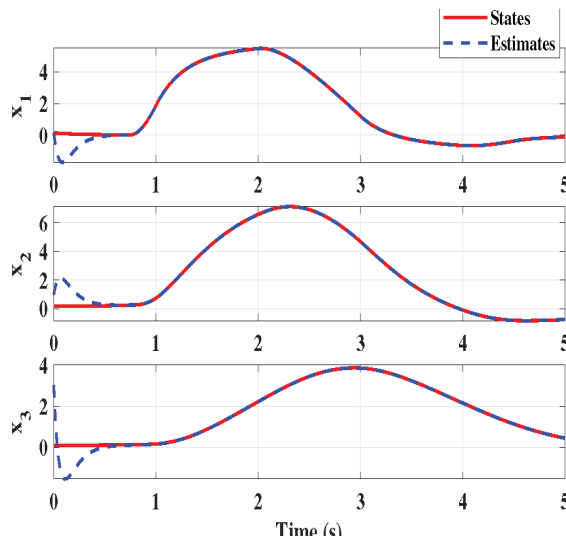


Figure 4. States and their estimates.

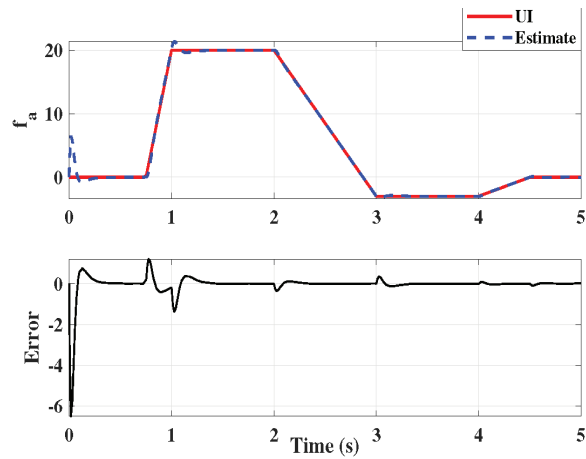


Figure 5. Unknown input and the State estimation error.

#### 4. Conclusions

In this study, we focus on estimating states and unknown inputs in Takagi-Sugeno systems that have unmeasurable premise variables, utilizing a Proportional Multiple Integral (PMI) observer. We define the stability conditions using Linear Matrix Inequalities to ensure robust performance. To validate the PMI observer's efficacy, we conduct a simulation using the Continuous Stirred Tank Reactor (CSTR) system as a practical example.

**Author Contributions:** Conceptualization, K.M., W.H. and M.Y.H.; methodology, K.M.; software, K.M. and W.H.; validation, K.M.; investigation, K.M., W.H. and M.Y.H.; writing—original draft preparation, K.M.; writing—review and editing, K.M. and W.H.; visualization, K.M.; supervision, M.Y.H.; project administration, M.Y.H. All authors have read and agreed to the published version of the manuscript.

**Funding:** This research received no external funding.

**Institutional Review Board Statement:** Not applicable.

**Informed Consent Statement:** Not applicable.

**Data Availability Statement:** Data are contained within the article.

**Conflicts of Interest:** The authors declare no conflicts of interest.

#### References

1. Hamdi, W.; Hammoudi, M.Y.; Hamiane, M. Proportional Multi-Integral Observer Design for Takagi-Sugeno Systems with Unmeasurable Premise Variables: Conservatism Reduction via Polyquadratic Lyapunov Function. *Eur. J. Control* **2023**, *75*, 100915. [CrossRef]
2. Bzioui, S.; Channa, R. Robust Tracking Control for the Non-isothermal Continuous Stirred Tank Reactor. *Int. J. Bioautom.* **2020**, *24*, 131–142. [CrossRef]
3. Bzioui, S.; Channa, R. An adaptive observer design for nonlinear systems affected by unknown disturbance with simultaneous actuator and sensor faults. application to a CSTR. *Biointerface Res. Appl. Chem.* **2021**, *12*, 4847–4856.
4. Asadi, S.; Moallem, M.; Wang, G.G. Simultaneous Sensor and Actuator Fault Reconstruction by Using a Sliding Mode Observer, Fuzzy Stability Analysis, and a Nonlinear Optimization Tool. *Sensors* **2022**, *22*, 6866. [CrossRef] [PubMed]
5. Orjuela, R.; Marx, B.; Ragot, J.; Maquin, D. Conception d'un observateur PI pour un multimodèle découplé. In Proceedings of the 8ème conférence internationale des Sciences et Techniques de l'Automatique, STA'2007, Sousse, Tunisia, 5–7 November 2007.
6. Pas, M.S.; Taghirad, H.D. Disturbance retrieving unknown input proportional integral observer for generalized linear systems: Application to fault diagnosis. In Proceedings of the ICCAS, Gyeonggi-do, Republic of Korea, 27–30 October 2010.
7. Hadi, A.S.; Shaker, M.S. A new estimation/decoupling approach for robust observer-based fault reconstruction in nonlinear systems affected by simultaneous time varying actuator and sensor faults. *J. Frankl. Inst.* **2020**, *357*, 8956–8979. [CrossRef]

8. Boukhlof, A.; Hammoudi, M.Y.; Saadi, R.; Benbouzid, M.E. Hardware-in-the-loop implementation of an unknown input observer for synchronous reluctance motor. *ISA Trans.* **2023**, *133*, 485–494. [CrossRef] [PubMed]
9. Ichalal, D.; Marx, B.; Ragot, J.; Maquin, D. Simultaneous state and unknown inputs estimation with PI and PMI observers for Takagi Sugeno model with unmeasurable premise variables. In Proceedings of the 17th Mediterranean Conference on Control and Automation, Thessaloniki, Greece, 24–26 June 2009.
10. Mimoune, K.; Hammoudi, M.Y.; Hamdi, W.; Mimoune, S.M. Observer design for Takagi–Sugeno fuzzy systems with unmeasured premise variables: Conservatism reduction using line integral Lyapunov function. *ISA Trans.* **2023**, *142*, 626–634. [CrossRef] [PubMed]
11. Mimoune, K.; Hammoudi, M.Y.; Saadi, R.; Benbouzid, M.; Boukhlof, A. Real-Time Implementation of Non Linear Observer Based State Feedback Controller for Induction Motor Using Mean Value Theorem. *J. Electr. Eng. Technol.* **2023**, *18*, 615–628. [CrossRef]

**Disclaimer/Publisher’s Note:** The statements, opinions and data contained in all publications are solely those of the individual author(s) and contributor(s) and not of MDPI and/or the editor(s). MDPI and/or the editor(s) disclaim responsibility for any injury to people or property resulting from any ideas, methods, instructions or products referred to in the content.



MDPI AG  
Grosspeteranlage 5  
4052 Basel  
Switzerland  
Tel.: +41 61 683 77 34

*Engineering Proceedings* Editorial Office  
E-mail: [engproc@mdpi.com](mailto:engproc@mdpi.com)  
[www.mdpi.com/journal/engproc](http://www.mdpi.com/journal/engproc)



Disclaimer/Publisher's Note: The statements, opinions and data contained in all publications are solely those of the individual author(s) and contributor(s) and not of MDPI and/or the editor(s). MDPI and/or the editor(s) disclaim responsibility for any injury to people or property resulting from any ideas, methods, instructions or products referred to in the content.







Academic Open  
Access Publishing

[mdpi.com](https://www.mdpi.com)

ISBN 978-3-7258-1288-2